

Joint Institute for Nuclear Research



**XV Advanced Research Workshop
on High Energy Spin Physics
(DSPIN-13)**

Dubna, October 8–12, 2013

Proceedings

Edited by *A.V. Efremov* and *S.V. Goloskokov*

Dubna 2014

УДК [539.12.01 + 539.12 ... 14 + 539.12 ... 162.8](063)

ББК [22.382.1 + 22.382.2 + 22.382.3]я431

A20

Advisory body: International Committee for Spin Physics:

R.G. Milner (Chair) MIT, E. Steffens (Past-Chair) Erlangen, M. Anselmino (Torino),
E. Aschenauer BNL, A. Belov INR Moscow, H. Gao Duke, P. Lenisa Ferrara,
B.-Q. Ma Peking, N. Makins Illinois, A. Martin Trieste, A. Milstein Novosibirsk,
M. Poelker JLab, R. Prepost Wisconsin, T. Roser Brookhaven, N. Saito KEK, H. Sakai Tokyo,
H. Stroehrer Juelich, O. Teryaev JINR Dubna, F. Bradamante* Trieste, E.D. Courant* BNL,
D.G. Crabb* Virginia, A.V. Efremov* JINR Dubna, G. Fidecaro* CERN,
W. Haeberli* Wisconsin, A.D. Krisch* Michigan, A. Masaïke* Kyoto, C.Y. Prescott* SLAC,
V. Soergel* Heidelberg, W.T.H. van Oers* Manitoba.

* Honorary Members

Organizing Committee: A. Efremov (chair), Dubna; M. Finger (co-chair), Prague;
A. Sandacz (co-chair), Warsaw; S. Goloskokov (sc. secretary), Dubna; O. Teryaev (sc.
secretary), Dubna; E. Russakovich (secretary), Dubna; E. Kolganova, Dubna; K. Kurek,
Warsaw; V. Ladygin, Dubna; S. Nurushev, Protvino; Yu. Panebrattsev, Dubna; N. Piskunov,
Dubna; I. Savin, Dubna; O. Selyugin, Dubna.

Sponsored by:

Joint Institute for Nuclear research,
International Committee for Spin Physics Symposia,
Russian Foundation for Basic Research.
“DYNASTY” Foundation,
European Physical Society
Physics-Online.ru

The contributions are reproduced from the originals presented by the Organizing Committee.

A20

Advanced Research Workshop on High Energy Spin Physics (13; 2013; Dubna).

Proc. of XV Advanced Research Workshop on High Energy Spin Physics (DSPIN-13)(Dubna,
October 8–12, 2013). — Dubna, JINR. — 423p.

ISBN 978-5-9530-0315-3

The collection includes contributions presented at the XV Advanced Research Workshop on High Energy Spin Physics (DSPIN-13), (Dubna, October 8–12, 2013), on different theoretical, experimental and technical aspects of this branch of physics.

Рабочее совещание по физике спина при высоких энергиях (15; 2013; Дубна).

Труды XV Рабочего совещания по физике спина при высоких энергиях (DSPIN-13)(Дубна,
8–12 октября 2013 г.) — Дубна: ОИЯИ, 2014. — 423 с.

ISBN 978-5-9530-0377-3

В сборник включены доклады представленные на XV рабочее совещание по физике спина при высоких энергиях (Дубна, 8–12 октября 2013 г.), по теоретическим, экспериментальным и техническим аспектам этой области физики.

УДК [539.12.01 + 539.12 ... 14 + 539.12 ... 162.8](063)

ББК [22.382.1 + 22.382.2 + 22.382.3]я431

ISBN 978-5-9530-0377-3

©Joint Institute for Nuclear Research, 2014

Contents

Welcome address	
<i>JINR Vice-Director R. Lednicky</i>	9
Violent collisions of spinning protons and polarized beams: past, present & perhaps at NICA, FERMILAB, AGS and J-PARC	
<i>A.D. Krisch</i>	10
Theory of spin physics	11
The study of the different scaling variables on target mass corrected polarized structure functions	
<i>F. Abdolghafari</i>	13
Nuclear effects in the polarization phenomena	
<i>V.V. Abramov</i>	17
Z' -boson effects at high energy colliders	
<i>V.V. Andreev</i>	21
NLO light cone sum rules for the nucleon electromagnetic form factors	
<i>I.V. Anikin</i>	25
Decomposition of sea quark flavours from QCD analysis of polarized DIS and SIDIS world data	
<i>F. Arbabifar</i>	29
Theoretical considerations for a jet simulation with spin	
<i>X. Artru</i>	33
Collins asymmetry in field ionization of hydrogen	
<i>X. Artru</i>	41
Large- x factorization of transverse-distance dependent parton densities	
<i>I.O. Cherednikov</i>	45
The axial form factor and polarization of the final nucleon in quasi-elastic $\nu - N$ scattering	
<i>E. Christova</i>	49
Magnetic polarizability of diquarks in baryons	
<i>P. Filip</i>	53
Role of transversity in spin effects in meson leptonproduction.	
<i>S.V. Goloskokov</i>	57
On energy-momentum and spin/helicity of quark and gluon fields	
<i>F.W. Hehl</i>	65
Anomalous nonperturbative quark-gluon chromomagnetic interaction and spin effects in high energy reactions	
<i>N.S. Korchagin</i>	75
The singlet contribution to the Bjorken polarized sum rule	
<i>S.A. Larin</i>	79
Femtoscopic correlations of two identical particles with nonzero spin in the model of one-particle multipole sources	
<i>V.V. Lyuboshitz</i>	83

Nambu-Poisson formulation of the spinning particle dynamics in the (accelerator) external fields <i>N.V. Makhaldiani</i>	87
Generalised parton distributions of photon <i>Sreeraj Nair</i>	91
Absence of the non-uniqueness problem of the Dirac theory in a curved spacetime spin-rotation coupling is not physically relevant <i>V.P. Neznamov</i>	95
JEDI (EDM@Juelich). Learning the systematic limitations on EDM at COSY <i>N.N. Nikolaev</i>	101
Spin dependence of e^-e^+ pair production by an electron in a strong magnetic field <i>O.P. Novak</i>	107
Conservation laws and covariant equations of motion for spinning particles <i>Yu.N. Obukhov</i>	110
Flavor dependence of the spin-independent and spin-dependent parts of GPDs($x, t, \xi = 0$) <i>O.V. Selyugin</i>	116
Formulas of connection between the different QCD orders for parton distribution and fragmentation functions <i>O.Yu. Shevchenko</i>	120
Importance of semi-inclusive DIS processes in determining fragmentation functions <i>A.V. Sidorov</i>	124
Spin-1/2 particles in arbitrary strong gravitational fields <i>A.J. Silenko</i>	131
Statistical description of the flavor structure of the nucleon sea <i>J. Soffer</i>	137
Truncated moments of parton densities in applications to spin physics <i>D. Strózik-Kotlorz</i>	143
Unique heavy lepton mixing signature in W^+W^- pair production at LC with polarized beams <i>A.V. Tsytrinov</i>	147
Spin observables of pd -scattering within the Glauber model and test of T-invariance <i>Yu.N. Uzikov</i>	151
Exoplanetary searches with gravitational microlensing: polarization aspects <i>A.F. Zakharov</i>	155
Spin-orbital composition in relativistic many-fermion systems <i>P. Zavada</i>	161
To the memory of A.P. Bakulev <i>S. V. Mikhailov and N. G. Stefanis</i>	169
APT/FAPT applications in the low-energy QCD domain <i>V.L. Khandramai</i>	171
Widths and transition form factors of mesons: consideration from axial anomaly <i>A.G. Oganesian</i>	177

Comparing vacuum and hadronic higher twists <i>O.V. Teryaev</i>	183
--	-----

Experimental results 189

Results on the transverse double spin asymmetries in the elastic pp -scattering at $\sqrt{s} = 200$ GeV <i>I. Alekseev</i>	191
PHENIX spin program: recent results & prospects <i>K.N. Barish</i>	195
Transverse spin and transverse momentum structure of the nucleon from the COMPASS experiment <i>F. Bradamante</i>	201
Study of nucleon spin and TMDs at JLab <i>Jian-Ping Chen</i>	209
Hadron multiplicities and quark fragmentation functions at COMPASS <i>N. du Fresne von Hohenesche</i>	217
The Q_{weak} experiment. First direct measurement of the proton's weak charge <i>J.R. Hoskins</i>	221
Measurement of spin-dependent structure function g_1^p with 200 GeV beam at COMPASS (CERN) <i>A.V. Ivanov</i>	227
Investigation of deuteron beam interaction with carbon and polyethylene targets at intermediate energies by means of GEANT4 simulation <i>M. Janek</i>	231
Investigation of the deuteron short-range spin structure at Nuclotron <i>P.K. Kurilkin</i>	235
Experimental program for baryonic matter studies <i>V.P. Ladygin</i>	239
Polarization effects in the quasi-elastic $(p, 2p)$ -reaction with nuclei at 1 GeV <i>O.V. Miklukho</i>	247
Recent results from HERMES <i>W.-D. Nowak</i>	255
Longitudinal double spin asymmetry A_1^p and spin-dependent structure function g_1^p of the proton at low x and low Q^2 from COMPASS <i>A.S. Nunes</i>	263
The polarized beam tagging system of the experimental set-up SPASCHARM <i>S.B. Nurushev</i>	267
The η -meson production with the polarized proton beam with WASA-at-COSY <i>I. Ozerianska</i>	273
The flavor structure of the nucleon sea <i>J.C. Peng</i>	277
The three form factor recoil polarization experiments at Jefferson Lab <i>C.F. Perdrisat</i>	285
The Dp non-mesonic breakup data at 300–500 MeV of the deuteron energy obtained at Nuclotron <i>S.M. Piyadin</i>	291

Proton form factor measurements at Jefferson Lab in 12 GeV era	
<i>Vina Punjabi</i>	295
Spin and parity determination of 125 GeV particle with the CMS detector	
<i>A. Rinkevicius</i>	301
The GPD program at COMPASS	
<i>A. Sandacz</i>	307
Spin observables in antihyperon-hyperon production with PANDA	
<i>K. Schönning</i>	315
Uncertainties in the transverse double spin asymmetries due to the luminosity normalization	
<i>D.N. Svirida</i>	319
Exclusive meson production at COMPASS	
<i>P. Sznajder</i>	323
Spin asymmetry in forward polarized pp scattering and a brief summary from workshop on "High-energy scattering at zero degree"	
<i>K. Tanida</i>	327
Recent spin results from the STAR experiment at RHIC	
<i>Qinghua Xu</i>	333
Study of the spin and parity of Higgs boson with ATLAS detector	
<i>Yaquan Fang</i>	341
NICA SPD	345
Polarized deuterons and protons at NICA: the design concept development	
<i>A.D. Kovalenko</i>	345
Proton and deuteron polarization control in NICA collider using small solenoids	
<i>Yu.N. Filatov</i>	351
Proposal on the Spin Physics Detector (SPD) at NICA	
<i>G.V. Meshcheryakov</i>	355
The feasibility of Drell–Yan processes at NICA	
<i>R.R. Akhunzyanov</i>	359
Spin physics with direct photons at NICA SPD	
<i>A. Guskov</i>	363
Possibilities for the spin-dependent observables measurement in elastic NN scattering at NICA	
<i>V.I. Sharov</i>	367
Orbital parameters of proton beam in Nuclotron with solenoid Siberian snake	
<i>M.A. Kondratenko</i>	371
Comparison of solenoid, helix and dipole Siberian snakes in the NICA collider	
<i>A.M. Kondratenko</i>	375

Technics and new developments **379**

Absolute pp polarimeter for calibration of the beam tagging system at the SPASCHARM set-up	
<i>A.A. Bogdanov</i>	381
Polarized target for Drell–Yan experiment at COMPASS	
<i>J. Matoušek</i>	385

The method of assembly functions in the problem of a momentum restoring of charged particles <i>I.P. Yudin</i>	389
---	-----

Related problems **393**

Kerr geometry as a bridge from theory of superstrings to spinning particles <i>A.Ya. Burinskii</i>	395
Electromagnetic singular soliton as particle with spin and magnetic moment <i>A.A. Chernitskii</i>	399
On the disputed $\pi_1(1600)$ and observation of a new iso-vector resonance <i>F. Nerling</i>	402
QCD effective coupling and spectra of $(q\bar{q})$, (gg) states within infrared confinement <i>Gurjav Ganbold</i>	408
Perspective studies of strong interactions and hadronic matter in antiproton-proton annihilation <i>M.Yu. Barabanov</i>	412
Summary. An analytical review of DSPIN-13 <i>A.V. Efremov and J. Soffer</i>	416
List of participants of DSPIN-13	421

WELCOME ADDRESS
by JINR Vice-Director R. Lednicky

Dear Colleagues,

Ladies and Gentlemen, on behalf of the Directorate of Joint Institute for Nuclear Research it is a pleasure for me to welcome you here in Dubna at the 15-th International Workshop on High Energy Spin Physics.

Unfortunately, I should start my talk from bad news. To the great sorrow of all of us, the prominent theorist in the field of spin physics, one of the founders of this field in Dubna, Vladimir Luboshitz, passed away this year. He will be remembered by many of his friends and colleagues. His son, Valery, will present here a talk based on their common work. Another great lost is the sudden death of Alexander Bakulev, the leading member of Dubna QCD group. In dedicated session, there will be several presentations reflecting his scientific interests and achievements. I would like to ask you to honor the memory of both of them by the minute of silence.

JINR has a long-lasting tradition of experimental and theoretical studies of spin phenomena. Back in 1981, the first workshop in high energy spin physics was organized in Dubna by Lev Lapidus. These meetings became regular thanks to Anatoly Efremov, their chairman for many years.

The current workshop is taking place in the important period of development of particle physics at JINR related with the construction of the NICA accelerator complex based on the existing Nuclotron facility. The main physics goal of NICA project is a study of hot and dense QCD matter.

The investigation of important properties of this matter, like critical point and mixed phase, doesn't require very large energies. These properties are expected to show up just in NICA energy range. The NICA program is complementary to the CBM project at FAIR and will continue the program of Beam energy scan at RHIC with much higher luminosity. Besides the heavy ion program in the collider mode, the sophisticated fixed target experiment – Baryonic Matter at Nuclotron – is under preparation and will be presented at the workshop.

The spin physics program represents another important direction of experiments at NICA in both collider and fixed target modes. It assumes the use of polarized deuteron and proton beams and construction of the dedicated Spin Physics Detector (SPD) in the second intersection point. The main goal is a study of Single Spin Asymmetries in Drell-Yan processes and investigation of new distribution functions. There are also plans to study spin asymmetries in the production of heavy quarkonia, spin-related signals in heavy ion collisions and spin asymmetries in elastic scattering (the Krisch effect). There will be a special session dedicated to the spin physics program at NICA. We are very much interested in the assistance of the international spin physics community in preparation of the competitive program on this new facility and formation of a wide international collaboration for its realisation.

The Workshop is supported by Russian Foundation for Basic Research, “Dynasty” Foundation, International Committee of Spin Physics, Physics-Online.ru and, of course, by JINR. I would like to thank the organizers, wish you interesting talks, illuminating discussions and a nice stay here in Dubna and JINR. The workshop is opened.

VIOLENT COLLISIONS OF SPINNING PROTONS AND POLARIZED BEAMS: PAST, PRESENT & PERHAPS AT NICA, FERMILAB, AGS AND J-PARC

A.D. Krisch[†]

Spin Physics Center, University of Michigan, Ann Arbor, Michigan 48109-1040, USA

[†] [†]*E-mail: krisch@umich.edu*

Abstract

I will first discuss the history of polarized proton beams and of unpolarized and polarized elastic and inclusive scattering, including the still unexplained large transverse spin effects found several decades ago in high energy proton-proton spin experiments at ZGS, CERN, AGS, Fermilab and RHIC. I will then briefly discuss possible transverse spin experiments on violent elastic and inclusive collisions of polarized protons at Fermilab's new high-intensity Main Injector, NICA, J-PARC and AGS. I will end by describing a new single 4-twist helix snake which might efficiently maintain the proton polarization at these facilities in the 3-120 GeV range.

Since much of my talk was about the history of Spin Physics with polarized beams, which is a topic that I discussed at many conferences, it seems improper to again publish an almost identical talk. Thus, I am only submitting references to some of these earlier history talks [1,2] and articles [3,4] along with the last reference for a recent paper posted on ArXiv [5]. This is about a new snake design which might allow the acceleration of polarized protons in Fermilab's 120 GeV Main Injector and Dubna's now-being-constructed NICA 20 GeV collider, as well as other accelerators and colliders. To see this talk's figures and photos see Ref [6]. The details of my talk could be also found at the site

<http://theor.jinr.ru/~spin/2013/>

References

- [1] A.D. Krisch, Hard collisions of spinning protons: Past, present and future, Eur. Phys. J. A31, 417-423 (2007)
- [2] Ibid, Hard Collisions of spinning protons: history & future, Proc. DSPIN09, 11-21. (2008)
- [3] Ibid, The Spin of the Proton, Scientific American, 240, 68 (May 1979)
- [4] Ibid, Collisions of Spinning,Protons, Scientific American, 257, 3241, 42 (Aug 1987)
- [5] F. Antoulinakis et al., One 4-Twist Helix Snake to Maintain Polarization in 8-120 GeV Proton Rings.
ArXiv: 1110.3042 (4 September 2013)
- [6] <http://theor.jinr.ru/~spin/2013/talks/krisch.pdf>

THEORY OF SPIN PHYSICS

THE STUDY OF THE DIFFERENT SCALING VARIABLES ON TARGET MASS CORRECTED POLARIZED STRUCTURE FUNCTIONS

F. Abdolghafari¹, S. Taheri Monfared ^{2†} and S. M. Moosavi Nejad^{1,2}

(1) *Physics Department, Yazd University, Yazd, Iran*

(2) *School of Particles and Accelerators, Institute for Research in Fundamental Sciences (IPM), P.O.Box 19395-5531, Tehran, Iran*

† *sara.taheri@ipm.ir*

Abstract

We study the effect of target mass corrections (TMCs) to the polarized structure functions $g_1(x, Q^2)$ and $g_2(x, Q^2)$ at Next-to-Leading Order (NLO) approximation following the method suggested by Georgi and Politzer. We compare three different scaling variables which give certain corrections to the Bjorken scaling in the low-to-moderate Q^2 region. Our results are compared with experimental data.

1 Introduction

Deep Inelastic Scattering (DIS) has played a basic role in the development of our present understanding of the sub-structure of elementary particles. Discovering the Bjorken scaling variable in the Quark Parton Model (QPM) and the other scaling variables motivated physicists to consider the proton as a composite particle which is made of partons (i.e. quarks and gluons). As the precision of the recent lepton-hadron scattering data has improved, it is necessary for the theoretical analysis to keep pace. Therefore, it is important to consider all sources of corrections which may contribute at a comparable magnitude, such as quark and target mass corrections [1]. Understanding TMCs, which formally are sub-leading $1/Q^2$ corrections to leading twist structure functions, is very important. Their effects are mostly pronounced at large- x and moderate- Q^2 , which coincide with the region where parton distribution functions (PDFs) are not very well determined.

In this paper, we firstly introduce the Nachtmann, Weizmann and Bloom-Gilman scaling variables [2] and then study the effect of target mass corrections to the polarized structure functions g_1 and g_2 in the Operator Product Expansion (OPE). In fact, the polarized DIS process involving the collision of a longitudinally polarized lepton beam with a longitudinally or transversely polarized target, provides complementary and equally important insight into the structure of the nucleon.

2 Different Scaling Variables

Many precise experiments have recently proved that the measured structure functions do not exactly scale in the Bjorken variable, $x = \frac{Q^2}{2M\nu}$. Here, $Q^2 = -q^2$ where q is the four-momenta transferred from the lepton to the nucleon, M is the target nucleon mass and $\nu = E - E'$ is the energy transferred to the hadronic system in which the

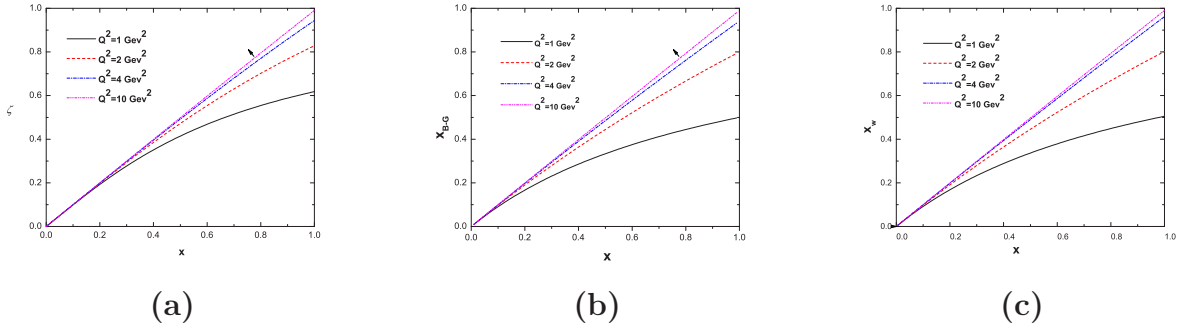


Figure 1: The Nachtmann variable ξ , Bloom-Gilman variable x_{B-G} and Weizmann variable x_w as a function of Bjorken scaling variable x at $Q^2 = 1, 2, 4, 10 \text{ GeV}^2$.

energies of the initial and final leptons are denoted by E and E' , respectively. It was commonly recognized that such scaling violation effects are clear evidence for validity of the Quantum Chromodynamics (QCD), however there were some other attempts to re-establish the scaling behavior by introducing new scaling variables. These new variables have a more general meaning than the Bjorken variable and partly contain the target mass corrections. Those are Nachtmann, Bloom-Gilman and Weizmann variables which are listed here:

- At finite Q^2 and for massless quarks, the parton light-cone fraction is given by the Nachtmann variable. This variable, $\xi = \frac{Q^2}{M(\nu + \sqrt{\nu^2 + Q^2})}$, can be understood theoretically by the energy conservation of quasi-elastic lepton-quark scattering in parton language and naturally appears in the OPE frame.
- The Bloom-Gilman variable [3], $x_{B-G} = \frac{Q^2}{(2M\nu + M^2)}$, makes the data scale at Q^2 region which is not so large in comparison with M^2 .
- The Weizmann variable [4], $x_w = \frac{(Q^2 + m^2)}{(2M\nu + M^2)}$ which includes the quark mass (m), produces scaling even down to $Q^2 = 0$.

In Fig. 1, we plotted the Nachtmann, Bloom-Gilman and Weizmann variables versus the Bjorken variable at $Q^2 = 1, 2, 4, 10 \text{ GeV}^2$. As it was expected, they turn to be the Bjorken one at $Q^2 \sim 10 \text{ GeV}^2$. The x_{B-G} , x_w scaling variables behave quite identical due to very low mass effects of quarks. In Fig. 2, target mass corrected polarized structure function xg_1^{TMC} is plotted in terms of the different variables at $Q^2 = 2 \text{ GeV}^2$. Among all the variables, only the Nachtmann variable could be understood theoretically by energy conservation of quasi-elastic lepton-quark scattering in parton language. The Bloom-Gilman variable and the Weizmann variable are

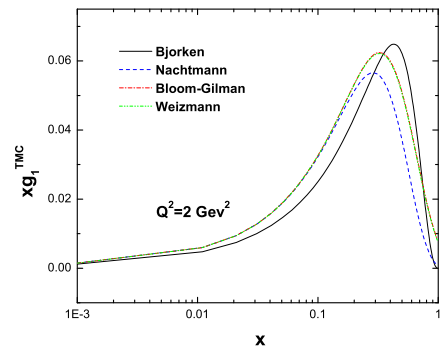


Figure 2: The polarized structure function xg_1^{TMC} considering the target mass corrections for the different variables at $Q^2 = 2 \text{ GeV}^2$.

lacking in clear theoretical reasoning. In next section, we use the Nachtmann variable to consider TMCs into the polarized structure functions.

3 Polarized Structure Functions

To get TMCs into the nucleons polarized structure functions, we follow the method proposed by Georgi and Politzer [5–7]. The explicit twist-2 expression of target mass corrected g_1 and g_2 are:

$$g_1^{\text{TMC}}(x, Q^2) = \frac{xg_1(\xi, Q^2; M=0)}{\xi(1+4M^2x^2/Q^2)^{3/2}} + \frac{4M^2x^2}{Q^2} \frac{x+\xi}{\xi(1+4M^2x^2/Q^2)^2} \int_{\xi}^1 \frac{d\xi'}{\xi'} g_1(\xi', Q^2; M=0) - \frac{4M^2x^2}{Q^2} \frac{(2-4M^2x^2/Q^2)}{2(1+4M^2x^2/Q^2)^{5/2}} \int_{\xi}^1 \frac{d\xi'}{\xi'} \int_{\xi'}^1 \frac{d\xi''}{\xi''} g_1(\xi'', Q^2; M=0), \quad (1)$$

$$g_2^{\text{TMC}}(x, Q^2) = -\frac{xg_1(\xi, Q^2; M=0)}{\xi(1+4M^2x^2/Q^2)^{3/2}} + \frac{x(1-4M^2x\xi/Q^2)}{\xi(1+4M^2x^2/Q^2)^2} \int_{\xi}^1 \frac{d\xi'}{\xi'} g_1(\xi', Q^2; M=0) - \frac{3}{2} \frac{4M^2x^2/Q^2}{(1+4M^2x^2/Q^2)^{5/2}} \int_{\xi}^1 \frac{d\xi'}{\xi'} \int_{\xi'}^1 \frac{d\xi''}{\xi''} g_1(\xi'', Q^2; M=0). \quad (2)$$

The above g_2^{TMC} satisfies the well-known Wandzura-Wilcek (WW) relation [8]. In our analysis, we utilize the fit result of Ref. [9] in which the Polarized PDFs are determined based on the Jacobi polynomial expansion method. TMCs are performed on their fit results and the effect of different scaling variables are studied. Figures 3 and 4 display

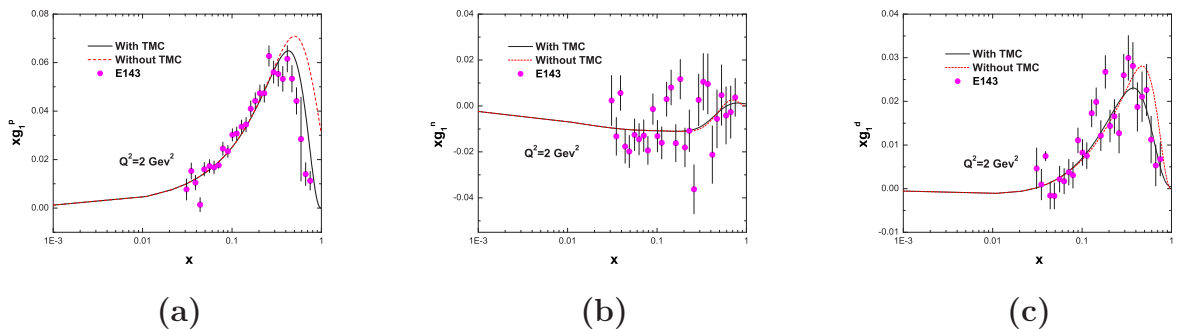


Figure 3: The polarized structure functions xg_1^p , xg_1^n and xg_1^d as a function of x for $Q^2 = 2 \text{ GeV}^2$

our results for the polarized structure functions g_1 and g_2 at $Q^2 = 2 \text{ GeV}^2$, respectively. For comparison, we also show the results obtained by E143 experimental data [10]. The data are generally well described within error.

4 Results

Although, the Bjorken variable is a standard variable at finite Q^2 but it does not contain any mass effects. The best available scaling variable is the Nachtmann one. In this analysis, considering the target mass corrections we obtained the polarized structure functions

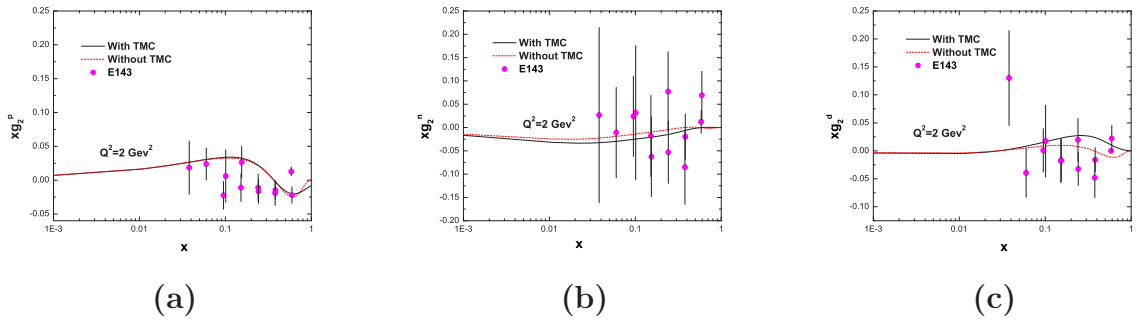


Figure 4: The polarized structure functions xg_2^p , xg_2^n and xg_2^d as a function of x for $Q^2 = 2 \text{ GeV}^2$

g_1 and g_2 for Proton, Neutron and Deuteron and we compared them with the experimental data. The polarized structure function xg_1^{TMC} is plotted for all defined variables. Our results showed that TMCs play a remarkable role on the nucleon structure functions. In fact, we found good agreement with the experimental data by applying these corrections.

References

- [1] Ingo.Schienbein et al J. Phys. G **35**, (2008) [arxiv:0709.1775 [hep-ph]].
- [2] Bo-Qiang Ma Phys. Lett. B **176**, (1986) 179.
- [3] E.D. Bloom and F.J. Gilman, Phys. Rev. D **4**, (1971) 2901.
- [4] V. Rittenberg and H.R. Rubinstein, Phys. Lett. B **35**, (1971) 50.
F.W. Brasse et al, Nucl. Phys. B **39**, (1972) 421.
- [5] Y.B.Dong, Phys. Lett. B **641**, (2006) 272.
- [6] A. Piccione, G. Ridolfi, Nuc. Phys. B **513**, (1998) 301.
- [7] J. Blumlein, N. Kochelev Phys. Lett. B **381**, (1996) 296.
J. Blumlein, N. Kochelev Nucl. Phys. B **489**, (1997) 285.
J. Blumlein,A. Tkabladze, Nucl. Phys. B **553**, (1999) 427.
J. Blumlein,A. Tkabladze, [arXiv:9812331 [hep-ph]].
- [8] S. Wandzura, F. Wilczek, Phys. Lett. B **72**, (1977) 195.
- [9] A. N. Khorramian, S. Atashbar Tehrani, S. Taheri Monfared, F. Arbabifar and F. I. Olness, Phys. Rev. D **83**, 054017 (2011) [arXiv:1011.4873 [hep-ph]].
- [10] K. Abe et al, [E143 collaboration], Phys. Rev. D **58**, 112003 (1998) [arXiv:9802357 [hep-ph]].

NUCLEAR EFFECTS IN THE POLARIZATION PHENOMENA

V.V. Abramov^{1†}

(1) *Institute for High Energy Physics, Protvino, Russia*

† *E-mail: Victor.Abramov@ihep.ru*

Abstract

Atomic weight dependence of hyperon polarization and single spin asymmetry is studied within the framework of chromomagnetic quark polarization model. Predictions are given for polarization of antihyperons, P_N , produced by protons on different nuclear targets. Oscillation of $P_N(x_F)$ is predicted, which is due to anti-quark spin precession in the strong chromomagnetic field, created by the fast moving spectator quarks.

Polarization phenomena, such as hyperon polarization (P_N) and hadron single spin asymmetry (A_N) are often studied using nuclear beams and/or targets. In order to compare the data, measured on different targets, we have to use a model, which is able to describe the dependence of polarization effects on atomic weights, A_1 and A_2 of colliding particles. The chromomagnetic quark polarization model (CQPM), which is known also as “effective color field model”, is used to describe the polarization data for 80 different inclusive reactions, including reactions with nuclear beam and/or target [1–3].

The main assumptions of the CQP model are: 1) The creation of effective color field (ECF) after initial color exchange, which has a linear chromoelectric and transverse circular chromomagnetic components; 2) Microscopic Stern-Gerlach like mechanism for generation of polarization phenomena in the ECF, created by relativistic spectator quarks; 3) Quark spin precession in the ECF; 4) Quark counting rules for the ECF (field, created by spectator quarks and antiquarks, from projectile and from the target, is a linear function of their numbers with weights, depending on color factors). Quark flow diagrams are used to count the number of the spectator quarks. 5) Circular transverse chromomagnetic field has a focusing or defocusing effect on a probe quark color charge and this can lead to a resonance like energy dependence of polarization observables, such as P_N and A_N .

The global analysis is performed for the following type of polarization data: the hadron asymmetry A_N , the hyperon polarization P_N , the vector meson alignment ρ_{00} and polarization $\alpha = (\sigma_T - 2\sigma_L)/(\sigma_T + 2\sigma_L)$. In total, there are 80 inclusive reactions for hh, hA, AA and lepton-A interactions, with 3160 data points and 99 free model parameters.

It is assumed, that the model parameters have the power A-dependence: $\sim A_1^a A_2^b$, where the powers a and b are found for each particular parameter from the global fit.

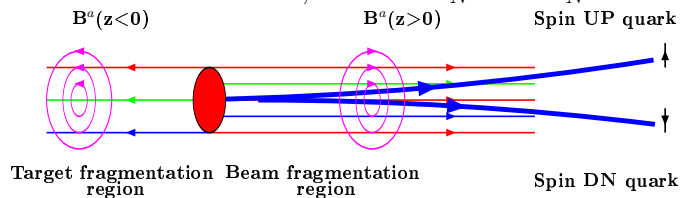


Figure 1: Pictorial view of the microscopic Stern-Gerlach device for a quark, which is moving through a circular transverse chromomagnetic field, created by spectator quarks. The probe quark gets polarized in the color field.

The microscopic Stern-Gerlach effect, which causes the polarization phenomena, in the framework of the CQP model, is explained in Fig. 1. Spectator quarks, which are the fragmentation products of the colliding hadrons, are moving, in the c.m.s. reference frame, along the z -axis. As a result, the color currents and surrounding them transverse circular chromomagnetic field B^a are created in the $z < 0$ and $z > 0$ regions. The probe quark from the detected hadron gets, after passing the region of inhomogeneous chromomagnetic field, an additional transverse momentum $\delta p_x^{\uparrow\downarrow}$, which is directed to the left or to the right, for the quark spin directed up or down, respectively. The trajectories of quarks with spin up and down are separating from each other, as is shown in Fig. 1. The probe quark could be not only a valence quark from the colliding hadrons, but also a sea antiquark, created in the interaction process. Even in this case the antiquark, after passing the inhomogeneous chromomagnetic field, gets an additional transverse momentum $\delta p_x^{\uparrow\downarrow}$, which causes, for example, the antihyperon polarization in the baryon-baryon collisions.

Since, in general, the local direction of the B^a field and the quark spin ξ are not parallel, the quark spin precession is taken into account and it is described by the equation (1), which is similar to the BMT one [1]:

$$d\xi/dt = g_s[\xi \mathbf{B}^a](g_Q^a - 2 + 2M_Q/E_Q)/2M_Q, \quad (1)$$

where M_Q and E_Q – quark mass and its energy. The electric charge in (1) is replaced by a color quark charge (g_s), and the magnetic g -factor is replaced by a quark chromomagnetic g_Q^a -factor.

Large value of quark anomalous chromomagnetic moment $\Delta\mu^a = (g^a - 2)/2 \approx -0.4$ was predicted in the framework of the instanton model in the mean field approximation and assuming the dynamical quark mass $m = 170$ MeV [5]. From the global data analysis of polarization data the value $\Delta\mu^a = -0.471 \pm 0.007$ is estimated for the u, c -quarks with charge $+2/3$ and the value, which is smaller by a factor $\sqrt{2/3}$, for the d, s, b -quarks with electric charge $-1/3$.

The polarization P_N and asymmetry A_N are given by a set of equations:

$$A_N = C(\sqrt{s})F(p_T, A)[G(\phi_A) - \sigma G(\phi_B)]; \quad (2)$$

$$G(\phi) = (1 - \cos \phi)/\phi + \epsilon \cdot \phi, \quad (3)$$

$$\phi_A = \omega_A^0 y_A, \quad \phi_B = \omega_B^0 y_B, \quad (4)$$

$$C(\sqrt{s}) = v_0/[(1 - E_R/\sqrt{s})^2 + \delta_R^2]^{1/2}, \quad (5)$$

$$F(p_T, A) = (1 - \exp[-(p_T/p_T^0)^\delta])(1 - \alpha_A \ln A), \quad A \leq A_T; \quad (6)$$

$$F(p_T, A) = (1 - \exp[-(p_T/p_T^0)^\delta])(1 - \alpha_A \ln A_T), \quad A > A_T; \quad (7)$$

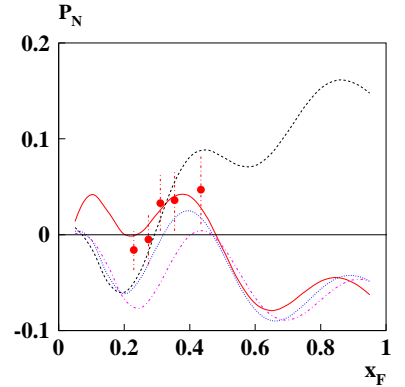


Figure 2: Dependence $P_N(x_F)$ in the reaction $pA \rightarrow \Xi^{0+} X$ [6]. Calculation are for pp, pC, pCu and pPb-interactions and $\sqrt{s} = 38, 78$ GeV.

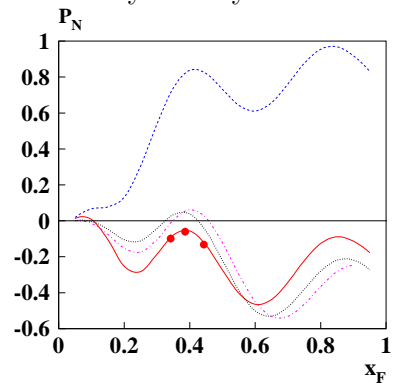


Figure 3: Dependence $P_N(x_F)$, in the reaction $pA \rightarrow \Xi^+ X$ [7]. Calculation are for pp, pBe, pCu pPb-interactions and $\sqrt{s} = 38, 78$ GeV.

$$y_A = x_A - (E_0/\sqrt{s} + f_A)(1 + \cos \theta^{cm}) + a_0(1 - \cos \theta^{cm}), \quad (8)$$

$$y_B = x_B - (E_0/\sqrt{s} + f_B)(1 - \cos \theta^{cm}) + a_0(1 + \cos \theta^{cm}), \quad (9)$$

$$v_0 = \frac{-Dg_Q^a \xi_y^0 (\theta^{cm} - \theta_0)}{2\rho(g_Q^a - 2)}, \quad (10)$$

$$\xi_y^0(x) = \frac{\pm 1}{1 + \exp(-x \ln(\sqrt{s/s_0}/\kappa))}, \quad (11)$$

$$\omega_{A(B)}^0 = \frac{g_s \alpha_s \nu_{A(B)} S_0 (g_Q^a - 2)}{M_Q c \rho^2}, \quad (12)$$

where θ^{cm} is the hadron C registration angle in the c.m.s., $\sqrt{s_0} = 1$ GeV, $\delta = 2.47 \pm 0.11$, $A_T = 56.4 \pm 9.0$, $\kappa = 0.0071 \pm 0.0092$ and $\epsilon = -0.004759 \pm 0.00011$ are the global model parameters, $D_r = D/\rho$, ω_A^0 , ω_B^0 , f_A , f_B , a_0 , E_0 , E_R , δ_R , σ , p_T^0 , α_A and θ_0 are the local parameters, describing a particular reaction. Function $\xi_y^0 \approx \pm \Theta(\theta^{cm} - \theta_0)$ takes into account the value and the sign of u and d -quark polarization in the polarized proton. It takes also into account the threshold dependence of $A_N(\theta^{cm})$ on the production angle θ^{cm} in the nucleon-nucleon c.m.s. reference frame. For the polarization P_N the factor $\xi_y^0 \equiv 1$. In (12) are used the following values: $(g_Q^a - 2)/2$ - the quark Q anomalous chromomagnetic moment, where $Q = d, u, s, c, b$, α_s - the strong running coupling constant, $g_s = \pm \sqrt{4\pi\alpha_s}$ - the color quark charge, M_Q - its mass, c - the speed of light, ρ - the transverse radius of region, occupied by chromomagnetic field, created by one quark, and S_0 - the parameter, which describes the longitudinal size of the field.

The A-dependence of the CQP model parameters is estimated from the global fit of polarization data for 80 inclusive reactions and is presented below:

$$E_0 = \begin{cases} E_0(1, 1)A_1^{2\alpha}, & x_F > 0; \\ E_0(1, 1)A_2^{2\alpha}, & x_F < 0; \\ E_0(1, 1)(A_1 A_2)^\alpha, & x_F = 0; \end{cases} \quad (13)$$

$$E_R = \begin{cases} E_R(1, 1)A_1^{2\alpha}, & x_F > 0; \\ E_R(1, 1)A_2^{2\alpha}, & x_F < 0; \\ E_R(1, 1)(A_1 A_2)^\alpha, & x_F = 0; \end{cases} \quad (14)$$

$$\delta_R = \delta_R(1, 1)(A_1 A_2)^\alpha, \quad p_N = p_N(1, 1)/(A_1 A_2)^{2\alpha/3}, \quad (15)$$

$$D_r = D_r(1, 1)(A_2/A_1)^{2\alpha/3}, \quad \sigma = \sigma(1, 1)(A_1/A_2)^\beta, \quad (16)$$

$$p_T^0 = p_T^0(1, 1)(A_1 A_2)^{\gamma/2}, \quad a_0 = a_0(1, 1)/A_1^\gamma, \quad (17)$$

where $\alpha = 0.0390 \pm 0.0027$, $\beta = 0.2423 \pm 0.0071$, $\gamma = \alpha + \beta$. The parameters f_A and f_B do not depend on A_1, A_2 . There is one exclusion from the above rules. For the reaction $pA \rightarrow \Lambda^\dagger X$ the dependence of p_T^0 on A_1 and A_2 is the following:

$$p_T^0 = p_T^0(1, 1)/A_2^\alpha. \quad (18)$$

Understanding the antihyperon polarization P_N in baryon-nucleus collisions is crucial for the theory of strong interactions. Most of the models predict zero P_N due to absence of valence quarks from the colliding hadrons in the observed antihyperon. The experiments

show the non-zero polarization. The CQP model predicts non-zero $P_N(x_F)$, which oscillates due to the antiquark spin precession in a strong chromomagnetic field, created by the six spectator quarks. An example of $P_N(x_F)$ dependence for the reaction $pA \rightarrow \bar{\Xi}^{0\uparrow} X$ is shown in Fig. 2, where the CQP model predictions are also shown [6]. The solid curve is for C target, while the dashed one is for the proton target.

Polarization in the process $pA \rightarrow \bar{\Xi}^{+\uparrow} X$ is shown Fig. 3, with the data measured on Be target [7]. The dashed curve is for the proton and the solid one is for the Be target, respectively.

Polarization in the process $pA \rightarrow \bar{\Lambda}^{\uparrow} X$ is shown in Fig. 4, with the data measured in the experiment E766 on the proton target [8]. Since at higher energies zero polarization was measured, the result of E766 means resonance-like energy dependence, described by eq. (5), which is due to the focusing properties of a circular transverse chromomagnetic field [3]. The curves are the calculations within the CQP model, which are made for the proton (solid), Be (dashed), Cu (dotted) and Pb (dash-dotted) targets, respectively.

Conclusion: the A-dependence of antihyperons, produced in proton-nucleus collisions could be significant. The polarization is positive for the proton target and $x_F > 0.4$, while for heavier nuclei with $A \geq 9$ it is negative.

This work was partially supported by the RFBR grant 12-02-00737.

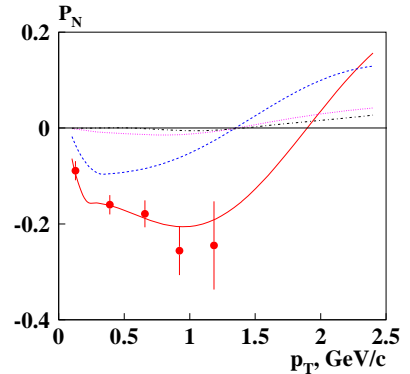


Figure 4: Dependence $P_N(p_T)$ in the reaction $pA \rightarrow \bar{\Lambda}^{\uparrow} X$ [8]. Calculations are made for $x_F = -0.229$, $\sqrt{s} = 7.31$ GeV and $A=1, 9.01, 63.55$ and 207.2 .

References

- [1] V.V. Abramov, Phys. At. Nucl. **72** (2009) 1872.
- [2] V.V. Abramov, Proc. of the 19th. Int. Spin Physics Symposium, SPIN2010, J. Phys.: Conf. Ser. **295** (2011) 012086.
- [3] V.V. Abramov, Proc. of the 20th. Int. Spin Physics Symposium, SPIN2012, Phys. Part. Nucl. **45**, No. 1, (2014) 62.
- [4] V. Bargman, L. Michel and V. Telegdy, Phys. Rev. Lett. **2** (1959) 435.
- [5] N. Kochelev and N. Korchagin, Anomalous Quark Chromomagnetic Moment and Single-Spin Asymmetries, (2013) arXiv:1308.4857 [hep-ph].
- [6] E. Abouzaid et al., Phys. Rev. **D75** (2007) 012005.
- [7] P.M. Ho et al., Phys. Rev. Lett. **65** (1990) 1713.
- [8] J. Felix (E766 Collab.), Inclusive $\bar{\Lambda}$ polarization in pp collisions at 27 GeV: Proc. of the Adriatico Research Conference on Trends in Collider Spin Physics, edited by Y. Onel, N. Paver, A. Penzo. Trieste, 5-8 December 1995.: Singapore, River Edge, N.J.: World Scientific, 1997. P. 231.

Z' BOSON EFFECTS AT HIGH ENERGY COLLIDERS

V.V. Andreev^{1,★}, A.A. Pankov^{2,†}

(1) *The F. Skoryna Gomel State University, Gomel, Belarus*

(2) *The Abdus Salam ICTP Affiliated Centre, Technical University of Gomel, Gomel, Belarus*

★ *E-mail: quarks@gsu.by* † *E-mail: pankov@ictp.it*

Abstract

We discuss the expected sensitivity to Z' boson effects of the W^\pm boson production process at the Large Hadron Collider (LHC). The results of model dependent analysis of Z' boson effects are presented in terms of Z - Z' mixing angle ϕ and Z' boson mass $M_{Z'}$. We find that the process $pp \rightarrow W^+W^- + X$ allows to place stringent constraints on the $Z - Z'$ mixing angle which is of order $\sim 10^{-4} - 10^{-3}$ for $M_{Z'} = 3$ TeV at the nominal LHC energy and luminosity.

1 Introduction

Although the Standard Model (SM) of the electroweak and strong interactions describes nearly all experimental data available today [1], it is widely believed that it is not the ultimate theory. There is a number of Grand Unified Theories that predict the existence of new neutral gauge bosons that can be accessible at current and/or future colliders [2].

The search for these Z' particles is an important aspect of the experimental physics program of current and future high-energy colliders. Present limits from direct production at the LHC and virtual effects at LEP, through interference or mixing with the Z boson, imply that new Z' bosons are rather heavy and mix very little with the Z boson. Depending on the considered models, Z' masses of the order of 2.5–3.0 TeV (LHC) [3, 4] and Z - Z' mixing angles at the level of $\sim 10^{-3}$ are excluded [5]. A Z' boson, if lighter than ~ 5 TeV, could be discovered at the LHC with $\sqrt{s} = 14$ TeV in the Drell-Yan process

$$p + p \rightarrow Z' \rightarrow \ell^+ + \ell^- + X \quad (1)$$

with $\ell = e, \mu$. Future e^+e^- International linear collider (ILC) with high c.m. energies and longitudinally polarized beams could indicate the existence of Z' bosons via its interference effects in fermion pair production processes, with masses up to about $6 \times \sqrt{s}$ while $Z - Z'$ mixing will be constrained up to $\sim 10^{-4} - 10^{-3}$ in process $e^+e^- \rightarrow W^+W^-$ [2].

After the discovery of a Z' boson at the LHC, some diagnosis of its coupling and $Z - Z'$ mixing needs to be done in order to identify the correct theoretical frame. In this note we study a potential of the LHC to discover $Z - Z'$ mixing effects in the process

$$p + p \rightarrow W^+ + W^- + X \quad (2)$$

and compare it with that expected at the ILC.

Process (2) is important for studying the electroweak gauge symmetry at the LHC. Properties of the weak gauge bosons are closely related to electroweak symmetry breaking and the structure of the gauge sector in general. In this letter, we examine the feasibility of observing the Z' boson in process (2) at the LHC, which is not the principal discovery channel as Drell-Yan process, but can help to understand the origin of new gauge bosons.

2 Cross section of $pp \rightarrow W^+W^- + X$ process

At high energies the process (2) can be described by the mechanism analogous to Drell-Yan that is indicated in Fig. 1.

The cross section of process (2) is written as

$$d\sigma = \sum_q \int \int d\xi_1 d\xi_2 \left\{ [f_{q|P_1}(\xi_1)f_{\bar{q}|P_2}(\xi_2) + f_{\bar{q}|P_1}(\xi_1)f_{q|P_2}(\xi_2)] d\hat{\sigma}(q\bar{q} \rightarrow W^+W^-) \right\}, \quad (3)$$

where $f_{q|P_i}, f_{\bar{q}|P_i}$ are parton distribution functions in P_1 and P_2 protons, while $\xi_{1,2}$ determine the part of proton momentum carried by q and \bar{q} .

It is convenient to replace $\xi_{1,2}$ variables with rapidities using the following relations:

$$\xi_1 = \frac{M}{\sqrt{s}} e^y, \quad \xi_2 = \frac{M}{\sqrt{s}} e^{-y}. \quad (4)$$

Taking into account the experimental bounds on pseudo-rapidities obtained at the LHC ($|\eta| < \eta_{\text{cut}}$) one should change the integration limits in (3) [6, 7]:

$$|y| \leq Y = \min [\ln(\sqrt{s}/M), \eta_{\text{cut}}], \quad (5)$$

$$|z| \leq z_{\text{cut}} = \min [\tanh(Y - |y|)/\beta_W, 1], \quad (6)$$

where $\beta_W = \sqrt{1 - 4M_W^2/\hat{s}}$, $\hat{s} = \xi_1\xi_2s = M^2$ and M_W is a W boson mass.

As a result, the resonance $R(= Z')$ production cross section with its subsequent decay into a pair of W^\pm bosons can be obtained by integrating the subprocess cross section over z ($z = \cos\theta$) within the interval $|z| \leq z_{\text{cut}}$, over rapidity of W^\pm -pair $|y| \leq Y$ and over invariant mass M near resonance peak ($M_R - \Delta M/2, M_R + \Delta M/2$).

$$\sigma(pp \rightarrow W^+W^- + X) = \int_{M_R - \Delta M/2}^{M_R + \Delta M/2} dM \int_{-Y}^Y dy \int_{-z_{\text{cut}}}^{z_{\text{cut}}} dz \frac{d\sigma_{q\bar{q}}}{dM dy dz}. \quad (7)$$

In the experimental discovery of a narrow resonance the observed width is determined by the diboson W^\pm invariant mass resolution, that we may associate to the size of the bin ΔM introduced above. For the ATLAS detector, the bin size ΔM at invariant diboson mass M measured in TeV units, can be parameterized as:

$$\Delta M = 24 (0.625M + M^2 + 0.0056)^{1/2} \text{ GeV}. \quad (8)$$

Throughout the paper we will use Eq. (8) for the bin size.

Differential cross section in (7) can be written as:

$$\frac{d\sigma_{q\bar{q}}}{dM dy dz} = K \frac{2M}{3s} \sum_q \left\{ [f_{q|P_1}(\xi_1)f_{\bar{q}|P_2}(\xi_2) + f_{\bar{q}|P_1}(\xi_1)f_{q|P_2}(\xi_2)] \frac{d\hat{\sigma}_{q\bar{q}}}{dz} \right\}, \quad (9)$$

where K is the so-called K -factor that accounts for higher-order QCD corrections. In the leading order to α_s , one has $K \simeq 1.10$ - 1.15 (depending on the W^\pm pair invariant mass) [8].

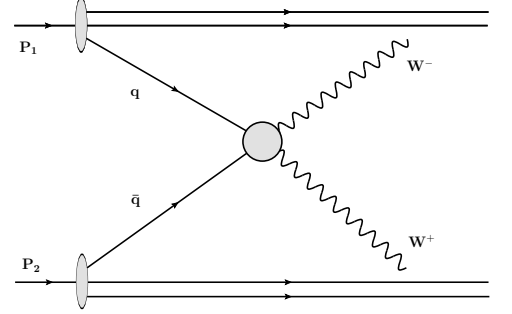


Figure 1: Schematic diagram representation of W^+W^- pair production in $p_1p_2 \rightarrow W^+W^- + X$ process.

We use the CTEQ6 parton distributions [9] with renormalization and factorization scales $\mu_F^0 = \mu_R^0 = \sqrt{(p_T^{\ell+2} + p_T^{\ell-2})}/2$ for pure leptonic final states.

Hadron production of vector Z_2 bosons in proton-proton collisions with their subsequent decay into a pair of W^\pm bosons at parton level is described by subprocess

$$q\bar{q} \rightarrow \gamma, Z_1, Z_2 \rightarrow W^+W^-, \quad (10)$$

Feynman diagrams of which in the Born approximation are presented in Fig. 1.

Differential cross section of process (10) is the following:

$$\frac{d\sigma_{q\bar{q}}}{dz} = \frac{\beta_W}{32\pi\hat{s}} \sum_{\lambda, \lambda', \tau, \tau'} |F_{\lambda\lambda'\tau\tau'}(\hat{s}, \theta)|^2. \quad (11)$$

Here, $\lambda = -\lambda' = \pm 1/2$ are the quark helicities, the helicities of the W^- and W^+ are denoted by $\tau, \tau' = \pm 1, 0$. The helicity amplitudes $F_{\lambda\lambda'\tau\tau'}(\hat{s}, \theta)$ have a structure presented in [6]. In evaluating Γ_2 , we took into account the channels of Z_2 -boson decay into fermions (quarks and leptons) and bosons predicted by the SM.

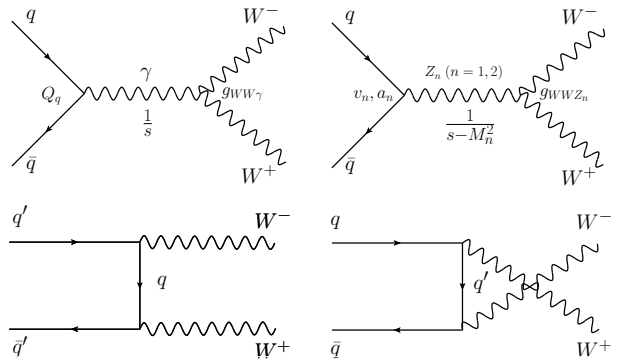


Figure 2: Feynman diagrams of $q\bar{q}(q'\bar{q}') \rightarrow W^+W^-$ process in the presence of Z_2 boson.

3 Z - Z' mixing

We start discussing the observability of the Z' signal in the leptonic W^\pm decay channels with both equal and different flavor leptons in the final state. In the case of different flavor leptons, the Z' signal in process $pp \rightarrow Z' \rightarrow W^+W^- \rightarrow \ell^+\ell'^-\nu_l\nu_{l'}$ (l and l' stand for electrons and muons) possesses SM backgrounds coming from the production of W^+W^- pairs, as well as, from $t\bar{t}$ pairs where the top quarks decay semi-leptonically. In the case that the final state leptons in reaction $pp \rightarrow Z' \rightarrow W^+W^- \rightarrow \ell^+\ell'^-\nu_l\nu_{l'}$ have the same flavor (ee or $\mu\mu$), there are additional backgrounds originating from Drell-Yan lepton pair production, as well as ZZ pair production with one Z decaying into charged leptons and the other decaying invisibly or with both Z decaying into charged leptons two of which escape undetected. After applying cuts described in [10] all backgrounds can be reduced.

In order to obtain constraints on Z' boson parameters (ϕ and M_2) we evaluate the ratio of cross sections, $(\sigma \times B)_{Z'}$ and $(\sigma \times B)_{lim}$. Here, $(\sigma \times B)_{Z'}$ is the resonant cross section calculated within some Z' model (for arbitrary ϕ and M_2), while $(\sigma \times B)_{lim}$ is the cross section required for a significance of 2σ (95% C.L.). A discovery reach in a Z' scenario is obtained by using the following criterion [11]:

$$(\sigma \times B)_{Z'} / (\sigma \times B)_{lim} \leq 1. \quad (12)$$

Fig. 3 shows the discovery reach (at a 95% C.L.) in the plane spanned by the $Z - Z'$ mixing angle and the Z_2 boson mass for the Z'_χ model from E_6 obtained from the analysis of the cross sections of process (2) at the LHC taking into account the pure leptonic decay channels of W^\pm bosons. The corresponding limits are indicated by solid lines in Fig. 3. Also, Fig. 3 shows the discovery reaches obtained from analysis of the polarized

cross sections of process $e^+e^- \rightarrow W^+W^-$ at the ILC [2]. Two options of energy and time integrated luminosity have been chosen, namely, $\sqrt{s} = 0.5$ TeV and $\mathcal{L}_{\text{int}} = 0.5 \text{ ab}^{-1}$ (dashed lines) and $\sqrt{s} = 1.0$ TeV and $\mathcal{L}_{\text{int}} = 1 \text{ ab}^{-1}$ (dot-dashed lines). In addition, the Z' mass limits obtained from the Drell-Yan process (1) in the current experiments at the LHC at $\sqrt{s} = 8$ TeV and $\mathcal{L}_{\text{int}} = 20 \text{ fb}^{-1}$ as well as at nominal energy and luminosity, $\sqrt{s} = 14$ TeV and $\mathcal{L}_{\text{int}} = 100 \text{ fb}^{-1}$, are depicted in Fig. 3 by horizontal lines.

One can see that the ILC with energy of 0.5 TeV is able to place the limits on the $Z - Z'$ mixing angle at the level of $\text{few} \times 10^{-3}$ that comparable with those obtained from the global analysis of electroweak data. It turns out that doubling energy and luminosity leads to further improvement of the limit on $Z - Z'$ mixing angle up to $|\phi| \sim \text{few} \times 10^{-4}$. The Fig. 3 also demonstrates a high ability of the LHC to study the $Z - Z'$ mixing effects that comparable with those obtained at the ILC for $\sqrt{s} = 1$ TeV. From the comparison of numerical results relevant to the potentials of LHC and ILC to study $Z - Z'$ mixing effects one can conclude that these colliders would provide a complementary information on $Z - Z'$ mixing angle.

Acknowledgments. The research was partially supported by the Abdus Salam ICTP TRIL Programme and the Belarusian Republican Foundation for Fundamental Research.

References

- [1] J. Beringer *et al.* (Particle Data Group), Phys. Rev. D **86**, 010001 (2012).
- [2] Vas. V. Andreev, G. Moortgat-Pick, P. Osland, A. A. Pankov and N. Paver, Eur. Phys. J. C **72**, 2147 (2012).
- [3] S. Chatrchyan *et al.* [CMS Collaboration], Phys. Lett. **B714**, 158-179 (2012).
- [4] G. Aad *et al.* [ATLAS Collaboration], JHEP **1211**, 138 (2012).
- [5] J. Erler, P. Langacker, S. Munir, E. Rojas, JHEP **0908**, 017 (2009).
- [6] E. Nuss, Z. Phys. C **76**, 701 (1997).
- [7] P. Osland, A. Pankov, N. Paver, A. Tsytrinov, Phys. Rev. D **78**, 035008 (2008).
- [8] Yu-Ming Bai *et al.*, Phys. Rev. D **85**, 016008 (2012).
- [9] J. Pumplin *et al.*, JHEP **0207**, 012 (2002).
- [10] A. Alves *et al.*, Phys. Rev. D **80**, 073011 (2009).
- [11] D. Benchekroun, C. Driouichi, A. Hoummada, Eur. Phys. J. direct C **3**, N3 (2001).

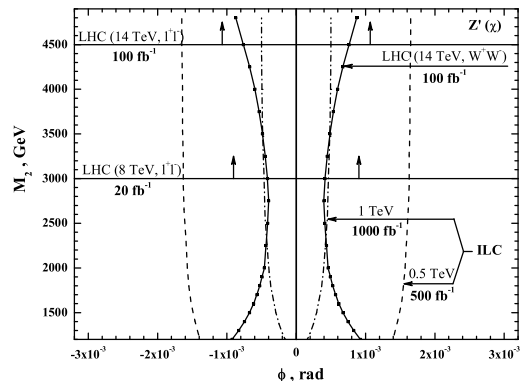


Figure 3: Discovery reach (95% C.L.) for Z'_χ model obtained from analysis of process (2) at the LHC for leptonic channel (thick solid lines). The limits obtained from analysis of the polarized cross sections of process $e^+e^- \rightarrow W^+W^-$ with $P_L = \pm 0.8$ and $\overline{P}_L = \pm 0.5$ at the ILC are also shown. Two options of energy and time integrated luminosity have been taken: $\sqrt{s} = 0.5$ TeV, $\mathcal{L}_{\text{int}} = 0.5 \text{ ab}^{-1}$ (dashed lines) and $\sqrt{s} = 1.0$ TeV, $\mathcal{L}_{\text{int}} = 1 \text{ ab}^{-1}$ (dot-dashed lines).

NLO LIGHT CONE SUM RULES FOR THE NUCLEON ELECTROMAGNETIC FORM FACTORS

I.V. Anikin^{1,†}, V.M. Braun² and N. Offen²

(1) *Bogoliubov Laboratory of Theoretical Physics, JINR, 141980 Dubna, Russia*

(2) *Institut für Theoretische Physik, Universität Regensburg, D-93040 Regensburg, Germany*

† *E-mail: anikin@theor.jinr.ru*

Abstract

We study the electromagnetic nucleon form factors within the approach based on light-cone sum rules.

Introduction. We derive light-cone sum rules (LCSRs) for the electromagnetic nucleon form factors including the next-to-leading-order corrections for the contribution of twist-three and twist-four operators and a consistent treatment of the nucleon mass corrections. The soft Feynman contributions are calculated in terms of small transverse distance quantities using dispersion relations and duality. The form factors are expressed in terms of nucleon wave functions at small transverse separations (DAs), without any additional parameters. The distribution amplitudes can be extracted from the comparison with the experimental data on form factors and compared to the results of lattice QCD simulations. A self-consistent picture emerges, with the three valence quarks carrying 40% : 30% : 30% of the proton momentum.

Our work can be split on three essential parts: (i) calculations within LCSR; (ii) derivation of the factorized amplitude at the leading order (LO) up to twist-6 and at the next-to-leading order (NLO) up to twist-4. We calculated 22 coefficient functions at NLO and 20 of them are new ones. To avoid the mixture with the so-called evanescent operators, we use the renormalization procedure for operators with open Dirac indices; (iii) study of the corresponding distribution amplitudes. In particular, the light-cone expansion to the twist-4 accuracy of the three-quark matrix elements with generic quark positions.

The LCSR approach allows one to calculate the form factors in terms of the nucleon (proton) DAs. To this end we consider the correlation function

$$T_\nu(P, q) = i \int d^4x e^{iqx} \langle 0 | T [\eta(0) j_\nu^{\text{em}}(x)] | P \rangle \quad (1)$$

where $\eta(0)$ is the Ioffe interpolating current with $\langle 0 | \eta(0) | P \rangle = \lambda_1 m_N N(P)$. The matrix element of the electromagnetic current $j_\mu^{\text{em}}(x)$ taken between nucleon states is conventionally written in terms of the Dirac and Pauli form factors $F_1(Q^2)$ and $F_2(Q^2)$ or in terms of the electric $G_E(Q^2)$ and magnetic $G_M(Q^2)$ Sachs form factors. We also define a light-like vector n_μ by the condition $q \cdot n = 0$, $n^2 = 0$ and introduce the second light-like vector as $p_\mu = P_\mu - n_\mu m_N^2 / (2P \cdot n)$, $p^2 = 0$, and $g_{\mu\nu}^\perp = g_{\mu\nu} - (p_\mu n_\nu + p_\nu n_\mu) / (pn)$. We consider the

“plus” spinor projection of the correlation function involving the “plus” component of the electromagnetic current, which can be parametrized in terms of two invariant functions

$$\Lambda_+ T_+ = p_+ \{m_N \mathcal{A}(Q^2, P'^2) + \hat{q}_\perp \mathcal{B}(Q^2, P'^2)\} N^+(P), \quad (2)$$

where $Q^2 = -q^2$ and $P'^2 = (P - q)^2$ and $N^\pm(P) = \Lambda^\pm N(P)$, $\Lambda^+ = \hat{p}\hat{n}/(2pn)$, $\Lambda^- = \hat{n}\hat{p}/(2pn)$. Further, making use of the Borel transformation $(s - P'^2)^{-1} \longrightarrow e^{-s/M^2}$, one obtains the following sum rules:

$$2\lambda_1 F_1(Q^2) = \frac{1}{\pi} \int_0^{s_0} ds e^{(m_N^2 - s)/M^2} \text{Im} \mathcal{A}^{\text{QCD}}(Q^2, s), \quad (3)$$

$$\lambda_1 F_2(Q^2) = \frac{1}{\pi} \int_0^{s_0} ds e^{(m_N^2 - s)/M^2} \text{Im} \mathcal{B}^{\text{QCD}}(Q^2, s). \quad (4)$$

Each of the functions has a perturbative expansion which we write as $\mathcal{A} \cong \mathcal{A}^{\text{LO}} + \alpha_s(\mu) \mathcal{A}^{\text{NLO}}/3\pi$ and similar for \mathcal{B} ; μ is the renormalization scale. For consistency with our NLO calculation, we rewrite our results in a different form, expanding all kinematic factors in powers of m_N^2/Q^2 . We keep all corrections $\mathcal{O}(m_N^2/Q^2)$ but neglect terms $\mathcal{O}(m_N^4/Q^4)$ etc. which is consistent with taking into account contributions of twist-three, -four, -five (and, partially, twist-six) in the operator product expansion (OPE). After calculations, the NLO corrections read (see all details in [1]).

$$\begin{aligned} Q^2 \mathcal{A}_q^{\text{NLO}} = & \int [dx_i] \left\{ \sum_{k=1,3} \left[\mathbb{V}_k(x_i) C_q^{\mathbb{V}_k}(x_i, W) + \mathbb{A}_k(x_i) C_q^{\mathbb{A}_k}(x_i, W) \right] \right. \\ & \left. + \sum_{m=1,2,3} \left[\mathbb{V}_2^{(m)}(x_i) C_q^{\mathbb{V}_2^{(m)}}(x_i, W) + \mathbb{A}_2^{(m)}(x_i) C_q^{\mathbb{A}_2^{(m)}}(x_i, W) \right] \right\} + \mathcal{O}(\text{twist-5}) \end{aligned} \quad (5)$$

and

$$Q^2 \mathcal{B}_q^{\text{NLO}} = \int [dx_i] \left[\mathbb{V}_1(x_i) D_q^{\mathbb{V}_1}(x_i, W) + \mathbb{A}_1(x_i) D_q^{\mathbb{A}_1}(x_i, W) \right] + \mathcal{O}(\text{twist-5}). \quad (6)$$

Notice that $C_d^{\mathbb{V}_2^{(1)}}(x_i, W) = C_d^{\mathbb{A}_2^{(1)}}(x_i, W) = 0$. The explicit expressions for all coefficient functions have rather cumbersome forms and can be found in [1].

Results. In this paragraph, we discuss very shortly the main our results. The full and comprehensive analysis and discussion of all input parameters, form factors and DAs can be found in [1]. It is instructive to write down schematically the structure of all our form factors as

$$\mathcal{F} = \mathcal{F}_0 + \frac{f_N}{\lambda_1} \mathcal{F}_{f_N} + \sum_{i=0,1} \eta_{1i} \mathcal{F}_{\eta_{1i}} + \frac{f_N}{\lambda_1} \sum_{i=1}^2 \sum_{j=0; j \leq i}^2 \varphi_{ij} \mathcal{F}_{\varphi_{ij}}. \quad (7)$$

Main nonperturbative input in the LCSR calculation of form factors is provided by normalization constants, f_N , λ_1 , and shape parameters of nucleon DAs, φ_{ij} and η_{ij} . The existing information, together with our final choices explained below, is summarized in Table 1 and Table 2. As it is seen, one exists quantitative estimates for f_N/λ_1 and the

Model	Method	f_N/λ_1	φ_{10}	φ_{11}	φ_{20}	φ_{21}	φ_{22}	Reference
ABO1	LCSR (NLO)	-0.17	0.05	0.05	0.075	-0.027	0.17	this work
ABO2	LCSR (NLO)	-0.17	0.05	0.05	0.038	-0.018	-0.13	this work
BLW	LCSR (LO)	-0.17	0.0534	0.0664	-	-	-	[2]
BK	pQCD	-	0.0357	0.0357	-	-	-	[3]
COZ	QCDSR (LO)	-	0.163	0.194	0.41	0.06	-0.163	[4]
KS	QCDSR (LO)	-	0.144	0.169	0.56	-0.01	-0.163	[5]
	QCDSR (NLO)	-0.15	-	-	-	-	-	[6]
BS(HET)	QCDSR(LO)	-	0.152	0.205	0.65	-0.27	0.020	[7]
LAT09	LATTICE	-0.083	0.043	0.041	0.038	-0.14	-0.47	[8]
LAT13	LATTICE	-0.075	0.038	0.039	-0.050	-0.19	-0.19	[9]

Table 1: Parameters of the nucleon distribution amplitudes at the scale $\mu^2 = 2 \text{ GeV}^2$.

Model	Method	η_{10}	η_{11}	Reference
ABO1	LCSR (NLO)	-0.039	0.140	this work
ABO2	LCSR (NLO)	-0.027	0.092	this work
BLW	LCSR (LO)	0.05	0.0325	[2]
BK	pQCD	-	-	[3]
COZ	QCDSR (LO)	-	-	[4]
KS	QCDSR (LO)	-	-	[5]
	QCDSR (NLO)	-	-	[6]
LAT09	LATTICE	-	-	[8]
LAT13	LATTICE	-	-	[9]

Table 2: Parameters of the nucleon distribution amplitudes at the scale $\mu^2 = 2 \text{ GeV}^2$.

first-order shape parameters φ_{10} , φ_{11} of the leading twist-3 DA. The other parameters, in contrast, are very weakly constrained. From the comparison with the experimental data, the larger values of f_N/λ_1 are preferred so that we fix $f_N/\lambda_1 = -0.17$ and also take $\varphi_{10} = \varphi_{11} = 0.05$ in agreement with lattice calculations and the previous LO LCSR studies [2]. We then make a fit to the experimental data on the magnetic proton form factor $G_M^p(Q^2)$ and G_E^p/G_M^p in the interval $1 < Q^2 < 8.5 \text{ GeV}^2$ with all other entries as free parameters. We separate fits for $M^2 = 1.5 \text{ GeV}^2$ and $M^2 = 2 \text{ GeV}^2$ that are referred as ABO1 and ABO2, respectively. The resulting values of shape parameters are collected in Table 1 and Table 2 and the corresponding form factors (solid curves for the set ABO1 and dashed for ABO2) are shown in Fig. 1 for the proton (left two panels) and the neutron (right two panels). The ratio $Q^2 F_2^p(Q^2)/F_1^p(Q^2)$ of Pauli and Dirac form factors in the proton is demonstrated in Fig. 2. The quality of the two fits of the proton data is roughly similar, whereas the description of neutron form factors is slightly worse for ABO2 compared to ABO1. In both fits the neutron magnetic form factor comes out to be 20-30% below the data.

Conclusions. In conclusion, our calculation incorporates the following new elements as compared to previous studies:

- (i) NLO QCD corrections to the contributions of twist-three and twist-four DAs;
- (ii) the exact account of “kinematic” contributions to the nucleon DAs of twist-four and twist-five induced by lower geometric twist operators (Wandzura-Wilczek terms);

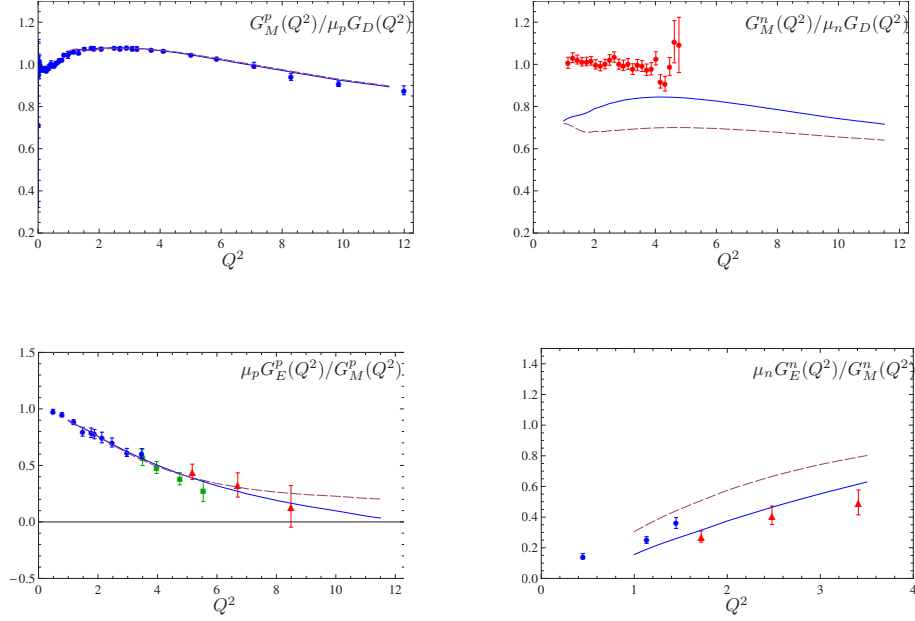


Figure 1: Nucleon electromagnetic form factors from LCSRs compared to the experimental data [1].

- (iii) the light-cone expansion to the twist-four accuracy of the three-quark matrix elements with generic quark positions;
- (iv) a new calculation of twist-five off-light cone contributions;
- (v) a more general model for the leading-twist DA, including contributions of second-order polynomials.

This work was supported by the German Research Foundation (DFG), grant BR 2021/6-1 and in part by the RFBR (grant 12-02-00613) and the Heisenberg-Landau Program.

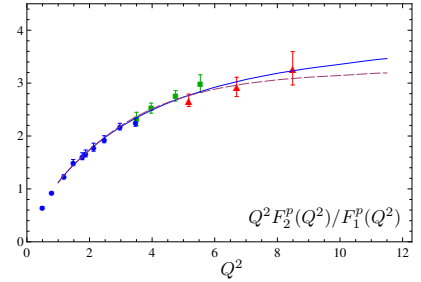


Figure 2: The ratio of Pauli and Dirac electromagnetic proton form factors from LCSRs compared to the experimental data [1].

References

- [1] I. V. Anikin, V. M. Braun and N. Offen, Phys. Rev. **D88** (2013) 114021.
- [2] V. M. Braun, A. Lenz and M. Wittmann, Phys.Rev. **D73** (2006) 094019.
- [3] J. Bolz and P. Kroll, Z. Phys. **A356** (1996) 327.
- [4] V. L. Chernyak, A. A. Ogloblin and I. R. Zhitnitsky, Z. Phys. **C42** (1989) 583.
- [5] I. D. King and C. T. Sachrajda, Nucl. Phys. **B279** (1987) 785.
- [6] M. Gruber, Phys. Lett. **B699** (2011) 169.
- [7] N. G. Stefanis, Eur. Phys. J. direct **C7** (1999) 1.
- [8] V. M. Braun *et al.* [QCDSF Collaboration], Phys. Rev. **D79** (2009) 034504.
- [9] R. Schiel *et al.*, *Wave functions of the Nucleon and the $N^*(1535)$* , invited talk at the 31st International Symposium on Lattice Gauge Theory, July 29 – August 03 (2013), Mainz, Germany.

DECOMPOSITION OF SEA QUARK FLAVOURS FROM QCD ANALYSIS OF POLARIZED DIS AND SIDIS WORLD DATA

F. Arbabifar^{1,2†}, Ali N. Khorramian^{1,2} and M. Soleymaninia^{1,2}

(1) *Physics Department, Semnan University, Semnan, Iran*

(2) *School of Particles and Accelerators, Institute for Research in Fundamental Sciences (IPM), P.O.Box 19395-5531, Tehran, Iran*

† *E-mail: farbabifar@ipm.ir*

Abstract

We present the results of our new QCD analysis of polarized parton distributions of the nucleon at NLO accuracy in the fixed-flavor number scheme. Performing a combined QCD fit on the global sets of all available inclusive and semi-inclusive polarized deep inelastic scattering data, we are able to extract new polarized parton distribution functions (PPDFs) at the input scale $Q_0^2 = 1 \text{ GeV}^2$. Particularly, we have calculated PPDFs considering light sea-quark decomposition and the results are in good agreement with the experimental data and the most precise theoretical models obtained by recent analyses of DSSV and LSS. Also the uncertainties of PPDFs are determined using the standard Hessian method.

1 Introduction

In the recent years the determination of the spin projections of nucleon partonic composition from polarized high energy experimental data has improved remarkably and the extracted polarized parton distributions have very essential role in the study of hard scattering processes phenomenology.

In addition to the QCD analysis on polarized DIS experiments [1, 2], semi inclusive deep inelastic scattering (SIDIS) experimental data [3] have been also included by some of the theoretical groups recently [4, 11]. The extracted PPDFs of different analyses are lightly different in valence quarks comparison but the PPDFs of sea quarks and gluon are more different. The difference is caused by datasets selection, parametrization forms of PPDFs and the method of evolution and QCD analysis. The impact of different PPDFs and the spin Physics on the determination of fragmentation functions (FFs) have been studied recently in Ref. [6]. Here we focus on the effect of SIDIS data on determination of PPDFs, specially sea quarks distribution separation which was not considered in our last DIS data analysis and we present the comparison between both results. The impact of RHIC polarized proton proton collision data will be studied in a separate publication in near future.

2 Polarized asymmetries

The polarized structure function $g_1(x, Q^2)$ can be predicted in perturbative QCD in terms of PPDFs and strong coupling constant up to NLO approximation. The ratio of polarized

and unpolarized structure functions, g_1 and F_1 , is related to the measurable asymmetries by [3]

$$\frac{g_1}{F_1} = \frac{1}{1 + \gamma^2} [A_1 + \gamma A_2] . \quad (1)$$

The value of A_2 can be neglected in a good approximation and it is being suppressed by the small value of kinematic factor γ in the limit $m^2 \ll Q^2$.

In our QCD analysis we perform fit procedure on A_1 or g_1/F_1 for DIS data

$$A_1(x, Q^2) = \frac{g_1(x, Q^2)}{F_1(x, Q^2)} (1 + \gamma^2) . \quad (2)$$

Note that such a procedure is equivalent to a fit to $(g_1)_{exp}$, but it is more precise than the fit to the g_1 data themselves presented by the experimental groups because here the g_1 data are extracted in the same way for all of the data sets.

Unlike the inclusive polarized deep inelastic scattering wherein g_1 structure function is measured by detecting only the final state lepton, the particle detected in semi inclusive polarized deep inelastic experiments are charged hadrons in addition to scattered lepton. The double-spin asymmetry in SIDIS experiments for the production of hadron h is

$$A_{1N}^h(x, z, Q^2) = \frac{g_{1N}^h(x, z, Q^2)}{F_{1N}^h(x, z, Q^2)} . \quad (3)$$

The structure functions g_1^h and F_1^h are fully determined in terms of polarized and unpolarized distributions respectively up to NLO approximation and are fully presented in Ref. [3]. Thus we will determine g_1 and g_{1N}^h from Eqs. 2 and 3 in the analysis and extract polarized parton distribution functions. We utilize two types of data sets from DIS and SIDIS experiments which come from relevant experiments done at DESY, SLAC, JLAB and CERN [3].

2.1 PPDFs Parametrization

In our analysis we choose an initial scale for the evolution of $Q_0^2 = 1 \text{ GeV}^2$ and assume the PPDFs to have the following functional form

$$x \delta q = \mathcal{N}_q \eta_q x^{a_q} (1 - x)^{b_q} (1 + c_q x^{0.5} + d_q x) , \quad (4)$$

with $\delta q = \delta u + \delta \bar{u}$, $\delta d + \delta \bar{d}$, $\delta \bar{u}$, $\delta \bar{d}$, $\delta \bar{s}$ and δg . The Normalization constants \mathcal{N}_q are chosen such that η_q are the first moments of $\delta q(x, Q_0^2)$ and $B(a, b)$ is the Euler beta function.

Since the present SIDIS data are not yet sufficient to distinguish s from \bar{s} , we assume $\delta s(x, Q^2) = \delta \bar{s}(x, Q^2)$ throughout. To control the behavior of PPDFs, we have to consider some extra constraints; so we get $a_{u+\bar{u}} = a_{\bar{u}}$ and $a_{d+\bar{d}} = a_{\bar{d}} = a_s$ to control the small x behavior of \bar{u} , \bar{d} and $s = \bar{s}$. Also in the primary fitting procedures we find out that the parameters $b_{\bar{u}}$, $b_{\bar{d}}$, $b_{s=\bar{s}}$ and b_g become very close to each other, around 10. We understand that they are not strongly determined by the fit, so we fix them to 10 which is their preferred value to fulfill the positivity condition, $|\delta q_i(x, Q_o^2)| \leq q_i(x, Q_o^2)$, and also it controls the behavior of polarized sea quarks at large x region. In addition, we find

flavor	η	a	b	c	d
$u + \bar{u}$	0.783	0.409 ± 0.0025	2.733 ± 0.0368	0.0*	80.855 ± 1.4115
$d + \bar{d}$	-0.485	0.123 ± 0.0036	4.249 ± 0.0280	0.0*	83.345 ± 13.9609
\bar{u}	0.051 ± 0.0022	0.409 ± 0.0025	10.0*	10.016 ± 13.5510	-32.424 ± 15.8386
\bar{d}	-0.081 ± 0.0020	0.123 ± 0.0036	10.0*	116.235 ± 81.2783	902.567 ± 615.0900
\bar{s}	-0.072 ± 0.0077	0.123 ± 0.0036	10.0*	0.0*	-16.045 ± 4.7815
g	-0.156 ± 0.0039	2.453 ± 0.0334	10.0*	0.0*	-3.922 ± 0.0659

Table 1: Final parameter values and their statistical errors at the input scale $Q_0^2 = 1 \text{ GeV}^2$, those parameters marked with (*) are fixed.

that the parameter c_q is very close to zero for $\delta q = \delta u + \delta \bar{u}$, $\delta d + \delta \bar{d}$, $\delta \bar{s}$ and δg so we fix them at 0.

Generally PPDFs analysis use two well-known sum rules relating the first moments of PPDFs to F and D quantities which are evaluated in neutron and hyperon β -decays under the assumption of SU(2) and SU(3) flavor symmetries. A new reanalysis of F and D parameters with updated β -decay constants acquired [6] $F = 0.464 \pm 0.008$ and $D = 0.806 \pm 0.008$, so we make use of these evaluations in our present analysis. Since we do not focus on flavor symmetry and we have $\delta \bar{u} \neq \delta \bar{d} \neq \delta \bar{s}$, we can use the following relations in the analysis

$$\begin{aligned}
\Delta u + \Delta \bar{u} &= 0.9275 + \Delta s + \Delta \bar{s} , \\
\Delta d + \Delta \bar{d} &= -0.3415 + \Delta s + \Delta \bar{s} ,
\end{aligned}
\tag{5}$$

so we exclude the parameters define the first moment of $(\delta u + \delta \bar{u})$ and $(\delta d + \delta \bar{d})$ (i.e. $\eta_{u+\bar{u}}$ and $\eta_{d+\bar{d}}$) from the analysis and obtain them by Eq. 5. The evolution and computational method of the current analysis are fully discussed in Ref. [3]

3 Results

The values of obtained parameters attached to the input PPDFs are summarized in Table 1. We find $\chi^2/\text{d.o.f.} = 1171.571/1132 = 1.03$ which yields an overlay acceptable fit to the experimental data. In Fig. 1 we present the polarized parton distributions and their comparison to parameterizations from DSSV09 [11] and LSS10 [4] at input scale $Q_0^2 = 1 \text{ GeV}^2$. Examining the $x(\delta u + \delta \bar{u})$ and $x(\delta d + \delta \bar{d})$ distributions we see that all of the fits are in agreement. For the $x\delta \bar{u}$ and $x\delta \bar{d}$ distributions, the curves, specially our model and DSSV09, are very close; $\delta \bar{d}$ is negative for any x in the measured x region while $\delta \bar{u}$ passes zero around $x = 0.1 - 0.2$ and becomes negative for large x for all presented models. For the strange sea-quark density $x\delta s$, the main difference between the presented model, LSS10 and DSSV09 sets is that for $x < 0.03$ LSS10 is less negative than others, also both of current model and LSS10 are less positive than DSSV09 for $x > 0.03$.

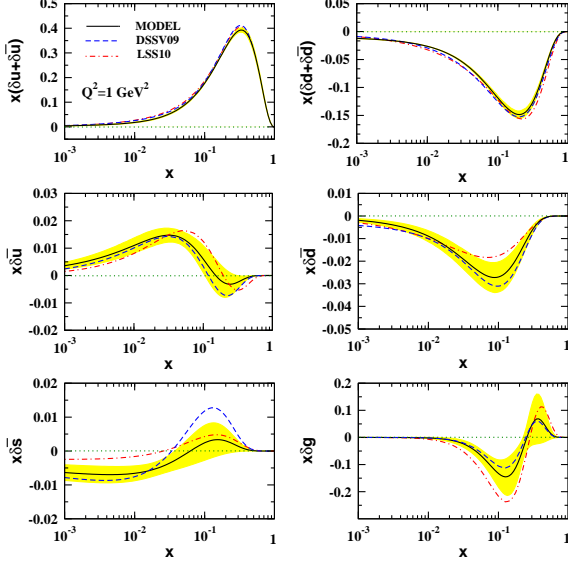


Figure 1: The result of our analysis for quark helicity distributions at $Q_0^2 = 1 \text{ GeV}^2$ in comparison with DSSV09 [11] and LSS10 [4].

By employing SIDIS data a flavour decomposition of the polarized sea quarks is obtained and the light antiquark polarized densities $\delta\bar{u}$, $\delta\bar{d}$ and $\delta s = \bar{s}$ are determined separately, Fig. 2 shows the difference between $\delta\bar{u}$, $\delta\bar{d}$ in the current analysis comparing to other models and experimental data. Also in the present parametrization we use a term $(1 + c_s x^{0.5} + d_s x)$ in the input strange sea-quark distribution to let a sign changing for $\delta s = \delta\bar{s}$, which was not considered in the standard scenario [2]. The comparison of polarized light sea-quark distributions ($x\delta s$, $x\delta\bar{u}$, $x\delta\bar{d}$) in the standard scenario and current model are presented in Ref. [3] and shows that the behavior of the polarized strange quark density remains puzzling.

References

- [1] J. Blumlein and H. Bottcher, Nucl. Phys. B **841** (2010) 205.
- [2] A. N. Khorramian, S. Atashbar Tehrani, S. Taheri Monfared, F. Arbabifar and F. I. Olness, Phys. Rev. D **83** (2011) 054017.
- [3] F. Arbabifar, A. N. Khorramian and M. Soleymaninia, arXiv:1311.1830 [hep-ph].
- [4] E. Leader, A. V. Sidorov and D. B. Stamenov, Phys. Rev. D **82** (2010) 114018.
- [5] D. de Florian, R. Sassot, M. Stratmann and W. Vogelsang, Phys. Rev. D **80** (2009) 034030.
- [6] M. Soleymaninia, A. N. Khorramian, S. M. Moosavinejad and F. Arbabifar, Phys. Rev. D **88**, 054019 (2013).
- [7] C. Amsler et al. (Particle Data Group), Phys. Lett. B **667** (2008) 1.

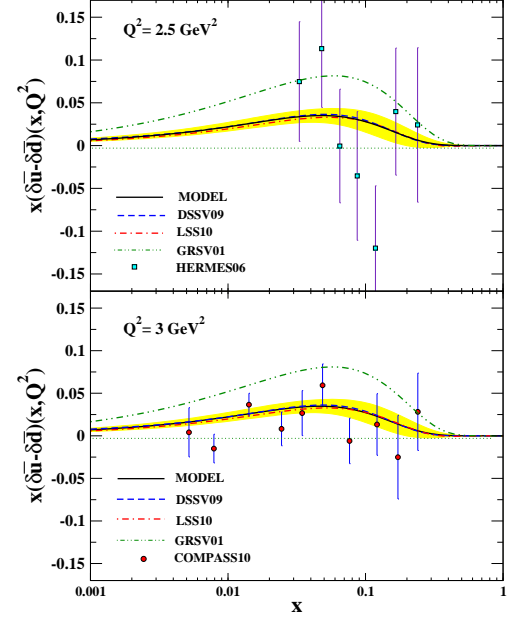


Figure 2: The quark helicity distributions for the difference $x(\delta\bar{u} - \delta\bar{d})$ at $Q^2 = 2.5, 3 \text{ GeV}^2$ comparing to other models and experimental data [3].

THEORETICAL CONSIDERATIONS FOR A JET SIMULATION WITH SPIN

X. Artru^{1†} and Z. Belghobsi^{2‡}

(1) *Université de Lyon, CNRS/IN2P3 and Université Lyon 1, IPNL, France*

(2) *Laboratoire de Physique Théorique, Université de Jijel, Algeria*

† *x.artru@ipnl.in2p3.fr* ‡ *z.belghobsi@univ-jijel.dz*

Abstract

A first part lists basic rules, taken from the string- and multiperipheral models, that a recursive quark fragmentation model should obey. A second part describes spin effects given by the classical “string + 3P0” mechanism of quark-antiquark pair creation, in pseudoscalar and vector meson production: Collins effect, jet handedness and “hidden spin” effects in unpolarized experiments. The last part constructs a recursive quantum-mechanical model of spin-dependent fragmentation. In a “*ab initio*” approach an integral equation must be solved as a preliminary task. With a “renormalized input”, this task is reduced to an ordinary integration. A spin-dependent generalization of the symmetric Lund model is obtained.

1 Introduction

A jet model which takes into account the quark spin degree of freedom must start with *quantum amplitudes* rather than probabilities. A “toy model” [1] using Pauli spinors and inspired from the multiperipheral model and the classical *string + ³P₀* mechanism [2, 3] followed this principle. Collins- and *longitudinal jet handedness* [4] effects were generated. However hadron mass-shell constraints were ignored. These constraints are satisfied in an improved model [5], which is a *symmetric-Lund* model endowed with spin factors. In the *ab initio* approach of [5] the inputs are quark *propagators* and quark-hadron *vertices* derived from a string action. The recursive *splitting function* is obtained by solving an integral equation. We will show that, starting from a *renormalized input*, this preliminary task is replaced by an ordinary integration.

Section 2 lists the rules and approximations of a *bona fide* recursive jet model. Spin effects produced by the classical *string + ³P₀* mechanism or the “toy model” are sketched in Sec.3. The next sections develop the model of Ref. [5] in three stages: the *ab initio* approach, the *renormalized input* approach and the application with string amplitudes.

2 Rules and approximations for a recursive model

We take the example of W^\pm decay into $q_A + \bar{q}_B$ and no gluon (lower part of Fig.1-left) followed by a hadronisation into mesons and no baryon (upper part of Fig.1-left),

$$q_A + \bar{q}_B \rightarrow h_1 + h_2 \dots + h_N. \quad (1)$$

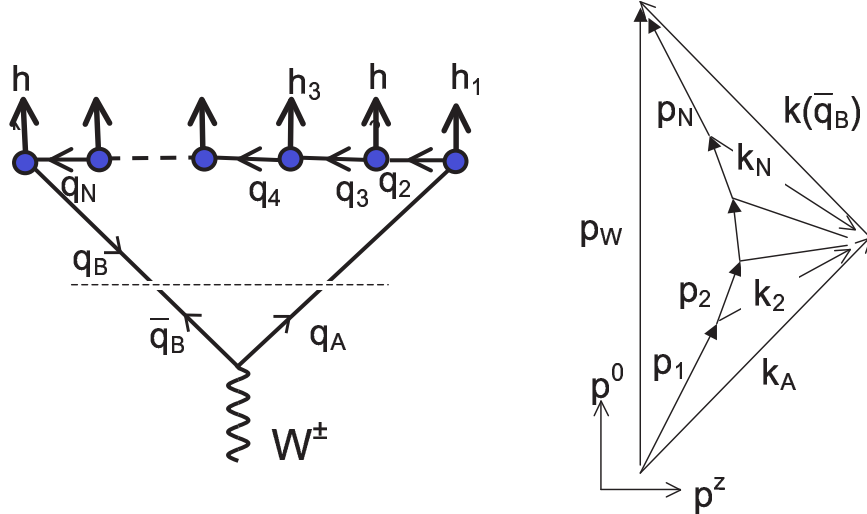


Figure 1: Left: quark-diagram of a hadronic decay of W^\pm . Right: associated momentum diagram, projected on the (p^0, p^z) plane.

In the multiperipheral picture, (1) is decomposed in recursive *quark splittings*

$$q_1 \rightarrow h_1 + q_2, \quad q_2 \rightarrow h_2 + q_3, \dots, \quad q_N \rightarrow h_N + q_B, \quad (2)$$

with $q_1 \equiv q_A$; h_n is the meson of *rank* $n \leq N$; $q_B \equiv q_{N+1}$ is the charge conjugate of \bar{q}_B and “propagates backward in time”.

Factorization. We assume the approximate *probability* convolution

$$\mathcal{P}_{\text{event}} \simeq \int d\Omega \frac{d\mathcal{P}(W^\pm \rightarrow q_A \bar{q}_B)}{d\Omega} \times \mathcal{P}(q_A + \bar{q}_B \rightarrow h_1 + h_2 \dots + h_N). \quad (3)$$

$\mathcal{P}_{\text{event}}$ is the exclusive N -particle distribution of the whole event. $d\mathcal{P}/d\Omega$ is the angular distribution of the quark momentum \mathbf{k}_A in the W^\pm rest frame. The last factor is the exclusive N -particle distribution of reaction (1). $\mathbf{k}_A/|\mathbf{k}_A| = \hat{\mathbf{z}}$ defines the *jet axis*. In a more rigorous approach the convolution should bear on the *amplitudes*. k_A is an internal momentum of the loop diagram of Fig.1-left and $\mathcal{P}_{\text{event}}$ is a double integral: in k_A for the amplitude and in k'_A for the complex conjugate amplitude. Factorization (3) ignores the pure quantum-mechanical quantity $k_A - k'_A$.

Multiperipheral dynamics. Each splitting conserves 4-momentum: $k_n = p_n + k_{n+1}$. These relations are exhibited in the momentum diagram of Fig.1-right. A basic ingredient of the multiperipheral model is the cutoff in the quark virtualities $-k^2$. It implies:

- a cutoff in $|k^+ k^-| \equiv (k^0 + k^z) |k^0 - k^z|$, which insures the approximate ordering of h_1, h_2, \dots, h_N in rapidity and the *leading particle effect* (or *favoured fragmentation*).
- a cutoff in \mathbf{k}_T leading to the *Local Compensation of Transverse Momenta* (LCTM) [6]. It leads to a cutoff in \mathbf{p}_T of the hadrons^{1,2}.

¹The converse is not true: the \mathbf{p}_T cutoff alone, used in some models, does not lead to a \mathbf{k}_T cutoff.

²The symmetric Lund splitting function reinforces the \mathbf{p}_T cutoff by the factor $\exp[-b(m_h^2 + p_T^2)/Z]$.

Ladder approximation. A same hadronic final state can be obtained with several multiperipheral diagrams which differ by permutations. In the *ladder approximation* the interferences between these diagrams are neglected. Most often only one diagram is important, the others having rank ordering too far from the rapidity ordering.

String dynamics. The same properties are found in the String Fragmentation Model. Fig.2 represents the world sheet of the massive string or *dart* stretched by q_A and \bar{q}_B and decaying into hadrons, in a classical 1+1 dimensional model with massless quarks. It is a particular type of quark multiperipheral model, if one orders the Q -corners according to the null-plane time variable $X^- = t - z$ and make the correspondance³

$$t(Q_n) - t(O) = k_n^z/\kappa, \quad z(Q_n) - z(O) = k_n^0/\kappa, \quad (4)$$

where $\kappa \simeq 1$ GeV/fm is the string tension (hereafter we take $\kappa = 1$). For a string breaking point Q the condition that there is no other breaking in its past cone leads to the suppression of large $(OQ)^2 \equiv -k^+k^-$ by a factor

$$\exp(-b|k^+k^-|) \quad (5)$$

where $2b$ is the string "fragility" in units $\kappa = 1$. Quarks with masses and transverse momenta are thought to be produced by a tunneling mechanism similar to the Schwinger one for e^+e^- creation in strong electric field. It provides the k_T cutoff factor

$$\exp[-\pi(m_q^2 + k_T^2)/\kappa]. \quad (6)$$

3 Properties of the classical *string* + 3P_0 mechanism

Fig.3 depicts the decay of the dart as if all Q_n were at equal time. Assuming that a $q_n\bar{q}_n$ pair is created at Q_n in the 3P_0 state and with zero 4-momentum, one predicts a correlation between the antiquark polarization $\bar{\mathbf{S}}_n$ and transverse momentum $\bar{\mathbf{k}}_{n,T}$: $\langle \bar{\mathbf{k}}_n \cdot (\hat{\mathbf{z}} \times \bar{\mathbf{S}}_n) \rangle$ is positive. A similar effect is predicted in atomic physics [7].

Case where h_1, h_2, \dots are pseudoscalar mesons. In that case q_n and \bar{q}_{n+1} forming h_n have antiparallel spins. Combined with the $\langle \bar{\mathbf{k}} \cdot (\hat{\mathbf{z}} \times \bar{\mathbf{S}}) \rangle$ correlations it gives:

- a Collins effect toward $\mathbf{S}_1 \times \hat{\mathbf{z}}$ for the "favored" meson h_1 ,
- Collins effects of alternate sides for the next mesons,
- a large Collins effect for h_2 ,
- *Relative* Collins Effects (or *IFF*) larger than from "single-Collins" + LCTM alone.

³ $k = \text{canonical quark momentum} = \text{mechanical momentum} + \text{string momentum flow through } OQ.$

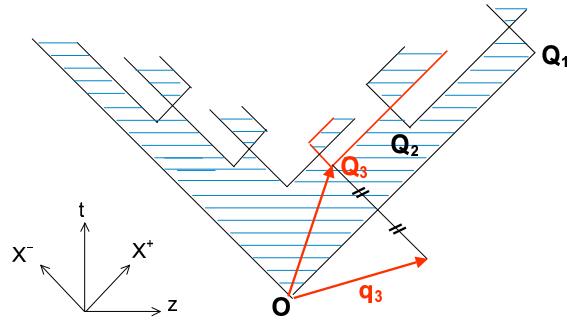


Figure 2: Relation (4) between the quark momentum q_3 in the multiperipheral picture and the point Q_3 where the $q_3\bar{q}_3$ pair is created in the classical string fragmentation model with $m_q = 0$, $k_T = 0$.

Case where h_1 is a leading vector meson. In a vector meson of linear polarization \mathbf{A} (being known from the decay products), the q and \bar{q} polarizations are symmetrical about the plane perpendicular to \mathbf{A} (Fig.3b). Let us consider a 1st-rank vector meson:

- if $\mathbf{A} \parallel \hat{\mathbf{z}}$ the Collins asymmetry is opposite to that of a leading pseudoscalar meson,
- if $\mathbf{A} \perp \hat{\mathbf{z}}$ the Collins asymmetry is in the azimuth $2\phi(\mathbf{A}) - \phi(\mathbf{S}_1) - \pi/2$,
- if both $A_z \neq 0$ and $\mathbf{A}_T \neq 0$ and if q_1 is helicity-polarized, $S_{1z} A_z \mathbf{A} \cdot \langle \hat{\mathbf{z}} \times \mathbf{p} \rangle$ is positive.

This is a *longitudinal jet-handeness* [4] effect.

These three effects are reproduced by the “toy model”. They correspond respectively to lines 3, 5 and 6 of Eq.(27) of [1]. On the average, the Collins effect is -1/3 that of the pseudoscalar meson [8].

Hidden spin effects. Whether q_A is polarized or not, the $\langle \bar{\mathbf{k}} \cdot (\hat{\mathbf{z}} \times \bar{\mathbf{S}}) \rangle$ correlation of the *string* $+^3P_0$ mechanism has an impact on the \mathbf{p}_T distribution of the rank ≥ 2 mesons:

- for a pseudoscalar meson, $\langle \mathbf{p}_T^2 \rangle_{\text{meson}} > 2 \langle \mathbf{k}_T^2 \rangle_{\text{quark}}$,
- for a vector meson linearly polarized along $\hat{\mathbf{z}}$, $\langle \mathbf{p}_T^2 \rangle_{\text{meson}} < 2 \langle \mathbf{k}_T^2 \rangle_{\text{quark}}$,
- for a vector meson linearly polarized along $\hat{\mathbf{x}}$, $\langle p_x^2 \rangle < 2 \langle \mathbf{k}_T^2 \rangle < \langle p_y^2 \rangle$.

On the average, $\langle \mathbf{p}_T^2 \rangle_{\text{V-meson}} < \langle \mathbf{p}_T^2 \rangle_{\text{PS-meson}}$. These ”hidden spin” effects allow an unexpensive test of the *string* $+^3P_0$ mechanism (note that the *Schwinger mechanism* predicts no $\langle \bar{\mathbf{k}} \cdot (\hat{\mathbf{z}} \times \bar{\mathbf{S}}) \rangle$ correlation [9]). At least they suggest that quark spin plays a role even in unpolarized experiments and should be included in any jet model.

4 The *ab initio* approach

The starting point is the multiperipheral hadronization amplitude

$$\langle k_B, s_B | \mathcal{M}_N \{ q_A \bar{q}_B \rightarrow h_1 h_2 \cdots h_N \} | k_A, s_A \rangle = \langle k_B, s_B | \mathcal{D} \{ q_B \} \mathcal{V} \{ q_B, h_N, q_N \} \cdot \mathcal{D} \{ q_3 \} \mathcal{V} \{ q_3, h_2, q_2 \} \mathcal{D} \{ q_2 \} \mathcal{V} \{ q_2, h_1, q_A \} \mathcal{D} \{ q_A \} | k_A, s_A \rangle. \quad (7)$$

$|k_B, s_B\rangle$ is the negative energy state whose hole is $|k(\bar{q}_B), s(\bar{q}_B)\rangle$. Inside curly brackets, $\{q\} = (f, k)$ gathers the quark flavor f and 4-momentum k . For a meson $\{h\} = (h, p, s_h)$ gathers the species h , the 4-momentum and the spin state. The quark propagator $\mathcal{D}\{q\} \equiv \mathcal{D}(f, k)$ and the vertex function $\mathcal{V}\{f', h, f\} \equiv \mathcal{V}_{f', h, f}(k', k)$ are the *inputs* of the model. In a *step-by-step* covariant model, $|k_A, s_A\rangle$ and $|k_B, s_B\rangle$ would be Dirac spinors and \mathcal{D} and \mathcal{V} would be 4×4 matrices, *e.g.*, $\mathcal{D}\{q\} = D(f, k^2) (m_f + \gamma \cdot k)$. However Lorentz covariance is

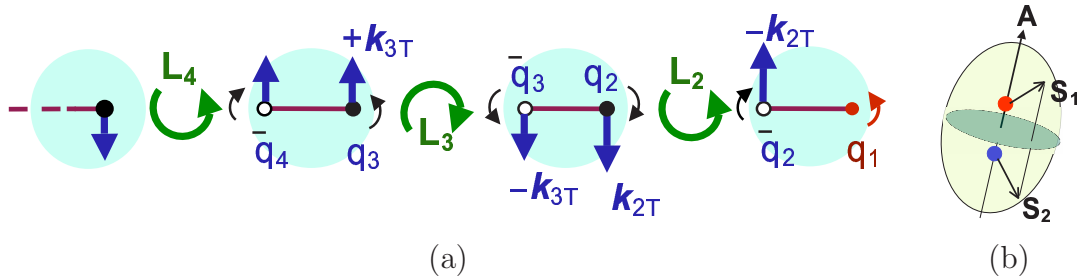


Figure 3: (a) string decay into pseudoscalar mesons with the *string* $+^3P_0$ mechanism. (b) spin correlation of the quark and antiquark in a vector meson linearly polarized along \mathbf{A} .

required only *globally* for the whole process of Fig.1. Together with P and C conservation, this requires the invariance of \mathcal{M} under

- (a) rotations about $\hat{\mathbf{z}}$,
- (b) Lorentz transformations along $\hat{\mathbf{z}}$,
- (c) reflection about any plane containing $\hat{\mathbf{z}}$,
- (d) *quark chain reversal* or “left-right symmetry” [2], *i.e.*, interchanging q_A and \bar{q}_B .

These invariances can be realized with *Pauli* spinors, *e.g.*, $\mathcal{D}\{q\} = \mu_f + \sigma_z \sigma \cdot \mathbf{k}_T$. Doing so, we do not take into account the whole information (2 q-bits) carried by an off-mass-shell Dirac spinor. We leave this question for further studies.

Hadronization “cross section” of quark q_n . In the ladder approximation one can define the hadronization “cross section” of an initial or intermediate polarized quark q_n ,

$$\mathcal{H}\{\bar{q}_B + \uparrow q_n \rightarrow X\} = \text{Tr } \mathcal{R}\{q_n\} \rho\{q_n\}, \quad (8)$$

where $\rho\{q_n\} = (\mathbf{I} + \sigma \cdot \mathbf{S}_n)/2$ is the spin density matrix of q_n ,

$$\mathcal{R}\{q_n\} = \frac{1}{2} \sum_{N \geq n} \int d\{h_n\} \cdots d\{h_N\} \mathcal{M}_{N-n}^\dagger \mathcal{M}_{N-n} \delta^4[p_n + \cdots + p_N - k_A - k(\bar{q}_B)] \quad (9)$$

and $\int d\{h\} \cdots$ stands for $\sum_h \sum_{s(h)} \int d^3\mathbf{p}/p^0 \cdots$. We are interested in the q_A fragmentation region, that is why we will took \bar{q}_B unpolarized. $\mathcal{R}\{q\}$ obeys the *ladder* integral equation (illustrated by Fig.4):

$$\mathcal{R}\{q\} = \int d\{h\} T^\dagger\{q', h, q\} \mathcal{R}\{q'\} T\{q', h, q\} + \sum_h \mathcal{M}_1^\dagger \mathcal{M}_1 \delta[(k - k_B)^2 - m_h^2] \quad (10)$$

with $T\{q', h, q\} \equiv \mathcal{V}\{q', h, q\} \mathcal{D}\{q\}$. At large $m_X^2 \simeq |k_B^-| k^+$,

$$\mathcal{R}\{q\} \simeq \mathcal{B}\{q\} (m_X^2)^{\alpha_R}, \quad (11)$$

$$\mathcal{B}\{q\} = \beta(f, \mathbf{k}_T^2) [1 + A(f, \mathbf{k}_T^2) \sigma \cdot \tilde{\mathbf{n}}(\mathbf{k})], \quad (12)$$

with $\tilde{\mathbf{n}}(\mathbf{k}) \equiv \hat{\mathbf{z}} \times \mathbf{k} / |\hat{\mathbf{z}} \times \mathbf{k}|$. In ordinary multiperipheral models α_R and $\mathcal{B}\{q\}$ are the intercept and residue of the *output Regge trajectory*. $A(f, \mathbf{k}_T^2)$ is the single-spin asymmetry of $\uparrow q + \bar{q}_B \rightarrow X$. $A(f, 0) = 0$. $\mathcal{B}\{q\}$ is semi-positive definite: $\beta > 0$, $|A| \leq 1$.

Recursive Monte-Carlo algorithm. Suppose that we have already generated $n-1$ steps of (2) and recorded the density matrix $\rho\{q_n\}$. The simulation of the next step $\uparrow q_n \rightarrow h_n + \uparrow q_{n+1}$ (hereafter rewritten $\uparrow q \rightarrow h + \uparrow q'$) proceeds in two sub-steps:

1) **generate the species and momentum of h .** From Eqs.(10-11) the type and momentum distribution of the next-rank particle is proportional to

$$d\mathcal{H}\{\bar{q}_B + \uparrow q\} = \frac{dZ d^2\mathbf{p}_T}{Z} |k_B^- k'^+|^{\alpha_R} \sum_{s(h)} \text{Tr} [\mathcal{B}\{q'\} T\{q', h, q\} \rho\{q\} T^\dagger\{q', h, q\}], \quad (13)$$

with $Z \equiv p^+/k^+$, $k' = k - p$.

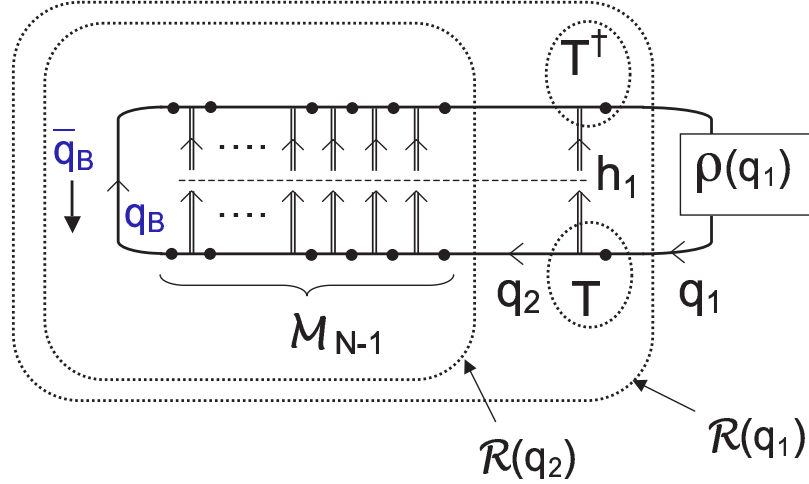


Figure 4: Ladder unitarity diagram associated to Eqs.(8-10) with $n=1$, $q = q_1$, $q' = q_2$. Black bullets represent quark propagators. The summation over N is understood.

2) **calculate the polarization of $\uparrow q'$.** It is given by

$$\rho\{q'\} = \sum_{s(h)} [T\{q', h, q\} \rho\{q\} T^\dagger\{q', h, q\}] / \text{Tr}[\text{idem}]. \quad (14)$$

If h has nonzero spin and one wants to simulate its decay, a more complicated algorithm is needed, following the rules of [11] (see also Sec.5.1 of [12]).

In this *ab initio* approach one must calculate α_R and the functions $\beta(f, \mathbf{k}_T^2)$ and $A(f, \mathbf{k}_T^2)$ from the integral equation (10), as a preliminary numerical task.

5 The *renormalized input* approach

The physical properties (*e.g.*, the multi-particle distributions) are unchanged by two kinds of “renormalization” of the propagators and vertices:

$$\begin{aligned} (a) \quad & \text{new } \mathcal{D}\{q\} = |k^- k^+|^\lambda \mathcal{D}\{q\}, \quad \text{new } \mathcal{V}\{q', h, q\} = |k'^+ k^-|^\lambda \mathcal{V}\{q', h, q\} \\ (b) \quad & \text{new } \mathcal{D}\{q\} = \Lambda\{q\} \mathcal{D}\{q\} \Lambda\{q\}, \quad \text{new } \mathcal{V}\{q', h, q\} = \Lambda^{-1}\{q'\} \mathcal{V}\{q', h, q\} \Lambda^{-1}\{q\}, \end{aligned} \quad (15)$$

where $\Lambda\{q\} \equiv \Lambda(f, \mathbf{k}_T)$ is a matrix in spin space. Under (a) α_R is shifted by 2λ . Under (b), *new* $\mathcal{B}\{q\} = \Lambda^\dagger\{q\} \mathcal{B}\{q\} \Lambda\{q\}$. Let us combine (a) and (b) with $\lambda = -\alpha_R/2$ and $\Lambda = \mathcal{B}^{-\frac{1}{2}} (\mathcal{D}^\dagger/\mathcal{D})^{\frac{1}{4}}$ (these matrices commute). We get *new* $\alpha_R = 0$, *new* $\mathcal{R}\{q\} = \text{new } \mathcal{B}\{q\} = \mathbf{I}$. Taking the renormalized $\mathcal{V}\{q', h, q\}$ as unique input, the renormalized propagator is obtained from (10):

$$\mathcal{D}\{q\} = U^{-\frac{1}{2}}\{q\} \quad \text{with} \quad U\{q\} \equiv \sum_h \int \frac{d^3\mathbf{p}}{p^0} \mathcal{V}^\dagger\{q', h, q\} \mathcal{V}\{q', h, q\}. \quad (16)$$

The preliminary task is now to evaluate (16). It is much easier than solving the integral equation (10). Besides, (13) is simplified by the absence of $|k_B^- k'^+|^{\alpha_R}$ and $\mathcal{B}\{q'\}$.

6 Application with string amplitudes

An *ab initio* string hadronization amplitude [5] can be expressed in the multiperipheral form with the propagator and vertex

$$\mathcal{D}\{q\} = (k^- k^+ - i0)^{\alpha\{q\}} \exp[(i - b) k^- k^+ / 2] d\{q\}, \quad (17)$$

$$\mathcal{V}\{q', h, q\} = (p^+ / k'^+)^{\alpha\{q'\}} \exp[(b - i) k'^- k^+ / 2] (-p^- / k^-)^{\alpha\{q\}} g\{q', h, q\}. \quad (18)$$

$d\{q\} = d(f, \mathbf{k}_T)$ and $g\{q', h, q\} = g_{f', h, f}(\mathbf{k}'_T, \mathbf{k}_T)$ are spin matrices and $\alpha\{q\} = \alpha(f, \mathbf{k}_T^2)$. In the ladder approximation one can remove the phases of the exponential factors and of $(k^- k^+ - i0)^{\alpha\{q\}}$. This does not change the probabilities. After renormalization,

$$\mathcal{V}\{q', h, q\} = (k'^+ / p^+)^{a\{q'\}/2} \exp(-b k'^- k^+ / 2) (-k^- / p^-)^{a\{q\}/2} g\{q', h, q\}, \quad (19)$$

with a new $g\{q', h, q\}$ and $a\{q\} = \text{old}(\alpha_R - 2 \text{Re } \alpha\{q\})$. The right Eq.(16) becomes

$$U\{q\} = u\{q\} / \mathcal{E}_q(k^- k^+) \quad \text{with} \quad \mathcal{E}_q(x) \equiv x^{-a\{q\}} e^{-bx}, \quad (20)$$

$$u\{q\} = \sum_{h, s(h)} \int d^2 \mathbf{p}_T \frac{dZ}{Z} \left(\frac{1-Z}{Z} \right)^{a\{q'\}} \mathcal{E}_q \left(\frac{m_h^2 + \mathbf{p}_T^2}{Z} \right) g^\dagger\{q', h, q\} g\{q', h, q\}. \quad (21)$$

Example: $a\{q\} = \text{constant}$ and

$$g\{q', h, q\} = e^{-B(\mathbf{k}'_T + \mathbf{k}_T)^2} (\mu_{f'} + \sigma_z \sigma \cdot \mathbf{k}'_T) \Gamma(\mu_f + \sigma_z \sigma \cdot \mathbf{k}_T) \quad (22)$$

with $\Gamma = \sigma_z$ for a pseudoscalar meson and $\Gamma = G_L V_z^* \mathbf{I} + G_T \sigma \cdot V_T^* \sigma_z$ for a vector meson, like in the ‘‘toy model’’ [1]. A complex μ_f with $\text{Im} \mu_f > 0$ reproduces the effects of the *string* $+^3 P_0$ mechanism.

The recipe (13-14) becomes

1. generate the species and momentum of h following the distribution

$$d^2 \mathbf{p}_T \frac{dZ}{Z} \left(\frac{1-Z}{Z} \right)^{a\{q'\}} \mathcal{E}_q \left(\frac{m_h^2 + \mathbf{p}_T^2}{Z} \right) \sum_{s(h)} \text{Tr}(t\{q', h, q\} \rho\{q\} t^\dagger\{q', h, q\}) \quad (23)$$

with $t\{q', h, q\} = g\{q', h, q\} u^{-\frac{1}{2}}\{q\}$,

2. calculate the polarization of $\uparrow q'$ with

$$\rho\{q'\} = \left[\sum_{s(h)} t\{q', h, q\} \rho\{q\} t^\dagger\{q', h, q\} \right] / \text{Tr}[\text{idem}]. \quad (24)$$

If quark spin is ignored, $g\{q', h, q\} = g_{f', h, f}(\mathbf{k}'_T, \mathbf{p}_T, \mathbf{k}_T)$, $u\{q\} = u(f, \mathbf{k}_T)$ and one recovers the symmetric Lund model. $U\{q\}$ and $\langle j | \mathcal{V}^\dagger\{q', h, q\} | j' \rangle \langle i' | \mathcal{V}\{q', h, q\} | i \rangle$ are the spin-dependent generalizations of $\rho_\nu(V)$ and $\rho_{\nu, \nu'}(V, V')$ in [10].

7 Conclusion

We have built a *bona fide* recursive quark fragmentation model including the quark spin degree of freedom. For pseudo-scalar and vector mesons the model can reproduce the Collins effects of the classical *string* +³ P_0 mechanism and also give longitudinal jet handedness. It can be a guide for quark polarimetry and may also account for "hidden spin" effects in unpolarized quark fragmentation. The *ab initio* input consists in quark propagators and vertices. Using it, an integral equation has to be solved in order to fix the splitting distribution. Starting from the *renormalized input*, which consists in exponents $a\{q\} = a(f, \mathbf{k}_T^2)$ and vertex matrices $g\{q', h, q\} = g_{f', h, f}(\mathbf{k}'_T, \mathbf{k}_T)$, only an ordinary integration is needed. Putting vertices derived from the semiclassical string action in 1+1 dimension, one obtains a spin-dependent generalization of the symmetric Lund model which may be implemented in a Monte-Carlo code of quark jet simulation.

References

- [1] X. Artru, Proc. of XIII Advanced Research Workshop on High Energy Spin Physics (2009), p.33 ; arXiv:1001.1061.
- [2] B. Andersson, G. Gustafson, G. Ingelman and T. Sjöstrand, Phys. Rep. **97** (1983) 31.
- [3] X. Artru, J. Czyżewski and H. Yabuki, Zeit. Phys. **C73** (1997) 527.
- [4] O. Nachtmann, Nucl. Phys. **B127** (1977) 314 ; J.F. Donoghue, Phys. Rev. **D19** (1979) 2806 ; A.V. Efremov, L. Mankiewicz and N.A. Törnqvist, Phys. Lett. **B284** (1992) 394.
- [5] X. Artru and Z. Belghobsi, (a) Proc. of XIV Advanced Research Workshop on High Energy Spin Physics (2011), p.45 ; (b) AIP Conf. Proc. **1444** (2012) 97 ; (c) X. Artru, Problems of Atomic Science and Technology, N 1. Series Nuclear Physics Investigations **57** (2012) 173.
- [6] A. Krzywicki and B. Petersson, Phys. Rev. **D6** (1972) 924.
- [7] E. Redouane-Salah and X. Artru AIP, Conf. Proc. **1444** (2012) 157 (<http://hal.in2p3.fr/in2p3-00672604>) ; X. Artru and E. Redouane-Salah, these proceedings.
- [8] J. Czyżewski, Acta Physica Polonica **27** (1996) 1759.
- [9] X. Artru and J. Czyżewski, Acta Physica Polonica **B29** (1998) 2115 ; ArXiv:hep-ph/9805463.
- [10] X. Artru, Z. Phys. C - Particles and Fields **26** (1984) 23.
- [11] I.G. Knowles, Nucl. Phys. **B304** (1988) 767 ; J.C. Collins, *ibid.* 794.
- [12] X. Artru, M. Elchikh, J.-M. Richard, J. Soffer and O.V. Teryaev, Phys. Rep. **470** (2009) 1-92.

COLLINS ASYMMETRY IN FIELD IONIZATION OF HYDROGEN

X. Artru^{1†} and E. Redouane-Salah^{2†}

(1) *Université de Lyon, CNRS/IN2P3 and Université Lyon 1, IPNL, France*

(2) *Université de M'sila, Faculté des Sciences, Département de Physique
and LPMPS, Université de Constantine 1, Algeria*

† *E-mail: x.artru@ipnl.in2p3.fr*

Abstract

An effect similar to the Collins asymmetry is found in the ionization of a hydrogen atom by a static electric field \mathbf{E} . When the initial electron possesses an orbital angular momentum $\langle \mathbf{L} \rangle$ transverse to the field, the mean transverse velocity of the final electron points in the direction of $\mathbf{E} \times \langle \mathbf{L} \rangle$. However $\langle \mathbf{L} \rangle$ is oscillating in time due to the linear Stark effect, making $\langle \mathbf{v}_T \rangle$ oscillate.

Introduction. An atom can be ionized by a sufficiently strong static electric field \mathbf{E} thanks to the tunnel effect. This process has a strong similarity with the production of a quark-antiquark pair ($q\bar{q}$) in a QCD string. If the initial electron has an orbital angular momentum perpendicular to \mathbf{E} , the average transverse velocity $\langle \mathbf{v}_T \rangle$ should be nonzero and in the direction of $\langle \mathbf{L} \rangle \times \mathbf{F}$, where $\mathbf{F} = -e\mathbf{E}$ is the external force [1]. We refer to it as the $\mathbf{v} \cdot (\mathbf{L} \times \mathbf{F})$ asymmetry. The mechanism (Fig.1-left) looks like the *string* + 3P_0 mechanism (Fig.1-right) of hyperon polarization [2] and Collins effect [1, 3].

At variance with the string + 3P_0 mechanism, the *Schwinger mechanism* of $q\bar{q}$ pair creation yields no $\mathbf{v} \cdot (\mathbf{L} \times \mathbf{F})$ asymmetry [1]. Thus the question of such an asymmetry in string breaking remains open. It is at least instructive to study it in atomic physics.

1 Behavior of an H atom in an external electric field

We consider an hydrogen atom in an static electric field $\mathbf{E} = -(F/e)\hat{\mathbf{z}}$. At small F the *linear* Stark effect just splits the n^{th} energy level in $2n - 1$ sublevels separated by¹ $\omega = 3nF/2$. *Stark states* are the eigenstates of $H_0 - Fz = \mathbf{p}^2/2 - 1/r - Fz$ in the $F \rightarrow 0$ limit. For large enough F ionization by tunneling becomes important and Stark states move into resonances of complex energy $E = E_R - i\gamma/2$. Using the parabolic coordinates $\xi=r-z$, $\eta=r+z$, $\varphi=\arg(x+iy)$, their wave functions have the separable form [4]

$$\Psi = \xi^{-1/2} \Phi(\xi) \eta^{-1/2} \chi(\eta) e^{im\varphi}, \quad (1)$$

where $\Phi(\xi)$ verifies

$$\partial^2 \Phi / \partial \xi^2 + [E/2 + Z_\xi/\xi - (m^2 - 1)/(4\xi^2) - F\xi/4] \Phi(\xi) = 0 \quad (2)$$

and $\chi(\eta)$ an analogous equation with $F \rightarrow -F$ and $Z_\xi \rightarrow Z_\eta = 1 - Z_\xi$. Stark states are labeled $|n_\xi, n_\eta, m\rangle$, where n_ξ and n_η are the numbers of nodes of $\Phi(\xi)$ and $\chi(\eta)$, linked

¹In this paper we use atomic units: $\hbar/(m_e\alpha c) = 0.0529$ nm for length, $\hbar/(m_e\alpha^2 c^2) = 2.42 \cdot 10^{-17}$ s for time, $m_e\alpha^2 c^2 = 27,2$ eV for energy and $m_e^2\alpha^3 c^2/\hbar = 5.14 \cdot 10^9$ eV/cm for force.

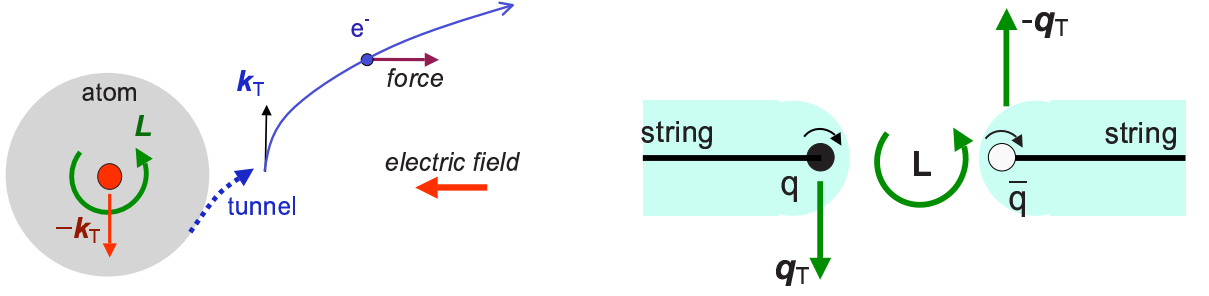


Figure 1: Left: semi-classical motion of the electron extracted from the hydrogen atom by a strong field \mathbf{E} , when the electron is initially in a $L_y = +1$ state. Right: String + 3P_0 mechanism correlating the transverse momentum and the transverse polarization of a quark created in string decay [3, 1].

by $n_\eta + n_\xi + |m| + 1 = n$ and fixing $Z_\xi = (n + n_\xi - n_\eta)/(2n)$. With the change of variables $\sqrt{\xi/n} e^{i\varphi} = \hat{x} + i\hat{y}$, $\hat{\Phi}(\hat{x}, \hat{y}) \equiv \xi^{-1/2} \Phi(\xi) e^{im\varphi}$ is the wave function of a 2-dimensional harmonic oscillator of angular momentum m and energy $\epsilon_\xi = 2nZ_\xi = 2n_\xi + |m| + 1$.

L_\perp oscillations. Stark states are also eigenstates of A_z , where \mathbf{A} is the Laplace-Runge-Lenz-Pauli vector

$$\mathbf{A} = \mathbf{r}/r + (\mathbf{L} \times \mathbf{p} - \mathbf{p} \times \mathbf{L})/2. \quad (3)$$

For $F=0$, $\langle A_z \rangle = 2\langle z \rangle / (3n^2) = (n_\eta - n_\xi)/n$. For $F \neq 0$ the transverse components (L_x, L_y) and (A_x, A_y) are not conserved. Starting from a L_y eigenstate, $\langle L_y \rangle$ oscillates in quadrature with $\langle A_x \rangle$, as pictured in Fig.2, with the period $2\pi/\omega$. Let us take as an example the initial state $|n=2, L_y=+1\rangle$, whose wave function is

$$\Psi(\mathbf{r}, 0) = 8^{-1}\pi^{-1/2} (z + ix) e^{-r/2} = 0.5(|010\rangle - |100\rangle + i|001\rangle + i|00-1\rangle). \quad (4)$$

At $t \neq 0$ it evolves as

$$\Psi(t) = 0.5 e^{it/8} (e^{+i\omega t} |010\rangle - e^{-i\omega t} |100\rangle + i|001\rangle + i|00-1\rangle) \quad (5)$$

$$= e^{it/8} \left[\cos^2 \frac{\omega t}{2} |L_y=+1\rangle - \sin^2 \frac{\omega t}{2} |L_y=-1\rangle + \frac{i}{\sqrt{2}} \sin(\omega t) |l=0\rangle \right]. \quad (6)$$

Thus the atom oscillates between three L_y eigenstates.

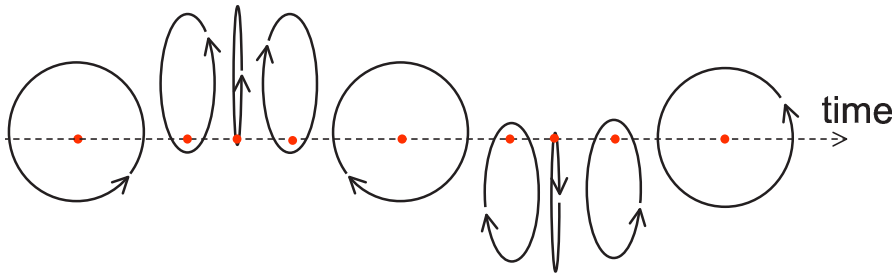


Figure 2: Classical picture of the Stark oscillations of L_y and A_x .

2 Tunneling amplitudes

The external force is confining in ξ and changes $\Phi(\xi)$ only little. Tunneling bears on $\chi(\eta)$. The wave function at large η describes the escaped electron. Using, as in Ref. [4], the JWKB method to lowest order in F , one obtains for the state $|i\rangle \equiv |n_\xi, n_\eta, m\rangle$

$$\Psi_i(\mathbf{r}, t)_{\eta \rightarrow \infty} \simeq a_i \hat{\Phi}_i(\hat{x}, \hat{y}) \exp\{(-i\delta E_i - \gamma_i/2)t'\} B(\eta, t) \quad (7)$$

a_i is the tunneling amplitude normalized to $|a_i|^2 = \gamma_i$, δE_i is the Stark shift, $\hat{\Phi}_i(\hat{x}, \hat{y})$ is the 2-D oscillator wave function normalized to $\langle \hat{\Phi}_i | \hat{\Phi}_i \rangle = 1$ and

$$B(\eta, t) = (4F\eta^3)^{-1/4} \exp\left[(i/3)\sqrt{F}(\eta - \eta_F)^{3/2} + it/8 + 5i\pi/4\right]. \quad (8)$$

$\eta_F \equiv 1/(n^2F)$ is near the tunnel exit and $t' \equiv t - \sqrt{(\eta - \eta_F)/F}$ is the classical electron exit time. For $n=2$ the amplitudes are

$$\begin{aligned} a_1 &\equiv a_{010} = iq a_{00+1}, \\ a_2 &\equiv a_{00+1} = a_{00-1} = 2^{-5/2} F^{-1} \exp[-1/(24F)], \\ a_3 &\equiv a_{100} = a_{00+1}/(iq), \end{aligned} \quad (9)$$

with $q = e^{-3/2}/\sqrt{2F}$. The widths $\gamma_i = |a_i|^2$ agree with Slavjanov's result [5].

3 $\mathbf{v} \cdot (\mathbf{L} \times \mathbf{F})$ asymmetry for the initial state $|n=2, L_y = +1\rangle$

With the initial state (4) the escaped electron density is, according to (5,7-8),

$$|\Psi(\mathbf{r}, t)|_{\eta \rightarrow \infty}^2 = (4F\eta^3)^{-1/2} \left| \hat{\Phi}(\hat{x}, \hat{y}, t') \right|^2 \quad (10)$$

with $\eta \simeq 2z$, $(\hat{x}, \hat{y}) \simeq (x, y)/\sqrt{2nz}$. In the $n=2$ case,

$$\hat{\Phi}(t') = 0.5 \left\{ a_1 \hat{\Phi}_{010} e^{(i\omega - \gamma_1/2)t'} - a_3 \hat{\Phi}_{100} e^{(-i\omega - \gamma_3/2)t'} + ia_2 (\hat{\Phi}_{00+1} + \hat{\Phi}_{00-1}) e^{-\gamma_2 t'/2} \right\}. \quad (11)$$

$|\Psi(\mathbf{r}, t)|^2$ looks like the density of a classical electron cloud falling freely in the force field \mathbf{F} . An electron leaving the tunnel at time t' with the transverse velocity \mathbf{v}_\perp follows the parabola of fixed $(\hat{x}, \hat{y}) \simeq \mathbf{v}_\perp/\sqrt{2F}$. The interference between even- and odd- m terms of $\hat{\Phi}(t')$ yields the $\mathbf{v} \cdot (\mathbf{L} \times \mathbf{F})$ asymmetry, which is t' -dependent. A measure of it is

$$A(t') \equiv \langle v_x \rangle / \Delta v_x = \langle \hat{\Phi}(t') | \hat{x} | \hat{\Phi}(t') \rangle / \sqrt{\langle \hat{\Phi}(t') | \hat{x}^2 | \hat{\Phi}(t') \rangle}; \quad (12)$$

$$A(t'=0) = 8^{1/2} (q^2 + 8 + 3q^{-2})^{-1/2}. \quad (13)$$

Like L_y , $A(t')$ changes sign at the Stark frequency, giving the "crawling snake" of Fig.3 [6].

Conclusion. This study shows that the $\mathbf{v} \cdot (\mathbf{L} \times \mathbf{F})$ effect does exist in field ionisation, but is oscillating in time. Several constraints make its search challenging:

- Radiative transition may compete with field ionization.
- The initial asymmetry $A(0)$ is small if the $|a_i|$'s differ too much (see Eqs.13 and 9).

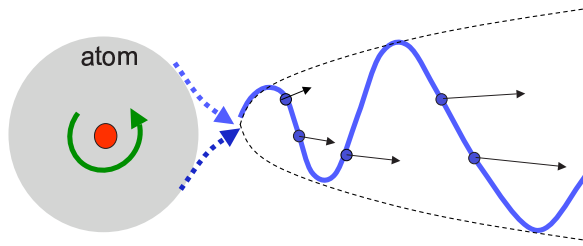


Figure 3: "Crawling snake" motion of $\langle x \rangle$ versus z of the escaping electron. As t grows the undulations move to the right.

- $A(t')$ is fast oscillating, therefore one may only measure its time-averaged $\langle A \rangle$. This one is large only if $\gamma_i \gtrsim \omega$, so that ionization is faster than oscillation.

These constraints are satisfied with a large enough field. In the $n=2$ case this field is too strong to be produced in laboratory. Hopefully, our results can be generalized to large n (Rydberg states), where the required field scales like n^{-4} [7]. The \mathbf{v}_T distribution can be measured by the *photoelectron imaging* techniques [8, 9].

Our formulae, obtained at lowest order in F , cannot be applied at the required field. Accurate numerical methods are given in [10, 11]. Nevertheless the above conclusions should remain qualitatively correct.

References

- [1] X. Artru and J. Czyzewski, *Acta Phys. Polonica C* **B29** (1998) 2015.
- [2] B. Andersson, G. Gustafson, G. Ingelman and T. Sjöstrand, *Phys. Rep.* **97** (1983) 31.
- [3] X. Artru, J. Czyzewski and H. Yabuki, *Zeit. Phys. C* **73** (1997) 527.
- [4] L.D. Landau, E.M. Lifshitz, *Course of theoretical physics, Vol. 3, Quantum Mechanics*, Pergamon press, London.
- [5] Yu. Slavjanov, *Problemi Matematicheskoi Fiziki* (Leningrad: Leningrad State University, 1970), pp 125-34.
- [6] E. Redouane-Salah and X. Artru, *AIP Conf. Proc.* **1444**, 157 (2012).
- [7] X. Artru and E. Redouane-Salah, in preparation.
- [8] Yu.N. Demkov, V.D. Kondratovich and V.N. Ostrovskii, *Pis'ma Zh. Eksp. Teor. Fiz.* **34**, 425 (1981) [*JETP Lett.* **34**, 403 (1981)].
- [9] A.S. Stodolna, A. Rouze, F. Lépine, S. Cohen, F. Robicheaux, A. Gijsbertsen, J.H. Jungmann, C. Bordas and M.J.J. Vrakking, *Phys. Rev. Lett.* **110**, 213001 (2013).
- [10] R.J. Damburg and V.V. Kolosov, *J. Phys. B* **9**, 3149 (1976), **B 11**, 1921 (1978), **B 12**, 2637 (1979).
- [11] T. Yamabe, A. Tachibana and H.J. Silverstone, *Phys. Rev. A* **16** (1977) 877.

LARGE- x FACTORIZATION OF TRANSVERSE-DISTANCE DEPENDENT PARTON DENSITIES

I.O. Cherednikov^{1,2,†}

(1) *EDF, Universiteit Antwerpen, B-2020 Antwerpen, Belgium*

(2) *BLTP JINR, RU-141980, Dubna, Russia*

† *E-mail: igor.cherednikov@uantwerpen.be*

Abstract

We discuss a large- x QCD factorization framework, which implies some practical applications to the phenomenology of the TDDs accessible in future experimental programs to be started at the Jefferson Lab 12 GeV and the Electron-Ion Collider. This approach suggests extraction of the three-dimensional parton distribution functions as a convolution of a collinear jet function and soft transverse-distance dependent (TDD) function defined as a vacuum average of a partially light-like Wilson loop.

Transverse structure of the nucleon is encoded in the transverse-momentum dependent PDFs what finalizes the three-dimensional picture in the momentum representation (see, e.g., [1] and Refs. therein). An interesting opportunity to unravel the 3D PDFs at large Bjorken x is provided by the forthcoming energy upgrade from 6 to 12 GeV to CEBAF at Jefferson Lab. Given that CEBAF is a fixed-target facility, this upgrade will enable probing the region $0.1 < x < 0.7$, where valence quarks prevail. On the other hand, smaller x for the similar Q^2 can be reached at the planned Electron-Ion Collider, which will explore the nucleon's sea as well [1]. In total, the kinematic range of both experiments is executed to be about $10^{-3} < x < 1$ and $2 \text{ GeV}^2 < Q^2 < 100 \text{ GeV}^2$. This coverage will allow one to make precision tests and compare various TMD factorization methods, as well as to look for important relations between nuclear and high-energy phenomenology. Having in mind the kinematical set up of the above-mentioned experiments, we will discuss the generic 3D-correlation functions in the large- x limit which is easier to analyze within an appropriate factorization scheme. We will show, moreover, how the theory of the large- x PDFs can profit from the study of properties of the generalized loop space.

We start from a generic gauge-invariant *transverse-distance dependent* (TDD) correlation function defined as a Fourier transform of the *transverse-momentum dependent* (TMD) hadronic matrix element $\mathcal{F}(x, \mathbf{k}_\perp; P^+, n^-, \mu^2)$

$$\begin{aligned} \mathcal{F}(x, \mathbf{b}_\perp; P^+, n^-, \mu^2) &= \int d^2 k_\perp e^{-ik_\perp \cdot \mathbf{b}_\perp} \mathcal{F}(x, \mathbf{k}_\perp; P^+, n^-, \mu^2) = \\ &= \int \frac{dz^-}{2\pi} e^{-ik^+ z^-} \left\langle P \left| \bar{\psi}(z^-, \mathbf{b}_\perp) \mathcal{U}_n^\dagger[z^-, \mathbf{b}_\perp; \infty^-, \mathbf{b}_\perp] \mathcal{U}_l^\dagger[\infty^-, \mathbf{b}_\perp; \infty^-, \infty_\perp] \right. \right. \\ &\quad \left. \left. \times \mathcal{U}_l[\infty^-, \infty_\perp; \infty^-, \mathbf{0}_\perp] \mathcal{U}_n[\infty^-, \mathbf{0}_\perp; 0^-, \mathbf{0}_\perp] \psi(0^-, \mathbf{0}_\perp) \right| P \right\rangle, \end{aligned} \quad (1)$$

which is supposed to contain the information about quark distribution in the longitudinal one-dimensional momentum space and two-dimensional impact-parameter coordinate

space. Generic semi-infinite Wilson line evaluated along a certain four-vector w_μ are defined as

$$\mathcal{U}_w[\infty; z] \equiv \mathcal{U}_\gamma = \mathcal{P} \exp \left[-ig \int_0^\infty d\tau w_\mu \mathcal{A}^\mu(z + w\tau) \right], \quad (2)$$

where the vector w_μ parametrizes the path γ : $w_\mu\sigma$, $\sigma \in [0, \infty]$, the latter containing, in general, light-like, longitudinal non-light-like, and transversal parts [2]. Large- x factorization scheme for the gauge-invariant integrated PDFs has been proposed and developed in Ref. [3]. Here we generalize this method to include the 3D-PDF, Eq. (2), see Ref. [4].

First we notice that at the large- x , the struck quarks moves as fast as the parent nucleon, that is, in the infinite momentum frame, the soft-gluon contribution is factorized into the eikonal operators [5]. Thus we re-write Eq. (2) as

$$\begin{aligned} \mathcal{F}(x, \mathbf{b}_\perp; P^+, n^-, \mu^2) &= \int \frac{dz^-}{2\pi} e^{-ik^+z^-} \left\langle P \left| \bar{\psi}(z) \mathcal{U}_P[z; \infty] \mathcal{U}_P^\dagger[z; \infty] \mathcal{U}_{n^-}^\dagger[z] \right. \right. \\ &\times \left. \left. \mathcal{U}_{n^-}[\infty; 0] \mathcal{U}_P[\infty; 0] \mathcal{U}_P^\dagger[\infty; 0] \psi(0) \right| P \right\rangle, \end{aligned} \quad (3)$$

where $z = (0^+, z^-, \mathbf{b}_\perp)$. For the sake of simplicity, we work in what follows in covariant gauge, so the transverse segments of the path are omitted. The eikonal approximation assumes that very fast quark having the momentum k_μ can be considered as a classical particle moving parallel to the nucleon momentum P , so that instead of the quark fields we use

$$\Psi_{\text{jet}}(0) = \mathcal{U}_P^\dagger[\infty; 0] \psi(0), \quad \bar{\Psi}_{\text{jet}}(z) = \bar{\psi}(z) \mathcal{U}_P[z; \infty], \quad (4)$$

where the fields $\bar{\Psi}_{\text{in-jet}}, \Psi_{\text{in-jet}}$ stand for the incoming-collinear jets in initial and final states [5, 3]. Before going over to the large- x approximation, we insert in Eq. (4) two full sets of intermediate states

$$\begin{aligned} \mathcal{F}(x, \mathbf{b}_\perp; P^+, n^-, \mu^2) &= \sum_q \sum_{q'} \int \frac{dz^-}{2\pi} e^{-ik^+z^-} \left\langle P \left| \bar{\psi}(z) \mathcal{U}_P[z; \infty] \right| q \right\rangle \\ &\times \left\langle q \left| \mathcal{U}_P^\dagger[z; \infty] \mathcal{U}_{n^-}^\dagger[z; \infty] \mathcal{U}_{n^-}[\infty; 0] \mathcal{U}_P[\infty; 0] \right| q' \right\rangle \left\langle q' \left| \mathcal{U}_P^\dagger[\infty; 0] \psi(0) \right| P \right\rangle, \end{aligned} \quad (5)$$

Now one observes that the large- x regime suggests the struck quark takes almost all momentum of the parent nucleon:

$$k_\mu \approx P_\mu. \quad (6)$$

Given that in the infinite-momentum frame the transverse component of the nucleon momentum vanishes, the transverse momentum of the incoming quark \mathbf{k}_\perp is acquired completely due to the interactions with gluons. The following properties of the large- x regime will be used from now on:

1. All real radiation can only by soft, that is the intermediate states in Eq. (6) carry zero momenta in the leading approximation:

$$q_\mu, q'_\mu \sim (1-x)P_\mu \quad (7)$$

2. Quark radiation is negligible in the leading-twist; virtual gluons can be either soft or collinear, collinear gluons can only be virtual;

3. Rapidity divergences (known also as “light-cone singularities”) originate only from the soft contributions. This important observation can be justified as follows: given that the rapidity divergence take place in the soft region of the integration over momenta, that is at small virtual gluon momenta $\kappa^+ \rightarrow 0$, one concludes that the minus-infinite rapidity region is responsible for their existence, whose gluons move parallel to the outgoing jet, not incoming-collinear jet, where the rapidity is positive;
4. As distinct from the collinear PDFs, real contributions are ultraviolet-finite due to the transverse distance \mathbf{b}_\perp acting as a large-momentum cutoff. They may, however, contain rapidity singularities and exhibit non-trivial x - and \mathbf{b}_\perp -dependence.

It follows immediately from the property (1) that the leading contribution to the large- x TDD (6) is given by the vacuum intermediate state $|0\rangle = |q, q' = 0\rangle$:

$$\begin{aligned} \mathcal{F}(x, \mathbf{b}_\perp; P^+, n^-, \mu^2) = & \\ & \int \frac{dz^-}{2\pi} e^{-ik^+z^-} \langle P | \bar{\psi}(z) \mathcal{U}_P[z; \infty] | 0 \rangle \langle 0 | \mathcal{U}_P^\dagger[\infty; 0] \psi(0) | P \rangle \cdot \\ & \times \langle 0 | \mathcal{U}_P^\dagger[z; \infty] \mathcal{U}_{n^-}^\dagger[z; \infty] \mathcal{U}_{n^-}[\infty; 0] \mathcal{U}_P[\infty; 0] | 0 \rangle . \end{aligned} \quad (8)$$

Using Eq. (4), we write (in the $x \rightarrow 1$ regime)

$$\mathcal{F}(x, \mathbf{b}_\perp; P^+, n^-, \mu^2) = \int \frac{dz^-}{2\pi} e^{-ik^+z^-} \langle P | \bar{\Psi}_{\text{in-jet}}(z) | 0 \rangle \langle 0 | \Psi_{\text{in-jet}}(0) | P \rangle \quad (9)$$

$$\begin{aligned} & \times \langle 0 | \mathcal{U}_P^\dagger[z; \infty] \mathcal{U}_{n^-}^\dagger[z; \infty] \mathcal{U}_{n^-}[\infty; 0] \mathcal{U}_P[\infty; 0] | 0 \rangle = |\mathcal{J}_{\text{in-jet}}(P)|^2 \\ & \times \int \frac{dz^-}{2\pi} e^{-i(1-x)P^+z^-} \cdot \langle 0 | \mathcal{U}_P^\dagger[z; \infty] \mathcal{U}_{n^-}^\dagger[z; \infty] \mathcal{U}_{n^-}[\infty; 0] \mathcal{U}_P[\infty; 0] | 0 \rangle , \end{aligned} \quad (10)$$

where $\mathcal{J}_{\text{jet}}(P)$ is the jet matrix element [6] which obeys

$$\begin{aligned} & \langle P | \bar{\Psi}_{\text{jet}}(z) | 0 \rangle \langle 0 | \Psi_{\text{jet}}(0) | P \rangle = \\ & e^{-iP^+z^-} \langle P | \bar{\Psi}_{\text{jet}}(P) | 0 \rangle \langle 0 | \Psi_{\text{jet}}(P) | P \rangle = e^{-iP^+z^-} |\mathcal{J}_{\text{jet}}(P)|^2 . \end{aligned} \quad (11)$$

We have shown, therefore, that the following large- x factorization scheme is valid

$$\mathcal{F}(x, \mathbf{b}_\perp; P^+, n^-, \mu^2) |_{x \rightarrow 1} = \mathcal{H}(\mu^2, P^2) \cdot \Phi(x, \mathbf{b}_\perp; P^+, n^-, \mu^2) , \quad (12)$$

where the contribution of incoming-collinear partons is accumulated in the x -independent jet function \mathcal{H} , while the soft function Φ reads

$$\Phi(x, \mathbf{b}_\perp; P^+, n^-, \mu^2) = \int dz^- e^{-i(1-x)P^+z^-} \langle 0 | \mathcal{U}_P^\dagger[z; \infty] \mathcal{U}_{n^-}^\dagger[z; \infty] \mathcal{U}_{n^-}[\infty; 0] \mathcal{U}_P[0; \infty] | 0 \rangle , \quad (13)$$

with two sorts of the Wilson lines: incoming-collinear (off-light-cone, $P^2 \neq 0$), \mathcal{U}_P , and outgoing-collinear (light-like, $(n^-)^2 = 0$), \mathcal{U}_{n^-} .

The properties (2 – 4) allow us to formulate the rapidity and renormalization-group evolution equations for the factorized TDD (12):

$$\mu \frac{d}{d\mu} \ln \mathcal{F}(x, \mathbf{b}_\perp; P^+, n^-, \mu^2) = \mu \frac{d}{d\mu} \ln \mathcal{H}(\mu^2) + \mu \frac{d}{d\mu} \ln \Phi(x, \mathbf{b}_\perp; P^+, \mu^2) , \quad (14)$$

$$P^+ \frac{d}{dP^+} \ln \mathcal{F}(x, \mathbf{b}_\perp; P^+, n^-, \mu^2) = P^+ \frac{d}{dP^+} \ln \Phi(x, \mathbf{b}_\perp; P^+, \mu^2) . \quad (15)$$

Note that the r.h.s. of Eq. (14) is \mathbf{b}_\perp -independent and shows up only single-logarithmic dependence on the rapidity [7]. The r.h.s. of Eq. (15) corresponds hence to the Collins-Soper-Sterman kernel \mathcal{K}_{CSS} [8].

The rapidity associated with the plus-component of the momentum P is formally infinite and must be supplied with proper regularization [6, 7] $Y_P = \lim_{\eta \rightarrow 0} \frac{1}{2} \ln \frac{(P \cdot n^-)}{\eta}$, where η is a rapidity cutoff.

Taking into account that the variation of the scalar product $\delta(P \cdot n^-) = \delta S_P$ corresponds to a conformal transformation of the area restricted by the planar part of the path γ^* on which the Wilson loop is defined

$$\mathcal{U}_{\gamma^*} \equiv \mathcal{U}_P^\dagger[z; \infty] \mathcal{U}_{n^-}^\dagger[z; \infty] \mathcal{U}_{n^-}[\infty; 0] \mathcal{U}_P[0; \infty] , \quad (16)$$

that is

$$\gamma^* = P_\mu \sigma \cup n_\mu^- \sigma' \cup n_\mu^- \tau \cup P_\mu \sigma , \quad (17)$$

with $\sigma \in [-\infty; 0]$, $\sigma' \in [0; \infty]$, $\tau \in [\infty; 0]$, $\sigma \in [0; \infty]$. Therefore, implies the simple relationship holds between rapidity and area logarithmic derivatives:

$$P^+ \frac{d}{dP^+} = \frac{d}{d \ln S_P} \sim \frac{d}{dY_P} .$$

Hence the rapidity evolution of the soft function (13) can be related to the area transformation law of a certain class of the paths. Moreover, in the recent work [9] we have shown that the non-local classically conformal path variations can be introduced in terms of the so-called Fréchet derivative associated to a diffeomorphism in generalised loop space, which makes the whole approach mathematically consistent.

References

- [1] D. Boer, *et al.*, arXiv:1108.1713 [nucl-th];
J. Dudek, *et al.*, Eur. Phys. J. **A48** (2012) 187.
- [2] A.V.Belitsky, X. Ji, F. Yuan, Nucl. Phys. **B656** (2003) 165;
D. Boer, P.J. Mulders, F. Pijlman, Nucl. Phys. **B667** (2003) 201.
- [3] G.P. Korchemsky, G. Marchesini, Nucl. Phys. **B406** (1993) 225.
- [4] I.O. Cherednikov, T. Mertens, P. Taels, F.F. Van der Veken, Int. J. Mod. Phys. Conf. Ser. **25** (2014) 1460006;
I.O. Cherednikov, T. Mertens, F.F. Van der Veken, Phys. Rev. **D86** (2012) 085035.
- [5] A. Bassetto, M. Ciafaloni, G. Marchesini, Phys. Rept. **100** (1983) 201.
- [6] H.-n. Li, Phys. Rev. **D55** (1997) 105; arXiv:1308.0413 [hep-ph].
- [7] I.O. Cherednikov, N.G. Stefanis, Phys. Rev. **D77** (2008) 094001; Nucl. Phys. **B802** (2008) 146; Phys. Rev. **D80** (2009) 054008.
- [8] J.C. Collins, D.E. Soper, Nucl. Phys. **B193** (1981) 381; J.C. Collins, D.E. Soper, G.F. Sterman, Nucl. Phys. **B250** (1985) 199.
- [9] I.O. Cherednikov, T. Mertens, arXiv:1401.2721 [hep-th].

THE AXIAL FORM FACTOR AND POLARIZATION OF THE FINAL NUCLEON IN QUASI-ELASTIC $\nu - N$ SCATTERING¹

S.M. Bilenky^{a†} and E. Christova^{b††},

(a) *JINR, Dubna, Russia*

(b) *Institute for Nuclear Research and Nuclear Energy, Bulgarian Academy of Sciences, Sofia, Bulgaria*

E-mail: †bilenky@gmail.com; ††echristo@inrne.bas.bg;

Abstract

We have calculated the polarization of the final nucleon in charged current quasi-elastic $\nu - N$ scattering. We show that the longitudinal and transverse polarizations, as well as their ratio exhibit simple dependence on the axial form factor and their sensitivity to the axial mass is much stronger than that of the cross section. This suggests that measurements of the polarization of the nucleon in the high-statistics neutrino experiments could provide important information on the axial form factor.

1 Introduction

Important for understanding the electromagnetic structure of the nucleon are the two, Dirac and Pauli, electromagnetic form factors (FFs) $F_1(Q^2)$ and $F_2(Q^2)$, that determine elastic electron-nucleon scattering.

There are two ways of extracting $F_{1,2}$, or the more convenient experimentally charge and magnetic FFs $G_E = F_1 - \tau F_2$ and $G_M = F_1 + F_2$, $\tau = Q^2/4M^2$. The standard, Rosenbluth, procedure is based on the unpolarized cross section and determines G_E and G_M separately with a limited sensitivity to G_E^p at higher Q^2 . It was found:

1. At relatively low $Q^2 \lesssim 5 \text{ GeV}^2$ the magnetic FFs exhibit approximately the *same* dipole Q^2 -dependence, $G_D(Q^2) = (1 + Q^2/0.71 \text{ GeV}^2)^{-2}$:

$$G_M^p = \mu_p G_D(Q^2), \quad G_M^n = \mu_n G_D(Q^2). \quad (1)$$

2. Up to $Q^2 \lesssim 6 \text{ GeV}^2$ all data exhibit "scaling" of the proton FFs:

$$\mathcal{R}(Q^2) = \frac{\mu_p G_E^p(Q^2)}{G_M^p(Q^2)} \simeq 1. \quad (2)$$

which implies the *same* Q^2 -dependence for G_E^p and G_M^p .

In the late 90-ies Jefferson Lab. started series of new type of experiments that allowed a direct measurement of \mathcal{R} . In 1968 it was shown [1] that the ratio of the transverse P_\perp and longitudinal P_\parallel polarization of the recoil proton is directly proportional to \mathcal{R} :

$$\frac{P_\perp}{P_\parallel} = -\frac{G_E^p}{G_M^p} \sqrt{\frac{2\varepsilon}{\tau(1+\varepsilon)}}, \quad (3)$$

where $\varepsilon = [1 + 2(1 + \tau)\tan^2\theta/2]^{-1}$, θ is the scattering angle. JLab measured the ratio P_\perp/P_\parallel in the energy range $Q^2=[0.5 - 8.5] \text{ GeV}^2$ and unexpected results were obtained [2]:

¹The paper is supported by a priority Grant between Bulgaria and JINR. S.M. Bilenky acknowledges the support of AvH Stiftung (contract Nr. 3.3-3-RUS/1002388) and RFBR Grant N 13-02-01442.

1. "Scaling" *does not* hold. The form factor $G_E^p(Q^2)$ decreases much faster than $G_M^p(Q^2)$: $\mathcal{R} = 1$ at $Q^2 \simeq 1 \text{ GeV}^2$ and falls down to $\mathcal{R} = 0.2$ at $Q^2 = 5.6 \text{ GeV}^2$.
2. There is a clear discrepancy between the two methods in extracting \mathcal{R} .

Polarization experiments drastically changed our knowledge about the e.m. FFs and raised the important questions about radiative corrections and 2-photon exchange.

The JLab results strongly motivated our studies of the recoil nucleon polarization in charged current quasi-elastic (CCQE) $\nu(\bar{\nu}) - N$ scattering as a source of independent information about the axial form factor. We obtain analytic expressions for the polarization and estimate numerically the sensitivity of the polarization and the cross sections to the axial mass. Most of the presented results can be found in more details in [3].

2 The weak charged current form factors

We study the CCQE processes:

$$\nu + p \rightarrow \mu^+ + n, \quad \bar{\nu} + n \rightarrow \mu^- + p \quad (4)$$

which are the dominant processes at low neutrino energies and give a direct information on the charged current (CC) weak form factors.

The matrix elements of (4) is determined by the 4 weak CC FFs – $F_{1,2}^{CC}$, G_A and G_P :

$$\mathcal{M} = \frac{G_F}{\sqrt{2}} (\bar{u}_\mu \gamma^m (1 \pm \gamma_5) u_\nu) \cdot \langle N' | J_\mu^{CC} | N \rangle \quad (5)$$

$$\langle N' | J_\mu^{CC} | N \rangle = \bar{u}_{N'} \left(\gamma_\mu F_1^{CC} + \frac{i\sigma_{\mu\nu} q^\nu}{2M} F_2^{CC} + \gamma_\mu \gamma_5 G_A + \frac{q_\mu}{2M} \gamma_5 G_P \right) u_N \quad (6)$$

Due to CVC $F_{1,2}^{CC}$ are related to the e.m. FFs:

$$F_{1,2}^{CC}(Q^2) = F_{1,2}^p(Q^2) - F_{1,2}^n(Q^2), \quad (7)$$

where $F_{1,2}^p$ and $F_{1,2}^n$ are the Dirac and Pauli form factors of the proton and neutron, known at present in a wide region of Q^2 [2]. The hypothesis for partial conservation of the axial current (PCAC) implies that the contribution of $G_P(Q^2)$ can be neglected. Thus, study of the CCQE processes (4) will give information about the axial form factor $G_A(Q^2)$.

In analogy with the electromagnetic FFs, G_A is usually parameterized by the dipole formula:

$$G_A(Q^2) = \frac{g_A}{(1 + \frac{Q^2}{M_A^2})^2}. \quad (8)$$

Here $g_A = 1.2701 \pm 0.0025$ is the axial constant, known from the neutron β -decay data and M_A is a parameter – the "axial mass". At present, experiments on measurements of the CCQE cross section, performed at different neutrino energies and on different nuclear targets suggest different values for M_A [4]:

$$\begin{aligned} d \text{ or } H - \text{target} & \quad M_A = 1.03 \pm 0.02 \text{ GeV} \\ Fe - \text{target} & \quad M_A = 1.26_{-0.10}^{+0.12+0.08} \text{ GeV}, \quad \text{MINOS} \\ H_2O - \text{target} & \quad M_A = 1.20 \pm 0.12 \text{ GeV}, \quad \text{K2K} \\ C - \text{target} & \quad M_A = 1.05 \pm 0.02 \pm 0.06 \text{ GeV}, \quad \text{NOMAD} \\ C - \text{target} & \quad M_A = 1.35 \pm 0.17 \text{ GeV}, \quad \text{MiniBooNE} \end{aligned} \quad (9)$$

Though compatible within 2σ errors, these results show a clear discrepancy for the central values of M_A , that could originate in different reasons. The precise determination of the axial FF is important not only for understanding the nucleon structure, but it is a basic ingredient in interpretation of the neutrino oscillation experiments. Here we suggest that measurement of the final nucleon polarization could provide an important independent information about G_A .

3 Polarization of the final nucleon

T-invariance implies that the polarization vector of the final nucleons in (4) lays in the scattering plane. We define its longitudinal s_{\parallel} and transverse s_{\perp} components:

$$\vec{s} = s_{\perp} \vec{e}_{\perp} + s_{\parallel} \vec{e}_{\parallel}, \quad (10)$$

where \vec{e}_{\perp} and \vec{e}_{\parallel} are two orthogonal unit vectors in the scattering plane, $\vec{e}_{\parallel} = \vec{p}'/|\vec{p}'|$, p' is the 4-momentum of the final nucleon. We obtain:

- The transverse polarization exhibits a simple linear dependence on G_A :

$$(J_0 s_{\perp})^{\nu, \bar{\nu}} = \frac{-2E' \sin \theta}{|\vec{q}|} [\pm y G_M^{CC} + (2-y)G_A] G_E^{CC} \quad (11)$$

- The longitudinal polarization s_{\parallel} is expressed solely in terms of G_A and G_M^{CC} , i.e. the best known magnetic form factors of the proton and neutron, the poorly known G_E^{CC} does not enter:

$$(J_0 s_{\parallel})^{\nu, \bar{\nu}} = -\frac{q_0}{|\vec{q}|} [\pm y G_M^{CC} + (2-y)G_A] \left[(2-y)G_M^{CC} \pm \left(y + \frac{2M}{E} \right) G_A \right]. \quad (12)$$

- If the neutrino detector is in a magnetic field, then both s_{\perp} and s_{\parallel} could be measured (like in elastic $e-p$ scattering). Their ratio exhibits a simple linear dependence on G_A :

$$\left(\frac{s_{\parallel}}{s_{\perp}} \right)^{\nu, \bar{\nu}} = \frac{q_0}{2E' \sin \theta} \frac{[(2-y)G_M^{CC} \pm G_A(y + 2M/E)]}{G_E^{CC}}. \quad (13)$$

- The quantity $J_0^{\nu, \bar{\nu}}$ is determined via the differential cross section:

$$J_0^{\nu, \bar{\nu}} = \frac{d\sigma^{\nu, \bar{\nu}}}{dQ^2} \cdot \frac{4\pi}{G_F^2}, \quad (14)$$

and is given by the expression:

$$J_0^{\nu, \bar{\nu}} = 2(1-y) \left[G_A^2 + \frac{\tau(G_M^{CC})^2 + (G_E^{CC})^2}{1+\tau} \right] + \frac{My}{E} \left[G_A^2 - \frac{\tau(G_M^{CC})^2 + (G_E^{CC})^2}{1+\tau} \right] + y^2 (G_M^{CC} \mp G_A)^2 \pm 4y G_M^{CC} G_A. \quad (15)$$

Here y , q_0 , $|\vec{q}|$ are kinematic factors, E' is the energy of the final lepton.

4 Numerical results

Using the commonly used parametrizations for the e.m. FFs, we examined the sensitivity of s_{\parallel} and s_{\perp} , and their ratio s_{\parallel}/s_{\perp} on the axial mass for the following values of M_A :

- 1) $M_A = 1.016$ – full (black) line
 - 2) $M_A = 1.20$ – dashed (red) line
 - 3) $M_A = 1.35$ – dash – dotted (blue) line
- (16)

We compared it to the sensitivity of the cross section.

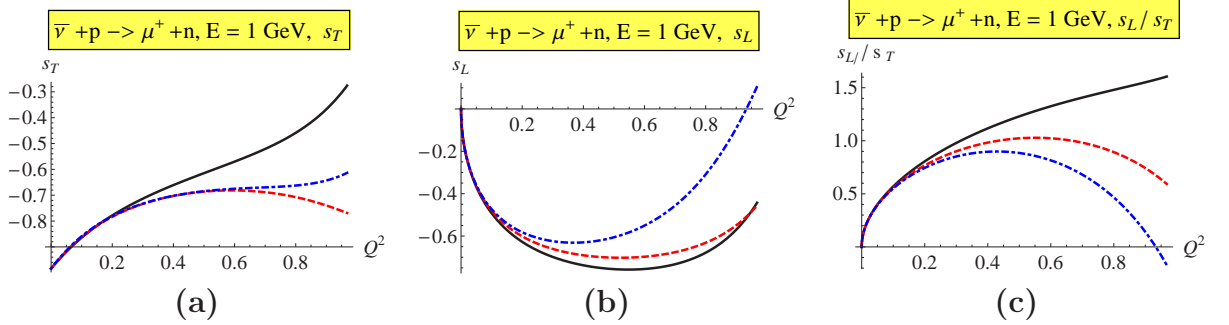


Figure 1: The dependence of the transverse s_T and longitudinal s_L polarizations of the neutron at $E=1$ GeV ((a) and (b)), and their ratio s_L/s_T (c) on the values of M_A (eq. (16)) in $\bar{\nu}_\mu + p \rightarrow \mu^+ + n$.

Fig. 12 shows that there is a clear sensitivity in the polarization of the final neutron in $\bar{\nu}_\mu + p \rightarrow \mu^+ + n$. It is most clearly pronounced for s_{\parallel} and, respectively, for the ratio s_{\parallel}/s_{\perp} . An advantage of s_{\parallel}/s_{\perp} is that many of the systematic uncertainties and radiative corrections cancel, however a magnetic field should be applied to the detector in order to measure s_{\parallel} . This sensitivity holds also for higher values of neutrino energies E . In contrast, Fig. 13 shows that the cross section exhibits very weak sensitivity to M_A .

There is almost no sensitivity to the polarization of the proton in $\nu_\mu + n \rightarrow \mu^- + p$, but the polarizations are big and could present an independent measurement of G_A .

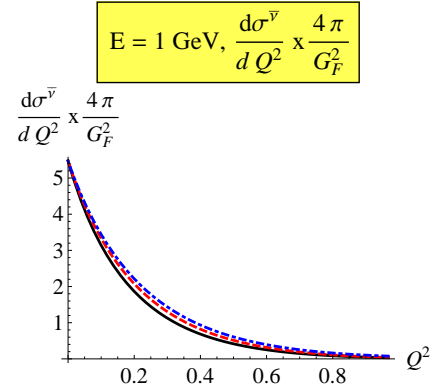


Figure 2: The dependence on M_A (see eq. (16)) of the cross section of $\bar{\nu}_\mu + p \rightarrow \mu^+ + n$ at $E=1$ GeV.

References

- [1] A.I.Akhiezer and M. Rekalov *Sov. Phys. Dokl.* **13** (1968) 572
- [2] C.F. Perdrisat, V. Punjabi and M. Vanderhaeghen *Prog. Part. Nucl. Phys.* **59** (2007) 694 (arXiv:hep-ph/0612014)
- [3] S.M.Bilenky and E. Christova, *J. Phys. G* **40** (2013) 075004 (arXiv:1303.3710)
- [4] R.D.Ransome, arXiv:1111.1154, contribution to "Physics in Collisions" 2011, Vancouver

MAGNETIC POLARIZABILITY OF DIQUARKS IN BARYONS

P. Filip

*Institute of Physics, Slovak Academy of Sciences
Dúbravská cesta 9, Bratislava 845 11, Slovakia
E-mail: Peter.Filip@savba.sk*

Abstract

We study the response of diquark wave function in Λ -type baryons to strong magnetic fields. It is found that quantum state of $J=0$ diquark (ud) in the magnetic field changes due to magnetic polarizability, and constituent quarks in (ud) diquark become polarized. The phenomenon influences polarized quark distribution functions $\Delta u(x)$ and $\Delta d(x)$, which therefore may be sensitive to the internal electromagnetic fields in hypernuclei. We also speculate, that strange quark polarization in nucleon may originate from the interaction of virtual $s\bar{s}$ quark pairs with the intrinsic magnetic field of nucleon $B \approx 10^{13}\text{T}$.

1 Introduction

It has been suggested many years ago [1], that baryons and mesons contain fractionally charged fermions - constituent quarks. According to Dirac equation, magnetic moment of charged particles with spin $s = 1/2$ is $\mu = \hbar Q/2m^*$, and therefore, constituent quarks should have magnetic moments. For baryons this concept works surprisingly well, and measured magnetic moments of hyperons $\Omega^-, \Xi^0, \Xi^-, \Sigma^+, \Sigma^-, \Lambda^0$, proton and neutron, can be understood as originating from the magnetic moments $\mu_u = 1.85\mu_N$, $\mu_d = -0.97\mu_N$, $\mu_s = -0.61\mu_N$ of quarks with constituent masses $m_u^*, m_d^* \approx 330\text{MeV}$ and $m_s^* = 510\text{MeV}$.

Consequently, open-flavor vector mesons should also have magnetic moments. For example, K^{*+} meson (bound state of u, \bar{s} quarks with parallel spins) may be expected to have magnetic moment $\mu_{K^{*+}} = |\mu_u| + |\mu_s| = 2.5\mu_N$ (here $\mu_N = 3.1 \cdot 10^{-14}\text{MeV/T}$).

The response of pseudoscalar mesons and scalar diquarks to external magnetic fields can be understood using the analogy of (qq') bound states with muonium ($e^-\mu^+$) and positronium (e^-e^+). Similarly to singlet ($J=0$) ground state of positronium or muonium, mesons $\eta_c, \eta_b, \eta', \pi, K, D, B$ should have zero magnetic moment [2]. In the magnetic field however, due to magnetic polarizability of pseudoscalar mesons, induced magnetic moment $\tilde{\mu}[B]$ is expected to appear [3], due to partial polarization of $q\bar{q}$ pair in $J=0$ quantum state. If the analogy with positronium behavior [4] is indeed correct, wave function $(\uparrow\downarrow + \downarrow\uparrow)/\sqrt{2}$ of ($m_z=0$) substate of vector mesons can acquire the admixture of pseudoscalar state $(\uparrow\downarrow - \downarrow\uparrow)/\sqrt{2}$ in the magnetic field, and quenching [5] of $\Psi(c\bar{c}), \Upsilon(b\bar{b})$ and $\varphi(s\bar{s})$ meson decays may occur [6] in static external fields $B \approx 10^{14} - 10^{15}\text{T}$.

Internal spin structure of scalar diquarks [7] in Λ -type baryons resembles quantum state of pseudoscalar mesons: $(\uparrow\downarrow - \downarrow\uparrow)/\sqrt{2}$. In strong magnetic field, a superposition of ($J=0$) diquark with its excited state ($J=1, m_z=0$) can take place. In this contribution we discuss the magnetic polarizability of diquarks in baryons due to fields $B \approx 10^{11}-10^{14}\text{T}$.

2 Spin structure of Λ baryons

Internal spin structure of $\Lambda_{1/2}^0(1116)$ baryon differs from that of proton, neutron and other spin 1/2 hyperons [8]. Typical $s = 1/2$ baryon contains two quarks (diquark) in ($J=1$) triplet state accompanied with the third quark, as described by naive $SU(6)$ function $\Psi_{1/2}^T$ in Eq.(1). One may directly guess that ground state wave function of proton (uud) is similar to Σ^+ (uus), since both they contain quarks (uu) accompanied by third d or s quark. Almost equal masses of Σ^+ , Σ^- , Σ^0 hyperons then suggest, that their constituent quantum spin structure is similar, (given by $\Psi_{1/2}^T$) as in the case of proton and neutron.

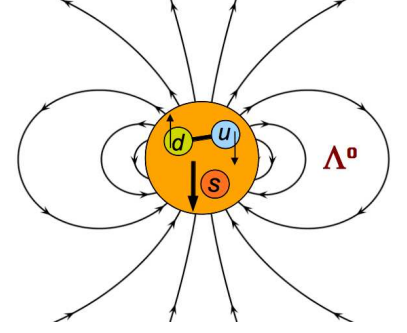


Figure 1: Scalar diquark (ud) in Λ^0 hyperon. The field is generated by magnetic moment μ_s of s -quark.

$$\Psi_{1/2}^S = \frac{(\uparrow\downarrow - \downarrow\uparrow)\uparrow}{\sqrt{2}} \quad \Psi_{1/2}^T = \frac{\sqrt{2}\uparrow\uparrow\downarrow - (\uparrow\downarrow + \downarrow\uparrow)\uparrow/\sqrt{2}}{\sqrt{3}} \quad \Psi_{3/2} = (\uparrow\uparrow\uparrow) \quad (1)$$

However, constituent quarks (uds) of $\Sigma_{1/2}^0$ hyperon can enter a lower-energy quantum state $\Psi_{1/2}^S$, with different configuration of quark spins. Such state is observed experimentally as $\Lambda_{1/2}^0(1116)$. Mass difference ($\delta M=77\text{MeV}$) between $\Sigma^0(1193)$ and Λ^0 baryon comes from different interaction energy of constituent quark color-magnetic moments.

Quantum structure of Λ^0 hyperon thus contains scalar ($J=0$) diquark accompanied with the third quark, which is then responsible for the spin of such baryon. A question, which quarks enter the scalar ($J=0$) diquark state in flavor-degenerate baryons of type $\Lambda^0(uds)$, $\Xi_c^+(usc)$ or $\Omega_{cb}^0(sc b)$ has been discussed already by Franklin et al. [10]. The conclusion was that two quarks with similar masses form a scalar diquark state, with small admixture of other diquark flavor configurations. For $\Lambda^0(uds)$, $\Lambda_c^+(udc)$, $\Lambda_b^0(udb)$ this means that scalar diquark (ud) is accompanied with heavier s , c or b quark.

If all three constituent quark spins are oriented in parallel, baryon has spin $s=3/2$, which corresponds to experimentally observed Ω hyperon and Δ , Σ^* and Ξ^* resonances. Spin wave function $\Psi_{3/2}$ of such baryons is shown Eq.(1).

3 Internal hyperfine magnetic fields in baryons

Within the framework of MIT bag model [9], constituent quarks are bound together in a small ($R \approx 1\text{fm}$) volume, which contains strong gluon fields and also virtual partons. Constituent quarks are the source of magnetic dipole and electric fields, which are not screened by the external vacuum. In a simplified picture of Λ^0 hyperon as purely (ud)- s state, the measured magnetic moment $\mu_\Lambda = -0.613\mu_N$ is to be generated by s -quark: $\mu_\Lambda = \mu_s$, because diquarks in quantum state $\Psi^S = (\uparrow\downarrow - \downarrow\uparrow)\sqrt{2}$ (as well as pseudoscalar mesons) should have zero magnetic moment.

However, the above said is not completely true. Magnetic dipole field lines, which constitute the dipole field of Λ^0 hyperon are contained in (penetrating) the "bag" volume of baryon (see Fig.1). Therefore, scalar (ud) diquark state, described by the spin wave function Ψ^S can be altered in the magnetic field, and achieve (due to its magnetic polarizability) an induced magnetic moment $\tilde{\mu}[B]$, as discussed for the η -meson case in [3].

In such picture, virtual quark-antiquark pairs and scalar diquarks are swimming in a deconfined QCD medium (the "bag") containing also gluons and strong magnetic field.

Let us estimate the strength of hyperfine magnetic field inside baryons: Since the source of the magnetic dipole field is localized inside the hadronic "bag" volume, we shall assume, that dipole magnetic moment $\mu = c_1 \cdot \mu_N$ of baryon comes from the fictious current loop of radius $R_B = r_o [10^{-15} \text{m}]$ (for proton $c_1 = 2.79$, for Λ hyperon $c_1 = -0.61$). One has

$$\mu = I \cdot S = I \cdot \pi R_B^2 \quad \longrightarrow \quad I = (c_1 / \pi r_o^2) \mu_N 10^{30} \approx 5 (c_1 / \pi r_o^2) 10^3 A \quad (2)$$

using $\mu_N = 5 \cdot 10^{-27} \text{ J/T}$. Magnetic field B_{int} at the center of such current loop is

$$B_{int} = \mu_o I / 2 R_B \quad \longrightarrow \quad B_{int} \approx (2 c_1 / r_o^3) 10^{12} T, \quad (3)$$

if magnetic permeability $\mu_o = 4\pi \cdot 10^{-7} \text{ NA}^{-2}$ of vacuum is used. For Λ^0 hyperon we then obtain internal magnetic field $B_{int}^\Lambda \approx 4 \cdot 10^{12} \text{ T}$ (assuming $r_o = 0.67 \text{ [fm]}$), and for proton $B_{int}^p \approx 10^{13} \text{ Tesla}$, assuming fictious current loop radius $r_o = 0.82 \text{ [fm]}$.

4 Scalar diquarks in the magnetic field

External and intrinsic magnetic field of baryons can influence quantum state of scalar diquarks via interaction term: $H_{int} = -\vec{\mu}_q \cdot \vec{B}$. Similarly to the case of Positronium and Muonium, spin-singlet state $\tilde{\Psi}^S[B]$ becomes a quantum superposition of triplet and singlet states [4], and induced magnetic moment [6] of scalar (ud) diquark appears

$$\tilde{\Psi}^S[B] = \frac{c_\alpha - s_\alpha}{\sqrt{2}} |\uparrow\downarrow\rangle - \frac{c_\alpha + s_\alpha}{\sqrt{2}} |\downarrow\uparrow\rangle; \quad \langle \tilde{\Psi}^S | \hat{\mu} | \tilde{\Psi}^S \rangle = (|\mu_u| + |\mu_d|) \sin(2\alpha) = \Delta\mu \quad (4)$$

where $s_\alpha = \sin(\alpha) = y / \sqrt{1 + y^2}$, $c_\alpha = \cos(\alpha) = \sqrt{1 - s_\alpha^2}$, and $y = x / (1 + \sqrt{1 + x^2})$ depends on magnetic field B via parameter $x = 2(|\mu_u| + |\mu_d|)B / \Delta E_{hf}$. Hyperfine splitting ΔE_{hf} is $(M_\Lambda - M_\Sigma) = 77 \text{ MeV}$ for Λ^0 hyperon, and 166 MeV and 194 MeV for Λ_c^+ and Λ_b hyperons. In the limit $B \rightarrow \infty$, $\alpha = 45^\circ$, and scalar diquark becomes fully polarized $\tilde{\Psi}^S = -|\downarrow\uparrow\rangle$ in its ($J=0$) state: quark magnetic moments become oriented along field \vec{B} direction, while their spins are anti-parallel. In such extreme case, polarized quark distribution functions $\Delta u(x)$ and $\Delta d(x)$ of Λ^0 baryon are substantially affected.

Induced magnetic moment $\Delta\mu$ of scalar diquark should contribute to the magnetic moment of Λ^0 hyperon, as pointed out already by Franklin et al. [10]. In the limiting case $\Delta\mu \rightarrow |\mu_u| + |\mu_d| = 2.8\mu_N$. For our intrinsic magnetic field $B = 4 \cdot 10^{12} \text{ T}$ in Λ^0 hyperon: $\sin(2\alpha) \approx x = 2(|\mu_u| + |\mu_d|)B / \Delta E_{hf} = 0.0091$ and $\Delta\mu = 0.026\mu_N$, which is 4% of μ_Λ . Here, we did not take into account the full wave function $\Psi_{1/2}^T$ of Σ baryon (see Eq.1), which contains term $(\uparrow\downarrow + \downarrow\uparrow)\sqrt{2}$ with probability $(1/\sqrt{3})^2$. Magnetic polarizability of scalar (us) and (ds) diquarks in Ξ_c hyperons originates from the same mechanism: the superposition of Ψ^S with Ψ^T triplet state of Ξ_c' hyperons (they correspond to Σ^0). Due to different quark magnetic moment orientation relative to quark spin in (us) and (ds) diquarks, magnetic polarizability $\beta_0 = 2\langle \Psi^S | \hat{\mu}_{ds} | \Psi^T \rangle^2 / \Delta E_{hf}$ of (ds) diquark is expected to be much smaller compared to (us) and (ud) diquarks (see Eq.10 and Eq.11 in [2]).

The interaction of color-magnetic dipole moments of quarks induces additional hyperfine mixing [8, 10] of wave functions Ψ^T and Ψ^S , which is independent from purely electromagnetic effects we study here.

5 Virtual $s\bar{s}$ pairs polarization in nucleon

Similarly to virtual e^+e^- pairs, which contribute to anomalous magnetic moments of electron and muon, virtual $(s\bar{s})$ pairs can influence nucleon properties. Various experimental results suggest, that $(s\bar{s})$ quark pairs in nucleon are polarized: $\Delta s = -0.1 \pm 0.02$ [11].

Let us assume here, that intrinsic magnetic field $B_{int} \approx 10^{13}\text{T}$ in nucleon affects quantum state of virtual $(s\bar{s})$ pairs. Inside the hadronic bag, without any external fields, virtual $s\bar{s}$ pairs would appear in pure $J=0^{+-}$ singlet state $\Psi^S = (\uparrow\downarrow - \downarrow\uparrow)/\sqrt{2}$, or in $J=1^{--}$ triplet state. Due to its smaller energy, pseudoscalar configuration Ψ^S should be more probable. If internal magnetic field $B_{int} \approx 10^{13}\text{T}$ in nucleon modifies the wave function $\tilde{\Psi}^S[B]$ of scalar $s\bar{s}$ pairs as described by Eq.(4), induced magnetic moment of $J=0$ $(s\bar{s})$ pairs appears: $\langle \hat{\mu} \rangle_{s\bar{s}} = 2|\mu_s| \sin(2\alpha)$, which may contribute to the nucleon magnetic moment. At the same time, net polarization of virtual s quarks occurs.

6 Conclusions

We have discussed that quantum state of scalar diquarks in Λ^0 - type hyperons can be influenced by internal and external magnetic fields. Our estimate of the intrinsic (hyperfine) magnetic field for Λ^0 hyperon is $B_{int} = 4 \cdot 10^{12}\text{T}$. We suggest, that polarized quark distribution functions $\Delta q(x)$ of Λ^0 - type hyperons can be modified due to polarization of scalar (ud) diquark in strong electromagnetic field, which may be remotely related to EMC effect. We also suggest, that virtual $s\bar{s}$ pairs in nucleon are effectively polarized due to the intrinsic magnetic field of nucleon $B_{int} \approx 10^{13}\text{T}$.

Acknowledgement: This work is supported by Slovak Grant Agency VEGA (2/0197/14).

References

- [1] M. Gell-Mann, Phys. Lett. **8** (1964) 214; G. Zweig, CERN Report No.8419/TH.412.
- [2] P. Filip, Nuclear Physics - Proceedings Supplements **B245** (2013) 251.
- [3] P. Filip, Physics of Particles and Nuclei **45** (2014) 7.
- [4] O. Halpern, Phys. Rev. **94** (1954) 904; A. Rich, Rev. Mod. Phys. **53** (1981) 127.
- [5] V.W. Hughes, S. Marder, C.S. Wu, Phys. Rev. **98** (1955) 1840.
- [6] P. Filip, Proceedings of Science (CPOD 2013) 035, in Proc. of 8th Int. Workshop on Critical Point and Onset of Deconfinement, March 11-15, 2013, California, USA.
- [7] M. Anselmino et al, Rev. Mod. Phys. **65** (1993) 1199.
- [8] J. Franklin, Phys. Rev. **172** (1968) 1807; N. Isgur, Phys. Rev. **D21** (1980) 779.
- [9] A. Chodos, V.F. Weisskopf et al., Phys. Rev. **D9** (1974) 3471.
- [10] J. Franklin, Phys. Rev. **D24** (1981) 2910; *ibid* **D55** (1997) 425.
- [11] M.G. Shaposhnikov, Nucl. Phys. **A692** (2001) 63c.

ROLE OF TRANSVERSITY IN SPIN EFFECTS IN MESON LEPTOPRODUCTION.

S.V. Goloskokov[†]

*Bogoliubov Laboratory of Theoretical Physics, Joint Institute for Nuclear Research, Dubna
141980, Moscow region, Russia*

[†] *E-mail: goloskkv@theor.jinr.ru*

Abstract

We analyze the light meson leptonproduction within the handbag approach. We show that effects determined by the transversity Generalized Parton Distributions (GPDs), H_T and \bar{E}_T are essential in the description of pseudoscalar and vector meson leptonproduction.

1 Introduction

In our papers [1], we calculated the processes of light meson leptonproduction within the handbag approach, where the amplitudes factorize into hard subprocesses and in (GPDs) [2] which encode soft physics. The modified perturbative approach [3], where the quark transverse degrees of freedom accompanied by Sudakov suppressions are taken into account, was used to calculate the hard subprocess amplitudes. We discuss some details of this approach for vector meson (VM) production in section 2.

The pseudoscalar meson (PM) production was analyzed in [4, 5]. It was found that the transversity GPDs H_T and \bar{E}_T are essential in the description of these reactions at low Q^2 . Within the handbag approach the transversity GPDs are accompanied by twist-3 meson distribution amplitudes. These transversity contributions provide large transverse cross sections for most of the pseudoscalar meson channels [5] (see section 3)

The role of transversity GPDs in the VM leptonproduction [6] is discussed in section 4. The importance of the transversity GPDs was examined in the Spin Density Matrix Elements (SDMEs) and in asymmetries measured with a transversely polarized target. For the transversity GPDs H_T and \bar{E}_T we used the same parameterizations as in our study of the PM leptonproduction. Our results for SDMEs are in good agreement with HERMES experimental data on the ρ^0 production. We also estimated the moments of transverse target spin asymmetries A_{UT} which contain the transversity contributions. The $A_{UT}^{\sin(\phi_s)}$ asymmetry is found to be not small [6] at COMPASS energies.

2 Meson leptonproduction and handbag approach

The amplitude of meson leptonproduction at large Q^2 is assumed to factorize [2] into a hard subprocess amplitude \mathcal{H} and a soft proton matrix element, parameterized in terms of GPDs $F(\bar{x}, \xi, t)$, $E(\bar{x}, \xi, t)$, ...

The proton non-flip and spin-flip amplitude can be expressed in terms of gluons, quarks or sea contributions

$$\mathcal{M}_{\mu'+,\mu+} \propto \int_{-1}^1 dx \mathcal{H}_{\mu'+,\mu+}^a F^a(x, \xi, t), \quad \mathcal{M}_{\mu'-,\mu+} \propto \frac{\sqrt{-t}}{2m} \int_{-1}^1 dx \mathcal{H}'_{\mu'+,\mu+}^a E^a(x, \xi, t). \quad (1)$$

The subprocess amplitude is calculated within the MPA [3]. The amplitude \mathcal{H}^a is a contraction of the hard part \mathcal{F}^a which includes the transverse quark momentum \mathbf{k}_\perp in the propagators and the nonperturbative meson wave function $\Psi(\mathbf{k}_\perp)$ [7]. The gluonic corrections are treated in the form of the Sudakov factors. The resummation and exponentiation of the Sudakov corrections S can be performed in the impact parameter space \mathbf{b} [3], and the amplitude reads as

$$\mathcal{H}_{0\lambda,0\lambda}^a \propto \int d\tau d^2b \Psi(\tau, -\mathbf{b}) \mathcal{F}_{0\lambda,0\lambda}^a(\bar{x}, \xi, \tau, Q^2, \mathbf{b},) \alpha_s \exp[-S(\tau, \mathbf{b}, Q^2)].$$

Here τ is the momentum fraction of the quark that enters into the meson.

The GPDs contain extensive information about the hadron structure. Hadron form factors and parton angular momenta can be related with GPDs. At zero skewness ξ and momentum transfer GPDs are equal to ordinary PDFs

$$F^a(x, 0, 0) = f^a(x), \quad E^a(x, 0, 0) = e^a(x). \quad (2)$$

Here quarks (valence and sea) and gluon PDFs f^a are determined from CTEQ6 parameterization [8]. The PDFs e^a are taken from the Pauli form factor [9].

The GPDs are estimated using the double distribution representation [10] which connects GPDs with PDFs through the double distribution function ω . For the valence quark contribution it looks like

$$\omega_i(x, y, t) = h_i(x, t) \frac{3}{4} \frac{[(1-|x|)^2 - y^2]}{(1-|x|)^3}. \quad (3)$$

The functions h are determined in the terms of PDFs and parameterized in the form

$$h(x, t) = N e^{bot} x^{-\alpha(t)} (1-x)^n. \quad (4)$$

Here the t -dependence is considered in a Regge form and $\alpha(t)$ is the corresponding Regge trajectory. The parameters in (4) are obtained from the known information about PDFs e.g, [8, 9].

The handbag approach was successfully applied to light meson leptonproduction [1]. In Fig.1, we show our results for Q^2 and W dependencies of the ρ leptonproduction which are in good agreement with experimental data. It can be seen in Fig. 1, (left) that the leading twist results do not reproduce data at low Q^2 . The power k_\perp^2/Q^2 corrections in the propagators of hard subprocess amplitude are important in the description of the data. Corrections can be regarded as effective consideration of the higher twist effects. From Fig 1 (right) we see that the model describes the ρ meson leptonproduction quite well for $W > 4\text{GeV}$. The rapid growth of the cross section at lower energies has not been understood within the handbag model till now.

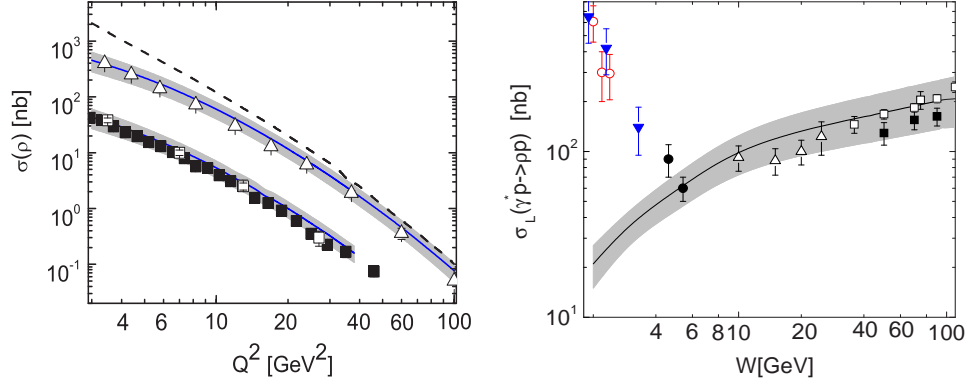


Figure 1: Left: Cross sections of the ρ production at $W = 75\text{GeV}/10$ and $W = 90\text{GeV}$. Dashed line: leading twist results. Right: The longitudinal cross section for the ρ^0 production at $Q^2 = 4.0\text{GeV}^2$. References to experimental data can be found in [1]

3 Transversity in pseudoscalar mesons production

Exclusive electroproduction of PM was studied within the handbag approach [4, 5]. It was shown that the asymptotically dominant leading-twist contributions, which are determined by the GPDs \tilde{H} and \tilde{E} , are not sufficient to describe the experimental results on electroproduction of PM at low Q^2 . It can be seen, for example, from $A_{UT}^{\sin(\phi_s)}$ asymmetry

$$A_{UT}^{\sin(\phi_s)} \propto \text{Im}[M_{0-,++}^* M_{0+,0+}]. \quad (5)$$

This asymmetry was found to be small in the handbag model based on the leading twist amplitudes. This result is inconsistent with the data where $A_{UT}^{\sin(\phi_s)} \sim 0.5$.

A new twist-3 contribution to the $M_{0-,++}$ amplitude, which is not small at $t' \sim 0$, is needed to understand the data. The inclusion in our consideration of the $M_{0+,++}$ amplitude which has a similar twist-3 nature is also extremely important to explain the PM production at low Q^2 . We estimate these contributions by the transversity GPD H_T , \bar{E}_T in conjugation with the twist-3 pion wave function in the hard subprocess amplitude $\mathcal{H}_{0-, \mu+}$ [5]

$$\mathcal{M}_{0-, \mu+}^{M, tw-3} \propto \int_{-1}^1 d\bar{x} \mathcal{H}_{0-, \mu+}(\bar{x}, \dots) H_T^M; \quad \mathcal{M}_{0+, \mu+}^{M, tw-3} \propto \frac{\sqrt{-t'}}{4m} \int_{-1}^1 d\bar{x} \mathcal{H}_{0-, \mu+}(\bar{x}, \dots) \bar{E}_T^M. \quad (6)$$

The H_T GPD is connected with transversity PDFs as

$$H_T^a(x, 0, 0) = \delta^a(x); \quad \text{and} \quad \delta^a(x) = C N_T^a x^{1/2} (1-x) [q_a(x) + \Delta q_a(x)]. \quad (7)$$

We parameterize the PDF δ (see [4, 5]) by using the model [11]. The double distribution (3) is used to calculate GPD H_T .

At the moment, the information on \bar{E}_T is very poor. Some results were obtained only in the lattice QCD [12]. The lower moments of \bar{E}_T^u and \bar{E}_T^d were found to be of the same sign, similar in size and quite large. At the same time, H_T^u and H_T^d have different signs. These properties of GPDs provide essential compensation of the \bar{E}_T contribution in the π^+ amplitude, but H_T effects are not small there. For the π^0 production we have the opposite case – the \bar{E}_T contributions are large and the H_T effects are small.

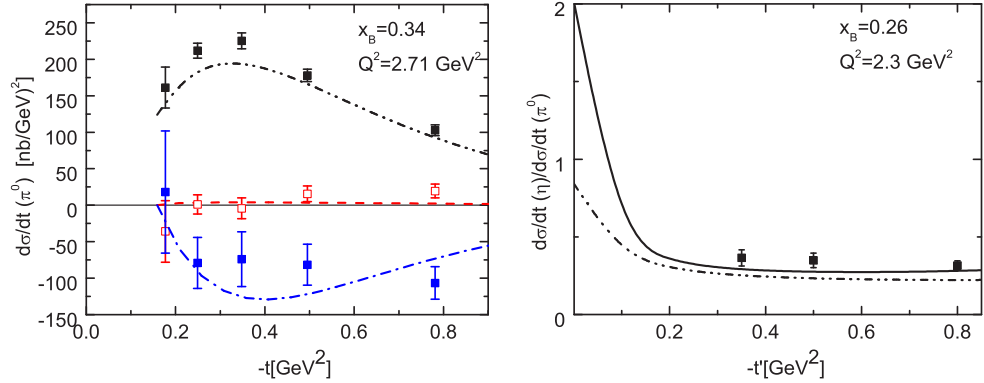


Figure 2: Left: π^0 production in the CLAS energy range together with the data [14]. Dashed-dot-dotted line- $\sigma = \sigma_T + \epsilon\sigma_L$, dashed line- σ_{LT} , dashed-dotted- σ_{TT} . Right: η/π^0 production ratio in the CLAS energy range together with preliminary data [15].

In Fig. 2 (left), we present our results for the cross section of the π^0 production. The transverse cross section where the \bar{E}_T and H_T contributions are important [4] dominates. At small momentum transfer the H_T contribution is visible and provides a nonzero cross section. At $-t' \sim 0.2\text{GeV}^2$ the \bar{E}_T contribution becomes essential and gives a maximum in the cross section. A similar contribution from \bar{E}_T is observed in the interference cross section σ_{TT} . The fact that we describe well both unseparated σ and σ_{TT} cross sections can indicate that transversity effects were probably observed in CLAS [14]. In Fig. 2 (right), we show the η and π^0 cross section ratio obtained in the model (for details see [5]). At small momentum transfer this ratio is controlled by the H_T contribution. At larger $-t'$ the E_T contributions become important. The value about $1/3$ for the cross section ratio in the momentum transfer $-t' > 0.2\text{GeV}^2$ is a consequence of the flavor structure of the η and π^0 amplitudes. This result was confirmed by the preliminary CLAS data [15].

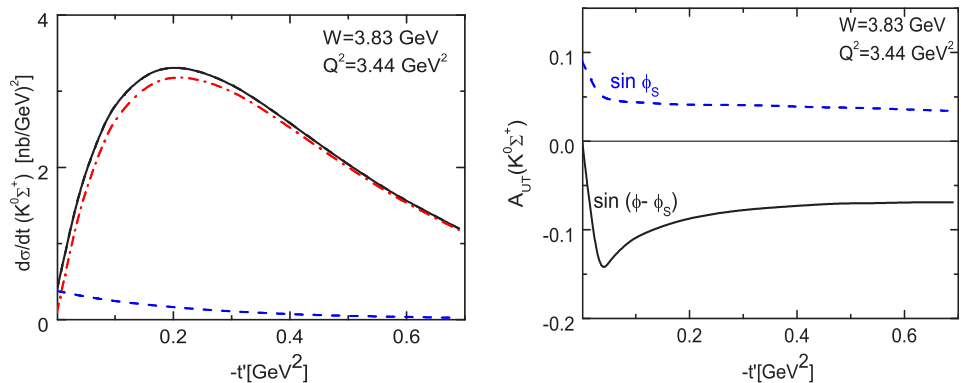


Figure 3: Left: Cross sections of the $K^0\Sigma^+$ production at HERMES energies. Right: Predicted moments of A_{UT} asymmetries for the $K^0\Sigma^+$ channel at HERMES.

A similar essential transversity E_T contribution is observed in the kaon production. An example of our results for the $K^0\Sigma^+$ cross section is shown in Fig. 3 (left). As in the π^0 production, we find here a dip near $-t' = 0$. It was found that the longitudinal cross

section σ_L , which is expected to play an important role, is much smaller with respect to the transverse cross section σ_T at low Q^2 - see Fig 3 (left). At sufficiently large Q^2 the leading-twist σ_L contribution will dominate because transversity twist-3 effects, which contribute to σ_T , decrease quickly with Q^2 growing. The same result was found in the π^0 production [16]. The predicted asymmetries in $K^0\Sigma^+$ channel are shown in Fig. 3 (right).

4 Transversity in vector mesons production

Now we extend our analysis of transversity effects to the VM production [6]. Transversity will be essential in the amplitudes with a transversely polarized photon and a longitudinally polarized vector meson. The twist-3 amplitudes have a form of (6) where the transversity GPDs occur in combination with twist-3 meson wave functions. The asymptotic form for the twist-3 chiral-odd DA $h_{||V}^{(s)} = 6\tau(1 - \tau)$ is used.

Note that the transversity contribution in the VM production contains the parameter $m_V = 0.77\text{GeV}$ instead of $\mu_\pi = 2\text{GeV}$ for PM production [6]. As a result, the transversity contribution to the VM amplitudes is parametrically about 3 times smaller with respect to PM case. In calculation of the amplitude we use the same parameterizations for transversity GPDs H_T and \bar{E}_T which was obtained in our study of the PM leptonproduction in the section 3.

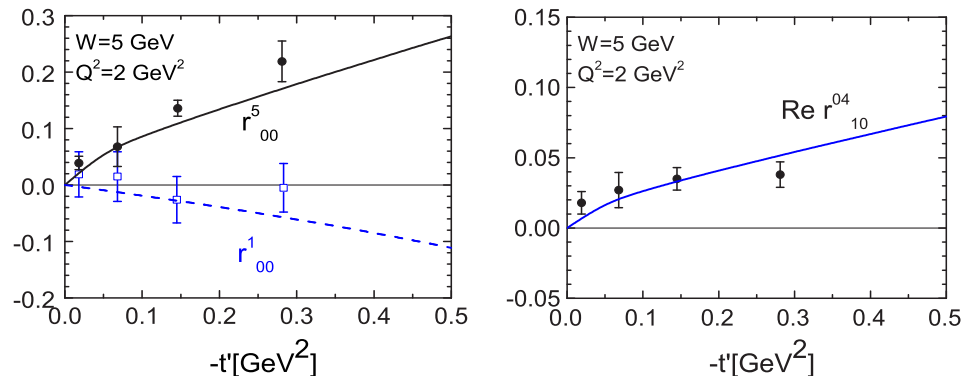


Figure 4: Transversity effects at SDMEs at $W = 5$ GeV together with HERMES data [17].

The importance of the transversity GPDs was examined in the SDMEs and in asymmetries measured with a transversely polarized target. The $M_{0+,++} = \langle \bar{E}_T \rangle$ amplitude is essential in some SDMEs. Really,

$$r_{00}^5 \sim \text{Re}[M_{0+,0+}^* M_{0+,++}]; \quad r_{00}^1 \sim -|M_{0+,++}|^2; \quad r_{10}^{04} \sim \text{Re}[M_{+,++}^* M_{0+,++}]. \quad (8)$$

Our results for these the SDMEs in the ρ^0 meson production at HERMES are shown in Fig. 4. These values and signs are in good agreement with HERMES experimental data [17]. We observe that large \bar{E}_T effects found in the π^0 channel are compatible with SDME of the ρ production at HERMES energies.

In Fig. 5, we show our results for the $\sin(\phi - \phi_s)$ moment of the A_{UT} asymmetry

$$A_{UT}^{\sin(\phi - \phi_s)} \sim \text{Im}[M_{0-,0+}^* M_{0+,0+} - M_{0-,++}^* M_{0+,++}] \quad (9)$$

at HERMES and COMPASS energies. This asymmetry is determined essentially by interference of the $\langle \bar{E} \rangle$ and $\langle F \rangle$ contributions (1) and is consistent with the data. The effects of transversity are quite small here.

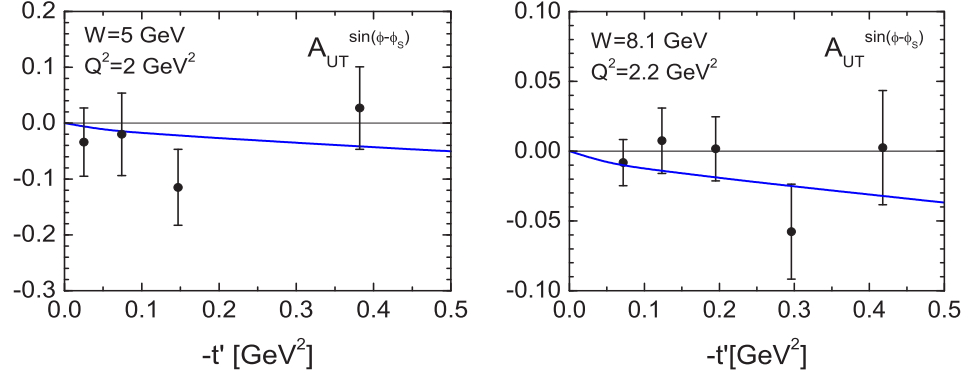


Figure 5: Model results for the $A_{UT}^{\sin(\phi-\phi_s)}$ asymmetry. Left: at HERMES. Right: at COMPASS energy. Data are from [18, 19].

The $\sin(\phi_s)$ moment of the A_{UT} asymmetry is determined by the H_T GPDs.

$$A_{UT}^{\sin(\phi_s)} \sim \text{Im}[M_{0-,++}^* M_{0+,0+}]; \quad M_{0-,++} = \langle H_T \rangle \quad (10)$$

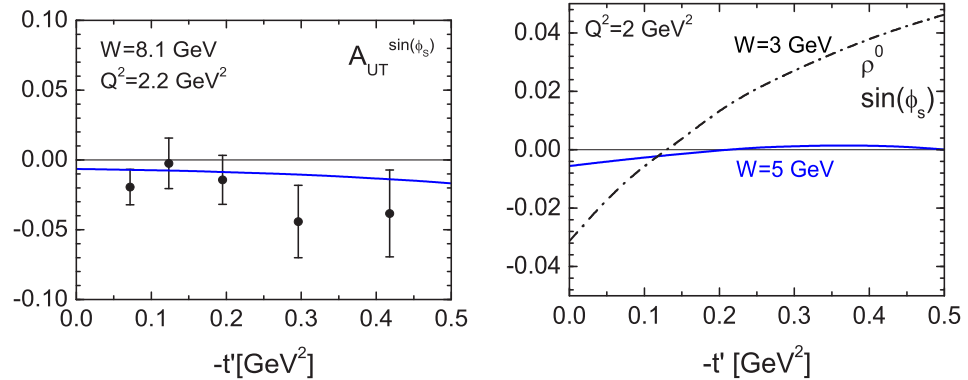


Figure 6: Left: $A_{UT}^{\sin(\phi_s)}$ asymmetry as COMPASS. Data are from [19]. Right: Predicted $A_{UT}^{\sin(\phi_s)}$ asymmetry at HERMES and CLAS energies.

This asymmetry is found to be not small at COMPASS [6] and compatible with the data [19] Fig 6 (left). The energy dependence of $A_{UT}^{\sin(\phi_s)}$ from CLAS to HERMES is quite rapid and shown in Fig. 6 (right). This prediction can be verified in a future CLAS experiment to test the x -dependence of GPDs H_T .

In Fig.7, we show the Q^2 dependencies of $A_{UT}^{\sin(\phi_s)}$ and $A_{LT}^{\cos(\phi_s)}$ which is determined by a similar to (10) equation only with the replacement of the imaginary to the real part there. The model results are close to experimental data.

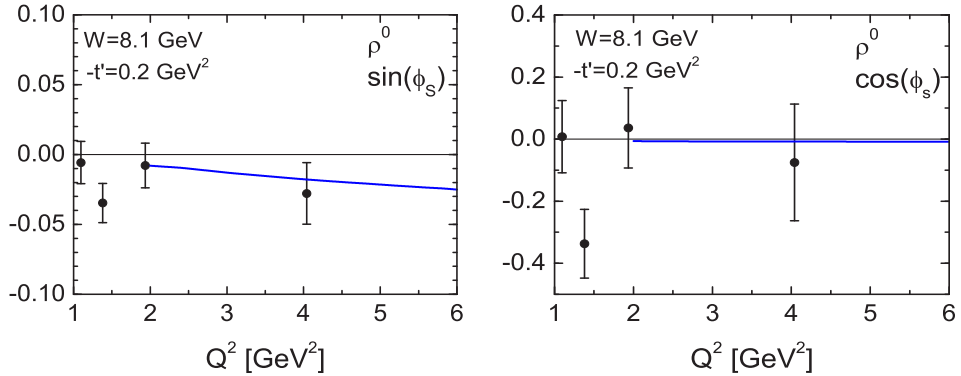


Figure 7: Q^2 dependences of Left: $A_{UT}^{\sin(\phi_s)}$ asymmetry. Right: $A_{LT}^{\cos(\phi_s)}$ asymmetry at COMPASS together with data [19].

5 Conclusion

The handbag approach, where the amplitudes factorize into the hard subprocesses and GPDs [2], was successfully applied to light meson production. The results based on this approach on cross sections and various spin observables were found to be in good agreement with data at HERMES, COMPASS and HERA energies at high Q^2 [1].

At the leading-twist accuracy the PM production is only sensitive to the GPDs \tilde{H} and \tilde{E} which contribute to the amplitudes for longitudinally polarized virtual photons. It was found that the leading twist contributions are not sufficient to describe spin observables in PM production at sufficiently low photon virtualities Q^2 . We observe that the experimental data on the PM leptonproduction also require contributions from the transversity GPDs from H_T and \bar{E}_T . Within the handbag approach the transversity GPDs are accompanied by twist-3 meson distribution amplitudes. These transversity contributions provide large transverse cross sections for most of the pseudoscalar meson channels [5]. There is some indication that large transversity effects are available now at CLASS [14]. Thus, the transversity GPDs are extremely essential in understanding spin effects in the PM production.

The role of transversity GPDs in the VM leptonproduction was investigated within the handbag approach [6]. The transversity GPDs in combination with twist-3 meson wave functions occur in the amplitudes with the transversely polarized virtual photon and a longitudinal polarized vector meson. The importance of the transversity GPDs was examined in the SDMEs and in asymmetries measured with a transversely polarized target. The SDMEs for the light VM production were found to be in good agreement with HERMES experimental data on the ρ^0 production [17]. We also estimated the $A_{UT}^{\sin(\phi-\phi_s)}$ transverse target spin asymmetry [6]. The results are consistent with HERMES and COMPASS data [18, 19]. The $A_{UT}^{\sin(\phi_s)}$ asymmetry is found in the model to be not small at COMPASS [6] and also compatible with the data [19]. Our predictions were compared with the COMPASS experimental data in the COMPASS paper [19].

We described well the cross section and spin observables for various meson productions. Thus, we can conclude that the information on GPDs discussed above should not be far from reality. Future experimental results at COMPASS, JLAB12 can give important

information on the role of transversity effects in these reactions.

This work is supported in part by the Russian Foundation for Basic Research, Grant 12-02-00613 and by the Heisenberg-Landau program.

References

- [1] S.V. Goloskokov, P. Kroll, Euro. Phys. J. **C42**, 281-301 (2005); *ibid* **C50** 829, (2007); *ibid* **C53** 367, (2008); *ibid* **C59**, 809-819 (2009).
- [2] X. Ji, Phys. Rev. **D55**, (1997) 7114;
A.V. Radyushkin, Phys. Lett. **B380**, (1996) 417;
J.C. Collins, et al., Phys. Rev. **D56**, (1997) 2982.
- [3] J. Botts and G. Sterman, Nucl. Phys. **B325**, (1989) 62.
- [4] S.V. Goloskokov, P. Kroll, Euro. Phys. J. **C65**, (2010) 137.
- [5] S.V. Goloskokov, P. Kroll, Euro. Phys. J. **A47**, (2011) 112.
- [6] S.V. Goloskokov, P. Kroll, arXiv: 1310.1472 [hep-ph] (2013).
- [7] R. Jakob, P. Kroll, Phys. Lett. **B315**, (1993) 463;
J. Bolz, J.G. Körner, P. Kroll, Z. Phys. **A350**, (1994) 145.
- [8] J. Pumplin, et al., JHEP **0207**, (2002) 012.
- [9] M. Diehl, T. Feldmann, R. Jakob and P. Kroll, Euro. Phys. J. **C39**, (2005) 1.
- [10] I.V. Musatov and A.V. Radyushkin, Phys. Rev. **D61**, (2000) 074027.
- [11] M. Anselmino, M. Boglione, U. D'Alesio, A. Kotzinian, F. Murgia, A. Prokudin and S. Melis, Nucl. Phys. Proc. Suppl. **191**, (2009) 98.
- [12] M. Gockeler *et al.* [QCDSF Collaboration and UKQCD Collaboration], Phys. Rev. Lett. **98**, (2007) 222001.
- [13] L. L. Frankfurt, P. V. Pobylitsa, M. V. Polyakov and M. Strikman, Phys. Rev. **D60**, (1999) 014010.
- [14] I. Bedlinskiy, et al. (CLAS Collaboration) Phys. Rev. Lett. **109**, (2012) 112001.
- [15] V. Kubarovsky et al., Proc. of DSPIN-11, Dubna, September 2011, p. 258.
- [16] S.V. Goloskokov. Proc. of DSPIN-11, Dubna, September 2011, p. 71.
- [17] A. Airapetian et al. (HERMES Collab.), Euro. Phys. J. **C62**, (2009) 659.
- [18] A. Rostomyan et al. (HERMES Collab.), arXiv: 0707.2486 [hep-ex].
- [19] C. Adolph, et al. (COMPASS Collaboration) arXiv: 1310.1454 [hep-ex] (2013).

ON ENERGY-MOMENTUM AND SPIN/HELICITY OF QUARK AND GLUON FIELDS

Friedrich W. Hehl^{1,†}

(1) *Institute for Theoretical Physics, University of Cologne, 50923 Köln, Germany
and Dept. of Physics & Astronomy, University of Missouri, Columbia, MO 65211, USA*

† *E-mail: hehl@thp.uni-koeln.de*

Abstract

In special relativity, quantum matter can be classified according to mass-energy and spin. The corresponding field-theoretical notions are the *energy-momentum-stress* tensor \mathfrak{T} and the *spin* angular momentum tensor \mathfrak{S} . Since each object in physics carries energy and, if fermionic, also spin, the notions of \mathfrak{T} and \mathfrak{S} can be spotted in all domains of physics. We discuss the \mathfrak{T} and \mathfrak{S} currents in Special Relativity (SR), in General Relativity (GR), and in the Einstein-Cartan theory of gravity (EC). We collect our results in 4 theses: (i) The quark energy-momentum and the quark spin are described correctly by the canonical (Noether) currents \mathfrak{T} and \mathfrak{S} , respectively. (ii) The gluon energy-momentum current is described correctly by the (symmetric and gauge invariant) Minkowski type current. Its (Lorentz) spin current vanishes, $\mathfrak{S} = 0$. However, it carries helicity of plus or minus one. (iii) GR contradicts thesis (i), but is compatible with thesis (ii). (iv) Within the viable EC-theory, our theses (i) and (ii) are fulfilled and, thus, we favor this gravitational theory.

1. Introduction. The *nucleon spin* and how it is built up in terms of spin and orbital angular momentum contributions of the quark and gluon fields is still under discussion. Recently, in this context, the problem has been addressed of the appropriate energy-momentum and spin tensors of quark and gluon fields, see the review paper of Leader and Lorcé [1]. They emphasize the importance of the splitting of the angular momentum of the gluon field into orbital and spin parts. However, since the energy-momentum and angular momentum distributions of a field are interrelated via the *orbital* angular momentum, the angular momentum question can only be answered if the energy-momentum distribution is treated at the same time. This is an expression of the *semi*-direct product structure of the Poincaré group $P(1,3) := T(4) \rtimes SO(1,3)$; here $T(4)$ denotes the translation group and $SO(1,3)$ the Lorentz group.

These facts are, of course, recognized by Leader and Lorcé [1] perfectly well, as can be seen by their discussion of the so-called Belinfante and the canonical energy-momentum tensors of both, the gluon and the quark fields. Even though they mention general relativity (GR) in this context, their main arguments are taken from special-relativistic quantum field theory. On the other side it is known—we only remind of Weyl’s verdict [2] that only “*the process of variation to be applied to the metrical structure of the world, leads to a true definition of the energy*” of matter—that an appropriate gravitational theory is obligatory in order to get a clear insight into the energy-momentum distribution of matter.

Why is this true? In Newton's gravitational theory the mass density of matter is the source of gravity; in GR, by an appropriate generalization, it is the (symmetric) Hilbert energy-momentum tensor ${}^{\text{Hi}}\mathbf{t}_{ij}$, which is computed by variation of the matter Lagrangian \mathcal{L} with respect to the metric tensor g_{ij} , namely ${}^{\text{Hi}}\mathbf{t}_{ij} := 2\delta\mathcal{L}/\delta g^{ij}$. Consequently, we have to assume that the energy-momentum distribution is, in the classical limit, a measurable quantity and that this localized energy-momentum distribution, with its 10 components, is the source of the gravitational field. *As long as we subscribe to GR*, the Hilbert energy-momentum tensor is the only viable energy-momentum tensor of matter, a fact that is put into doubt by Leader and Lorcé.¹

Teryaev [3] already pointed out that the energy-momentum tensor of matter will play a decisive role at the interface between quantum chromodynamics (QCD) and gravity, see also [16]. He discussed the gravitational moments of Dirac particles, as done earlier by Kobzarev and Okun [5] and by Hehl et al. [6].

Let us recall the eminent importance of the Poincaré group. Wigner's mass-spin classification of elementary (or fundamental) particles [7] is at the basis of the standard model of particle physics, the quark and the gluon are particular examples of it. The mass-spin classification, by means of a scalar and a vector quantity, underlines the particle aspect of matter. The corresponding notions for elementary fields in classical field theory, are the energy-momentum current² and the spin current. Thus, the mass-spin classification of matter is mirrored on the field-theoretical side by the canonical (Noether) energy-momentum current $\mathfrak{T}_i{}^k$, with 4×4 components, and the canonical (Noether) spin current $\mathfrak{S}_{ij}{}^k = -\mathfrak{S}_{ji}{}^k$ with its 6×4 components. The relation of the Hilbert and the Noether energy-momentum currents will be discussed further down.

On the gravitational side, some developments took place that are not without implications for the understanding of the energy-momentum and the spin distribution of matter fields, see also the thermodynamic considerations of Becattini & Tinti [8]. GR got a competitor in the Einstein-Cartan(-Sciama-Kibble) theory of gravitation (EC) or, more generally, in the Poincaré gauge theory of gravitation (PG). A short outline and the classical papers of the subject can be found in Blagojević and Hehl [9], see also the review paper [10].

The EC is a viable gravitational theory that can be distinguished from GR at very high densities or at very small distances occurring in early cosmology. The critical distance is $\ell_{\text{EC}} \approx (\lambda_{\text{Co}}\ell_{\text{Pl}}^2)^{1/3}$, with the Compton wave length λ_{Co} of the particle involved, about 10^{-26} cm for the nucleon, and the Planck length $\ell_{\text{Pl}} \approx 10^{-33}$ cm. Mukhanov [11] has argued the the data of the Planck satellite support GR up to distances of the order of 10^{-27} cm, that is, the same order of magnitude where the deviations of EC are supposed to set in.

The EC-theory is a simple case of a PG-theory. The PG-theory is formulated in a Riemann-Cartan (RC) spacetime with torsion $C_{ij}{}^k (= -C_{ji}{}^k)$ and curvature $R_{ij}{}^{kl} (= -R_{ji}{}^{kl} = -R_{ij}{}^{lk})$. The gravitational Lagrangian of PG-theory is, in general, quadratic in the field strengths torsion and curvature. EC-theory is the simplest case, when the Lagrangian, apart from the cosmological term, consists only of a linear curvature piece $\sim R_{ij}{}^{ji}$ (summation!), the Riemann-Cartan generalization of the Hilbert-Einstein La-

¹“...we feel that the fundamental versions are the canonical and the Belinfante ones, since they involve at least local fields...”, see [1], page 92.

²We use, for energy-momentum and spin, the notions ‘tensor’ and ‘current’ synonymously.

grangian. Then, additionally to the gravitational effects of GR, we find a very weak spin-spin-contact interaction that is governed by Einstein’s gravitational constant. But what is more relevant in the present context is that in PG-theory—hence also in EC-theory—the source of the Newton-Einstein type gravity is the *canonical energy-momentum* and the source of a Yang-Mills type strong gravity the *canonical spin*.

However, one has to be careful in the details: Gauge field, like the electromagnetic or the gluon field, do *not* carry canonical (Lorentz) spin, but rather only *helicity*, see [12]. In this case, the canonical energy-momentum turns out to be what is conventionally called the symmetrized energy-momentum. This will be explained in detail. With these provisos in mind, we can state that the canonical tensors for energy-momentum and spin play the role of sources of gravity in the PG-theory. Here we have an interface between gravity and hadron physics as stressed by Teryaev [3].

2. Action principle, translational invariance. We consider classical matter field $\Psi(x)$ (scalar, Weyl, Dirac, Maxwell, Proca, Rarita-Schwinger, Fierz-Pauli etc.) in special relativity (SR). The Minkowski spacetime M_4 , with Cartesian coordinates x^i ($i, j, \dots = 0, 1, 2, 3$), carries a Lorentz metric $g_{ij} \stackrel{*}{=} o_{ij} := \text{diag}(+ - - -)$. An isolated material system with first order action $W_{\text{mat}} := \frac{1}{c} \int d\Omega \mathcal{L}(\Psi, \partial\Psi)$ (see [14, 13]) is invariant under 4 translations, $x'^i = x^i + a^i$. The Noether theorem and $\delta\mathcal{L}/\delta\Psi = 0$ yield the energy-momentum conservation in the form

$$\boxed{\partial_j \mathfrak{T}_i{}^j = 0}, \quad \underbrace{\mathfrak{T}_i{}^j}_{4 \times 4} := \frac{\partial \mathcal{L}}{\partial \partial_j \Psi} \partial_i \Psi - \mathcal{L} \delta_i^j, \quad (1)$$

with the canonical (Noether) energy-momentum tensor of type $\binom{1}{1}$, also called momentum current density. It is, in general, asymmetric and has 16 independent components.

With metric we can lower the upper index of $\mathfrak{T}_i{}^j$ and can decompose \mathfrak{T}_{ij} irreducibly with respect to the Lorentz group³ (here $\mathfrak{F}_{ij} := \mathfrak{T}_{(ij)} - \frac{1}{4}g_{ij}\mathfrak{T}_k{}^k$):

$$\begin{aligned} \mathfrak{T}_{ij} &= \mathfrak{F}_{ij} + \mathfrak{T}_{[ij]} + \frac{1}{4}g_{ij}\mathfrak{T}_k{}^k, \\ 16 &= 9(\text{sym.tracefree}) \oplus 6(\text{antisym.}) \oplus 1(\text{trace}). \end{aligned} \quad (2)$$

An ansatz for a simple classical fluid (“dust”) is

$$\underbrace{\mathfrak{T}_i{}^j}_{\text{mom. curr. d.}} = \underbrace{\mathbf{p}_i}_{\text{mom. d.}} \underbrace{u^j}_{\text{velocity}} \quad (\text{observe natural index positions}). \quad (3)$$

If the momentum density is transported in the direction of the velocity, $\mathbf{p}_i = \rho g_{ik} u^k$, with ρ as mass-energy density, then $\mathfrak{T}_{[ij]} = 0$. A bit more refined is the classical ideal (perfect, Euler) fluid, with p as pressure:

$$\mathfrak{T}_{ij} = (\rho + p)u_i u_j - p g_{ij}, \quad \mathfrak{T}_{[ij]} = 0, \quad \mathfrak{T}_k{}^k = \rho - 3p. \quad (4)$$

Superfluid ${}^3\text{He}$ in the A-phase is a spin fluid of the convective type, see Eq.(8) below. The angular momentum law, as formulated for the A-phase on p. 427 of Vollhardt & Wölfle [16], is a proof of this stipulation. This is an irrefutable result that asymmetric stress tensors do exist in nature, a fact doubted in many texts.

³The Bach parentheses are $(ij) := \frac{1}{2}\{ij + ji\}$, $[ij] := \frac{1}{2}\{ij - ji\}$, see Schouten [15].

The quark current, as spin 1/2 current, should be of a similar type as the superfluid ${}^3\text{He}$ in the A-phase. That is, the (physically correct) energy-momentum current of the quark field should be asymmetric and most probably the canonical (Noether) current \mathfrak{T}_i^j of Eq.(1).

In *electromagnetism*, only \mathfrak{X}_{ij} survives (9 components), since it is massless, that is, $\mathfrak{T}_k^k = 0$, and carries *helicity*, but no (Lorentz) spin, i.e., $\mathfrak{T}_{[ij]} = 0$. The analogous should be true for the gluon field, since, like the Maxwell (photon) field, it is a gauge field, see below for some more details.

From where did Einstein take the symmetry of the energy-momentum tensor? Einstein, in [17] on the pages 48 and 49, discussed the symmetry of the energy-momentum tensor of Maxwell's theory. Subsequently, on page 50, he argued: "*We can hardly avoid making the assumption that in all other cases, also, the space distribution of energy is given by a symmetrical tensor, $T_{\mu\nu}$, ...*" This is hardly a convincing argument if one recalls that the Maxwell field is massless. As we saw, the A-phase of ${}^3\text{He}$ contradicts Einstein's assumption. Asymmetric energy-momentum tensors are legitimate quantities in physics and, the symmetry of an energy-momentum tensor has to retire as a generally valid rule.

3. Lorentz invariance. Invariance under 3+3 infinitesimal Lorentz transformations, $x'^i = x^i + \omega^{ij}x_j$, with $\omega^{(ij)} = 0$, yields, via the Noether theorem and $\delta\mathcal{L}/\delta\Psi = 0$, angular momentum conservation,

$$\partial_k \left(\underbrace{\mathfrak{S}_{ij}^k}_{\text{spin}} + \underbrace{x_{[i}\mathfrak{T}_{j]}^k}_{\text{orb. angular mom.}} \right) = 0, \quad \underbrace{\mathfrak{S}_{ij}^k}_{6 \times 4} := -\frac{\partial\mathcal{L}}{\partial\partial_k\Psi} \underbrace{f_{ij}}_{\text{Lor. gen.}} \Psi = -\mathfrak{S}_{ji}^k. \quad (5)$$

The canonical (Noether) spin \mathfrak{S}_{ij}^k , the spin current density, is a tensor of type $(\frac{1}{2})$, plays a role in the interpretation of the Einstein-de Haas effect (1915). If we differentiate in (5)₁ the second term and apply $\partial_k\mathfrak{T}_i^k = 0$, then we find a form of angular momentum conservation that can be generalized to curved and contorted spacetimes (x^i is not a vector in general):

$$\partial_k (\mathfrak{S}^{ijk} + x^{[i}\mathfrak{T}^{j]k}) = 0 \quad \Longrightarrow \quad \boxed{\partial_k \mathfrak{S}^{ijk} - \mathfrak{T}^{[ij]} = 0}. \quad (6)$$

If $\mathfrak{S}^{ijk} = 0$, then $\mathfrak{T}^{[ij]} = 0$, that is, the energy-momentum tensor is symmetric, but not necessarily vice versa.

The irreducible decomposition of \mathfrak{S}^{ijk} , with the axial vector piece ${}^{\text{AX}}\mathfrak{S}_{ijk} := \mathfrak{S}_{[ijk]}$ and the vector piece ${}^{\text{VEC}}\mathfrak{S}_{ij}^k := \frac{2}{3}\mathfrak{S}_{[i|\ell}\delta_{|j]}^k$, reads:

$$\begin{aligned} \mathfrak{S}_{ij}^k &= \text{TEN}\mathfrak{S}_{ij}^k + \text{VEC}\mathfrak{S}_{ij}^k + \text{AX}\mathfrak{S}_{ij}^k, \\ 24 &= 16 \oplus 4 \oplus 4, \end{aligned} \quad (7)$$

The Weyssenhoff ansatz for a classical spin fluid is again of the convective type:

$$\underbrace{\mathfrak{T}_i^j}_{\text{mom. curr. d.}} = \underbrace{\mathbf{p}_i}_{\text{mom. d.}} \underbrace{u^j}_{\text{velocity}} \quad \text{and} \quad \underbrace{\mathfrak{S}_{ij}^k}_{\text{spin curr. d.}} = \underbrace{\mathfrak{s}_{ij}}_{\text{spin d.}} \underbrace{u^k}_{\text{velocity}} = -\mathfrak{S}_{ji}^k. \quad (8)$$

The momentum density \mathbf{p}_i is no longer proportional to the velocity, as it was in (3). Usually, the constraint $\mathfrak{s}_{ij}u^j = 0$ is assumed.

For the Dirac field, which cannot be described by a Wessenhoff ansatz, the spin current is totally antisymmetric, $\overset{D}{\mathfrak{S}}_{ijk} = \overset{D}{\mathfrak{S}}_{[ijk]}$. Thus, only the axial vector spin current survives, $\overset{AX}{\mathfrak{S}}_{ijk} \neq 0$. The Dirac field is highly symmetric. Accordingly, we can introduce the spin flux *vector*

$$\mathcal{S}^i := \frac{1}{3!} \epsilon^{ijkl} \mathfrak{S}_{jkl} \quad \sim \quad (\text{spin flux density 1 comp., spin density 3 comps.}). \quad (9)$$

The 3d spin flux density distribution is spatially isotropic.

4. Poincaré invariance. We collect our results: The Poincaré invariance of the action yields the 4 + 6 conservation laws,

$$\partial_k \mathfrak{T}_i^k = 0 \quad (\text{energy-momentum conservation}), \quad (10)$$

$$\partial_k \mathfrak{S}_{ij}^k - \mathfrak{T}_{[ij]} = 0 \quad (\text{angular momentum conservation}). \quad (11)$$

These field theoretical notions \mathfrak{T}_i^k and \mathfrak{S}_{ij}^k have their analogs in a the particle description of matter. The Lie algebra of the Poincaré group reads (see [18] for details, $\hbar = 1$):

$$\begin{aligned} [P_i, P_j] &= 0, \\ [J_{ij}, P_k] &= 2i g_{k[i} P_{j]} \quad (\text{transl. and Lorentz transf. mix, as in } \mathfrak{S}_{ijk} + x_{[i} \mathfrak{T}_{j]k}), \\ [J_{ij}, J_{kl}] &= 2i (g_{k[i} J_{j]l} - g_{l[i} J_{j]k}). \end{aligned} \quad (12)$$

We recognize its semidirect product structure, as it is manifest in the existence of orbital angular momentum. The “square roots” of the Casimir operators P^2 (mass square) and W^2 (spin square), with the Pauli-Lubański vector $W^i := \frac{1}{2} \epsilon^{ijkl} J_{jk} P_l$, correspond to \mathfrak{T}_i^k and \mathfrak{S}_{ij}^k .

5. Exterior calculus in a Riemann-Cartan (RC) space, the electromagnetic gluon energy-momentum, and the Dirac field. We introduce the generally covariant calculus of *exterior differential forms* that is valid not only in Minkowski space, but also in the RC-spacetime of the Poincaré gauge theory of gravity, see [19]. We work with an orthonormal coframe (tetrad) $\vartheta^\alpha = e_i^\alpha dx^i$ and a Lorentz connection $\Gamma^{\alpha\beta} = \Gamma_i^{\alpha\beta} dx^i = -\Gamma^{\beta\alpha}$; the fields are exterior forms (0-forms, 1-forms,..., 4-forms) with values in the algebra of some Lie group; the frame (or anholonomic) indices are in Greek, $\alpha, \beta, \dots = 0, 1, 2, 3$. The electromagnetic potential is a 1-form $A = A_i dx^i$, the field strength a 2-form $F := dA = \frac{1}{2} F_{ij} dx^i \wedge dx^j$, the exterior derivative is denoted by d , the gauge covariant exterior derivative is by D , for details see [20].

The matter currents translate from tensor to exterior calculus as follows: Energy-momentum 3-form $\mathfrak{T}_\alpha = \mathfrak{T}_\alpha^\gamma \star \vartheta_\gamma = \delta L_{\text{mat}} / \delta \vartheta^\alpha$, spin 3-form $\mathfrak{S}_{\alpha\beta} = \mathfrak{S}_{\alpha\beta}^\gamma \star \vartheta_\gamma = \delta L_{\text{mat}} / \delta \Gamma^{\alpha\beta}$, with the Hodge star \star . Here we displayed already the variational expression, which will be explained below.

Maxwell’s vacuum field $A(x)$ is a 1-form, a geometrical object independent of coordinates and frames. As such, it has vanishing Lorentz-spin, $\mathfrak{S}_{\alpha\beta} = 0$, but helicity ± 1 . The analogous is true for the gluon field. As a consequence, in exterior calculus, its canonical (i.e. Noether) energy-momentum 3-form is symmetric and gauge invariant directly, see [19], footnote 53. Conventionally, see [14], the *coordinate dependent* components A_i of

A are used in the Lagrangian formalism, see also the clarifying considerations of Benn et al. [21].

Thesis 1: *The energy-momentum current 3-form of the free gluon field $F = DA$ is given by the Minkowski type expression [22]*

$$\mathfrak{T}_\alpha = \frac{1}{2}[F \wedge (e_\alpha \lrcorner F) - {}^*F \wedge (e_\alpha \lrcorner F)] \quad \text{or} \quad \mathfrak{T}_i{}^j = \frac{1}{4}\delta_i^j F_{kl}F^{kl} - F_{ik}F^{jk}. \quad (13)$$

The (Lorentz) spin current of the gluon field vanishes, $\mathfrak{S}_{\alpha\beta\gamma} = 0$, the gluon orbital angular momentum current is given by $x_{[\alpha}\mathfrak{T}_{\beta]}$ and represents the total angular momentum. As a gauge potential, the gluon is described by a 1-form and has helicity ± 1 .

The second example, Dirac field in exterior calculus for illustration. Its Lagrangian reads,

$$L_D = \frac{i}{2}(\overline{\Psi} \star \gamma \wedge D\Psi + \overline{D\Psi} \wedge \star \gamma \Psi) + {}^*m\overline{\Psi}\Psi, \quad (14)$$

with $\gamma := \gamma_\alpha \vartheta^\alpha$ and $\gamma_{(\alpha}\gamma_{\beta)} = o_{\alpha\beta}\mathbf{1}_4$. The 3-forms of the canonical momentum and spin current densities are ($D_\alpha := e_\alpha \lrcorner D$, here \lrcorner denotes the interior product sign):

$$\mathfrak{T}_\alpha = \frac{i}{2}(\overline{\Psi} \star \gamma \wedge D_\alpha \Psi + \overline{D_\alpha \Psi} \wedge \star \gamma \Psi), \quad \mathfrak{S}_{\alpha\beta} = \frac{1}{4}\vartheta_\alpha \wedge \vartheta_\beta \wedge \overline{\Psi} \gamma_5 \Psi. \quad (15)$$

In Ricci calculus $\mathfrak{S}_{\alpha\beta\gamma} = \mathfrak{S}_{[\alpha\beta\gamma]} = \frac{1}{4}\epsilon_{\alpha\beta\gamma\delta}\overline{\Psi}\gamma_5\gamma^\delta\Psi$. Because of the equivalence principle, the *inertial currents* \mathfrak{T}_α and $\mathfrak{S}_{\alpha\beta}$ are, at the same time, the gravitational currents of the classical Dirac field. A decomposition of $(\mathfrak{T}_\alpha, \mathfrak{S}_{\alpha\beta})$ à la Gordon, yields the *gravitational* moment densities of the Dirac field [6]; it is a special case of relocalization, see below.

Thesis 2: *The canonical (Noether) energy-momentum and the canonical (Noether) spin current 3-forms of a Dirac/quark field are given by the expressions in Eq.(15).*

6. Relocalization of energy-momentum and spin distribution. We redefine the canonical currents $\mathfrak{T}_i{}^j$ and $\mathfrak{S}_{ij}{}^k$ by adding curls, see [23, 6],

$$\widehat{\mathfrak{T}}_i{}^j := \mathfrak{T}_i{}^j + \partial_k Y_i{}^{jk}, \quad \widehat{\mathfrak{S}}_{ij}{}^k := \mathfrak{S}_{ij}{}^k + Y_{[ij]}{}^k + \partial_l Z_{ij}{}^{kl}, \quad (16)$$

with the arbitrary antisymmetric super-potentials $Y_i{}^{jk} = -Y_i{}^{kj}$ and $Z_{ij}{}^{kl} = -Z_{ij}{}^{lk} = -Z_{ji}{}^{kl}$. We substitute (16)₁ and the partial derivative of (16)₂ into (10) and (11), Then we recognize that these *relocalized* currents fulfill the original conservation laws:

$$\partial_j \widehat{\mathfrak{T}}_i{}^j = 0, \quad \partial_k \widehat{\mathfrak{S}}_{ij}{}^k - \widehat{\mathfrak{T}}_{[ij]} = 0. \quad (17)$$

The integrated *total* energy-momentum and the *total* angular momentum of an insular material system are invariant under relocalization [23]. However, “relocalization invariance” under the transformations specified in (16) is *not* a generally valid physical principle. It should rather be understood as a formal trick to compute the total energy-momentum and angular momentum in a most convenient way.

It is convenient to introduce a new superpotential U that is equivalent to Y by

$$U_{ij}{}^k := -Y_{[ij]}{}^k = -U_{ji}{}^k \quad \implies \quad Y_i{}^{jk} = -U_i{}^{jk} + U^{jk}{}_i - U_i{}^k{}^j. \quad (18)$$

The *Belinfante* relocalization (1939) is a special case: Belinfante [24] effectively required $\widehat{\mathfrak{S}}_{kl}{}^j = 0$. Then, by (16)₂ and (18)₁, $\mathfrak{S}_{ij}{}^k = U_{ij}{}^k - \partial_l Z_{ij}{}^{kl}$ and the relocalized energy-momentum, ${}^{\text{Bel}}\mathfrak{t}_i{}^j := \widehat{\mathfrak{T}}_i{}^j$, with $\widehat{\mathfrak{S}}_{kl}{}^j = 0$, reads

$${}^{\text{Bel}}\mathfrak{t}_i{}^j = \mathfrak{T}_i{}^j - \partial_k \left(\mathfrak{S}_i{}^{jk} - \mathfrak{S}{}^{jk}{}_i + \mathfrak{S}{}^{k.i}{}_j \right) \quad \text{with} \quad \boxed{\partial_j {}^{\text{Bel}}\mathfrak{t}_i{}^j = 0, \quad {}^{\text{Bel}}\mathfrak{t}_{[kl]} = 0.} \quad (19)$$

For the Dirac field, because of the total antisymmetry of \mathfrak{S}_{ijk} , we find simply ${}^{\text{Bel}}\mathfrak{t}_{ij} = {}^{\text{Bel}}\mathfrak{t}_{(ij)}$, see [25]. Incidentally, the Gordon relocalization, mentioned above, *differs* from the Belinfante relocalization.

7. Dynamic Hilbert energy-momentum in general relativity. How can we choose amongst the multitude of the relocalized energy-momentum tensors and spin tensors? After all, as physicists we are convinced that the energy and the spin distribution of matter (but not of gravity!) are observable quantities, at least in the classical domain. There must exist physically correct and unique energy-momentum and spin tensors in nature. The Belinfante recipe was to kill $\mathfrak{T}_{[kl]}$ in order to tailor the energy-momentum for the application in Einstein’s field equation.

Already in 1915, Hilbert defined the dynamic energy-momentum as the response of the matter Lagrangian to the variation of the metric [26]:

$${}^{\text{Hi}}\mathfrak{t}_{ij} := 2\delta\mathfrak{L}_{\text{mat}}(g, \Psi, \overset{\{\}}{\nabla}\Psi) / \delta g^{ij}; \quad (20)$$

g^{ij} (or its reciprocal g_{kl}) is the gravitational potential in GR. The matter Lagrangian is supposed to be *minimally coupled* to g^{ij} , in accordance with the equivalence principle. Only in gravitational theory, in which spacetime can be deformed, we find a real local definition of the material energy-momentum tensor. The Hilbert definition is analogous to the relation from elasticity theory “stress $\sim \delta(\text{elastic energy})/\delta(\text{strain})$ ”. Recall that strain is defined as $\varepsilon^{ab} := \frac{1}{2} \left({}^{(\text{defo})}g^{ab} - {}^{(\text{undefo})}g^{ab} \right)$, see [27]. Even the factor 2 is reflected in the Hilbert formula.

Rosenfeld (1940) has shown [28], via Noether type theorems, that the Belinfante tensor ${}^{\text{Bel}}\mathfrak{t}_{ij}$, derived within SR, coincides with the Hilbert tensor ${}^{\text{Hi}}\mathfrak{t}_{ij}$ of GR. Thus, the Belinfante-Rosenfeld recipe yields...

Thesis 3: *In the framework of GR, the Hilbert energy-momentum tensor*

$${}^{\text{Hi}}\mathfrak{t}_i{}^j = {}^{\text{Bel}}\mathfrak{t}_i{}^j = \mathfrak{T}_i{}^j - \nabla_k \left(\mathfrak{S}_i{}^{jk} - \mathfrak{S}{}^{jk}{}_i + \mathfrak{S}{}^{k.i}{}_j \right) = {}^{\text{Hi}}\mathfrak{t}{}^j{}_i, \quad (21)$$

localizes the energy-momentum distribution correctly; here $(\mathfrak{T}_i{}^j, \mathfrak{S}_{ij}{}^k)$ are the canonical Noether currents. The spin tensor attached to ${}^{\text{Hi}}\mathfrak{t}_i{}^j$ vanishes.

The Rosenfeld formula (21) identifies the Belinfante with the Hilbert tensor. In other words, the Belinfante tensor provides the correct source for Einstein’s field equation. As long as we accept GR as the correct theory of gravity, the localization of energy-momentum and spin of matter is solved. This state of mind is conventionally kept till today by most theoretical physicists. In passing, one should note that the spin of matter has a rather auxiliary function in this approach. After all, the spin of the Hilbert-Belinfante-Rosenfeld tensor simply vanishes.

However, the Poincaré gauge theory of gravity (PG; Sciama, Kibble 1961, see [9] for a review), in particular the viable Einstein-Cartan theory (EC) with the curvature scalar as gravitational Lagrangian, has turned the Rosenfeld formula (21) upside down.

8. Dynamic Sciama-Kibble spin in Poincaré gauge theory. The gauging of the Poincaré group identifies as gauge potentials the orthonormal coframe $\vartheta^\alpha = e_i^\alpha dx^i$ and the Lorentz connection $\Gamma^{\alpha\beta} = \Gamma_i^{\alpha\beta} dx^i = -\Gamma^{\beta\alpha}$. The spacetime arena of the emerging Poincaré gauge theory of gravity (PG) is a Riemann-Cartan space with Cartan's *torsion* and with Riemann-Cartan *curvature* as gauge field strength, respectively [10]:

$$C_{ij}{}^\alpha := \nabla_{[i} e_{j]}^\alpha, \quad R_{ij}{}^{\alpha\beta} := \text{“}\nabla\text{”}_{[i} \Gamma_{j]}^{\alpha\beta} \quad (\text{or } C^\alpha = D\vartheta^\alpha, \quad R^{\alpha\beta} = \text{“}D\text{”}\Gamma^{\alpha\beta}). \quad (22)$$

The energy-momentum and angular momentum laws generalize to

$$\overset{*}{\nabla}_k \mathfrak{T}_i{}^k = \underbrace{C_{ik}{}^\ell}_{\text{torsion}} \mathfrak{T}_\ell{}^k + \underbrace{R_{ik}{}^{lm}}_{\text{curvature}} \mathfrak{S}_{lm}{}^k, \quad \overset{*}{\nabla}_k \mathfrak{S}_{ij}{}^k - \mathfrak{T}_{[ij]} = 0; \quad (23)$$

here $\overset{*}{\nabla}_k := \nabla_k + C_{k\ell}{}^\ell$. GR is the subcase for $\mathfrak{S}_{ij}{}^k = 0$, see also [30, 29]. The material currents are defined by variations with respect to the potentials (minimal coupling!):

$$\boxed{\text{SK}\mathfrak{T}_\alpha{}^i = \delta\mathfrak{L}_{\text{mat}}(e, \Psi, \overset{\Gamma}{D}\Psi)/\delta e_i{}^\alpha, \quad \text{SK}\mathfrak{S}_{\alpha\beta}{}^i = \delta\mathfrak{L}_{\text{mat}}(e, \Psi, \overset{\Gamma}{D}\Psi)/\delta\Gamma_i{}^{\alpha\beta}.} \quad (24)$$

This Sciama-Kibble definition of the spin (1961) in equation (24) is only possible in the Riemann-Cartan spacetime of PG. It is analogous to the relation “moment stress $\sim \delta(\text{elastic energy})/\delta(\text{contortion})$ ” in a Cosserat type medium, the contortion being a “rotational strain”, see [31].

The application of the Lagrange-Noether machinery to the minimally coupled action function yields, after a lot of algebra, the final result, see [19]:

$$\text{SK}\mathfrak{T}_\alpha{}^i = \mathfrak{T}_\alpha{}^i, \quad \text{SK}\mathfrak{S}_{\alpha\beta}{}^i = \mathfrak{S}_{\alpha\beta}{}^i. \quad (25)$$

The dynamically defined energy-momentum and spin currents à la Sciama-Kibble coincide with the canonical Noether currents of classical field theory.

Thesis 4: *Within PG, the quark energy-momentum and the quark spin are distributed in accordance with the canonical Noether currents $\mathfrak{T}_\alpha{}^i$ and $\mathfrak{S}_{\alpha\beta}{}^i$, respectively.*

This is in marked contrast to the doctrine in the context of GR.

We express the canonical energy-momentum tensor in terms of the Hilbert one (see [32]):

$$\text{SK}\mathfrak{T}_\alpha{}^i = \mathfrak{T}_\alpha{}^i = \text{Hi}\mathfrak{t}_\alpha{}^i + \overset{*}{\nabla}_k (\mathfrak{S}_\alpha{}^{ik} - \mathfrak{S}^{ik}{}_\alpha + \mathfrak{S}_\alpha{}^k{}^i), \quad \text{SK}\mathfrak{S}_{\alpha\beta}{}^i = \mathfrak{S}_{\alpha\beta}{}^i. \quad (26)$$

The new Rosenfeld formula (26)₁ reverses its original meaning in (21). Within PG, the canonical tensor $\mathfrak{T}_\alpha{}^i$ represents the correct energy-momentum distribution of matter and the (sym)metric Hilbert tensor now plays an auxiliary role. In GR, it is the other way round. Moreover, we are now provided with a dynamic definition of the canonical spin tensor. In GR, the spin was only a *kinematic* quantity floating around freely.

These results on the correct distribution of material energy-momentum and spin in the framework of PG are *independent* of a specific choice of the *gravitational* Lagrangian. However, if we choose the RC curvature scalar as a gravitational Lagrangian, we arrive at the Einstein-Cartan(-Sciama-Kibble) theory of gravitation, which is a viable theory of gravity competing with GR.

9. An algebra of the momentum and the spin currents? We discussed exclusively classical field theory. Can we learn something for a corresponding quantization of gravity? Our classical analysis has led us to the gravitational currents \mathfrak{T}_α and $\mathfrak{S}_{\alpha\beta}$. They represent the sources of gravity.

In strong and in electroweak interaction, before the standard model had been worked out, one started with the current algebra of the phenomenologically known *strong* and the *electroweak* currents (see Sakurai [33], Fritzsche et al. [34], and also Cao [35]).

Schwinger (1963) studied, for example, the equal time commutators of the components of the Hilbert energy-momentum tensor [8]. Should one try to include also the spin tensor components and turn to the canonical tensors?

In the Sugawara model (1968), “*A field theory of currents*” was proposed [37] with 8 vector and 8 axial vector currents for strong interaction and a symmetric energy-momentum current for gravity that was expressed bilinearly in terms of the axial and the vector currents. Now, when we have good arguments that the gravitational currents are \mathfrak{T}_α and $\mathfrak{S}_{\alpha\beta}$, one may want to develop a corresponding current algebra by determining the equal time commutator of these currents....

Acknowledgments. I’d like to thank Anatoly Efremov, Chair of DSPIN-13, and Oleg Teryaev for the invitation and for their hospitality in Dubna. For discussions I am most grateful to Francesco Becattini (Frankfurt & Florence), Yuri Obukhov (Moscow), Oleg Teryaev (Dubna), and Sasha Silenko (Dubna & Minsk). Helpful remarks by Jim Nester (Chung-li) and Erhard Scholz (Wuppertal) are appreciated. I acknowledge support by the German-Russian Heisenberg-Landau program.

References

- [1] E. Leader and C. Lorcé, Phys. Repts. (submitted to) [arXiv:1309.4235].
- [2] H. Weyl, *Space–Time–Matter*, transl. from the 4th German ed., Dover, New York (1952) p. 237.
- [3] O. V. Teryaev, [arXiv:hep-ph/9904376].
- [4] O. V. Teryaev, Czech. J. Phys. **53** (2003) Supplement A [arXiv:hep-ph/0306301]; AIP Conf. Proc. **915** (2007) 260–263 [arXiv:hep-ph/0612205].
- [5] I. Y. Kobzarev and L. B. Okun, Sov. Phys. JETP **16** (1963) 343–346.
- [6] F. W. Hehl, A. Macías, E. W. Mielke, Yu. N. Obukhov, in: Festschrift for E. Schucking, A. Harvey, ed., Springer, Berlin (1997/98) [arXiv:gr-qc/9706009].
- [7] E. P. Wigner, Annals Math. **40** (1939) 149–204.
- [8] F. Becattini and L. Tinti, Phys. Rev. D **84**, 025013 (2011) [arXiv:1101.5251]; Phys. Rev. D **87**, 025029 (2013) [arXiv:1209.6212].
- [9] M. Blagojević and F. W. Hehl (eds.), *Gauge Theories of Gravitation, a Reader with Commentaries*, Imperial College Press/World Scientific, London/Singapore (2013).
- [10] F. Gronwald and F. W. Hehl, *On the Gauge Aspects of Gravity*, Invited Erice Lecture, May 1995 [arXiv:gr-qc/9602013].
- [11] V. Mukhanov, Physics Colloquium, University of Bonn, July 2013.

- [12] E. Leader, *Spin in Particle Physics*, Cambridge Univ. Press, Cambridge (2001).
- [13] E. M. Corson, *Introduction to Tensors, Spinors, and Relativistic Wave Equations*, Blackie, London (1953).
- [14] L. D. Landau and E. M. Lifshitz: *The Classical Theory of Fields*, Vol.2 of *Course of Theoretical Physics*; transl. from the Russian, Pergamon, Oxford (1962).
- [15] J. A. Schouten, *Ricci-Calculus*, 2nd ed., Springer, Berlin (1954).
- [16] D. Vollhardt and P. Wölfle, *The Superfluid Phases of Helium 3*, Taylor & Francis, London (1990) [reprinted with corrections by Dover, Mineola, NY (2013)].
- [17] A. Einstein, *The Meaning of Relativity*, 5th ed., Princeton Univ. Press, Princeton (1955).
- [18] W.-K. Tung, *Group Theory in Physics*, World Scientific, Philadelphia (1985).
- [19] F. W. Hehl, J. D. McCrea, E. W. Mielke, and Y. Ne'eman, Phys. Repts. **258** (1995) 1–171.
- [20] F. W. Hehl and Yu. N. Obukhov, *Foundations of Classical Electrodynamics: Charge, flux, and metric*, Birkhäuser, Boston (2003).
- [21] I. M. Benn, T. Dereli and R. W. Tucker, Phys. Lett. B **96** (1980) 100–104.
- [22] H. Minkowski, Nachr. Königl. Wiss. Ges. Göttingen, math.-phys. Kl. (1908) 53–111; for a modern evaluation, see F. W. Hehl, Ann. Phys. (Berlin) **17** (2008) 691–704.
- [23] F. W. Hehl, Repts. Math. Phys. (Torun) **9** (1976) 55–82.
- [24] F. J. Belinfante, Physica **6** (1939) 887–898; **7** (1940) 449–474.
- [25] H. Tetrode, Z. Physik **49** (1928) 858–864.
- [26] D. Hilbert, Nachr. Ges. Wiss. Göttingen, math.-phys. Kl. (1915) 395–407.
- [27] L. D. Landau and E. M. Lifshitz: *Theory of Elasticity*, Vol.7, Oxford (1959).
- [28] L. Rosenfeld, Mém. Acad. Roy. Belgique, Cl. Sc. **18** (1940) fasc. 6.
- [29] R. R. Lompay, [arXiv:1401.2549].
- [30] R. R. Lompay, and A. N. Petrov, J. Math. Phys. **54** (2013) 062504.
- [31] F. W. Hehl and Yu. N. Obukhov, *Elie Cartan's torsion in geometry and in field theory, an essay*, Ann. Fond. Louis de Broglie **32** (2007) 157–194 [arXiv:0711.1535].
- [32] W. Kopczyński, J. D. McCrea and F. W. Hehl, Phys. Lett. A **135** (1989) 89–91.
- [33] J. J. Sakurai, Ann. Phys. (NY) **11** (1960) 1–48.
- [34] H. Fritzsche, M. Gell-Mann and H. Leutwyler, Phys. Lett. B **47** (1973) 365–368.
- [35] T. Y. Cao, *From Current Algebra to Quantum Chromodynamics*, Cambridge Univ. Press, Cambridge (2010).
- [36] J. Schwinger, Phys. Rev. **130** (1963) 406–409.
- [37] H. Sugawara, Phys. Rev. **170** (1968) 1659–1662.

ANOMALOUS NONPERTURBATIVE QUARK-GLUON CHROMOMAGNETIC INTERACTION AND SPIN EFFECTS IN HIGH ENERGY REACTIONS

N.I. Kochelev¹, N.S. Korchagin²

*Bogoliubov Laboratory of Theoretical Physics, Joint Institute for Nuclear Research, Dubna,
Moscow region, 141980, Russia*

(1) *E-mail: kochelev@theor.jinr.ru*

(2) *E-mail: korchagin@theor.jinr.ru*

Abstract

We discuss a new nonperturbative mechanism for spin effects in high energy reactions with hadrons. This mechanism is based on the existence of a large anomalous quark chromomagnetic moment (AQCM) induced by the nontrivial topological structure of QCD vacuum. As an example, we estimate the contribution of this interaction to the single spin asymmetry (SSA) in the inclusive pion production in the proton-proton scattering. We show that SSA induced by AQCM is large and its value is in qualitative agreement with experimental data.

The explanation of the large spin effects in high energy reactions with hadrons is one of the long-standing problems in QCD (see [1, 2] and references therein). It is well known that QCD has a complicated structure of vacuum which leads to the phenomenon of spontaneous chiral symmetry breaking (SCSB) in strong interaction. The instanton liquid model of QCD vacuum [3, 4] is one of the models in which the SCSB phenomenon arises in a very natural way due to the quark chirality-flip in the field of strong fluctuation of vacuum gluon fields called instantons. As the result, instantons lead to the anomalous quark-gluon chromomagnetic vertex with a large quark spin-flip [5]¹. Therefore, they can give an important contribution to the spin dependent cross sections.

In this Letter, we discuss the mechanism of spin effects based on the quark spin-flip by the nonperturbative contribution coming from AQCM. As an example, we present the estimation of the AQCM contribution to SSA in the inclusive pion production in the high energy proton-proton interaction².

The general quark-gluon vertex with the AQCM contribution is

$$V_\mu(q^2)t^a = -g_s t^a (\gamma_\mu + \frac{\mu_a F_2(q^2)}{2M_q} \sigma_{\mu\nu} q_\nu), \quad (1)$$

where the first term is the conventional pQCD quark-gluon vertex and the second term in our model comes from the nonperturbative sector of QCD. In Eq.1, the form factor F_2 describes nonlocality of the interaction, μ_a is AQCM, q^2 is the virtuality of the gluon and M_q is the dynamical quark mass.

¹The importance of SCSB phenomenon for quark spin-flip was also mentioned in the recent paper [6] in the different aspect.

²The details of calculation of the AQCM contribution to SSA at the quark level can be found in [7].

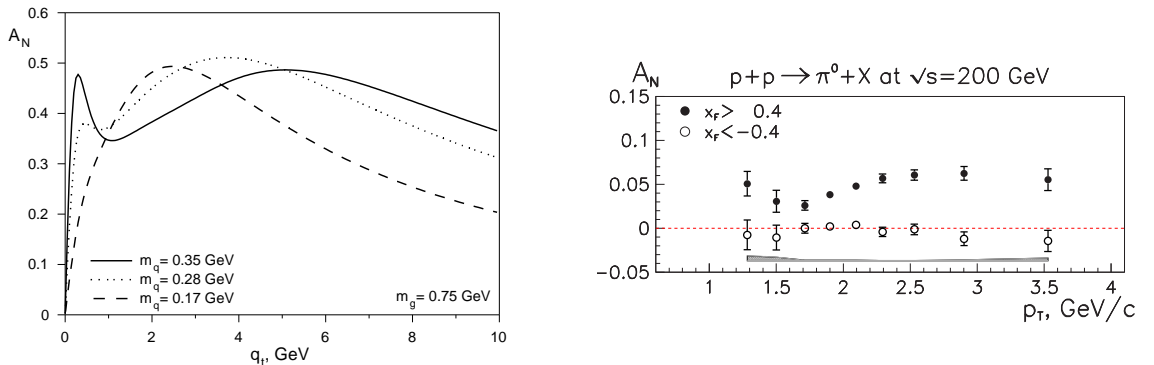


Figure 2: Left panel: the q_t dependence of SSA for the different values of the dynamical quark mass and fixed value for the dynamical gluon mass $m_g = 0.75$ GeV. Right panel: STAR data for inclusive π^0 production [9].

a rather soft power-like form factor in the quark-gluon vertex, Eq.2, and a small average size of an instanton, $\rho_c \approx 1/3$ fm [3]. Such a flat dependence has been observed by the STAR collaboration in the inclusive π^0 production in high energy proton-proton collision, right panel of Fig.2, and was not expected in the models based on the so-called TMD factorization [10]. Finally, the sign of the SSA is defined by the sign of AQCM and should be positive. This sign is very important for explanation of the signs of SSA observed for the inclusive production of π^+ , π^- and π^0 mesons in proton-proton and proton-antiproton high energy collisions. We can estimate asymmetry at the hadron level for the inclusive production of pions in the proton-proton scattering by using some simple assumptions. Let us consider only leading fragmentation of pions from the final quark. In this case, SSA for the different charge of pions is

$$A_N^{\pi}(q_t) \approx \frac{\Delta q_t}{q} A_N^q(q_t), \quad (6)$$

where $A_N^q(q_t)$ is SSA at the quark level presented in the left panel in Fig.2, Δq_t is the transverse polarization of the quark with the given flavor in the transversely polarized proton and q is the number of the corresponding quark in the proton. Using the additional assumption $\Delta q_t \approx \Delta q$, where Δq is the longitudinal polarization of the quark in the longitudinally polarized proton we have got

$$A_N^{\pi^+}(q_t) \approx 0.383 A_N^q(q_t), \quad A_N^{\pi^-}(q_t) \approx -0.327 A_N^q(q_t), \quad A_N^{\pi^0}(q_t) \approx 0.146 A_N^q(q_t), \quad (7)$$

where we used values $\Delta u = 0.766$ and $\Delta d = -0.327$ from [11]. Finally, one can verify that our estimation given by Eq.7 is in qualitative agreement with the available experimental data [9, 12, 13] for the large x_F region.

In summary, we discussed the spin effects in high energy reactions induced by AQCM. This phenomenon appears from the anomalous strong spin-flip quark-gluon interaction induced by the topologically nontrivial configuration of the vacuum gluon fields called instantons. As an example, we estimated the contribution of AQCM to SSA in the inclusive production of the pions in the proton-proton scattering and showed that it was large. Additional arguments for the importance of AQCM for spin effects in high

energy reactions can be found in [14] where its contribution to the elastic proton-proton scattering at large momentum transfer was considered. We would like to mention that the mechanism of spin effects based on AQCM is quite general and might happen in any nonperturbative QCD model with SCSB. The attractive feature of the instanton model is that within this model this phenomenon comes from rather small distances $\rho_c \approx 0.3$ fm. As the result, it allows one to understand the origin of large observed spin effects at large transverse momenta.

The authors are very grateful to A.V. Efremov for the invitation to DSPIN-13 Workshop and for the discussion.

References

- [1] A. D. Krisch, arXiv:1001.0790 [hep-ex].
- [2] E. Leader, Camb. Monogr. Part. Phys. Nucl. Phys. Cosmol. **15** (2001) 1.
- [3] T. Schäfer and E.V. Shuryak, Rev. Mod. Phys. **70** (1998) 1323.
- [4] D. Diakonov, Prog. Par. Nucl. Phys. **51** (2003) 173.
- [5] N. I. Kochelev, Phys. Lett. **B426** (1998) 149.
- [6] S. M. Troshin and N. E. Tyurin, Phys. Rev. D **88** (2013) 017502.
- [7] N. Kochelev and N. Korchagin, Phys. Lett. B **729** (2014) 117.
- [8] N. Kochelev, Phys. Part. Nucl. Lett. **7** (2010) 326.
- [9] B. I. Abelev *et al.* [STAR Collaboration], Phys. Rev. Lett. **101** (2008) 222001.
- [10] J. Collins, Foundation of perturbative QCD, Cambridge University Press (2011).
- [11] D. de Florian, R. Sassot, M. Stratmann and W. Vogelsang, Phys. Rev. D **80** (2009) 034030.
- [12] J. H. Lee *et al.* [BRAHMS Collaboration], AIP Conf. Proc. **915** (2007) 533.
- [13] D. L. Adams *et al.* [FNAL-E704 Collaboration], Phys. Lett. B **264** (1991) 462.
- [14] N. Kochelev and N. Korchagin, arXiv:1312.5094 [hep-ph], to be published in Phys.Rev.D.

THE SINGLET CONTRIBUTION TO THE BJORKEN POLARIZED SUM RULE

S.A. Larin^{1†}

(1) *Institute for Nuclear Research of the Russian Academy of Sciences, 60th October
Anniversary Prospect 7a, Moscow 117312, Russia*

† *E-mail: larin@inr.ac.ru*

Abstract

It is shown that the existing four-loop result for the Bjorken polarized sum rule for deep inelastic electron-nucleon scattering obtained within perturbative Quantum Chromodynamics should be supplemented by the calculation of the diagrams of the so called singlet type. We also suggest a new exact relation which connects the Bjorken polarized sum rule and the the Gross-Llewellyn Smith sum rule.

Since the discovery of the asymptotic freedom [1] there was the enormous progress in perturbative calculations in Quantum Chromodynamics (QCD). In particular calculations of the Bjorken sum rule for polarized deep inelastic electron-nucleon scattering [2] have now some history. The leading $O(\alpha_s)$ correction in the strong coupling constant α_s was calculated in [3]. The next-to-leading $O(\alpha_s^2)$ approximation was obtained in [4] and the $O(\alpha_s^3)$ correction was found in [5]. Quite recently the $O(\alpha_s^4)$ approximation was published [6].

In the present contribution we demonstrate that the calculation [6] should be supplemented by the calculation of the diagrams of the so called singlet type. We determine this singlet contribution up to an overall constant using the Crewther relation [7].

We also suggest a new exact relation which connects the Bjorken polarized sum rule and the the Gross-Llewellyn Smith sum rule.

The Bjorken sum rule for polarized deep inelastic scattering has the following form

$$\int_0^1 (g_1^{ep}(x, Q^2) - g_1^{en}(x, Q^2)) dx = \frac{g_A}{6} C_{Bjp}(a_s(Q^2)) + \text{nonperturbative terms}, \quad (1)$$

where g_1^{ep} and g_1^{en} are the structure functions of polarized electron-proton and electron-nucleon deep inelastic scattering, $g_A \approx 1.22$ is the axial constant of the neutron β -decay, Q^2 is the Euclidean momentum transfer squared, $a_s = \alpha_s/\pi$ is the strong coupling.

The coefficient function $C_{Bjp}(a_s) = 1 + O(a_s)$ enters the following short-distance operator product expansion (OPE)

$$i \int d^4x e^{iqx} T [J_\mu(x) J_\nu(0)] = (q_\mu q_\nu - g_{\mu\nu} q^2) \Pi^{EM}(Q^2) + \epsilon_{\mu\nu\lambda\rho} \frac{q_\rho}{q^2} [C_{Bjp}^a(a_s) A_\lambda^a(0) + C_{EJ}(a_s) A_\lambda(0)] + \text{higher twists}, \quad (2)$$

where the summation over repeated indexes is assumed, J_μ is the electromagnetic quark current, $\Pi^{EM}(Q^2)$ is the polarization function, $A_\lambda^a = \bar{\psi} \gamma_\lambda \gamma_5 t^a \psi$ is the non-singlet (NS)

axial quark current, t^a being the (diagonal) generator of the flavor $SU(n_f)$ -group, n_f being the number of quark flavors. $A_\lambda = \bar{\psi}\gamma_\lambda\gamma_5\psi$ is the singlet (SI) axial quark current.

To calculate the coefficient function $C_{Bjp}^a(a_s)$ at the multiloop level one uses the method of projections [8] which gives

$$i \int d^4x e^{iqx} \langle 0 | T [\bar{\psi}(p)\gamma_\sigma\gamma_5 t^a \psi(-p) J_\mu(x) J_\nu(0)] | 0 \rangle \Big|_{p=0}^{amputated} = \quad (3)$$

$$const \epsilon_{\mu\nu\sigma\rho} \frac{q_\rho}{q^2} C_{Bjp}^a(a_s) Z_A,$$

where $\psi(p)$ is the Fourier transform of the quark field carrying the momentum p . Quark legs are amputated. Z_A is the renormalization constant of the non-singlet axial current. $const$ is the normalization constant. The technique how to deal with the γ_5 -matrix in multiloop calculations within dimensional regularization and minimal subtraction scheme is given in [9].

The coefficient function $C_{Bjp}^a(a_s)$ receives contributions from two types of diagrams. The first type, the non-singlet one (with both electromagnetic vertexes attached to the fermion line of external quark legs) produces the flavor factor $Tr(Q_f^2 t^a)$, where Q_f is the (diagonal) quark charge matrix $Q_f = diag(2/3, -1/3, -1/3, \dots)$. The second, the singlet type (when one electromagnetic vertex is attached to the fermion line of external quark legs and another to the internal quark loop) gives the flavor factor $Tr(Q_f)Tr(Q_f t^a)$. The ratio of these flavor factors does not depend on the index a

$$\frac{Tr(Q_f)Tr(Q_f t^a)}{Tr(Q_f^2 t^a)} = 3 \sum_{i=1}^{n_f} q_i \quad (4)$$

where q_i are electromagnetic quark charges. That is why one can factorize from $C_{Bjp}^a(a_s)$ the a -independent coefficient function $C_{Bjp}(a_s)$ which enters the sum rule (1)

$$C_{Bjp}^a(a_s) = Tr(Q_f^2 t^a) C^{NS}(a_s) + Tr(Q_f) Tr(Q_f t^a) C^{SI}(a_s) = \quad (5)$$

$$\left(C^{NS}(a_s) + 3 \left(\sum_{i=1}^{n_f} q_i \right) C^{SI} \right) Tr(Q_f^2 t^a) = C_{Bjp}(a_s) Tr(Q_f^2 t^a).$$

It is the contribution of the singlet type C^{SI} which is missed in the calculation [6] of the α_s^4 -correction to the Bjorken polarized sum rule. It is interesting to note that individual diagrams of the singlet type give non-zero contributions to the sum rule already in the a_s^3 order but their total sum nullifies [5] in this order. It can be explained by using the generalized Crewther relation [7]. The relation states that

$$C_{Bjp}(a_s) D^{NS}(a_s) = d_R \left(1 + \frac{\beta(a_s)}{a_s} K(a_s) \right), \quad (6)$$

$$K(a_s) = a_s K_1 + a_s^2 K_2 + a_s^3 K_3 + \dots,$$

where K_i are calculable in QCD coefficients, d_R is the dimension of the quark representation ($d_R = 3$ in QCD), $\beta(a_s)$ is the renormalization group β -function

$$\beta(a_s) = \mu^2 \frac{\partial a_s}{\partial \mu^2} = \sum_{i \geq 0} \beta_i a_s^{i+2} \quad (7)$$

with the well known first coefficient $\beta_0 = -\frac{11}{12}C_A + \frac{1}{3}T_F n_f$, C_A being the quadratic Casimir operator of the adjoint representation of the group and T_F being the trace normalization of the fundamental representation.

The Adler function $D^{NS}(a_s)$ is defined as

$$D^{EM}(a_s) = -12\pi^2 Q^2 \frac{d}{dQ^2} \Pi^{EM}(Q^2), \quad (8)$$

$$D^{EM}(a_s) = \left(\sum_i q_i^2 \right) D^{NS}(a_s) + \left(\sum_i q_i \right)^2 D^{SI}(a_s).$$

The singlet diagrams contributing to $C_{Bjp}(a_s)$ at the a_s^3 and the a_s^4 levels are proportional to the color factor $d^{abc}d^{abc}$, where d^{abc} are the symmetric structure constants of the $SU(N_c)$ color group (for QCD with the $SU(3)$ group one gets $d^{abc}d^{abc} = 40/3$). At the a_s^3 level the sum of the singlet diagrams should nullify since the color factor $d^{abc}d^{abc}$ is the complete color factor for these diagrams and the coefficient β_0 can not be factorized which is in the contradiction with the Crewther relation (6). At the a_s^4 level there are enough loops (four) to generate the color structure $\beta_0 d^{abc}d^{abc}$ in accordance with the relation (6). Thus one can get the non-zero singlet contribution to the Bjorken polarized sum rule in the order a_s^4

$$C_{Bjp}(a_s) = C^{NS}(a_s) + X a_s^4 \beta_0 \sum_{i=1}^{n_f} q_i d^{abc}d^{abc} + O(a_s^5), \quad (9)$$

where the non-singlet contribution was calculated up to and including the order a_s^4 in [6]. The numerical constant X is still to be calculated to get the complete $O(a_s^4)$ correction.

In principle it is possible that after calculating the singlet contribution to $C_{Bjp}(a_s)$ one can see at the a_s^4 level the validity of the interesting relation which connects different physical quantities

$$[C^{NS}(a_s) + n_f C^{SI}(a_s)] D^{NS}(a_s) = C_{GLS}(a_s) [D^{NS}(a_s) + n_f D^{SI}(a_s)], \quad (10)$$

here $C_{GLS}(a_s)$ is the coefficient function of the Gross-Llewellyn Smith sum rule for deep inelastic neutrino-nucleon scattering [11]. $D^{NS}(a_s) + n_f D^{SI}(a_s) \equiv D(a_s)/n_f$, where $D(a_s)$ is the Adler function corresponding to the correlator of the flavor singlet quark currents.

This relation is valid at the a_s^3 level. To show that it can be valid in all orders let us consider OPE for the following 3-point function

$$T_{\mu\nu\lambda}^{ab}(p, q) = i \int \langle 0 | T [V_\mu(x) A_\lambda^a(y) V_\nu^b(0)] | 0 \rangle e^{ipx+iqy} dx dy, \quad (11)$$

where $V_\mu = \bar{\psi}\gamma_\mu\psi$ is the vector singlet quark current, $V_\nu^b = \bar{\psi}\gamma_\nu t^b\psi$ is the vector non-singlet quark current, A_λ^a is the axial vector current defined in eq.(2).

We can apply first the following OPE

$$i \int T [A_\lambda^a(y) V_\nu^b(0)] e^{iqy} dy = \delta^{ab} \epsilon_{\lambda\nu\alpha\beta} \frac{q_\beta}{Q^2} C_{GLS}(a_s) V_\alpha(0) + \dots \quad (12)$$

and substitute it into eq.(11) to get

$$T_{\mu\nu\lambda}^{ab}(p, q) = \delta^{ab} \epsilon_{\lambda\nu\alpha\beta} \frac{q_\beta}{Q^2} C_{GLS}(a_s) \int \langle 0 | T [V_\mu(x) V_\alpha(0)] | 0 \rangle e^{ipx} dx + \dots \quad (13)$$

For more formal derivation of the OPE for 3-point functions see [8].

On the other hand we can apply first the following OPE

$$i \int T [V_\mu(x) V_\nu^b(0)] e^{ipx} dx = \epsilon_{\mu\nu\alpha\beta} \frac{p_\beta}{P^2} [C^{NS}(a_s) + n_f C^{SI}(a_s)] A_\alpha^b(0) + \dots \quad (14)$$

and again substitute it into eq.(11) to obtain

$$T_{\mu\nu\lambda}^{ab}(p, q) = \epsilon_{\mu\nu\alpha\beta} \frac{p_\beta}{P^2} [C^{NS}(a_s) + n_f C^{SI}(a_s)] \times \quad (15)$$

$$\int \langle 0 | T [A_\lambda^a(y) A_\alpha^b(0)] | 0 \rangle e^{iqx} dq + \dots$$

Comparing eq.(13) and eq.(15) one can see a connection close to that of the relation (10). But presently we do not have a proof of this relation.

If eq.(10) is valid then one can determine the constant X in eq.(7) without explicit calculations of the singlet contribution to $C_{Bjp}(a_s)$ using results of ref. [10]: $X = -\frac{179}{384} + \frac{25}{48}\zeta_3 - \frac{5}{24}\zeta_5$.

Acknowledgments.

The author is grateful to collaborators of the Theory division of INR for helpful discussions. The work is supported in part by the grant for the Leading Scientific Schools NS-5590.2012.2.

References

- [1] D.J. Gross, F. Wilczek, Phys. Rev. Lett. **30** (1973) 1343;
H.D. Politzer, Phys. Rev. Lett. **30** (1973) 1346;
G. 't Hooft, report at the Marseille Conference on Yang-Mills Fields, 1972.
- [2] J.D. Bjorken, Phys. Rev. **148** (1966) 1467, **D1** (1970) 1376.
- [3] J. Kodaira, S. Matsuda, T. Muta, T. Uematsu and K. Sasaki, Phys. Rev. **D20** (1979) 627.
- [4] S.G. Gorishny and S.A. Larin, Phys. Lett. **B172** (1986) 109.
- [5] S.A. Larin and J.A.M. Vermaseren, Phys. Lett. **B259** (1991) 345.
- [6] P.A. Baikov, K.G. Chetyrkin, J.H. Kuhn, Phys. Rev. Lett. **104** (2010) 132004.
- [7] R.J. Crewther, Phys. Rev. Lett. **28** (1972) 1421; Phys. Lett. **B397** (1997) 137; hep-ph/9701321.
- [8] S.G. Gorishny, S.A. Larin and F.V. Tkachov, Phys. Lett. **B124** (1983) 217;
S.G. Gorishny and S.A. Larin, Nucl. Phys. **B283** (1987) 452.
- [9] S.A. Larin, Phys. Lett. **B303** (1993) 113.
- [10] P.A. Baikov, K.G. Chetyrkin, J.H. Kuhn, J. Rittinger, Phys. Lett. **B714** (2012) 62.
- [11] J.J. Gross, C.H. Llewellyn Smith, Nucl. Phys. **B14** (1969) 337.

FEMTOSCOPIC CORRELATIONS OF TWO IDENTICAL PARTICLES WITH NONZERO SPIN IN THE MODEL OF ONE-PARTICLE MULTIPOLE SOURCES

V.V. Lyuboshitz[†] and V.L. Lyuboshitz

*Joint Institute for Nuclear Research,
141980 Dubna, Moscow Region, Russia*

[†] *E-mail: Valery.Lyuboshitz@jinr.ru*

Abstract

The process of emission of two identical particles with nonzero spin and different helicities is theoretically investigated within the model of one-particle multipole sources. Taking into account the unitarity of the finite rotation matrix and symmetry relations for d -functions, the general expression for probability of emission of two identical particles by two multipole sources with angular momentum J , averaged over the projections of angular momentum and over the space-time dimensions of the generation region, has been obtained. For the case of unpolarized particles, the formula for two-particle correlation function at sufficiently large 4-momentum difference q is derived by the additional averaging over helicities. The concrete cases of emission of two unpolarized photons by dipole and quadrupole sources, and emission of two “left” neutrinos by sources with arbitrary J have been also considered, and the respective explicit expressions for the correlation function are obtained .

1. In the framework of the model of independent sources [1] with the angular momentum J and the projections of angular momentum onto the coordinate axis z , equaling M and M' , the amplitude of emission of two identical particles with the momentum \mathbf{p}_1 , helicity λ_1 and momentum \mathbf{p}_2 , helicity λ_2 has the following structure :

$$A_{MM'}(\mathbf{p}_1, \lambda_1; \mathbf{p}_2, \lambda_2) = D_{\lambda_1 M}^{(J)}(\mathbf{n}_1) D_{\lambda_2 M'}^{(J)}(\mathbf{n}_2) e^{i p_1 x_1} e^{i p_2 x_2} + D_{\lambda_2 M}^{(J)}(\mathbf{n}_2) D_{\lambda_1 M'}^{(J)}(\mathbf{n}_1) e^{i p_1 x_2} e^{i p_2 x_1}, \quad (1)$$

where x_1 and x_2 are the space-time coordinates of two multipole sources, $p_1 x_1 = E_1 t_1 - \mathbf{p}_1 \mathbf{x}_1$, $p_2 x_2 = E_2 t_2 - \mathbf{p}_2 \mathbf{x}_2$,

$$D_{\lambda_1 M}^{(J)}(\mathbf{n}_1) = D_{\lambda_1 M}^{(J)}(0, \theta_1, \phi_1) = (d_y(0, \theta_1, \phi_1) e^{i M \phi_1})_{\lambda_1 M},$$

$$D_{\lambda_2 M'}^{(J)}(\mathbf{n}_2) = D_{\lambda_2 M'}^{(J)}(0, \theta_2, \phi_2) = (d_y(0, \theta_2, \phi_2) e^{i M' \phi_2})_{\lambda_2 M'}, \quad (2)$$

are elements of the finite rotation matrix corresponding to the angular momentum J , $\mathbf{n}_1 = \mathbf{p}_1/|\mathbf{p}_1|$, $\mathbf{n}_2 = \mathbf{p}_2/|\mathbf{p}_2|$, θ_1, θ_2 and ϕ_1, ϕ_2 - polar and azimuthal angles of the momenta \mathbf{p}_1 and \mathbf{p}_2 , respectively .

Thus, in accordance with Eq. (1), the probability of emission of two identical particles with spin S , respective 4-momenta p_1, p_2 and helicities λ_1, λ_2 by two multipole sources

with the angular momentum J and projections M, M' of angular momentum onto the axis z amounts to :

$$W_{MM'}(p_1, \lambda_1; p_2, \lambda_2) = |D_{\lambda_1 M}^{(J)}(\mathbf{n}_1)|^2 |D_{\lambda_2 M'}^{(J)}(\mathbf{n}_2)|^2 + |D_{\lambda_1 M'}^{(J)}(\mathbf{n}_1)|^2 |D_{\lambda_2 M}^{(J)}(\mathbf{n}_2)|^2 + 2 (-1)^{2S} \operatorname{Re} \left(D_{\lambda_1 M}^{(J)}(\mathbf{n}_1) D_{\lambda_2 M}^{*(J)}(\mathbf{n}_2) D_{\lambda_1 M'}^{*(J)}(\mathbf{n}_1) D_{\lambda_2 M'}^{(J)}(\mathbf{n}_2) \right) \cos(qx), \quad (3)$$

where $q = p_1 - p_2$ is the difference of 4-momenta of two identical particles and $x = x_1 - x_2$ is the difference of 4-coordinates of two one-particle multipole sources.

Now let us average this expression over the angular momentum projections M, M' and over the space-time dimensions of the emission region . In doing so, we take into account that, due to the unitarity of the finite rotation matrix, the following relations hold :

$$\begin{aligned} \sum_{M=-J}^J |D_{\lambda_1 M}^{(J)}(\mathbf{n}_1)|^2 &= \sum_{M'=-J}^J |D_{\lambda_2 M'}^{(J)}(\mathbf{n}_2)|^2 = \\ &= \sum_{M=-J}^J |D_{\lambda_2 M}^{(J)}(\mathbf{n}_2)|^2 = \sum_{M'=-J}^J |D_{\lambda_1 M'}^{(J)}(\mathbf{n}_1)|^2 = 1. \end{aligned} \quad (4)$$

Let us remark that, without losing generality, we may choose the coordinate axis z as lying in the plane of the momenta \mathbf{p}_1 and \mathbf{p}_2 , with the axis y being perpendicular to this plane. Then the azimuthal angles of the momenta \mathbf{p}_1 and \mathbf{p}_2 will be equal to zero: $\phi_1 = \phi_2 = 0$, and the angle $\beta = \theta_1 - \theta_2$ will have the meaning of angle between the momenta \mathbf{p}_1 and \mathbf{p}_2 . In doing so, once again due to the unitarity of the finite rotation matrix, we obtain :

$$\begin{aligned} \sum_{M=-J}^J D_{\lambda_1 M}^{(J)}(\mathbf{n}_1) D_{M \lambda_2}^{*(J)}(\mathbf{n}_2) &= \sum_{M=-J}^J (e^{-i J_y \theta_1})_{\lambda_1 M} (e^{i J_y \theta_2})_{M \lambda_2} = \\ &= (e^{-i J_y (\theta_1 - \theta_2)})_{\lambda_1 \lambda_2} = (d_y^{(J)}(\beta))_{\lambda_1 \lambda_2}; \end{aligned} \quad (5)$$

$$\begin{aligned} \sum_{M'=-J}^J D_{\lambda_2 M'}^{(J)}(\mathbf{n}_2) D_{M' \lambda_1}^{*(J)}(\mathbf{n}_1) &= \sum_{M'=-J}^J (e^{-i J_y \theta_2})_{\lambda_2 M'} (e^{i J_y \theta_1})_{M' \lambda_1} = \\ &= (e^{i J_y (\theta_1 - \theta_2)})_{\lambda_2 \lambda_1} = (d_y^{(J)}(-\beta))_{\lambda_2 \lambda_1}. \end{aligned} \quad (6)$$

Using the well-known symmetry relation $(d_y^{(J)}(\beta))_{\lambda_1 \lambda_2} = (d_y^{(J)}(-\beta))_{\lambda_2 \lambda_1}$ [2], we come to the result :

$$\overline{W_{MM'}}(p_1, \lambda_1; p_2, \lambda_2) = \frac{1}{(2J+1)^2} \left(2 + 2 (d_{\lambda_1 \lambda_2}^{(J)}(\beta))^2 (-1)^{2S} \langle \cos(qx) \rangle \right). \quad (7)$$

Let us emphasize that the quantity $r = (d_{\lambda_1 \lambda_2}^{(J)}(\beta))^2$ has the meaning of the degree of non-orthogonality (non-distinguishability) of particle states with different helicities with respect to the momenta, the angle between which equals $\beta = \theta_1 - \theta_2$: $\langle \lambda_1 | \lambda_2 \rangle \neq 0$.

2. If the emitted identical particles with the momenta $\mathbf{p}_1, \mathbf{p}_2$ are unpolarized, then, after averaging over all the $(2S + 1)$ values of helicity allowed at spin S , we obtain:

$$\overline{W}(q) = \left(2(2S + 1)^2 + (-1)^{2S} 2 \sum_{\lambda_1 = -S}^S \sum_{\lambda_2 = -S}^S |d_{\lambda_1 \lambda_2}^{(J)}(\beta)|^2 \langle \cos(qx) \rangle \right) \frac{1}{(2J + 1)^2} \frac{1}{(2S + 1)^2} \quad (8)$$

At sufficiently large momentum differences q the correlation function, normalized by unity, will take the form :

$$R(q) = 1 + \frac{(-1)^{2S}}{(2S + 1)^2} \sum_{\lambda_1 = -S}^S \sum_{\lambda_2 = -S}^S |d_{\lambda_1 \lambda_2}^{(J)}(\beta)|^2 \langle \cos(qx) \rangle. \quad (9)$$

In particular, if $\beta = 0$, then we have $d_{\lambda_1 \lambda_2}^{(J)}(0) = \delta_{\lambda_1 \lambda_2}$, and formula (9) is simplified:

$$R(q) = 1 + (-1)^{2S} \frac{1}{2S + 1} \langle \cos(qx) \rangle. \quad (10)$$

Besides, taking into account the unitarity of the matrix $d_{\lambda_1 \lambda_2}^{(J)}(\beta)$, it is easy to see from Eq. (9) that at $J = S$ formula (10) is valid at any angles between the momenta \mathbf{p}_1 and \mathbf{p}_2 . Let us stress that Eq.(10) is related to particles with nonzero mass .

3. In the case of emission of two unpolarized photons, when the mass equals zero, spin $S = 1$ and each of the helicities λ_1, λ_2 takes only two $(2S)$ values: -1 and 1 , irrespective of the momentum direction, the correlation function for dipole sources has the form [3]:

$$R(q) = 1 + \frac{1}{4} \left[(d_{11}^{(1)}(\beta))^2 + (d_{-1,1}^{(1)}(\beta))^2 + (d_{-1,-1}^{(1)}(\beta))^2 + (d_{1,-1}^{(1)}(\beta))^2 \right] \langle \cos(qx) \rangle. \quad (11)$$

Taking into account the equalities:

$$d_{11}^{(1)}(\beta) = d_{-1,-1}^{(1)}(\beta) = \frac{1 + \cos \beta}{2}, \quad d_{1,-1}^{(1)}(\beta) = d_{-1,1}^{(1)}(\beta) = \frac{1 - \cos \beta}{2}, \quad (12)$$

we find:

$$R(q) = 1 + \frac{1}{4} (1 + \cos^2 \beta) \langle \cos(qx) \rangle. \quad (13)$$

At very small angles between the photon momenta ($\beta \ll 1$) we obtain:

$$R(q) = 1 + \frac{1}{2} \langle \cos(qx) \rangle. \quad (14)$$

For the case of quadrupole sources , the correlation function is as follows:

$$R(q) = 1 + \frac{1}{4} \left[(d_{11}^{(2)}(\beta))^2 + (d_{-1,1}^{(2)}(\beta))^2 + (d_{-1,-1}^{(2)}(\beta))^2 + (d_{1,-1}^{(2)}(\beta))^2 \right] \langle \cos(qx) \rangle. \quad (15)$$

Using the equalities:

$$d_{11}^{(2)}(\beta) = d_{-1,-1}^{(2)}(\beta) = \frac{1 + \cos \beta}{2} (2 \cos \beta - 1), \quad (16)$$

$$d_{1,-1}^{(2)}(\beta) = d_{-1,1}^{(2)}(\beta) = \frac{1 - \cos \beta}{2} (2 \cos \beta + 1), \quad (17)$$

we find the correlation function of two unpolarized photons emitted by the quadrupole sources :

$$R(q) = 1 + \frac{1}{4} (4 \cos^4 \beta - 3 \cos^2 \beta + 1) \langle \cos(qx) \rangle. \quad (18)$$

At $\beta \approx 0$ we have : $R(q) = 1 + \frac{1}{2} \langle \cos(qx) \rangle$, i.e. here we also obtain the standard formula (see Eq. (14)), corresponding to two directions of polarization for each of the photons [3].

Let us consider also the case of emission of two “left neutrinos (two “right” antineutrinos) , with helicity taking only one value $\lambda_1 = \lambda_2 = +\frac{1}{2}$. For this case, the correlation function in the model of multipole sources is as follows:

$$R(q) = 1 - (d_{\frac{1}{2}\frac{1}{2}}^{(J)}(\beta))^2 \langle \cos(qx) \rangle. \quad (19)$$

In particular, at $J = S = \frac{1}{2}$ we obtain :

$$R(q) = 1 - \cos^2 \frac{\beta}{2} \langle \cos(qx) \rangle. \quad (20)$$

In the limit $\beta \rightarrow 0$ Eq. (20) gives:

$$R(q) = 1 - \frac{1 + \cos(\beta/2)}{2} \langle \cos(qx) \rangle = 1 - \langle \cos(qx) \rangle. \quad (21)$$

References

- [1] M.I. Podgoretsky, EChAYa, **20** (1989) 266 .
- [2] L.D. Landau and E.M. Lifshitz, *Quantum Mechanics. Nonrelativistic theory* (Nauka, Moscow, 1989), par. 58.
- [3] V.L. Lyuboshitz and M.I. Podgoretsky, Yad. Fiz. **58** (1995) 33 [Phys. At. Nucl. **58** (1995) 30] .

NAMBU-POISSON FORMULATION OF THE SPINNING PARTICLE DYNAMICS IN THE (ACCELERATOR) EXTERNAL FIELDS

N.V. Makhaldiani[†]

Joint Institute for Nuclear Research, 141980 Dubna, Moscow Region, Russia

[†] *mnv@jinr.ru*

Abstract

Concise introduction in QCD Renormdynamics and Hamiltonization methods of the dynamical systems with application in heavy particle dynamics given.

Quantum field theory (QFT) and Fractal calculus provide universal language of fundamental physics (see e.g. [8]). In QFT existence of a given theory means, that we can control its behavior at some scales by renormalization theory [2, 3]. If the theory exists, than we want to solve it, which means to determine what happens on other scales. This is the problem (and content) of Renormdynamics. The result of the Renormdynamics, the solution of its discrete or continual motion equations, is the effective QFT on a given scale (different from the initial one). Perturbation theory series have the following qualitative form

$$f(x) = \sum_{n \geq 0} P(n)n!x^n = P(\delta)\Gamma(1 + \delta)\frac{1}{1-x}, \quad \delta = x \frac{d}{dx} \quad (1)$$

So, we reduce previous series to the standard geometric progression series. This series is convergent for $|x| < 1$ or for $|x|_p = p^{-k} < 1$, $x = p^k a/b$, $k \geq 1$, $p = 2, 3, 5, \dots, 29, \dots, 137, \dots$ With an appropriate normalization of the expansion parameter, the coefficients of the series are rational numbers and if experimental data indicates for some prime value, then we can take corresponding prime number and consider p-adic convergence of the series. In the Yukawa theory of strong interactions (see e.g. [2]), we take $\alpha = p = 13$,

$$f(p) = \sum f_n p^n, \quad f_n = n!P(n), \quad p = 13, \quad |f|_p \leq \sum |f_n|_p p^{-n} < \frac{1}{1-p^{-1}} \quad (2)$$

So, the series is convergent. If the limit is rational number, we consider it as an observable value of the corresponding physical quantity. In *MSSM* (see [6]) coupling constants unifies at $\alpha_u^{-1} = 26.3 \pm 1.9 \pm 1$. So, $23.4 < \alpha_u^{-1} < 29.2$

Question: how many primes are in this interval? (24, 25, 26, 27, 28, 29)

Only one! Proposal: take the value $\alpha_u^{-1} = 29.0\dots$ which will be two orders of magnitude more precise prediction and find the consequences for the *SM* scale observables.

The Goldberger-Treiman relation (GTR) [5] plays an important role in theoretical hadronic and nuclear physics. GTR relates the meson-nucleon coupling constants to the axial-vector coupling constant in β -decay: $g_{\pi N} f_\pi = g_{AMN}$. If we take

$$\alpha_{\pi N} = \frac{g_{\pi N}^2}{4\pi} = 13 \Rightarrow g_{\pi N} = 12.78; \quad f_\pi = \frac{130}{\sqrt{2}} = 91.9 \text{ MeV}, \quad m_N = 940 \text{ MeV}, \quad (3)$$

we find

$$g_A = \frac{f_\pi g_{\pi N}}{m_N} = \frac{91.9 \times \sqrt{52\pi}}{940} = 1.2496 \simeq 1.25 = \frac{5}{4}. \quad (4)$$

Renormdynamic equation

$$\dot{a} = \beta_1 a + \beta_2 a^2 + \dots \quad (5)$$

can be reparametrized,

$$\begin{aligned} a(t) &= f(A(t)) = A + f_2 A^2 + \dots + f_n A^n + \dots, \quad \dot{A} = b_1 A + b_2 A^2 + \dots \\ \dot{a} &= \dot{A} f'(A) = (b_1 A + b_2 A^2 + \dots)(1 + 2f_2 A + \dots + n f_n A^{n-1} + \dots) \\ b_1 &= \beta_1, \quad b_2 = \beta_2 + f_2 \beta_1 - 2f_2 b_1 = \beta_2 - f_2 \beta_1, \\ b_3 &= \beta_3 + 2f_2 \beta_2 + f_3 \beta_1 - 2f_2 b_2 - 3f_3 b_1 = \beta_3 + 2(f_2^2 - f_3) \beta_1, \\ b_4 &= \beta_4 + 3f_2 \beta_3 + f_2^2 \beta_2 + 2f_3 \beta_2 - 3f_4 b_1 - 3f_3 b_2 - 2f_2 b_3, \dots \\ b_n &= \beta_n + \dots + \beta_1 f_n - 2f_2 b_{n-1} - \dots - n f_n b_1, \dots \end{aligned} \quad (6)$$

so, by reparametrization, beyond the critical dimension ($\beta_1 \neq 0$) we can change any coefficient but β_1 . We can fix any higher coefficient with zero value. In the critical dimension of space-time, $\beta_1 = 0$, and we can change by reparametrization any coefficient but β_2 and β_3 . From the relations (6), in the critical dimension ($\beta_1 = 0$), we find that, we can define the minimal form of the RD equation

$$\dot{A} = \beta_2 A^2 + \beta_3 A^3, \quad (7)$$

then, as in the noncritical case, explicit solution for a will be given by reparametrization representation (6) [9]. If we know somehow the coefficients β_n , e.g. for first several exact and for others asymptotic values (see e.g. [7]) than we can construct reparametrization function (6) and find the dynamics of the running coupling constant. At any given scale by reparametrization $a = f(A)$ we can define new expansion parameter A as appropriate prime number. Statement: The reparametrization series for a is p-adically convergent, when β_n is rational numbers.

It was noted [12] that parton densities given by solution of the Altarelli-Parisi equation

$$\begin{aligned} \dot{M} &= AM, \quad M^T = (M_2, \bar{M}_2, M_2^s, M_2^G), \\ M_2 &= \int_0^1 dx x(u(x) + d(x)), \quad \bar{M}_2 = \int_0^1 dx x(\bar{u}(x) + \bar{d}(x)), \\ M_2^s &= \int_0^1 dx x(s(x) + \bar{s}(x)), \quad M_2^G = \int_0^1 dx x G(x), \end{aligned} \quad (8)$$

with the following valence quark initial condition at a scale m , $\bar{M}_2(m^2) = M_2^s(m^2) = M_2^G(m^2) = 0$, $M_2(m^2) = 1$ and $\alpha_s(m^2) = 2$, gives the experimental values $M_2 = 0.44$, $\bar{M}_2 = M_2^s = 0.04$, $M_2^G = 0.48$. So, for valence quark model, $\alpha_s(m^2) = 2$. We have seen, that for $\pi\rho N$ model $\alpha_{\pi\rho N} = 3$, and for πN model $\alpha_{\pi N} = 13$. It is nice that $\alpha_s^2 + \alpha_{\pi\rho N}^2 = \alpha_{\pi N}$. Note that to $\alpha_s = 2$ corresponds

$$g = \sqrt{4\pi\alpha_s} = 5.013 = 5 + . \quad (9)$$

Let us consider a general dynamical system

$$\dot{x}_n = v_n(x), \quad 1 \leq n \leq N. \quad (10)$$

The following Lagrangian and the corresponding motion equations

$$L = (\dot{x}_n - v_n(x))\psi_n, \quad \dot{x}_n = v_n(x), \quad \dot{\psi}_n = -\frac{\partial v_m}{\partial x_n}\psi_m, \quad (11)$$

extends the general system (10) by linear equation for the variables ψ . The extended system can be put in the Hamiltonian form

$$\dot{x}_n = \{x_n, H\}, \quad \dot{\psi}_n = \{\psi_n, H\}, \quad (12)$$

where the Hamiltonian and the bracket are defined as

$$H = v_n(x)\psi_n, \quad \{A, B\} = A\left(\overleftarrow{\frac{\partial}{\partial x_n}}\overrightarrow{\frac{\partial}{\partial \psi_n}} - \overleftarrow{\frac{\partial}{\partial \psi_n}}\overrightarrow{\frac{\partial}{\partial x_n}}\right)B. \quad (13)$$

In the Faddeev-Jackiw formalism [4] for the Hamiltonian treatment of systems defined by first-order Lagrangians and corresponding motion equations,

$$L = f_n(x)\dot{x}_n - H(x), \quad f_{mn}\dot{x}_n = \frac{\partial H}{\partial x_m}, \quad (14)$$

for the regular structure function f_{mn} , we have

$$\dot{x}_n = f_{nm}^{-1}\frac{\partial H}{\partial x_m} = \{x_n, x_m\}\frac{\partial H}{\partial x_m} = \{x_n, H\}, \quad (15)$$

where the fundamental Poisson (Dirac) bracket is

$$\{x_n, x_m\} = f_{nm}^{-1}, \quad f_{mn} = \partial_m f_n - \partial_n f_m. \quad (16)$$

The system (11) is an important example of the first order regular Hamiltonian systems. Indeed, in the new variables, $y_n^1 = x_n, y_n^2 = \psi_n$,

$$\begin{aligned} L &= (\dot{x}_n - v_n(x))\psi_n \Rightarrow \frac{1}{2}(\dot{x}_n\psi_n - \dot{\psi}_n x_n) - v_n(x)\psi_n \\ &= \frac{1}{2}y_n^a \varepsilon^{ab} y_n^b - H(y) = f_n^a(y)y_n^a - H(y), \quad f_n^a = \frac{1}{2}y_n^b \varepsilon^{ba}, \\ H &= v_n(y^1)y_n^2, \quad f_{nm}^{ab} = \frac{\partial f_m^b}{\partial y_n^a} - \frac{\partial f_n^a}{\partial y_m^b} = \varepsilon^{ab}\delta_{nm}; \\ \dot{y}_n^a &= \varepsilon_{ab}\delta_{nm}\frac{\partial H}{\partial y_m^b} = \{y_n^a, H\}, \quad \{y_n^a, y_m^b\} = \varepsilon_{ab}\delta_{nm}. \end{aligned} \quad (17)$$

In the canonical formulation, the equations of motion of a physical system are defined via a Poisson bracket and a Hamiltonian. In Nambu formulation, the Poisson bracket is replaced by the Nambu bracket with $n+1, n \geq 1$, slots. For $n=1$, we have the canonical formalism with one Hamiltonian. For $n \geq 2$, we have Nambu-Poisson formalism, with n Hamiltonians, [10], [13]. To study the strong interaction's spin dependence with polarized proton beams, one must preserve and control the polarization during acceleration and

storage. The quasi-classical description of the motion of a relativistic point particle with spin in accelerators and storage rings includes the equations of orbit motion

$$\begin{aligned} \dot{x}_n &= f_n(x), \quad f_n(x) = \varepsilon_{nm} \partial_m H, \quad n, m = 1, 2, \dots, 6; \quad x_n = q_n, \quad x_{n+3} = p_n, \\ H &= e\Phi + c\sqrt{\wp^2 + m^2 c^2}, \quad \wp_n = p_n - \frac{e}{c} A_n \end{aligned} \quad (18)$$

and Thomas-BMT equations [11, 1] of classical spin motion

$$\begin{aligned} \dot{s}_n &= \varepsilon_{nmk} \Omega_m s_k = \{H_1, H_2, s_n\}, \quad H_1 = \Omega \cdot s, \quad H_2 = s^2, \quad \{A, B, C\} = \varepsilon_{nmk} \partial_n A \partial_m B \partial_k C \\ \Omega_n &= \frac{-e}{m\gamma c} \left((1 + k\gamma) B_n - k \frac{(B \cdot \wp) \wp_n}{m^2 c^2 (1 + \gamma)} + \frac{1 + k(1 + \gamma)}{mc(1 + \gamma)} \varepsilon_{nmk} E_m \wp_k \right), \end{aligned} \quad (19)$$

where parameters e and m are the charge and the rest mass of the particle, c is the velocity of light, $k = (g - 2)/2$ quantifies the anomalous spin g factor, γ is the Lorentz factor, p_n are components of the kinetic momentum vector, E_n and B_n are the electric and magnetic fields, and A_n and Φ are the vector and scalar potentials. The spin motion equations we put in the Nambu-Poisson form. The general method of Hamiltonization of the dynamical systems we can use also in the spinning particle case. For this we invent for unified configuration space $q = (x, p, s)$, $x_n = q_n$, $p_n = q_{n+3}$, $s_n = q_{n+6}$, $n = 1, 2, 3$, the extended phase space, (q_n, ψ_n) , Hamiltonian and corresponding motion equations

$$H = H(q, \psi) = v_n \psi_n, \quad \dot{q}_n = v_n(q), \quad \dot{\psi}_n = -\frac{\partial v_m}{\partial q_n} \psi_m, \quad (20)$$

where v_n depends on external fields as control parameters which can be determined according to the optimal control criterium.

References

- [1] V. Bargmann, L. Michel, V.L. Telegdi, *Precession of the polarization of particles moving in a homogeneous electromagnetic field*, Phys. Rev. Lett., **2(10)** (1959) 435.
- [2] N.N. Bogoliubov and D.V. Shirkov, *Introduction to the Theory of Quantized Fields*, New York 1959.
- [3] J.C. Collins, *Renormalization*, Cambridge Univ. Press, London 1984.
- [4] L.D. Faddeev, R. Jackiw, Phys.Rev.Lett. **60** (1988) 1692.
- [5] M.L. Goldberger, S.B. Treiman, Phys. Rev. **110** (1958) 1178.
- [6] D.I. Kazakov, *Supersymmetric Generalization of the Standard Model of Fundamental Interactions*, Textbook, JINR Dubna 2004.
- [7] D.I. Kazakov, D.V. Shirkov, *Fortschr. d. Phys.* **28** (1980) 447.
- [8] N. Makhaldiani, *Fractal Calculus (H) and some Applications*, Physics of Particles and Nuclei Letters **8** (2011) 325.
- [9] N. V. Makhaldiani, *Renormdynamics, Multiparticle Production, Negative Binomial Distribution, and Riemann Zeta Function*, Physics of Atomic Nuclei, **76** (2013) 1169.
- [10] Y. Nambu, Phys.Rev. **D7** (1973) 2405.
- [11] L.H. Thomas, Philos. Mag. **3** (1927) 1.
- [12] M.B. Voloshin, K.A. Ter-Martyrosian, *Gauge Theory of Elementary Particles*, Atomizdat, Moscow 1984.
- [13] E.T. Whittaker, *A Treatise on the Analytical Dynamics*, Cambridge 1927.

GENERALISED PARTON DISTRIBUTIONS OF PHOTON

Asmita Mukherjee^{1†}, Sreeraj Nair¹ and Vikash Kumar Ojha¹

(1) *Indian Institute of Technology, Bombay*

† *E-mail: asmita.phy@iitb.ac.in*

Abstract

We studied the generalized parton distributions of photon using the overlap representation of light-front wave function and calculated both the helicity flip and the non-flip case.

1 Introduction

In recent years Generalised Parton Distribution(GPD) functions have emerged as an important tool for acquiring information about the structure of hadrons [1]. GPDs are special in the sense that they contain the combined information of the parton distribution function and the form factors. GPDs are also related to the total angular momentum of quarks inside the proton via Ji's [2] sum rule thus providing us with an handle on the elusive orbital angular momentum(OAM) of quarks inside the proton. GPDs are accessed via exclusive process like the deeply virtual Compton scattering(DVCS), $ep \rightarrow ep'\gamma$ where there is a finite momentum transfer between the initial and the final state with a real photon being observed at the final state.

In [3] deeply virtual Compton scattering (DVCS) $\gamma^*\gamma \rightarrow \gamma\gamma$ on a photon target was considered in the kinematic region of large center-of-mass energy, large virtuality (Q^2) but small squared momentum transfer ($-t$). The calculation was done at leading order in α and zeroth order in α_s when the momentum transfer was purely in the longitudinal direction. In another recent work [4], GPDs of the photon have been used to investigate analyticity properties of DVCS amplitudes and related sum rules for the GPDs. In this work we investigate the GPDs of photon when the momentum transfer is in both transverse and longitudinal direction and we also study the helicity flip and non-flip case of the real photon (target) state.

2 Generalised Parton Distributions of Photon

The GPDs for the photon can be expressed as the following off-forward matrix elements defined for the real photon (target) state [3]:

$$\begin{aligned} F^q &= \int \frac{dy^-}{8\pi} e^{-\frac{iP^+y^-}{2}} \langle \gamma(P', \lambda') | \bar{\psi}(0)\gamma^+\psi(y^-) | \gamma(P, \lambda) \rangle; \\ \tilde{F}^q &= \int \frac{dy^-}{8\pi} e^{-\frac{iP^+y^-}{2}} \langle \gamma(P', \lambda') | \bar{\psi}(0)\gamma^+\gamma^5\psi(y^-) | \gamma(P, \lambda) \rangle. \end{aligned} \quad (1)$$

F^q and \tilde{F}^q contributes when the photon is unpolarized and polarized respectively. We have chosen the light-front gauge $A^+ = 0$. We use the Fock space expansion of the photon state to calculate F^q and \tilde{F}^q . We express the GPDs in terms of photon light-front wave functions (LFWFs) and calculate them analytically using these LFWFs.

By taking a Fourier transform (FT) with respect to the transverse momentum transfer Δ^\perp we get the GPDs in the transverse impact parameter space.

$$q(x, b^\perp) = \frac{1}{(2\pi)^2} \int d^2\Delta^\perp e^{-i\Delta^\perp \cdot b^\perp} F^q = \frac{1}{2\pi} \int \Delta d\Delta J_0(\Delta b) F^q;$$

$$\tilde{q}(x, b^\perp) = \frac{1}{(2\pi)^2} \int d\Delta e^{-i\Delta^\perp \cdot b^\perp} \tilde{F}^q = \frac{1}{2\pi} \int \Delta d\Delta J_0(\Delta b) \tilde{F}^q.$$

where $J_0(z)$ is the Bessel function. The impact parameter distribution for a polarized photon is given by $\tilde{q}(x, b^\perp)$.

In Fig. 1(a) we have plotted the unpolarized photon GPD F^q as a function of x for a fixed value of ζ and different values of t . With $\Delta^\perp \neq 0$ the symmetry with respect to $x = 0.5$ is lost and also the GPDs become independent of t as $x \rightarrow 1$ because in this limit all the momentum is carried by the quark in the photon. In Fig. 1(b) we have plotted the Fourier transform (FT) of F^q with respect to Δ^\perp as a function of b and for fixed x . In all the plots we have taken $0 < x < 1$ for which the contribution comes from the active quark in the photon ($q\bar{q}$). The smearing in b^\perp space reveals the partonic substructure of the photon and its 'shape' in transverse space. The behavior in impact parameter space is qualitatively different than a dressed quark target and also from phenomenological models of proton GPDs. In the case of a photon there is no single particle contribution, and the distribution in b space purely reveals the internal $q\bar{q}$ structure of the photon. Here near $x \approx 1/2$ the peak in b space is very broad which means that the parton distribution is more dispersed when the q and \bar{q} share almost equal momenta. The parton distribution is sharper both for smaller x and larger x .

We extract the GPD that involves a helicity flip of the target photon from the non-vanishing coefficient of the combination $(\epsilon_{+1}^1 \epsilon_{-1}^{1*} + \epsilon_{-1}^2 \epsilon_{+1}^{2*})$. The GPD with helicity flip can be calculated analytically and is given by:

$$E_1 = \frac{\alpha e_q^2}{2\pi} x(1-x)^3 ((\Delta^1)^2 - (\Delta^2)^2) \quad (2)$$

$$\left[\int_0^1 dq \frac{(q^2 - q)}{\left(m^2 \left(1 - x(1-x) \right) + q(1-q)(1-x)^2 (\Delta^\perp)^2 \right)} \right]$$

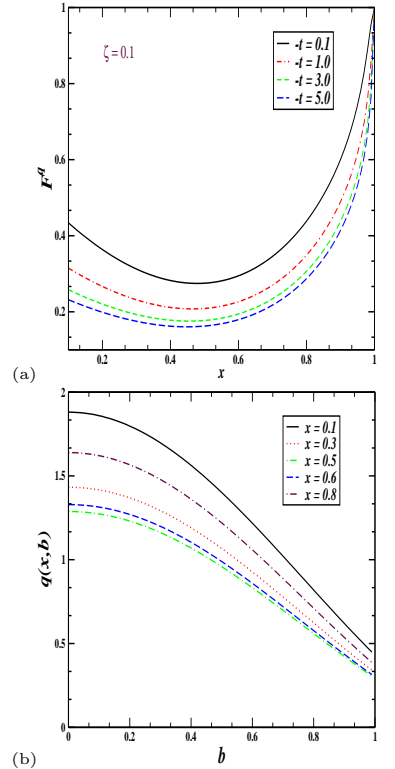


Figure 1: (Color online.) Plots of helicity non-flip ($\lambda = \lambda'$) Photon GPD. (a) Plot of unpolarized GPD F^q vs x for fixed values of $-t$ in GeV^2 for $\zeta = 0.1$ and (b) FT of unpolarized GPD $q(x, b)$ vs b for fixed values of x .

The above has the expected quadrupole structure coming from $((\Delta^1)^2 - (\Delta^2)^2)$. As the photon is a spin one particle, in order to flip its helicity, the overlapping light-front wave functions should have a difference of orbital angular momentum of two units, which manifests itself in the quadrupole structure. This is in accordance with a similar observation for the helicity-flip GPD E for the proton, which needs overlapping light-front wave functions of orbital angular momentum ± 1 unit [5,9]. Like the GPD E of a spin 1/2 particle for example a dressed electron/quark [7], the helicity flip photon GPD has no logarithmic term depending on the hard scale of the process Q^2 , which is the virtuality of the probing photon.

Starting from the expressions of photon GPDs, we define the parton distributions [8] with the helicity flip of the photon in transverse impact parameter space as:

$$q_1(x, b^\perp) = \frac{\alpha e_q^2}{4\pi^3} \int_0^\infty \Delta d\Delta \int_0^\pi d\theta \int_0^1 dq \left\{ \left(\frac{(b_1^2 - b_2^2)\Delta \sin\theta}{b^3} \right) \frac{\left(b\Delta \cos(b\Delta \sin\theta) \sin\theta - \sin(b\Delta \sin\theta) \right) (q^2 - q)x(1-x)^3}{\left(m^2(1-x(1-x)) + q(1-q)(1-x)^2(\Delta^\perp)^2 \right)} \right\} \quad (3)$$

In Fig. 2 we have plotted the helicity flip photon GPD $E_1(x, \Delta^\perp)$ vs. x for different values of t and a fixed value of $\phi = \tan^{-1} \frac{\Delta^2}{\Delta^1}$. The peak of $E_1(x, \Delta^\perp)$ increases with $-t$ and also shifts towards higher x . The GPD is zero when $\Delta^\perp = 0$ because in order to flip the helicity one needs non-zero OAM in the two-particle LFWFs and the OAM is zero when there is no momentum transfer in the transverse direction. There is no OAM contribution at $x = 0$ and $x = 1$ since all momenta are carried by either the quark or the antiquark in the photon. The upper limit of the Δ^\perp integration ideally should be ∞ . But in the numerical calculation we have a cutoff denoted by Δ_{max} . Fig. 3 shows a plot of $q_1(x, b^\perp)$ vs. b^1 and b^2 for a fixed value of $x = 0.3$ and different values of Δ_{max} . As Δ_{max} increases the peaks become sharper, which means that the distortion in b^\perp space moves closer to the origin.

3 Conclusion

We discussed the calculations for the generalized parton distributions of the photon for both the helicity flip as well as the non-flip case. We calculated at zeroth order in α_s and leading order in α . We also calculated the respective GPDs in the impact parameter space.

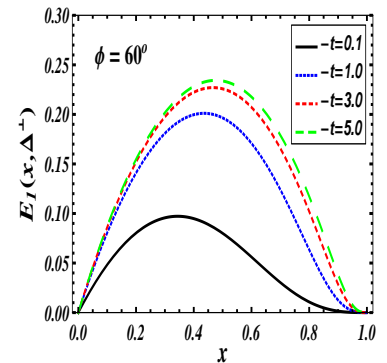


Figure 2: (Color online) Plots of $E_1(x, \Delta^\perp)$ vs x for different values of $t(\text{GeV}^2)$.

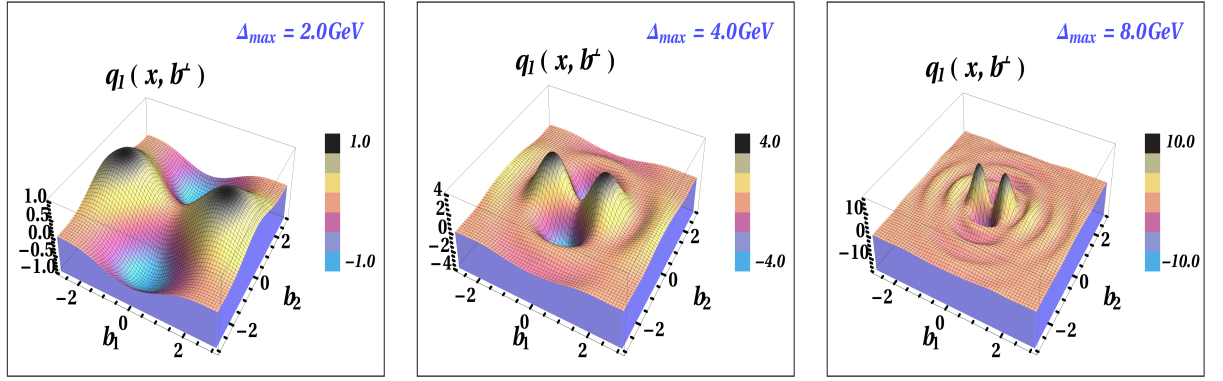


Figure 3: (Color online) Plots of $q_1(x, b^\perp)$ vs. b^1, b^2 for different values of Δ_{max} . b^1 and b^2 are in GeV^{-1} and Δ_{max} is in GeV . $x = 0.3$.

4 Acknowledgements

I thank the organizers of DSPIN-13 for the kind invitation and all the support provided. This work is supported by the DST project SR/S2/HEP-029/2010, Govt. of India.

References

- [1] For reviews on generalized parton distributions, and DVCS, see M. Diehl, Phys. Rept, **388**, 41 (2003); A. V. Belitsky and A. V. Radyushkin, Phys. Rept. **418** 1, (2005); K. Goeke, M. V. Polyakov, M. Vanderhaeghen, Prog. Part. Nucl. Phys. **47**, 401 (2001).
- [2] J.Xiangdong Phys. Rev. Lett. **78**, 6107A5613 (1997)
- [3] S. Friot, B. Pire, L. Szymanowski, Phys. Lett. **B 645** 153 (2007).
- [4] I. R. Gabdrakhmanov, O. V. Teryaev, Phys. Lett. **B 716**, 417 (2012).
- [5] S. J. Brodsky, M. Diehl, D. S. Hwang, Nucl. Phys. **B 596**, 99 (2001); M. Diehl, T. Feldman, R. Jakob, P. Kroll, Eur. Phys. J. **C 39**, 1 (2005).
- [6] S. J. Brodsky, D. S. Hwang, B-Q. Ma, I. Schmidt, Nucl. Phys. **B 593**, 311 (2001).
- [7] D. Chakrabarti and A. Mukherjee, Phys.Rev.**D72**, 034013 (2005); Phys. Rev. **D71**, 014038 (2005).
- [8] M. Burkardt, Int. J. Mod. Phys. **A 18**, 173 (2003); M. Burkardt, Phys. Rev. **D 62**, 071503 (2000), Erratum- ibid, **D 66**, 119903 (2002); J. P. Ralston and B. Pire, Phys. Rev. **D 66**, 111501 (2002).
- [9] A. Mukherjee, Sreeraj Nair, Phys. Lett. **B 706** 77 (2011).
- [10] A. Mukherjee, Sreeraj Nair, Phys. Lett. **B 707** 99 (2012).
- [11] A. Mukherjee, Sreeraj Nair, Vikash Kumar Ojha, Phys. Lett. **B 721** 284 (2013).

ABSENCE OF THE NON-UNIQUENESS PROBLEM OF THE DIRAC THEORY IN A CURVED SPACETIME SPIN-ROTATION COUPLING IS NOT PHYSICALLY RELEVANT

M.V. Gorbatenko and V.P. Neznamov^{1†}

*Russian Federal Nuclear Center – All-Russian Research Institute of Experimental Physics,
Sarov, Mira 37, Nizhni Novgorod region, Russia, 607188*

^{1†} *E-mail: neznamov@vniief.ru*

In the recent time, Arminjon's publications have emerged again [1–4], which declare and provide grounds for the assertion that the Dirac theory is non-unique in a curved and even flat spacetime. The proof is based on the demonstration that the form of Dirac Hamiltonians depends on the choice of tetrads. In our opinion, this is absolutely insufficient. To demonstrate the non-equivalence of Dirac Hamiltonians, one should find the difference in physical characteristics of a system under consideration with different choices of tetrads. Such characteristics may include energy spectra of Hamiltonians, mean values of physical quantities, various transition amplitudes and so on.

We share the conclusions of previous studies [5, 6] on the independence of physical characteristics of the Dirac theory on the choice of tetrads.

In [7–9], using the methods of pseudo-Hermitian quantum mechanics [10–12] for arbitrary, including time-dependent, gravitational fields, we developed an algorithm to transform any Dirac Hamiltonian in a curved spacetime with an arbitrary choice of tetrads into the η -representation, in which the Hamiltonian becomes self-conjugate, and the scalar product of wave functions becomes flat. The choice of different tetrads for the same physical system can lead in the η -representation to different forms of self-conjugate Hamiltonians. However, they will always be related by unitary transformations associated with spacetime rotations of Dirac matrices. It is evident that such Hamiltonians are physically equivalent. The choice of tetrads by a researcher is governed by convenience considerations. One can handle Dirac Hamiltonians in a curved spacetime using Parker's weight operator in the scalar product of wave functions [13], or treat them in the η -representation with a flat scalar product, using the common apparatus of quantum mechanics. In both cases physical characteristics of the systems remain identical.

Thus, as opposed to statements in [4] we show in papers [7–9] that the non-uniqueness problem of the Dirac theory in a curved spacetime from the point of view of receipt of different physical results for one and the same physical system does not exist.

Let us give some examples to illustrate this.

Example 1. In [7], three Hamiltonians, corresponding to three tetrad fields, and a self-conjugate Hamiltonian in the η -representation are derived for a weak Kerr field.

a) Killing tetrad field

$$\begin{aligned}
 H_k = im\gamma_0 - im\frac{M}{R}\gamma_0 - i\gamma_0\gamma^k\frac{\partial}{\partial x^k} + 2i\frac{M}{R}\gamma_0\gamma^k\frac{\partial}{\partial x^k} + \\
 \frac{i}{2}\frac{MR_k}{R^3}\gamma_0\gamma^k + 2i\frac{M(J_{kl}R_l)}{R^3}\frac{\partial}{\partial x^k} - 2im\frac{M(J_{kl}R_l)}{R^3}\gamma^k + \\
 2i\frac{M(J_{ml}R_l)}{R^3}S_{mk}\frac{\partial}{\partial x^k} - \frac{i}{2}\left\{\frac{M}{R^3}J_k - 3\frac{M(J_l R_l)R_k}{R^5}\right\}\gamma_5\gamma_0\gamma_k.
 \end{aligned} \tag{4}$$

$$\rho = 1 + \frac{3M}{R} + 2\frac{M(J_{km}R_m)}{R^3}\gamma_0\gamma_k; \tag{5}$$

b) tetrad field in symmetric gauge

$$H_s = im\gamma_0 - i\gamma_0\gamma_k \frac{\partial}{\partial x^k} - im\frac{M}{R}\gamma_0 + 2i\frac{M}{R}\gamma_0\gamma^k \frac{\partial}{\partial x^k} + \frac{i}{2}a\frac{MR_k}{R^3}\gamma_0\gamma^k + 2i\frac{M(J_{kl}R_l)}{R^3}\frac{\partial}{\partial x^k} - im\frac{M(J_{kl}R_l)}{R^3}\cdot\gamma^k + i\frac{M(J_{m1}R_l)}{R^3}S_{mk}\frac{\partial}{\partial x^k}. \quad (6)$$

$$\rho = 1 + \frac{3M}{R} + \frac{MJ_{km}R_m}{R^3}\gamma_0\gamma_k; \quad (7)$$

c) tetrad field of Hehl and Ni [14]

$$H_{H-N} = im\gamma_0 - im\frac{M}{R}\gamma_0 - i\gamma_0\gamma_k \frac{\partial}{\partial x^k} + 2i\frac{M}{R}\gamma_0\gamma^k \frac{\partial}{\partial x^k} + \frac{i}{2}\frac{MR_k}{R^3}\gamma_0\gamma^k + 2i\frac{M(J_{kl}R_l)}{R^3}\frac{\partial}{\partial x^k} + \frac{i}{2}\left\{\frac{M}{R^3}J_k - 3\frac{M(J_l R_l)R_k}{R^5}\right\}\gamma_5\gamma_0\gamma_k. \quad (8)$$

$$\rho = 1 + \frac{3M}{R}; \quad (9)$$

d) self-conjugate Hamiltonian in the η -representation

$$H_\eta = im\gamma_0 - im\frac{M}{R}\gamma_0 - i\gamma_0\gamma_k \frac{\partial}{\partial x^k} + 2i\frac{M}{R}\gamma_0\gamma^k \frac{\partial}{\partial x^k} - i\frac{MR_k}{R^3}\gamma_0\gamma^k + 2i\frac{M(J_{kl}R_l)}{R^3}\frac{\partial}{\partial x^k} + \frac{i}{2}\left\{\frac{M}{R^3}J_k - 3\frac{M(J_l R_l)R_k}{R^5}\right\}\gamma_5\gamma_0\gamma_k. \quad (10)$$

$$\rho = 1. \quad (11)$$

In (1) - (11), M is the mass of a source of the Kerr gravitational field, J_{km} is the angular momentum tensor of the Kerr field, $S_{mk} = \frac{1}{2}(\gamma_m\gamma_k - \gamma_k\gamma_m)$.

Each of the Hamiltonians (1), (6), (3), (12) differ from each other in their form. However, with the transition to the η -representation, all the Hamiltonians become the same, which proves their physical equivalence.

Example 2. We know that a free Dirac Hamiltonian in spherical coordinates of Minkowski space can be written in two ways resulting in substantially different expressions (see, e.g., [15])

$$H_1 = im\gamma_0 - i\gamma_0\left\{\gamma_1\left(\frac{\partial}{\partial r} + \frac{1}{r}\right) + \frac{1}{r}\gamma_2\left(\frac{\partial}{\partial\theta} + \frac{1}{2}ctg\theta\right) + \frac{1}{r\sin\theta}\gamma_3\frac{\partial}{\partial\phi}\right\}, \quad (12)$$

$$H_2 = im\gamma_0 - i\gamma_0\left\{\gamma_r\frac{\partial}{\partial r} + \gamma_\theta\frac{1}{r}\frac{\partial}{\partial\theta} + \gamma_\phi\frac{1}{r\sin\theta}\frac{\partial}{\partial\phi}\right\}. \quad (13)$$

In (13),

$$\begin{aligned} \gamma_r &= \sin\theta[\gamma_1\cos\phi + \gamma_2\sin\phi] + \gamma_3\cos\theta = R\gamma_1R^{-1} \\ \gamma_\theta &= \cos\theta[\gamma_1\cos\phi + \gamma_2\sin\phi] - \gamma_3\sin\theta = R\gamma_2R^{-1} \\ \gamma_\phi &= -\gamma_1\sin\phi + \gamma_2\cos\phi = R\gamma_3R^{-1}. \end{aligned} \quad (14)$$

The set $\{\gamma_r, \gamma_\theta, \gamma_\phi\}$ is related to the set $\{\gamma_1, \gamma_2, \gamma_3\}$ by a unitary matrix R ,

$$\begin{aligned} R &= R_1T_1R_2T_2 \\ R_1 &= \exp\left(-\frac{\phi}{2}\gamma_1\gamma_2\right); \quad T_1 = \frac{1}{\sqrt{2}}\gamma_5\gamma_1(E + \gamma_1\gamma_2) \\ R_2 &= \exp\left(-\frac{\theta}{2}\gamma_2\gamma_3\right); \quad T_2 = \frac{1}{\sqrt{2}}\gamma_5\gamma_2(E + \gamma_3\gamma_1). \end{aligned} \quad (15)$$

This shows that the Hamiltonians (12), (13) are physically equivalent, because they are related by the unitary transformation (15)

$$H_2 = RH_1R^{-1}, \quad R^{-1} = R^+. \quad (16)$$

Example 3. In [9], the following form of a Dirac Hamiltonian in Boyer-Lindquist coordinates is derived for a weak Kerr field:

$$\begin{aligned}
H_{B-L} = & im \left(1 - \frac{r_0}{2r}\right) \gamma_0 - i \left(1 - \frac{r_0}{r}\right) \gamma_0 \gamma_1 \left(\frac{\partial}{\partial r} + \frac{1}{r}\right) - \\
& i \left(1 - \frac{r_0}{2r}\right) \frac{1}{r} \left[\gamma_0 \gamma_2 \left(\frac{\partial}{\partial \theta} + \frac{1}{2} ctg \theta\right) + \gamma_0 \gamma_3 \frac{1}{\sin \theta} \frac{\partial}{\partial \phi} \right] - \\
& i \gamma_0 \gamma_1 \frac{r_0}{2r^2} - i \frac{r_0 a}{r^3} \frac{\partial}{\partial \phi} - i \frac{3}{4} \frac{r_0 a}{r^3} \gamma_3 \gamma_1 \sin \theta.
\end{aligned} \tag{17}$$

Let us compare this Hamiltonian with Hamiltonian (12). We rewrite (12) using somewhat different notation

$$\begin{aligned}
H_\eta = & im \left(1 - \frac{r_0}{2r}\right) \gamma_0 - i \left(1 - \frac{r_0}{r}\right) \gamma_0 \gamma_{\underline{k}} \frac{\partial}{\partial x^k} - \\
& i \frac{r_0}{2r^3} \gamma_0 \gamma_{\underline{k}} x_k - i \frac{r_0 a}{r^3} \left(x_1 \frac{\partial}{\partial x_2} - x_2 \frac{\partial}{\partial x_1}\right) + \\
& i \frac{r_0 a}{4r^3} \left[\gamma_1 \gamma_2 \left(1 - 3 \frac{x_3^2}{r^2}\right) - \gamma_2 \gamma_3 \frac{3x_3 x_1}{r^2} - \gamma_3 \gamma_1 \frac{3x_3 x_2}{r^2} \right].
\end{aligned} \tag{18}$$

In (18), $r_0 = 2M$, $\mathbf{J} = Ma$, $\mathbf{a} = (0, 0, a)$.

The summands with the momentum of rotation a in (17), (18) differ substantially from each other. However, in [9], these terms in (17), (18) are shown to be also physically equivalent using matrices (14), (15).

Example 4. For the solution

$$ds^2 = V^2(\mathbf{x}) dt^2 - W^2(\mathbf{x}) d\mathbf{x}^2 \tag{19}$$

Obukhov [16] obtained a self-conjugate Hamiltonian with a flat scalar product of wave functions

$$H_{Ob} = \beta m V + \frac{1}{2} \left[\boldsymbol{\alpha} \mathbf{p} \frac{V}{W} + \frac{V}{W} \boldsymbol{\alpha} \mathbf{p} \right] \tag{20}$$

In (20), $\beta = \gamma^0$, $\alpha^k = \gamma^0 \gamma^k$.

Then, after the unitary Eriksen-Kolsrud transformation [17], in the approximation of a weak gravitational field, Hamiltonian (20) becomes equal to

$$\begin{aligned}
H_{E-K} = & \beta \left(m V + \frac{\mathbf{p}^2}{2m} \right) - \frac{\beta}{4m} \{p^2, V - 1\} + \\
& \frac{\beta}{2m} \{ \mathbf{p}^2, \frac{V}{W} - 1 \} + \frac{\beta}{4m} [2\boldsymbol{\Sigma}(\mathbf{f} \times \mathbf{p}) + \nabla \mathbf{f}] + \frac{1}{2} (\boldsymbol{\Sigma} \Phi).
\end{aligned} \tag{21}$$

In (21), $\Phi = \nabla V$; $f = \nabla \left(\frac{V}{W}\right)$; $\boldsymbol{\Sigma} = \begin{pmatrix} \boldsymbol{\sigma} & 0 \\ 0 & \boldsymbol{\sigma} \end{pmatrix}$. However, for correct classical interpretation of individual summands in the Hamiltonian, initial expression (20) should be subjected to a unitary Foldy-Wouthuysen transformation [18], [19], [20].

As a result, A.Silenko and O. Teryaev [19] obtained the following expression for the transformed Hamiltonian:

$$\begin{aligned}
H_{FW} = & \beta \left(m V + \frac{\mathbf{p}^2}{2m} \right) - \frac{\beta}{4m} \{p^2, V - 1\} + \frac{\beta}{2m} \{ \mathbf{p}^2, \frac{V}{W} - 1 \} + \\
& \frac{\beta}{4m} [2\boldsymbol{\Sigma}(\mathbf{f} \times \mathbf{p}) + \nabla \mathbf{f}] - \frac{\beta}{8m} [2\boldsymbol{\Sigma}(\Phi \times \mathbf{p}) + \nabla \Phi].
\end{aligned} \tag{22}$$

The last summand in (22), instead of direct interaction between spin and gravity ($\frac{1}{2} \boldsymbol{\Sigma} \Phi$), describes the spin-orbital and contact interaction of a Dirac particle similarly to the interaction with an electromagnetic field [18].

Note that all the three Hamiltonians (20), (21), (22), are physically equivalent, because they are related to each other by unitary transformations. However, for the quasi-classical interpretation of Hamiltonian terms, one should use the Foldy-Wouthuysen representation [19], [20].

Now we consider the example given in one of the last works of Arminjon [3], in which he demonstrates the non-uniqueness (in his opinion) of the Dirac theory even in the flat Minkowski space.

Example 5. Arminjon considers a flat Minkowski space, (t', x', y', z') , with a free Dirac Hamiltonian

$$H' = \boldsymbol{\alpha}' \mathbf{p}' + \beta' m. \quad (23)$$

Then he considers a set of other time-dependent Dirac matrices

$$\begin{aligned} \beta &= \beta' \\ \alpha^1 &= \alpha'^1 \cos \omega t + \alpha'^2 \sin \omega t \\ \alpha^2 &= \alpha'^2 \cos \omega t - \alpha'^1 \sin \omega t \\ \alpha^3 &= \alpha'^3. \end{aligned} \quad (24)$$

As a result, for the new tetrads leading to the set of matrices α^k (24), a new Hamiltonian is obtained:

$$H = \boldsymbol{\alpha} \mathbf{p}' + \beta m - \frac{\omega}{2} \Sigma^3, \quad (25)$$

where $\Sigma^3 = i\alpha'^1 \alpha'^2 = i\alpha^1 \alpha^2 = \Sigma^3$.

Comparing (23), (25) Arminjon [3, 4] concludes that the Dirac theory is non-unique even in the flat Minkowski space.

In fact, as opposite to the initial Hamiltonian (23), the Hamiltonian (25) depends on time clearly (see. (24)). In addition, the Hamiltonian (25) has a complementary term $-\frac{\omega}{2} \Sigma^3$ and therefore in [3], [4] a question of physical significance of the direct spin-rotation coupling is discussed.

However, note that the matrices α^i (24) are related to the initial matrices α'^i by a unitary transformation matrix $R(t)$

$$\alpha^i = R \alpha'^i R^+, \quad (26)$$

where

$$R(t) = e^{\frac{\omega t}{2} \alpha'^1 \alpha'^2}; \quad R^+(t) = e^{-\frac{\omega t}{2} \alpha'^1 \alpha'^2}. \quad (27)$$

Considering that $R(t)$ is time dependent, we see that the Hamiltonians (25) and (23) are related by the unitary transformation

$$H = R H' R^+ - i R \frac{\partial R^+}{\partial t}. \quad (28)$$

Consequently, the Hamiltonians (23) and (25) are physically equivalent. If the free Hamiltonian (23) transforms to the Foldy-Wouthuysen representation, we obtain the known Hamiltonian [18]

$$H_{FW} = \beta \sqrt{m^2 + \mathbf{p}'^2}. \quad (29)$$

In [4] Arminjon attempted to define the difference between the mean values $\langle H \rangle$ and $\langle H' \rangle$ exactly. However, at averaging of the physical quantities for the spin particles it is

necessary to average also over spin states with appropriate change of normalizing condition $\sum_{\pm s} \int \psi^+(\mathbf{x}', s)\psi(\mathbf{x}', s) d\mathbf{x}' = \sum_{\pm s} \int \psi'^+(\mathbf{x}', s)\psi'(\mathbf{x}', s) d\mathbf{x}' = 1$. Then

$$\langle H \rangle - \langle H' \rangle = -\frac{\omega}{2} \sum_{\pm s} \int \psi^+(\mathbf{x}', s) \frac{\Sigma' \mathbf{p}'}{|\mathbf{p}'|} \psi(\mathbf{x}', s) d\mathbf{x}' = -\frac{\omega}{2} \sum_{\pm s} \int \psi'^+(\mathbf{x}', s) \Sigma'^3 \psi'(\mathbf{x}', s) d\mathbf{x}' = 0. \quad (30)$$

In (30) we choose a movement particle direction along z' coordinate ($|\mathbf{p}'| = p'^3$). As opposite to [4] following (30) the mean values of the Hamiltonians H and H' coincide.

Hence, the spin-rotation coupling in (25) is not physically relevant. It can manifest itself with a choice of a specific tetrad field, but it has no effect on the magnitude of final physical characteristics of the system under consideration (absolute analogy with direct spin-gravitation coupling in Example 4).

Example 6. In his work [3], Arminjon also considers a rotating frame of reference:

$$\begin{aligned} t &= t' \\ x &= x' \cos \omega t + y' \sin \omega t \\ y &= -x' \sin \omega t + y' \cos \omega t \\ z &= z'. \end{aligned} \quad (31)$$

The metric corresponding to coordinates (31) is expressed as

$$ds^2 = [1 - \omega^2 (x^2 + y^2)] dt^2 + 2\omega (y dx - x dy) dt - (dx^2 + dy^2 + dz^2). \quad (32)$$

In (32), to ensure that $g_{00} > 0$, the condition $\omega \sqrt{x^2 + y^2} < 1$ should be satisfied. γ -matrices corresponding to the chosen tetrad field have the form

$$\begin{aligned} \gamma^0 &= \gamma'^0 \\ \gamma^1 &= \gamma'^1 \cos \omega t + \gamma'^2 \sin \omega t + \gamma'^0 \omega y \\ \gamma^2 &= -\gamma'^1 \sin \omega t + \gamma'^2 \cos \omega t - \gamma'^0 \omega x \\ \gamma^3 &= \gamma'^3. \end{aligned} \quad (33)$$

As a result, we can obtain a self-conjugate Hamiltonian,

$$H_\omega = \boldsymbol{\alpha}' \mathbf{p}' + \beta m - \omega \left(y \frac{\partial}{\partial x} - x \frac{\partial}{\partial y} \right). \quad (34)$$

With another set of tetrads, Arminjon in [3] obtains the following form of γ -matrices:

$$\begin{aligned} \gamma_{Ar.}^0 &= \gamma'^0 \\ \gamma_{Ar.}^1 &= \gamma'^1 + \gamma'^0 \omega y \\ \gamma_{Ar.}^2 &= \gamma'^2 - \gamma'^0 \omega x \\ \gamma_{Ar.}^3 &= \gamma'^3. \end{aligned} \quad (35)$$

The self-conjugate Hamiltonian has the following form:

$$H_{Ar.} = \alpha_{Ar.} \mathbf{p}' + \beta m - i\omega \left(y \frac{\partial}{\partial x} - x \frac{\partial}{\partial y} \right) - \frac{\omega}{2} \Sigma'^3. \quad (36)$$

Note that the matrices γ^1, γ^2 in (33) can be written as

$$\begin{aligned} \gamma^1 &= R^+ \gamma'^1 R + \gamma'^0 \omega y \\ \gamma^2 &= R^+ \gamma'^2 R - \gamma'^0 \omega x. \end{aligned} \quad (37)$$

One can see from this that the matrices (35) and (33) are related by the unitary transformation

$$\gamma_{Ar.}^\mu = R\gamma^\mu R^+. \quad (38)$$

The Hamiltonians (36) and (34), similarly to the Hamiltonians (25), (23), are physically equivalent, because they are related by the unitary transformation $R(t)$

$$H_{Ar.} = RH_\omega R^+ - iR\frac{\partial R^+}{\partial t}. \quad (39)$$

Thus, as a result of our consideration, we can draw the following conclusions:

1. The problem of non-uniqueness of the Dirac theory in a curved spacetime does not exist. If treated properly, Dirac Hamiltonians will always determine correct physical characteristics of the systems under consideration irrespective of the choice of tetrads.

2. The spin-rotation coupling for Dirac particles in the context of [3, 4] does not represent a physically relevant quantity. It can manifest itself with a certain choice of tetrads, but the spin-rotation coupling has no effect on the final physical characteristics of the quantum mechanical systems under consideration.

References

- [1] M.Arminjon and F.Reiffer. Ann. Phys. (Berlin) 523, 531-551 (2011); arxiv: 0905.3686 [gr-qc].
- [2] M. Arminjon. Ann. Phys. (Berlin) 523, 1008-1028 (2011); arxiv: 1107.4556v2 [gr-qc].
- [3] M. Arminjon. arxiv: 1211.1855v1 [gr-qc].
- [4] M.Arminjon. Int. J. Theor. Phys. Vol. 52, issue 7 (2013); arxiv: 1302.5584 [gr-qc].
- [5] D.R. Brill and J.A.Wheeler. Rev. Modern Physics, 29 (1957), 465-479 (1957). Erratum: Rev. Modern. Phys. 33, 623-624 (1961).
- [6] T.C.Chapman and D.J.Leiter. Ann. J.Phys. 44, 9, 858-862 (1976).
- [7] M.V.Gorbatenko, V.P.Neznamov. Phys. Rev. D 82, 104056 (2010); arxiv: 1007.4631 [gr-qc].
- [8] M.V.Gorbatenko, V.P.Neznamov. Phys. Rev. D 83, 105002 (2011); arxiv: 1102.4067v1 [gr-qc].
- [9] M.V.Gorbatenko, V.P.Neznamov. arxiv: 1107.0844 [gr-qc].
- [10] C. M. Bender, D. Brody and H. F. Jones. Phys.Rev.Lett. **89**, 2704041 (2002); Phys. Rev. D70, 025001 (2004).
- [11] A. Mostafazadeh. J.Math Phys. (N.Y.) **43**, 205 (2002), **43**, 2814 (2002), **43**, 3944 (2002); arXiv: 0810.5643v3[quant-ph].
- [12] B. Bagchi, A. Fring. Phys. Lett. A 373, 4307 (2009).
- [13] L. Parker. Phys. Rev. D22. 1922 (1980).
- [14] F. W. Hehl and W. T. Ni. Phys. Rev. D42. 2045 (1990).
- [15] S.R.Dolan. Trinity Hall and Astrophysics Group, Cavendish Laboratory. Dissertation, 2006.
- [16] Yu.N.Obukhov. Phys. Rev. Lett. 86, 192 (2001); Forsch. Phys. 50, 711 (2002).
- [17] E.Eriksen and M.Kolsrud, Nuovo Cim. 18 (1960); A.G.Nikitin, J.Phys. A: Math Gen. A31, 3297 (1998).
- [18] L.L.Foldy, S.A.Wouthuysen. Phys. Rev. 78. p.29 (1950).
- [19] A.J.Silenko and +.V.Teryaev, Phys. Rev. D71, 064016 (2005).
- [20] V.P.Neznamov, A.J.Silenko. J. Math. Phys. 2009. v. 50. p.122302.
- [21] S.Chandrasekhar, Proc. R.Soc.Lond. A.349, 571-575 (1976).
- [22] E.T.Newman and R.Penrose, J.Math.Phys. 3, 566 (1962).

JEDI (EDM@Juelich): LEARNING THE SYSTEMATIC LIMITATIONS ON EDM AT COSY

N.N. Nikolaev^{1,2†}, F. Rathmann², M. Rosenthal³ and A. Saleev^{1,2}

(1) *L.D. Landau Institute for Theoretical Physics, 142432 Chernogolovka, Russia*

(2) *Institut für Kernphysik, Jülich Center for Hadron Physics,
Forschungszentrum Jülich, Jülich, Germany*

(3) *III. Physikalisches Institut, RWTH Aachen, Aachen, Germany*

† *E-mail: nikolaev@itp.ac.ru*

Abstract

The search for the EDM of charged particles is only possible at storage rings. At the moment, COSY at IKP, Forschungszentrum Juelich, is a unique facility in the world to study the relevant spin dynamics and to perform the precursor measurements of the proton and deuteron EDM. Such studies are must before embarking a construction of the dedicated EDM storage rings. The recently formed JEDI Collaboration aims at exploring the emerging tremendous scientific and technological challenges. This talk summarizes a status of the project and principal plans for 2014 and beyond, with an emphasis on the theoretical understanding of prominent systematic errors.

1. Introduction. The motivations for the search for electric dipole moments (EDMs) for charged particles have been extensively reviewed in the talk at the previous DSPIN-2011 [1] and should not be repeated here at length. The nonvanishing EDM is only possible if P- and CP-invariance are broken symmetries. The CP-violation is one of Sakharov's criterions for the Big Bang baryogenesis. A fundamental issue is that, while the CP violation in the kaon and B-decays can be parameterized in terms of the SM CKM matrix, the SM fails miserably with the experimentally known baryon content of the Universe. Consequently, our very existence is the best proof that the CKM mechanism is not the end of the story. On the pure dimensional counting, a natural scale for the EDM, $d \sim 10^{-24}$ e-cm, is set by the magnetic moment (MDM) times $\sim 10^{-7}$ fo the parity nonconservation times $\sim 10^{-3}$ for the CP-violation. With the CKM mechanism one needs the weak interaction to two orders, so that $d_{SM} \sim 10^{-31}$ e-cm. The current upper bound on the neutron EDM, $d_n < 3 \cdot 10^{-26}$ e-cm, does not preclude a possibility of a much larger proton and deuteron EDMs, $d_{p,d} \sim 10^{-24}$ e-cm.

The ultimate goal of the JEDI Collaboration, which enrolled about 100 physicists from about 30 Institutions, is to carry out direct measurement of the proton and deuteron EDMs. The road to this goal is paved by tremendous scientific and technological challenges. The immediate target is studies of the spin coherence time (SCT) and systematic errors - the issues common to all future storage ring experiments. Subsequent goals include first direct measurements of the proton and deuteron EDMs at the *magnetic* storage ring COSY using RF techniques, and the development of a dedicated, primarily *electric* storage ring for light ion (p , d , ${}^3\text{He}$) EDM searches.

2. Frenkel-Thomas-BMT equation and the EDM signal at storage rings. For a spinning particle at rest the spin interaction with the \vec{B} - and \vec{E} -fields reads $H = -\vec{\mu} \cdot \vec{B} - \vec{d} \cdot \vec{E} = -\vec{S} \cdot (\mu \vec{B} + d \vec{E})$. Notice a fundamental duality: EDM in an electric field is doing on spin exactly

the same job as MDM does in a magnetic field. The EDM observable is a precession of the spin in an electric field. The charged particles can be subjected to an electric field only in a storage ring. On the closed-orbit for a reference equilibrium particle $\vec{\beta} \cdot \vec{B} = \vec{\beta} \cdot \vec{E} = 0$. The spin precession is described by the familiar Frenkel-Thomas-Bargmann-Michel-Telegdi equation

$$\frac{d\vec{S}}{dt} = \vec{\Omega} \times \vec{S},$$

$$\vec{\Omega} = -\frac{e}{m} \left\{ \underbrace{G\vec{B} + \left(\frac{1}{\beta^2} - G - 1\right) \vec{\beta} \times \vec{E}}_{\text{MDM}} + \underbrace{\eta \left(\vec{E} + \vec{\beta} \times \vec{B}\right)}_{\text{EDM}} \right\}, \quad (1)$$

where G is the anomalous G -factor, we undebraced the MDM and EDM contributions to the spin precession, and $\eta = dm/e$.

The default prediction from the CP-violation models is $\eta \sim 10^{-10}$ and the only way to enhance the EDM signal is to let the EDM contribution to drive the imperfection spin resonance.

The dedicated, frozen spin, EDM rings will operate at $K = 0$ imperfection resonance. In the simplest case of protons it will be an MDM-transparent, pure electric ring run at $\beta^2 = 1/(G + 1)$, $p \approx 0.7$ GeV/c, such that the spin tune $\nu_s = K = 0$. Then, for an infinitely long time, the injected pure longitudinal spin will be subject to driven up-down oscillations with the angular velocity $\vec{\Omega}_o = (e\eta E/m)\vec{e}_x$. In practice, the observation time will be limited by the longitudinal spin decoherence time, τ_{SC} , and the attainable EDM signal - the vertical polarization, S_y , will be limited by $S_y \leq \Omega_o \tau_{SC} \ll 1$.

At the moment, we are interested in a pure magnetic ring like COSY. The interaction of the EDM with the static motional electric field tilts the stable spin axis,

$$\vec{\Omega} = -\frac{e}{m} \left\{ G\vec{B} + \eta\vec{\beta} \times \vec{B} \right\} = \Omega_R \frac{G\gamma}{\cos \xi} \left\{ \cos \xi \vec{e}_y + \sin \xi \vec{e}_x \right\}, \quad (2)$$

and modifies the spin tune,

$$\nu_s = \frac{G\gamma}{\cos \xi}, \quad \tan \xi = \eta.$$

Here one starts with injection of the vertical spin and rotates it onto the ring plane by a radio-frequency radial electric field resonant to the spin-tune frequency plus/minus the ring frequency harmonics [1],

$$\nu_{\text{RF}} = \nu_s + K, \quad K = 0, \pm 1, \pm 2, \dots,$$

where $\nu_s = G\gamma$ is the spin tune for an idle precession, which is a principal feature of all-magnetic rings. In a pure magnetic ring, $\vec{E} = 0$, the interaction of the EDM with the motional electric field mimics the interaction of the MDM with the radial imperfection magnetic fields.

Adding a proper vertical RF B-field, one can make the RF device an MDM-transparent one, in which the motional magnetic field is compensated for by the B-field. Such an RF-E \times B spin flipper provides spin kicks around the Ox axis, $\chi_x \neq 0$. The second option is the RF E \times B Wien filter, where one adjusts B-field such that the Lorentz force exerted on the beam is zero,

$$\vec{E} + \vec{\beta} \times \vec{B} = 0.$$

Thereby, the excitation of coherent betatron oscillations of the beam, inherent to the spin flipper, is avoided. According to the FT-BMT equation, the RF E \times B Wien filter is an EDM transparent device, which only produces a pure magnetic kick χ_y to the phase of the spin precession around the Oy axis, which thereby changes from the idle one to the RF-modulated

one. As Y. Semertzidis observed, under the resonance condition, this frequency modulation conspires with the EDM interaction with the motional electric field to entail the nonvanishing driven up-down spin oscillation tune,

$$\nu_o = \nu_{\text{EDM}} = \frac{1}{2\pi} \xi \chi_y.$$

By a remarkable duality, the two devices with identical RF radial E-field generate identical EDM signals,

$$\nu_{\text{EDM}} = \frac{1}{2\pi} \chi_x = \frac{1}{2\pi} \xi \chi_y$$

Unfortunately, by the same token, this frequency modulation of the spin tune would generate the background ν_{MDM} by the interaction of the MDM with the imperfection magnetic fields. On the other hand, the EDM rotation by the MDM-transparent RF $E \times B$ spin flipper is free of the background from the imperfection magnetic fields. The RF ExB spin flipper is unacceptable, though, since it excites the coherent betatron oscillations. The possible scheme to temper these oscillations has been discussed in Ref. [1], whether it is feasible at COSY or not calls for further studies.

A pattern of the EDM-driven oscillations is common to all the spin rotators, including the familiar MDM rotation by the RF solenoid. Let Oy' be the normal to the ring plane at the running particle position and $X'Y'$ be a vertical plane which rotates with respect to the tangent to the ring with the spin-tune frequency $\nu_s f_R$. The oscillating spin lies in the $X'Y'$ plane and the Oz' axis serves as a running spin axis. The driven spin oscillation tune,

$$\nu_o = \nu_{\text{EDM}} + \nu_{\text{MDM}},$$

is common to $S_{y'} = S_y$ and $S_{x'}$. Driven oscillations modulate the idle precession, and the resulting Fourier spectrum of the horizontal spin would consist of two side bands,

$$\nu_h = \nu_s \pm \nu_o,$$

which could be resolved by the fast time-stamp (≈ 90 ps/tick) polarimetry of the horizontal polarization developed at COSY [2]. Simultaneously, one can measure ν_o directly from driven up-down oscillations of S_y . Such a doublet Fourier spectrum of horizontal spin precession under the driven oscillations has indeed been observed experimentally in the September 2013 run at COSY. The preliminary analysis of the spin tune data indicates an unprecedented precision of 10^{-8} per 4 second time interval, and even higher precision of 10^{-10} can be reached.

Evidently, the momentum spread in the beam causes a spread of the the spin tune,

$$\Delta\nu_s = G\gamma\beta^2 \frac{\delta p}{p}.$$

Should δp stay constant, the spin would decohere instantly, $\tau_{CS} \sim 1/f_R \Delta\nu_s$, at the millisecond scale. Such a runaway spin decoherence is stopped by the RF cavity. Still, one has to eliminate/minimize the effects of chromatic aberrations caused by the synchrotron and betatron oscillations and the coupling between the momentum changes and betatron oscillations - the 2012 runs (COSY experiment #176 [3]) gave a convincing evidence this can be achieved by proper tuning of the arc sextupoles [4, 5]. An enhancement of the spin coherence time to the record ~ 300 sec has been achieved, confirming the earlier findings at e^+e^- colliders in Novosibirsk [6]. The momentum spread changes the beam revolution time, which changes the phase of the RF EB field and, thus, decoheres the driven oscillations - further experiments with more sextupole families are planned in 2014.

2.1. Mapping the imperfections at COSY. COSY has never been intended to be used as a machine to determine particle EDMs. At the present stage, the primary goal is to test the ideas behind the spin dynamics which would be an integral part of all the dedicated EDM rings, and to set an upper bound on the proton and deuteron EDMs, or η as a convenient dimensionless parameter. Because the ballpark value of η is so small, one must be able to control the MDM to imperfection coupling driven background to a very high accuracy. To this end, the imperfection field properties of COSY remain an open issue. Furthermore, they are subject to steering the closed orbit.

Imperfection spin kicks add up all over the particle trajectory in the ring. This effect is coherent for all particles, because imperfection fields are static. Although an invariant spin axis exists, it is not strictly vertical. In case of a purely vertical invariant spin axis, the spin tune would be $\nu_s = G\gamma$ (G is the anomalous magnetic moment, and γ the relativistic Lorentz factor). Now we comment on the task of mapping the static imperfections.

We illustrate the principal idea on an example of localized longitudinal static imperfection magnetic fields. Let χ_i be the corresponding average spin kicks per single crossing. First we cite the familiar case of a single imperfection,

$$\cos \pi \nu_s = \cos(\pi G\gamma) \cos\left(\frac{1}{2}\chi\right) \quad (3)$$

For the deuteron with small $G \approx -0.14$, the imperfection clearly increases the spin tune.

Consider next two imperfections opposite to each other in the ring. Then it is easy to derive the spin tune

$$\cos \pi \nu_s = \cos^2\left(\frac{1}{2}\pi G\gamma\right) \cos y_+ - \sin^2\left(\frac{1}{2}\pi G\gamma\right) \cos y_- . \quad (4)$$

$$y_{\pm} = \frac{1}{2}(\chi_1 \pm \chi_2) . \quad (5)$$

Obviously, the extremum of the $\cos \pi \nu_s$ is a saddle point at $\chi_1 = \chi_2 = 0$, at which $\nu_s = G\gamma$. If either $\chi_1 = 0$ or $\chi_2 = 0$, one would recover the single-imperfection result.

An interplay of an intrinsic imperfection of the ring with two static solenoids placed in opposite straight sections is more tricky. We cite the result for an intrinsic imperfection with the integrated kick α_x , located at the phase θ^* in the ring, which is corrected for by two artificial spin kicks, χ_1 and χ_2 , produced by static solenoid magnets, each located in one of the straight sections, as in the previous example:

$$\begin{aligned} & \cos(\pi \nu_s) = \\ & = \cos\left(\frac{1}{2}\pi G\gamma\right) \left[\cos\left(\frac{\alpha_x}{2}\right) \cos\left(\frac{1}{2}\pi G\gamma\right) \cos(y_+) - \sin\left(\frac{\alpha_x}{2}\right) \cos\left(\frac{1}{2}(\pi - 2\theta^*)G\gamma\right) \sin(y_+) \right] - \\ & - \sin\left(\frac{1}{2}\pi G\gamma\right) \left[\cos\left(\frac{\alpha_x}{2}\right) \sin\left(\frac{1}{2}\pi G\gamma\right) \cos(y_-) - \sin\left(\frac{\alpha_x}{2}\right) \sin\left(\frac{1}{2}(\pi - 2\theta^*)G\gamma\right) \sin(y_-) \right] \quad (6) \end{aligned}$$

As a function of the relevant spin kicks from the two solenoids, one would again have a saddle-point structure, but the intrinsic imperfections shall offset the saddle point location from the origin. Obviously, this offset would depend on the beam energy. To which extent just two solenoids could compensate for the generic distributed imperfection fields, needs more scrutiny. At COSY, mapping of the imperfection fields can be performed using two straight section solenoids, which are used as magnetic guide fields for the electron beams in the 30 kV and in the 2 MV electron cooler. The aim is to recable one of the compensation solenoids of the 30 kV electron cooler with a separate power supply, whereby field integrals of ≈ 0.15 Tm would become available. The main solenoid of the 2 MV cooler provides field integrals of about 0.54 Tm, and will be used as a second solenoid.

2.2. Disentangling the EDM from static machine and RF imperfections.

Mapping the imperfection is but a starting point. One must not be discouraged by a nonideal cancellation of the ring imperfection field effects. Indeed, consider the case of the RF Wien filter. The EDM interaction with the motional electric field in the ring and the MDM interaction with the imperfection magnetic field combine into the EDM-like spin kick around the running spin axis,

$$\begin{aligned}\nu_o &= \frac{1}{2}\psi\sqrt{\xi^2 - 2\xi\alpha_x \cos\theta^* + \alpha_x^2}. \\ &\approx \frac{1}{2}\psi(\alpha_x - \xi \cos\theta^*)\end{aligned}\quad (7)$$

The effective position of the imperfection field must be kept stable, but varying the phase of the RF amounts to moving the Wien around the ring, which amounts to varying the phase θ^* . Then, the θ^* -dependence of ν_o will be used to constrain the EDM signal by the measurement of the doublet splitting of the idle precession Fourier spectrum or of the up-down oscillation frequency. To this end, one would use the above described manipulation with artificial imperfections to maximize the variation of ν_o .

One might benefit from a larger splitting of the doublet of side-bands in the Fourier spectrum of the horizontal spin. One option is to add an RF solenoid run from the same source as the RF Wien filter. In the imperfection-free ring one would find

$$\nu_o = \nu_{\text{sol}} + \nu_{\text{EDM}} \cos\theta^* \quad (8)$$

where now θ^* stands for the relative phase shift between two kicks, which can be controlled radiotechnically. This way, one could vary the interference of the two kicks from the constructive to destructive and thus deduce the EDM signal.

In 2014 the RF ExB dipole (stripline), operated in the Wien-filter mode, will be installed at COSY. Within the momentum range of COSY, it will be operated at the first few harmonics of the spin tune ($\gamma G + K$). Initially, it will provide the radial magnetic field with the vertical electric field of ≈ 76 kV/m. Its principal action on a spin will be a rotation of the MDM around the radial axis. As such, it will simulate the RF ExB EDM flipper, but will be free of parasitic excitation of coherent betatron oscillations. As we stated above, the RF-E \times B flipper generated EDM signal is free of the background generated by static imperfection fields. This feature can be experimentally tested with the RF-ExB Wien filter, which will operate in precisely the RF-E \times B EDM flipper mode. One must run it simultaneously with the above discussed static solenoids and verify that the tune of up-down spin oscillations is independent of the solenoid strengths.

3. Outlook for a future JEDI studies. The long range activities related to mapping out the imperfection content of COSY can be summarized as follows:

1. Spin tune studies vs static solenoid field strength under idle precession. The result will be a determination of the intrinsic imperfection properties of the COSY ring.
2. Runs with the RF ExB Wien filter would check, that regarding the driven up-down oscillations, the device is doing the same job as the RF solenoid in all the aspects.
3. Studies of the driven up-down oscillation frequency and idle-precession frequency vs artificial imperfections induced by the static solenoids.
4. Run simultaneously the frequency-locked RF solenoid and the horizontal RF Wien filter to study their interference vs the relative phase shift. Here one of the RF devices can be viewed as an RF EDM rotator.

5. The above items describe experiments with the RF ExB Wien filter operated with the radial RF B-field, thus simulating the MDM-transparent RF-E flipper. Rotate the RF Wien filter into an upright position with vertical RF magnetic field, so that it will frequency modulate the spin tune. Use the MDM interaction with static solenoid(s) to simulate the EDM interaction with the motional electric field in the ring. First thing is to check that the FM modulation of the spin tune would exhibit the resonance coupling to static imperfection magnetic fields. Varying the RF of the Wien filter around the spin tune frequency one can measure the width of the resonance line. That would be a direct proof of the utility of the RF ExB wien filter as the resonance EDM rotator.
6. Run simultaneously the frequency locked RF solenoid and the *upright* RF Wien filter to study their interference vs the relative phase shift and to investigate a utility of the splitting of the Fourier spectrum of the horizontal spin under driven oscillations to determine the strength of the up-down spin rotator.
7. Tilting the RF Wien filter from the pure vertical to pure horizontal orientation of its magnetic field will test a significance of the misalignment of the Wien filter as a source of possible systematic errors.

The above set of experiments would basically exhaust a simulation of all possible systematic effects which will be encountered with RF EDM rotators. Remarkably, already in 2014 JEDI will be in possession of all the instrumentation to conduct preliminary studies of all the above items. Stay tuned to new results to be reported at the next Workshop.

References

- [1] A. Lehrach, B. Lorentz, W. Morse, N. Nikolaev, F. Rathmann, Precursor Experiments to Search for Permanent Electric Dipole Moments (EDMs) of Protons and Deuterons at COSY, Proceedings of XIV Workshop on High Energy Spin Physics, Dubna, 2011, pp/283-302, arXiv:1201.5773 [hep-ph].
- [2] Z. Bagdasarian et al., Submitted to *Phys. Rev. ST Accel. Beams* (2013).
- [3] A. Lenisa and E. Stephenson, COSY proposal #176: Extending the In-Plane Spin Coherence Time of a Polarized Deuteron Beam in a Storage Ring Using Higher Order Fields; A. Lehrach, F. Rathmann and J. Pretz, COSY proposal #216: Search for Permanent Electric Dipole Moments at COSY - Stage 1: Spin coherence and systematic error studies.
- [4] P. Benati et al., *Phys. Rev. ST Accel. Beams* **15** (2012) 124202.
- [5] P. Benati et al., *Phys. Rev. ST Accel. Beams* **16** (2012) 049901.
- [6] S. Serednyakov et al., *Phys. Lett. B* **66** (1977) 102; I. Vasserman et al., *Phys. Lett. B* **187** (1977) 172; *Phys. Lett. B* **198** (1977) 302.

SPIN DEPENDENCE OF e^-e^+ PAIR PRODUCTION BY AN ELECTRON IN A STRONG MAGNETIC FIELD

O. P. Novak

Institute of Applied Physics, NAS of Ukraine, Sumy 40000, Ukraine

E-mail: novak-o-p@ukr.net

Abstract

The trident production process $e^- \rightarrow e^- + e^- + e^+$ in a background magnetic field has been studied in the lowest Landau levels (LLL) approximation. The process rate is determined by the resonant case, when the second-order Feynman graph decomposes into two first-order diagrams which correspond to radiation and photoproduction processes. It is shown, that the process rate is maximum with the initial electron spin along the field and the final electron spins opposite to the field. This implies spin-flip radiation process which is not suppressed for transitions from a relativistic initial state to the lowest energy levels.

Pair production by an electron is not possible in free space, thus, strong enough background field is needed to make such process noticeable. In quantum electrodynamics (QED), the measure of strong field is the critical field $B_c \approx 4.41 \cdot 10^{13}$ G. In laboratory conditions the highest feasible magnetic field strength is only $\sim 10^7$ G which is still much less than the critical one [1].

Nevertheless, astrophysics has long-standing interest in the physics of QED processes in a magnetic field [2]. Neutron stars are believed to have surface magnetic field with magnitude from 10^9 to 10^{15} G. Particularly, pair production processes in a pulsar magnetosphere are essential for understanding the pulsar radiation mechanism.

The present study of pair production by an electron in a magnetic field is partially motivated by the experimental observation of the similar process in the field of a light wave at SLAC National Accelerator Laboratory, reported in 1997 [3].

According to the theorem proved by Nikishov [4], a process in constant electromagnetic field involving relativistic particles can be described by the rate of the same process in constant crossed fields, $\vec{E} \perp \vec{B}$ and $E = B$. This includes the case of an electromagnetic wave though an additional averaging over the wave period is needed. Thus, it is possible to estimate the number of events in the SLAC experiment using the rate of magnetic production. Such comparison was done in Refs. [5, 6], which showed reasonably good agreement with the experimental data. However, in Ref. [5, 6] the simplest case of pair production to ground levels was considered. The purpose of the present work is to study pair production to excited Landau levels in the reaction

$$e^- \longrightarrow e^- + e^- + e^+. \quad (1)$$

The Feynman diagrams of the process (1) are shown in Fig. 1. The calculations have been carried out in the frame of Furry picture and the solutions of the Dirac equation in a magnetic field were used for the electron and positron scattering states.

An electron in a magnetic field occupies discrete energy levels with eigenvalues

$$E = \sqrt{p_z^2 c^2 + m^2 c^4 + 2lb m^2 c^4}, \quad (2)$$

where l is the Landau level number, p_z is the parallel to the field momentum, and $b = B/B_c$ is magnetic field strength in the units of B_c . The motion of the initial electron along the field can be excluded without loss of generality by Lorentz transformation, $p_{iz} = 0$. We will consider the case when the final particles occupy low energy levels (lowest Landau levels approximation) and the magnetic term in (2) is small in comparison with the electron rest energy,

$$l_1 b \ll 1, \quad l_2 b \ll 1, \quad l_+ b \ll 1. \quad (3)$$

At the same time, the initial electron energy E_i should exceed the threshold value to produce a pair,

$$E_i \geq (\tilde{m}_1 + \tilde{m}_2 + \tilde{m}_+) c^2, \quad \tilde{m}_j = m\sqrt{1 + 2l_j b}. \quad (4)$$

We assume that the initial electron energy is close to the threshold value.

It is known that two-vertex QED processes exhibit resonant behavior. The process rate diverges when the virtual photon momentum fulfill the usual relativistic relation $k_\nu k^\nu = 0$. Resonant divergences can be eliminated by introducing the width Δ to the virtual state in accordance with Breit-Wigner prescription [7], $\omega \rightarrow \omega - i\Delta/2$. Resonances are not kinematically separated in the considered process and the rate is determined by the resonant regime.

The calculations has been carried out within standard QED perturbation theory. The obtained rate has the greatest order of magnitude when the spin projections are

$$\begin{aligned} s_{iz} &= +1/2, & s_{1z} &= -1/2, \\ s_{+z} &= +1/2, & s_{2z} &= -1/2. \end{aligned} \quad (5)$$

The potential energy of spin-field interaction is negative in this spin state. The resulting expression of the rate looks like

$$W_{--+}^+ = \alpha^2 \left(\frac{mc^2}{\hbar} \right)^2 \frac{b\sqrt{\pi} \Omega^{2L} e^{-2\Omega^2} \Gamma(L + 1/2)}{3\sqrt{3} \Delta l_i! l_1! l_2! l_+! L!}, \quad (6)$$

$$L = l_1 + l_2 + l_+, \quad \Omega = 2/b. \quad (7)$$

The superscript denotes spin projection of the initial electron, and the subscripts denote spin projections of the final electrons and the positron respectively.

At the resonance a two-vertex process can be viewed as a cascade of two first-order processes, namely photon radiation and photoproduction in the present case. The indicated spin projections (5) mean that the initial electron makes spin-flip radiative transition, though it is known that photon emission with change of the electron spin projection is

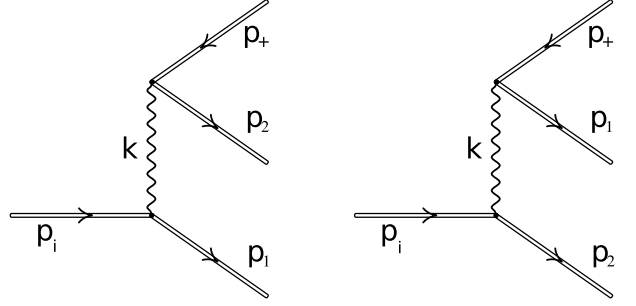


Figure 1: Feynman diagrams of e^-e^+ pair production by an electron in a magnetic field. Double lines represent solutions of Dirac equation in a magnetic field.

not probable [8]. Nevertheless, if an electron transits from a high energy level to a near-ground level, the probability to change spin projection from the positive to the negative value increases and become comparable with the probability of the no-spin-flip process [9]. The considered case of resonant pair production near the threshold includes such transition, which explains the issue.

There are 16 possible spin states in all. The corresponding rates, expressed in the units of W_{--+}^+ , are

$$\begin{aligned}
w_{--+}^+ &= 1, & w_{+--+}^+ &= \frac{5\delta}{3} l_1 b, & w_{--+}^- &= \frac{4\delta}{3}, & w_{+--+}^- &= \frac{1}{2} l_1 b, \\
w_{---}^+ &= \frac{\delta}{3} l_+ b, & w_{-+++}^+ &= \frac{5\delta}{3} l_2 b, & w_{---}^- &= l_+ b, & w_{-+++}^- &= \frac{1}{2} l_2 b, \\
w_{-+-}^+ &= \frac{1}{8} l_2 l_+ b^2, & w_{++++}^+ &= \frac{1}{4} l_1 l_2 b^2, & w_{-+-}^- &= \frac{2\delta}{3} l_2 l_+ b^2, & w_{++++}^- &= \frac{\delta}{3} l_1 l_2 b^2, \\
w_{+--}^+ &= \frac{1}{8} l_1 l_+ b^2, & w_{++++}^+ &= \frac{\delta}{4} l_1 l_2 l_+ b^3, & w_{+--}^- &= \frac{2\delta}{3} l_1 l_+ b^2, & w_{++++}^- &\longrightarrow 0,
\end{aligned} \tag{8}$$

where $\delta = (\tilde{m}_i - \tilde{m}_1 - \tilde{m}_2 - \tilde{m}_+)/m$.

There is a simple pattern in the above expressions. When a final particle is created with unfavorable spin orientation (spin up for an electron and spin down for a positron), then the rate contains small factor (lb) with the corresponding level number. When all particles spins are oriented in the energetically high way, the leading order cancels and the rate become negligibly small within the accuracy of the considered approximation, $w_{++++}^- \rightarrow 0$.

Such behavior of the rate is inherited from one-photon pair production [9], which is the second stage in the resonant process (1).

References

- [1] A. D. Sakharov, Usp. Fiz. Nauk 161 (5), 29 (1991) [Sov. Phys.–Usp. 34 (5), 375 (1991)].
- [2] A. K. Harding, Science, **251**, 1033–1038 (1991).
- [3] D. L. Burke et al., Phys. Rev. Lett., **79**, 1626 (1997).
- [4] A. I. Nikishov, Proc. of P.N. Lebedev Fiz. Inst. , AS USSR **111**, 152 (1979) (in Russian).
- [5] O. P. Novak, R. I. Kholodov and P. I. Fomin, JETP **110**, 978-982 (2010).
- [6] O. P. Novak and R. I. Kholodov. Phys. Rev. D, **86** 105013 (2012).
- [7] C. Graziani, A. K. Harding, R. Sina, Phys. Rev. D **51**, 7097 (1995).
- [8] A. A. Sokolov and I. M. Ternov, *Synchrotron Radiation from Relativistic Electrons* (American Institute of Physics, New York, 1986).
- [9] O. P. Novak, R. I. Kholodov, Phys. Rev. D, **80** 025025 (2009).

CONSERVATION LAWS AND COVARIANT EQUATIONS OF MOTION FOR SPINNING PARTICLES

Yu.N. Obukhov^{1†} and D. Puetzfeld^{2‡}

- (1) *IBRAE, Russian Academy of Sciences, B.Tulskaya 52, 115191 Moscow, Russia*
 (2) *ZARM, University of Bremen, Am Fallturm, 28359 Bremen, Germany*
 † *E-mail: obukhov@ibrae.ac.ru* ‡ *E-mail: dirk.puetzfeld@zarm.uni-bremen.de*

Abstract

We derive the Noether identities and the conservation laws for general gravitational models with arbitrarily interacting matter and gravitational fields. These conservation laws are used for the construction of the covariant equations of motion for test bodies with minimal and nonminimal coupling.

Metric-affine gravity [1] provides a general framework for the discussion of dynamics of arbitrarily interacting matter and gravitational field. In this formalism, one can analyse minimal coupling of matter with or without microstructure, along with extended nonminimal coupling schemes, in any spacetime geometry. The gravitational field potentials are the independent metric tensor g_{ij} and the linear connection Γ_{ki}^j . The corresponding field strengths [1] are the curvature, the torsion, and the nonmetricity:

$$R_{kli}{}^j = \partial_k \Gamma_{li}^j - \partial_l \Gamma_{ki}^j + \Gamma_{kn}^j \Gamma_{li}^n - \Gamma_{ln}^j \Gamma_{ki}^n, \quad (1)$$

$$T_{kl}{}^i = \Gamma_{kl}^i - \Gamma_{lk}^i, \quad (2)$$

$$Q_{kij} = -\nabla_k g_{ij} = -\partial_k g_{ij} + \Gamma_{ki}^l g_{lj} + \Gamma_{kj}^l g_{il}. \quad (3)$$

The deviation from Riemannian geometry (specified by the Christoffel connection $\tilde{\Gamma}_{kj}^i = \frac{1}{2}g^{il}(\partial_j g_{kl} + \partial_k g_{lj} - \partial_l g_{kj})$ and marked by tilde) is measured by the *distorsion* tensor

$$N_{kj}{}^i = \tilde{\Gamma}_{kj}^i - \Gamma_{kj}^i. \quad (4)$$

Noether identities arise from the symmetries of the action $I = \int d^4x \mathcal{L}$. Here we study the case when the Lagrangian density $\mathcal{L} = \mathcal{L}(\psi^A, \nabla_i \psi^A, g_{ij}, R_{kli}{}^j, T_{kl}{}^i, Q_{kij}, N_{kj}{}^i)$ is a function of the metric, the curvature (1), the torsion (2), the nonmetricity (3), the matter field ψ^A , and its *covariant derivative* $\nabla_k \psi^A = \partial_k \psi^A - \Gamma_{ki}^j (\sigma^A_B)_j{}^i \psi^B$. We assume that the action is invariant under general coordinate transformations of the gravitational and the matter fields: $x^i \rightarrow x^i + \delta x^i$, $g_{ij} \rightarrow g_{ij} + \delta g_{ij}$, $\Gamma_{ki}^j \rightarrow \Gamma_{ki}^j + \delta \Gamma_{ki}^j$, and $\psi^A \rightarrow \psi^A + \delta \psi^A$

$$\delta x^i = \xi^i(x), \quad (5)$$

$$\delta g_{ij} = -(\partial_i \xi^k) g_{kj} - (\partial_j \xi^k) g_{ik}, \quad (6)$$

$$\delta \psi^A = -(\partial_i \xi^j) (\sigma^A_B)_j{}^i \psi^B, \quad (7)$$

$$\delta \Gamma_{ki}^j = -(\partial_k \xi^l) \Gamma_{li}^j - (\partial_i \xi^l) \Gamma_{kl}^j + (\partial_l \xi^j) \Gamma_{ki}^l - \partial_{ki}^2 \xi^j. \quad (8)$$

The generators $(\sigma^A_B)_j{}^i$ of the coordinate transformations satisfy commutation relations

$$(\sigma^A_C)_j{}^i (\sigma^C_B)_l{}^k - (\sigma^A_C)_l{}^k (\sigma^C_B)_j{}^i = (\sigma^A_B)_l{}^i \delta_j^k - (\sigma^A_B)_j{}^k \delta_l^i. \quad (9)$$

After a straightforward computation, we find for the variation of the action

$$\delta I = - \int d^4x \left[\xi^k \Omega_k + (\partial_i \xi^k) \Omega_k^i + (\partial_{ij}^2 \xi^k) \Omega_k^{ij} + (\partial_{ijn}^3 \xi^k) \Omega_k^{ijn} \right], \quad (10)$$

where explicitly

$$\begin{aligned} \Omega_k &= \frac{\delta \mathcal{L}}{\delta g_{ij}} \partial_k g_{ij} + \frac{\delta \mathcal{L}}{\delta \psi^A} \partial_k \psi^A + \partial_i \left(\frac{\partial \mathcal{L}}{\partial \partial_i \psi^A} \partial_k \psi^A - \delta_k^i \mathcal{L} \right) \\ &+ \partial_i \left(\frac{\partial \mathcal{L}}{\partial \partial_i g_{mn}} \partial_k g_{mn} \right) + \frac{\partial \mathcal{L}}{\partial \Gamma_{ln}^m} \partial_k \Gamma_{ln}^m + \frac{\partial \mathcal{L}}{\partial \partial_i \Gamma_{ln}^m} \partial_k \partial_i \Gamma_{ln}^m, \end{aligned} \quad (11)$$

$$\begin{aligned} \Omega_k^i &= 2 \frac{\delta \mathcal{L}}{\delta g_{ij}} g_{kj} + \frac{\delta \mathcal{L}}{\delta \psi^A} (\sigma^A_B)_k^i \psi^B + \frac{\partial \mathcal{L}}{\partial \partial_i \psi^A} \partial_k \psi^A - \delta_k^i \mathcal{L} \\ &+ 2 \partial_n \left(\frac{\partial \mathcal{L}}{\partial \partial_n g_{ij}} g_{jk} \right) + \frac{\partial \mathcal{L}}{\partial \partial_i g_{mn}} \partial_k g_{mn} + \partial_j \left(\frac{\partial \mathcal{L}}{\partial \partial_j \psi^A} (\sigma^A_B)_k^i \psi^B \right) \\ &+ \frac{\partial \mathcal{L}}{\partial \Gamma_{li}^j} \Gamma_{lk}^j + \frac{\partial \mathcal{L}}{\partial \Gamma_{il}^j} \Gamma_{kl}^j - \frac{\partial \mathcal{L}}{\partial \Gamma_{lj}^k} \Gamma_{lj}^i + \frac{\partial \mathcal{L}}{\partial \partial_i \Gamma_{ln}^m} \partial_k \Gamma_{ln}^m \\ &+ \frac{\partial \mathcal{L}}{\partial \partial_n \Gamma_{il}^m} \partial_n \Gamma_{kl}^m + \frac{\partial \mathcal{L}}{\partial \partial_n \Gamma_{li}^m} \partial_n \Gamma_{lk}^m - \frac{\partial \mathcal{L}}{\partial \partial_n \Gamma_{lm}^k} \partial_n \Gamma_{lm}^i, \end{aligned} \quad (12)$$

$$\begin{aligned} \Omega_k^{ij} &= \frac{\partial \mathcal{L}}{\partial \partial_{(i} \psi^A} (\sigma^A_B)_{k}^{j)} \psi^B + \frac{\partial \mathcal{L}}{\partial \Gamma_{(ij)k}^m} + \frac{\partial \mathcal{L}}{\partial \partial_{(i} \Gamma_{j)l}^m} \Gamma_{kl}^m \\ &+ 2 \frac{\partial \mathcal{L}}{\partial \partial_{(i} g_{j)n}} g_{kn} + \frac{\partial \mathcal{L}}{\partial \partial_{(i} \Gamma_{|l|j)}^m} \Gamma_{lk}^m - \frac{\partial \mathcal{L}}{\partial \partial_{(i} \Gamma_{|ln|}^k} \Gamma_{ln}^{j)}. \end{aligned} \quad (13)$$

$$\Omega_k^{ijn} = \frac{\partial \mathcal{L}}{\partial \partial_{(n} \Gamma_{ij)k}^m}. \quad (14)$$

Invariance of the action, $\delta I = 0$, yields the four Noether identities:

$$\Omega_k = 0, \quad \Omega_k^i = 0, \quad \Omega_k^{ij} = 0, \quad \Omega_k^{ijn} = 0. \quad (15)$$

General coordinate symmetry is due to the fact that the density \mathcal{L} is constructed from covariant objects. Denoting $\rho^{ijk}_l = \frac{\partial \mathcal{L}}{\partial R_{ijk}^l}$, $\sigma^{ij}_k = \frac{\partial \mathcal{L}}{\partial T_{ij}^k}$, $\nu^{kij} = \frac{\partial \mathcal{L}}{\partial Q_{kij}}$, $\mu^{ij}_k = \frac{\partial \mathcal{L}}{\partial N_{ij}^k}$, we find

$$\frac{\partial \mathcal{L}}{\partial \Gamma_{ij}^k} = - \frac{\partial \mathcal{L}}{\partial \nabla_i \psi^A} (\sigma^A_B)_k^j \psi^B + 2\nu^{ij}_k + 2\sigma^{ij}_k + 2\rho^{inl}_k \Gamma_{nl}^j + 2\rho^{nij}_l \Gamma_{nk}^l - \mu^{ij}_k, \quad (16)$$

$$\frac{\partial \mathcal{L}}{\partial \partial_i \Gamma_{jk}^l} = 2\rho^{ijk}_l, \quad \frac{\partial \mathcal{L}}{\partial \partial_k g_{ij}} = -\nu^{kij} + \frac{1}{2} (\mu^{(ki)j} + \mu^{(kj)i} - \mu^{(ij)k}). \quad (17)$$

As a result, we verify that $\Omega_k^{ij} = 0$ and $\Omega_k^{ijn} = 0$ are satisfied identically. Using (16) and (17), we then recast the Noether identities (11) and (12) into

$$\begin{aligned} \Omega_k &= \frac{\delta \mathcal{L}}{\delta g_{ij}} \partial_k g_{ij} + \frac{\delta \mathcal{L}}{\delta \psi^A} \partial_k \psi^A + \partial_i \left(\frac{\partial \mathcal{L}}{\partial \nabla_i \psi^A} \nabla_k \psi^A - \delta_k^i \mathcal{L} \right) \\ &+ \widehat{\nabla}_j \left(\frac{\partial \mathcal{L}}{\partial \nabla_j \psi^A} (\sigma^A_B)_m^n \psi^B \right) \Gamma_{kn}^m + \frac{\partial \mathcal{L}}{\partial \nabla_l \psi^A} (\sigma^A_B)_m^n \psi^B R_{lkn}^m \\ &- \left[\widehat{\nabla}_j \nu^{jmn} - \frac{1}{2} \check{\nabla}_i (\mu^{(im)n} + \mu^{(in)m} - \mu^{(mn)i}) \right] \partial_k g_{mn} \\ &+ \rho^{iln}_m \partial_k R_{iln}^m + \sigma^{ln}_m \partial_k T_{ln}^m + \mu^{ln}_m \partial_k N_{ln}^m + \nu^{lmn} \partial_k Q_{lmn} = 0, \end{aligned} \quad (18)$$

$$\begin{aligned}
\Omega_k{}^i &= 2\frac{\delta\mathcal{L}}{\delta g_{ij}}g_{kj} + \frac{\delta\mathcal{L}}{\delta\psi^A}(\sigma^A{}_B)_k{}^i\psi^B + \frac{\partial\mathcal{L}}{\partial\nabla_i\psi^A}\nabla_k\psi^A - \delta_k^i\mathcal{L} \\
&\quad - \widehat{\nabla}_j\left(2\nu^{ji}{}_k - \frac{\partial\mathcal{L}}{\partial\nabla_j\psi^A}(\sigma^A{}_B)_k{}^i\psi^B\right) + \check{\nabla}_n(\mu^{(ni)j} + \mu^{(nj)i} - \mu^{(ij)n})g_{jk} \\
&\quad - \mu^{ln}{}_k N_{ln}{}^i + \mu^{il}{}_n N_{kl}{}^n + \mu^{li}{}_n N_{lk}{}^n + 2\sigma^{il}{}_n T_{kl}{}^n - \sigma^{ln}{}_k T_{ln}{}^i \\
&\quad + 2\rho^{iln}{}_m R_{kln}{}^m + \rho^{lni}{}_m R_{lnk}{}^m - \rho^{lnm}{}_k R_{lmn}{}^i + \nu^{imn}Q_{kmn} = 0. \tag{19}
\end{aligned}$$

An arbitrary tensor density $\mathcal{A}^n{}_{i\dots j\dots}$ is mapped into a density of the same weight by

$$\widehat{\nabla}_n\mathcal{A}^n{}_{i\dots j\dots} = \partial_n\mathcal{A}^n{}_{i\dots j\dots} + \Gamma_{nl}{}^j\mathcal{A}^n{}_{i\dots l\dots} - \Gamma_{ni}{}^l\mathcal{A}^n{}_{l\dots j\dots}, \tag{20}$$

A similar covariant derivative, defined by the Riemannian connection, is denoted

$$\check{\nabla}_n\mathcal{A}^n{}_{i\dots j\dots} = \partial_n\mathcal{A}^n{}_{i\dots j\dots} + \widetilde{\Gamma}_{nl}{}^j\mathcal{A}^n{}_{i\dots l\dots} - \widetilde{\Gamma}_{ni}{}^l\mathcal{A}^n{}_{l\dots j\dots}, \tag{21}$$

It is worthwhile to note that the variational derivative with respect to the metric is an explicitly covariant density. This follows from the fact that the Lagrangian depends on g_{ij} not only directly, but also through the objects Q_{kij} and $N_{ki}{}^j$. Explicitly, we find

$$\frac{\delta\mathcal{L}}{\delta g_{ij}} = \frac{d\mathcal{L}}{dg_{ij}} - \partial_n\left(\frac{\partial\mathcal{L}}{\partial\partial_n g_{ij}}\right) = \frac{\partial\mathcal{L}}{\partial g_{ij}} + \widehat{\nabla}_n\nu^{nij} - \frac{1}{2}\check{\nabla}_n(\mu^{(ni)j} + \mu^{(nj)i} - \mu^{(ij)n}). \tag{22}$$

The Noether identity (18) is apparently noncovariant in contrast to (19). To fix this, we replace $\Omega_k = 0$ by an equivalent covariant identity: $\overline{\Omega}_k = \Omega_k - \Gamma_{kn}{}^m\Omega_m{}^n = 0$. Explicitly,

$$\begin{aligned}
\overline{\Omega}_k &= \frac{\delta\mathcal{L}}{\delta\psi^A}\nabla_k\psi^A + \widehat{\nabla}_i\left(\frac{\partial\mathcal{L}}{\partial\nabla_i\psi^A}\nabla_k\psi^A - \delta_k^i\mathcal{L}\right) - \left(\frac{\partial\mathcal{L}}{\partial\nabla_i\psi^A}\nabla_l\psi^A - \delta_l^i\mathcal{L}\right)T_{ki}{}^l \\
&\quad + \left[\widehat{\nabla}_n\nu^{nij} - \frac{1}{2}\check{\nabla}_n(\mu^{(ni)j} + \mu^{(nj)i} - \mu^{(ij)n}) - \frac{\delta\mathcal{L}}{\delta g_{ij}}\right]Q_{kij} + \frac{\partial\mathcal{L}}{\partial\nabla_l\psi^A}(\sigma^A{}_B)_m{}^n\psi^B R_{lkn}{}^m \\
&\quad + \rho^{iln}{}_m\nabla_k R_{iln}{}^m + \sigma^{ln}{}_m\nabla_k T_{ln}{}^m + \nu^{lmn}\nabla_k Q_{lmn} + \mu^{ln}{}_m\nabla_k N_{ln}{}^m = 0. \tag{23}
\end{aligned}$$

When the matter fields satisfy the field equations $\delta\mathcal{L}/\delta\psi^A = 0$, the Noether identities (19) and (23) reduce to the *conservation laws* for the energy-momentum and hypermomentum, respectively.

Nonminimal coupling models [2–4] have attracted considerable attention recently. Using our results above, we can analyse a large class of models with the Lagrangian

$$\mathcal{L} = \sqrt{-g}FL_{\text{mat}}. \tag{24}$$

The coupling function $F = F(g_{ij}, R_{kli}{}^j, T_{kl}{}^i, Q_{kij}, N_{kl}{}^i)$ depends arbitrarily on its arguments, whereas the matter Lagrangian $L_{\text{mat}} = L_{\text{mat}}(\psi^A, \nabla_i\psi^A, g_{ij})$ has the usual form.

The matter is characterized by the canonical energy-momentum tensor, the canonical hypermomentum tensor, and the metrical energy-momentum tensor

$$\Sigma_k{}^i = \frac{\partial L_{\text{mat}}}{\partial\nabla_i\psi^A}\nabla_k\psi^A - \delta_k^i L_{\text{mat}}, \quad \Delta^n{}_k{}^i = -\frac{\partial L_{\text{mat}}}{\partial\nabla_i\psi^A}(\sigma^A{}_B)_k{}^n\psi^B, \quad t_{ij} = \frac{2}{\sqrt{-g}}\frac{\delta(\sqrt{-g}L_{\text{mat}})}{\delta g^{ij}}. \tag{25}$$

The usual spin arises as an antisymmetric part of the hypermomentum, $\tau_{ij}{}^k = \Delta_{[ij]}{}^k$, whereas the trace $\Delta^k = \Delta^i{}_i{}^k$ is the dilation current. The symmetric traceless part describes the proper hypermomentum [1].

The conservation laws are derived from (19) and (23), and they read

$$F\Sigma_k^i = Ft_k^i + \nabla_n^* (F\Delta_k^i{}^n), \quad (26)$$

$$\nabla_i^* (F\Sigma_k^i) = F \left(\Sigma_l^i T_{ki}{}^l - \Delta_n^m{}^l R_{klm}{}^n - \frac{1}{2} t^{ij} Q_{kij} \right) - L_{\text{mat}} \nabla_k F. \quad (27)$$

The so-called modified covariant derivative is defined as $\nabla_i^* = \nabla_i + N_{ki}{}^k$. These results generalize our previous findings [5–7].

The equations of motion of extended bodies are obtained from the conservation laws, see the historic overview in [8]. There exist various schemes using the so-called multipole expansion technique in which the motion of an extended body, sweeping a finite world tube, is approximated by the motion of a point particle, which is characterized by a (infinite, in general) set of moments. The latter are defined as integrated quantities derived from the Noether currents that describe body's matter. Here we use the covariant expansion approach of Synge [9, 10].

In Synge's formalism, two-points tensors (or bitensors) are introduced as tensorial functions of two spacetime points. Most important among them is the world-function $\sigma(x, y)$, which measures the interval (distance) along a unique geodesic curve connecting the two points x and y , and the parallel propagator $g^y{}_x(x, y)$ that transfers tensorial objects along this geodesic. Covariant derivatives of the world-function are denoted by $\sigma_y := \nabla_y \sigma$, etc.

Let us consider, for now, the special case when the microstructure of matter is reduced to the spin $\tau_{ij}{}^k$ and the geometry of spacetime, accordingly, is characterized by the vanishing nonmetricity $Q_{kij} = 0$. The general equations of motion based on the conservation laws (26) and (27) will be analysed elsewhere.

The lowest (pole and dipole) integrated moments are $p^{y_0} = \int_{\Sigma(s)} g^{y_0}{}_{x_0} \tilde{\Sigma}^{x_0 x_2} d\Sigma_{x_2}$, and

$$p^{y_1 y_0} = - \int_{\Sigma(s)} \sigma^{y_1} g^{y_0}{}_{x_0} \tilde{\Sigma}^{x_0 x_2} d\Sigma_{x_2}, \quad s^{y_0 y_1} = - \int_{\Sigma(s)} g^{y_0}{}_{x_0} g^{y_1}{}_{x_1} \tilde{\tau}^{[x_0 x_1] x_2} d\Sigma_{x_2}. \quad (28)$$

The tilde denotes densitized canonical energy-momentum and spin tensors, and the integration is done over the spatial cross-section $\Sigma(s)$ of a world tube of a body at the value s of the proper time parameter along the representative world line $x^i(s)$.

Performing the appropriate integrations of the conservation laws (26) and (27), we obtain the equations of motion in the pole-dipole approximation [11]

$$\frac{D}{ds} \mathcal{P}^a = \frac{1}{2} \tilde{R}^a{}_{bcd} \mathcal{J}^{cd} v^b + f^a, \quad \frac{D}{ds} \mathcal{J}^{ab} = -2v^{[a} \mathcal{P}^{b]} + f^{ab}. \quad (29)$$

Here $v^a = dx^a/ds$ is the 4-velocity of the body, and we construct the generalized total energy-momentum vector and the total angular momentum tensor

$$\mathcal{P}^a = F \left(p^a - \frac{1}{2} N^a{}_{cd} S^{cd} \right) + (p^{ba} - S^{ab}) \nabla_b F, \quad \mathcal{J}^{ab} = F (L^{ab} + S^{ab}), \quad (30)$$

from the integrated 4-momentum p^a of the body, the integrated orbital angular momentum $L^{ab} = 2p^{[ab]}$, and the integrated spin angular momentum $S^{ab} = -2s^{ab}$.

The Mathisson-Papapetrou equations (29) contain an additional force and torque due to the higher multipole moments and the nonminimal coupling (with $A_i = \nabla_i \log F$):

$$f^a = F\Theta^{bc}{}_{,d}\tilde{\nabla}^a T_{bc}{}^d - 2q^{bcd}N_{dc}{}^a\nabla_b F + 2Fq^{acd}\nabla_d A_c - \xi\nabla^a F + \xi^b\tilde{\nabla}_b\nabla^a F, \quad (31)$$

$$f^{ab} = 2F\Theta^{cd[a}T_{cd}{}^{b]} + 4F\Theta^{[a}{}_{cd}T^{b]cd} - 4q^{[a|c|b]}\nabla_c F - 2\xi^{[a}\nabla^{b]}F. \quad (32)$$

Here $\xi = \int_{\Sigma(s)} \tilde{L}_{\text{mat}} w^{x_2} d\Sigma_{x_2}$, $\xi^y = \int_{\Sigma(s)} \sigma^y \tilde{L}_{\text{mat}} w^{x_2} d\Sigma_{x_2}$, $\Theta^{bca} = \frac{1}{2}(q^{bca} + q^{bac} - q^{cab})$, and

$$q^{y_0 y_1 y_2} = \int_{\Sigma(s)} g^{y_0}{}_{x_0} g^{y_1}{}_{x_1} g^{y_2}{}_{x_2} \tilde{T}^{[x_0 x_1] x_2} w^{x_3} d\Sigma_{x_3}. \quad (33)$$

For the definition of w^x see [10].

Interestingly, the form of the torsion-dependent pieces of the additional force and torque exactly reproduces the contribution of the quadrupole translational moment studied for fermionic matter in [12, 13]. An important next step would be to establish the complete structure of the equations of motion up to the quadrupole order both in the rotational and translational moments. Such a study can be most conveniently done along the lines of the approach of Bailey and Israel [14].

Our covariant equations of motion (29) extend and confirm previous results on the dynamics of extended bodies with spin [15, 16] and [8]. In particular, when the coupling is minimal ($F = 1$), we immediately verify that the post-Riemannian geometrical structure of spacetime can be detected only by using test particles with *intrinsic spin*. Rotating macroscopic bodies are thus, so to say, neutral to the torsion.

Nevertheless, it is worthwhile to notice that even structureless massive point particles can be affected by the post-Riemannian gravitational field when the coupling function F depends on the torsion and nonmetricity. Such single-pole particles do not move along geodesic curves (in contrast to minimally coupled point particles). A ‘‘pressure’’ like force arises as the gradient of the coupling function:

$$m\dot{v}^a = \xi(\delta_b^a - v^a v_b)\nabla^b \log F. \quad (34)$$

A similar force determines the nongeodesic motion of test particles in the scalar-tensor theory of gravitation [17, 18] where the gravitational coupling constant is replaced by the scalar coupling function.

Acknowledgements D.P. was supported by the Deutsche Forschungsgemeinschaft (DFG) through the grant LA-905/8-1/2. Y.N.O. thanks the Organizing Committee for the invitation and support.

References

- [1] F. W. Hehl, J. D. McCrea, E. W. Mielke, and Y. Ne’eman. *Phys. Rep.* **258** (1995) 1.
- [2] T. Koivisto. *Class. Quantum Grav.* **23** (2006) 4289.
- [3] O. Bertolami, C. G. Böhmer, T. Harko, and F. S. N. Lobo. *Phys. Rev. D* **75** (2007) 104016.
- [4] M. Mohseni. *Phys. Rev. D* **81** (2010) 124039.

- [5] D. Puetzfeld and Yu. N. Obukhov. *Phys. Rev. D* **78** (2008) 121501.
- [6] D. Puetzfeld and Yu. N. Obukhov. *Phys. Rev. D* **87** (2013) 044045.
- [7] Yu.N. Obukhov and D. Puetzfeld. *Phys. Rev. D* **87** (2013) 081502.
- [8] D. Puetzfeld and Yu. N. Obukhov. *Phys. Rev. D* **76** (2007) 084025.
- [9] J.L. Synge. *Relativity: The general theory*. North-Holland, Amsterdam, 1960.
- [10] W.G. Dixon. *Nuovo Cim.* **34** (1964) 317.
- [11] D. Puetzfeld and Yu. N. Obukhov. *Phys. Rev. D* **88** (2013) 064025.
- [12] F.W. Hehl, A. Macías, E. W. Mielke, and Yu. N. Obukhov. *On Einstein's Path – Essays in honor of Engelbert Schucking*, Alex Harvey (Ed.), Springer, New York, 1998, p. 257.
- [13] Yu. N. Obukhov. *Acta Phys. Pol. B* **29** (1998) 1131.
- [14] I. Bailey and W. Israel. *Comm. Math. Phys.* **42** (1975) 65.
- [15] W. R. Stoeger and P. B. Yasskin. *Gen. Rel. Grav.* **11** (1979) 427.
- [16] P. B. Yasskin and W. R. Stoeger. *Phys. Rev. D* **21** (1980) 2081.
- [17] C. Brans and R. H. Dicke, *Phys. Rev.* **124** (1961) 925.
- [18] Y. Fujii and K. Maeda. *The scalar-tensor theory of gravitation*. Cambridge University Press, Cambridge, 2003.

FLAVOR DEPENDENCE OF THE SPIN-INDEPENDENT AND SPIN-DEPENDENT PARTS OF GPDs($x, t, \xi = 0$)

O.V. Selyugin¹

¹*BLTP, Joint Institute for Nuclear Research, Dubna, Russia*

Abstract

The different sets of PDF with the new form of t -dependence of generalized parton distributions (GPDs) were examined in the descriptions of the electromagnetic form factors of the proton and neutron. One of the purposes was to minimize the number of fitting parameters. We found that main flavor difference related to the spin-dependent of PDF incoming as part in GPDs. Hence, contrary to some other work, our result shows a little flavor dependence of the t -dependence of the $GPDs(x, t, \xi = 0)$.

The parton picture of the hadron is in most part represented by the parton distribution functions (PDFs). They are determined in the deep inelastic processes. The next step in the development of the picture of the hadron was made by introducing the non-forward structure functions - general parton distributions - GPDs [1] with spin-independent the $H(x, \xi, t)$ and the spin-dependent $E(x, \xi, t)$ parts. Generally, GPDs depend on the momentum transfer t , the average momentum fraction $x = 0.5(x_i + x_f)$ of the active quark, and the skewness parameter $2\xi = x_f - x_i$ that measures the longitudinal momentum transfer. Some of the advantages of GPDs were presented by the sum rules [1]

$$F_1^q(t) = \int_0^1 dx \mathcal{H}^q(x, \xi = 0, t), \quad F_2^q(t) = \int_0^1 dx \mathcal{E}^q(x, \xi = 0, t). \quad (1)$$

Now we cannot obtain the t -dependence of GPDs from the first principles, but it can be obtained from the phenomenological description by $GPDs$ of the nucleon electromagnetic form factors. Many different forms of the t -dependence of GPDs were proposed. In the quark diquark model [2, 3] the form of GPDs consist of three parts - PDFs, function distribution and Regge-like.

$$F_q(x, t) = N_q G_{M_x^{I,II}}^{\lambda,II}(x, t) R_{P_q}^{\alpha_q \alpha'_q}(x, t). \quad (2)$$

The parameters have the flavor dependence for the all three parts. As a result, they came to the conclusion: "The data show, in particular, a suppression of d quarks with respect to u quarks at large momentum transfer". In other works (see e.g. [4]) the description of the t -dependence of GPDs was developed in a more complicated picture using the polynomial forms with respect to x . Note that in [5] it was shown that at large $x \rightarrow 1$ and momentum transfer the behavior of GPDs requires a larger power of $(1 - x)^n$ in the t -dependent exponent:

$$\mathcal{H}^q(x, t) \sim \exp[a(1 - x)^n t] q(x). \quad (3)$$

¹selugin@theor.jinr.ru

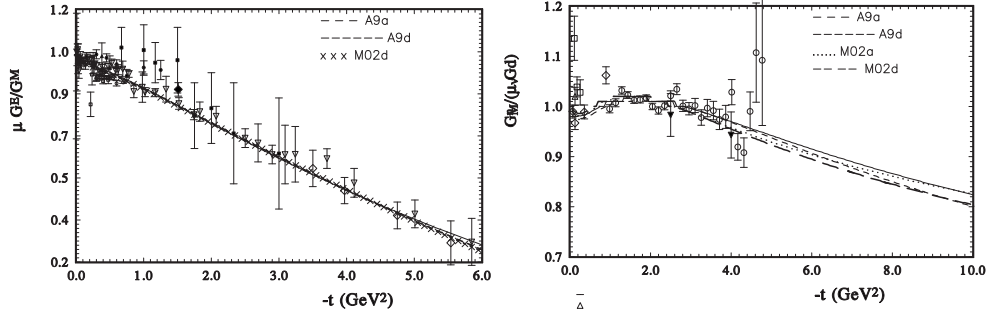


Figure 1: The model description of the electromagnetic form factors for the proton(left) $\mu G_E^p/G_M^p$ and the neutron (right) $G_M^n/(\mu G_d)$ with the different PDFs.

with $n \geq 2$. It was noted that $n = 2$ naturally leads to the Drell-Yan-West duality between parton distributions at large x and the form factors.

Let us modify the original Gaussian ansatz and choose the t -dependence of GPDs in the simple form

$$\mathcal{H}^q(x, t) = q(x) \exp[a_+ (1-x)^2/x^m t]. \quad (4)$$

The value of the parameter $m = 0.4$ is fixed by the low t experimental data while the free parameters a_{\pm} (a_+ - for \mathcal{H} and a_- - for \mathcal{E}) were chosen to reproduce the experimental data in the whole t region. The isotopic invariance can be used to relate the proton and neutron GPDs. Hence, we do not change any parameter and keep the same t -dependence of GPDs as in the case of proton.

In our first work [6] the function $q(x)$ is based on the MRST02 global fit [6]. In all calculations we restrict ourselves to the contributions of only valence u and d quarks. Following the standard representation we have for the Pauli form factor F_2

$$\begin{aligned} \mathcal{E}^q(x, t) &= \mathcal{E}^q(x) \exp[a_- (1-x)^2/x^{0.4} t]; \\ \mathcal{E}^u(x) &= k_u/N_u (1-x)^{\kappa_1} u(x), \quad \mathcal{E}^d(x) = k_d/N_d (1-x)^{\kappa_2} d(x), \end{aligned} \quad (5)$$

where $\kappa_1 = 1.53$ and $\kappa_2 = 0.31$ [8]. According to the normalization of the Sachs form factors, we have $k_u = 1.673$, $k_d = -2.033$, $N_u = 1.53$, $N_d = 0.946$

Now many PPDs, proposed by different Collaborations, were examined to compare the descriptions of the electromagnetic form factors of the proton and neutron. We take 464 experimental data and take into account only statistical errors. As a result, we find that the different PDF sets, which well describe the deep inelastic processes, gave the large difference in the description of the form factors [9]. The whole sets of the results will be published. Now we note that a better description of the form factors was given by PDFs of the [10, 11] and [12]. The obtained description of the electromagnetic form factors is shown on Fig. 1 (left) for the proton and Fig.1(right) for the neutron. Note that at small momentum transfer practically all PDFs gave the same descriptions. However, at large t we obtain the different description for the different PDFs.

Now let us examine separate contributions of the u and d quarks to the electromagnetic form factors in our model of the t -dependence of GPDs. We take PDFs of [10] which give the one of the best descriptions of the electromagnetic form factors. We analyze the two cases: first - the base variant of GPDs with only 4 free variation parameters, second -

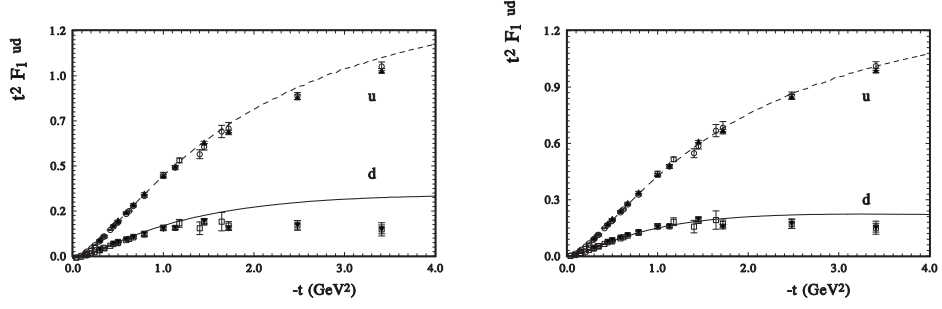


Figure 2: The u and d quarks contributions to the $t^2 F_1(t)$: - the fit with 4 free parameters (left) and with 10 free parameters (right). The data take from [13].

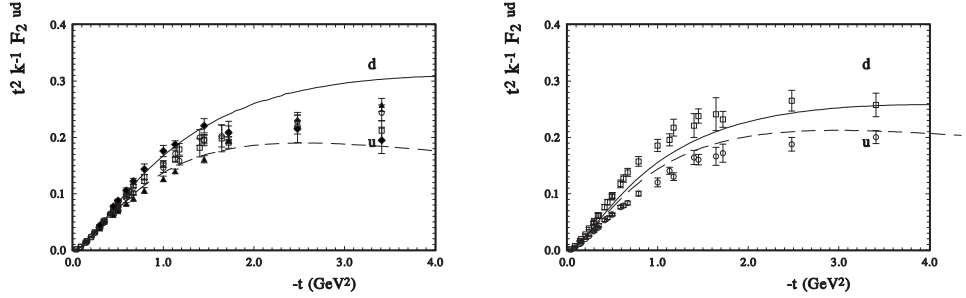


Figure 3: The same as in Fig.2 for the $k^{-1}t^2 F_2(t)$.

with the maximum number of free variation parameters - 10.

$$\mathcal{H}^q(x, t) = q(x)_u \exp[\alpha (a_5 x(1-x) + (1-x)^{a_1}/(\epsilon+x)^{a_2} t)] \quad (6)$$

$$+ q(x)_d \exp[\alpha a_3 (a_6 x(1-x) + (1-x)^{a_1 a_4}/(\epsilon+x)^{a_2} t)]. \quad (7)$$

$$\mathcal{E}^q(x, t) = q(x)_u (1-x)^{k_1} \exp[\alpha (a_5 x(1-x) + (1-x)^{a_1}/(\epsilon+x)^{a_2} t)]$$

$$+ q(x)_d (1-x)^{k_2} \exp[\alpha a_3 (a_6 x(1-x) + (1-x)^{a_1 a_4}/(\epsilon+x)^{a_2} t)].$$

Here the parameters a_3, a_4, a_5, a_6 represent the flavor dependence of the Regge part of GPDs and the parameters k_1, k_2 are responsible for the flavor dependence of the spin-dependent part of PDFs. If we take the PDFs sets from [10] we obtain the small difference in $\sum \chi^2$ in the descriptions of the electromagnetic form factors in these two cases, only 25%. However, the number of free parameters differs essentially: 4 and 10. Further increase in the number of free parameters leads to a very small decrease in $\sum \chi^2$.

The u and d quark contributions to $F_1(t)$ multiplied by t^2 is shown in Fig.2. We compare the fits with 4 free parameters (left) and 10 free parameters (right). It is clear that the difference is very small. Only the d quark contribution is slightly less in the last case. However, the t -dependence in both the cases is practically the same. In Fig.2, we present the same calculations for $F_2(t)$. Again, the contribution of the d quark decreases in the case of a large number of free parameters. Despite the large number of the free parameters, our calculations better coincide with extractions of the u and d quark contributions up to $-t = 2 \text{ GeV}^2$ [13]. The u and d quark contributions to $F_1(t)$ (left) and $F_2(t)$ (right) at large momentum transfer are shown in Fig.3. It is clear that at large t the behavior of the u and d quark contributions is the same.

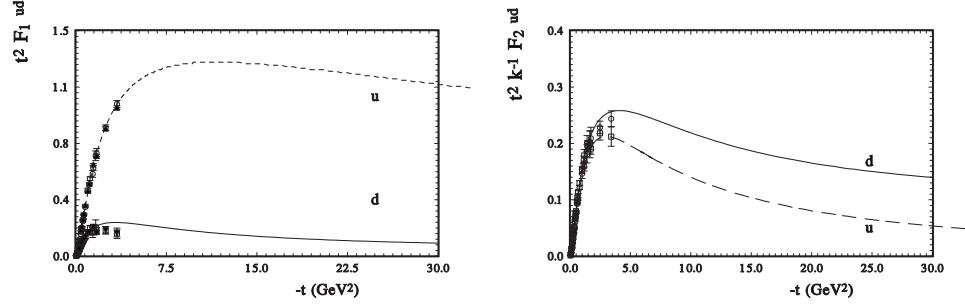


Figure 4: The u and d quarks contributions in $F_1(t)$ (left) and in $F_2(t)$ (right) at large momentum transfer.

Our analysis of PDFs sets of the different Collaborations show a large difference in the descriptions of the electromagnetic form factors of the proton and neutron. The best result can be obtained with PDFs sets of [10] and [11]. These sets lead to minimum of $\sum \chi^2$. They also show the small dependence of the GPDs on the increasing different free parameters. The obtained t dependence of GPDs has a simple form and a small number of the free parameters.

The flavor dependence in these cases in most part comes from the spin dependent part of PDFs. We obtained the good descriptions of the electric and magnetic form factors of the proton and neutron simultaneously. We found that different PDFs gave almost the same descriptions of the proton form factors at small momentum transfer. The difference appear only at large t . Our calculations of the u and d quark contributions show the same t dependence at large t .

References

- [1] X.D. Ji, Phys. Lett. **78**, (1997) 610; Phys. Rev D **55** (1997) 7114; D. Muller *et al.*, Fortsch. Phys. **42**, (1994) 101; Radyushkin, A.V., Phys. Rev. D **56**, 5524 (1997).
- [2] G.R. Goldstein, J.O. Hernandez, S. Liuti, Phys.Rev. **D84** 034007 (2011).
- [3] J.O. Gonsales-Hernandes *et al.*, arXiv:1206.1876 v3.
- [4] M.Diehl *et al.*, Eur.Phys. J. C **39** (2005) 1.
- [5] F. Yuan, Phys. Rev. D, **69**, 051501(R) (2004) .
- [6] O. Selyugin, O. Teryaev, Phys. Rev. **D 79** 033003 (2009);
- [7] A.D. Martin *et al.*, Phys. Lett. B **531** (2002) 216.
- [8] M. Guidal, *et al.*, Phys. Rev. D **72**, 054013 (2005) .
- [9] O. Selyugin Intern. Symposium "SPIN in High Energy Physics", Dubna, (2012), arXiv:1304.2127.
- [10] S. Alekhin *et al.*, Phys.Rev. **D81**, 014032 (2010).
- [11] S. Alekhin, J. Blu"mlein, and S. Moch, Phys.Rev. **D86**, 054009 (2012).
- [12] H. Khanpour *et al.*, arXiv:1205.5194.
- [13] G.D. Gates *et al.*, Phys.Rev.Lett. **106** 252003 (2011); I.A. Qattan and J. Arrington, Phys.Rev. **C86** 065210 (2012).

FORMULAS OF CONNECTION BETWEEN THE DIFFERENT QCD ORDERS FOR PARTON DISTRIBUTION AND FRAGMENTATION FUNCTIONS

O.Yu. Shevchenko

Joint Institute for Nuclear Research, Dubna, Russia

Abstract

The formulas directly connecting parton distribution functions (PDFs) and fragmentation functions (FFs) at the next to leading order (NLO) QCD with the same quantities at the leading order (LO) are derived. These formulas are universal, i.e. have the same form for all kinds of PDFs and FFs, differing only in the respective splitting functions entering there.

Recently [1] the formulas directly connecting parton distribution functions (PDFs) and fragmentation functions (FFs) at the next to leading order (NLO) QCD with the same quantities at the leading order (LO) were derived. To obtain these formulas only the DGLAP evolution equations and the asymptotic condition that PDFs (FFs) at different QCD orders become the same in the Bjorken limit were used as an input. Due to universality of this input the obtained connection formulas are also universal, i.e. they are valid for any kind of PDFs (FFs) we deal with, differing only in the respective splitting functions entering there. Moreover, operating in the same way as in Ref. [1] one can also establish the connection of PDFs (FFs) at LO (as well as at NLO) with these quantities at any higher QCD order (NNLO, NNNLO, ...) (will be published elsewhere).

Let us discuss the derivation of the connection formulas in some detail. We start with some necessary notation and definitions. For the flavor non-singlet and singlet quantities we introduce the notation Q_{NS} and $\mathbf{V} = (Q_S, G)$, where Q_{NS} can be either q_{NS} (non-singlet combinations of quark densities), or Δq_{NS} (non-singlet combinations of helicity PDFs), or combinations of transversity PDFs $\Delta_T q(\bar{q}) \equiv h_{1q,\bar{q}}, \dots$, or D_{NS}^h ("non-singlet" combination of FFs D_q^h), ..., while Q_S can be q_S , Δq_S , D_S^h, \dots , G can be g , Δg , D_g^h, \dots . In this notation the DGLAP evolution equations (see [2] for review) look as

$$Q^2 d\mathbf{V}(Q^2, x)/dQ^2 = (\alpha_s/2\pi)[\mathbf{P}^{(0)}(x) + (\alpha_s/2\pi)\mathbf{P}^{(1)}(x) + O(\alpha_s^2)] \otimes \mathbf{V}(Q^2, x), \quad (1)$$

where the convolution (\otimes) is given by

$$(A \otimes B)(x) = \int_0^1 dx_1 \int_0^1 dx_2 \delta(x - x_1 x_2) A(x_1) B(x_2) = \int_x^1 \frac{dy}{y} A\left(\frac{x}{y}\right) B(y),$$

and analogously for Q_{NS} with the replacement $\mathbf{P}(x, \alpha_s) \rightarrow P(x, \alpha_s) = P^{(0)}(x) + (\alpha_s/2\pi)P^{(1)}(x) + O(\alpha_s^2)$. Here \mathbf{P} is 2×2 matrix with the elements $P_{qq}, P_{qg}, P_{gq}, P_{gg}$, and the splitting functions for unpolarized PDFs and helicity PDFs can be found in the review [3], for transversity PDFs – in the review [4], for FFs – in Ref. [5] and references therein.

Following [6] it is convenient to define the evolution operators \mathbf{E} and \mathbf{E} (2×2 matrix with the elements $E_{qq}, E_{qg}, E_{gq}, E_{gg}$) as

$$Q_{NS}(Q^2, x) = \mathbf{E}(Q^2, x) \otimes Q_{NS}(Q_0^2, x), \quad \mathbf{V}(Q^2, x) = \mathbf{E}(Q^2, x) \otimes \mathbf{V}(Q_0^2, x). \quad (2)$$

Here we are interested in the initial conditions¹

$$\mathbf{E}(Q^2 = Q_0^2, x) = \delta(1 - x), \quad \mathbf{E}(Q^2 = Q_0^2, x) = \mathbf{1} \delta(1 - x), \quad (3)$$

which allow to evolve Q_{NS} and \mathbf{V} from the initial scale Q_0^2 to an arbitrary scale Q^2 .

It is also convenient to use, following [6], the evolution variable $t = (2/\beta_0) \ln(\alpha_s(Q_0^2)/\alpha_s(Q^2))$ instead of the standard variable $\ln(Q^2/\mu^2)$. Besides, we introduce the notation

$$A|_{LO} \equiv \hat{A}, \quad A|_{NLO} \equiv A, \quad (4)$$

for any quantity A at LO and NLO, respectively.

From now on we consider only the nontrivial singlet case. Transition to the simple non-singlet case will be easily done in the end of calculations by making the replacement of the matrices with the respective commuting quantities.

In terms of quantities t and \mathbf{E} the DGLAP equations are rewritten in LO as

$$\frac{d}{dt} \hat{\mathbf{E}}(\hat{t}, x) = \mathbf{P}^{(0)} \otimes \hat{\mathbf{E}}(\hat{t}, x), \quad (5)$$

while in NLO they look as

$$\frac{d}{dt} \mathbf{E}(t, x) = \left[\mathbf{P}^{(0)}(x) + \frac{\alpha_s}{2\pi} \mathbf{R}(x) + O(\alpha_s^2) \right] \otimes \mathbf{E}(t, x), \quad (6)$$

where

$$\mathbf{R}(x) \equiv \mathbf{P}^{(1)}(x) - \frac{\beta_1}{2\beta_0} \mathbf{P}^{(0)}(x). \quad (7)$$

Solution of (5) with the initial condition (3) $\hat{\mathbf{E}}(\hat{t} = 0, x) = \mathbf{1} \delta(1 - x)$ reads [6]

$$\hat{\mathbf{E}}(\hat{t}, x) = \text{Exp}(\mathbf{P}^{(0)}(x) \hat{t}) = \mathbf{1} \delta(1 - x) + \hat{t} \mathbf{P}^{(0)}(x) + \frac{\hat{t}^2}{2!} \mathbf{P}^{(0)}(x) \otimes \mathbf{P}^{(0)}(x) + \dots, \quad (8)$$

while to solve NLO equation (6) one can apply the elegant method of Ref. [6] based on the analogy with the perturbative quantum mechanics (see Eqs. (5.47)–(5.54) in Ref. [6]). Operating in this way one obtains the general solution of (6) in the form (for a moment we omit x dependence and $\delta(1 - x)$)

$$\mathbf{E}(t) = \left\{ \hat{\mathbf{E}}(t) \otimes \left[\mathbf{1} + \frac{\alpha_s(Q_0^2)}{2\pi} \int_{t'}^t d\tau e^{-\beta_0 \tau/2} \hat{\mathbf{E}}(-\tau) \otimes \mathbf{R} \otimes \hat{\mathbf{E}}(\tau) \right] \otimes \hat{\mathbf{E}}(-t') \right\} \otimes \mathbf{E}(t'). \quad (9)$$

Putting $t' \rightarrow \infty$ in (9) one reproduces the solution (Eq. (5.54) in Ref. [6]) satisfying the boundary condition $\mathbf{E} \rightarrow \hat{\mathbf{E}}$ as $t \rightarrow \infty$. In turn, putting $t' = 0$ in (9) one gets the solution

$$\mathbf{E}(t) = \left[\mathbf{1} + \frac{\alpha_s(Q^2)}{2\pi} \int_0^t d\tau e^{\beta_0 \tau/2} \hat{\mathbf{E}}(\tau) \otimes \mathbf{R} \otimes \hat{\mathbf{E}}(-\tau) \right] \otimes \hat{\mathbf{E}}(t), \quad (10)$$

satisfying the boundary condition (3) we deal with.

The *key point* to proceed is the condition that all PDFs and FFs should take the same values in LO and NLO (as well as in NNLO, ...) as $Q^2 \rightarrow \infty$:

$$Q_{NS}(Q^2 \rightarrow \infty, x) = \hat{Q}_{NS}(Q^2 \rightarrow \infty, x), \quad \mathbf{V}(Q^2 \rightarrow \infty, x) = \hat{\mathbf{V}}(Q^2 \rightarrow \infty, x). \quad (11)$$

¹We do not consider the asymptotic conditions [6] $\mathbf{E}(\mathbf{E}) \rightarrow \hat{\mathbf{E}}(\hat{\mathbf{E}})$ as $Q^2 \rightarrow \infty$ (see Eq. (5.57) in [6]), since we deal only with particular realization (2) of the general conditions given by Eqs. (5.18) in [6].

Though this asymptotic condition seems to be intuitively clear, let us argue it in some detail because of its great importance for what follows.

Imagine that two researchers analyse in LO (the first) and NLO (the second) the same “ideal” data – the data available with tremendous statistics even in the Bjorken “sub-limit” (so high Q^2 values are accessible that the Bjorken scaling violation becomes invisible even within extremely small uncertainties on measured asymmetries and cross-sections). For determinacy and simplicity let us suppose that they analyse the imaginary “ideal” polarized SIDIS data on pion production and extract the valence helicity PDFs Δu_V , Δd_V from the proton and deuteron difference asymmetries (see Ref. [7] and references therein) measured in the Bjorken “sub-limit”. The first uses LO formulas $A_p^{\pi^+-\pi^-} \sim (4\Delta u_V - \Delta d_V)/(4u_V - d_V)$ and $A_d^{\pi^+-\pi^-} \sim (\Delta u_V + \Delta d_V)/(u_V + d_V)$ (i.e., performs the analysis analogous to one of COMPASS [8]), and the second their NLO generalization (Eqs. (6-10) in Ref. [7]). Besides, for self-consistency, both imaginary researches do not use the existing parametrizations on u_V , d_V but extract these quantities themselves (as well as the integrated over cut in z difference² $D_1 - D_2$ of favored and unfavored pion FFs) using the same SIDIS data on pion production averaged over spin and studying the quantities $F_{2p(d,^3\text{He},\dots)}^{\pi^+} - F_{2p(d,^3\text{He},\dots)}^{\pi^-}$, where in both LO and NLO only u_V , d_V and $D_1 - D_2$ survive. It is obvious that all terms with convolutions \otimes (see Eqs. (6-10) in Ref. [7]) distinguishing NLO and LO equations for finding Δu_V , Δd_V and u_V , d_V , $D_1 - D_2$ just disappear as one approaches the Bjorken limit, so that comparing the results on these quantities obtained in the Bjorken “sub-limit” both researchers could not discriminate between them.

So, let us pass to limit $Q_0^2 \rightarrow \infty$ in Eq. (2) using the asymptotic condition (11). Then, on the one hand (NLO evolution)

$$\mathbf{V}(Q^2, x) = \mathbf{E}(t \rightarrow -\infty, x) \otimes \mathbf{V}(Q_0^2 \rightarrow \infty, x) = \mathbf{E}(t \rightarrow -\infty, x) \otimes \hat{\mathbf{V}}(Q_0^2 \rightarrow \infty, x), \quad (12)$$

and, on the other hand (inverse LO evolution)

$$\hat{\mathbf{V}}(Q_0^2 \rightarrow \infty, x) = \hat{\mathbf{E}}(\hat{t} \rightarrow \infty, x) \otimes \hat{\mathbf{V}}(Q^2, x). \quad (13)$$

Combining Eqs. (12) and (13) one obtains

$$\mathbf{V}(Q^2, x) = \left[\lim_{Q_0^2 \rightarrow \infty} \mathbf{E}(t, x) \otimes \hat{\mathbf{E}}(-\hat{t}, x) \right] \otimes \hat{\mathbf{V}}(Q^2, x). \quad (14)$$

Using Eqs. (8), (10) and the relation $\lim_{Q^2 \rightarrow \infty} (\alpha_s/\hat{\alpha}_s) = 1$ we arrive at the connection formula between NLO and LO flavour singlet PDFs (FFs) \mathbf{V} and $\hat{\mathbf{V}}$ at the same finite Q^2 value

$$\begin{aligned} \mathbf{V}(Q^2, x) = & \left[\mathbf{1} \delta(1-x) - \frac{\alpha_s(Q^2)}{2\pi} \int_{-\infty}^0 d\tau e^{\beta_0\tau/2} \hat{\mathbf{E}}(\tau, x) \otimes \mathbf{R}(x) \otimes \hat{\mathbf{E}}(-\tau, x) \right] \\ & \otimes \text{Exp} \left(-\frac{2}{\beta_0} \ln \frac{\alpha_s(Q^2)}{\hat{\alpha}_s(Q^2)} \mathbf{P}^{(0)}(x) \right) \otimes \hat{\mathbf{V}}(Q^2, x), \end{aligned} \quad (15)$$

where all dependence on the unreachable infinite point Q_0^2 just cancels out.

In the non-singlet case the relation (15) is significantly simplified. The terms $\hat{E}(\tau, x) \equiv \text{Exp}(\tau P^{(0)}(x))$ and $\hat{E}(-\tau, x)$ cancel out each other in the integrand and one easily obtains

$$\begin{aligned} Q_{NS}(Q^2, x) = & \left[\delta(1-x) + \frac{\alpha_s(Q^2)}{2\pi} \left(\frac{\beta_1}{\beta_0^2} P^{(0)}(x) - \frac{2}{\beta_0} P^{(1)}(x) \right) \right] \\ & \otimes \text{Exp} \left(-\frac{2}{\beta_0} \ln \frac{\alpha_s(Q^2)}{\hat{\alpha}_s(Q^2)} P^{(0)}(x) \right) \otimes \hat{Q}_{NS}(Q^2, x). \end{aligned} \quad (16)$$

²On simultaneous determination of valence PDFs and $D_1 - D_2$ from the SIDIS data see, for example, [9].

Eqs. (15) and (16) connecting flavour singlet and non-singlet quantities in NLO with the same quantities in LO is the *main result* of the paper. Let us briefly discuss their practical use.

There are not any problems with application of Eq. (16) and the task of reconstruction of NLO non-singlet quantities from LO ones is reduced just to the trivial calculation of the integrals entering the convolutions \otimes . Indeed, the parameter $\epsilon \equiv -(2/\beta_0) \ln(\alpha_s/\hat{\alpha}_s)$ is very small even at the minimal (the lower boundary of the experimental cut on Q^2 is usually about 1 GeV^2) really available Q^2 values, so that one can achieve very good accuracy keeping only few first terms in the expansion $\text{Exp}(\epsilon P^{(0)}(x)) = \delta(1-x) + \epsilon P^{(0)}(x) + (\epsilon^2/2!) P^{(0)}(x) \otimes P^{(0)}(x) + \dots$. Certainly, the same statement holds for term $\text{Exp}(\epsilon \mathbf{P}^{(0)}(x))$ in Eq. (15), but there arises an additional problem how to deal with the integral over τ . As usual, the problem is easily solved in the space of Mellin moments. Notice that Q^2 independent integral over τ in Eq. (15) just coincides³ with the quantity $-U(x)$ in Ref. [6] (see Eq. (5.45) in [6]), which enters the solution of DGLAP with the boundary conditions $\lim_{Q^2 \rightarrow \infty} \mathbf{E}(E) = \hat{\mathbf{E}}(\hat{E})$ (see footnote 2). Then, applying the inverse Mellin transformation, one easily obtains instead of (15) the formula suitable⁴ for numerical calculations

$$\mathbf{V}(Q^2, x) = \left[\mathbf{1} \delta(1-x) + \frac{\alpha_s(Q^2)}{2\pi} \int_{C-i\infty}^{C+i\infty} dn \frac{x^{-n}}{2\pi i} U(n) \right] \otimes \text{Exp}(\epsilon(Q^2) \mathbf{P}^{(0)}(x)) \otimes \hat{\mathbf{V}}(Q^2, x), \quad (17)$$

where 2×2 matrix $U(n) \equiv \int_0^1 dx x^{n-1} U(x)$ is given by Eq. (5.41) in Ref. [6].

In summary, the formulas allowing to transform LO parton distribution and fragmentation functions to NLO ones are derived. To obtain these formulas we use as an input only the DGLAP evolution equations and the asymptotic condition that PDFs (FFs) at different QCD orders become the same in the Bjorken limit. Due to universality of this input the connection formulas are also universal, i.e. they are valid for any kind of PDFs (FFs) we deal with. Besides, it is obvious that operating in the same way one can also establish the connection of PDFs (FFs) at LO (as well as at NLO) with these quantities at any higher QCD order (NNLO, NNNLO, ...), and the only restriction here is the knowledge of the respective splitting functions.

References

- [1] O. Yu. Shevchenko, Phys. Rev. **D87** (2013) 114004.
- [2] G. Altarelli, Phys. Rept. **81** (1982) 1.
- [3] B. Lampe and E. Reya, Phys. Rept. **332** (2000) 1.
- [4] V. Barone, A. Drago and P. G. Ratcliffe, Phys. Rept. **359** (2002) 1.
- [5] P. Nason and B. R. Webber, Nucl. Phys. B **421** (1994) 473.
- [6] V. Furmanski and R. Petronzio, Z. Phys. C **11** (1982) 293.
- [7] O. Y. Shevchenko, R. R. Akhunzyanov and V. Y. Lavrentyev, Eur. Phys. J. C **71** (2011) 1713.
- [8] M. Alekseev *et al.* [COMPASS Collaboration], Phys. Lett. B **660** (2008) 458.
- [9] M. Arneodo *et al.* [European Muon Collaboration], Nucl. Phys. B **321** (1989) 541.
- [10] A. Vogt, Comput. Phys. Commun. **170** (2005) 65 (hep-ph/0408244).

³Using Eq. (5.28) in Ref. [6] for U and the obvious relation $Q^2 d[\text{Exp}((2/\beta_0) \ln \hat{\alpha}_s \mathbf{P}^{(0)}) \otimes \hat{\mathbf{V}}]/dQ^2 = 0$ one can immediately check that r.h.s. of Eq. (15) indeed satisfies the NLO DGLAP equation (1).

⁴In Ref. [10] one can find the efficient algorithm for the numerical calculation of the integral over n (proper choice of the integration contour, etc. – see discussion around Eq. (3.2) in Ref. [10]).

IMPORTANCE OF SEMI-INCLUSIVE DIS PROCESSES IN DETERMINING FRAGMENTATION FUNCTIONS¹

E. Leader^a, A.V. Sidorov^{b†} and D.B. Stamenov^c

(a) *Imperial College, Prince Consort Road, London SW7 2BW, England*

(b) *Joint Institute for Nuclear Research, 141980 Dubna, Russia*

(c) *Institute for Nuclear Research and Nuclear Energy, Bulgarian Academy of Sciences, Blvd. Tsarigradsko Chaussee 72, Sofia 1784, Bulgaria*

† *E-mail: sidorov@theor.jinr.ru*

Abstract

A NLO QCD analysis of the HERMES and COMPASS data on pion multiplicities is presented. Sets of pion fragmentation functions are extracted from fits to the data and compared with those obtained from other groups before these data were available. The consistency between HERMES and COMPASS data is discussed. We point out a possible inconsistency between the the HERMES $[x, z]$ and $[Q^2, z]$ presentations of their data.

In the absence of charged current neutrino data, the experiments on polarized inclusive deep inelastic lepton-nucleon scattering (DIS) yield information only on the sum of quark and anti-quark parton densities $\Delta q + \Delta \bar{q}$ and the polarized gluon density ΔG . In order to extract separately Δq and $\Delta \bar{q}$ other reactions are needed. One possibility is to use the *polarized* semi-inclusive lepton-nucleon processes (SIDIS) $l + N \rightarrow l' + h + X$, where h is a detected hadron (pion, kaon, etc) in the final state. In these processes new physical quantities appear - the fragmentation functions $D_{q,\bar{q}}^h(z, Q^2)$ which describe the fragmentation of quarks and antiquarks into hadrons. Due to the different fragmentation of quarks and anti-quarks, the polarized parton densities Δq and $\Delta \bar{q}$ can be determined separately from a combined QCD analysis of the data on inclusive and semi-inclusive asymmetries. The key role of the fragmentation functions (FFs) for the correct determination of sea quark parton densities $\Delta \bar{q}$ was discussed in [1]. There are different sources to extract the fragmentation functions themselves: The semi-inclusive $e^+ e^-$ annihilation data, single-inclusive production of a hadron h at a high transverse momentum p_T in hadron-hadron collisions, unpolarized semi-inclusive DIS processes. It is important to mention that the data on hadron multiplicities in unpolarized SIDIS processes are crucial for a reliable determination of FFs, because only then one can separate $D_q^h(z, Q^2)$ from $D_{\bar{q}}^h(z, Q^2)$. Such data have been used *only* by the DSS group in their global analysis [2]. As a result, the properties of the extracted set of FFs significantly differ, especially in the kaon sector, from those of the other sets of FFs [3]. Unfortunately, the new properties of the DSS FFs are based on the *unpublished* HERMES'05 SIDIS data on hadron multiplicities which are not confirmed by the final HERMES data [4]. It turns out that not only the DSS FFs, but all other sets of pion and kaon FFs are NOT in agreement with the recent HERMES and COMPASS data [5] on hadron multiplicities.

¹This research was supported by the JINR-Bulgaria Collaborative Grant and the RFBR Grants (Nrs 11-01-00182, 12-02-00613 and 13-02-01005).

In this talk we present our results on new pion fragmentation functions extracted from a NLO QCD fit to the HERMES and COMPASS (the first ref. in [5]) data on the pion multiplicities. While COMPASS reports data only on a deuteron target, HERMES presents data on both the proton and deuteron targets.

The multiplicity $M_{p(d)}^\pi(x, Q^2, z)$ of pions using a proton (deuteron) target are defined as the number of pions produced, normalized to the number of DIS events, and can be expressed in terms of the semi-inclusive cross section $\sigma_{p(d)}^\pi$ and the inclusive cross section $\sigma_{p(d)}^{DIS}$:

$$\begin{aligned} M_{p(d)}^\pi(x, Q^2, z) &= \frac{d^3 N_{p(d)}^\pi(x, Q^2, z)/dx dQ^2 dz}{d^2 N_{p(d)}^{DIS}(x, Q^2)/dx dQ^2} = \frac{d^3 \sigma_{p(d)}^\pi(x, Q^2, z)/dx dQ^2 dz}{d^2 \sigma_{p(d)}^{DIS}(x, Q^2)/dx dQ^2} \\ &= \frac{(1 + (1 - y^2))2x F_{1p(d)}^h(x, Q^2, z) + 2(1 - y)x F_{Lp(d)}^h(x, Q^2, z)}{(1 + (1 - y^2))2x F_{1p(d)}(x, Q^2) + 2(1 - y)F_{Lp(d)}(x, Q^2)}. \end{aligned} \quad (1)$$

In Eq. (1) F_1^h, F_L^h and F_1, F_L are the semi-inclusive and the usual nucleon structure function respectively, which are expressed in terms of the unpolarized parton densities and the fragmentation functions (F_1^h, F_L^h), and by the unpolarized parton densities (F_1, F_L).

Let's start our discussion with the results of the fit to COMPASS deuteron data. In our fit we have used the $[y, x(Q^2), z]$ presentation of the data, where $y = Q^2/2ME_x$ is the fractional energy of the virtual photon, and M and E are the mass of the nucleon and the energy of the muon beam, respectively. The data on the multiplicities are distributed in five y -bins as functions of z at different fixed values of (x, Q^2) . The total number of the data points is 398, 199 for π^+ and 199 for π^- multiplicities. The errors used are quadratic combinations of the statistical and systematic errors. The number of free parameters, attached to the input parametrizations of the pion FFs [$D_u^{\pi^+}(z), D_{\bar{u}}^{\pi^+}(z), D_g^{\pi^+}(z)$] at $Q^2 = 1 \text{ GeV}^2$ and determined from the fit, is 12. The assumption that all unfavored pion FFs are equal is used. For the unpolarized parton densities we use the NLO MRST'02 set of PDFs [6]. The charm contribution to the multiplicities is not taken into account. For the value of χ^2/DOF corresponding to the best fit to the data we obtain $283.12/386=0.73$. An excellent description of the COMPASS pion data is achieved. The quality of the fit is illustrated for the y_3 -bin [0.2-0.3] (see Fig. 1 for π^+ and Fig. 2 for

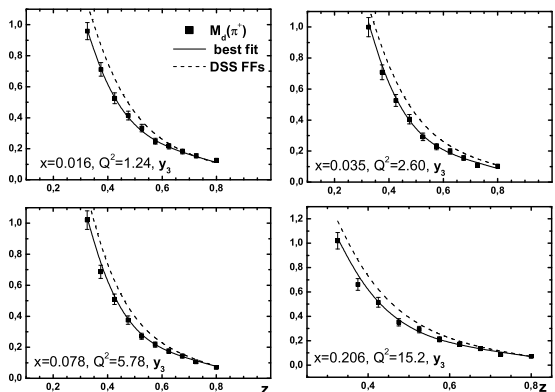


Figure 1: Comparison of our NLO QCD results for COMPASS π^+ multiplicities with the data. The multiplicities computed with the DSS FFs are also shown.

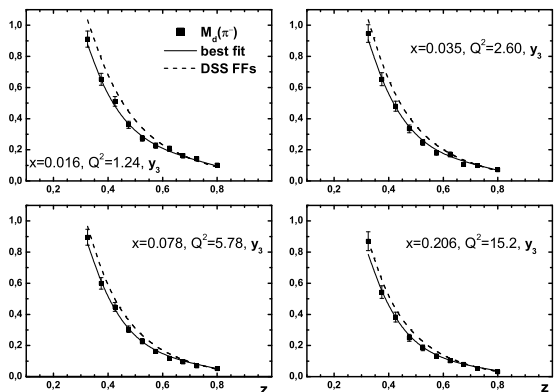


Figure 2: Comparison of our NLO QCD results for COMPASS π^- multiplicities with the data. The multiplicities computed with the DSS FFs are also shown.

π^- multiplicities). In the figures are presented also the multiplicities at the COMPASS kinematics calculated using the DSS FFs (dashed curves). The extracted pion FFs will be presented later and compared to those obtained from our fit to the HERMES data, as well as to some of the FFs sets available at present. Here we would like only to mention that it is obvious that the COMPASS data are in disagreement with the DSS FFs.

Let us discuss now our results on the pion FFs extracted from a NLO QCD fit to the HERMES proton and deuteron data on pion multiplicities, corrected for exclusive vector meson production [4]. In our analysis we have used the $[x, z]$ as well as the $[Q^2, z]$ presentation of the data. The pion multiplicities are given for 4 z -bins $[0.2-0.3; 0.3-0.4; 0.4-0.6; 0.6-0.8]$ as functions of x for the $[x, z]$ or functions of Q^2 for the $[Q^2, z]$ presentation. The total number of the π^+ and π^- data points is 144. It turned out that we can not find a reasonable fit to the HERMES $[x, z]$ data. Also, there is a strong indication that the HERMES $[x, z]$ and COMPASS data are not consistent. We observe a big discrepancy

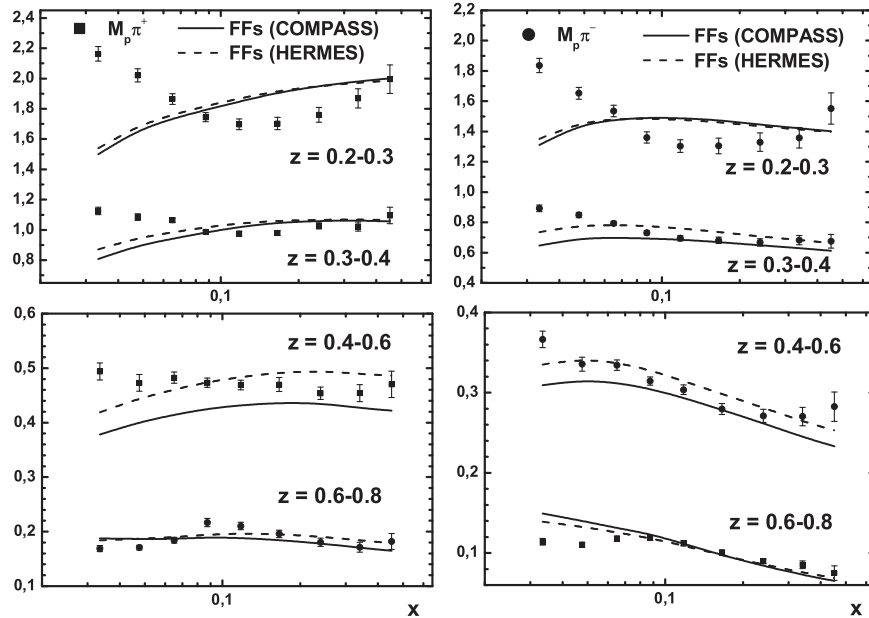


Figure 3: Comparison of HERMES $[x, z]$ proton data on π^+ (left) and π^- multiplicities (right) with the multiplicities at the same kinematic points calculated by our FFs extracted from the COMPASS data (solid curves) and from HERMES $[Q^2, z]$ data (dashed curves).

between the values of the HERMES data on pion multiplicities and multiplicities at the same kinematic points computed with our FFs extracted from the COMPASS data (see solid curves in Fig. 3 for proton and Fig. 4 for deuteron data).

We were very surprised to find that the situation is dramatically changed if the HERMES data on pion multiplicities in $[Q^2, z]$ presentation are used in the QCD analysis. In this case a reasonable fit to the data is achieved, $\chi^2/DOF = 151.73/132 = 1.15$. The errors used in the fit are quadratic combinations of the statistical and point-to-point systematic errors. As in the COMPASS case: *a)* isospin symmetry for FFs is imposed, *b)* we assume that all unfavored pion FFs are equal and *c)* the same parametrizations for the

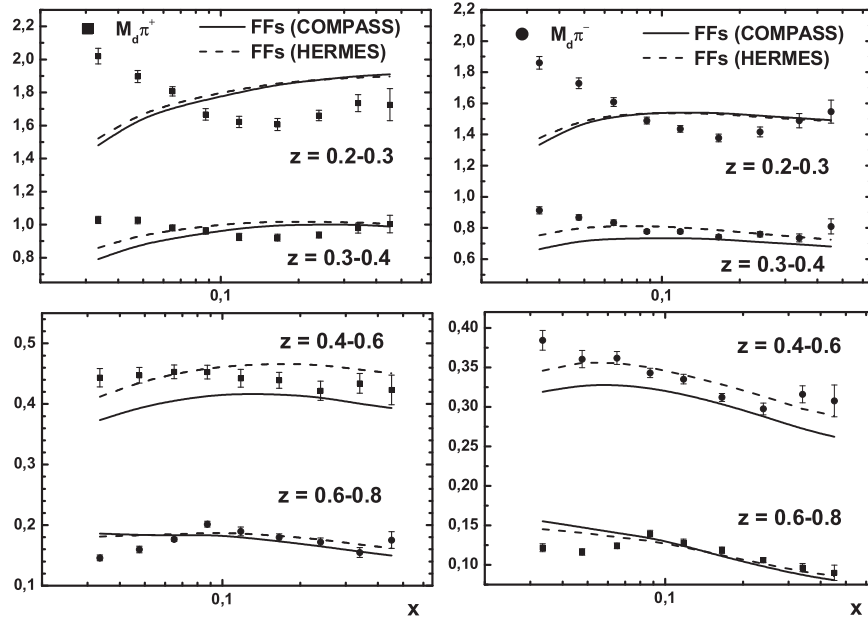


Figure 4: Comparison of HERMES $[x, z]$ deuteron data on π^+ (left) and π^- multiplicities (right) with the multiplicities at the same kinematic points calculated by our FFs extracted from the COMPASS data (solid curves) and from HERMES (Q^2, z) data (dashed curves).

input FFs are used in the analysis. We find that the description of the proton data (the mean value of χ^2 per point is equal to 0.96 for π^+ and 0.70 for π^- multiplicities) is better than that of the deuteron data (where the mean value of χ^2 per point is equal to 1.25 for π^+ and 1.31 for π^- multiplicities). The quality of the fit to the data is illustrated in Fig. 5 (for the proton target) and Fig. 6 (for the deuteron target).

Using the extracted FFs from the HERMES data on multiplicities in the $[Q^2, z]$ presentation we have calculated the multiplicities at the kinematic points for the $[x, z]$ presentation. The obtained value for χ^2 is huge, 2093.3 for 144 experimental points. The results are shown (dash curves) in Fig. 3 for a proton and in Fig. 4 for a deuteron target. As seen from the figures, the discrepancy is very large for both the proton and deuteron targets for the first z -bin $[0.2-0.3]$, as well as at lowest x , for all z -bins. It follows from this observation that the $[x, z]$ and $[Q^2, z]$ presentation of the *same* data leads to different physical results. A further study of this unusual situation is urgently needed.

The extracted pion FFs from the fit to COMPASS data (solid curves) and from the fit to HERMES data on pion multiplicities (dash curves) are presented in Fig. 7, and compared to those determined by DSS [2] and HKNS (the 2nd reference in [3]) in Fig. 8. Due to the visible difference in the z region $[0.4-0.6]$ between the favored fragmentation functions D_u^+ extracted from HERMES and COMPASS data, and the large difference between the corresponding gluon FFs, the dashed curves in Fig. 5 and Fig. 6 corresponding to the multiplicities at the HERMES $[Q^2, z]$ data points calculated by the FFs (COMPASS), lie systematically lower than the data points for the same z -bin. Combined

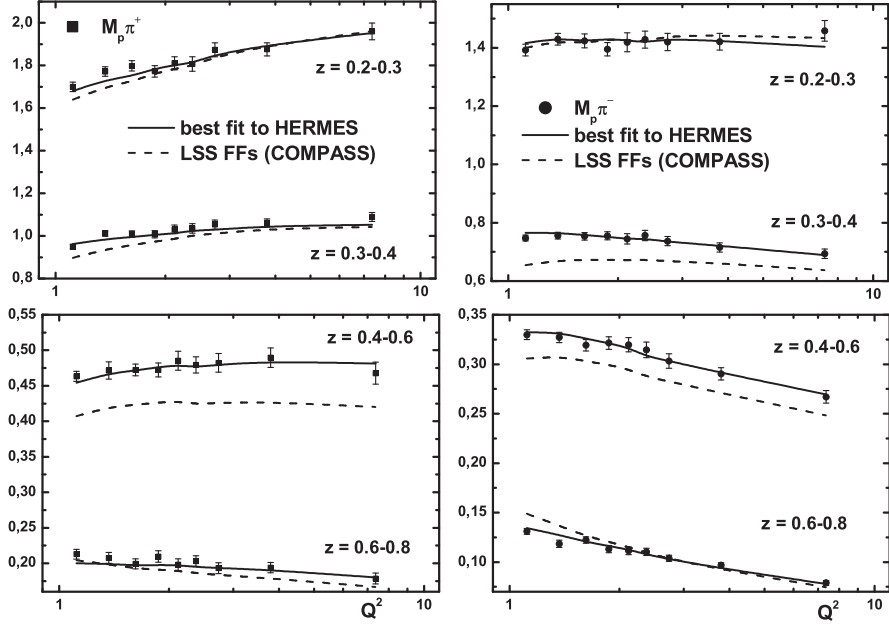


Figure 5: Comparison of HERMES $[Q^2, z]$ proton data on π^+ (left) and π^- multiplicities (right) with the best fit curves. The dashed curves correspond to the multiplicities at the same kinematic points calculated using our FFs extracted from the COMPASS data.

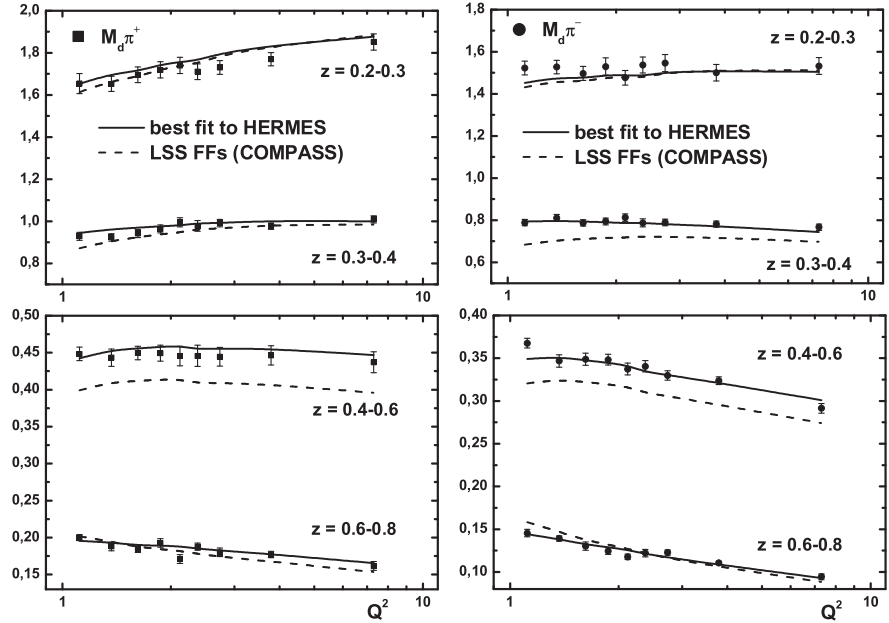


Figure 6: Comparison of HERMES $[Q^2, z]$ deuteron data on π^+ (left) and π^- multiplicities (right) with the best fit curves. The dashed curves correspond to the multiplicities at the same kinematic points calculated using our FFs extracted from the COMPASS data.

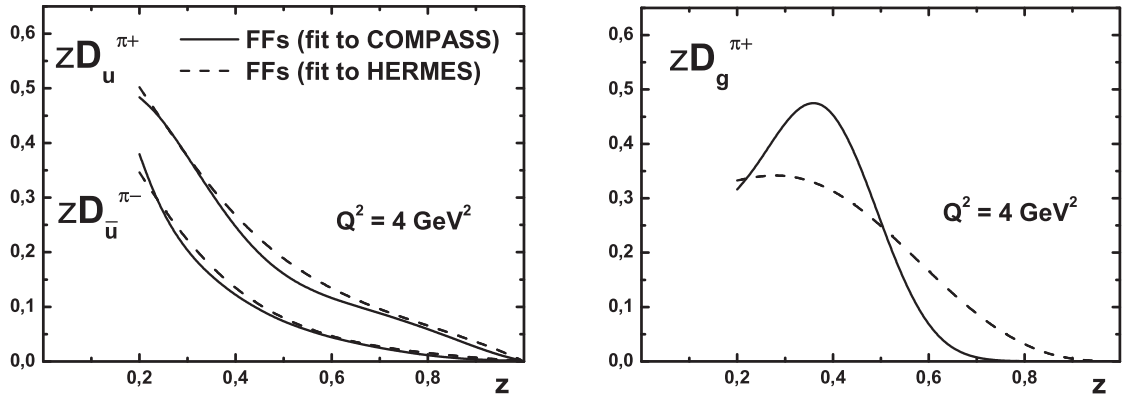


Figure 7: Our FFs extracted from the fit to COMPASS data (solid curves) and HERMES (Q^2, z) data (dashed curves).

fits to the COMPASS and HERMES [Q^2, z] data on pion multiplicities will answer the important question if the discrepancy between the two data sets, shown in Figs. 5 and 6, will be removed, or more generally, if the HERMES [Q^2, z] and COMPASS data are or are not consistent.

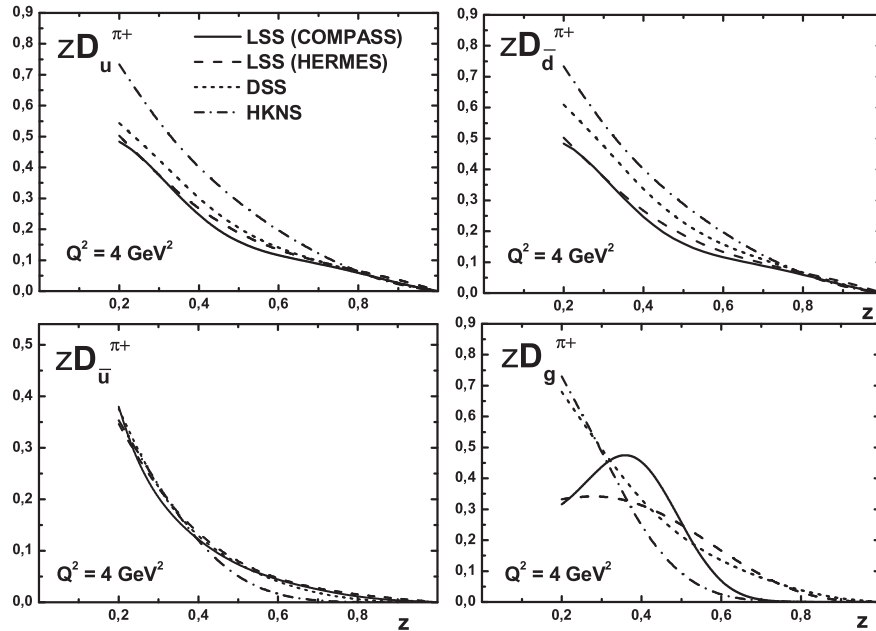


Figure 8: Comparison between the new pion FFs and those of DSS and HKNS.

One can see from Fig. 8 that the new sets of pion FFs for the quarks are close to that of DSS. The differences, however, between $D_g^{\pi^+}$ corresponding to the different sets, are large. Also, for the DSS set the favored fragmentation function $D_d^{\pi^+}$ is larger than $D_u^{\pi^+}$

because in their analysis a violation of isospin symmetry was allowed. This is the main reason that the values of the multiplicities calculated by the DSS FFs for the COMPASS kinematics (dashed curves in Figs 1 and 2) are systematically larger than the experimental values. The situation is the same for the HERMES data.

In conclusion, new sets of pion FFs are determined from the fits to the recent HERMES and COMPASS data on pion multiplicities. They differ from those of DSS and HKNS obtained before these data were available. There is a strong indication that the $[x, z]$ and $[Q^2, z]$ presentations of the HERMES data on the pion multiplicities are not equivalent and lead to different physical results, which suggests that there might be something wrong with the extraction of the data presentations from the measured experimental values. We find also that the COMPASS and HERMES $[x, z]$ data are not consistent. The situation about the consistency between the COMPASS and HERMES $[Q^2, z]$ data looks much better. Here the discrepancy is mainly for the third z -bin for the π^+ and for the second and third z -bins for the π^- multiplicities. So, the important questions as to the consistency between COMPASS and HERMES $[Q^2, z]$ data will depend on the results of a combined fit to the data, which is under way.

References

- [1] E. Leader, A.V. Sidorov, D.B. Stamenov, Phys. Rev. **D84** (2011) 014002.
- [2] D. de Florian, R. Sassot, M. Stratmann, Phys. Rev. **D75** (2007) 114010;
Phys. Rev. **D76** (2007) 074033.
- [3] S. Kretzer, Phys. Rev. **D62** (2000) 054001;
M. Hirai, S. Kumano, T.-H. Nagai, K. Sudoh, Phys. Rev. **D75** (2007) 094009;
S. Albino, B. A. Kniehl, G. Kramer, Nucl. Phys. **B803** (2008) 42.
- [4] A. Airapetain et al., Phys. Rev. **D87** (2013) 074029.
- [5] N. Makke (for COMPASS collaboration), 21th Int. Workshop DIS'2013, Marseille, April, 2013;
Proc. of the 20th Int. Workshop on DIS'2012, C12-03-26.1, p.741-744.
- [6] A.D. Martin, R.G. Roberts, W.J. Stirling, R.S. Thorne, Eur. Phys. J. **C28** (2003) 455.

SPIN-1/2 PARTICLES IN ARBITRARY STRONG GRAVITATIONAL FIELDS

Y.N. Obukhov¹, A.J. Silenko^{2,3†} and O.V. Teryaev²

(1) *Theoretical Physics Laboratory, Nuclear Safety Institute, RAS, Moscow 115191, Russia*

(2) *Bogoliubov Laboratory of Theoretical Physics, JINR, Dubna 141980, Russia*

(3) *Research Institute for Nuclear Problems, Belarusian State University, Minsk 220030, Belarus*

† *E-mail: alsilenko@mail.ru*

Abstract

We find the Hermitian Dirac Hamiltonian for an arbitrary classical external field (including the gravitational and electromagnetic ones). We further apply the Foldy-Wouthuysen transformation, and derive the quantum equations of motion for the spin and position operators. We analyze the semiclassical limit of these equations and compare the results with the dynamics of a classical spinning particle. The comparison of the quantum-mechanical and classical equations describing a spinning particle in an arbitrary gravitational field shows their complete agreement.

1 Introduction

In this paper, we present the results of our investigations of the Dirac fermions based on the new method [1] of the Foldy-Wouthuysen (FW) transformation. Earlier, we analyzed the dynamics of spin in weak static and stationary gravitational fields [2–5] and in strong stationary gravitational fields [6] of massive compact sources. These previous results are now extended on the general case of a completely arbitrary gravitational field.

Our notations and conventions are the same as in Ref. [3]. The world indices of the tensorial objects are denoted by Latin letters $i, j, k, \dots = 0, 1, 2, 3$ and the first letters of the Greek alphabet label the tetrad indices, $\alpha, \beta, \dots = 0, 1, 2, 3$. Spatial indices of 3-dimensional objects are denoted by Latin letters from the beginning of the alphabet, $a, b, c, \dots = 1, 2, 3$. Temporal and spatial tetrad indices are distinguished by hats.

2 Dirac particle in a gravitational field

The massive particle is quite generally characterized by its position in spacetime, $x^i(\tau)$, depending on the proper time τ , and by the spin tensor $S^{\alpha\beta} = -S^{\beta\alpha}$. We denote 4-velocity of a particle $U^\alpha = e_i^\alpha dx^i/d\tau$. In view of the choice of parametrization by the proper time, it is normalized by the standard condition $g_{\alpha\beta} U^\alpha U^\beta = c^2$ where $g_{\alpha\beta} = \text{diag}(c^2, -1, -1, -1)$ is the flat Minkowski metric. We use the tetrad e_i^α (or coframe) to describe the dynamics of spinning particles on a spacetime manifold in arbitrary curvilinear coordinates.

We use the notations t and x^a ($a = 1, 2, 3$) for the coordinate time and the spatial local coordinates, respectively. A convenient parametrization of the spacetime metric

was proposed by De Witt [7] in the context of the canonical formulation of the quantum gravity. The general form of the line element of an arbitrary gravitational field reads

$$ds^2 = V^2 c^2 dt^2 - \delta_{\hat{a}\hat{b}} W^{\hat{a}}{}_c W^{\hat{b}}{}_d (dx^c - K^c dt) (dx^d - K^d dt). \quad (1)$$

One needs the orthonormal frames to discuss the spinor field and to formulate the Dirac equation. From the mathematical point of view, the tetrad is necessary to “attach” a spinor space at every point of the spacetime manifold. Tetrads (coframes) are naturally defined up to a local Lorentz transformations, and one usually fixes this freedom by choosing a gauge. We discussed the choice of the tetrad gauge in [5] and have demonstrated that a physically preferable option is the Schwinger gauge [8, 9], namely the condition $e_{\hat{a}}^0 = 0, a = 1, 2, 3$. Accordingly, for the general metric (1) we will work with the tetrad

$$e_{\hat{i}}^{\hat{0}} = V \delta_i^0, \quad e_{\hat{i}}^{\hat{a}} = W^{\hat{a}}{}_b (\delta_i^b - c K^b \delta_i^0), \quad a = 1, 2, 3. \quad (2)$$

The inverse tetrad, such that $e_{\alpha}^i e_j^{\alpha} = \delta_j^i$,

$$e_{\hat{0}}^i = \frac{1}{V} (\delta_0^i + \delta_a^i c K^a), \quad e_{\hat{a}}^i = \delta_b^i W^b{}_{\hat{a}}, \quad a = 1, 2, 3, \quad (3)$$

also satisfies the similar Schwinger condition, $e_{\hat{a}}^0 = 0$. Here we introduced the inverse 3×3 matrix, $W^a{}_{\hat{c}} W^{\hat{c}}{}_b = \delta_b^a$.

A classical massive particle moves along a world line $x^i(\tau), i = 0, 1, 2, 3$, parametrized by the proper time τ . Its 4-velocity is defined as usual by the derivatives $U^i = dx^i/d\tau$. With respect to a given orthonormal frame, the velocity has the components $U^{\alpha} = e_{\hat{i}}^{\alpha} U^i, \alpha = 0, 1, 2, 3$. It is convenient to describe the 4-velocity by its 3 spatial components $v^{\hat{a}}, a = 1, 2, 3$, in an anholonomic frame. Then $U^{\alpha} = (\gamma, \gamma v^{\hat{a}})$, with the Lorentz factor $\gamma^{-1} = \sqrt{1 - v^2/c^2}$, and, consequently,

$$U^0 = \frac{dt}{d\tau} = e_{\alpha}^0 U^{\alpha} = \frac{\gamma}{V}, \quad (4)$$

$$U^a = \frac{dx^a}{d\tau} = e_{\alpha}^a U^{\alpha} = \frac{\gamma}{V} (c K^a + V W^a{}_{\hat{b}} v^{\hat{b}}). \quad (5)$$

We used (3) here. Dividing (5) by (4) and denoting $\mathcal{F}^a{}_b = V W^a{}_{\hat{b}}$, we find for the velocity with respect to the coordinate time

$$\frac{dx^a}{dt} = \mathcal{F}^a{}_b v^b + c K^a. \quad (6)$$

The Dirac equation in a curved spacetime reads [10, 11]

$$(i\hbar\gamma^{\alpha} D_{\alpha} - mc)\Psi = 0, \quad \alpha = 0, 1, 2, 3, \quad (7)$$

$$D_{\alpha} = e_{\alpha}^i D_i, \quad D_i = \partial_i + \frac{iq}{\hbar} A_i + \frac{i}{4} \sigma^{\alpha\beta} \Gamma_{i\alpha\beta}.$$

Here the Lorentz connection is $\Gamma_i^{\alpha\beta} = -\Gamma_i^{\beta\alpha}$, and $\sigma^{\alpha\beta} = \frac{i}{2} (\gamma^{\alpha}\gamma^{\beta} - \gamma^{\beta}\gamma^{\alpha})$ are the generators of the local Lorentz transformations of the spinor field. The transformation [6]

$$\psi = (\sqrt{-g} e_{\hat{0}}^0)^{\frac{1}{2}} \Psi. \quad (8)$$

yields the Dirac equation in the Schrödinger form with the *Hermitian* Hamiltonian [6]

$$\mathcal{H} = \beta mc^2 V + q\Phi + \frac{c}{2} (\pi_b \mathcal{F}^b_a \alpha^a + \alpha^a \mathcal{F}^b_a \pi_b) + \frac{c}{2} (\mathbf{K} \cdot \boldsymbol{\pi} + \boldsymbol{\pi} \cdot \mathbf{K}) + \frac{\hbar c}{4} (\boldsymbol{\Xi} \cdot \boldsymbol{\Sigma} - \Upsilon \gamma_5). \quad (9)$$

Here $\mathbf{K} = \{K^a\}$, and the kinetic momentum operator $\boldsymbol{\pi} = \{\pi_a\}$ with $\pi_a = -i\hbar\partial_a + qA_a = p_a + qA_a$ accounts for the interaction with the electromagnetic field $A_i = (\Phi, A_a)$. To remind the notation: $\beta = \gamma^0$, $\boldsymbol{\alpha} = \{\alpha^a\}$, $\boldsymbol{\Sigma} = \{\Sigma^a\}$, where the 3-vector-valued Dirac matrices have their usual form; namely, $\alpha^a = \gamma^0 \gamma^a$ ($a, b, c, \dots = 1, 2, 3$) and $\Sigma^1 = i\gamma^2 \gamma^3$, $\Sigma^2 = i\gamma^3 \gamma^1$, $\Sigma^3 = i\gamma^1 \gamma^2$. We also introduced a pseudoscalar Υ and a 3-vector $\boldsymbol{\Xi} = \{\Xi_a\}$ by [6]

$$\Upsilon = V \epsilon^{\widehat{abc}} \Gamma_{\widehat{abc}} = -V \epsilon^{\widehat{abc}} \mathcal{C}_{\widehat{abc}}, \quad \Xi_{\widehat{a}} = \frac{V}{c} \epsilon_{\widehat{abc}} \Gamma_{\widehat{0}^{\widehat{bc}}} = \epsilon_{\widehat{abc}} \mathcal{Q}^{\widehat{bc}}. \quad (10)$$

For the static and stationary rotating configurations, the pseudoscalar invariant vanishes ($\epsilon^{\widehat{abc}} \mathcal{C}_{\widehat{abc}} = 0$), and thus the corresponding term was absent in the special cases considered in Refs. [5, 6]. But in general this term contributes to the Dirac Hamiltonian.

3 The Foldy-Wouthuysen transformation

We do not make any assumptions and/or approximations for the functions $V, W^{\widehat{a}}_b, K^a$. The Planck constant \hbar will be treated as the only small parameter. In accordance with this strategy, we retain in the FW Hamiltonian all the terms of the zero and first orders in \hbar . The leading nonvanishing terms of order \hbar^2 have been calculated in both nonrelativistic and weak field approximations in our previous works [2, 5, 6] for the more special cases. These terms describe the gravitational contact (Darwin) interaction.

We obtain the Foldy-Wouthuysen Hamiltonian in the following form:

$$\mathcal{H}_{FW} = \mathcal{H}_{FW}^{(1)} + \mathcal{H}_{FW}^{(2)}. \quad (11)$$

Here the two terms read, respectively [12],

$$\mathcal{H}_{FW}^{(1)} = \beta\epsilon' + \frac{\hbar c^2}{16} \left\{ \frac{1}{\epsilon'}, (2\epsilon^{cae} \Pi_e \{p_b, \mathcal{F}^d_c \partial_d \mathcal{F}^b_a\} + \Pi^a \{p_b, \mathcal{F}^b_a \Upsilon\}) \right\} + \frac{\hbar mc^4}{4} \epsilon^{cae} \Pi_e \left\{ \frac{1}{\mathcal{T}}, \{p_d, \mathcal{F}^d_c \mathcal{F}^b_a \partial_b V\} \right\}, \quad (12)$$

$$\mathcal{H}_{FW}^{(2)} = \frac{c}{2} (K^a p_a + p_a K^a) + \frac{\hbar c}{4} \Sigma_a \Xi^a + \frac{\hbar c^2}{16} \left\{ \frac{1}{\mathcal{T}}, \left\{ \Sigma_a \{p_e, \mathcal{F}^e_b\}, \left\{ p_f, \left[\epsilon^{abc} \left(\frac{1}{c} \dot{\mathcal{F}}^f_c - \mathcal{F}^d_c \partial_d K^f + K^d \partial_d \mathcal{F}^f_c \right) - \frac{1}{2} \mathcal{F}^f_d (\delta^{db} \Xi^a - \delta^{da} \Xi^b) \right] \right\} \right\} \right\}, \quad (13)$$

$$\epsilon' = \sqrt{m^2 c^4 V^2 + \frac{c^2}{4} \delta^{ac} \{p_b, \mathcal{F}^b_a\} \{p_d, \mathcal{F}^d_c\}}, \quad \mathcal{T} = 2\epsilon'^2 + \{\epsilon', mc^2 V\}. \quad (14)$$

The equation of motion of spin is given by

$$\frac{d\boldsymbol{\Pi}}{dt} = \frac{i}{\hbar} [\mathcal{H}_{FW}, \boldsymbol{\Pi}] = \boldsymbol{\Omega}_{(1)} \times \boldsymbol{\Sigma} + \boldsymbol{\Omega}_{(2)} \times \boldsymbol{\Pi}. \quad (15)$$

Here the 3-vectors $\mathbf{\Omega}_{(1)}$ and $\mathbf{\Omega}_{(2)}$ are the operators of the angular velocity of spin precessing in the exterior classical gravitational field. Their components read explicitly as follows [12]:

$$\begin{aligned} \Omega_{(1)}^a &= \frac{mc^4}{2} \left\{ \frac{1}{T}, \{p_e, \epsilon^{abc} \mathcal{F}^e_b \mathcal{F}^d_c \partial_d V\} \right\} \\ &+ \frac{c^2}{8} \left\{ \frac{1}{\epsilon'}, \{p_e, (2\epsilon^{abc} \mathcal{F}^d_b \partial_d \mathcal{F}^e_c + \delta^{ab} \mathcal{F}^e_b \Upsilon)\} \right\} \end{aligned} \quad (16)$$

and

$$\begin{aligned} \Omega_{(2)}^a &= \frac{\hbar c^2}{8} \left\{ \frac{1}{T}, \left\{ \{p_e, \mathcal{F}^e_b\}, \left\{ p_f, \left[\epsilon^{abc} \left(\frac{1}{c} \dot{\mathcal{F}}^f_c - \mathcal{F}^d_c \partial_d K^f \right. \right. \right. \right. \right. \\ &\left. \left. \left. \left. + K^d \partial_d \mathcal{F}^f_c \right) - \frac{1}{2} \mathcal{F}^f_d (\delta^{db} \Xi^a - \delta^{da} \Xi^b) \right] \right\} \right\} \right\} + \frac{c}{2} \Xi^a. \end{aligned} \quad (17)$$

One may notice that the two different matrices, $\mathbf{\Sigma}$ and $\mathbf{\Pi}$, appear on the right-hand side of Eq. (15). This is explained by the fact that the vector $\mathbf{\Omega}_{(1)}$ contains odd number of components of the momentum operator, whereas the vector $\mathbf{\Omega}_{(2)}$ contains even number of p_a . Actually, both $\mathbf{\Omega}_{(1)}$ and $\mathbf{\Omega}_{(2)}$ depend only on the combination \mathcal{F}^b_{apb} . However, the velocity operator is proportional to an additional β factor. As a result, the operator $\mathbf{\Omega}_{(1)}$ also acquires an additional β factor [5], when it is rewritten in terms of the velocity operator \mathbf{v} . Note also that only the upper part of β proportional the unit matrix is relevant in the FW representation. Therefore, the appearance of β does not lead to any physical effects.

Equations (15)-(17) yield the following explicit semiclassical equations describing the motion of the average spin (the vector product is defined by $\{\mathbf{A} \times \mathbf{B}\}_a = \epsilon_{abc} A^b B^c$) [12]:

$$\frac{d\mathbf{s}}{dt} = \mathbf{\Omega} \times \mathbf{s} = (\mathbf{\Omega}_{(1)} + \mathbf{\Omega}_{(2)}) \times \mathbf{s}, \quad (18)$$

$$\Omega_{(1)}^a = \frac{c^2}{\epsilon'} \mathcal{F}^d_c p_d \left(\frac{1}{2} \Upsilon \delta^{ac} - \epsilon^{aef} V \mathcal{C}_{ef}^c + \frac{\epsilon'}{\epsilon' + mc^2 V} \epsilon^{abc} W^e_{\hat{b}} \partial_e V \right), \quad (19)$$

$$\Omega_{(2)}^a = \frac{c}{2} \Xi^a - \frac{c^3}{\epsilon'(\epsilon' + mc^2 V)} \epsilon^{abc} Q_{(bd)} \delta^{dn} \mathcal{F}^k_n p_k \mathcal{F}^l_c p_l. \quad (20)$$

Here, in the semiclassical limit,

$$\epsilon' = \sqrt{m^2 c^4 V^2 + c^2 \delta^{cd} \mathcal{F}^a_c \mathcal{F}^b_d p_a p_b}. \quad (21)$$

We can substitute the results obtained into the FW Hamiltonian (11) and recast the latter in a compact and transparent form:

$$\mathcal{H}_{FW} = \beta \epsilon' + \frac{c}{2} (\mathbf{K} \cdot \mathbf{p} + \mathbf{p} \cdot \mathbf{K}) + \frac{\hbar}{2} (\mathbf{\Pi} \cdot \mathbf{\Omega}_{(1)} + \mathbf{\Sigma} \cdot \mathbf{\Omega}_{(2)}). \quad (22)$$

We can use Eq. (22) to derive the velocity operator in the semiclassical approximation:

$$\frac{dx^a}{dt} = \frac{i}{\hbar} [\mathcal{H}_{FW}, x^a] = \beta \frac{\partial \epsilon'}{\partial p_a} + c K^a = \beta \frac{c^2}{\epsilon'} \mathcal{F}^a_b \delta^{bc} \mathcal{F}^d_c p_d + c K^a. \quad (23)$$

The explicit expression for the force operator reads [12]

$$F_{\hat{a}} = \frac{1}{2} \left\{ \dot{W}^b_{\hat{a}}, p_b \right\} + \frac{1}{4} \left\{ p_b, \left\{ \frac{\partial \mathcal{H}_{FW}}{\partial p_c}, \partial_c W^b_{\hat{a}} \right\} \right\} - \frac{1}{2} \left\{ W^b_{\hat{a}}, \partial_b \mathcal{H}_{FW} \right\}, \quad (24)$$

$$\frac{\partial \mathcal{H}_{FW}}{\partial p_c} = \beta \frac{c^2}{4} \delta^{ad} \left\{ \frac{1}{\epsilon'}, \{p_b, \mathcal{F}^b_a \mathcal{F}^c_d\} \right\} + c K^c + \frac{\hbar}{2} \mathfrak{T}^c, \quad (25)$$

where we introduced the following compact notation

$$\mathfrak{T}^c = \frac{\partial \mathcal{U}}{\partial p_c}, \quad \mathcal{U} := \mathbf{\Pi} \cdot \mathbf{\Omega}_{(1)} + \mathbf{\Sigma} \cdot \mathbf{\Omega}_{(2)}. \quad (26)$$

Corrections due to the noncommutativity of operators are of order of \hbar^2 and can be neglected in (24). Let us split the total force operator into the terms of the zeroth and first orders in the Planck constant:

$$F_{\hat{a}} = F_{\hat{a}}^{(0)} + F_{\hat{a}}^{(1)}. \quad (27)$$

The zeroth order terms read as follows

$$F_{\hat{a}}^{(0)} = \frac{1}{2} \left\{ \dot{W}_{\hat{a}}, p_b \right\} - \frac{1}{2} \left\{ W_{\hat{a}}, \partial_b \left[\beta \epsilon' + \frac{c}{2} (K^a p_a + p_a K^a) \right] \right\} + \frac{1}{4} \left\{ p_b, \left\{ \left(\beta \frac{c^2}{4} \delta^{ad} \left\{ \frac{1}{\epsilon'}, \{p_b, \mathcal{F}^b{}_a \mathcal{F}^c{}_d\} \right\} + c K^c \right), \partial_c W_{\hat{a}} \right\} \right\}. \quad (28)$$

These terms describe the influence of the gravitational field on the particle without taking into account its internal structure. The first term in Eq. (28) is important for the motion of the particle in nonstationary spacetimes, for example, in cosmological context. The next term describes the Newtonian force, the related relativistic corrections, and the Coriolis-like force proportional to \mathbf{K} . The last term also contributes to the relativistic corrections to the force acting in static spacetimes that arise in addition to the velocity-independent Newtonian force. All the terms of the first order in \hbar collectively represent the quantum-mechanical counterpart of the Mathisson force similar to the Stern-Gerlach force in electrodynamics. This force is given by, recall the notation (26),

$$F_{\hat{a}}^{(1)} = \frac{\hbar}{8} \left\{ p_b, \left\{ \mathfrak{T}^c, \partial_c W_{\hat{a}} \right\} \right\} - \frac{\hbar}{4} \left\{ W_{\hat{a}}, \partial_b \mathcal{U} \right\}. \quad (29)$$

Equations (28) and (29) reproduce all known quantum-mechanical results [2, 3, 5, 6].

4 Classical spinning particles

It is important to compare the classical and quantum Hamiltonians of a spinning particle. It was proven in Ref. [12] that the classical Hamiltonian has the following structure:

$$\mathcal{H}_{class} = \sqrt{m^2 c^4 V^2 + c^2 \delta^{cd} \mathcal{F}^a{}_c \mathcal{F}^b{}_d \pi_a \pi_b} + c \mathbf{K} \cdot \boldsymbol{\pi} + q \Phi + \mathbf{s} \cdot \mathbf{\Omega}. \quad (30)$$

In the general case, $\mathbf{\Omega}$ includes both electromagnetic and gravitational contributions.

The obvious similarity of quantum (22) and classical (30) Hamiltonians is another demonstration of complete agreement of the quantum-mechanical and classical equations of motion. The consistency is also confirmed by the computation of the force. Switching off the electromagnetic field, we find the classical equation for the force:

$$F_{\hat{a}}^{class} = p_b \dot{W}_{\hat{a}}^b + p_b \frac{\partial \mathcal{H}_{class}}{\partial p_c} \partial_c W_{\hat{a}}^b - W_{\hat{a}}^b \partial_b \mathcal{H}_{class}. \quad (31)$$

Rewriting Eq. (24) in terms of the spin operator, $\mathbf{s} = \hbar \mathbf{\Sigma} / 2$, shows its consistency with Eq. (31).

5 Conclusions

In this paper, we consider the case of an arbitrary spacetime metric and generalize our results obtained for the weak fields and for the special static and stationary field configurations [2–6, 12]. The convenient parametrization in terms of the functions $V(t, x^c)$, $K^a(t, x^c)$, and $W^{\hat{a}}_b(t, x^c)$ provides a unified description of all possible inertial and gravitational fields. We derive the Hermitian Dirac Hamiltonian (9), apply the FW transformation [1] and construct the FW Hamiltonian (11) for an *arbitrary Riemannian spacetime geometry*. Our results further confirm the earlier conclusions [5, 6] and demonstrate that the classical spin dynamics is fully consistent with the semiclassical one. Finally, the complete consistency of the quantum-mechanical and classical descriptions of spinning particles is also established using the Hamiltonian approach.

The work was supported in part by the JINR, the Belarusian Republican Foundation for Fundamental Research (Grant No. Φ 12D-002), and the Russian Foundation for Basic Research (Grants No. 11-02-01538, 11-01-12103).

References

- [1] A.J. Silenko, Phys. Rev. A **77** (2008), 012116.
- [2] A.J. Silenko and O.V. Teryaev, Phys. Rev. D **71** (2005), 064016.
- [3] A.J. Silenko and O.V. Teryaev, Phys. Rev. D **76** (2007), 061101(R).
- [4] A.J. Silenko, Acta Phys. Polon. B Proc. Suppl. **1** (2008), 87.
- [5] Yu.N. Obukhov, A.J. Silenko, and O.V. Teryaev, Phys. Rev. D **80** (2009), 064044.
- [6] Yu.N. Obukhov, A.J. Silenko, and O.V. Teryaev, Phys. Rev. D **84** (2011), 024025.
- [7] B.S. DeWitt, Phys. Rev. **160** (1967), 1113.
- [8] J. Schwinger, Phys. Rev. **130** (1963), 800; 1253.
- [9] P.A.M. Dirac, Interacting gravitational and spinor fields, in: *Recent developments in general relativity. Festschrift for Infeld* (Pergamon Press, Oxford and PWN, Warsaw, 1962) pp. 191-200.
- [10] D.W. Sciama, On the analogy between charge and spin in general relativity, in: *Recent Developments in General Relativity. Festschrift for Infeld*. Pergamon Press, Oxford; PWN, Warsaw (1962), pp. 415-439.
- [11] T.W.B. Kibble, J. Math. Phys. **2** (1961), 212.
- [12] Yu.N. Obukhov, A.J. Silenko, and O.V. Teryaev, Phys. Rev. D **88** (2013), 084014.

STATISTICAL DESCRIPTION OF THE FLAVOR STRUCTURE OF THE NUCLEON SEA

Jacques Soffer

Department of Physics, Temple University Philadelphia, Pennsylvania 19122-6082, USA
E-mail: jacques.soffer@gmail.com

Claude Bourrely

*Aix-Marseille Université, Département de Physique, Faculté des Sciences de Luminy,
F-13288 Marseille, Cedex 09, France*
E-mail: claude.bourrely@univ-amu.fr

Franco Buccella

INFN, Sezione di Napoli, Via Cintia, Napoli, I-80126, Italy
E-mail: buccella@na.infn.it

Abstract

The theoretical foundations of the quantum statistical approach to parton distributions are reviewed together with the phenomenological motivations from a few specific features of Deep Inelastic Scattering data. The chiral properties of QCD lead to strong relations between quarks and antiquarks distributions and automatically account for the flavor and helicity symmetry breaking of the sea. We are able to describe both unpolarized and polarized structure functions in terms of a small number of parameters. The extension to include their transverse momentum dependence will be also briefly considered.

1 Basic review on the statistical approach

Let us first recall some of the basic components for building up the parton distribution functions (PDF) in the statistical approach, as oppose to the standard polynomial type parametrizations, based on Regge theory at low x and counting rules at large x . The fermion distributions are given by the sum of two terms [1], the first one, a quasi Fermi-Dirac function and the second one, a flavor and helicity independent diffractive contribution equal for light quarks. So we have, at the input energy scale Q_0^2 ,

$$xq^h(x, Q_0^2) = \frac{AX_{0q}^h x^b}{\exp[(x - X_{0q}^h)/\bar{x}] + 1} + \frac{\tilde{A}x^{\bar{b}}}{\exp(x/\bar{x}) + 1} , \quad (1)$$

$$x\bar{q}^h(x, Q_0^2) = \frac{\bar{A}(X_{0q}^{-h})^{-1}x^{\bar{b}}}{\exp[(x + X_{0q}^{-h})/\bar{x}] + 1} + \frac{\tilde{A}x^{\bar{b}}}{\exp(x/\bar{x}) + 1} . \quad (2)$$

It is important to remark that x is indeed the natural variable, since all sum we will use are expressed in terms of x . Notice the change of sign of the potentials and helicity for the antiquarks. The parameter \bar{x} plays the role of a *universal temperature* and X_{0q}^{\pm} are the two *thermodynamical potentials* of the quark q , with helicity $h = \pm$. We would like to stress that the diffractive contribution occurs only in the unpolarized distributions

$q(x) = q_+(x) + q_-(x)$ and it is absent in the valence $q_v(x) = q(x) - \bar{q}(x)$ and in the helicity distributions $\Delta q(x) = q_+(x) - q_-(x)$ (similarly for antiquarks). The *nine* free parameters ¹ to describe the light quark sector (u and d), namely X_u^\pm , X_d^\pm , b , \bar{b} , \tilde{b} , \tilde{A} and \bar{x} in the above expressions, were determined at the input scale from the comparison with a selected set of very precise unpolarized and polarized Deep Inelastic Scattering (DIS) data [1]. The additional factors X_q^\pm and $(X_q^\pm)^{-1}$ come from the transverse momentum dependence (TMD), as explained in Refs. [2, 3] (See below). For the gluons we consider the black-body inspired expression

$$xG(x, Q_0^2) = \frac{A_G x^{b_G}}{\exp(x/\bar{x}) - 1}, \quad (3)$$

a quasi Bose-Einstein function, with b_G , the only free parameter, since A_G is determined by the momentum sum rule. We also assume a similar expression for the polarized gluon distribution $x\Delta G(x, Q_0^2) = \tilde{A}_G x^{\tilde{b}_G} / [\exp(x/\bar{x}) - 1]$. For the strange quark distributions, the simple choice made in Ref. [1] was greatly improved in Ref. [4]. Our procedure allows to construct simultaneously the unpolarized quark distributions and the helicity distributions. This is worth noting because it is a very unique situation. Following our first paper in 2002, new tests against experimental (unpolarized and polarized) data turned out to be very satisfactory, in particular in hadronic collisions, as reported in Refs. [5, 6].

2 Some selected results

Let us first come back to the important question of the flavor asymmetry of the light antiquarks. Our determination of $\bar{u}(x, Q^2)$ and $\bar{d}(x, Q^2)$ is perfectly consistent with the violation of the Gottfried sum rule, for which we found $I_G = 0.2493$ for $Q^2 = 4\text{GeV}^2$. Nevertheless there remains an open problem with the x distribution of the ratio \bar{d}/\bar{u} for $x \geq 0.2$. According to the Pauli principle this ratio should be above 1 for any value of x . However, the E866/NuSea Collaboration [7] has released the final results corresponding to the analysis of their full data set of Drell-Yan yields from an 800 GeV/c proton beam on hydrogen and deuterium targets and they obtain the ratio, for $Q^2 = 54\text{GeV}^2$, \bar{d}/\bar{u} shown in Fig. 1 (Left). Although the errors are rather large in the high x region, the statistical approach disagrees with the trend of the data. Clearly by increasing the number of free parameters, it is possible to build up a scenario which leads to the drop off of this ratio for $x \geq 0.2$. For example this was achieved in Ref. [8], as shown by the dashed curve in Fig. 1 (Left). There is no such freedom in the statistical approach, since quark and antiquark distributions are strongly related. One way to clarify the situation is, to improve the statistical accuracy on the Drell-Yan yields which seems now possible, since there are new opportunities for extending the measurement of the $\bar{d}(x)/\bar{u}(x)$ ratio to larger x up to $x = 0.7$, with the ongoing E906 experiment at the 120 GeV Main Injector at FNAL [9] and a proposed experiment at the new 30-50 GeV proton accelerator at J-PARC [10].

Another way is to call for the measurement of a different observable sensitive to $\bar{u}(x)$ and $\bar{d}(x)$. One possibility is the ratio of the unpolarized cross sections for the production of W^+ and W^- in pp collisions, which will directly probe the behavior of the $\bar{d}(x)/\bar{u}(x)$ ratio. Let us recall that if we denote $R_W(y) = (d\sigma^{W^+}/dy)/(d\sigma^{W^-}/dy)$, where y is the W

¹ A and \bar{A} are fixed by the following normalization conditions $u - \bar{u} = 2$, $d - \bar{d} = 1$.

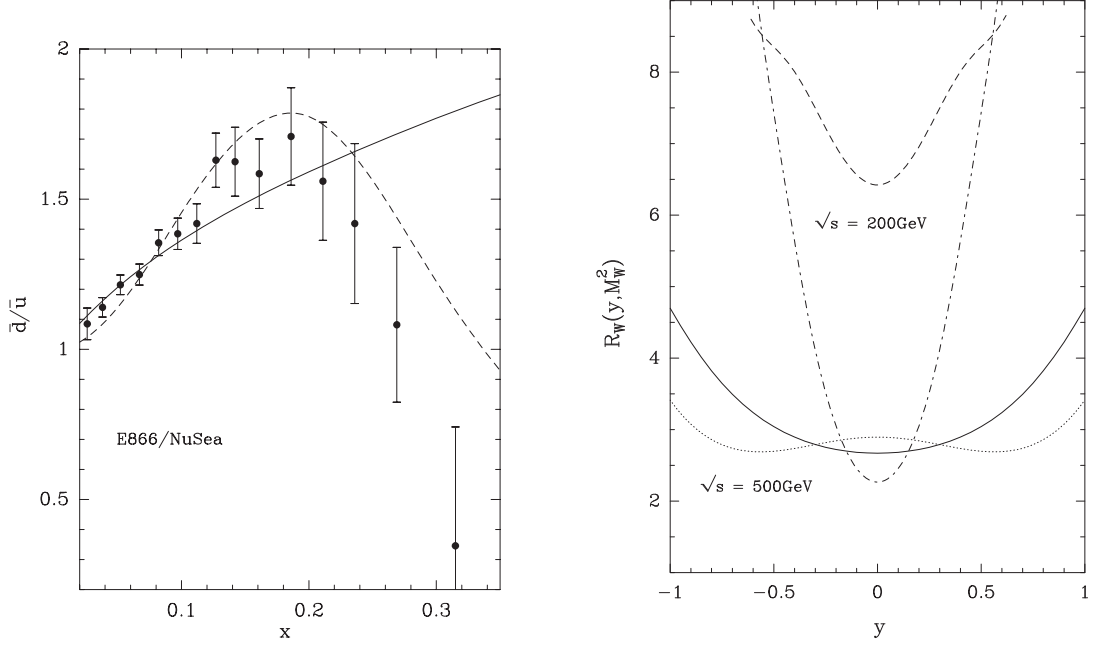


Figure 1: *Left*: Comparison of the data on $(\bar{d}/\bar{u})(x, Q^2)$ from E866/NuSea at $Q^2 = 54\text{GeV}^2$ [7], with the prediction of the statistical model (solid curve) and the set 1 of the parametrization proposed in Ref. [8] (dashed curve). *Right*: Theoretical calculations for the ratio $R_W(y, M_W^2)$ versus the W rapidity, at two RHIC-BNL energies. Solid curve ($\sqrt{s} = 500\text{GeV}$) and dashed curve ($\sqrt{s} = 200\text{GeV}$) are the statistical model predictions. Dotted curve ($\sqrt{s} = 500\text{GeV}$) and dashed-dotted curve ($\sqrt{s} = 200\text{GeV}$) are the predictions obtained using the $\bar{d}(x)/\bar{u}(x)$ ratio from Ref. [8].

rapidity, we have [11] at the lowest order

$$R_W(y, M_W^2) = \frac{u(x_a, M_W^2)\bar{d}(x_b, M_W^2) + \bar{d}(x_a, M_W^2)u(x_b, M_W^2)}{d(x_a, M_W^2)\bar{u}(x_b, M_W^2) + \bar{u}(x_a, M_W^2)d(x_b, M_W^2)}, \quad (4)$$

where $x_a = \sqrt{\tau}e^y$, $x_b = \sqrt{\tau}e^{-y}$ and $\tau = M_W^2/s$. This ratio R_W , such that $R_W(y) = R_W(-y)$, is accessible with a good precision at RHIC-BNL [12] and at $\sqrt{s} = 500\text{GeV}$ for $y = 0$, we have $x_a = x_b = 0.16$. So $R_W(0, M_W^2)$ probes the $\bar{d}(x)/\bar{u}(x)$ ratio at $x = 0.16$. Much above this x value, the accuracy of Ref. [7] becomes poor. In Fig. 1 (Right) we compare the results for R_W using two different calculations. In both cases we take the u and d quark distributions obtained from the present analysis, but first we use the \bar{u} and \bar{d} distributions of the statistical approach (solid curve in Fig. 1 (Right)) and second the \bar{u} and \bar{d} from Ref. [8] (dashed curve in Fig. 1 (Right)). For $y = \pm 1$, which corresponds to x_a or x_b near 0.43, one sees that the predictions are very different. Notice that the energy scale M_W^2 is much higher than in the E866/NuSea data, so one has to take into account the Q^2 evolution. At $\sqrt{s} = 200\text{GeV}$ for $y = 0$, we have $x_a = x_b = 0.40$ and, although the W^\pm yield is smaller at this energy, the effect on $R_W(0, M_W^2)$ is strongly enhanced, as seen in Fig. 1 (Right). This is an excellent test, which needs to be revisited and should be done in the near future. The subject of the strange quark distributions is also very important and challenging, in particular because the HERMES Collaboration has presented recently a new data set at variance with the previous one. For lack of space we are unable to cover it here.

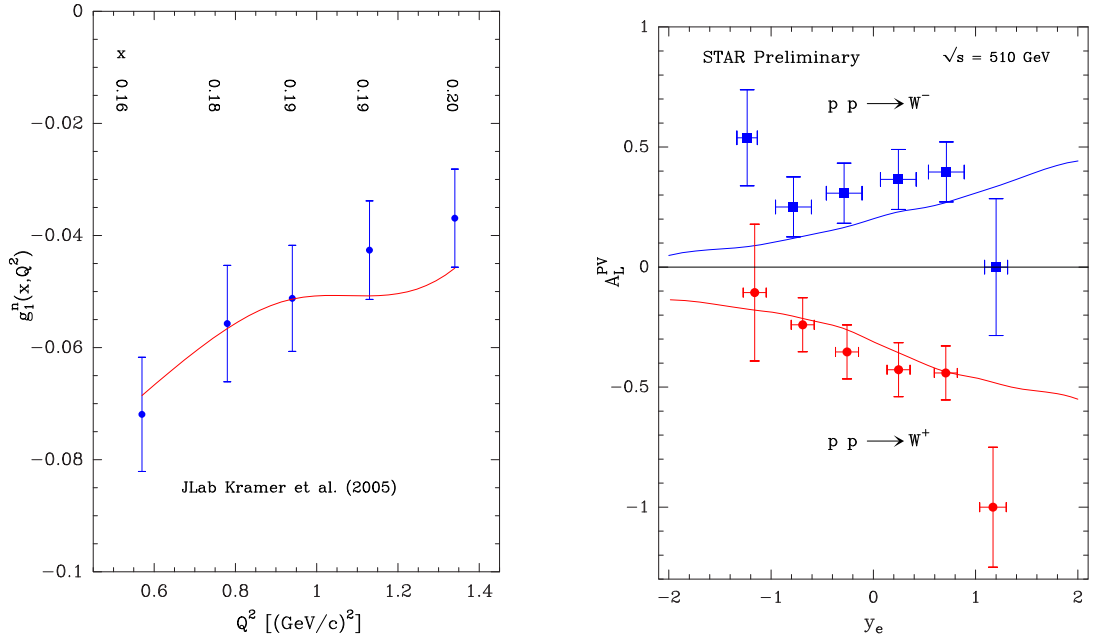


Figure 2: *Left:* Comparison of the $g_1^n(x)$ data at low Q^2 from [13] with the prediction of the statistical model. *Right:* Predicted parity-violating asymmetries A_L^{PV} for charged-lepton production at BNL-RHIC, through production and decay of W^\pm bosons. y_e is the the charged-lepton rapidity and the data points are from Ref. [15] (Taken from [14]).

We now turn to two specific examples of spin-dependent observables to illustrate the predictive power of our approach for helicity quark and antiquark distributions. First, let us consider the neutron structure function $g_1^n(x, Q^2)$ measured in polarized DIS with a neutron target. Although it has been measured extensively by different collaborations, some accurate data obtained at JLab, in the low Q^2 region, have been largely ignored so far [13]. In Fig. 2 (Left) we compare our predictions with these data, dominated by Δd and $\Delta \bar{d}$ which are negative, and one observes a remarkable agreement. Another example is the helicity asymmetry in the charged-lepton production through production and decay of W^\pm bosons. As explained in Ref. [14], the W^- asymmetry is very sensitive to the sign and magnitude of $\Delta \bar{u}$ and the successful results of the statistical approach are displayed in Fig. 2 (Right).

3 Transverse momentum dependence of the parton distributions

The parton distributions $p_i(x, k_T^2)$ of momentum k_T , must obey the momentum sum rule $\sum_i \int_0^1 dx \int k_T^2 p_i(x, k_T^2) dk_T^2 = 1$. In addition it must also obey the transverse energy sum rule $\sum_i \int_0^1 dx \int p_i(x, k_T^2) \frac{k_T^2}{x} dk_T^2 = M^2$. From the general method of statistical thermodynamics we are led to put $p_i(x, k_T^2)$ in correspondance with the following expression $\exp(\frac{-x}{\bar{x}} + \frac{-k_T^2}{x\mu^2})$, where μ^2 is a parameter interpreted as the transverse temperature. So we have now the main elements for the extension to the TMD of the statistical PDF. We obtain in a natural

way the Gaussian shape with **no** x, k_T factorization, because the quantum statistical distributions for quarks and antiquarks read in this case

$$xq^h(x, k_T^2) = \frac{F(x)}{\exp(x - X_{0q}^h)/\bar{x} + 1} \frac{1}{\exp(k_T^2/x\mu^2 - Y_{0q}^h) + 1}, \quad (5)$$

$$x\bar{q}^h(x, k_T^2) = \frac{\bar{F}(x)}{\exp(x + X_{0q}^{-h})/\bar{x} + 1} \frac{1}{\exp(k_T^2/x\mu^2 + Y_{0q}^{-h}) + 1}. \quad (6)$$

Here $F(x) = \frac{Ax^{b-1}X_{0q}^h}{\ln(1+\exp Y_{0q}^h)\mu^2} = \frac{Ax^{b-1}}{k\mu^2}$, where Y_{0q}^h are the thermodynamical potentials chosen such that $\ln(1 + \exp Y_{0q}^h) = kX_{0q}^h$, in order to recover the factors X_{0q}^h and $(X_{0q}^h)^{-1}$, introduced earlier. Similarly for \bar{q} we have $\bar{F}(x) = \bar{A}x^{2b-1}/k\mu^2$. The determination of the 4 potentials Y_{0q}^h can be achieved with the choice $k = 3.05$. Finally μ^2 will be obtained from the transverse energy sum rule and one finds $\mu^2 = 0.198\text{GeV}^2$. Detailed results are shown in Refs. [2, 3].

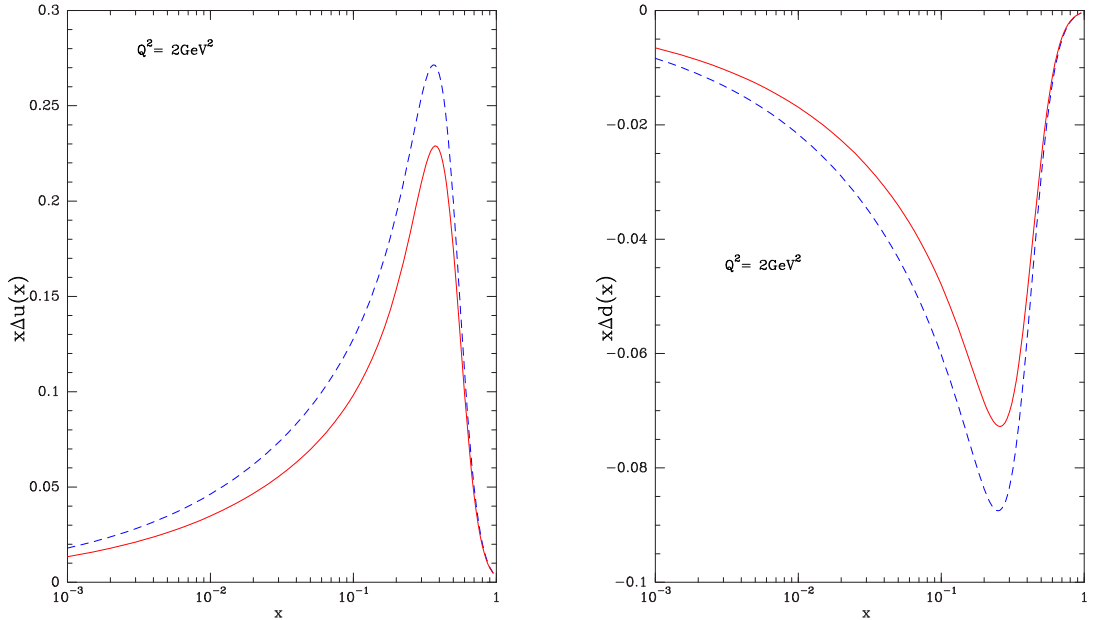


Figure 3: The u and d quark helicity distributions versus x : $x\Delta q(x)$ (dashed line) and $x\Delta q^{MW}(x)$ (solid line). (Taken from Ref. [3]).

Before closing we would like to mention an important point. So far in all our quark or antiquark TMD distributions, the label “ h ” stands for the helicity along the longitudinal momentum and not along the direction of the momentum, as normally defined for a genuine helicity. The basic effect of a transverse momentum $k_T \neq 0$ is the Melosh-Wigner rotation, which mixes the components q^\pm in the following way $q^{+MW} = \cos^2\theta q^+ + \sin^2\theta q^-$ and $q^{-MW} = \cos^2\theta q^- + \sin^2\theta q^+$, where for massless partons, $\theta = \arctan(\frac{k_T}{p_0 + p_z})$, with $p_0 = \sqrt{k_T^2 + p_z^2}$. It vanishes when either $k_T = 0$ or p_z , the quark longitudinal momentum, goes to infinity. Consequently $q = q^+ + q^-$ remains unchanged since $q^{MW} = q$, whereas we have $\Delta q^{MW} = (\cos^2\theta - \sin^2\theta)\Delta q$.

For illustration we display in Fig. 3, $x\Delta q(x)$ and $x\Delta q^{MW}(x)$ for $Q^2 = 2\text{GeV}^2$, which shows the effect of the Melosh-Wigner rotation, mainly in the low x region.

A new set of PDF is constructed in the framework of a statistical approach of the nucleon. All unpolarized and polarized distributions depend upon a small number of free parameters, with some physical meaning. New tests against experimental (unpolarized and polarized) data on DIS, semi-inclusive DIS and hadronic processes are very satisfactory. It has a good predictive power but some special features remain to be verified, specially in the high x region. The extension to TMD has been achieved and must be checked more accurately together with Melosh-Wigner effects in the low x region, for small Q^2 .

Acknowledgments

JS is grateful to the organizers of DSPIN-13 for their warm hospitality at JINR and for their invitation to present this talk. Special thanks go to Prof. A.V. Efremov for providing a full financial support and for making, once more, this meeting so successful.

References

- [1] C. Bourrely, F. Buccella and J. Soffer, Eur. Phys. J. **C23**, (2002) 487.
- [2] C. Bourrely, F. Buccella and J. Soffer, Phys. Rev. **D83**, (2011) 074008.
- [3] C. Bourrely, F. Buccella and J. Soffer, Int. J. of Modern Physics **A28** (2013) 1350026.
- [4] C. Bourrely, F. Buccella and J. Soffer, Phys. Lett. **B648**, (2007) 39.
- [5] C. Bourrely, F. Buccella and J. Soffer, Mod. Phys. Lett. **A18**, (2003) 771.
- [6] C. Bourrely, F. Buccella and J. Soffer, Eur. Phys. J. **C41**, (2005) 327.
- [7] R.S. Towell, *et al.*, Phys. Rev. **D64**, (2001) 052002.
- [8] A. Daleo, C.A. García Canal, G.A. Navarro and R. Sassot, Int. J. of Modern Physics **A17** (2002) 269.
- [9] D.F. Geesaman, *et al.* [E906 Collaboration], FNAL Proposal E906, April 1, 2001.
- [10] J.C. Peng, *et al.*, hep-ph/0007341.
- [11] C. Bourrely and J. Soffer, Nucl. Phys. B **423**, (1994) 329.
- [12] G. Bunce, N. Saito, J. Soffer and W. Vogelsang, Ann. Rev. Nucl. Part. Sci. **50**, (2000) 525.
- [13] K. Kramer, *et al.*, Phys. Rev. Lett. **95**, (2005) 142005.
- [14] C. Bourrely, F. Buccella and J. Soffer, Phys. Lett. **B726**, (2013) 296.
- [15] B. Surrow, arXiv:1310.7974 [hep-ex].

TRUNCATED MOMENTS OF PARTON DENSITIES IN APPLICATIONS TO SPIN PHYSICS

S.V. Mikhailov¹, D. Strózik-Kotlorz^{2†} and O.V. Teryaev¹

(1) *JINR, Dubna, Russia*

(2) *Division of Physics, Opole University of Technology*

† *E-mail: dorota@theor.jinr.ru*

Abstract

We review our main results on the truncated Mellin moments approach and present a novel generalization of DGLAP equations. We also demonstrate applications to the Bjorken sum rule analysis.

Study of polarized processes provides knowledge about the spin structure of the nucleon. Recent experimental data and NLO analysis suggest that valence quarks carry the expected fraction of the nucleon spin, but the main questions are still open: how the nucleon spin is distributed among its constituents: quarks (particularly sea quarks with negative helicity) and gluons and how the dynamics of these constituent interactions depends on spin. New experimental data in the resonance region from Jefferson Lab together with complementary data from HERMES, COMPASS and RHIC, are a crucial step towards better understanding of not only the flavor decomposition and gluon contributions to the nucleon spin but also the quark-hadron duality. The main goal of present polarized experiments is to determine the nucleon spin structure functions $g_1(x, Q^2)$, $g_2(x, Q^2)$ and their moments which are essential in testing QCD sum rules. The theoretical approach usually used in the description of these experimental results are the QCD evolution equations for the parton densities which change with Q^2 according to the well-known DGLAP equations [1–4]. This standard DGLAP approach operates on the parton densities q ; hence their moments, which are, e.g., the contributions to the proton spin and other sum rules, can be obtained by the integration of the parton densities q over Bjorken- x .

One can also directly study the Q^2 evolution of the Mellin moments of the parton densities. The moments originate from OPE - the basic formalism of quantum field theory and provide a natural framework in QCD analysis. The DGLAP-type diagonal integro-differential evolution equations for the single and double truncated moments of the parton distribution functions were derived in [5], [6] and [7] (previously, there were known the non-diagonal differential evolution equations in which the n th truncated moment coupled to all higher ones [8–11]). Evolution equations for double truncated moments and their application to study the quark-hadron duality were also discussed in [12].

The main finding of the truncated Mellin moments (TMM) approach is that the n th moment of the parton distribution obeys also the DGLAP equation but with a rescaled splitting function $P'(z) = z^n P(z)$ [5]. This approach allows one to restrict the analysis to the experimentally available Bjorken- x region. Here, we present a novel generalization of DGLAP equations and applications to the Bjorken sum rule analysis for the low scale Q^2 based on the TMM approach.

1 Generalization of DGLAP equations

The strong interactions between quarks and gluons cause changes in the parton densities. For medium and large x , the Q^2 evolution of the parton distributions is described by the standard DGLAP equations [1–4]. In the DGLAP approach, the main role is played by the PDFs while in our TMM approach we study directly the Q^2 evolution of the truncated moments of the PDFs. In [5], we found that the single truncated moments of the parton distributions $q(x, Q^2)$, defined as

$$q_n(x_0, Q^2) = \int_{x_0}^1 dx x^{n-1} q(x, Q^2), \quad (1)$$

obey also the DGLAP-like equation

$$\frac{dq_n(x_0, Q^2)}{d \ln Q^2} = \frac{\alpha_s(Q^2)}{2\pi} (P' \otimes q_n)(x_0, Q^2). \quad (2)$$

A role of the splitting function is played here by $P'(n, y)$:

$$P'(n, y) = y^n P(y). \quad (3)$$

Double truncated moments

$$q_n(x_{min}, x_{max}, Q^2) = \int_{x_{min}}^{x_{max}} dx x^{n-1} q(x, Q^2), \quad (4)$$

which are a subtraction of two single truncated ones also satisfy the DGLAP-type evolution Eq. (2)-(3) [6, 7, 12]. In higher order analysis Wilson coefficients rescale in the same way as the splitting functions:

$$C'_i(n, x) = x^n C_i(x). \quad (5)$$

Here we present a generalization of the above results, obtained for multi integration of the original function. Namely, if $f(x, Q^2)$ is a solution of the nonsinglet DGLAP equation with the kernel $P(y)$:

$$Q^2 \frac{d}{dQ^2} f(z, Q^2) \equiv \dot{f}(z) = P * f(z) \equiv \int_0^1 P(y) f(x, Q^2) \delta(z - x \cdot y) dy dx, \quad (6)$$

then the multi-integrated function $f_k(z; \{n\}_k)$

$$\begin{aligned} f_k(z; \{n\}_k) &\equiv f_k(z; n_1, n_2, \dots, n_k) \\ &= \int_z^1 z_k^{n_k-1} dz_k \int_{z_k}^1 z_{k-1}^{n_{k-1}-1} dz_{k-1} \dots \int_{z_2}^1 z_1^{n_1-1} f(z_1, Q^2) dz_1, \end{aligned} \quad (7)$$

which is a generalization of the truncated moments is also the solution of DGLAP equation

$$\dot{f}_k(z; \{n\}_k) = \mathcal{P}_k * f_k(z; \{n\}_k) \equiv \int_0^1 \mathcal{P}_k(y) f_k(x; \{n\}_k) \delta(z - x \cdot y) dy dx \quad (8)$$

with the kernel

$$\mathcal{P}_{\mathbf{k}}(y) = P(y) \cdot y^{n_1+n_2+\dots+n_k}. \quad (9)$$

The general solution (7) is the source of various partial solutions. E.g. from (8,9) at $k = 1$ follows

$$\dot{f}_1(z; n_1) = \int_0^1 P(y) y^{n_1} f_1(x; n_1) \delta(z - x \cdot y) dx dy, \quad (10)$$

which is simply the known equation (2). If one puts $z = 0$ in (10) it reduces to

$$\dot{f}_1(0; n_1) = \left(\int_0^1 P(y) y^{n_1-1} dy \right) \cdot f_1(0; n_1) \equiv -\gamma(n_1) \cdot f_1(0; n_1), \quad (11)$$

that is the renormalization group equation for the standard untruncated moments $f_1(0; n_1)$.

Based on Eq.(7,8,9) different interesting partial solutions of DGLAP can be constructed and applied to analysis of the experimental data in different restricted x -regions, respectively.

2 Analysis of the Bjorken sum rule at low- Q^2

The Bjorken sum rule (BSR) refers to the first moment of nonsinglet part of the structure function $g_1(x, Q^2)$

$$\Gamma_1^{p-n}(Q^2) = \int_0^1 [g_1^p(x, Q^2) - g_1^n(x, Q^2)] dx \quad (12)$$

and must be hold as a rigorous prediction of QCD in the limit of the infinite momentum transfer $Q^2 \rightarrow \infty$. Usually, the Q^2 dependence of BSR is represented in the form

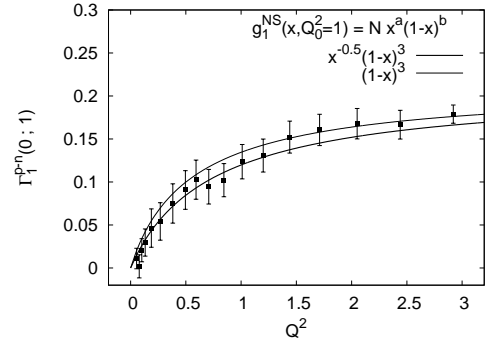


Figure 1: Theoretical LO predictions for $\Gamma_1^{p-n}(Q^2)$, incorporating 'shift' (15). Comparison with JLab data [13].

$$\Gamma_1^{p-n}(Q^2) = \underbrace{\frac{g_A}{6} \left[1 - \frac{\alpha_s}{\pi} - 3.58 \frac{\alpha_s^2}{\pi^2} - 20.21 \frac{\alpha_s^3}{\pi^3} + \dots \right]}_{\text{leading twist}} + \underbrace{\sum_{i=2}^{\infty} \frac{\mu_{2i}(Q^2)}{Q^{2i-2}}}_{\text{higher twists}}, \quad (13)$$

where $g_A = F + D = 1.267 \pm 0.004$ denotes neutron β -decay constant. The presently available experimental data for g_1 and its moments are restricted in both x and Q^2 ranges so, in fact, experiments provide data for truncated moments and cut contributions to sum rules:

$$\Gamma_1^{p-n}(x_{min}, x_{max}, Q^2) = \int_{x_{min}}^{x_{max}} [g_1^p(x, Q^2) - g_1^n(x, Q^2)] dx. \quad (14)$$

In our analysis we focused on the low Q^2 JLAB data [13], testing a method allowing to apply pQCD evolution equations to the low (nonperturbative) $Q^2 \rightarrow 0$ region. Imposing that the parton distributions at the initial Q^2 scale (which are of the nonperturbative

origin) should be regular functions of x for any Q^2 , we use ‘shift’ in Q^2 variable, including in this way in our analysis the limit $Q^2 \rightarrow 0$. Shift of the Q^2 scale as an IR regulator has been introduced and discussed in many works, see eg. [14]. As both kinematic variables x and Q^2 are not independent, we propose in our approach such shift in Q^2 which implies also shift in Bjorken- x , respectively:

$$Q^2 \longrightarrow Q^2 + M^2; \quad x \longrightarrow \bar{x} = \frac{Q^2 + M^2}{W^2 + Q^2 + M^2} = x \frac{1 + \alpha}{1 + \alpha x}, \quad (15)$$

where $\alpha \equiv M^2/Q^2$.

In Fig.1 we compare our theoretical predictions for $\Gamma_1^{p-n}(Q^2)$ with experimental JLab data [13]. We used ‘shift’ approach (15) and TMM evolution in the limit $x_0 \rightarrow 0$, assuming $M = 1\text{GeV}$. The obtained results show that the scaling of variables Q^2 and x can mimic higher-twists resummation in the low- Q^2 region.

References

- [1] V.N. Gribov and L.N. Lipatov, Sov. J. Nucl. Phys. **15** (1972) 438.
- [2] V.N. Gribov and L.N. Lipatov, Sov. J. Nucl. Phys. **15** (1972) 675.
- [3] Yu.L. Dokshitzer, Sov. Phys. JETP **46** (1977) 641.
- [4] G. Altarelli and G. Parisi, Nucl. Phys. **B126** (1977) 298.
- [5] D. Kotlorz and A. Kotlorz, Phys. Lett. **B644** (2007) 284.
- [6] D. Kotlorz and A. Kotlorz, Acta Phys. Pol. **B40** (2009) 1661.
- [7] D. Kotlorz and A. Kotlorz, Acta Phys. Pol. **B42** (2011) 1231.
- [8] S. Forte and L. Magnea, Phys. Lett. **B448** (1999) 295.
- [9] S. Forte, L. Magnea, A. Piccione and G. Ridolfi, Nucl. Phys. **B594** (2001) 46.
- [10] A. Piccione, Phys. Lett. **B518** (2001) 207.
- [11] S. Forte, J. Latorre and L. Magnea Nucl. Phys. **B643** (2002) 477.
- [12] A. Psaker, W. Melnitchouk, M.E. Christy and C. Keppel, Phys. Rev. **C78** (2008) 025206.
- [13] A. Deur et all, Phys. Rev. **D78** (2008) 032001.
- [14] A. Donnachie and P.V. Landshoff, Z. Phys. **C61** (1994) 139;
 B. Badelek and J. Kwiecinski, Rev. Mod. Phys. **68** (1996) 445;
 B.I. Ermolaev, M. Greco and S.I. Troyan, Riv. Nuovo Cim. **033** (2010) 57;
 D.V. Shirkov, PEPAN Letters, **20** (2013) 1.

UNIQUE HEAVY LEPTON MIXING SIGNATURE IN W^+W^- PAIR PRODUCTION AT LC WITH POLARIZED BEAMS

A.A. Pankov, A.V. Tsytrinov[†]

The A. Salam ICTP Affiliated Centre, Technical University of Gomel, 246746 Gomel, Belarus

[†] *E-mail: tsytrin@rambler.ru*

Abstract

We explore the effects of neutrino and electron mixing with exotic heavy leptons in the W -pair production within E_6 models. We examine the possibility of uniquely distinguishing and identifying such effects of heavy neutral lepton exchange from $Z - Z'$ mixing within the same class of models and also from analogous ones due to competitor models with anomalous trilinear gauge couplings that can lead to very similar experimental signatures at a Linear Collider.

Detailed examination of the process

$$e^+ + e^- \rightarrow W^+ + W^- \quad (1)$$

at the ILC allows to observe a manifestation of New Physics (NP) that may appear beyond the Standard Model (SM). In the SM, the process (1) is described by the amplitudes mediated by photon and Z boson exchange in the s -channel and by neutrino exchange in the t -channel. This reaction is quite sensitive to both the leptonic vertices and the trilinear couplings to W^+W^- of the SM Z and of any new heavy neutral boson or a new heavy lepton that can be exchanged in the s -channel or t -channel, respectively. A popular example in this regard, is represented by E_6 models [1, 2]. Specifically, for the leptons we shall limit ourselves to the case where the considered new fermions are doublets under the gauge symmetry $SU(2)$. We also assume that the new, “exotic” fermions only mix with the standard ones within the same family (the electron and its neutrino being the ones relevant to process (1)), which assures the absence of tree-level generation changing neutral currents. The needed fermion mixing formalism has been introduced, e.g., in [3]. Basically, denoting by ν , e , N and E the mass eigenstates, the neutral current couplings of leptons to Z and Z' can be written, respectively, as

$$g_a^e = g_a^{e^0} c_{1a}^2 + g_a^{E^0} s_{1a}^2; \quad g_a^{e'} = g_a^{e'^0} c_{1a}^2 + g_a^{E'^0} s_{1a}^2, \quad (2)$$

where $f^0 \equiv e^0$, E^0 are gauge-eigenstates, and $a = L, R$. Moreover, in Eq. (2) $c_{1a} = \cos \psi_{1a}$ and $s_{1a} = \sin \psi_{1a}$, with ψ_{1a} the mixing angle between the two charged leptons.

The charged current couplings are given by:

$$\begin{aligned} G_L^\nu &= c_{1L}c_{2L} - 2T_{3L}^E s_{1L}s_{2L}; & G_R^\nu &= -2T_{3R}^E s_{1R}s_{2R}, \\ G_L^N &= -s_{2L}c_{1L} - 2T_{3L}^E c_{2L}s_{1L}; & G_R^N &= -2T_{3R}^E c_{2R}s_{1R}, \end{aligned} \quad (3)$$

and, analogously to (2), $c_{2a} = \cos \psi_{2a}$ and $s_{2a} = \sin \psi_{2a}$ refer to the mixing between the neutral leptons.

In turn, Z - Z' mixing is introduced through the relation

$$\begin{pmatrix} Z_1 \\ Z_2 \end{pmatrix} = \begin{pmatrix} \cos \phi & \sin \phi \\ -\sin \phi & \cos \phi \end{pmatrix} \begin{pmatrix} Z \\ Z' \end{pmatrix}, \quad (4)$$

where Z , Z' are weak-eigenstates, Z_1 , Z_2 are mass-eigenstates and ϕ is the Z - Z' mixing angle.

As a class of models where lepton mixing and Z - Z' mixing can be simultaneously present, we will consider in the sequel the case of E_6 models. In these extended schemes, the fermion couplings to Z are the familiar SM ones:

$$g_a^{f0} = \left(T_{3a}^{f0} - Q_{em,a}^2 s_W^2 \right) g_Z, \quad (5)$$

with $s_W^2 = \sin^2 \theta_W$ and $g_Z = 1/s_W c_W$, and the couplings to Z' are:

$$\begin{aligned} g_L^{e0} &= (3A + B) g_{Z'}; & g_R^{e0} &= (A - B) g_{Z'} \\ g_L^{E0} &= -(2A + 2B) g_{Z'}; & g_R^{E0} &= (-2A + 2B) g_{Z'}. \end{aligned} \quad (6)$$

In Eq. (6): $g_{Z'} = g_Z s_W$, $A = \cos \beta / 2\sqrt{6}$, $B = \sqrt{10} \sin \beta / 12$, with β specifying the orientation of the $U(1)'$ generator in the E_6 group space. The most commonly considered models are Z'_χ , Z'_ψ and $-Z'_\eta$ models, which are specified by $\beta = 0$, $\pi/2$ and $(\pi - \arctan \sqrt{5/3})$, respectively.

Finally, taking Eq. (4) into account, the leptons neutral current couplings to Z_1 and Z_2 are, respectively:

$$g_{1a}^f = g_a^f \cos \phi + g_a^{f'} \sin \phi; \quad g_{2a}^f = -g_a^f \sin \phi + g_a^{f'} \cos \phi. \quad (7)$$

Obviously, the SM case is reobtained when all (fermion and gauge boson) mixing angles are put equal to zero.

Current lower limits on $M_{Z'}$ obtained from dilepton pair production at the LHC with $\sqrt{s} = 8$ TeV and $\mathcal{L}_{int} \approx 20 \text{ fb}^{-1}$ range in the interval $\sim 2.6 - 3.0$ TeV, depending on the particular Z' model being tested. Already these masses are too high for a Z' to be directly seen at the ILC. However, even at such high masses, Z' exchanges can manifest themselves indirectly *via* deviations of cross sections, and in general of the reaction observables, from the SM predictions.

The polarized cross section for the process (1) can be written as [3]

$$\begin{aligned} \frac{d\sigma(P_L^-, P_L^+)}{d\cos\theta} &= \frac{1}{4} \left[(1 + P_L^-) (1 - P_L^+) \frac{d\sigma^{RL}}{d\cos\theta} + (1 - P_L^-) (1 + P_L^+) \frac{d\sigma^{LR}}{d\cos\theta} \right. \\ &\quad \left. + (1 + P_L^-) (1 + P_L^+) \frac{d\sigma^{RR}}{d\cos\theta} + (1 - P_L^-) (1 - P_L^+) \frac{d\sigma^{LL}}{d\cos\theta} \right], \end{aligned} \quad (8)$$

where P_L^- (P_L^+) are degrees of longitudinal polarization of e^- (e^+), θ the scattering angle of the W^- with respect to the e^- direction. The superscript ‘‘RL’’ refers to a right-handed electron and a left-handed positron, and similarly for the other terms. The relevant polarized differential cross sections for $e_a^- e_b^+ \rightarrow W_\alpha^- W_\beta^+$ contained in Eq. (8) can be expressed as [3]

$$\frac{d\sigma_{\alpha\beta}^{ab}}{d\cos\theta} = C \sum_{k=0}^{k=2} F_k^{ab} \mathcal{O}_{k\alpha\beta}, \quad (9)$$

where $C = \pi\alpha_{e.m.}^2\beta_W/2s$, $\beta_W = (1 - 4M_W^2/s)^{1/2}$ the W velocity in the CM frame, and the helicities of the initial e^-e^+ and final W^-W^+ states are labeled as $ab = (RL, LR, LL, RR)$ and $\alpha\beta = (LL, TT, TL)$, respectively. The \mathcal{O}_k are functions of the kinematical variables dependent on energy \sqrt{s} , the scattering angle θ and the W mass, M_W , which characterize the various possibilities for the final W^+W^- polarizations ($TT, LL, TL + LT$ or the sum over all W^+W^- polarization states for unpolarized W 's).

The F_k are combinations of lepton and trilinear gauge boson couplings, g_{WWZ_1} and g_{WWZ_2} , including lepton and Z - Z' mixing as well as propagators of the intermediate states. For instance, for the LR case the first term F_0^{LR} describes the contributions to the cross section caused by neutrino ν and heavy neutral lepton N exchanges in the t -channel while the second one, F_1^{LR} , is responsible for s -channel exchange of the photon γ and the gauge bosons Z_1 and Z_2 . The interference between s - and t -channel amplitudes is contained in the term F_2^{LR} . The RL case is simply obtained by exchanging $L \rightarrow R$.

For the LL and RR cases there is only N -exchange contribution,

$$F_0^{LL} = F_0^{RR} = \frac{1}{16s_W^4} r_N^2 (G_L^{Ne} G_R^{Ne})^2. \quad (10)$$

By ‘‘identification’’ we shall here mean *exclusion* of a certain set of competitive models, including the SM, to a certain confidence level. For this purpose, the double beam polarization asymmetry, defined as

$$A_{\text{double}} = \frac{\sigma(P_1, -P_2) + \sigma(-P_1, P_2) - \sigma(P_1, P_2) - \sigma(-P_1, -P_2)}{\sigma(P_1, -P_2) + \sigma(-P_1, P_2) + \sigma(P_1, P_2) + \sigma(-P_1, -P_2)}, \quad (11)$$

is very useful¹. Here $P_1 = |P_L^-|$, $P_2 = |P_L^+|$, and $\sigma(\pm P_1, \pm P_2)$ denotes the polarized integrated cross section determined within the allowed range of the W^- scattering angle (or $\cos\theta$). From Eqs. (8) and (11) one finds for the A_{double} of the process (1)

$$A_{\text{double}} = P_1 P_2 \frac{(\sigma^{RL} + \sigma^{LR}) - (\sigma^{RR} + \sigma^{LL})}{(\sigma^{RL} + \sigma^{LR}) + (\sigma^{RR} + \sigma^{LL})}. \quad (12)$$

We note that this asymmetry is only available if both initial beams are polarized.

It is important to also note that the SM gives rise only to σ^{LR} and σ^{RL} such that the structure of the integrated cross section has the form

$$\sigma_{\text{SM}} = \frac{1}{4} [(1 + P_L^-) (1 - P_L^+) \sigma_{\text{SM}}^{RL} + (1 - P_L^-) (1 + P_L^+) \sigma_{\text{SM}}^{LR}]. \quad (13)$$

This is also the case for anomalous gauge couplings (AGC), and Z' -boson exchange (including Z - Z' mixing and Z_2 exchange). The corresponding expressions for those cross sections can be obtained from (13) by replacing the specification $\text{SM} \rightarrow \text{AGC}$ and Z' , respectively. Accordingly, the double beam polarization asymmetry has a common form for all those cases:

$$A_{\text{double}}^{\text{SM}} = A_{\text{double}}^{\text{AGC}} = A_{\text{double}}^{Z'} = P_1 P_2 = 0.48, \quad (14)$$

where the numerical value corresponds to the product of the electron and positron degrees of polarization: $P_1 = 0.8$, $P_2 = 0.6$. Eq. (14) demonstrates that $A_{\text{double}}^{\text{SM}}$, $A_{\text{double}}^{\text{AGC}}$ and $A_{\text{double}}^{Z'}$

¹For details of the analysis and original references see [4].

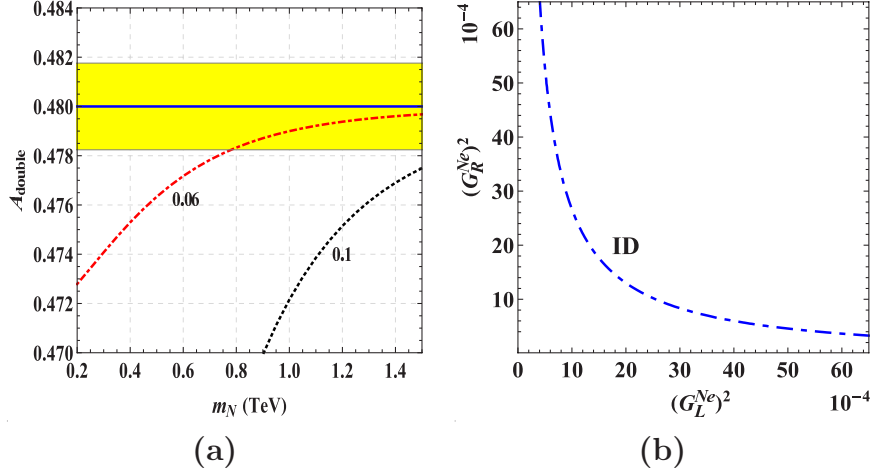


Figure 1: (a) A_{double} vs. neutral heavy lepton mass m_N at the ILC with $\sqrt{s} = 1$ TeV, $\mathcal{L}_{\text{int}} = 1$ ab $^{-1}$. The solid line corresponds to $A_{\text{double}}^{\text{SM}} = A_{\text{double}}^{Z'} = A_{\text{double}}^{\text{AGC}}$. The error bands indicate the expected uncertainty in the SM case at the 1- σ level. (b) Identification reaches at 95% CL obtained from a combined analysis of polarized differential cross sections ($P_L^- = \pm 0.8$, $P_L^+ = \mp 0.6$), and exploiting the A_{double} for $m_N = 0.6$ TeV.

are indistinguishable for any values of NP parameters, AGC or Z' mass and strength of Z - Z' mixing, i.e. $\Delta A_{\text{double}} = A_{\text{double}}^{\text{AGC}} - A_{\text{double}}^{\text{SM}} = A_{\text{double}}^{Z'} - A_{\text{double}}^{\text{SM}} = 0$.

On the contrary, the heavy neutral lepton N -exchange in the t -channel will induce non-vanishing contributions to σ^{LL} and σ^{RR} , and thus force A_{double} to a smaller value, $\Delta A_{\text{double}} = A_{\text{double}}^N - A_{\text{double}}^{\text{SM}} \propto -P_1 P_2 r_N^2 (G_L^{Ne} G_R^{Ne})^2 < 0$ irrespectively of the simultaneous lepton and Z - Z' mixing contributions to σ^{RL} and σ^{LR} . A value of A_{double} below $P_1 P_2$ can provide a signature of heavy neutral lepton N -exchange in the process (1). All those features in the A_{double} behavior are shown in Fig. 1(a), where we consider unpolarized W s. The identification reach (ID) on the plane of heavy lepton coupling ($(G_L^{Ne})^2$, $(G_R^{Ne})^2$) (at 95% C.L.) plotted in Fig. 1(b) is obtained from conventional χ^2 analysis with A_{double} . Note that identification is possible in the region labeled as “ID”. The hyperbola-like limit of the identification reach is due to the appearance of a product of the squared couplings $(G_L^{Ne})^2$ and $(G_R^{Ne})^2$ in the deviation from the SM cross section, given by Eq. (10). It should be stressed that the identification reach is independent of the Z' model assumed, whereas the discovery reach is not.

Acknowledgements. This research has been partially supported by the Abdus Salam ICTP under the TRIL and Associates Scheme and the Belarusian Republican Foundation for Fundamental Research.

References

- [1] P. Langacker, Rev. Mod. Phys. **81** (2009) 1199.
- [2] A. Leike, Phys. Rept. **317** (1999) 143.
- [3] A.A. Babich, A.A. Pankov and N. Paver, Phys. Lett. **B346** (1995) 303.
- [4] G. Moortgat-Pick, P. Osland, A.A. Pankov and A.V. Tsytrinov, Phys. Rev. **D87** (2013) 095017.

SPIN OBSERVABLES OF pd -SCATTERING WITHIN THE GLAUBER MODEL AND TEST OF T-INVARIANCE

A.A. Temerbayev¹, Yu.N. Uzikov^{2†}

(1) *L.N. Gumilyov Eurasian National University, Astana, Kazakhstan*

(2) *Joint Institute for Nuclear Research, Dubna, Russia*

† *E-mail: uzikov@jinr.ru*

Abstract

The total polarized proton-deuteron cross section for the case of vector polarization of the incident proton p_y^p and tensor polarization P_{xz} of the deuteron target provides a null test for the time-invariance violating but P-parity conserving effects. The dedicated experiment is planned by the PAX collaboration at COSY at proton beam energies 135 MeV. We use the Glauber theory for pd elastic scattering in order to calculate total polarized pd cross sections for T-even, P-even interaction and estimate on this basis a part of the background of the planned measurement.

1 Introduction

CP violation established in physics of kaons and B-mesons leads to simultaneous violation of CP and P-invariance. Under assumption of CPT-invariance this implies existence of T-odd P-odd interactions. These effects are parametrized in the standard model by CP violating phase of the Kabibo-Kabayashi-Maskawa matrix. Another source for T-odd P-odd effects is the QCD θ -term, which can be related to electric dipole moments (EDM) of elementary particles and atoms in their ground states.

On the contrary, time-reversal-non-invariant (T-odd) P-parity conserving (P-even) flavor conserving interactions do not arise on the fundamental level within the standard model, although can be generated as weak radiative corrections to the T-odd P-odd interaction. Khriplovich found [1] that the relative strength of this interaction does not exceed $\alpha_T \sim 2 \times 10^{-6}$. Furthermore, as mentioned in Ref. [2], if a T-odd and P-even term arises from T-odd P-odd term, one should have one additional P-odd term in the effective interaction, that leads to effective interaction with a coupling $g \sim M^4 G_F^2 \sin \delta \sim 10^{-10}$, where δ is the CP-violating phase, G_F is the Fermi constant and M is the nucleon mass.

On the other hand, much larger g is not excluded [2] as the low energy limit of some unknown interaction. Existing experimental constraints on the T-odd P-even effects in physics of nuclei are rather weak. So, test of the detailed balance performed for the reactions $^{27}\text{Al}(p, \alpha)^{24}\text{Mg}$ and $^{24}\text{Mg}(\alpha, p)^{27}\text{Al}$ and complemented by numerous statistical analyses of nuclear energy-level fluctuations leads to $\alpha_T < 2 \times 10^{-3}$ [3]. Another type of experiment, i.e. polarized neutron transmission through polarized ^{165}Ho target gives $\alpha_T \leq 7.1 \times 10^{-4}$ (or $\bar{g}_\rho \leq 5.9 \times 10^{-2}$) [4]. Here \bar{g}_ρ is the T-odd P-even coupling constant of the charged ρ -meson with the nucleon introduced in Ref. [5] to classify the T-odd P-even interactions in terms of boson exchanges. Charge symmetry breaking determined as difference in scattering of polarized proton off unpolarized neutron $\vec{p}n$ and polarized

neutrons off unpolarized protons $\bar{n}p$ gives $\alpha_T \leq 8 \times 10^{-5}$ (or $\bar{g}_p < 6.7 \times 10^{-3}$) [5]. One should add that indirect estimation based on existing constraints on EDM gives $\alpha_T \leq 1.1 \times 10^{-5}$ ($\bar{g}_p \leq \times 10^{-3}$) [6].

The goal of the TRIC experiment [7] is the measurement of the total polarized cross section $\tilde{\sigma}$ of the proton-deuteron scattering with vector polarization of the proton p_y^p and tensor polarization of the deuteron P_{xz} (see below Eq. (2)). As was shown in Ref. [8], this observable constitutes the null-test of T-odd P-even effects. The well known statement on non-existence of null experiments [9] that would unambiguously test the time-reversal invariance independently on dynamical assumptions holds for bilinear (in respect of the reaction amplitude F_{fi}) observables only and, therefore, does not include transmission experiments which measure total cross sections, i.e. the linear in F_{fi} observables. Experiment [7] will be done at beam energy 135 MeV. The aim of this experiment is to improve the results of previous measurement [4] on $\bar{n}^{167}\text{Ho}$ scattering by one order of magnitude. In this case, detailed information on the ordinary T-even P-even spin observables at this energy is required in order to determine magnitude of possible false-effects caused by pure strong and Coulomb interaction due to non-ideal conditions of the experiment. So, one has to know angular dependence of the spin-correlation parameters $C_{y,y}$, $C_{xz,y}$ for elastic scattering in forward hemisphere and the total polarized cross sections σ_1 and σ_3 (for definitions see Eq.(2)). However, experimental data on these observables at this energy are rather poor.

In the present work we use the Glauber theory [10] to calculate unpolarized differential cross section and spin observables of the elastic pd scattering and total polarized pd cross sections. The spin-dependent formalism of the pd -elastic scattering is recently developed in Ref. [11]. The formalism includes full spin dependence of elementary pN -amplitudes and S- and D-components of the deuteron wave function. We further develop the formalism to calculate spin-correlation and spin-transfer parameters and account for Coulomb effects. Furthermore, the formalism of Ref. [11] is developed for a non-Madison reference frame and, therefore, cannot be applied straightforwardly to direct comparison with the existing experimental data [12, 13] presented in the Madison-type reference frame. We properly modify the formalism of Ref. [11] to provide comparison with the existing experimental data [12, 13].

2 Results and discussion

T-even P-even interactions lead to the transition amplitude of pd scattering at zero degree [14]

$$e'^*_{\beta} \hat{F}_{\alpha\beta} e_{\alpha} = g_1[\mathbf{e} \mathbf{e}'^* - (\hat{\mathbf{k}}\mathbf{e})(\hat{\mathbf{k}}\mathbf{e}'^*)] + g_2(\hat{\mathbf{k}}\mathbf{e})(\hat{\mathbf{k}}\mathbf{e}'^*) + ig_3\{\boldsymbol{\sigma}[\mathbf{e} \times \mathbf{e}'^*] - (\boldsymbol{\sigma}\hat{\mathbf{k}})(\hat{\mathbf{k}} \cdot [\mathbf{e} \times \mathbf{e}'^*])\} + ig_4(\boldsymbol{\sigma}\hat{\mathbf{k}})(\hat{\mathbf{k}} \cdot [\mathbf{e} \times \mathbf{e}'^*]), \quad (1)$$

where \mathbf{e} (\mathbf{e}') is the polarization vector of the initial (final) deuteron, $\hat{\mathbf{k}}$ is the unit vector along the beam momentum, $\boldsymbol{\sigma}$ is the Pauli matrix, g_i ($i = 1, \dots, 4$) are complex amplitudes. Adding to the right-hand side of Eq.(1) the T-odd P-even term in a very general form $g_5\{(\boldsymbol{\sigma} \cdot [\hat{\mathbf{k}} \times \mathbf{e}])(\mathbf{k} \cdot \mathbf{e}'^*) + (\boldsymbol{\sigma} \cdot [\hat{\mathbf{k}} \times \mathbf{e}'^*])(\mathbf{k} \cdot \mathbf{e})\}$ and using the generalized optical theorem, one can find the total cross section of the pd scattering as

$$\sigma_{tot} = \sigma_0 + \sigma_1 \mathbf{p}^p \cdot \mathbf{p}^d + \sigma_2 (\mathbf{p}^p \cdot \hat{\mathbf{k}})(\mathbf{p}^d \cdot \hat{\mathbf{k}}) + \sigma_3 P_{zz} + \tilde{\sigma} p_y^p P_{xz}^d, \quad (2)$$

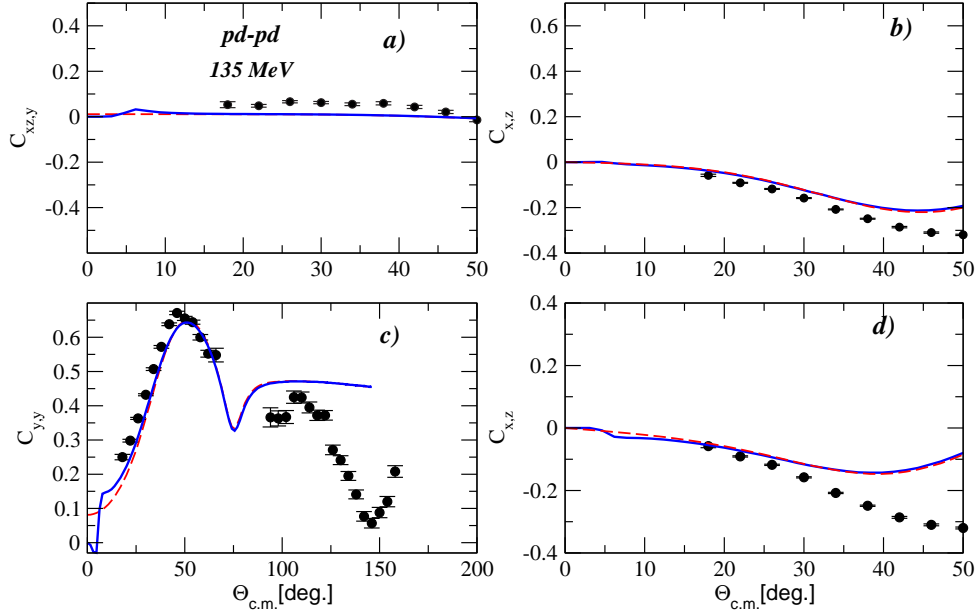


Figure 1: Result of present calculation of spin observables $C_{xz,y}$ (a), $C_{x,z}$ (b), $C_{y,y}$ (c) and $C_{x,z}$ (d) of the pd elastic scattering in comparison with the data [13] at 135 MeV: without Coulomb (dashed line) and with Coulomb included (full).

where \mathbf{p}^p (\mathbf{p}^d) is the vector polarization of the initial proton (deuteron) and P_{zz} and P_{xz} are the tensor polarizations of the deuteron. The OZ axis is directed along the proton beam momentum.

In Eq. (2) the terms σ_i with $i = 0, 1, 2, 3$ are non-zero only for T-even P-even interaction and the last term $\tilde{\sigma}$ is non-zero if the T-odd P-even interaction effects occur. Thus, this term constitutes the-null test signal of T-invariance violation with P-parity conservation. This term can be measured in transmission experiment as difference of counting rates for the cases with $p_y^p P_{xz}^d > 0$ and $p_y^p P_{xz}^d < 0$.

The results of our calculations for unpolarized differential cross section, vector A_y and tensor A_{ij} analysing powers, spin correlations parameters $C_{i,j}$, $C_{ij,k}$ and spin-transfer coefficients $K_j^{i'}$ at 135 MeV and 250 MeV are in reasonable agreement with the available experimental data at small scattering angles ($< 30^\circ$) and/or Faddeev calculations [12,13]. Some part of our calculations is shown in Fig. 1. Coulomb effects are taken into account within the single scattering mechanism. We found that Coulomb effects essentially improve agreement with the data on the non-polarized differential cross section and vector analysing powers A_y^p and A_y^d at these energies at angles $\theta_{cm} \leq 20^\circ - 30^\circ$. The total hadronic polarized cross sections σ_1 and σ_3 are calculated using the optical theorem, whereas Coulomb effects are taken into account in the line of Ref. [15].

Let us consider possible false-effects. One source of these effects is connected with non-zero vector polarization of the deuteron $p_y^d \neq 0$ directed along the vector polarization of the proton beam p_y^p . In this case the term $\sigma_1 p_y^p p_y^d$ in Eq. (2) contributes to the asymmetry A corresponding to the cases $p_y^p P_{xz}^d > 0$ and $p_y^p P_{xz}^d < 0$ which is planned to be measured in the TRIC experiment [7]. According to our calculation, at beam energy 135 MeV the total cross sections are $\sigma_0 = 78.5$ mb, $\sigma_1 = 3.7$ mb, $\sigma_2 = 17.4$ mb, and $\sigma_3 = -1.1$ mb. Therefore, the ratio $r = \sigma_1/\sigma_0$ is equal to ≈ 0.05 . If the TRIC project is going to

measure the ratio $R_T = \tilde{\sigma}/\sigma_0$ with an uncertainty about $\leq 10^{-6}$ (an upper limit for R), then one can find from this ratio r that the vector polarization of the deuteron p_y^d has to be less than $\approx 2 \times 10^{-6}$. When making this estimation, we assume that the ratio of the background-to-signal is $p_y^d \sigma_1 / \tilde{\sigma} \sim 10^{-1}$.

Acknowledgements. We are thankful to D. Eversheim and Yu. Valdau for fruitful discussion of the details of the TRIC project.

References

- [1] I.B. Khriplovich, Nucl.Phys. **B 352** (1991) 385.
- [2] V.Gudkov, Phys. Rep. **212** (192) 77.
- [3] J.B. French et al. Phys. Rev. Lett. **54** (1985) 2313.
- [4] P.R. Huffman et al. Phys. Rev. C **55** (1997) 2684.
- [5] M. Simonius, Phys. Rev. Lett. **78** (1997) 4163.
- [6] W.C. Haxton, A. Höring, M.J. Musolf, Phys. Rev. D **50** (1994) 3422.
- [7] COSY Proposal N 215, "Test of Time reversal invariance in proton-deuteron scattering at COSY", Spokespersons: D. Eversheim, B. Lorentz, Yu. Valdau, available from [http://donald.cc.kfa-juelich.de/wochenplan/List of all COSY-Proposals.shtml](http://donald.cc.kfa-juelich.de/wochenplan/List%20of%20all%20COSY-Proposals.shtml)
- [8] H.E. Conzett, Phys. Rev. C **48** (1993) 423.
- [9] F.Arash, M.J. Moravcsik, G.R. Goldstein, Phys. Rev. Lett. **54** (1985) 2649.
- [10] R.J. Glauber, V.Franco, Phys. Rev. **156** (1967) 1685.
- [11] M.N. Platonova, V.I. Kukulín. Phys. Rev. C **81** (2010) 014004.
- [12] K. Sekiguchi et al. Phys. Rev. C **65** (2002) 034003.
- [13] B. von Przewoski et al. Phys. Rev. C **74** (2006) 064003.
- [14] M.P. Rekaló et al., N.M. Piskunov, I.M. Sitnik, Few-Body Syst. **23**, (1998) 187.
- [15] Yu.N. Uzikov, J. Haidenbauer. Phys. Rev. C **79** (2009) 024617.

EXOPLANETARY SEARCHES WITH GRAVITATIONAL MICROLENSING: POLARIZATION ASPECTS

A. F. Zakharov^{1,2,3†}, G. Inghosso⁴, F. De Paolis⁴, A.A. Nucita⁴, F. Strafella⁴,
S. Calchi Novati^{5,6} and Ph. Jetzer⁷

(1) *Institute of Theoretical and Experimental Physics, Moscow, 117218, Russia*

(2) *Bogoliubov Laboratory of Theoretical Physics, JINR, Dubna, 141980 Russia*

(3) *North Carolina Central University, Durham, NC 27707, USA*

(4) *Dipartimento di Matematica e Fisica “Ennio De Giorgi”, Università del Salento, CP 193, I-73100 Lecce, Italy & INFN Sezione di Lecce, CP 193, I-73100 Lecce, Italy*

(5) *Dipartimento di Fisica “E.R. Caianiello”, Università di Salerno, I-84081 (SA), Italy*

(6) *Istituto Internazionale per gli Alti Studi Scientifici (IIASS), Vietri Sul Mare (SA), Italy*

(7) *Institute for Theoretical Physics, University of Zürich, CH-8057, Zürich, Switzerland*

† *E-mail: zakharov@itep.ru*

Abstract

There are different methods for finding exoplanets such as radial spectral shifts, astrometrical measurements, transits, timing etc. Gravitational microlensing (including pixel-lensing) is among the most promising techniques with the potentiality of detecting Earth-like planets at distances about a few astronomical units from their host star or near the so-called snow line with a temperature in the range $0 - 100^0$ C on a solid surface of an exoplanet. We emphasize the importance of polarization measurements which can help to resolve degeneracies in theoretical models. In particular, the polarization angle could give additional information about the relative position of the lens with respect to the source.

Already before the discovery of exoplanets it was shown how efficient is gravitational microlensing as a tool to search for extrasolar planets, including the low mass ones, even at relatively large distances from their host stars. Later on, observations and simulations gave the opportunity to confirm the robustness of conclusions. Exoplanets near the snow line may be also detected with this technique. Moreover, in contrast with conventional methods, such as transits and Doppler shift measurements, gravitational microlensing gives a chance to find exoplanets not only in the Milky Way, but also in nearby galaxies, such as the Andromeda galaxy [1, 2], so pixel-lensing towards M31 provides an efficient tool to search for exoplanets and indeed an exoplanet might have been already discovered in the PA-N2-99 event [1]. Since source stars for pixel-lensing towards M31 are basically red giants (and therefore, their typical diameters are comparable to Einstein diameters and the caustic sizes) one has to take into account the source finiteness effect. In the case of relatively small size sources, the probability to have features due to binary lens (or planet around star) in the light curves is also small since it is proportional to the caustic area. Giant star sources have large angular sizes and relatively higher probability to touch caustics [1]. In the paper we point out an importance of polarization observations for microlensing event candidates to support (or reject) microlensing model and resolve degeneracies of binary (exoplanetary) microlens models.

Table 1: Exoplanets discovered with microlensing. 24 exoplanets have been found in 22 systems, in particular, there are two exoplanets in OGLE-2006-BLG-109L (lines 5,6) and there are two exoplanets in OGLE-2012-BLG-0026 (lines 18,19).

#	Star Mass (M_{\odot})	Planet Mass	Star-planet Separation (AU)
1	$0.63^{+0.07}_{-0.09}$	$830^{+250}_{-190}M_{\oplus}$	$4.3^{+2.5}_{-0.8}$
2	0.46 ± 0.04	$(1100 \pm 100)M_{\oplus}$	(3.6 ± 0.2)
3	$0.22^{+0.21}_{-0.11}$	$5.5^{+5.5}_{-2.7}M_{\oplus}$	$2.6^{+1.5}_{-0.6}$
4	$0.49^{+0.23}_{-0.29}$	$13^{+6.0}_{-8.0}M_{\oplus}$	$2.7^{+1.7}_{-1.4}$
5	$0.51^{+0.05}_{-0.04}$	$(230 \pm 19)M_{\oplus}$	(2.3 ± 0.5)
6	$0.51^{+0.05}_{-0.04}$	$(86 \pm 7)M_{\oplus}$	$4.5^{+2.1}_{-1.0}$
7	$0.64^{+0.21}_{-0.26}$	$20^{+7}_{-8}M_{\oplus}$	$3.3^{+1.4}_{-0.8}$
8	$0.084^{+0.015}_{-0.012}$	$3.2^{+5.2}_{-1.8}M_{\oplus}$	$0.66^{+0.19}_{-0.14}$
9	$0.30^{+0.19}_{-0.12}$	$260.54^{+165.22}_{-104.85}M_{\oplus}$	$0.72^{+0.38}_{-0.16}/6.5^{+3.2}_{-1.2}$
10	0.67 ± 0.14	$28^{+58}_{-23}M_{\oplus}$	$1.4^{+0.7}_{-0.3}$
11	$0.38^{+0.34}_{-0.18}$	$50^{+44}_{-24}M_{\oplus}$	$2.4^{+1.2}_{-0.6}$
12	$0.19^{+0.30}_{-0.12}$	$2.6^{+4.2}_{-1.6}M_J$	$1.8^{+0.9}_{-0.7}$
13	0.56 ± 0.09	$10.4 \pm 1.7M_{\oplus}$	$3.2^{+1.9}_{-0.5}$
14	$0.44^{+0.27}_{-0.17}$	$2.4^{+1.2}_{-0.6}M_J$	$1.0 \pm 0.1/3.5 \pm 0.5$
15	$0.67^{+0.33}_{-0.13}$	$1.5^{+0.8}_{-0.3}M_J$	2^{+3}_{-1}
16	$0.75^{+0.33}_{-0.41}$	$3.7 \pm 2.1M_J$	$8.3^{+4.5}_{-2.7}$
17	0.26 ± 0.11	$0.53 \pm 0.21M_J$	$2.72 \pm 0.75/1.50 \pm 0.50$
18	0.82 ± 0.13	$0.11 \pm 0.02M_J$	3.82 ± 0.30
19	0.82 ± 0.13	$0.53 \pm 0.21M_J$	4.63 ± 0.37
20	0.022 ± 0.002	$1.88 \pm 0.19M_J$	0.88 ± 0.03
21	0.44 ± 0.07	$2.73 \pm 0.43M_J$	3.45 ± 0.26
22	0.11 ± 0.01	$9.2 \pm 2.2M_{\oplus}$	0.92 ± 0.16
23	0.025 ± 0.001	$9.4 \pm 0.5M_J$	0.19 ± 0.01
24	0.018 ± 0.001	$7.2 \pm 0.5M_J$	0.31 ± 0.01

s

Since the existence of planets around lens stars leads to the violation of circular symmetry of lens system and, as a result, to the formation of fold and cusp type caustics, one can detect extra peaks in the microlensing light curve due to caustic crossing by the star source as a result of its proper motion.

A list of exoplanets detected with microlensing searches toward the Galactic bulge is given in Table 1. For some planetary systems two probable regions for the planet-to-star distance are given due to the planet and star-lens parameter degeneracy, see rows 9, 14, 17 in Table 1. In these searches we have a continuous transition from massive exoplanets to brown dwarfs, since an analysis of the anomalous microlensing event, MOA-2010-BLG-073 has been done, where the primary of the lens is an M-dwarf with $M_{L1} = 0.16 \pm 0.03M_{\odot}$ while the companion has $M_{L2} = 11.0 \pm 2.0M_J^1$, at a perpendicular distance around 1.21 ± 0.16 AU from the host star, so the low mass component of the system

¹According to the definition of a "planet" done by the working group of the International Astronomical Union on February 28, 2003 has the following statement: "... Objects with true masses below the limiting mass for thermonuclear fusion of deuterium (currently calculated to be 13 Jupiter masses for objects of solar metallicity) that orbit stars or stellar remnants are "planets" (no matter how they formed).."

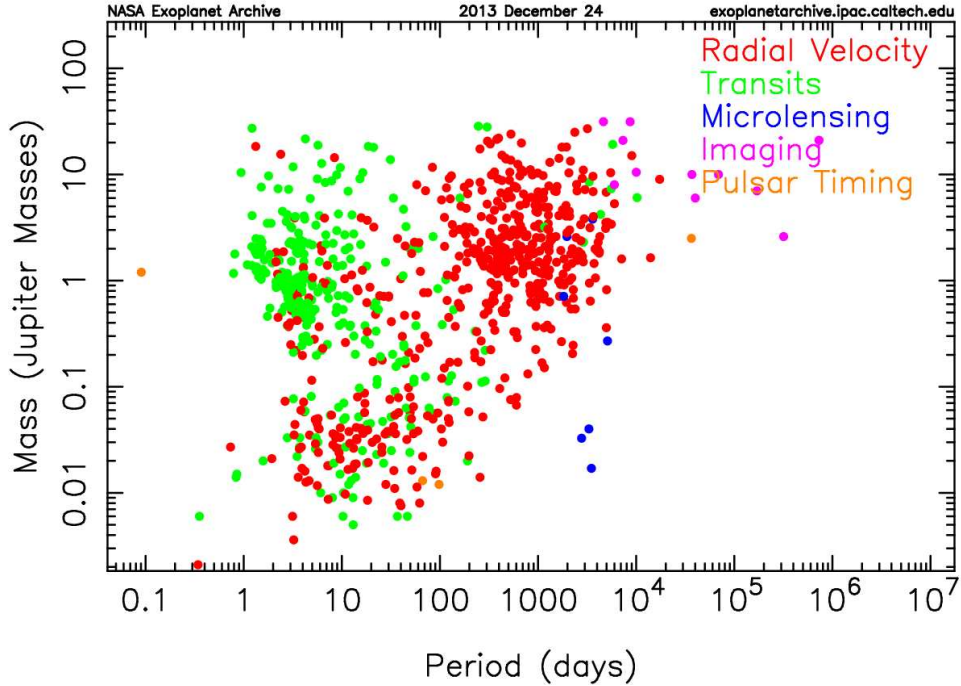


Figure 1: All exoplanets found with different techniques until December 24, 2013, see <http://exoplanetarchive.ipac.caltech.edu/exoplanetplots/>.

is near a boundary between planets and brown dwarfs. It is remarkable that the first exoplanet has been discovered by the MOA-I collaboration with only a 0.6 m telescope. This microlensing event was also detected by the OGLE collaboration, but the MOA observations with a larger field of view CCD, made about 5 exposures per night for each of their fields. This was an important advantage and shows that even observations with modest facilities (around 1 meter telescope size and even smaller) can give a crucial contribution in such discoveries. Until now four super-Earth exoplanets (with masses about $10M_{\oplus}$) have been discovered by microlensing (see Table 1 and Fig. 1), showing that this technique is very efficient in detecting Earth mass exoplanets at a few AU from their host stars, since a significant fraction of all exoplanets discovered with different techniques and located in the region near the so-called snow line (or the habitable zone) found with gravitational microlensing. Some of these exoplanets are among the highest exoplanets see lines 3 and 8 in Table 1. For comparison, Doppler shift measurements help to detect an Earth-mass planet orbiting our neighbor star a Centauri B. The planet has an orbital period of 3.236 days and is about 0.04 AU from the star. Recently, a sub-Mercury size exoplanet Kepler-37b has been discovered with a transit technique. It means that the existence of cool rocky planets is a common phenomenon in the Universe. Moreover, recently, it was claimed that around 17% of stars host Jupiter-mass planets ($0.3 - 10 M_J$), cool Neptunes ($10 - 30M_{\oplus}$) and super-Earths ($10 - 30M_{\oplus}$) have relative abundances per star in the Milky Way such as 52% and 62%, respectively. Analysis of Kepler space telescope data also shows that a significant fraction of all stars has to have exoplanets. Pixel-lensing towards M31 may provide an efficient tool to search for exoplanets in that galaxy [1], and indeed an exoplanet might be already discovered in the PA-N2-99 event [1]. As it is well known the amplifications for a finite source and for a point-like source are different because there is a gradient of amplification in respect of

a source area. If the source size is rather small, the probability to produce features of binary lens (or planet around star) is proportional to the caustic area. However, giant stars have large angular sizes and relatively higher probability to touch planetary caustics (see [1], for more details).

For point-like lens polarization could reach 0.1% while for binary lens it could reach a few percent since the magnification gradient is much greater near caustics. It has been shown that polarization measurements could resolve degeneracies in theoretical models of microlensing events. Calculations of polarization curves for microlensing events with features in the light curves induced by the presence of an exoplanet and observed towards the Galactic bulge have been done [3, 4]. Here we emphasize that measurements of then polarization angle could give additional information about the gravitational microlensing model.² If polarization measurements are possible, in principle, one could measure polarization as a function of direction for an orientation of polarimeter and an instant for microlensing event. If a polarimeter is fixed one has an additional function of time to explain observational data, but if a polarimeter could be rotated, polarization is an additional function of direction at each instant. Such an information could help to resolve degeneracies and confirm (or disprove) microlensing models for observed phenomena.

For instance, for a point-like lens the direction for the maximal polarization at the instant when an amplification is also maximal (which is perpendicular to the line connecting star and lens) may allow to infer the direction of lens proper motion, thus allowing to eventually pinpoint the lens in following observations. Even in the case of binary lens, the orientation of polarization vector corresponds to the orientation of the fold caustic (or more correctly to the tangent vector to the fold caustic at the intersection point with the path of source), provided the source size is small enough.

In Fig. 2, the light curve, the polarization curve and the polarization angle are shown for the OGLE-2005-BLG-169 event, where a binary system formed by a main sequence star with mass $M_{\odot} \sim 0.5 M_{\odot}$ and a Neptune-like exoplanet with mass about $13 M_{\oplus}$ is expected from the light curve analysis. The event parameters are $t_E = 42.27$ days, $u_0 = 1.24 \times 10^{-3}$, $b = 1.0198$, $q = 8.6 \times 10^{-5}$, $\alpha = 117.0$ deg, $\rho_* = 4.4 \times 10^{-4}$, where $t_E, u_0, b, q, \alpha, \rho_*$ are the Einstein time, the impact parameter, the projected distance of the exoplanet to the host star, the binary component mass ratio, the angle formed by the source trajectory and the separation vector between the lenses, and the source star size, respectively (all distances are given in R_E units). The effect of the source transiting the caustic is clearly visible both in the polarization curve (see the middle panel in Fig. 2) and in the flip of the polarization angle (see the bottom panel). We would like to stress that the high peak magnification ($A \simeq 800$) of the OGLE-2005-BLG-169 event leading to I -magnitude of the source about 13 mag at the maximum gives the opportunity to measure the polarization signal for such kind of events by using present available facilities. In this case, polarization measurements might give additional information about the caustic structure, thus potentially allowing to distinguish among different models of exoplanetary systems. Recently, it was found that a variable giant star source mimics exoplanetary signatures in the MOA-2010-BLG-523S event. In this respect, we emphasize that polarization measurements may be helpful in distinguishing exoplanetary features from other effects in the light curves.

The polarization curve and the polarization angle for the MOA-2008-BLG-310Lb event is shown in Fig. 3. For this event it was expected the existence of a sub-Saturn exoplanet

²We call polarization angle the angle which corresponds to a direction with the maximal polarization.

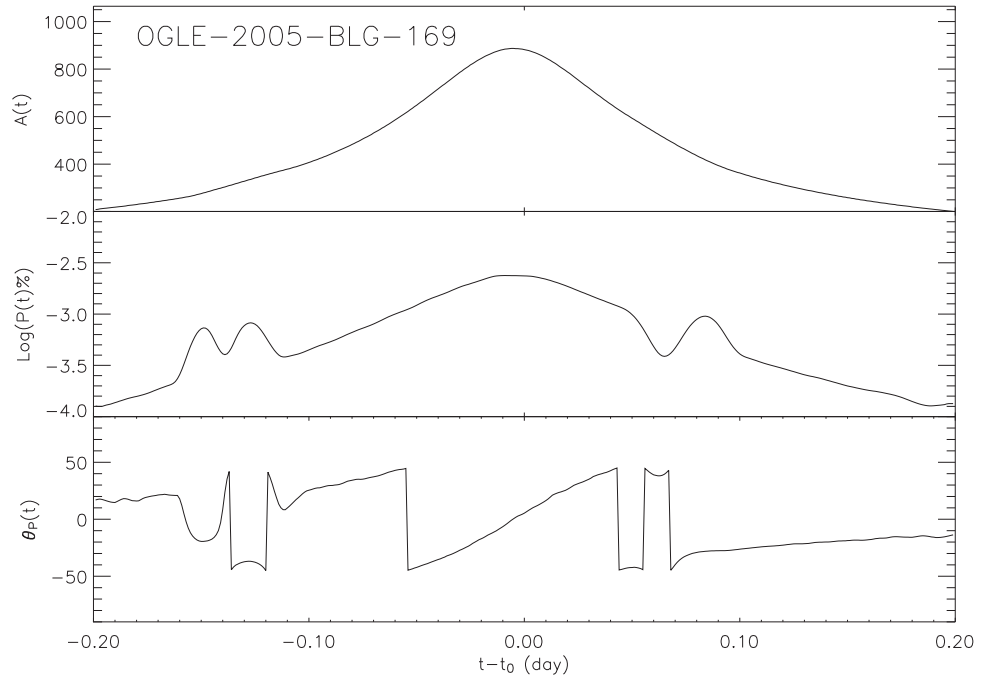


Figure 2: Light curve (top panel), polarization curve (middle panel) and polarization angle (bottom panel) for the OGLE-2005-BLG-169 event.

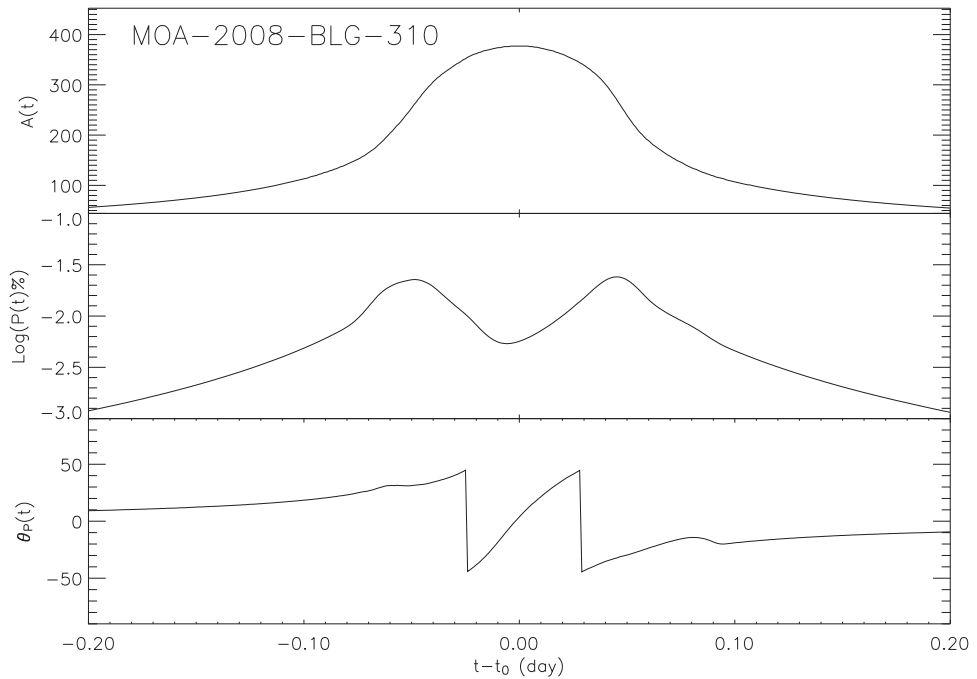


Figure 3: Light curve (top panel), polarization curve (middle panel) and polarization angle (bottom panel) for the MOA-2008-BLG-310 event.

with mass $m = 74 \pm 17 M_{\oplus}$. The event parameters are $t_E = 11.14$ days, $u_0 = 3. \times 10^{-3}$, $b = 1.085$, $q = 3.31 \times 10^{-4}$, $\alpha = 69.33$ deg, $\rho_* = 4.93 \times 10^{-3}$. In particular, the event is characterized by large finite source effect since $\rho_*/u_0 > 1$, leading to polarization features similar to those of single lens events. Nevertheless, in this case we can see the variability in the polarization signal that arises when the source touches the first fold caustic at $t_1 \simeq t_0 - 0.07$ days, the source enters the primary lens at $t_2 \simeq t_0 - t_E \sqrt{\rho_*^2 - u_0^2}$ days, the source exits the primary lens at $t_3 \simeq t_0 + t_E \sqrt{\rho_*^2 - u_0^2}$ days and touches the second fold caustic $t_4 \simeq t_0 + 0.09$ days.

Now there are campaigns of wide field observations by Optical Gravitational Lensing Experiment (OGLE) and Microlensing Observations in Astrophysics (MOA) and a couple of follow-up observations, including MicroFUN³ and PLANET⁴. It is important to note that small size (even less than one meter diameter) telescopes acting in follow-up campaigns contributed in discoveries of light Earth-like exoplanets and it is a nice illustration that a great science can be done with modest facilities. As it was shown by [3] polarization measurements are very perspective to remove uncertainties in exoplanet system determination and they give an extra proof for a conventional gravitational microlens model with suspected exoplanets. Moreover, an orientation of polarization angle near the maximum of polarizations (and light) curves gives information on direction of proper motion in respect to gravitational microlens system which could include exoplanet. Such an information could be important for possible further observations of the gravitational lens system in future. The contribution is a short version of paper [5], where one can find a more detailed references and discussion.

AFZ thanks organizers of DSPIN-13, especially prof. A.V. Efremov, for the kind attention to our contribution, and acknowledges also a partial support of the NSF (HRD-0833184) and NASA (NNX09AV07A) grants at NCCU (Durham, NC, USA).

References

- [1] G. Ingresso et al., *Mon. Not. R. Astron. Soc.*, **399** (2009) 219.
- [2] G. Ingresso et al., *Gen. Rel. Grav.*, **43** (2011) 1047.
- [3] G. Ingresso et al., *Mon. Not. R. Astron. Soc.*, **426** (2012) 1496.
- [4] G. Ingresso et al., *Physica Scripta* (accepted); arXiv:1310.5866v1[astro-ph.SR].
- [5] A.F. Zakharov et al., *Advances in Space Research* (accepted); arXiv:1312.3468v1 [astro-ph.SR].

³<http://www.astronomy.ohio-state.edu/microfun/microfun.html>.

⁴<http://planet.iap.fr/>.

SPIN-ORBITAL COMPOSITION IN RELATIVISTIC MANY-FERMION SYSTEMS

P. Zavada

Institute of Physics of the AS CR, Na Slovance 2, CZ-182 21 Prague 8, Czech Republic
E-mail: zavada@fzu.cz

Abstract

The interplay of spins and orbital angular moments of the fermions play an important role for the structure of the many-fermion systems like atoms, nuclei, nucleons (baryons) or mesons. We start our study from the one-fermion eigenstates of angular momentum represented by the spinor spherical harmonics. Afterwards we study the properties of many-fermion states resulting from a multiple angular momentum composition of the one-fermion states, giving the total angular momentum $J = \langle L \rangle + \langle S \rangle$, which is identified with the spin of the composite particle. We demonstrate how the composition rules affect the relativistic interplay between the sums of the spins $\langle S \rangle$ and orbital angular moments $\langle L \rangle$ of the constituents, which collectively generate the spin of composite particle. It is suggested that in a relativistic case, when the masses of the constituent fermions are much less than their energy (in the rest frame of the composite particle), then the spin of the composite particle is dominated by the orbital angular moments $\langle L \rangle$ of the constituents, while $|\langle S \rangle| \leq J/3$. A special attention is paid to the case $J = 1/2$ that is related e.g. to the spin of proton generated by the composition of spins and orbital angular moments of the quarks.

1 Eigenstates of angular momentum

The solutions of free Dirac equation represented by eigenstates of the total angular momentum (AM) with quantum numbers j, j_z are the spinor spherical harmonics [1–3], which in the *momentum representation* reads

$$|j, j_z\rangle = \Phi_{jl_p j_z}(\omega) = \frac{1}{\sqrt{2\epsilon}} \begin{pmatrix} \sqrt{\epsilon + m} \Omega_{jl_p j_z}(\omega) \\ -\sqrt{\epsilon - m} \Omega_{j\lambda_p j_z}(\omega) \end{pmatrix}, \quad (1)$$

where ω represents the polar and azimuthal angles (θ, φ) of the momentum \mathbf{p} with respect to the quantization axis z , $l_p = j \pm 1/2$, $\lambda_p = 2j - l_p$ (l_p defines the parity), energy $\epsilon = \sqrt{\mathbf{p}^2 + m^2}$, and

$$\begin{aligned} \Omega_{jl_p j_z}(\omega) &= \begin{pmatrix} \sqrt{\frac{j+j_z}{2j}} Y_{l_p, j_z-1/2}(\omega) \\ \sqrt{\frac{j-j_z}{2j}} Y_{l_p, j_z+1/2}(\omega) \end{pmatrix}; \quad l_p = j - \frac{1}{2}, \\ \Omega_{j\lambda_p j_z}(\omega) &= \begin{pmatrix} -\sqrt{\frac{j-j_z+1}{2j+2}} Y_{l_p, j_z-1/2}(\omega) \\ \sqrt{\frac{j+j_z+1}{2j+2}} Y_{l_p, j_z+1/2}(\omega) \end{pmatrix}; \quad l_p = j + \frac{1}{2}. \end{aligned} \quad (2)$$

j, j_z	$P_{j,j_z}(\omega)$
$\frac{1}{2}, \frac{1}{2}$	1
$\frac{3}{2}, \frac{3}{2}$	$\frac{3-3 \cos 2\theta}{4}$
$\frac{5}{2}, \frac{5}{2}$	$\frac{5+3 \cos 2\theta}{4}$
$\frac{7}{2}, \frac{7}{2}$	$\frac{45-60 \cos 2\theta+15 \cos 4\theta}{64}$

Table 1: The examples of the distributions (8). The common factor $1/4\pi$ is omitted.

In a relativistic case the quantum numbers of spin and orbital angular momentum (OAM) are not conserved separately, but only the total AM j and its projection $j_z = s_z + l_z$ can be conserved. The complete wave function reads

$$\Psi_{jl_p j_z}(\epsilon, \omega) = \phi_j(\epsilon) \Phi_{jl_p j_z}(\omega). \quad (3)$$

The function $\phi_j(\epsilon)$ or its equivalent representation (7) is the amplitude of probability that the fermion has energy ϵ . In fact the main results in this note depend only on the probability distribution $a_j^*(\epsilon) a_j(\epsilon)$ via the parameters (16). The spinors (1) are normalized as

$$\int \Phi_{j'l_p j'_z}^+(\omega) \Phi_{jl_p j_z}(\omega) d\omega = \delta_{j'j} \delta_{l'_p l_p} \delta_{j'_z j_z}, \quad (4)$$

where $d\omega = d \cos \theta d\varphi$. Then the normalization

$$\int \Psi_{j'l_p j'_z}^+(\epsilon, \omega) \Psi_{jl_p j_z}(\epsilon, \omega) d^3 \mathbf{p} = \delta_{j'j} \delta_{l'_p l_p} \delta_{j'_z j_z} \quad (5)$$

implies the condition for the amplitude ϕ_j ,

$$\int \phi_j^*(\epsilon) \phi_j(\epsilon) p^2 dp = 1. \quad (6)$$

In the next discussion it will be convenient also to use the alternative representation, which differs in normalization,

$$a_j(\epsilon) = \frac{\phi_j(\epsilon)}{2\sqrt{\pi}}; \quad \int a_j^*(\epsilon) a_j(\epsilon) d^3 \mathbf{p} = 1. \quad (7)$$

1.1 Angular moments of one-fermion states

A few examples of the corresponding probability distribution

$$P_{j,j_z}(\omega) = \Phi_{jl_p j_z}^+(\omega) \Phi_{jl_p j_z}(\omega); \quad \int P_{j,j_z}(\omega) d\omega = 1, \quad (8)$$

are given in Table 1. These distributions does not depend on the parameters φ and $l_p = j \pm 1/2$. The lowest value $j = 1/2$ generates rotational symmetry of the probability distribution, but for higher $j = 3/2, 5/2, \dots$ the distribution has axial symmetry only. The states (1) are not eigenstates of spin and OAM; nevertheless, one can always calculate the mean values of corresponding operators

$$s_z = \frac{1}{2} \begin{pmatrix} \sigma_z & 0 \\ 0 & \sigma_z \end{pmatrix}, \quad l_z = -i \left(p_x \frac{\partial}{\partial p_y} - p_y \frac{\partial}{\partial p_x} \right). \quad (9)$$

The related matrix elements are given by the relations [4]:

$$\begin{aligned}\langle s_z \rangle_{j,j_z} &= \int \Phi_{j_l p j_z}^+ s_z \Phi_{j_l p j_z} d\omega = \frac{1 + (2j + 1)\mu}{4j(j + 1)} j_z, \\ \langle l_z \rangle_{j,j_z} &= \int \Phi_{j_l p j_z}^+ l_z \Phi_{j_l p j_z} d\omega = \left(1 - \frac{1 + (2j + 1)\mu}{4j(j + 1)}\right) j_z,\end{aligned}\quad (10)$$

in which we have denoted

$$\mu = \pm \frac{m}{\epsilon}, \quad (11)$$

where the sign (\pm) corresponds to $l_p = j \mp 1/2$. The relations imply that in the nonrelativistic limit, when $\mu \simeq \pm 1$, we get for signs (\pm) correspondingly,

$$\langle s_z \rangle_{j,j_z} = \left\{ \begin{array}{c} \frac{j_z}{2j} \\ \frac{-j_z}{2(j+1)} \end{array} \right\}, \quad \langle l_z \rangle_{j,j_z} = \left\{ \begin{array}{c} \left(1 - \frac{1}{2j}\right) j_z \\ \left(1 + \frac{1}{2(j+1)}\right) j_z \end{array} \right\} \quad (12)$$

and in the relativistic case, when $\mu \rightarrow 0$, we have

$$\langle s_z \rangle_{j,j_z} = \frac{j_z}{4j(j + 1)}, \quad \langle l_z \rangle_{j,j_z} = \left(1 - \frac{1}{4j(j + 1)}\right) j_z. \quad (13)$$

The last two relations imply

$$\left| \langle s_z \rangle_{j,j_z} \right| \leq \frac{1}{4(j + 1)} \leq \frac{1}{6}, \quad \frac{\left| \langle s_z \rangle_{j,j_z} \right|}{\left| \langle l_z \rangle_{j,j_z} \right|} \leq \frac{1}{4j^2 + 4j - 1} \leq \frac{1}{2}. \quad (14)$$

For the complete wave function (3), the relations (10) are modified as

$$\begin{aligned}\langle\langle s_z \rangle\rangle_{j,j_z} &= \int \Psi_{j_l p j_z}^+ s_z \Psi_{j_l p j_z} d^3 \mathbf{p} = \frac{1 + (2j + 1)\langle\mu_j\rangle}{4j(j + 1)} j_z, \\ \langle\langle l_z \rangle\rangle_{j,j_z} &= \int \Psi_{j_l p j_z}^+ l_z \Psi_{j_l p j_z} d^3 \mathbf{p} = \left(1 - \frac{1 + (2j + 1)\langle\mu_j\rangle}{4j(j + 1)}\right) j_z,\end{aligned}\quad (15)$$

where

$$\langle\mu_j\rangle = \pm \int a_j^*(\epsilon) a_j(\epsilon) \frac{m}{\epsilon} d^3 \mathbf{p}, \quad |\langle\mu_j\rangle| \leq 1. \quad (16)$$

1.2 Many-fermion states

The system of fermions (or arbitrary particles) generating the state with quantum numbers J, J_z can be represented by the combination of one-particle states. For example the pair of states j_1, j_2 can generate the states

$$|(j_1, j_2)J, J_z\rangle = \sum_{j_{z1}=-j_1}^{j_1} \sum_{j_{z2}=-j_2}^{j_2} \langle j_1, j_{z1}, j_2, j_{z2} | J, J_z \rangle |j_1, j_{z1}\rangle |j_2, j_{z2}\rangle; \quad (17)$$

$$j_{z1} + j_{z2} = J_z, \quad |j_1 - j_2| \leq J \leq j_1 + j_2, \quad (18)$$

where $\langle j_1, j_{z1}, j_2, j_{z2} | J, J_z \rangle$ are Clebsch-Gordan coefficients, which are nonzero if the conditions (18) are satisfied. In this way one can repeat the composition and obtain the many-particle eigenstates of resulting J, J_z

$$|(j_1, j_2, \dots, j_n)_c J, J_z\rangle = \sum_{j_{z1}=-j_1}^{j_1} \sum_{j_{z2}=-j_2}^{j_2} \dots \sum_{j_{zn}=-j_n}^{j_n} c_j |j_1, j_{z1}\rangle |j_2, j_{z2}\rangle \dots |j_n, j_{zn}\rangle, \quad (19)$$

where the coefficients c_j are a product of the Clebsch-Gordan coefficients

$$c_j = \langle j_1, j_{z1}, j_2, j_{z2} | J_3, J_{3z} \rangle \langle J_3, J_{3z}, j_3, j_{z3} | J_4, J_{4z} \rangle \dots \langle J_n, J_{nz}, j_n, j_{zn} | J, J_z \rangle. \quad (20)$$

Let us remark that the set j_1, j_2, \dots, j_n does not define the resulting state unambiguously. The result depends on the pattern of their composition, e.g.

$$(((j_1 \oplus j_2)_{J_1} \oplus j_3)_{J_2} \oplus j_4)_J, \quad (((j_1 \oplus j_2)_{J_1} \oplus (j_3 \oplus j_4)_{J_2})_{J_3} \oplus j_5)_J, \quad (21)$$

where J_k represent intermediate AMs corresponding to the steps of composition:

$$j_1 \oplus j_2 = J_1, \quad J_1 \oplus j_3 = J_2, \quad J_2 \oplus j_4 = J. \quad (22)$$

Each binary composition " \oplus " is defined by Eq. (17). Different composition patterns are in (19) symbolically expressed by the subscript c . Apparently, the number of patterns increases with n very rapidly; however, in a real scenario with an interaction one can expect their probabilities will differ. The case $n = 3$ will be illustrated in more detail below.

From now we discuss only the composed states with resulting $J = J_z = 1/2$ ($J_z = -1/2$ gives the equivalent results). The corresponding n -fermion state (n is odd)

$$\Phi_{c,1/2,1/2}(\omega_1, \omega_2, \dots, \omega_n) = |(j_1, j_2, \dots, j_n)_c 1/2, 1/2\rangle, \quad (23)$$

or alternatively

$$\Psi_{c,1/2,1/2} = \phi_{j_1}(\epsilon_1) \phi_{j_2}(\epsilon_2) \dots \phi_{j_n}(\epsilon_n) \Phi_{c,1/2,1/2}(\omega_1, \omega_2, \dots, \omega_n) \quad (24)$$

generate the n -dimensional angular distribution

$$P_c(\omega_1, \omega_2, \dots, \omega_n) = \Phi_{c,1/2,1/2}^+ \Phi_{c,1/2,1/2}, \quad (25)$$

from which the corresponding average one-fermion distributions are obtained as

$$p_{c,k}(\omega_k) = \int P_c(\omega_1, \omega_2, \dots, \omega_n) \prod_{i \neq k}^n d\omega_i, \quad (26)$$

which gives [4]:

$$p_{c,k}(\omega) = \frac{1}{4\pi}. \quad (27)$$

It follows that the distribution

$$P_c(\omega) = \sum_{k=1}^n p_{c,k}(\omega) = \frac{n}{4\pi}, \quad (28)$$

which is generated by the state (23) has rotational symmetry similar to the distribution $P_{1/2,1/2}$ generated by the one-fermion state in Table 1. Therefore the angular probability distribution $P_c(\omega)$ related to the state $J = 1/2$ has rotational symmetry regardless of the number of involved particles. This rule suggests that e.g. in a nucleus $J = 1/2$, the probability distribution of nucleons, separately for protons and neutrons, has in the momentum space rotational symmetry. Spherical symmetry of probability distribution in the momentum space apparently implies spherical symmetry in coordinate representation.

What can be said about the mean values of the spin and OAM contributions

$$\begin{aligned} \langle \mathbb{S}_z \rangle_{c,1/2,1/2} &= \langle s_{z1} + s_{z2} + \dots + s_{zn} \rangle_c, & \langle \mathbb{L}_z \rangle_{c,1/2,1/2} &= \langle l_{z1} + l_{z2} + \dots + l_{zn} \rangle_c, \\ \langle \mathbb{S}_z \rangle_{c,1/2,1/2} + \langle \mathbb{L}_z \rangle_{c,1/2,1/2} &= \frac{1}{2}, \end{aligned} \quad (29)$$

corresponding to the state (23)? In the next we discuss this question in more detail for the case $n = 3$.

1.2.1 Three-fermion states

There are three patterns for composition of the three AMs j_a, j_b, j_c :

$$((j_a \oplus j_b)_{J_c} \oplus j_c)_{1/2}; \quad abc = 123, 312, 231. \quad (30)$$

Corresponding states are

$$\begin{aligned} \Phi_{c,1/2,1/2}(\omega_1, \omega_2, \omega_3) &= \sum_{j_{z1}=-j_1}^{j_1} \sum_{j_{z2}=-j_2}^{j_2} \sum_{j_{z3}=-j_3}^{j_3} \langle j_a, j_{za}, j_b, j_{zb} | J_c, J_{zc} \rangle \\ &\times \langle J_c, J_{zc}, j_c, j_{zc} | 1/2, 1/2 \rangle |j_1, j_{z1}\rangle |j_2, j_{z2}\rangle |j_3, j_{z3}\rangle. \end{aligned} \quad (31)$$

The conditions (18) give at most two possibilities for the intermediate values J_c , which must satisfy

$$J_c = j_c \pm 1/2, \quad |j_a - j_b| \leq J_c \leq j_a + j_b. \quad (32)$$

At the same time it holds

$$j_{z1} + j_{z2} + j_{z3} = 1/2, \quad j_{za} + j_{zb} = J_{zc}. \quad (33)$$

In this way two possible values J_c in three patterns (30) give six possibilities to create the state (31). Further, if we take into account two possible values $l_p = j \pm 1/2$ for each one-fermion state in (31) and defined by (1), then in general the total number of generated three-fermion states is $6 \times 2^3 = 48$. Due to orthogonality of the terms in sum (31) the three-fermion mean values (29) are calculated as

$$\begin{aligned} \langle \mathbb{S}_z \rangle_{c,1/2,1/2} &= \sum_{j_{z1}=-j_1}^{j_1} \sum_{j_{z2}=-j_2}^{j_2} \sum_{j_{z3}=-j_3}^{j_3} \langle j_a, j_{za}, j_b, j_{zb} | J_c, J_{zc} \rangle^2 \\ &\times \langle J_c, J_{zc}, j_c, j_{zc} | 1/2, 1/2 \rangle^2 (\langle s_{za} \rangle + \langle s_{zb} \rangle + \langle s_{zc} \rangle) \end{aligned} \quad (34)$$

j_1	j_2	j_3	$\langle S_z \rangle_3$	$\langle S_z \rangle_2$	$\langle S_z \rangle_1$	$\langle S_z \rangle_3$	$\langle S_z \rangle_2$	$\langle S_z \rangle_1$
1	1	1	$\frac{1+2\tilde{\mu}}{6}$	$\frac{1+2\tilde{\mu}}{6}$	$\frac{1+2\tilde{\mu}}{6}$	$\frac{1+2\tilde{\mu}}{6}$	$\frac{1+2\tilde{\mu}}{6}$	$\frac{1+2\tilde{\mu}}{6}$
2	1	2	\times	\times	$\frac{-1}{18}$	$\frac{-1}{18}$	$\frac{-1}{18}$	\times
3	1	3	\times	\times	$\frac{18}{1+3\tilde{\mu}}$	$\frac{18}{-1+6\tilde{\mu}}$	$\frac{18}{3+7\tilde{\mu}}$	$\frac{18}{3+7\tilde{\mu}}$
2	2	2	$\frac{6}{1+4\tilde{\mu}}$	$\frac{18}{1+4\tilde{\mu}}$	$\frac{18}{1+4\tilde{\mu}}$	$\frac{90}{1+4\tilde{\mu}}$	$\frac{30}{1+4\tilde{\mu}}$	$\frac{30}{1+4\tilde{\mu}}$
3	2	3	$\frac{6}{30}$	$\frac{18}{30}$	$\frac{18}{30}$	$\frac{90}{-5-4\tilde{\mu}}$	$\frac{30}{-5-4\tilde{\mu}}$	$\frac{30}{30}$
2	3	2	\times	\times	$\frac{-5-4\tilde{\mu}}{90}$	$\frac{-5-4\tilde{\mu}}{-1+29\tilde{\mu}}$	$\frac{-5-4\tilde{\mu}}{-1+29\tilde{\mu}}$	\times
3	3	3	$\frac{5+17\tilde{\mu}}{90}$	$\frac{5+17\tilde{\mu}}{90}$	$\frac{-1+2\tilde{\mu}}{90}$	$\frac{-1+29\tilde{\mu}}{90}$	$\frac{-1+29\tilde{\mu}}{90}$	$\frac{41+134\tilde{\mu}}{90}$
2	2	2	$\frac{1+2\tilde{\mu}}{13+38\tilde{\mu}}$	$\frac{13+38\tilde{\mu}}{13+38\tilde{\mu}}$	$\frac{13+38\tilde{\mu}}{13+38\tilde{\mu}}$	$\frac{630}{-23+2\tilde{\mu}}$	$\frac{630}{31+74\tilde{\mu}}$	$\frac{630}{31+74\tilde{\mu}}$
3	2	3	$\frac{6}{29+104\tilde{\mu}}$	$\frac{270}{23+152\tilde{\mu}}$	$\frac{270}{23+152\tilde{\mu}}$	$\frac{630}{-1+8\tilde{\mu}}$	$\frac{378}{55+232\tilde{\mu}}$	$\frac{378}{55+232\tilde{\mu}}$
2	3	2	$\frac{630}{1+6\tilde{\mu}}$	$\frac{1890}{1+6\tilde{\mu}}$	$\frac{1890}{1+6\tilde{\mu}}$	$\frac{210}{1+6\tilde{\mu}}$	$\frac{1890}{1+6\tilde{\mu}}$	$\frac{1890}{1+6\tilde{\mu}}$
3	3	3	$\frac{70}{70}$	$\frac{70}{70}$	$\frac{70}{70}$	$\frac{70}{70}$	$\frac{70}{70}$	$\frac{70}{70}$

Table 2: Mean values $\langle S_z \rangle_c$ of three-fermion states $|(j_1, j_2, j_3, J_c)1/2, 1/2\rangle$ with $J_c = j_c - 1/2$ and $J_c = j_c + 1/2$ (columns 4,5,6 and 7,8,9; $c = 3, 2, 1$) [see the first relation (32) and (34)]. The symbol \times denotes configuration for which the second condition (32) is not satisfied.

and similarly for $\langle \mathbb{L}_z \rangle_{c,1/2,1/2}$. Corresponding one-fermion values $\langle s_{z..} \rangle$ and $\langle l_{z..} \rangle$ are given by the relations (10). The results for a set of input values j_1, j_2, j_3 and $l_{pk} = j_k - 1/2$ are listed in Table 2 and the results corresponding to remaining sets $l_{pk} = j_k \pm 1/2$ are similar and differ only in terms proportional to $\tilde{\mu}$. Since

$$\langle S_z \rangle_{c,1/2,1/2} = -\langle S_z \rangle_{c,1/2,-1/2}, \quad \langle S_z \rangle_{c,1/2,\pm 1/2} + \langle \mathbb{L}_z \rangle_{c,1/2,\pm 1/2} = \pm 1/2,$$

we present only $\langle S_z \rangle_c \equiv \langle S_z \rangle_{c,1/2,1/2}$. The meaning of the parameter $\tilde{\mu}$ is as follows:

- (1) If one assumes the same parameter μ (11) for the three fermions in the state (31), then $\tilde{\mu} = \mu$.
- (2) In a general case, the complete wave function

$$\Psi_{c,1/2,1/2} = \phi_{j_1}(\epsilon_1) \phi_{j_2}(\epsilon_2) \phi_{j_3}(\epsilon_3) \Phi_{c,1/2,1/2}(\omega_1, \omega_2, \omega_3) \quad (35)$$

gives instead of (16) a more complicated expression [4]

$$\tilde{\mu} = f_c(\langle \mu_1 \rangle, \langle \mu_2 \rangle, \langle \mu_3 \rangle, j_1, j_2, j_3), \quad (36)$$

where the parameters $\langle \mu_i \rangle$ are defined by Eq. (16). The expression is simplified for $\langle \mu_1 \rangle = \langle \mu_2 \rangle = \langle \mu_3 \rangle = \langle \mu \rangle$,

$$f_c(\langle \mu \rangle, \langle \mu \rangle, \langle \mu \rangle, j_1, j_2, j_3) = \langle \mu \rangle. \quad (37)$$

Obviously the many-fermion system with $J = J_z = 1/2$ can be treated as a composed particle of the spin 1/2. This spin is generated by the spins and OAMs of the involved fermions. The relative weights of the spin and OAM contributions vary depending not only on the intrinsic values j_1, j_2, j_3 and the pattern of composition, but also on the mass-motion parameter $\tilde{\mu}$. The data in the table suggest that for any configuration in the relativistic limit $\tilde{\mu} \rightarrow 0$, we have

$$|\langle S_z \rangle| \leq \frac{1}{6} \quad (38)$$

similar to the case of the one-fermion states (14).

The table illustrates a complexity of the AM composition even for only three fermions. Is there a simple rule like (38) for $n > 3$? First, let us consider the composition

$$\Psi_{c,1/2,1/2} = |(j_1, j_2, \dots, j_n)_c 1/2, 1/2\rangle, \quad (39)$$

where all one-fermion AMs are the same, $j_i = j$ (like the rows 1,4,9 in the table). The corresponding spin reads

$$\langle \mathbb{S}_z \rangle = \frac{1 + (2j + 1) \tilde{\mu}}{8j(j + 1)} \quad (40)$$

regardless of n and details of composition. The proof of this relation is given in [4]. Apparently for $\tilde{\mu} \rightarrow 0$, the relation (38) is again satisfied. The situation with the composition of different AMs is getting much more complex for increasing n . However, an average value of the spin over all possible composition patterns of the state $|(j_1, j_2, \dots, j_n)_c 1/2, 1/2\rangle$ appears to safely satisfy (38). This is the case when there is no (e.g., dynamical) preference among various composition patterns.

Let us illustrate a possible role of the composition patterns by the simple example $j_1, j_2, j_3 = 1/2$. Eq. (31) gives the three states corresponding to $J_c = 1$,

$$\Psi_{abc,1/2,1/2} = \frac{\phi_{abc}}{\sqrt{6}} (|-1/2, 1/2, 1/2\rangle + |1/2, -1/2, 1/2\rangle - 2|1/2, 1/2, -1/2\rangle), \quad (41)$$

where

$$\phi_{abc} = \phi_a(\epsilon_a) \phi_b(\epsilon_b) \phi_c(\epsilon_c). \quad (42)$$

The indices abc define the composition in accordance with (30), and AM states are defined correspondingly, $|j_{za}, j_{zb}, j_{zc}\rangle$. The other three states correspond to $J_c = 0$,

$$\Psi_{abc,1/2,1/2} = \frac{\phi_{abc}}{\sqrt{2}} (|1/2, -1/2, 1/2\rangle - |-1/2, 1/2, 1/2\rangle). \quad (43)$$

The non-relativistic proton SU(6) wave function in a standard notation read:

$$|p \uparrow\rangle = \frac{1}{\sqrt{2}} \left\{ \frac{1}{\sqrt{6}} |d u u + u d u - 2 u u d\rangle \times \frac{1}{\sqrt{6}} |\downarrow \uparrow \uparrow + \uparrow \downarrow \uparrow - 2 \uparrow \uparrow \downarrow\rangle \right. \\ \left. + \frac{1}{\sqrt{2}} |d u u - u d u\rangle \frac{1}{\sqrt{2}} |\downarrow \uparrow \uparrow - \uparrow \downarrow \uparrow\rangle \right\}. \quad (44)$$

The comparison (41)–(43) with (44) suggests that the SU(6) wave function after substitution

$$\phi_a(\epsilon_a) = u_1, \quad \phi_b(\epsilon_b) = u_2, \quad \phi_c(\epsilon_c) = d$$

can be obtained as the superposition of wave functions generated by the AM compositions

$$((u_1 \oplus u_2)_J \oplus d)_{1/2}, \quad ((d \oplus u_1)_J \oplus u_2)_{1/2}, \quad ((u_2 \oplus d)_J \oplus u_1)_{1/2} \quad (45)$$

for $J = 1, 2$.

2 Conclusion

Our study was focused on the many-fermion system carrying spin $J = 1/2$, however the relation (38) can be generalized for arbitrary spin J

$$|\langle \mathbb{S}_z \rangle| \leq \frac{J}{3} \quad (46)$$

provided that:

(1) the intrinsic motion of the fermions inside the system (composite particle) is relativistic ($\tilde{\mu} \rightarrow 0$),

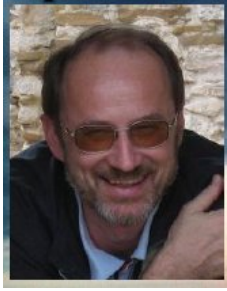
(2) mean value $\langle \mathbb{S}_z \rangle$ include an averaging over possible composition patterns (if the number of fermions $n \geq 3$)

The ratio $\tilde{\mu} = \langle m/\epsilon \rangle$ is of key importance, since it controls a "contraction" of the spin component (46) which is compensated by the OAM. It is a pure effect of relativistic quantum mechanic. The obtained results for $J = 1/2$ have been applied to the description of the proton spin structure in terms of the structure functions g_1 and g_2 in Ref. [4], where we have suggested the proton studied at polarized deep inelastic scattering is an ideal instrument for the study of this relativistic effect.

Acknowledgment: This work was supported by the project LG130131 of Ministry of Education, Youth and Sports of the Czech Republic.

References

- [1] L.D. Landau, E.M. Lifshitz et al., Quantum Electrodynamics (Course of Theoretical Physics, vol. 4), Elsevier Science Ltd., 1982.
- [2] L.C. Biedenharn, J.D. Louck, Angular Momentum in Quantum Physics: Theory and Application, Cambridge University Press 1985.
- [3] V.B. Berestetsky, A.Z. Dolginov and K.A. Ter-Martirosyan, Angular Functions of Particles with Spins (in Russian), JETP 20, 527-535 (1950).
- [4] P. Zavada, Phys. Rev. D **89**, 014012 (2014).



**Dedicated to the blessed memory
of Alexander Petrovich Bakulev
(25 June 1956 - 28 September, 2012)**

Our friend and colleague, the well-known theorist Alexander Petrovich Bakulev, passed away unexpectedly on September 28, 2012. This memorial section collects the reports which are related to his various scientific activities and presents some of the obtained results. It is by no means complete — it is rather a personal recollection.

Alexander (Sasha) Bakulev was born in Moscow on June 25, 1956 in a family with deep academic traditions. He graduated with honors from the Physical Faculty of the Moscow State University and completed in 1982 his postgraduate studies with a focus on statistical physics. After the defence of his Ph.D. thesis, he joined the Central Institute of Scientific Information (VINITI), where he worked as an editor of the physics department until his untimely death.

The career of Sasha took a decisive turn through Prof. A.V. Radyushkin who introduced him into the subject of Quantum Chromodynamics (QCD). In the year 1992, he became a member of Bogoliubov Laboratory of Theoretical Physics (BLTP), JINR, which remained his home institution for the rest of his life. His work with Radyushkin was successful. Their first publication [1] about the electromagnetic pion form factor (FF) is now well-known in the community. In the year 2000 it was followed by another successful common paper in collaboration with N. G. Stefanis on form factors in the space- and time- like region [2].

During his work at the BLTP, Sasha authored and coauthored more than 60 articles in peer-reviewed journals and proceedings' contributions to international conferences. Sasha developed during his career a strong scientific interest to various subjects in physics. However, his main attention was devoted to the studies of strong interactions within QCD. Indeed, working together with S. V. Mikhailov and N. G. Stefanis, he significantly improved and extended the method of QCD sum rules with nonlocal condensates in their applications to the meson form factors. This fruitful collaboration over a dozen of years provided insight into the pion structure in terms of the leading-twist pion distribution amplitude [3] — now with 135 citations in the arXiv. In a series of articles [4–6], Sasha and his collaborators have been able to describe the important process $\gamma\gamma^* \rightarrow \pi^0$ in good agreement with the experimental data using purely QCD without employing any fit parameter. These works found positive response and recognition from the physics community and have received two times the Second JINR Prize (2002 and 2013).

The other main subject in Sasha's research concerned the use of Analytic Perturbation Theory (APT), developed in the nineties by D.V. Shirkov and I.L. Solovtsov. Indeed, together with N.G. Stefanis and collaborators they applied APT with next-to-leading order accuracy to the pion electromagnetic FF [7] and were able to minimize the dependence on the renormalization-scheme and scale-setting parameters. In combination with the non-factorizable part of FF, they were able to reproduce the existing experimental data in a reasonable way. This work has found strong attention both by theorists and ex-

perimentalists and has currently 120 citations in the arXiv. Later A.P. Bakulev, S.V. Mikhailov and N.G. Stefanis generalized the original APT to the case of a fractional index of the APT couplings, giving rise to Fractional Analytic Perturbation Theory (FAPT) both for Euclidian [8] and Minkowski [9] spaces. Moreover, FAPT allows one to apply the renormalization-group method to nonpower series of the strong couplings and to consider a more general class of quantities in this framework [10]. This activity culminated in Sasha’s review [11] on FAPT in the year 2009, which is still topical and will remain so for the years to come.

Sasha has lived every instant of his life as being a gift from God — enthusiastically and cheerfully. He was even able to transfer this positive spirit to all people around him, making them forget their worries with his smile. He was always striving to be helpful to his colleagues considering it as a kind of “mission”, though for him it was just his natural way of life. Sasha will remain alive in our hearts.

Sergey V. Mikhailov and Nico G. Stefanis

References

- [1] A. P. Bakulev, A. V. Radyushkin, “Nonlocal condensates and QCD sum rules for the pion form-factor” Phys. Lett. **B271**, 223 (1991).
- [2] A. P. Bakulev, A. V. Radyushkin and N. G. Stefanis, “Form-factors and QCD in space - like and time - like region,” Phys. Rev. D **62**, 113001 (2000)
- [3] A. P. Bakulev, S. V. Mikhailov, N. G. Stefanis, “QCD-based pion distribution amplitudes confronting experimental data”, Phys. Lett. B **508**, 279 (2001) [Erratum-ibid. B **590**, 309 (2004)].
- [4] A. P. Bakulev, S. V. Mikhailov, N. G. Stefanis, “Unbiased analysis of CLEO data beyond LO and pion distribution amplitude”. Phys. Rev. D **67**, 074012 (2003). “CLEO and E791 data: A smoking gun for the pion distribution amplitude?” Phys. Lett. B **578**, 91 (2004).
- [5] A. P. Bakulev, S. V. Mikhailov, A. V. Pimikov, N. G. Stefanis, “Pion-photon transition—the new QCD frontier”, Phys. Rev. D **84**, 034014 (2011).
- [6] A. P. Bakulev, S. V. Mikhailov, A. V. Pimikov, N. G. Stefanis, “Comparing antithetic trends of data for the pion-photon transition form factor,” Phys. Rev. D **86**, 031501 (2012)
- [7] A. P. Bakulev, K. Passek-Kumericki, W. Schroers, N. G. Stefanis, “Pion form-factor in QCD: From nonlocal condensates to NLO analytic perturbation theory” Phys. Rev. **D70**, 033014 (2004) [Erratum-ibid. D **70**, 079906 (2004)].
- [8] A. P. Bakulev, S. V. Mikhailov, N. G. Stefanis, “QCD analytic perturbation theory: From integer powers to any power of the running coupling,” Phys. Rev. D **72**, 074014 (2005) [Erratum-ibid. D **72**, 119908 (2005)].

- [9] A. P. Bakulev, S. V. Mikhailov, N. G. Stefanis, “Fractional Analytic Perturbation Theory in Minkowski space and application to Higgs boson decay into a b anti-b pair,” *Phys. Rev. D* **75**, 056005 (2007) [Erratum-ibid. *D* **77**, 079901 (2008)].
 - [10] A. P. Bakulev, S. V. Mikhailov, N. G. Stefanis, “Higher-order QCD perturbation theory in different schemes: From FOPT to CIPT to FAPT,” *JHEP* **1006**, 085 (2010).
 - [11] A. P. Bakulev, “Global Fractional Analytic Perturbation Theory in QCD with Selected Applications”, *Phys. Part. Nucl.* **40**, 715 (2009).
-

APT/FAPT APPLICATIONS IN THE LOW-ENERGY QCD DOMAIN

V.L. Khandramai[†]

Gomel State Technical University, 246746 Gomel, Belarus

[†] *E-mail: v.khandramai@gmail.com*

Abstract

Analytic perturbation theory (APT) and its fractional generalization (FAPT) are the closed theoretical schemes without unphysical singularities and additional phenomenological parameters which allow one to combine renormgroup (RG) invariance, Q^2 -analyticity, compatibility with linear integral transformations and essentially incorporate nonperturbative structures. We provide a package “FAPT” based on the system *Mathematica* for QCD calculations in the framework of Analytic approach, which are needed to compute analytic couplings up to four-loops of RG running and to use it for both schemes: with fixed number of active flavours n_f , $\mathcal{A}_\nu(Q^2; n_f)$, $\mathfrak{A}_\nu(s; n_f)$, and the global one with taking into account all heavy-quark thresholds, $\mathcal{A}_\nu^{glob}(Q^2)$, $\mathfrak{A}_\nu^{glob}(s)$. Applications of this package to Bjorken sum rule higher-twist analysis considered.

1 Introduction

At a time when the precision of the Deep Inelastic Scattering data is being improved and the subtle effects such as higher twists contributions become topical task of studying, the improvement of the theoretical description of the low-energy QCD domain is necessary. One of the directions of such improvement is based on the Analytic Perturbation Theory and Fractional Analytic Perturbation Theory. The APT [1] yields a sensible description of hadronic quantities in QCD, though there are alternative approaches to the singularity of effective charge in QCD — in particular, with respect to the deep infrared region $Q^2 < \Lambda^2$. One of the main advantages of the APT analysis is much faster convergence of the APT nonpower series as compared with the standard PT power series. The APT approach was

applied to calculate properties of a number of hadronic processes (for a detailed review see [2, 3] and references therein).

The generalization of APT for the fractional powers of an effective charge was done in [4, 5]. The important advantage of FAPT in this case is that the perturbative results start to be less dependent on the factorization scale. This reminds the results obtained with the APT and applied to the analysis of the pion form factor in the $O(\alpha_s^2)$ approximation, where the results also almost cease to depend on the choice of the renormalization scheme and its scale. The process of the Higgs boson decay into a $b\bar{b}$ pair of quarks was studied within a FAPT-type framework in [6] and within the FAPT in [5, 7]. The results on the resummation of nonpower-series expansions of the Adler function of scalar D_S and a vector D_V correlators within the FAPT were presented in [8]. The interplay between higher orders of the perturbative QCD expansion and higher-twist contributions in the analysis of recent Jefferson Lab data on the lowest moment of the spin-dependent proton structure function, $\Gamma_1^p(Q^2)$, was studied in [9] using both the standard PT and APT/FAPT. The FAPT technique was also applied to analyse the structure function $F_2(x)$ [10, 11] and xF_3 [12], calculate binding energies and masses of quarkonia [13]. All these successful applications of APT/FAPT necessitate to have a reliable mathematical tool for extending the scope of these approaches. In this paper, we present the theoretical background which is necessary for the running of $\mathcal{A}_\nu[L]$ and $\mathfrak{A}_\nu[L]$ in the framework of APT and its fractional generalization, FAPT, and which is collected in the easy-to-use *Mathematica* package “FAPT” [14]. This task has been partially realized for APT as package *QCDAAPT* in [15]. We have organized “FAPT” in the same manner as the well-known package “RunDec” [16]. A few examples of APT and FAPT applications are given.

2 Basic relations

Let us start with the standard definitions used in “FAPT” for standard PT calculations. The perturbation theory in QCD in the region of space-like momentum transfer $Q^2 = -q^2 > 0$ is based on expansions in a series in powers of the running coupling $\alpha_s(\mu^2 = Q^2)$, which is defined through equation

$$\frac{da_{(\ell)}[L; n_f]}{dL} = - (a_{(\ell)}[L; n_f])^2 \left[1 + \sum_{k \geq 1}^{\ell} c_k(n_f) (a_{(\ell)}[L; n_f])^k \right], \quad (1)$$

where n_f is the number of active flavours, $b_k(n_f)$ are β -function coefficients [17], $L = \ln(Q^2/\Lambda^2)$ and Λ is the QCD scale, with the following notation: $\beta_f \equiv b_0(n_f)/4\pi$, $a_{(\ell)}(\mu^2; n_f) \equiv \beta_f \alpha_s^{(\ell)}(\mu^2; n_f)$ and $c_k(n_f) \equiv b_k(n_f)/b_0(n_f)^{k+1}$.

In the one-loop approximation ($c_k(n_f) = b_k(n_f) = 0$ for all $k \geq 1$) we have the well-known solution $a_{(1)}[L] = 1/L$ with the Landau pole singularity at $L \rightarrow 0$. In the two-loop approximation ($c_k(n_f) = b_k(n_f) = 0$ for all $k \geq 2$) the exact solution of Eq. (1) is also known [18]

$$a_{(2)}[L; n_f] = \frac{-c_1^{-1}(n_f)}{1 + W_{-1}(z_W[L])} \quad \text{with} \quad z_W[L] = -c_1^{-1}(n_f) e^{-1-L/c_1(n_f)}, \quad (2)$$

where $W_{-1}[z]$ is the appropriate branch of the Lambert function.

The three- ($c_k(n_f) = b_k(n_f) = 0$ for all $k \geq 3$) and higher-loop solutions $a_{(\ell)}[L; n_f]$ can be expanded in powers of the two-loop one, $a_{(2)}[L; n_f]$ (see [19] for details):

$$a_{(\ell)}[L; n_f] = \sum_{n \geq 1} C_n^{(\ell)} (a_{(2)}[L; n_f])^n. \quad (3)$$

The coefficients $C_n^{(\ell)}$ can be evaluated recursively. As has been shown in [19], this expansion has a finite radius of convergence, which appears to be sufficiently large for all values of n_f of practical interest.

The ℓ -loop solution $\alpha_s^{(\ell)}(Q^2)$ has an ℓ -root singularity of the type $L^{-1/\ell}$ at $L = 0$, which produces the pole as well in the ℓ -order term $d_\ell \alpha_s^\ell(Q^2)$. This prevents the application of perturbative QCD in the low-momentum space-like regime, $Q^2 \sim \Lambda^2$, with the effect that hadronic quantities, calculated at the partonic level in terms of a power-series expansion in $\alpha_s(Q^2)$, are not everywhere well defined.

The analytic couplings in the Euclidian $\mathcal{A}_\nu^{(\ell)}[L; n_f]$ and Minkowskian $\mathfrak{A}_\nu^{(\ell)}[L_s; n_f]$ domains calculated in APT with the spectral densities $\rho_\nu^{(\ell)}(\sigma; n_f)$ which enter into the Källén–Lehmann spectral representation:

$$\mathcal{A}_\nu^{(\ell)}[L; n_f] = \int_0^\infty \frac{\rho_\nu^{(\ell)}(\sigma; n_f)}{\sigma + Q^2} d\sigma = \int_{-\infty}^\infty \frac{\rho_\nu^{(\ell)}[L_\sigma; n_f]}{1 + \exp(L - L_\sigma)} dL_\sigma, \quad (4)$$

$$\mathfrak{A}_\nu^{(\ell)}[L_s; n_f] = \int_s^\infty \frac{\rho_\nu^{(\ell)}(\sigma; n_f)}{\sigma} d\sigma = \int_{L_s}^\infty \rho_\nu^{(\ell)}[L_\sigma; n_f] dL_\sigma, \quad (5)$$

where spectral functions are

$$\rho_\nu^{(\ell)}[L; n_f] \equiv \frac{1}{\pi} \mathbf{Im} (\alpha_s^{(\ell)}[L - i\pi; n_f])^\nu = \frac{\sin[\nu \varphi_{(\ell)}[L; n_f]]}{\pi (\beta_f R_{(\ell)}[L; n_f])^\nu}. \quad (6)$$

In the one-loop approximation the corresponding functions have the simplest form

$$\varphi_{(1)}[L] = \arccos\left(\frac{L}{\sqrt{L^2 + \pi^2}}\right), \quad R_{(1)}[L] = \sqrt{L^2 + \pi^2}, \quad (7)$$

whereas at the higher-loop orders they have a more complicated form and can not be simply calculated.

We developed a package “FAPT” performs the calculations of the basic required objects: $(\alpha_s^{(\ell)}[L, n_f])^\nu$, $\mathcal{A}_\nu^{(\ell)}[L, n_f]$ in Eq. (4) and $\mathfrak{A}_\nu^{(\ell)}[L, n_f]$ in Eq. (5) up to the N³LO approximation with a fixed number of active flavours n_f and the global one with taking into account all heavy-quark thresholds (for more details and description of procedures see [14]).

3 Applications to DIS

As an example of the APT application to DIS processes, we present the Bjorken sum rule (BSR) analysis. The BSR claims that the difference between the proton and neutron structure functions integrated over all possible values

$$\Gamma_1^{p-n}(Q^2) = \int_0^1 [g_1^p(x, Q^2) - g_1^n(x, Q^2)] dx, \quad (8)$$

of the Bjorken variable x in the limit of large momentum squared of the exchanged virtual photon at $Q^2 \rightarrow \infty$ is equal to $g_A/6$, where the nucleon axial charge $g_A = 1.2701 \pm 0.0025$ [17]. Commonly, one represents the Bjorken integral in Eq. (8) as a sum of perturbative and higher twist contributions

$$\Gamma_1^{p-n}(Q^2) = \frac{g_A}{6} \left[1 - \Delta_{\text{Bj}}(Q^2) \right] + \sum_{i=2}^{\infty} \frac{\mu_{2i}^{p-n}}{Q^{2i-2}}. \quad (9)$$

The perturbative QCD correction $\Delta_{\text{Bj}}(Q^2)$ has a form of the power series in the QCD running coupling $\alpha_s(Q^2)$. At the up-to-date four-loop level in the massless case in the modified minimal subtraction ($\overline{\text{MS}}$) scheme, for three active flavors, $n_f = 3$, it looks like [20]

$$\Delta_{\text{Bj}}^{\text{PT}}(Q^2) = 0.3183 \alpha_s(Q^2) + 0.3631 \alpha_s^2(Q^2) + 0.6520 \alpha_s^3(Q^2) + 1.804 \alpha_s^4(Q^2). \quad (10)$$

The perturbative representation (10) violates analytic properties due to the unphysical singularities of $\alpha_s(Q^2)$. To resolve the issue, we apply APT. In particular, the four-loop APT expansion for the perturbative part $\Delta_{\text{Bj}}^{\text{PT}}(Q^2)$ is given by the formal replacement

$$\Delta_{\text{Bj}}^{\text{PT}}(Q^2) = \sum_{k \leq 4} c_k \alpha_s^k(Q^2) \quad \Rightarrow \quad \Delta_{\text{Bj}}^{\text{APT}}(Q^2) = \sum_{k \leq 4} c_k \mathcal{A}_k(Q^2). \quad (11)$$

Previously, a detailed higher-twist analysis of the BSR in the framework of APT performed in [21, 9], where best convergence of both the higher orders and higher-twist series, weak μ -scale and loops dependence in Eq. (11) and as a main result a satisfactory description of the BSR data down to $Q \sim \Lambda \simeq 350$ MeV were founded.

In this paper we concentrate on the application of the FAPT approach by the example of the RG-evolution of the non-singlet higher-twist $\mu_4^{p-n}(Q^2)$ in Eq. (9). The evolution of the higher-twist terms $\mu_{6,8,\dots}^{p-n}$ is still unknown. The RG-evolution of $\mu_4^{p-n}(Q^2)$ in the standard PT reads

$$\mu_{4,PT}^{p-n}(Q^2) = \mu_{4,PT}^{p-n}(Q_0^2) \left[\frac{\alpha_s(Q^2)}{\alpha_s(Q_0^2)} \right]^\nu, \quad \nu = \gamma_0 / (8\pi\beta_0), \quad \gamma_0 = \frac{16}{3} C_F, \quad C_F = \frac{4}{3}. \quad (12)$$

In the framework of FAPT the corresponding expression reads as follows:

$$\mu_{4,APT}^{p-n}(Q^2) = \mu_{4,APT}^{p-n}(Q_0^2) \frac{\mathcal{A}_\nu^{(1)}(Q^2)}{\mathcal{A}_\nu^{(1)}(Q_0^2)}. \quad (13)$$

The best fits for $\mu_4^{p-n}(Q^2)$ taking into account the corresponding RG-evolution with $Q_0^2 = 1 \text{ GeV}^2$ as a normalization point and without the RG-evolution presented in Table 1. We do not take into account the RG-evolution in μ_4^{p-n} for the standard PT calculations and compare with FAPT since the only effect of that would be the enhancement of the Landau singularities by extra divergencies at $Q^2 \sim \Lambda^2$, whereas at higher $Q^2 \sim 1 \text{ GeV}^2$ the evolution is negligible with respect to other uncertainties. One can see from Table 1 that the fit results become more stable with respect to Q_{min} variations, which reduces the theoretical uncertainty of the BSR analysis.

Table 1: Results of higher twist extraction from the JLab data on BSR with inclusion and without inclusion of the RG-evolution of $\mu_4^{p-n}(Q^2)$ normalized at $Q_0^2 = 1 \text{ GeV}^2$.

Method	$Q_{min}^2, \text{ GeV}^2$	μ_4^{p-n}/M^2	μ_6^{p-n}/M^4	μ_8^{p-n}/M^6
	0.47	-0.055(3)	0	0
NNLO APT	0.17	-0.062(4)	0.008(2)	0
no evolution	0.10	-0.068(4)	0.010(3)	-0.0007(3)
	0.47	-0.051(3)	0	0
NNLO APT	0.17	-0.056(4)	0.0087(4)	0
with evolution	0.10	-0.058(4)	0.0114(6)	-0.0005(8)

4 Summary

To summarize, APT provides a natural way for the coupling constant and related quantities. These properties of the coupling constant are the universal loop-independent infrared limit and weak dependence on the number of loops. At the same time, FAPT provides an effective tool to apply the Analytic approach for RG improved perturbative amplitudes. This approaches was used in many applications.

The singularity-free, finite couplings $\mathcal{A}_\nu(Q^2)$, $\mathfrak{A}_\nu(s)$ appear in APT/FAPT as analytic images of the standard QCD coupling powers $\alpha_s^\nu(Q^2)$ in the Euclidean and Minkowski domains, respectively. In this paper, we presented the theoretical background, used in a package “FAPT” [14] based on the system **Mathematica** for QCD calculations in the framework of APT/FAPT, which are needed to compute these couplings up to N³LO of the RG running.

Acknowledgments

Author retains a deep sense of gratitude to excellent scientist and nice person Alexander Petrovich Bakulev. This talk is dedicated to implementing of his idea to give the public a convenient tool for calculations in Fractional APT.

I would like to thank S.V. Mikhailov, A.L. Kataev, O.P. Solovtsova, O.V. Teryaev and N.G. Stefanis for stimulating discussions and useful remarks. This work was supported in part by BelFBR Grants No. F12D-002 and No. F13M-143 and by RFBR Grant No. 11-01-00182.

References

- [1] D.V. Shirkov, I.L. Solovtsov, Phys. Rev. Lett. **79** (1997) 1209.
- [2] D.V. Shirkov, I.L. Solovtsov, Theor. Math. Phys. **150** (2007) 132.
- [3] A.P. Bakulev, Phys. Part. Nucl. **40** (2009) 715.
- [4] A.P. Bakulev, S.V. Mikhailov, N.G. Stefanis, Phys. Rev. **D72** (2005) 074014; *Erratum: ibid.* **D72** (2005) 119908(E).
- [5] A.P. Bakulev, S.V. Mikhailov, N.G. Stefanis, Phys. Rev. **D75** (2007) 056005; *Erratum: ibid.* **D77** (2008) 079901(E).

- [6] D.J. Broadhurst, A.L. Kataev, C.J. Maxwell, Nucl. Phys. **B592** (2001) 247.
- [7] N.G. Stefanis, Phys. Part. Nucl. **44** (2013) 494.
- [8] A.P. Bakulev, S.V. Mikhailov, N.G. Stefanis, JHEP **1006** (2010) 085.
- [9] R.S. Pasechnik, D.V. Shirkov, O.V. Teryaev, O.P. Solovtsova, V.L. Khandramai, Phys. Rev. **D81** (2010) 016010.
- [10] G. Cvetič, A.Y. Illarionov, B.A. Kniehl, A.V. Kotikov, Phys. Lett. **B679** (2009) 350.
- [11] A.V. Kotikov, V.G. Krivokhizhin, B.G. Shaikhatdenov, Phys. Atom. Nucl. **75** (2012) 507.
- [12] A.V. Sidorov, O.P. Solovtsova, arXiv:1312.3082 [hep-ph].
- [13] C. Ayala, G. Cvetič, Phys. Rev. **D87** (2013) 054008.
- [14] A.P. Bakulev, V.L. Khandramai, Comp. Phys. Comm. **184** (2013) 183.
- [15] A.V. Nesterenko, C. Simolo, Comp. Phys. Comm. **181** (2010) 1769.
- [16] K.G. Chetyrkin, J.H. Kühn, M. Steinhauser, Comp. Phys. Comm. **133** (2000) 43.
- [17] J. Beringer *et al.*, Phys. Rev. **D86** (2012) 010001.
- [18] E. Gardi, G. Grunberg, M. Karliner, JHEP **07** (1998) 007.
- [19] B.A. Magradze, Few Body Syst. **40** (2006) 71.
- [20] P.A. Baikov, K.G. Chetyrkin, J.H. Kühn, Phys. Rev. Lett. **104** (2010) 132004.
- [21] V.L. Khandramai, R.S. Pasechnik, D.V. Shirkov, O.P. Solovtsova, O.V. Teryaev, Phys. Lett. **B706** (2012) 340.

WIDTHS AND TRANSITION FORM FACTORS OF MESONS: CONSIDERATION FROM AXIAL ANOMALY.

Ya. Klopot^{2†}, A.G. Oganesian^{1,2} and O.V. Teryaev²

(1) *ITEP, Moscow, Russia*

(2) *JINR, Dubna, Russia*

† *E-mail: armen@itep.ru*

*This talk is dedicated to the memory
of our friend and colleague Aleksander Bakulev.*

Abstract

The approach of the calculation the transition formfactors (TFF) of pseudoscalar mesons, based on axial anomaly, is discussed. It is shown that in this approach TFF can be obtained both in space- and timelike regions. Obtained results are in good agreement with experiment.

Transition form factors (TFF) of pseudoscalar mesons are investigated in a very large number of paper, particularly in the framework of light cone sum rules [1–5], also by use of the flatlike modifications of the distribution amplitude [6, 7], and various other approaches, like a chiral quark model [8] and many others. In this talk we will discuss a new approach to investigate TFF of π^0 , η , η' mesons by use of the axial anomaly [9, 10]. The approach, based on relatively less known form of axial anomaly - the dispersion representation of it (see [11] for real photon case and [12–14] for virtual photons) allow one to describe the pseudoscalar mesons TFF at all Q^2 , even beyond the QCD factorization. The talk is based on our papers [15–17]. At the end of the talk we discuss a little the analytical continuation of our approach to time-like region.

The axial anomaly in QCD results in a non-vanishing divergence of axial current in the chiral limit. While singlet axial current acquires both electromagnetic and gluonic anomalous terms, diagonal components of the octet of axial currents, i.e., isovector $J_{\alpha 5}^{(3)} = \frac{1}{\sqrt{2}}(\bar{u}\gamma_\alpha\gamma_5 u - \bar{d}\gamma_\alpha\gamma_5 d)$ and octet $J_{\alpha 5}^{(8)} = \frac{1}{\sqrt{6}}(\bar{u}\gamma_\alpha\gamma_5 u + \bar{d}\gamma_\alpha\gamma_5 d - 2\bar{s}\gamma_\alpha\gamma_5 s)$ axial currents acquire an electromagnetic anomalous term only.

The vector-vector-axial triangle graph amplitude, where the axial anomaly occurs, contains an axial current $J_{\alpha 5}$ and two electromagnetic currents

$$T_{\alpha\mu\nu}(k, q) = \int d^4x d^4y e^{(ikx+iqy)} \langle 0 | T \{ J_{\alpha 5}(0) J_\mu(x) J_\nu(y) \} | 0 \rangle, \quad (1)$$

where k and q are the photons' momenta. In what follows, we limit ourselves to the case when one of the photons is on-shell ($k^2 = 0$).

Considering the unsubtracted dispersion relations, which result in the finite subtraction for the axial current divergence, one obtains the ASRs [13]:

$$\int_0^\infty A_3^{(a)}(s, q^2; m_i^2) ds = \frac{1}{2\pi} N_c C^{(a)}, \quad a = 3, 8, \quad (2)$$

where $N_c = 3$ is a number of colors, $C^{(3)} = \frac{1}{3\sqrt{2}}$ and $C^{(8)} = \frac{1}{3\sqrt{6}}$ are charge factors, m_i are quark masses and A_3 is the imaginary part of the invariant amplitude at the tensor structure $k_\nu \varepsilon_{\alpha\mu\rho\sigma} k^\rho q^\sigma$ in the variable $(k+q)^2 = s > 0$. The ASR (2) has a remarkable property – both perturbative and nonperturbative corrections to the integral are absent¹. The perturbative corrections are excluded because of the Adler-Bardeen theorem [18], while the nonperturbative corrections are also absent, as is expected from 't Hooft's principle. 't Hooft's principle in its original form [19] implies that the anomalies of the fundamental fields are reproduced on the hadron level. In the dispersive approach this means the absence of the corrections to the dispersive sum rules.

Let us stress that the spectral density $A_3^{(a)}(s, Q^2; m^2)$ itself can have both perturbative and nonperturbative corrections (however, the first-order correction $\propto \alpha_s$ is zero in the massless limit [20]), while the integral $\int_{4m^2}^{\infty} A_3^{(a)}(s, Q^2; m^2) ds$ equals exactly $\frac{1}{2\pi} N_c C^{(a)}$.

In what follows, we consider the case when one of the photons is real ($k^2 = 0$) while the other is real or virtual ($Q^2 = -q^2 \geq 0$).

Let us start with isovector case.

Saturating the three-point correlation function (1) with the resonances, singling out the lower one (pion) contribution and absorbing the higher resonances contributions by the ‘‘continuum’’ term $\int_{s_0^{(3)}}^{\infty} A_3^{(3)}(s, Q^2; m^2)$, we get the following (exact) relation

$$\pi f_\pi F_{\pi\gamma}(Q^2; m^2) = \frac{1}{2\pi} N_c C^{(3)} - \int_{s_0^{(3)}}^{\infty} A_3^{(3)}(s, Q^2; m^2) ds. \quad (3)$$

Here the coupling (decay) constants f_M^a are defined as $\langle 0 | J_{\alpha 5}^{(a)}(0) | M(p) \rangle = i p_\alpha f_M^a$, and the form factors $F_{M\gamma}$ of the transitions $\gamma\gamma^* \rightarrow M$ are defined as

$$\int d^4x e^{ikx} \langle M(p) | T \{ J_\mu(x) J_\nu(0) \} | 0 \rangle = \epsilon_{\mu\nu\rho\sigma} k^\rho q^\sigma F_{M\gamma}. \quad (4)$$

The lower limit $s_0^{(3)}$ of the integral has a sense of the interval of the duality of a pion (also often it is called ‘‘continuum threshold’’), Though it can be estimated from two-point sum rules (supposing, as usual, this parameter be the same for different 2 and 3-point correlator), but it can be determined directly from the ASR, as we will discuss later. The contribution to the spectral density $A_3^{(3)}(s, Q^2; m^2)$ for given flavor q is [13],

$$A_3^{(q)}(s, Q^2; m_q^2) = \frac{e_q^2}{2\pi} \frac{1}{(Q^2 + s)^2} \left(Q^2 R + 2m_q^2 \ln \frac{1+R}{1-R} \right), \quad (5)$$

where $R(s, m_q^2) = \sqrt{1 - \frac{4m_q^2}{s}}$.

From (3), (5), neglecting the quark mass, we obtain for the pion TFF,

$$F_{\pi\gamma}(Q^2; m^2) = \frac{1}{2\sqrt{2}\pi^2 f_\pi} \frac{s_0^{(3)}}{s_0^{(3)} + Q^2}. \quad (6)$$

The ASR are valid for all Q^2 , so our result (6) is also valid for all photon virtualities from zero to infinity. As we see, in the massless limit, the spectral density (5) is proportional to $\delta(s)$ at $Q^2 = 0$, so the continuum term in the ASR (3) goes to zero.

¹In the case of the singlet channel ($a = 0$), this property is violated because of the gluonic anomaly.

This corresponds to the well-known fact, that for the case of two real photons anomaly is saturated by pion only. From the other side for virtual photon case anomaly is not saturated by pion (it contribution quickly decreases), but with all infinite range of axial and pseudoscalar resonances, i.e. it become pure collective effect.

If we suppose, as usual, that duality region weakly depend on Q^2 (to be constant at first approximation), then $s_0^{(3)}$ can be determined directly from the high- Q^2 asymptotic of ASR. QCD factorization in this limit predicts $Q^2 F_{\pi\gamma}^{as} = \sqrt{2} f_\pi$ [21], so the high- Q^2 limit of (6) immediately leads to $s_0^{(3)} = 4\pi^2 f_\pi^2 = 0.67 \text{ GeV}^2$. This expression, substituted in (6) with, gives

$$F_{\pi\gamma}(Q^2; 0) = \frac{1}{2\sqrt{2}\pi^2 f_\pi} \frac{4\pi^2 f_\pi^2}{4\pi^2 f_\pi^2 + Q^2}, \quad (7)$$

so it proves the Brodsky-Lepage interpolation formula for the pion TFF [22], which was later confirmed by Radyushkin [23] in the approach of local quark-hadron duality.

Let us stress that in this way we found that it is a direct consequence of the anomaly sum rule (which is an exact nonperturbative QCD relation). Let me also note, that obtained value of $s_0^{(3)} = 0.67 \text{ GeV}^2$ is very close to those from two-point correlation function analysis ($s_0^{(3)} = 0.75 \text{ GeV}^2$) [24]. The result for pion TFF(6) together with the data from the CELLO [25], CLEO [26], BABAR [27] and Belle [29] collaborations is shown on Fig.1 by dashed line.

One can see, that while the anomaly predicted pion TFF is in good agreement with CLEO, CELLO and Belle results, but strongly contradict to BABAR result at large Q^2 . In our papers [16, 17] by use of pure dimension arguments it is shown, that possible nonperturbative contribution to spectral density of dimension 4 and higher can not resolve this contradiction with BABAR data. It was shown, that if BABAR data are correct, then unavoidably contribution of non OPE operator of dimension 2 should exist and the possible form of such contribution was offered. Then equation (6) modified as

$$F_{\pi\gamma}(Q^2) = \frac{1}{2\sqrt{2}\pi^2 f_\pi} \frac{s_0^{(3)}}{s_0^{(3)} + Q^2} \left[1 + \frac{\lambda Q^2}{s_0^{(3)} + Q^2} \left(\ln \frac{Q^2}{s_0^{(3)}} + \sigma \right) \right]. \quad (8)$$

where λ and σ are dimensionless parameters.

The fit of (8) to the whole set of data (CLEO+CELLO+Belle+BABAR)) gives $\lambda = 0.12$, $\sigma = -2.5$ with $\chi^2/d.o.f. = 0.9$ ($d.o.f. = 35$). The plot of $Q^2 F_{\pi\gamma}$ for these parameters is depicted in Fig.1 as a solid curve.

Let us emphasize that the correction (second term in brackets in 8) requires a log Q^2 term in spectral density A_3 itself and this is rather nontrivial requirement.

Finally we can conclude that if one do not suppose some new physics, than anomaly based result for pion TFF are in agreement of BELLE results at large Q^2 and contradict to BABAR data. If BABAR data is taken into account then anomaly indicate on the existence of contribution of dimension 2 operator. I would like to stress that our conclusion is in agreement of the extremely careful analysis done in [2, 3], where it was shown, that BABAR data can not be explained within usual OPE expansion.

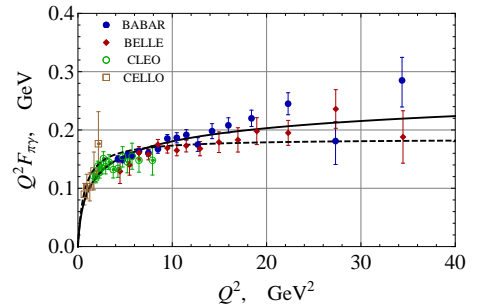


Figure 1: Pion TFF with and without correction (solid and dashed curves correspondingly).

The derivation of ASR for the octet channel, is like those for the isovector case we discuss before. In this case again only the electromagnetic anomaly gives a contribution and the gluonic anomaly is absent. However, in comparing to the isovector channel, here we have some differences. First, due to significant mixing in η - η' system, the η' meson contributes to the octet channel. Since η' decays into two real photons, it should be taken into account explicitly along with the η meson. Second, the strange mass contribution to spectral density in the octet channel $A_3^{(8)}$ is not negligible, but numerically is rather small, so in this paper we restrict ourselves to the leading approximation, where the quark mass corrections are neglected. Then treating the ASR in the same way as for the isovector channel gives

$$f_\eta^8 F_{\eta\gamma}(Q^2) + f_{\eta'}^8 F_{\eta'\gamma}(Q^2) = \frac{1}{2\sqrt{6}\pi^2} \frac{s_0^{(8)}}{s_0^{(8)} + Q^2}, \quad (9)$$

where $s_0^{(8)}$ is a continuum threshold (duality region) in the octet channel. It can be found in the same way as we discuss before for the isovector channel, i.e. considering the limit of large Q^2 . Then one can then found

$$s_0^{(8)} = 4\pi^2((f_\eta^8)^2 + (f_{\eta'}^8)^2 + 2\sqrt{2}[f_\eta^8 f_\eta^0 + f_{\eta'}^8 f_{\eta'}^0]). \quad (10)$$

Substituting (10) into (9) we can express the TFF directly in the terms of coupling constants without any free parameter. In order to find not only linear combination but the TFF $F_{\eta\gamma}$ and $F_{\eta'\gamma}$ separately, one can use widely discussed in the literature (see, e.g., [28]) hypothesis that the TFF of the nonphysical state $|q\rangle \equiv \frac{1}{\sqrt{2}}(|\bar{u}u\rangle + |\bar{d}d\rangle)$ is related to the pion form factor as $F_{q\gamma}(Q^2) = (5/3)F_{\pi\gamma}(Q^2)$. The states $|q\rangle$ and $|s\rangle \equiv |\bar{s}s\rangle$ are assumed to be expressed in terms of the physical states $|\eta\rangle, |\eta'\rangle$ via the quark-flavor mixing scheme ²

$$|q\rangle = \cos\phi|\eta\rangle + \sin\phi|\eta'\rangle, \quad |s\rangle = -\sin\phi|\eta\rangle + \sin\phi|\eta'\rangle. \quad (11)$$

Then one can relate the form factors:

$$\frac{5}{3}F_{\pi\gamma} = F_{\eta\gamma} \cos\phi + F_{\eta'\gamma} \sin\phi. \quad (12)$$

Now, incorporating this hypothesis into our approach, one can get

$$F_{\eta\gamma}(Q^2) = \frac{5}{12\pi^2 f_s f_\pi} \frac{s_0^{(3)}(\sqrt{2}f_s \cos\phi - f_q \sin\phi)}{s_0^{(3)} + Q^2} + \frac{1}{4\pi^2 f_s} \frac{s_0^{(8)} \sin\phi}{s_0^{(8)} + Q^2}, \quad (13)$$

$$F_{\eta'\gamma}(Q^2) = \frac{5}{12\pi^2 f_s f_\pi} \frac{s_0^{(3)}(\sqrt{2}f_s \sin\phi + f_q \cos\phi)}{s_0^{(3)} + Q^2} - \frac{1}{4\pi^2 f_s} \frac{s_0^{(8)} \cos\phi}{s_0^{(8)} + Q^2}, \quad (14)$$

where $s_0^{(3)} = 4\pi^2 f_\pi^2$, $s_0^{(8)} = (4/3)\pi^2(5f_q^2 - 2f_s^2)$.

The plot of Eqs. (13), (14) with constants from our analysis [17] $f_q = 1.20f_\pi$, $f_s = 1.65f_\pi$, $\phi = 38.1^\circ$ in comparison with experimental data is shown in Fig.2. One can observe a reasonably good agreement with the experimental data. For the decay constants of Ref. [30] one also gets a good description.

²Let me remind that quark-flavor mixing scheme is characterized by 3 parameters - constants f_q, f_s and mixing angle ϕ (see [30])

The agreement with the experimental data may indicate that the effect of a strong anomaly for the $\frac{1}{\sqrt{2}}|\bar{u}u + \bar{d}d\rangle$ state is small and the strong anomaly predominantly appears in the $\bar{s}s$ channel.

Finally let me say a little about time-like region of photon virtuality ($q^2 > 0$). As it was shown in the paper [31], due to the fact, that ASR (2) do not depend of q^2 , one can relatively easy make analytical continuation of this relation from space-like region ($q^2 < 0$) to the time like region ($q^2 > 0$), and then fulfilled our approach directly in time like region and obtain the TFFf at $q^2 > 0$. Surprisingly, the relation for TFF (6), (13), (14) remains the same (clearly Q^2 become negative). For example, the predictions for pion and η mesons TFF are shown in Fig. 3 and Fig. 4 The upper and low boundaries on Fig. 4 correspond to uncertainty of the mixing scheme parameters (taken from [17] and [30]). One can see a good agreements with present experimental data.

This work is supported in part by RFBR, research projects 12-02-00613a, 12-02-00284a, and by the Heisenberg-Landau program (JINR).

References

- [1] A. Khodjamirian, Int. J. Mod. Phys. A **25**, (2010) 513
- [2] S.V. Mikhailov, N.G. Stefanis, Mod. Phys. Lett. A **24**, (2009) 2858
- [3] A.P. Bakulev, S.V. Mikhailov, A.V. Pimikov, N. G. Stefanis, Phys. Rev. D **84**, (2011) 034014; Phys. Rev. D **86**, 031501 (2012)
- [4] S.S. Agaev, V.M. Braun, N. Offen, F.A. Porkert, Phys. Rev. D **83**, (2011) 054020
- [5] P. Kroll, Eur. Phys. J. C **71**, (2011) 1623
- [6] A.V. Radyushkin, Phys. Rev. D **80**, (2009) 094009
- [7] M.V. Polyakov, JETP Lett. **90**, (2009) 228
- [8] A.E. Dorokhov, arXiv:1003.4693 [hep-ph].
- [9] J.S. Bell, R. Jackiw, Nuovo Cim. **A60**, (1969) 47.
- [10] S.L. Adler, Phys. Rev. **177**, 2426-2438 (1969) 2426.
- [11] A.D. Dolgov, V. I. Zakharov, Nucl. Phys. **B27**, (1971) 525.
- [12] J. Horejsi, Phys. Rev. **D32**, (1985) 1029.
- [13] J. Horejsi, O. Teryaev, Z. Phys. **C65**, (1995) 681.
- [14] O.L. Veretin, O. V. Teryaev, Phys. Atom. Nucl. **58**, (1995) 2150.
- [15] Y.N. Klopov, A.G. Oganesian, O.V. Teryaev, Phys. Lett. B **695**, (2011) 130

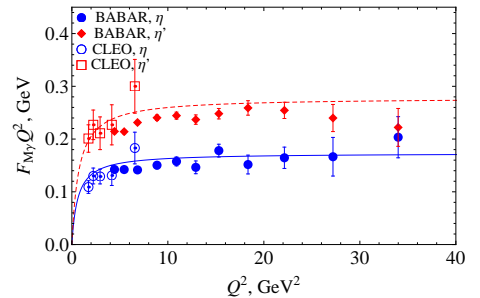


Figure 2: Combinations $F_{\eta\gamma}Q^2$ (blue solid line) and $F_{\eta'\gamma}Q^2$ (red dashed line).

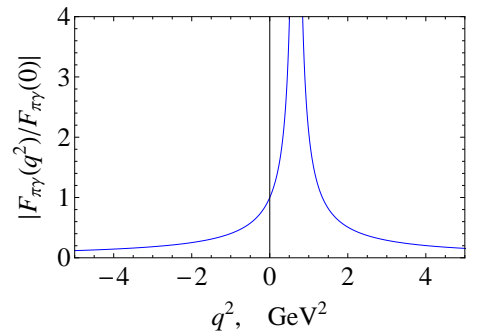


Figure 3: Pion TFF.

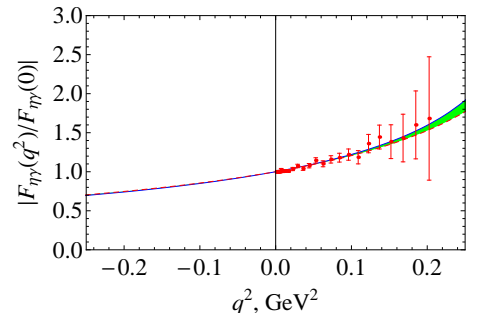


Figure 4: The η meson TFF and A2 Collaboration data [32].

- [16] Y.N. Klopot, A.G. Oganesian, O.V. Teryaev, Phys. Rev. D **84**, (2011) 051901; JETP Lett. **94**, 729 (2011) 729
- [17] Y. Klopot, A. Oganesian, O. Teryaev, Phys. Rev. D **87**, (2013) 036013
- [18] S.L. Adler, W.A. Bardeen, Phys. Rev. **182**, (1969) 1517.
- [19] G. 't Hooft in *“Recent developments in gauge theories”* ed. by G. 't Hooft *et al.*, Plenum Press, New York, 1980.
- [20] F. Jegerlehner, O.V. Tarasov, Phys. Lett. **B639**, (2006) 299.
- [21] G.P. Lepage, S.J. Brodsky, Phys. Rev. **D22**, (1980) 2157.
- [22] S.J. Brodsky, G.P. Lepage, Phys. Rev. **D24**, (1981) 1808.
- [23] A.V. Radyushkin, Acta Phys. Polon. **B26**, (1995) 2067.
- [24] M.A. Shifman, A.I. Vainshtein and V.I. Zakharov, Nucl. Phys. B **147**,(1979) 448.
- [25] H. J. Behrend *et al.* [CELLO Collaboration], Z. Phys. C **49**, 401 (1991).
- [26] J. Gronberg *et al.* [CLEO Collaboration], Phys. Rev. D **57**, (1998) 33.
- [27] B. Aubert *et al.* [BABAR Collaboration], Phys. Rev. D **80**, (2009) 052002.
- [28] P. del Amo Sanchez *et al.* [BABAR Collaboration], Phys. Rev. D **84**, (2011) 052001.
- [29] S. Uehara *et al.* [Belle Collaboration], Phys. Rev. D **86**, (2012) 092007.
- [30] T. Feldmann, P. Kroll and B. Stech, Phys. Rev. D **58**, (1998) 114006.
- [31] Y.N. Klopot, A.G. Oganesian and O.V. Teryaev, [arXiv:1312.1226 [hep-ph]]
- [32] P. Aguilar-Bartolome *et al.* [A2 Collaboration], arXiv:1309.5648 [hep-ex].

COMPARING VACUUM AND HADRONIC HIGHER TWISTS

O.V. Teryaev^{1,†}

(1) *Bogoliubov Laboratory of Theoretical Physics, JINR, Dubna 141980, Russia*

† *E-mail: teryaev@theor.jinr.ru*

Abstract

The similarity between non-local vacuum condensates and TMDs of hadrons is explored. The role of infinite sum of higher twists in inclusive (Bjorken sum rule in DIS) and semi-inclusive (SIDIS) processes is stressed. The hadronic D-term is compared to vacuum energy density (cosmological constant) and similarity of inflation and annihilation is suggested. The strangeness polarization due to axial anomaly is discussed.

1 Introduction

Higher twist (HT) corrections are very important for the applications of QCD at low scales. They correspond to the matrix elements of composite operators between the vacuum and hadronic states. These cases essentially differ as there is no longitudinal momentum in vacuum (and the twist basically reduces to dimension). Still one may look for the similarity between vacuum HTs and *transverse* degrees of freedom of hadronic HTs. In particular, I will address a case of *non-local vacuum condensates* (NLVC) and Transverse-Momentum Dependent Parton Distributions (TMDs) as their analogs.

Sasha Bakulev (together with Anatoly Radyushkin) made a crucial contribution [1] to the development and applications of the NLVC. Few years ago I discussed with him (only briefly, unfortunately) the possible relations between them and TMDs and he reacted with enthusiasm and encouragement, as he usually did. Like all of us, I am badly missing him and his judgment today.

The important property of NLVCs and TMDs is the appearance of infinite sums [2] of HTs. TMDs may be considered [3] as a (partial) sum of all HTs tower, while transverse moments (where Bessel moments [5] should naturally appear because transverse space is 2-dimensional) correspond [4] to definite twists.

The more simple case of all-twists relevance is that of (spin-dependent) DIS in real-photon limit, when contact with low-energy theorems (GDH sum rules) may be achieved [6]. Originally, this was realized by matching of the HT expansion in inverse powers of Q^2 (where QCD perturbative expansion in $\log Q^2$ was also included [7]) and "chiral" expansion in positive powers of Q^2 . It is also possible [2] to represent HT series in integral form, incorporating the analytic properties of virtual Compton amplitude. Even in its simplest version it leads to the rather accurate description of Bjorken sum rule at all Q^2 .

It is interesting, that vacuum analog of so-called Polyakov-Weiss D-term [8] in generalized parton distributions (GPDs) is represented by nothing else than cosmological constant. The observed definite (negative) sign of D-term may, in turn, be interpreted as a positive "effective" cosmological constant in the annihilation channel of respective gravitational formfactor establishing the relation between inflation and annihilation.

2 Resumming HT in spin-dependent DIS

Let us consider as a case study the lowest non-singlet moment of spin-dependent proton and neutron structure functions $g_1^{p,n}$ defined as

$$\Gamma_1^{p-n}(Q^2) = \int_0^1 dx g_1^{p-n}(x, Q^2), \quad (1)$$

with $x = Q^2/2M\nu$, the energy transfer ν , and the nucleon mass M . We imply the elastic contribution at $x = 1$ to be excluded, since the low- Q^2 behavior of “inelastic” $\Gamma_1^{p-n}(Q^2)$, i.e. the Bjorken Sum Rule (BSR), is constrained by the Gerasimov-Drell-Hearn (GDH) sum rule, which allows us to investigate continuation of the Bjorken integral $\Gamma_1^{p-n}(Q^2)$ to low Q^2 scales. As all the higher twists contributions are divergent when $Q^2 \rightarrow 0$, only infinite sum may be matched to GDH value. Let us consider the series

$$S(Q^2) = \sum_1^\infty a_n \left(\frac{M^2}{Q^2}\right)^n, \quad (2)$$

which may correspond either to non-perturbative part (HT) of Γ_1 or to $I_1 = 2M^2\Gamma_1/Q^2$ proportional to photoabsorption cross-sections constrained by GDHSR. By making the crucial step and representing a_n as a moments

$$a_n = \int_{-\infty}^\infty f(x)x^{n-1}, \quad (3)$$

the sum of HTs can be recasted as

$$S(Q^2) = \int_{-\infty}^\infty dx \frac{f(x)M^2}{Q^2 - xM^2}. \quad (4)$$

Such a representation in terms of moments may be compared to the similar one when the standard leading twist partonic expression is derived. The later, besides the nice physical picture, may be justified by correct analytical properties of virtual Compton amplitude, having s and u cuts produced by respective poles (at LO) and cuts in the partonic subprocess.

The similar arguments may be applied for HT resummation. If analytical properties of $S(Q^2)$ are represented by the cut residing at $Q^2 \leq 4m^2$ (m being the mass of the lightest particle in the respective channel), the integration in (3) should be limited to $(-\infty, -4m^2/M^2)$. If the function $f(x)$ has a definite sign it leads to the alternating HT series. Moreover, even for sign-changing $f(x)$ the series will be typically alternating unless fine-tuning of f is imposed.

It is crucially important that the leading twist contribution and respective perturbative (logarithmic) corrections has the same analytic properties, leading to the same properties of the full amplitude. This naturally selects the modified Analytic Perturbation Theory (APT) [9] which was successfully applied for the description of BSR [10]. These studies manifested the duality between the HT and perturbative corrections, so that HT decreased at NLO etc. Let me conjecture here, that the “real” HT should correspond to the piece which cannot be absorbed to perturbative series due to its asymptotic nature.

One may now continue S to $Q^2 = 0$ which is defined by first inverse moment

$$S(0) = - \int_{-\infty}^{-4m^2/M^2} dx \frac{f(x)}{x}. \quad (5)$$

Its sign will typically coincide with that of the first term of the series.

The derivatives of S at $Q^2 = 0$ are defined by higher inverse moments, say

$$S'(0) = - \int_{-\infty}^{-4m^2/M^2} dx \frac{f(x)}{M^2 x^2}. \quad (6)$$

If one neglect m (which corresponds to minimal APT in the perturbative part) this integral may diverge at $x \sim 0$. This divergence may be used to cancel the infinite slope of minimal APT contribution requiring that $f(x) \sim \rho_{pert}(s = M^2 x)$ for $x \sim 0$. This divergence is absent in the recently elaborated Massive Perturbation Theory (MPT [11], where $Q^2 \rightarrow \tilde{Q}^2 = Q^2 + M_{gl}^2$) which together with the VDM form of HT contribution $M_{HT}^2/(Q^2 + M_{HT}^2)$ lead to the reasonable description of BSR down to rather low Q^2 .

Note that VDM form of HT perfectly fits to (4) with the delta-function spectral density¹ while MPT expression has also the correct analytic properties provided relevant "gluonic mass" $M_{gl} \geq \Lambda_{QCD}$.

At the same time, the attempt to match the MPT description with GDHSR fails. The reason is obvious: the (average) slope of $\Gamma_1^{p-n}(Q^2)$ at low Q^2 is several times larger than the one following from GDHSR. This clearly supports the "two-component" approach [6] where slope is decomposed to the sum of "fast" rapidly decreasing component due to structure function g_2 and "slow" component due to structure function $g_T = g_1 + g_2$, which for BSR provides the slope [7] enhanced by factor $\mu_A^p/((\mu_A^n)^2 - (\mu_A^p)^2) \sim 4$ determined by proton and neutron anomalous magnetic moments.

It is therefore natural to combine MPT analysis with approach [6]. The fast component contribution is controlled by Butrkardt-Cottingham sum rule free from any corrections. GDH sum rule allows to relate HT and gluon masses (appearing to be close) so that there is single free parameter remained. The one-parameter fits [2] lead to the reasonable description of the data with the quality increasing with taking into account NLO MPT [11] and modifications of spectral density (4),

3 Hadronic vs vacuum matrix elements

3.1 Transverse Momentum Dependent Distributions and vacuum condensates

The TMDs can be conveniently defined [4] in coordinate (impact parameter) space. The representative case is Boer-Mulders function (in order to avoid consideration of gauge links/gluonic poles one may consider [4] Collins fragmentation function having the same Lorentz structure) when transverse coordinate is selected by the chiral-odd Dirac structure

$$\langle P | \bar{\psi}(0) \sigma^{\mu\nu} \psi(z) | P \rangle = M(P^\mu z^\nu - P^\nu z^\mu) I(z \cdot P, z^2) \quad (7)$$

¹The similar VDM form related to axial anomaly was discussed at this conference also in the talks of A. Oganesian.

Here the z^2 -dependence corresponds to k_T dependence in momentum space and contains all twists. The definite twists may be extracted by the expansion in Taylor series

$$I(z \cdot P, z^2) = \sum_{n=0}^{\infty} \frac{\partial^n}{n! \partial z^{2n}} I(z \cdot P, z^2)|_{z^2=0}, \quad (8)$$

which in the momentum space corresponds to the transverse moments of TMD. Note that the lowest twist is 3, which is seen from the appearance of factor M in the r.h.s. of (7). In the momentum space this factor is shifted to the denominator, as the transverse moment is taken over dk_T^2/M^2 [4].

Note that the expansion in z^2 may be performed only after the subtraction of the singular terms in z^2 , which in the collinear factorization are absorbed to coefficient function. For TMDs they constitute the power-like tail, after subtraction of which all the transverse moments became finite, indicating the Gaussian distributions.

The described situation is rather similar to non-local vacuum condensates (see [1] and Ref. therein) where one is dealing with vacuum matrix element

$$\langle 0 | \bar{\psi}(0) \psi(z) | 0 \rangle = \langle 0 | \bar{\psi}(0) \psi(0) | 0 \rangle F(z^2). \quad (9)$$

The Taylor expansion of F selects the local condensates of definite dimension, corresponding to the moments of suitably chosen Fourier transformed function being the complete analog of TMD. Note that subtraction of singular terms is performed here by subtraction of the perturbative contribution corresponding to quark propagator.

Generally, the hadronic matrix elements differ from the vacuum ones by the presence of essentially pseudo-Euclidian hadron momentum. At the same time, the Euclidian transverse dynamics may be more vacuum-like.

3.2 D-term and cosmological constant

Let us discuss one more interesting example of interplay between hadronic and vacuum matrix elements. It corresponds to so-called Polyakov-Weiss D-term [8] (appearing in analyticity based analysis as a subtraction constant [12]) whose moment is related to quadrupole gravitational formfactor

$$\langle P + q/2 | T^{\mu\nu} | P - q/2 \rangle = C(q^2)(g^{\mu\nu} q^2 - q^\mu q^\nu) + \dots \quad (10)$$

where gravitoelectric and gravitomagnetic formfactors [15] are dropped. C has definite (positive) sign in all the known cases including hadrons [8] (where also general stability arguments are discussed), photons [13], Q-balls [14].

For vacuum matrix element one has the famous cosmological constant

$$\langle 0 | T^{\mu\nu} | 0 \rangle = \Lambda g^{\mu\nu} \quad (11)$$

One may relate this matrix element in 2-dimensional transverse space orthogonal to P and q , so that effective 2-dimensional cosmological constant is

$$\Lambda = C(q^2) q^2 \quad (12)$$

The positive C leads to negative cosmological constant in the scattering process and to positive one in the annihilation process.

Note that scattering in the one-graviton approximation is similar to the motion of test particle in the classical gravitational field described by the solution of Einstein equation: the graviton propagator is related to their l.h.s., while the energy-momentum tensor of scattering particle corresponds to their r.h.s. The Born cross-section obviously contains the full information about the deflection angle θ dependence on the impact parameter b

$$\left| \frac{db^2}{d\theta} \right| = \frac{d\sigma}{\pi d\theta}. \quad (13)$$

Moreover, the ratio of helicity-flip and non-flip cross-section may be also calculated from the Born amplitude [16]. Passing to annihilation channel of one graviton exchange corresponds to exploration of crossing invariance and quantum effects for the produced particles while keeping the gravity on the classical level. The attracting possibility is to relate this process to Big Bang and inflation, The relation between annihilation and inflation! may not be so surprising due to known similarity between inflation and Schwinger pair production in the electric field [17].

The effective cosmological constant (12) corresponds to 2-dimensional space orthogonal to vectors Δ (which is purely time-like in the c.m. frame) and P which is purely space-like. It is of course very interesting whether real cosmological constant in our Universe may be understood as emerging from annihilation at extra dimensions. Qualitatively this is similar to brane cosmology, and one should stress that in the suggested scenario Big Bang is due to one-graviton annihilation. The specification of extra-dimensional states providing the cosmological constant of mass dimension 4 remains to be investigated.

4 Conclusions

The analyticity property continues to play the major role in developing of QCD approaches to low scale processes, being of most experimental interest. It allows one to justify the representation of infinite sums of higher twists contributions, providing, in particular, the accurate description of Bjorken Sum Rule data at low Q^2 .

The infinite series of higher twists are required to transverse momentum dependent parton distributions, having deep similarity to non-local vacuum condensates.

The vacuum/hadron matrix elements similarity allows to describe one-graviton annihilation as effective 2-dimensional cosmological constant, and this may be generalized to describe in a similar way cosmological constant in our Universe as emerging from one-graviton annihilation at extra dimension, which is the picture of a Big Bang in such a case.

Acknowledgment This work is supported in part by RFBR grants 12-02-00613 and 13-02-01060.

References

- [1] A. P. Bakulev and A. V. Radyushkin, Phys. Lett. B **271** (1991) 223.
- [2] O. Teryaev, Nucl. Phys. Proc. Suppl. **245** (2013) 195 [arXiv:1309.1985 [hep-ph]].

- [3] P. G. Ratcliffe and O. V. Teryaev, hep-ph/0703293; Mod. Phys. Lett. A **24** (2009) 2984 [arXiv:0910.5348 [hep-ph]].
- [4] O. V. Teryaev, Phys. Part. Nucl. **35** (2004) S24.
- [5] D. Boer, L. Gamberg, B. Musch and A. Prokudin, JHEP **1110** (2011) 021 [arXiv:1107.5294 [hep-ph]].
- [6] J. Soffer and O. Teryaev, Phys. Rev. Lett. **70** (1993) 3373; Phys. Rev. D **51** (1995) 25 [hep-ph/9405228].
- [7] J. Soffer and O. Teryaev, Phys. Rev. D **70** (2004) 116004 [hep-ph/0410228].
- [8] K. Goeke, M. V. Polyakov and M. Vanderhaeghen, Prog. Part. Nucl. Phys. **47** (2001) 401 [hep-ph/0106012].
- [9] D. V. Shirkov and I. L. Solovtsov, Phys. Rev. Lett. **79** (1997) 1209 [hep-ph/9704333]; Theor. Math. Phys. **150** (2007) 132 [hep-ph/0611229].
- [10] R. S. Pasechnik, D. V. Shirkov and O. V. Teryaev, Phys. Rev. D **78** (2008) 071902 [arXiv:0808.0066 [hep-ph]]; V. L. Khandramai, R. S. Pasechnik, D. V. Shirkov, O. P. Solovtsova and O. V. Teryaev, Phys. Lett. B **706** (2012) 340 [arXiv:1106.6352 [hep-ph]].
- [11] D. V. Shirkov, Phys. Part. Nucl. Lett. **10** (2013) 186 [arXiv:1208.2103 [hep-th]].
- [12] O. V. Teryaev, hep-ph/0510031. I. V. Anikin and O. V. Teryaev, Phys. Rev. D **76** (2007) 056007 [arXiv:0704.2185 [hep-ph]].
- [13] I. R. Gabdrakhmanov and O. V. Teryaev, Phys. Lett. B **716** (2012) 417 [arXiv:1204.6471 [hep-ph]].
- [14] M. Mai and P. Schweitzer, Phys. Rev. D **86** (2012) 076001 [arXiv:1206.2632 [hep-ph]]; *ibid.*, 096002 [arXiv:1206.2930 [hep-ph]].
- [15] O. V. Teryaev, hep-ph/9904376. A. J. Silenko and O. V. Teryaev, Phys. Rev. D **71** (2005) 064016 [gr-qc/0407015]. O. V. Selyugin and O. V. Teryaev, Phys. Rev. D **79** (2009) 033003 [arXiv:0901.1786 [hep-ph]].
- [16] O. V. Teryaev, Czech. J. Phys. **53** (2003) 47 [hep-ph/0306301].
- [17] Y. .B. Zeldovich and A. A. Starobinsky, Sov. Phys. JETP **34** (1972) 1159 [Zh. Eksp. Teor. Fiz. **61** (1971) 2161].

EXPERIMENTAL RESULTS

RESULTS ON THE TRANSVERSE DOUBLE SPIN ASYMMETRIES IN THE ELASTIC pp -SCATTERING AT $\sqrt{s} = 200$ GeV

Igor Alekseev^{1†} for the STAR collaboration

(1) *Institute for Theoretical and Experimental Physics, B. Chermushkinskaya 25, 117218,
Moscow, Russia*

† *E-mail: igor.alekseev@itep.ru*

Abstract

We present a new precise result on the transverse double spin asymmetries A_{NN} and A_{SS} in the proton-proton elastic scattering at $\sqrt{s} = 200$ GeV and very small momentum transferred. The data set includes about 20 million elastic events obtained in a run with dedicated optics by the STAR experiment at RHIC. The obtained preliminary values of $A_{NN} \sim A_{SS} \sim 5 \cdot 10^{-3}$ are small but distinguishable from zero.

One of the puzzles left in the Regge theory is that of odderon — a hypothetical counterpart of pomeron with odd charge parity. This Regge trajectory also does not vanish with energy and produces amplitudes which are 90 degrees rotated relative to pomeron ones. A visible effect of its existence could be sizable transverse double spin asymmetries A_{NN} and A_{SS} [1]. Nevertheless a careful estimation of the possible effect done later by T.L. Trueman [2] showed that it was not large and precise measurements are required.

Proton-proton elastic scattering at very small momentum transfer is described by the interference of the Coulomb and nuclear amplitudes (CNI region). The nuclear contribution is believed to be dominated by the classical pomeron exchange [3]. In this case no double spin flip amplitude is present in the nuclear term and only very small double spin asymmetries can be expected due to the electromagnetic component. The manifestation of non-negligible transverse double spin effects can point to possible contributions of other exchanges to the scattering amplitude [1, 2].

In terms of the helicity amplitudes, describing elastic scattering of identical spin-one-half particles, transverse double spin asymmetries are given as [4–6]:

$$\begin{aligned} A_{NN} \frac{d\sigma}{dt} &= \frac{4\pi}{s^2} [2|\phi_5|^2 + \text{Re}(\phi_1^* \phi_2 - \phi_3^* \phi_4)] , \\ A_{SS} \frac{d\sigma}{dt} &= \frac{4\pi}{s^2} \text{Re}(\phi_1^* \phi_2 + \phi_3^* \phi_4) . \end{aligned} \quad (1)$$

It would be more convenient for us to rewrite these equations in the form:

$$\begin{aligned} \frac{A_{NN} + A_{SS}}{2} \frac{d\sigma}{dt} &= \frac{4\pi}{s^2} [|\phi_5|^2 + \text{Re}(\phi_1^* \phi_2)] \approx \frac{4\pi}{s^2} \text{Re}(\phi_+^* \phi_2) , \\ \frac{A_{NN} - A_{SS}}{2} \frac{d\sigma}{dt} &= \frac{4\pi}{s^2} [|\phi_5|^2 - \text{Re}(\phi_3^* \phi_4)] \approx -\frac{4\pi}{s^2} \text{Re}(\phi_+^* \phi_4) , \end{aligned} \quad (2)$$

Spin-non-flip amplitude ϕ_+ is reasonably well known from unpolarized data [7] and single spin-flip amplitude ϕ_5 was already found compatible with zero in this experiment [8], so measurement of $(A_{NN} + A_{SS})/2$ and $(A_{NN} - A_{SS})/2$ gives us a direct knowledge of double spin-flip amplitudes ϕ_2 and ϕ_4 correspondingly. Amplitude ϕ_4 is kinematically suppressed and should vanish when $t \rightarrow 0$, while amplitude ϕ_2 can exist at $t = 0$. This fact is reflected in the standard parametrization of these hadronic amplitudes via dimensionless relative amplitudes r_2 and r_4 :

$$\phi_2^{had} = 2r_2 \text{Im}\phi_+ \text{ and } \phi_4^{had} = \frac{-t}{m^2} r_4 \text{Im}\phi_+. \quad (3)$$

The spin-dependent cross section, which is measured in the experiment, is also naturally expressed as a function of the same combinations $(A_{NN} + A_{SS})/2$ and $(A_{NN} - A_{SS})/2$:

$$2\pi \frac{d^2\sigma}{dt d\phi} = \frac{d\sigma}{dt} \left[1 + (P_B + P_Y) A_N \cos\varphi + P_B P_Y \left(\frac{A_{NN} + A_{SS}}{2} + \frac{A_{NN} - A_{SS}}{2} \cos 2\varphi \right) \right], \quad (4)$$

where P_B and P_Y are RHIC colliding beams polarizations. From this equation one can see that the term with $(A_{NN} + A_{SS})/2$ has no angular dependence and can be calculated only from the cross section difference between parallel and anti-parallel spin combinations. Such a measurement requires a good luminosity normalization and the normalization uncertainty directly contributes to the systematic error, providing equal false asymmetry. Details of the normalization are in the contribution by D. Svirida to these proceedings [9].

This analysis uses the same data set and the same elastic event selection as in the already published results on the single spin asymmetry A_N [8]. Raw double spin asymmetry as a function of azimuthal angle φ is given by the equation:

$$\varepsilon_2(\varphi) = \varepsilon'_2 + \varepsilon''_2 \cos 2\varphi = \frac{(K^{++}(\varphi) + K^{--}(\varphi)) - (K^{+-}(\varphi) + K^{-+}(\varphi))}{(K^{++}(\varphi) + K^{--}(\varphi)) + (K^{+-}(\varphi) + K^{-+}(\varphi))}, \quad (5)$$

where $K^{by}(\varphi) = N^{by}(\varphi)/L^{by}$ are normalized event counts in a certain small bin of azimuthal angle φ for certain spin combinations in 'blue' and 'yellow' beams $b, y = +$ or $-$. The plot of the raw double spin asymmetry ε_2 for the whole t -range is shown in fig. 1.

The results obtained for each of 5 t -ranges of the experiment are plotted in fig. 2. All points of $(A_{NN} - A_{SS})/2$ (the bottom panel) do not deviate from zero more than by two standard errors and the deviations are of different signs. The average is well compatible with zero. However slight negative slope can be imagined in the $(-t)$ dependence of the data, but it's difficult to state that it bears any physics meaning. On the contrary, $(A_{NN} + A_{SS})/2$ (the top panel) is significantly below zero and the absolute values are of the order of $5 \cdot 10^{-3}$. The distribution is approximately flat and the average is more than 6 standard deviations from zero. The three most important contributions to the systematic error come from background subtraction, luminosity

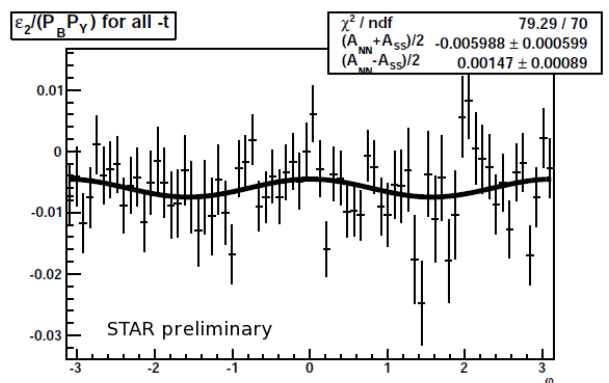


Figure 1: The raw double spin asymmetry ε_2 for the whole t -range. **STAR preliminary.**

normalization and beam polarization. The problem with the background is that though the background itself is very small (0.51% in average) it has quite different bunch structure, violating luminosity normalization, which makes it effectively highly polarized. This error is uncorrelated for different t -intervals. It was estimated for each point individually and added to statistical error in quadrature. The systematic error coming from the luminosity normalization of $8.4 \cdot 10^{-4}$ [9] is illustrated by the bar at the bottom of the panel. The product of the beam polarizations was $P_B P_Y = 0.372 \pm 0.052$, resulting in 14% scale uncertainty. The preliminary asymmetries averaged over the whole t -range of the data:

$$\begin{aligned} (A_{NN} + A_{SS})/2 &= \tau_{AY} 0.0051 \pm 0.0006(\text{stat}) \pm 0.0012(\text{sys}) \\ (A_{NN} - A_{SS})/2 &= 0.0005 \pm 0.0009(\text{stat}) \pm 0.0006(\text{sys}). \end{aligned}$$

This result is compatible with the measurements at RHIC polarized hydrogen jet, where A_{NN} was measured in the fixed target mode at $\sqrt{s} = 6.8$ and 13.7 GeV [10], but our result has higher precision.

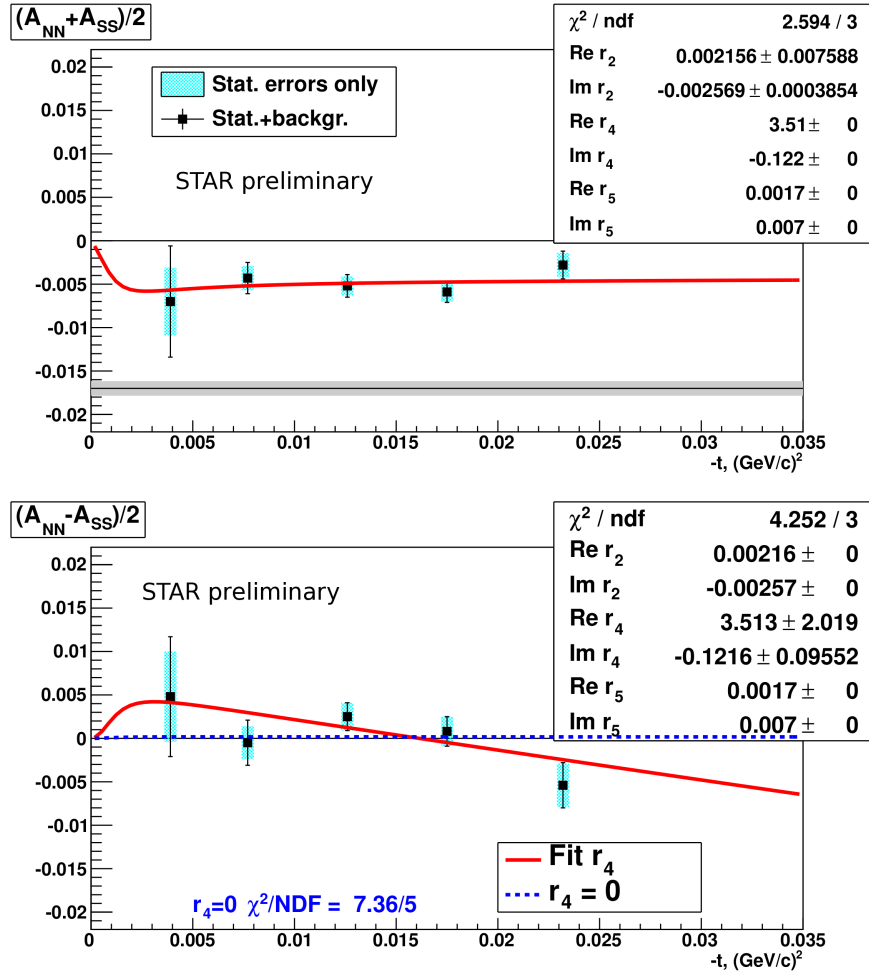


Figure 2: Double spin asymmetries as function of the 4-momentum transferred t . $(A_{NN} + A_{SS})/2$ - the top panel. $(A_{NN} - A_{SS})/2$ - the bottom panel. **STAR preliminary.**

Confidence ellipses of the relative amplitudes r_2 and r_4 obtained in the fits to $(A_{NN} + A_{SS})/2$ and $(A_{NN} - A_{SS})/2$ correspondingly are shown in fig. 3. A small negative $\text{Im}r_2$

is observed with $\text{Re} r_2$ and r_4 compatible to zero. The $(A_{NN} + A_{SS})/2$ obtained is small but different from zero. Its module is larger than the theory prediction in the absence of odderon, but its sign and t -dependence are different from the predictions which include odderon contribution [2].

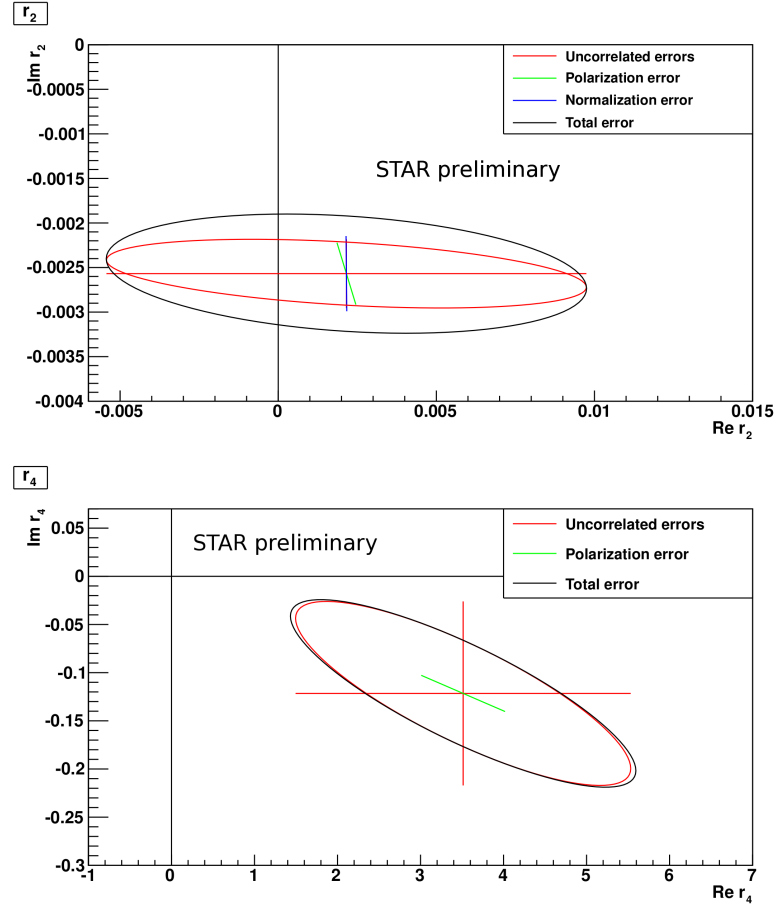


Figure 3: One- σ confidence regions for relative amplitudes r_2 (the top panel) and r_4 (the bottom panel). STAR Preliminary.

References

- [1] E. Leader and T.L. Trueman, Phys. Rev. **D61** (2000) 077504.
- [2] T.L. Trueman, [arXiv:hep-ph/0604153](https://arxiv.org/abs/hep-ph/0604153).
- [3] S. Nussinov, Phys. Rev. Lett. **34** (1975) 1286; S. Nussinov, Phys. Rev. **D14** (1976) 246.
- [4] N.H. Buttimore, E. Gotsman and E. Leader, Phys. Rev. **D18** (1978) 694.
- [5] T.L. Trueman, [arXiv:hep-ph/9610316](https://arxiv.org/abs/hep-ph/9610316).
- [6] N.H. Buttimore et al., Phys. Rev. **D59** (1999) 114010.
- [7] The COMPETE collaboration, <http://nuclth02.phys.ulg.ac.be/compete/predictor/>.
- [8] L. Adamczyk et al., STAR Collaboration. Phys. Lett. **B719** (2013) 62.
- [9] D. Svirida for the STAR collaboration, these Proceedings.
- [10] I.G. Alekseev et al., Phys. Rev. **D79** (2009) 094014.

PHENIX SPIN PROGRAM: RECENT RESULTS & PROSPECTS

Kenneth N. Barish^{1†} for the PHENIX Collaboration

(1) *University of California, Riverside, USA*

† *E-mail: Kenneth.Barish@ucr.edu*

Abstract

The PHENIX spin program utilizes polarized proton collisions in the Relativistic Heavy Ion Collider (RHIC) at Brookhaven National Laboratory to study the spin structure of the proton. We study different aspects of the nucleon spin structure by using longitudinally and transversely polarized beams and measuring single and double asymmetries for a variety of channels (e.g. pions, photons, and muons), primarily at center of mass energies of 200 and 500 GeV. Topics include the measurement of anti-quark helicity distribution functions via W production, the measurement of gluon helicity distribution functions, and the investigation of different mechanisms for the generation of transverse single spin asymmetries. We have reached an era of high enough luminosity and polarization (RHIC-II) to begin our investigation of low cross-section channels, such as the W. In this paper, I present selected recent results and discuss future prospects.

1 Proton Spin Structure at PHENIX

The PHENIX spin program has three major thrusts aimed at a detailed understanding of the spin structure of the proton's spin: (1) the measurement of the first moment of the spin dependent gluon distribution $\Delta g(x)$, (2) the measurement of the transversity and Sivers distributions, and (3) the flavor separation of the quark and anti-quark sea (Δq and $\Delta \bar{q}$). The RHIC accelerator has steadily progressed to the high luminosity and polarizations required for detailed studies of the proton spin structure (see Tables 1 & 2), and we have now entered the RHIC II luminosity era.

Table 1: PHENIX Longitudinally Polarized Runs.

Year	\sqrt{s}	Recorded L	Polarization	FoM P ⁴ L	FoM P ² L
2003 (Run 3)	200 GeV	0.35 pb ⁻¹	27%	1.9 nb ⁻¹	
2004 (Run 4)	200 GeV	0.12 pb ⁻¹	40%	3.1 nb ⁻¹	
2005 (Run 5)	200 GeV	3.40 pb ⁻¹	49%	200 nb ⁻¹	
2006 (Run 6)	200 GeV	7.50 pb ⁻¹	57%	790 nb ⁻¹	
2006 (Run 6)	62.4 GeV	0.08 pb ⁻¹	48%	4.2 nb ⁻¹	
2009 (Run 9)	500 GeV	10.0 pb ⁻¹	40%	260 nb ⁻¹	1600 nb ⁻¹
2009 (Run 9)	200 GeV	14.0 pb ⁻¹	57%	1400 nb ⁻¹	
2011 (Run 11)	500 GeV	16.7 pb ⁻¹	48%	880 nb ⁻¹	3800 nb ⁻¹
2012 (Run 12)	500 GeV	30.0 pb ⁻¹	52%	2200 nb ⁻¹	8100 nb ⁻¹
2013 (Run 13)	500 GeV	150.0 pb ⁻¹	55%	14000 nb ⁻¹	45500 nb ⁻¹

Table 2: PHENIX Transversely Polarized Runs.

Year	\sqrt{s}	Recorded L	Polarization	FoM P ² L
2001 (Run 2)	200 GeV	0.15 pb ⁻¹	15%	3.4 nb ⁻¹
2005 (Run 5)	200 GeV	0.16 pb ⁻¹	47%	35 nb ⁻¹
2006 (Run 6)	200 GeV	2.70 pb ⁻¹	51%	700 nb ⁻¹
2006 (Run 6)	62.4 GeV	0.02 pb ⁻¹	48%	4.6 nb ⁻¹
2008 (Run 8)	200 GeV	5.20 pb ⁻¹	46%	1100 nb ⁻¹
2012 (Run 12)	200 GeV	9.20 pb ⁻¹	58%	3100 nb ⁻¹

The PHENIX detector has a high rate capability utilizing a fast DAQ and specialized triggers, high granularity detectors, and good mass resolution and particle identification at the sacrifice of acceptance. Detection of π^0 , γ , and η utilize the finely grained central arm electromagnetic calorimeter ($|\eta| < 0.35$) and forward muon piston calorimeter (MPC) [$3.1 < |\eta| < 3.8$ (3.9) South (North)], charged pion detection uses the drift chamber and ring imaging Cherenkov detector, and J/ψ are detected with electrons in the central spectrometer ($|\eta| < 0.35$) and muons in our forward spectrometer consisting of Muon ID and Muon Tracker ($1.2 < |\eta| < 2.4$).

2 Gluon Polarization

PHENIX can measure Δg , the gluon contribution to the proton spin, through multiple channels covering a wide range of x_g leading to a robust measurement. Δg is extracted from measurements of the double spin longitudinal asymmetry (A_{LL}) for these various channels:

$$A_{LL} = \frac{\sigma_{++} - \sigma_{+-}}{\sigma_{++} + \sigma_{+-}} = \frac{1}{P_b P_y} \frac{N_{++} - RN_{+-}}{N_{++} + RN_{+-}}$$

where $++$ denotes same sign helicity, $+-$ denotes opposite sign helicity of colliding bunches, and A_{LL} is comprised of measurements of the beam polarization (P_b, P_y), helicity dependent particle yields (N), and the relative luminosity ($R = L_{+-}/L_{++}$). The relative luminosity is measured and evaluated by two global detectors, the BBC and ZDC which cover different pseudo-rapidity regions ($3.1 < |\eta| < 3.9$ and $|\eta| > 6.6$ respectively).

Extraction of $\Delta g(x)$ is based on a next-to-leading order (NLO) perturbative Quantum Chromodynamics (pQCD) framework, which has successfully described RHIC unpolarized cross section data [1]. RHIC π^0 A_{LL} results have been used in a NLO global fit (DSSV) of polarized parton densities [2]. While the results were found to be consistent with zero in the accessed range of the gluon momentum fraction, the more recent higher statistics data that include the 2009 data may indicate a non-zero $\Delta g(x)$ (see Fig. 1).

Currently, the main limitations are on the relative luminosity uncertainty, which is expected to be improved for the Run 9 final analysis, limited gluon x range probed and a poor sensitivity to the shape of $\Delta g(x)$ as several process contribute to inclusive hadron production at mid rapidity (principally gluon-gluon and quark-gluon scattering). The x -range is being widened by measurements at different center-of-mass energies and measurements in the forward direction. Additionally, correlation measurements, e.g., di-hadrons, will help better constrain the kinematics and hence determine the shape of $\Delta g(x)$. While some of these measurements have begun, their impact will be felt with the higher luminosity RHIC data and upgrades, particularly in the forward direction.

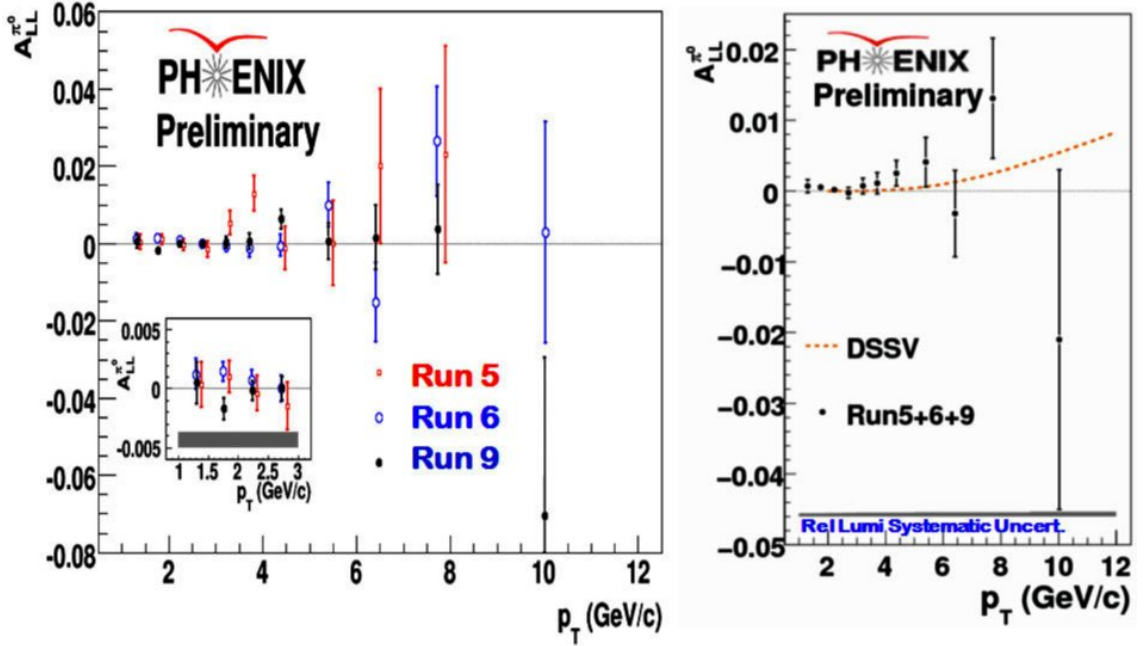


Figure 1: Double helicity asymmetry in inclusive π^0 production at 200 GeV as a function of p_T from runs 5, 6 and 9; dashed line corresponds to the DSSV global fit [2]. The data points tend to be above the curve corresponding to the DSSV fit, possibly indicating a non-zero Δg in the kinematic range measured ($0.02 < x < 0.3$).

3 Sea Quark Helicity

The production of W bosons in 500 GeV $p+p$ collisions provides a novel technique to extract the light quark and anti-quark polarizations through the measurement of longitudinal single spin asymmetries. W boson production selects the quark flavors through their charge. Additionally, it selects only one helicity of nearly massless quarks (left-handed helicity for quarks and right-handed helicity of anti-quarks) due to the maximally parity-violating nature of the weak interaction. Experimentally, we measure A_L of W^+ and W^- bosons via their decay lepton, as the sign of the decay lepton tags whether it came from a W^+ or W^- . We measure the decay leptons inclusively, which smears out the distinction of the quark and antiquark contributions as a function of rapidity due to the fixed helicity of the (anti)neutrino. While it enhances the forward-backward separation of the quarks and anti-quarks for negative leptons it is mixed for positive leptons. We are therefore most sensitive to the anti-quark polarization via measurement of $A_L(W^-)$ in the backward direction. However, ultimately we are still sensitive to anti-quark polarizations with enough statistics through the measurement of $A_L(W^+)$ in the central region.

First PHENIX results on the cross section and helicity asymmetry in W production at mid-rapidity in polarized $p+p$ collisions at 500 GeV from run 9 have been published [3]. The cross section was found to be consistent with theoretical expectations and we have observed a non-zero parity-violating asymmetry in W production via the electrons in the central arm from Run 9, 11, and 12, although the limited statistics do not yet allow for us to clearly distinguish between different scenarios of anti-quark polarization in the proton (see Fig. 2).

PHENIX implemented an upgrade, including the addition of resistive plate chambers

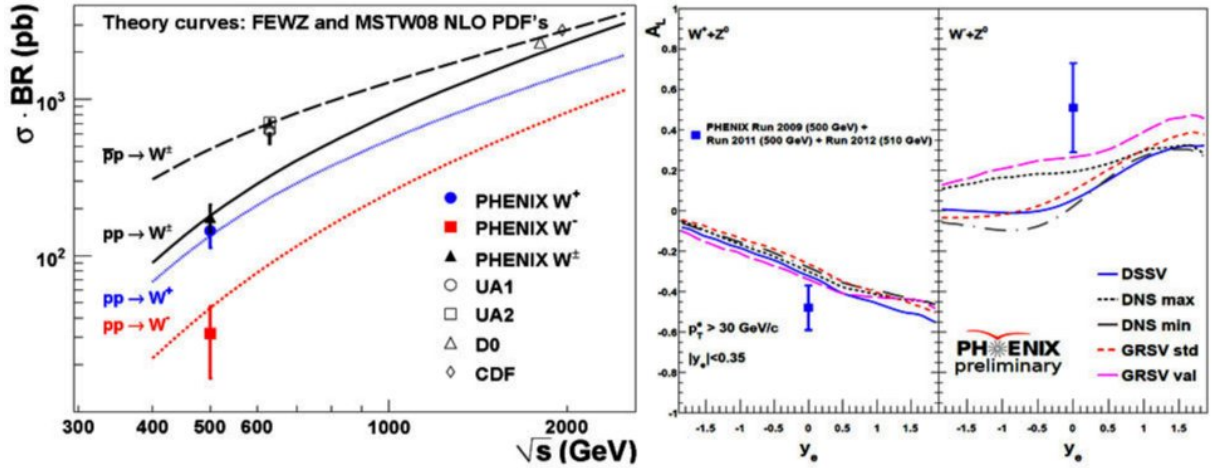


Figure 2: (left) W cross sections at 500 GeV compared to expectations based on higher energy data. (right) Preliminary positive and negative W single spin asymmetries measured in 500GeV $p+p$ collisions during Run 9, 11, and 12 via electrons in the PHENIX central arms. The lines represent models with different assumptions for the polarized anti-quark polarizations.

H(RPCs) and an upgrade of the front-end electronics from the existing muon trackers, facilitating the selection of forward and backward high momentum muons. Preliminary results from Run 12 are shown in Fig. 3. Run 13 produced a significantly increased luminosity and the muon trigger provided sufficient rejection to sample all W -events. The data is currently under analysis and is expected to yield a significant constraint on $\Delta\bar{u}$ and $\Delta\bar{d}$.

4 Transverse spin effects

Measured transverse spin asymmetries may have contributions from transversely asymmetric k_T quark distributions (the Sivers effect), spin-dependent fragmentation functions (the Collins effect), and quark-gluon field interference (Twist-3). The Sivers effect is related to the orbital angular momentum of the gluons and quarks in the proton and the Collins effect allows access to the transversity distribution, δq , which is a fundamental parton distribution function of the transverse polarization of quarks in a transversely polarized nucleon. The measurement of multiple channels in different kinematic regions are needed to disentangle the effects.

Fig. 4 shows the transverse single spin asymmetries at mid-rapidity for π^0 and η -mesons as measured in the PHENIX central arms. Compared to previous published results [4],

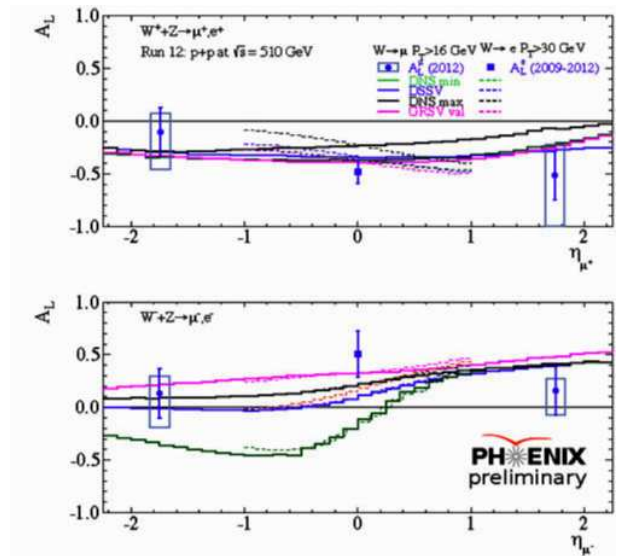


Figure 3: Preliminary positive (left) and negative (right) forward W single spin asymmetries measured in 500 GeV $p+p$ collisions during Run 11 via muons in the PHENIX forward spectrometer. The lines represent models with different assumptions for the polarized anti-quark polarizations.

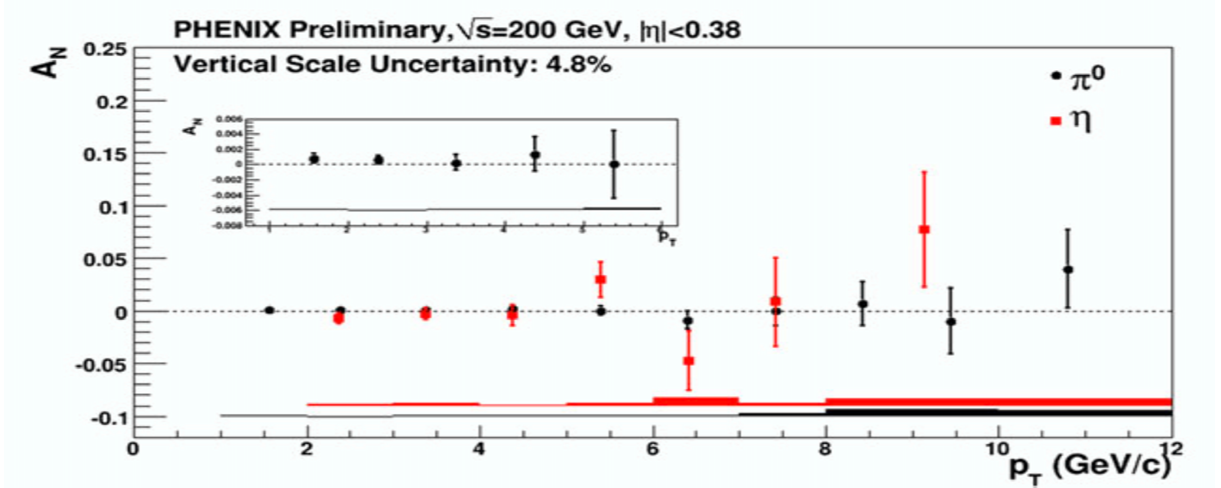


Figure 4: A_N at mid-rapidity for π^0 and η -mesons.

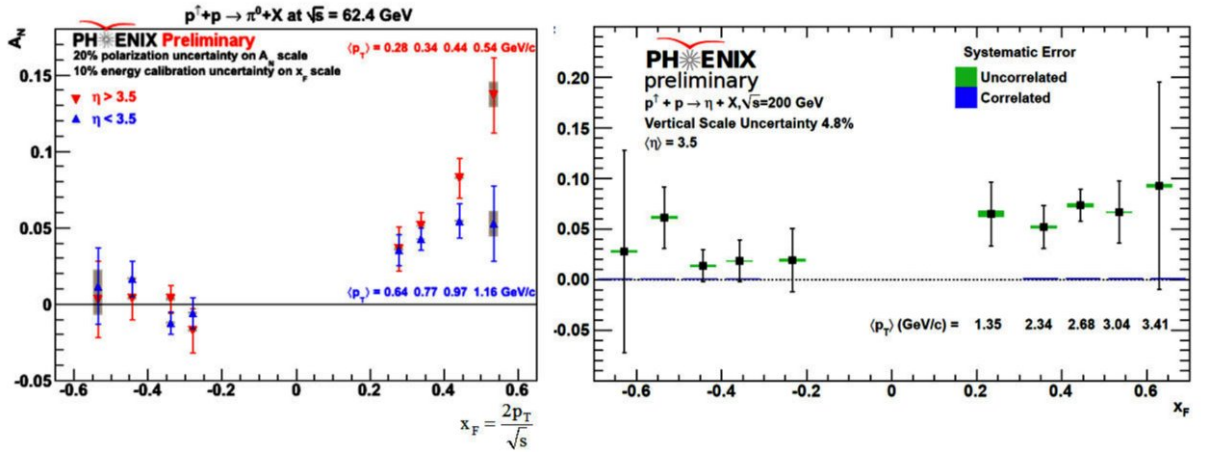


Figure 5: A_N in the forward and backward direction for π^0 's at 62.4 GeV (left) and η -mesons at 200 GeV (right).

the reach for π^0 has been extended to over 10 GeV/c, the statistical uncertainties have been reduced by a factor of over 20 at low p_T , and results for η -mesons are new. All mid-rapidity asymmetries are consistent with zero, leading to constraints on the gluon-Sivers effect as the gg and qg process are dominant and the transversity effect is suppressed [5].

Results are presented in Fig. 5 for neutral pions as function of x_F in the forward and backward directions using the Muon Piston Calorimeter (MPCs). The asymmetry scales with x_F , which is consistent with earlier observations from other experiments at lower center-of-mass energies [6]. The backward asymmetries are consistent with zero. PHENIX has also measured transverse asymmetries of η -mesons in forward rapidities with significant non-zero values for $x_F > 0$, see Fig. 5. They are comparable to the asymmetries of the π^0 in the same kinematic range, where there may be variations due to the isospin dependence, the fragmentation process, and the different masses. Backward asymmetries are close to being zero, although averaged over the whole $x_F < 0$ range they currently appear to be about 2σ positive.

In order to separate the various possible effects, PHENIX will measure asymmetries of different particles and particle correlations with greater precision in the near future. Correlations between particles at mid and forward rapidities will access certain partonic momentum ranges. The measurements require large luminosities and improved trigger.

5 Future Prospects

In the near term, PHENIX is adding a preshower tracker in front of the forward MPCs, allowing for π^0 rejection for the measurement of prompt photons. A measurement of the prompt photon A_N at $x_F > 0$ will provide key information about the process dependence of transverse momentum dependent parton distribution functions (TMDs) and provide a measurement of the quark Sivers effect [7, 6]. In the longer term, the PHENIX experiment is proposing to replace the current PHENIX spectrometer at mid-rapidity with sPHENIX [9], which also frees up space to allow for the possible addition of a spectrometer, fsPHENIX, in the forward direction ($1 < |\eta| < 4$) capable of measuring electrons, photons, and hadrons. It is being designed to measure jet correlations/structure and Drell-Yan. The measurements would allow the separation of Sivers & Collins and test TMD parton distribution factorization and universality. A subsequent upgrade adding an electron detector in the opposite direction would further evolve sPHENIX into a detector for inclusive, semi-inclusive and exclusive processes in deep inelastic electron-proton and electron-nucleus scattering, referred to as ePHENIX, utilizing a future high intensity electron beam at RHIC.

References

- [1] S.S. Adler *et al.* [PHENIX Collaboration], *Phys. Rev. Lett.* **91**, 241803 (2003), S.S. Adler *et al.*, (PHENIX), *Phys. Rev. Lett.* **97**, 012002 (2007), Adare *et al.* (PHENIX), *Phys. Rev. D* **76**, 051106 (2007).
- [2] D. de Florian, R. Sassot, M. Stratmann, and W. Vogelsang, *Phys. Rev. Lett.* **101**, 072001 (2008).
- [3] A. Adare *et al.* [PHENIX Collaboration], *Phys. Rev. Lett.* **106**, 062001 (2011).
- [4] S.S. Adler *et al.* [PHENIX Collaboration], *Phys. Rev. Lett.* **95**, 202001 (2005).
- [5] M. Anselmino, U. DAlesio, S. Melis, and F. Murgia, *Phys. Rev. D* **74**, 094011 (2006)
- [6] D.L. Adams *et al.* [E704], *Phys. Lett. B* **264**, 462 (1991).
- [7] Z.B. Kang, J-W Qiu, W. Vogelsang, F. Yuan, *Phys. Rev. D* **83**, 094001 (2011).
- [8] L.Gamberg, Z-B Kang, *Phys. Lett. B* **718**, 181 (2012).
- [9] C. Aidala *et al.* [PHENIX Collaboration], “sPHENIX: An Upgrade Concept from the PHENIX Collaboration”, arXiv:1207.6378 [nucl-ex].

TRANSVERSE SPIN AND TRANSVERSE MOMENTUM STRUCTURE OF THE NUCLEON FROM THE COMPASS EXPERIMENT

F. Bradamante^{1†}

on behalf of the COMPASS Collaboration

(1) *Dipartimento di Fisica, Università degli Studi di Trieste*

† *E-mail: Franco.Bradamante@cern.ch*

Abstract

A selection is presented of recent results from the COMPASS Collaboration on transverse spin and transverse momentum effects in semi-inclusive deeply inelastic scattering (SIDIS) of 160 GeV/c muons off proton and deuteron targets.

1. Introduction. The description of the partonic structure of the nucleon is one of the central problems of hadronic physics. In recent years considerable theoretical and experimental progress has been made and the relevance of the quark transverse spin and transverse momentum has been clearly assessed. In the present theoretical framework, eight transverse momentum dependent parton distribution functions (TMD PDFs) are required at leading twist for each quark flavour. They describe all possible correlations between the transverse momentum and spin of the quarks and the spin of the nucleon. When integrating over the quark transverse momentum five of these functions vanish, while three of them give the well known number, helicity and transversity distribution functions. Among these last three functions, the transversity distribution, which is the analogous of the helicity PDFs in the case of transversely polarized nucleons, was thoroughly studied only in the 90s and experimentally it is the least known one. On the experimental side, semi-inclusive deeply inelastic lepton scattering (SIDIS) is today the major source of information to access the TMD PDFs. It allows to access easily convolutions of the different TMD PDFs and fragmentation functions via high statistic measurements of asymmetries in the azimuthal distributions of the final-state hadrons. Also, using different (p , d , or n) targets and identifying the final state hadrons, one can separate the contributions of the quarks of different flavour. The clear non-zero spin asymmetries recently measured in SIDIS off transversely polarized targets by both HERMES at DESY and COMPASS at CERN at different beam energies, can be described quite well with the present formalism, and thus give much confidence in the overall picture [1].

COMPASS (COmmon Muon and Proton Apparatus for Structure and Spectroscopy) is a fixed-target experiment at the CERN SPS taking data since 2002. The COMPASS spectrometer is by now very well known in the scientific community and I will not spend any time in describing it, but only refer to the NIM paper of Ref. [2] and to the previous speaker [3]. An important part of the experimental programme consists in the study of the nucleon structure and SIDIS data have been collected using a 160 GeV longitudinally polarized muon beam and either longitudinally or transversely polarized proton (NH_3) and deuteron (^6LiD) targets. A selection of the results on the azimuthal asymmetries in $\mu N \rightarrow \mu' h^\pm X$ extracted from the data collected with transversely polarized targets is

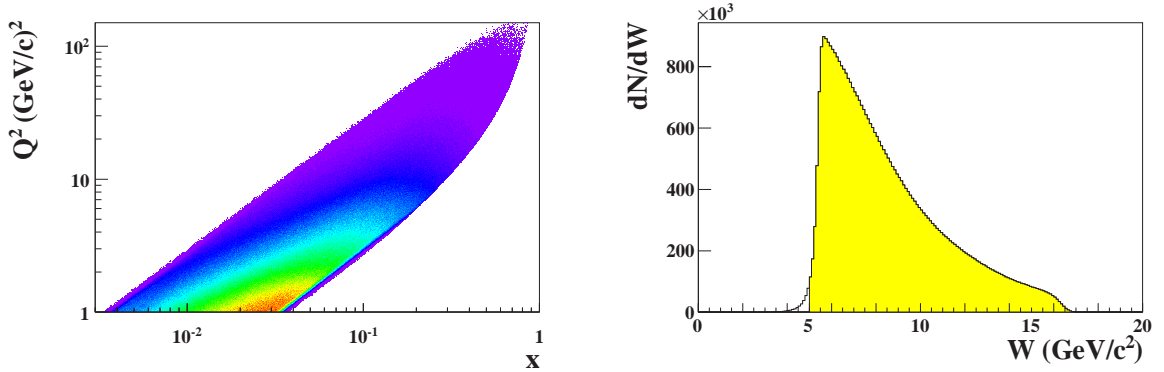


Figure 1: Left: $x - Q^2$ correlation for charged hadrons. Right: W distribution.

presented, with particular focus on the most recent measurements from the data collected in 2007 and 2010 with the proton target. These results exhibit clear signals for the Collins asymmetry, interpreted as a convolution of a non-zero transversity PDF and the Collins fragmentation function (FF), and for the Sivers asymmetry which is related to the Sivers function, the most famous and discussed of the TMD PDFs. At the same time six more transverse spin dependent azimuthal asymmetries have been obtained from the proton and the deuteron data. They have all their own interpretation in terms of the QCD parton model, preliminary results have already been presented at several conferences, but I have not enough space to include them in this written report. Large asymmetries have been measured in the production of oppositely charged hadron pairs (2-h) and the comparison between the Collins asymmetry and the 2-h asymmetry has led to interesting observations on the hadronisation mechanism of transversely polarised quarks. The data collected with the ${}^6\text{LiD}$ target, suitably averaged up to cancel possible target polarization effects, have also been analysed to search for the azimuthal modulations in the production of hadrons which are expected to be present in the unpolarised SIDIS cross-section. The azimuthal hadron asymmetries, which are related to the Boer-Mulders TMD PDF, show strong and somewhat puzzling kinematical dependences.

2. Collins and Sivers asymmetries. SIDIS data with a 160 GeV μ^+ beam and with the transversely polarised deuteron target (${}^6\text{LiD}$) were taken in the years 2002 to 2004. In 2007 and 2010 the transversely polarised proton target (NH_3) was used, again with the 160 GeV μ^+ beam.

The data analysis is very similar for all the years of data taking and the relevant cuts applied to select the “good events” are also the same. Only events with photon virtuality $Q^2 > 1$ $(\text{GeV}/c)^2$, fractional energy of the virtual photon $0.1 < y < 0.9$, and mass of the hadronic final state system $W > 5$ GeV/c^2 are considered. The charged hadrons are required to have at least 0.1 GeV/c transverse momentum p_T^h with respect to the virtual photon direction and a fraction of the available energy $z > 0.2$. The $x - Q^2$ correlation for charged hadrons from 2010 data is shown in Fig. 1 (left). As can be seen, the x range goes from $x \simeq 3 \cdot 10^{-3}$ to $x \simeq 0.7$ with relatively large Q^2 values in the valence region. Figure 1 (right) gives the corresponding W distribution. In the standard analysis, the transverse-spin asymmetries are measured separately for positive and negative hadrons (or pions or kaons) as functions of x , z or p_T^h . The complete definition (namely sign and kinematic factors) of the asymmetries can be found in the published papers [4].

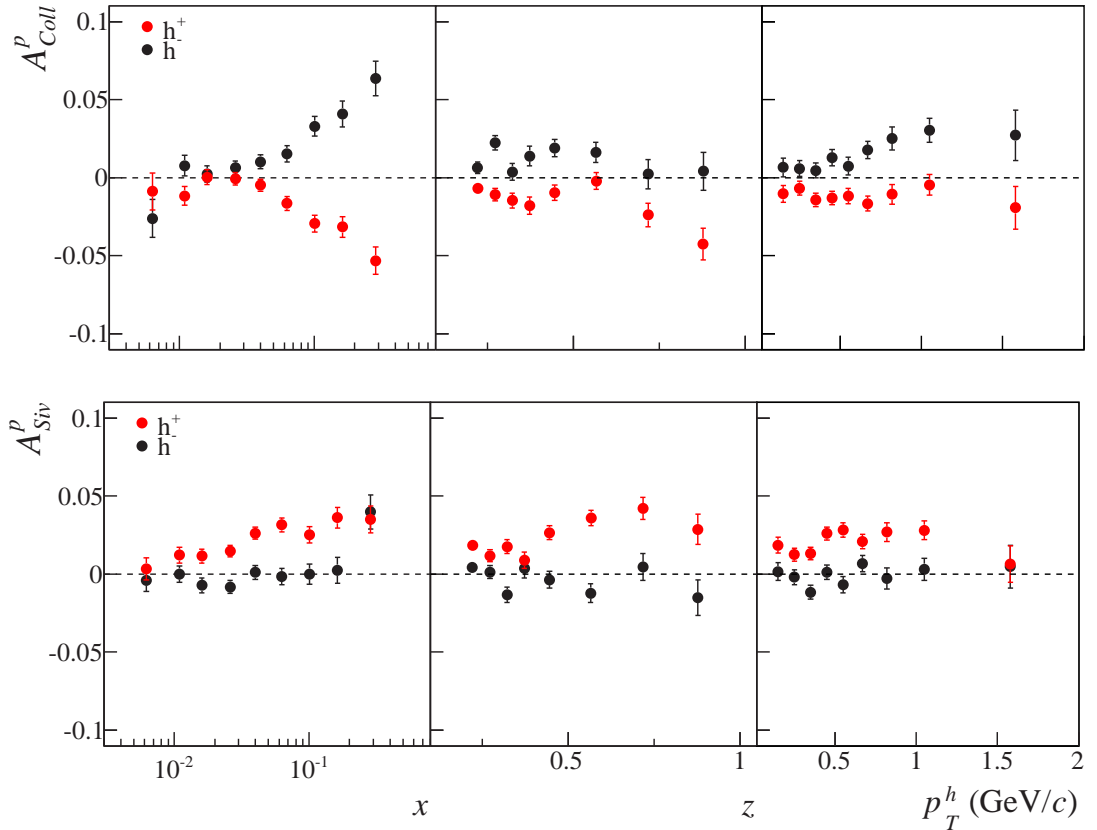


Figure 2: Collins (upper panel) and Sivers (lower panel) asymmetries for positive (red points) and negative (black points) hadrons as functions of x , z and p_T^h from the combined 2007 and 2010 proton data.

The Collins and Sivers asymmetries for positive and negative hadrons from the 2004 deuteron data [5] turned out to be compatible with zero within the few percent uncertainties, at variance with the non-zero results obtained by the HERMES experiment on proton [6]. These data could be understood in terms of cancellation between the u and d quark contributions in the deuteron target, and together with the Belle data of the $e + e^- \rightarrow hadrons$ process were used in global fits to extract the transversity and Sivers functions. Still today these COMPASS data are the only SIDIS data collected with a transversely polarised deuteron target.

The first results for the charged hadrons Collins and Sivers asymmetries on proton from COMPASS [7] came from the analysis of the 2007 data, while higher precision results have been obtained from the 2010 data [4]. Very recently, results for charged pions and kaons have also been produced [8].

The combined results for non-identified hadrons from 2007 and 2010 are shown in Fig. 2. The Collins asymmetries (upper plots) are compatible with zero in the previously unmeasured $x < 0.03$ region while at larger x they are clearly different from zero, with opposite sign for positive and negative hadrons and in nice agreement, both in sign and in magnitude, with the HERMES results [6]. There is no indication for lower values of the Collins asymmetry at the higher COMPASS Q^2 values as compared to the HERMES measurement.

The Sivers asymmetries for charged hadrons are given in the lower plots of Fig. 2. For

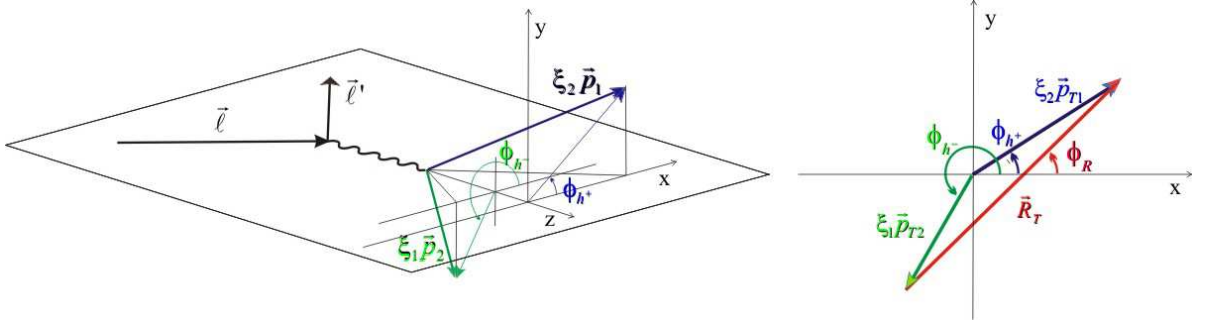


Figure 3: Kinematics of hadron pair production process in SIDIS. The 3-momenta \vec{l} and \vec{l}' of the incoming and scattered lepton define the scattering plane, the z axis (the direction of the virtual photon direction) and the x axis. The vectors \vec{p}_1 and \vec{p}_2 are the 3-momenta of the positive and negative hadron respectively. The vector \vec{R} is defined as $\vec{R} = (z_2 \vec{p}_1 - z_1 \vec{p}_2)/(z_1 + z_2) = \xi_2 \vec{p}_1 - \xi_1 \vec{p}_2$. The subscript T indicates the transverse component with respect to the virtual photon direction.

h^- they are compatible with zero with some indication for small negative values over the entire x range but in the last bin. In the case of h^+ , the Sivers asymmetry is positive down to very small x values and in the $x > 0.03$ region it is smaller than the same asymmetry measured by HERMES [6], a fact which can be understood in terms of the recent calculations on TMDs evolution.

3. Two-hadron asymmetry. An alternative approach to the transversity PDF in SIDIS utilises the transverse spin asymmetry in the production of pairs of oppositely charged hadrons, in the process $lN \rightarrow l'h^+h^-X$ [9]. In the SIDIS cross-section an azimuthal modulation is expected as a function of $\phi_{RS} = \phi_R + \phi_S - \pi$, whose amplitude is proportional to the product of the transversity PDF and a new chiral-odd FF, the Dihadron Fragmentation Function (DiFF) $H^{\angle}(z, M_{h^+h^-}, \cos \theta)$ [10]. The angle ϕ_R is the azimuthal angle of the relative momentum R of the two hadrons as depicted in Fig. 3, $\pi - \phi_S$ is the azimuthal angle of the spin vector of the struck quark, z is the sum of the fractional energy of the two hadrons, $M_{h^+h^-}$ is the invariant mass of the two hadrons, and θ is the polar angle of h^+ . First evidence for azimuthal asymmetries in leptonproduction of $\pi^+\pi^-$ pairs on transversely polarized protons was published by HERMES [11], while results on both proton and deuteron targets for unidentified charged hadrons pairs h^+h^- have been published by COMPASS [12]. Using these data and the Belle data on e^+e^- annihilation into two pairs of hadrons [13] a first extraction of the u and d quark transversity could be performed [14], which was in good agreement with the extraction of Ref. [15], based on the Collins asymmetry of single hadrons. The same procedure was applied to directly extract u and d quark transversities in the different x bins using COMPASS proton and deuteron results [16]. The data collected by COMPASS in 2010 on the transversely polarized proton target provided a sample of hadron pairs larger than the published one by a factor of three. Preliminary results were first shown at Transversity 2011 [17]. The selection of the two hadron events follows the same track than the single-hadron analysis, but more requirements are imposed. All possible combinations of oppositely charged hadron pairs originating from the vertex are taken into account in the analysis. At least three outgoing tracks are demanded for an interaction vertex, and each hadron has to have a fractional energy $z > 0.1$ and $x_F > 0.1$, to ensure that the hadrons are not produced in the target fragmentation. A cut of $R_T > 0.07$ GeV/c ensures a good definition

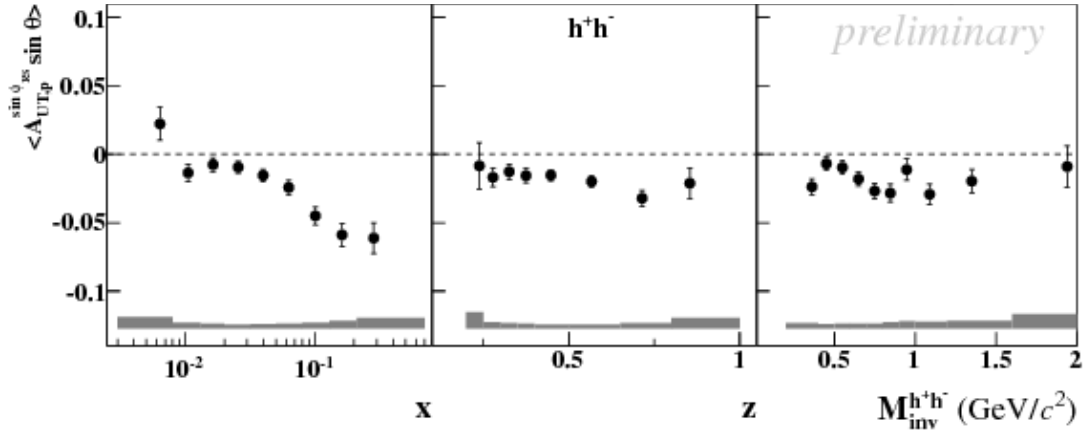


Figure 4: Unidentified 2-h asymmetries as functions of x, z and M_{h+h-} from the 2007 and the 2010 proton data.

of ϕ_{RS} . Within measurement errors, the 2-h asymmetry of the COMPASS deuteron data from the 2002-2004 runs are compatible with zero. On the other hand, the data on the proton target definitively show a non-zero signal, in particular in the x -valence region, as clear from Fig. 4, where the combined results from the 2007 and the 2010 runs are shown as a function of x, z and M_{h+h-} . These data are in good agreement with the only other existing measurement from the HERMES Collaboration, but the statistics of the COMPASS sample is considerably higher thanks to the larger phase space available. A remarkable similarity can thus be noted between the 2-h asymmetry and the Collins asymmetry for h^+ , which will be further discussed in Paragraph 5.

4. Azimuthal modulations in unpolarised SIDIS. Since the early times of the quark-parton model it was realised that a possible intrinsic transverse momentum of the target quark would cause measurable effects in the SIDIS cross-section, namely a $\cos \phi_h$ and a $\cos 2\phi_h$ modulation. Recently the study of these modulations has become particularly interesting within the framework of the new TMD approach to the PDFs and FFs. The amplitudes of these modulations, $A_{\cos \phi_h}^{UU}$ and $A_{\cos 2\phi_h}^{UU}$ are not only due to the kinematic of the scattering process (Cahn effect) but depend also on a new TMD PDF, the so-called Boer-Mulders function, which describes the correlation between the quark transverse spin and its transverse momentum in an unpolarised nucleon. In the amplitudes the Boer-Mulders function is convoluted with the Collins function, and its extraction from the unpolarised SIDIS cross section data is an important goal of the HERMES, CLAS and COMPASS Collaborations. COMPASS has extracted [18] the amplitudes $A_{\cos \phi_h}^{UU}$ and $A_{\cos 2\phi_h}^{UU}$ from a sample of data collected in 2004 on a ${}^6\text{LiD}$ target (to a good approximation, an isoscalar deuteron target). An $A_{\sin \phi_h}^{LU}$ asymmetry is also expected to be present due to higher twist effects and has been measured. It has no clear interpretation in terms of the parton model, it turns out to be small, and will be neglected in the following. To extract the azimuthal asymmetries one has to correct the measured azimuthal distributions by the ϕ_h dependent part of the apparatus acceptance and to fit the corrected distribution with the appropriate ϕ_h function. To reduce as much as possible the acceptance corrections, some tighter cuts have been applied to the SIDIS event selection as compared to the standard analysis. The final event and hadron selection is in this case: $Q^2 > 1 \text{ GeV}^2/c^2$, $W > 5 \text{ GeV}/c^2$, $0.003 < x < 0.13$, $0.2 < y < 0.9$, $\theta_{\gamma^*}^{lab} < 60 \text{ mrad}$, $0.2 < z < 0.85$ and $0.1 < p_T^h < 1.0 \text{ GeV}/c$.

The amplitudes of the azimuthal modulations have been obtained binning the data both separately in each of the relevant kinematic variables x , z or p_T^h and in a three-dimensional grid of these three variables. The amplitudes of the $\cos \phi_h$ and $\cos 2\phi_h$ modulations show strong kinematic dependences both for positive and negative hadrons. As an example, the preliminary results for $\cos \phi_h$ are shown in Fig. 5. Also $A_{\cos 2\phi_h}^{UU}$ shows a

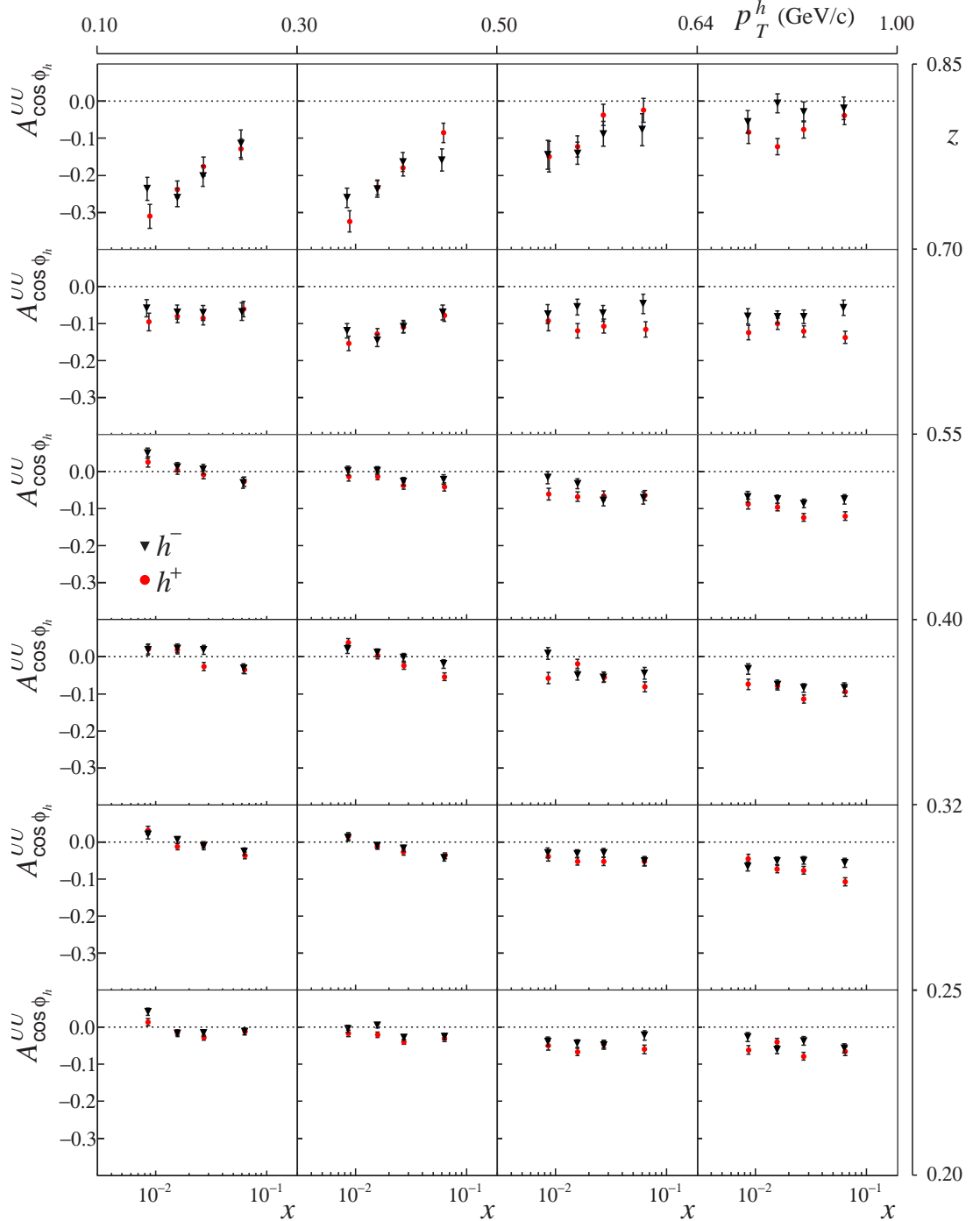


Figure 5: The preliminary results for the $\cos \phi_h$ asymmetries $A_{\cos \phi_h}^{UU}$ for positive and negative hadrons as functions of x in the different z and p_T^h bins from 2004 unpolarised ${}^6\text{LiD}$ data.

similarly strong dependence on the x , z and p_T^h variables, which up to now has not been reproduced with theoretical models.

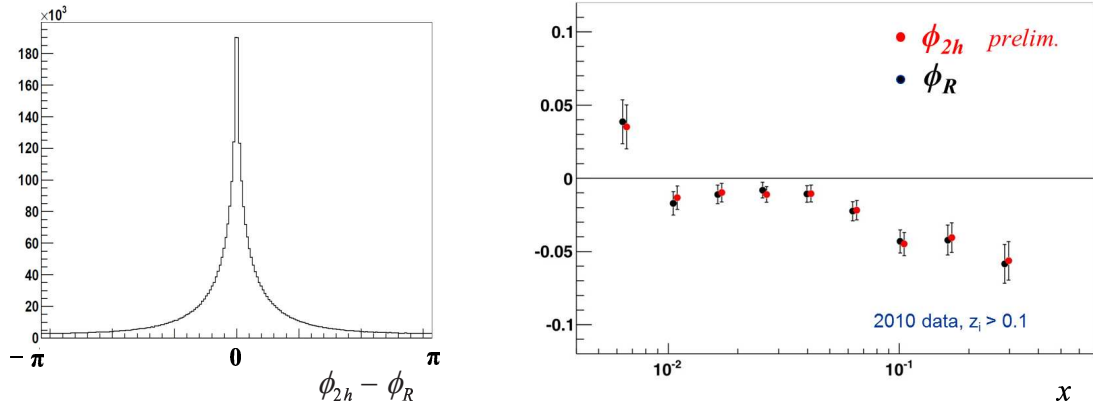


Figure 6: Left: difference between ϕ_{2h} and ϕ_R . Right: comparison between the 2-h asymmetries evaluated (see text) using ϕ_R (black points) and ϕ_{2h} (red points) from the 2010 data.

5. Interplay between Collins and dihadron asymmetries. There is a striking similarity between the Collins asymmetries in Fig. 2 and the 2-h asymmetries as functions of x shown in Fig. 4. First of all there is a mirror-symmetry between the Collins asymmetry for positive and for negative hadrons, the magnitude of the asymmetries being essentially identical and the sign being opposite in each x -bin. This symmetry has been phenomenologically described in terms of u quark dominance and almost opposite favoured and unflavoured Collins FFs [15].

The observation that the new COMPASS results on the 2-h asymmetries allow is that the values of the 2-h asymmetries are slightly higher but very close to the values of the Collins asymmetries for positive hadrons and to the mean of the values of the Collins asymmetry for positive and for negative hadrons, after changing the sign of the asymmetry of the negative hadrons. The hadron samples on which these asymmetries are evaluated are different, since at least one hadron with $z > 0.2$ is required to evaluate the Collins asymmetry while all the combinations of positive and negative hadrons with $z > 0.1$ are used in the case of the 2-h asymmetry. It has been checked however that the similarity between the two different asymmetries stays the same when measuring the asymmetries on the common hadron sample. This gives a strong indication that the analysing powers of the 1- and 2-h channels are almost the same, and their comparison will allow to access the contribution of the convolution over the transverse momenta in the Collins asymmetry.

More work has been done to understand the similarities between the Collins and the 2-h asymmetries [19]. The mirror symmetry of the Collins asymmetry for positive and negative hadrons suggests that when a transversely polarized quark fragments oppositely charged hadrons have azimuthal angles ϕ_{h+} and ϕ_{h-} differing by π . An anti-correlation between ϕ_{h+} and ϕ_{h-} is expected as a consequence of the local transverse momentum conservation in the fragmentation. The new and relevant point is that this correlation shows up also in the Collins asymmetry, so that the asymmetry exhibited by the hadron pair can be obtained in a way which is different from the one described in Par. 3. For each pair of oppositely charged hadrons, using the unit vectors of their transverse momenta we have evaluated the angle ϕ_{2h} which is the arithmetic mean (modulus π) of the azimuthal angles of the two hadrons after correcting ϕ_{h-} for the already mentioned π difference.

This azimuthal angle of the hadron pair is strongly correlated with ϕ_R , as can be seen in Fig. 6 (left) where the difference of the two angles is shown. By subtracting from

ϕ_{2h} the azimuthal angle $\pi - \phi_S$ as done in the standard analysis described in Par. 3, one obtains the angle ϕ_{2hS} which is simply the mean of the Collins angle of the positive and negative hadrons, namely a Collins angle for the hadron pair. The amplitude of the $\sin \phi_{2hS}$ modulation, which can be called the Collins asymmetries for the hadron pair, is shown as a function of x in Fig. 6 (right) for all the h^+h^- -pairs with $z > 0.1$ in the 2010 data, and compared with the 2-h asymmetries extracted from the same data sample. It is clear that the asymmetries are very close, hinting at a common physical origin for the Collins mechanism and the dihadron fragmentation, as originally suggested in the original 3P_0 Lund model and in the recursive string fragmentation model [20].

Acknowledgements. I'm grateful to Anatoly for his kind invitation, and to the COMPASS colleagues, in particular C. Braun, A. Martin and G. Sbrizzai, for valuable discussions and contributions to the work described in Par. 5.

References

- [1] C. A. Aidala, S. D. Bass, D. Hasch and G. K. Mallot, *Rev. Mod. Phys.* **85** (2013); 655. V. Barone, F. Bradamante and A. Martin, *Prog. Part. Nucl. Phys.* **65** (2010) 267.
- [2] P. Abbon *et al.* [COMPASS Collaboration], *Nucl. Instrum. Meth. A* **577** (2007) 455.
- [3] A. Bressan, these Proceedings.
- [4] C. Adolph *et al.* [COMPASS Collaboration], *Phys. Lett. B* **717** (2012) 376. C. Adolph *et al.* [COMPASS Collaboration], *Phys. Lett. B* **717** (2012) 383.
- [5] V. Y. Alexakhin *et al.* [COMPASS Collaboration], *Phys. Rev. Lett.* **94** (2005) 202002. E. S. Ageev *et al.* [COMPASS Collaboration], *Nucl. Phys. B* **765** (2007) 31.
- [6] A. Airapetian *et al.* [HERMES Collaboration], *Phys. Lett. B* **693** (2010) 11. A. Airapetian *et al.* [HERMES Collaboration], *Phys. Rev. Lett.* **103** (2009) 152002.
- [7] M. G. Alekseev *et al.* [COMPASS Collaboration], *Phys. Lett. B* **692** (2010) 240.
- [8] A. Martin [COMPASS Collaboration], Proceedings of The 20th INTERNATIONAL SYMPOSIUM on Spin Physics (SPIN2012), JINR, Dubna, Russia, September 17 - 22, 2012, arXiv:1303.2076 [hep-ex].
- [9] J. C. Collins, S. F. Heppelmann and G. A. Ladinsky, *Nucl. Phys. B* **420** (1994) 565.
- [10] A. Bacchetta and M. Radici, *Phys. Rev. D* **67** (2003) 094002.
- [11] A. Airapetian *et al.* [HERMES Collaboration], *JHEP* **06** (2008) 017.
- [12] C. Adolph *et al.* [COMPASS Collaboration], *Phys. Lett. B* **713** (2012) 10.
- [13] A. Vossen *et al.* [Belle Collaboration], *Phys. Rev. Lett.* **107** (2011) 072004.
- [14] A. Bacchetta, A. Courtoy and M. Radici, *JHEP* **1303** (2013) 119.
- [15] M. Anselmino *et al.*, *Phys. Rev. D* **87** (2013) 094019.
- [16] C. Elia, "Measurement of two-hadron transverse spin asymmetries in SIDIS at COMPASS", PhD Thesis, University of Trieste, 2012.
- [17] C. Braun [COMPASS Collaboration], *Nuovo Cim. C* **035N2** (2012) 115.
- [18] G. Sbrizzai [COMPASS Collaboration], Proceedings of The 20th INTERNATIONAL SYMPOSIUM on Spin Physics (SPIN2012), JINR, Dubna, Russia, September 17 - 22, 2012.
- [19] F. Bradamante [COMPASS Collaboration], "Interplay between collins asymmetry and two-hadron asymmetry", International workshop on the Structure of Nucleons and Nuclei, 10-14 June 2013, Como, Italy.
- [20] X. Artru, hep-ph/0207309.

STUDY OF NUCLEON SPIN AND TMDs AT JLab

Jian-Ping Chen[†]

(1) *Thomas Jefferson National Accelerator Facility, 12000 Jefferson Avenue, Newport News, VA 23606, USA*

[†] *E-mail: jpchen@jlab.org*

Abstract

The study of the nucleon spin and Transverse Momentum Dependent Distributions (TMDs) has been one of the main focuses of hadron physics. This paper will give an overview of the study of nucleon spin and TMDs at Jefferson Lab with focus on the experiments with transversely polarized targets. In inclusive Deep-Inelastic Scattering (DIS) with transversely polarized targets, several recent experiments at JLab made extensive measurements of g_2 structure function. The Burkhardt-Cottingham (B-C) sum rule [1] and the d_2 matrix, which is related to the quark-gluon correlations, were studied from the extracted moments of the g_2 . The initial exploratory Semi-Inclusive DIS (SIDIS) experiments with transversely polarized proton and deuteron targets from HERMES and COMPASS attracted great attentions and lead to very active efforts in both experimental and theoretical efforts to study the Transverse-Momentum-Dependent Distributions (TMDs). A SIDIS experiment on the neutron with a polarized ^3He target was performed at JLab. Recently published results as well as new preliminary results are shown. Precision TMD experiments are planned at JLab after the 12 GeV energy upgrade. Three approved experiments with a new SoLID spectrometer in Hall A will provide high precision TMD data in the valence quark region. TMD study is also planned with CLAS12 in Hall B. In the long-term future, an Electron-Ion Collider (EIC) as proposed in US (MEIC@JLab and e-RHIC@BNL) will provide precision TMD data of the gluons and the sea. A new opportunity just emerged in China that a low-energy EIC may provide precision TMD data in the sea and valence quark regions, complementary to the proposed EIC in US.

Introduction. Nucleon structure study has grown from mainly on the longitudinal structure and longitudinal spin [2] in the last forty years to recently rapidly increasing interests on the transverse structure and transverse spin. Transverse spin and Transverse Momentum Dependent Distribution (TMD) study has been the focus of hadron physics in recent years.

Measurements of g_2 and Extraction of Moments of g_2 . In polarized inclusive DIS experiments two spin structure functions, g_1 and g_2 , provide fundamental information of the nucleon structure. Polarized parton distribution functions (PDFs) have been extracted mainly from the first spin structure function, g_1 . Since g_1 is dominated by the lead twist (twist-2) (which provide information on PDFs) at high Q^2 , it is difficult to obtain clean information from g_1 on the quark-gluon correlations (the higher-twist effects). The second spin structure function, g_2 , is unique in providing clean access to the correlations between

quarks and gluons, because its twist-3 contribution is not suppressed (in terms of powers of Q^2) with respect to the leading twist (twist-2) contribution and the lead twist part (g_2^{WW}) can be obtained from the knowledge of g_1 through the Wandzura-Wilczek [3] relation: $g_2^{WW}(x, Q^2) = -g_1(x, Q^2) + \int_x^1 dy \frac{g_1(y, Q^2)}{y}$. In particular the 2nd moment of $g_2 - g_2^{WW}$, d_2 , is the twist-3 matrix element at high Q^2 , which can be interpreted as color polarizability [4] or color Lorentz force [5], and is directly related to the quark-gluon correlations. The zeroth moment is expected to be zero at all Q^2 as B-C sum rule [1] predicts. The measurements of g_2 requires transversely polarized targets, which is often technically challenging. SLAC E155x [6] performed the only dedicated g_2 measurement prior to JLab. At JLab, g_2 and its moments have been extensively measured for both the proton and the neutron (with polarized ^3He or deuterium targets) in a wide range of kinematics. The following table summarizes the JLab g_2 measurements.

Table 1: JLab Measurements of g_2 and Its Moments

Experiments	Halls	Particles	Q^2 (GeV 2)	Q^2 for Moments	Status
RSS [7]	C	p/d	1-2	1.3	published
SANE [8]	C	p	2-6	2-5	analysis
g2p [9]	A	p	0.02-0.3	0.02-0.3	analysis
E94-010 [10]	A	n (^3He)	0.1-1	0.1-0.9	published
E97-103 [11]	A	n (^3He)	0.6-1.3		published
E99-117 [12]	A	n (^3He)	3-5	5	published
E01-012 [13]	A	n (^3He)	1.2-3	1.2-3	submitted
E97-110 [14]	A	n (^3He)	0.01-0.3	0.01-0.3	preliminary
E06-014 [15]	A	n (^3He)	2-6	2-5	analysis

The precision data from E97-103 [11] show for the first time a clear deviation from g_2^{WW} , indicating that twist-3 effects are important at Q^2 around 1 GeV 2 .

The results of the zeroth moment of g_2 has been extracted for the neutron in the Q^2 range from 0.1 to 3 GeV 2 [10, 13] and for the proton at a Q^2 value of 1.3 GeV 2 [7]. The precision data are consistent with the B-C sum rule.

The second moment, d_2 , was extract for the proton [7] at a Q^2 of 1.3 GeV 2 and for the neutron [10, 13, 12] over a wide Q^2 range (0.1-3 and 5 GeV 2). d_2^n are expected to be extracted for both the neutron [15] and the proton [8] in a Q^2 range from 2 to 5 GeV 2 . These extensive set of measurements will allow a precision benchmark test of Lattice QCD calculations of the d_2 and help us to understand the quark-gluon correlations.

Transversity and TMD Distributions. The transverse spin (transversity) distributions, $\delta q(x, Q^2)$, are fundamental leading-twist (twist-2) quark distributions, similar to the unpolarized and polarized parton distributions, $q(x, Q^2)$ and $\Delta q(x, Q^2)$. In quark-parton models, they describe the net transverse polarization of quarks in a transversely polarized nucleon. Several special features of the transversity distributions make them uniquely interesting. The difference between the transversity and the longitudinal distributions is purely due to relativistic effects. The quark transversity distributions do not mix with gluonic effects [17] and have a valence-like behavior. The positivity of helicity amplitudes

leads to the Soffer's inequality [18] for the transversity: $|\delta q| \leq \frac{1}{2}(q + \Delta q)$. The lowest moment of δq measures the “tensor charge”, which can be calculated from lattice QCD.

Due to the chiral-odd nature of the transversity distribution, it cannot be measured in inclusive DIS experiments. In order to measure $\delta q(x, Q^2)$, an additional chiral-odd object is required, such as double-spin asymmetries in Drell-Yan processes, single target-spin azimuthal asymmetries in SIDIS reactions.

In the study of the unpolarized, longitudinally-polarized and transversely-polarized parton distributions, the parton transverse momenta are usually integrated over, so that the distributions depend only on the longitudinal momentum. Over 40-year's study has lead to precision information on the nucleon internal structure, but only in one dimension. The TMD distributions will provide a detailed map of the nucleon structure in 3-D momentum space. Study of TMDs will also allow us to learn about the orbital motion of the quarks and the effects from spin-orbital correlations. Furthermore, it provides a rich source of information on fundamental properties of QCD, such as the color gauge invariance. It will help to unravel the complexity of the quark-gluon interaction and shed light on the dynamics of the color confinement.

The first results of single target spin asymmetries in SIDIS from HERMES [19] (for the proton) and COMPASS [20] collaborations (for the deuteron and the proton) showed clear non-zero results for both the Collins and Sivers asymmetries for the proton, offering a first glimpse of possible effects caused by the transversity and TMD distributions. A global fit was performed on these data together with e^+e^- colliding data from Belle. Transversity, Sivers Function and Collins Functions were extracted from the global fit with some assumptions. [21]

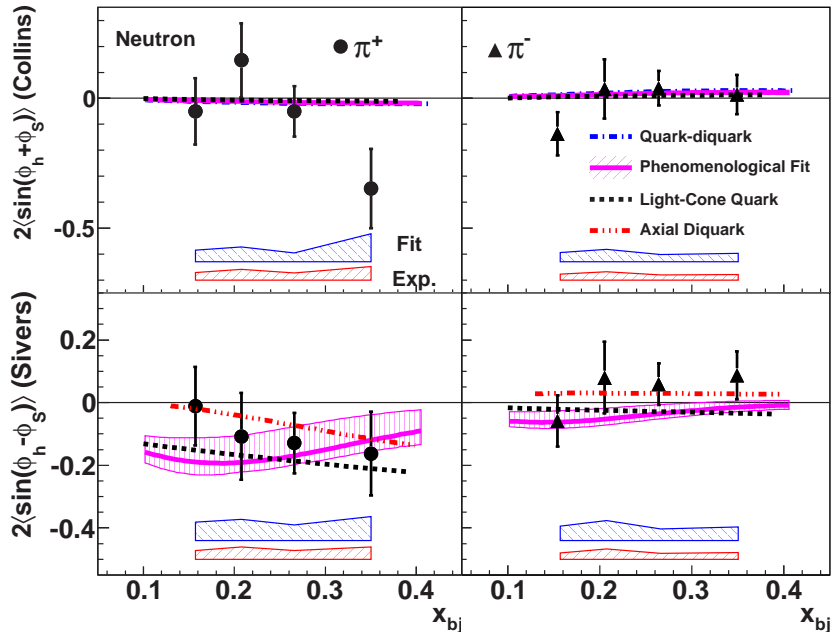


Figure 1: The extracted Collins/Sivers moments on neutron are shown together with uncertainty bands (see text) for both π^+ and π^- electro-production.

JLab E06-010: Study of the Neutron TMDs with a Transversely Polarized ^3He Target.

The first measurement of target single spin asymmetries for the neutron and ^3He was performed in the semi-inclusive $^3\text{He}(e, e'\pi)X$ reaction on a transversely polarized ^3He target. [22] The experiment, conducted at Jefferson Lab using a 5.9 GeV electron beam, covers a range of $0.14 < x < 0.34$ with $1.3 < Q^2 < 2.7 \text{ GeV}^2$. The Collins and Sivers moments were extracted from the azimuthal angular dependence of the measured asymmetries. The neutron results were extracted using the nucleon effective polarization and the measured cross section ratio of proton to ^3He and are show in Fig. 1. The Collins moments are compared with the phenomenological fit, [21] a light-cone quark model calculation [23] and quark-diquark model calculations. [24] The phenomenological fit and the model calculations predict small Collins asymmetries which are mostly consistent with our data. However, the π^+ Collins moment at $x = 0.34$ is suggestive of a noticeably more negative value at the 2σ level. Our data favor negative π^+ Sivers moments, while the π^- moments are close to zero.

Beam-target double spin asymmetry A_{LT} on a transversely polarized ^3He target was also measured in the same experiment [31]. The corresponding neutron A_{LT} asymmetries were extracted. These new data probe the transverse momentum dependent parton distribution function g_{1T}^q and therefore provide access to quark spin-orbit correlations. Our results indicate a positive azimuthal asymmetry for π^- production on ^3He and the neutron, while our π^+ asymmetries are consistent with zero.

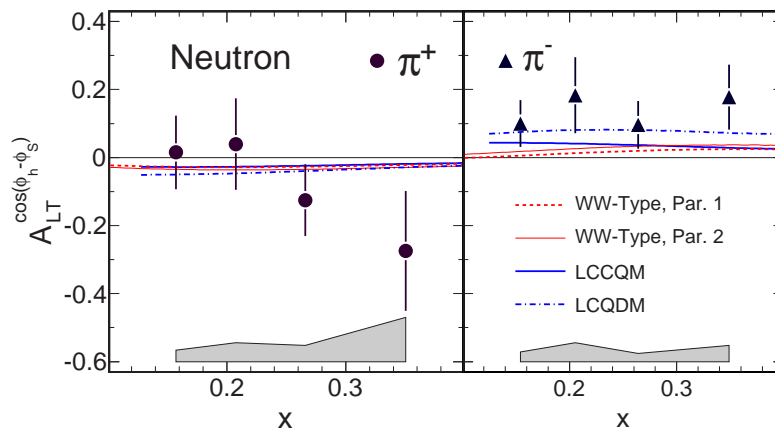


Figure 2: Neutron azimuthal asymmetry A_{LT} for positive (left) and negative (right) charged pions vs x .

The extracted A_{LT} results for the neutron are shown in Fig. 2 and are compared to several model calculations, including WW-type approximations with parametrizations [32], a light-cone constituent quark model (LCCQM) [33] and a light-cone quark-diquark model (LCQDM) [34]. While the extracted $A_{LT}^n(\pi^+)$ is consistent with zero within the uncertainties, $A_{LT}^n(\pi^-)$ is consistent in sign with these model predictions but favors a larger magnitude. While the π^+ and π^- data are consistent with the interplay between S-P and P-D wave interference terms predicted by the LCCQM and LCQDM models, the magnitude of the measured π^- asymmetry suggests a larger total contribution from such terms than that found in the LCCQM. In summary, a positive asymmetry was observed

for $n(e, e'\pi^-)X$, providing the first experimental indication of a nonzero A_{LT} , which at leading twist leads to a nonzero g_{1T} . When combined with measurements on proton and deuteron targets, these new data will aid the flavor-decomposition of the g_{1T} TMD PDFs.

From JLab E06-010, we also extracted Collins and Sivers asymmetries for charged Kaon production, thanks to the excellent hadron particle identifications in the HRS-L spectrometer. The total statistics for Kaons are significantly less than those for the pions, about 5% for K^+ to π^+ and about 1% for K^- to π^- . The extracted preliminary results [25], at an average x value of 0.22, of Collins and Sivers asymmetries on ^3He are consistent with zero for K^+ and negative, about 2σ away from zero, for K^- .

In addition to the coincidence data, we also took data on inclusive electron scattering and inclusive hadron productions. Single Spin Asymmetries were obtained. The preliminary results of SSA from inclusive DIS electron scattering on the vertically polarized neutron [26] show a clear non-zero value (about 3σ away from zero) with a value at the level of 10^{-2} . In the Born approximation (one photon exchange) and assuming the time-reversal invariance, the vertical SSA should be zero. The non-zero results are due to the two-photon-exchange contributions. Two groups of theoretical calculations [27,28], which assume two-photon exchange with quasi-free quarks, predicted the neutron asymmetry to be at the level of 10^{-4} to 10^{-2} . Our preliminary results are consistent in sign and order-of-magnitude with the model [28] where the two photons couple to different quarks.

The preliminary SSA results [29] of single charged pion production from vertically polarized ^3He target show clearly non-zero values with opposite sign between π^+ and π^- . Preliminary results on the charged Kaons production are also available but with significantly less statistics.

Planned JLab 12 GeV Program: Precision Study of TMDs with the SoLID Spectrometer and CLAS12 With 12 GeV energy upgrade of CEBAF, a new window opens up for precision study of the nucleon transverse spin and transverse momentum dependent distributions. To precisely map out the multi-dimensional (in momentum space) structure, both high luminosity and large acceptance spectrometers are necessary. A new spectrometer SoLID (Solenoidal Large Intensity Device) was proposed to be used for precision mapping of the multi-dimensional TMD asymmetries. Three SIDIS experiments were approved by the JLab Program Advisory Committees with the highest scientific rating (A). Two experiments will carry out precision measurements of Single target Spin Asymmetries (SSA) and Double target-beam Spin Asymmetries (DSA) from semi-inclusive electroproduction of charged pions from both a transversely polarized proton and a polarized ^3He target in DIS kinematics using 11 and 8.8 GeV electron beams. One experiment will be on a longitudinally polarized ^3He target. The proposed experiments will provide precise 4-D (x, z, P_T and Q^2) data on the Collins, Sivers, pretzelosity and Worm-Gear asymmetries for the proton and the neutron through the azimuthal angular dependence. The results from these experiments, when combined with the Collins fragmentation function determined from the e^+e^- collision data, will allow for a flavor separation of the quark tensor charge, and achieve a determination of the tensor charge of u and d quark to better than 10%. The extracted Sivers, pretzelosity and Worm-Gear asymmetries will provide important information to understand the correlation between the quark orbital angular momentum and the nucleon spin.

The projected results for π^+ Collins asymmetry at one typical kinematic bin is shown

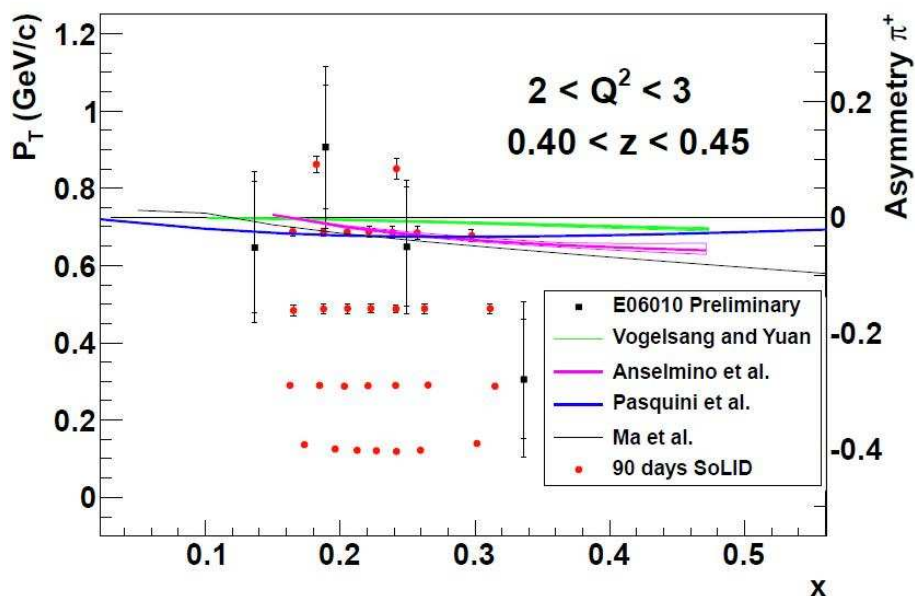


Figure 3: 12 GeV Projections with SoLID and a transversely polarized ^3He target for π^+ Collins asymmetries at $0.45 > z > 0.4, 3 > Q^2 > 2$.

in Fig. 3. The x-axis corresponds to the Bjorken x . The y-axis on the left side is P_T which is the transverse momentum. The y-axis on the right side shows the scale of the asymmetry. The y-position of the projections shows the average P_T value for the corresponding kinematic bin. The statistical uncertainties follow the scale on the right side of y-axis. The scale of the theoretical calculations follow the right side y-axis. Also shown in the figure are theoretical predictions from Anselmino *et al.* [21], Ma *et al.* [24], Pasquini *et al.* [33] and Vogelsang and Yuan [35] for the Collins asymmetry. Complete projections for π^+ (π^-) Collins/prezelocity/Sivers asymmetries in terms of 4-D (x, z, P_T and Q^2) kinematic bins can be found in Ref. [30]. These data will allow us to extract TMDs in the valence quark region with the ultimate precision. TMD study with a novel transversely polarized HD target was conditionally approved in Hall B with the CLAS12 spectrometer. The measurement will extend the kinematic range to higher Q^2 and higher P_T as well as extend to the Kaon production.

TMD Study with an Electron-Ion Collider. TMD study has been simulated for the cases of an EIC in US [37], namely the MEIC at JLab and e-RHIC at BNL. The Sivers function, as an example, is deemed as one golden measurement. While the medium and high energy EIC will provide precision map of TMDs of the gluons and the sea, a low energy EIC will play an important role in the TMD study, in particular in the sea-quark region and also in the valence quark region with high Q^2 . Such an opportunity is being seriously considered by the Chinese high-energy nuclear physics community. A new High Intensity heavy-ion Accelerator Facility (HIAF) was approved by the Chinese government, which can accelerate protons to 12 GeV and heavy ions up to Uranium to about 6 GeV/nucleon. The facility construction is planned to start in 2014 and complete by 2019. A new proposal [38] to add an electron ring to form a polarized EIC is being

considered. The proposed 1st stage will be a collider with 3 GeV polarized electrons on 12 GeV polarized protons with a luminosity up to 4×10^{32} e-nucleon/cm²/s. The physics program are under study. Possible golden experiments, including measurements of spin-flavor, TMD, GPD, hadronization, and pion/Kaon structure function, are being simulated. The proposal was discussed at several recent international conferences and was endorsed by the community.

Summary. Experimental study of g_2 and TMDs at JLab has been presented. Study of transverse spin and TMDs is one of the main focuses in hadron physics. Exploratory experiments already show many interest features. Results from a recent JLab experiment on the neutron with a transversely polarized ³He target are shown, including the published results and several new preliminary results. Precision experiments after JLab 12 GeV upgrade, including with a new proposed large acceptance spectrometer, SoLID, are discussed, which will provide high precision multi-dimensional mapping of the TMDs in the valence quark region. A new low-energy EIC in China is under consideration. Complementary to the JLab 12 GeV and the medium-to-high energy EIC in US.

References

- [1] H. Burkhardt and W. N. Cottingham, *Ann. Phys. (N.Y.)* **56**, 453 (1970).
- [2] S. E. Kuhn, J. P. Chen and E. Leader, *Prog. Part. Nucl. Phys.* **63** 1, (2009).
- [3] S. Wandzura and F. Wilczek, *Phys. Lett.* **B 72** (1977).
- [4] X. Ji and W. Melnitchouk, *Phys. Rev. D* **56**, 1 (1997).
- [5] M. Burkardt, arXiv:0812.2208 (2008).
- [6] P. L. Anthony, *et al.*, *Phys. Lett.* **B 553**, 18 (2003).
- [7] K. Slifer, *et al.*, *Phys. Rev. Lett.* **105**, 101601 (2010).
- [8] JLab E07-003, S. Choi, M. Jones, Z. E. Meziani and O. Randon, spokespersons.
- [9] JLab E08-027, A. Camsonne, J. P. Chen, D. Crabb and K. Slifer, spokespersons.
- [10] M. Amarian, *et al.*, *Phys. Rev. Lett.* **92**, 022301 (2004).
- [11] K. Kramer, *et al.*, *Phys. Rev. Lett.* **95**, 142002 (2005).
- [12] X. Zheng, *et al.*, *Phys. Rev. Lett.* **92**, 012004 (2004); *Phys. Rev. C* **70**, 065207 (2004).
- [13] P. Solvignon, *et al.*, *Phys. Rev. Lett* **101** 182502 (2008); arXiv:1304.4497 (2013).
- [14] JLab E97-110, J. P. Chen, A. Deur and F. Garibaldi, spokespersons.
- [15] JLab E06-014, S. Choi, X. Jiang, Z. E. Meziani and B. Sawatzky, spokespersons.
- [16] M. Gökeler, *et al.*, *Phys. Rev. D* **63**, 074506 (2001).
- [17] C. Bourrely, J. Soffer and O. V. Teryaev, *Phys. Lett.* **B420**, 375 (1998).
- [18] J. Soffer, *Phys. Rev. Lett.* **74**, 1292 (1995).
- [19] A. Airapetian, *et al.*, *Phys. Rev. Lett.* **94**, 012002 (2005).
- [20] The COMPASS collaboration, *Phys. Rev. Lett.* **94**, 202002 (2005); *Nucl. Phys.* **B765**, 31-70 (2007); *Phys. Lett.* **B717**, 376 (2012); *Phys. Lett.* **B717**, 383 (2012).
- [21] M. Anselmino *et al.*, *Phys. Rev.* **D72**, 094007 (2005); M. Anselmino *et al.*, *Phys. Rev.* **D75**, 054032 (2007).
- [22] JLab E06-010 Collaboration, X. Qian *et al.*, *Phys. Rev. Lett.* **107**, 072003 (2011).

- [23] S. Boffi *et al.*, *Phys. Rev.* **D79**, 094012 (2009); B. Pasquini *et al.*, *Phys. Rev.* **D78**, 034025 (2008).
- [24] J. She and B. Q. Ma, *Phys. Rev.* **D83**, 037502 (2011).
- [25] Y. Zhao, *et al.*, to be submitted.
- [26] J. Katich, *et al.*, arXiv:1311.0197 (2013).
- [27] A. Afanasev, M. Strikman and C. Weiss, *Phys. Rev. D* **77**, 014028 (2008).
- [28] A. Metz, *et al.*, *Phys. Rev. D* **86**, 094039 (2012).
- [29] K. Allada, *et al.*, arXiv:1311.1866 (2013).
- [30] JLab E12-10-006, Spokespersons: J. P. Chen, H. Gao, X. Jiang, X. Qian and J. C. Peng. JLab E12-11-007, Spokespersons: J. P. Chen, J. Huang, Y. Qiang and W. Yan. JLab E12-11-108, Spokespersons: K. Allada, J. P. Chen, H. Gao, X. Li and Z. E. Meziani.
- [31] JLab E06-010 Collaboration, J. Huang *et al.*, *Phys. Rev. Lett.* **108**, 052001 (2012).
- [32] A. Kotzinian, B. Parsamyan, and A. Prokudin, *Phys. Rev.* **D73**, 114017 (2006).
- [33] S. Boffi, A. V. Efremov, B. Pasquini, and P. Schweitzer, *Phys. Rev.* **D79**, 094012 (2009); B. Pasquini, S. Cazzaniga, and S. Boffi, *Phys. Rev.* **D78**, 034025 (2008).
- [34] J. Zhu and B.-Q. Ma, *Phys. Lett.* **B696**, 246 (2011).
- [35] W. Vogelsang and F. Yuan, private communications.
- [36] JLab C12-11-111, M. Contalbrigo and H. Avakian, spokespersons.
- [37] A. Accardi, *et al.*, EIC Whitepaper, arXiv:1212.1701 (2012).
- [38] <http://snst-hu.lzu.edu.cn/wiki/index.php/Eic>

HADRON MULTIPLICITIES AND QUARK FRAGMENTATION FUNCTIONS AT COMPASS

N. du Fresne von Hohenesche^{1†}
on behalf of the COMPASS collaboration

(1) *Institut für Kernphysik, Johannes Gutenberg-Universität*

† *E-mail: dufresne@cern.ch*

Abstract

Quark fragmentation functions (FF) $D_q^h(z, Q^2)$ describe final-state hadronisation of quarks q into hadrons h . The FFs can be extracted from hadron multiplicities in semi-inclusive deep inelastic scattering. The COMPASS collaboration has measured charged hadron multiplicities for identified pions and kaons using 160 GeV/c muons impinging on an isoscalar target. The data cover a large kinematical range and provide an important input for global QCD analyses at NLO, aiming at the determination of FFs, in particular in the strange quark sector. The latest results from COMPASS on pion and kaon multiplicities are presented.

Within the QCD parton model, semi-inclusive deep inelastic scattering can be factorised [1] into three components, the hard scattering cross section, the parton distribution functions (PDF), and the fragmentation functions (FF). The PDFs describe the structure of the initial-state hadrons, while the latter describe the hadronisation process as a collinear conversion of a single parton into final-state hadrons. While e^+e^- collider experiments provide precise measurements, only the sum of quark and anti-quark fragmentation functions can be extracted. In semi-inclusive deep inelastic scattering, flavour separated fragmentation functions can be determined in leading order from measured hadron multiplicities $M^h(Q^2, x, z)$, *i. e.* from the numbers of final-state hadrons normalised by the number of detected DIS events, using:

$$M^h(x, Q^2, z) = \frac{1}{\sigma^{DIS}} \frac{d\sigma^h}{dx dz dQ^2} \stackrel{\text{LO}}{=} \frac{\sum_q e_q^2 q(x, Q^2) D_q^h(z, Q^2)}{\sum_q e_q^2 q(x, Q^2)} \quad (1)$$

Here, $q(Q^2, x)$ are the parton distribution functions of the struck quarks, e_q the charge of the quark with the flavour q and $D_q^h(z, Q^2)$ the fragmentation function of quark q into hadron h . The kinematic variables are the virtual photon four-momentum squared Q^2 , the Bjorken variable x and the hadron energy fraction z . The current interest in FFs is motivated, *i. g.* by contradicting results of the strange quark helicity density. the contribution of the strange quarks to the nucleon spin, $\Delta s + \Delta \bar{s}$, can be extracted from an inclusive measurement [3] of the polarised structure function $g_1(x, Q^2)$ for proton and deuteron using pQCD. The result in NLO is negative. On the other hand, $\Delta s(x)$ can be extracted using semi-inclusive hadron asymmetries [4] in combination with a parametrisation of parton distribution functions and fragmentation functions. The integral over the measured x range tends to be zero, but strongly depends on the used parametrisation (*i. g.* EMC [5] and DSS [6]). The COMPASS experiment is an excellent facility to study

fragmentation functions from semi-inclusive muon nucleon scattering in a large kinematic range.

The COMPASS experiment [2] is located at the M2 beam line of the Super Proton Synchrotron at CERN. It uses a tertiary muon beam impinging on a isoscalar fixed-target. The set-up comprises a beam spectrometer, a target and two magnetic spectrometer stages. Both magnetic spectrometer stages have high resolution trackers and hadron as well as electromagnetic calorimetry. The first stage includes a Ring Imaging CHerenkov (RICH) detector for pion and kaon separation.

The analysis used data recorded in 2006 with a 160 GeV muon beam scattering off a polarised lithium-deuterid (${}^6\text{LiD}$) target. The polarisation cancels out as the direction was regularly reversed during data taking. After quality checks and geometric cuts on the interaction vertex of the beam muon and the target nucleon, DIS events are selected using $Q^2 > 1 \text{ GeV}^2$, $5 < W < 17 \text{ GeV}$ for the invariant mass of the final hadronic state, $0.004 < x < 0.7$ and $0.1 < y < 0.9$ for the relative virtual photon energy. In addition, hadrons are constrained to $0.2 < z < 0.85$. The lower limit is introduced to suppress contributions from target fragmentation and the upper limit to reduce contributions from production of exclusive vector mesons. To assure a good separation between pions and kaon, a hadron momentum cut of $10 \text{ GeV} < P_h < 40 \text{ GeV}$ has been applied for pions and kaons. The data are analysed in a three-dimensional binning of x , y and z . The obtained raw multiplicities are corrected for radiative QED effects, for the acceptance of

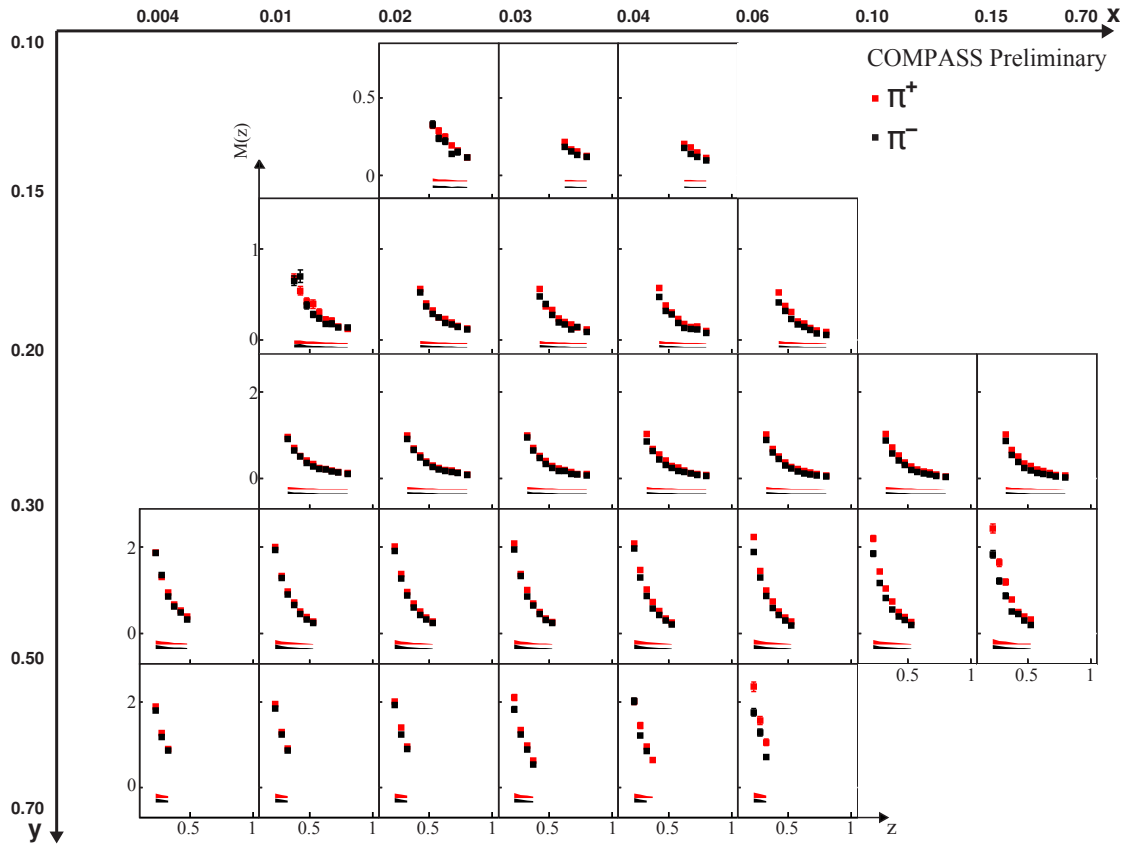


Figure 1: The preliminary, corrected pion hadron multiplicities in bins of x , y and z for positive pions (red) and negative pions (black). The systematic uncertainties are shown as error bands.

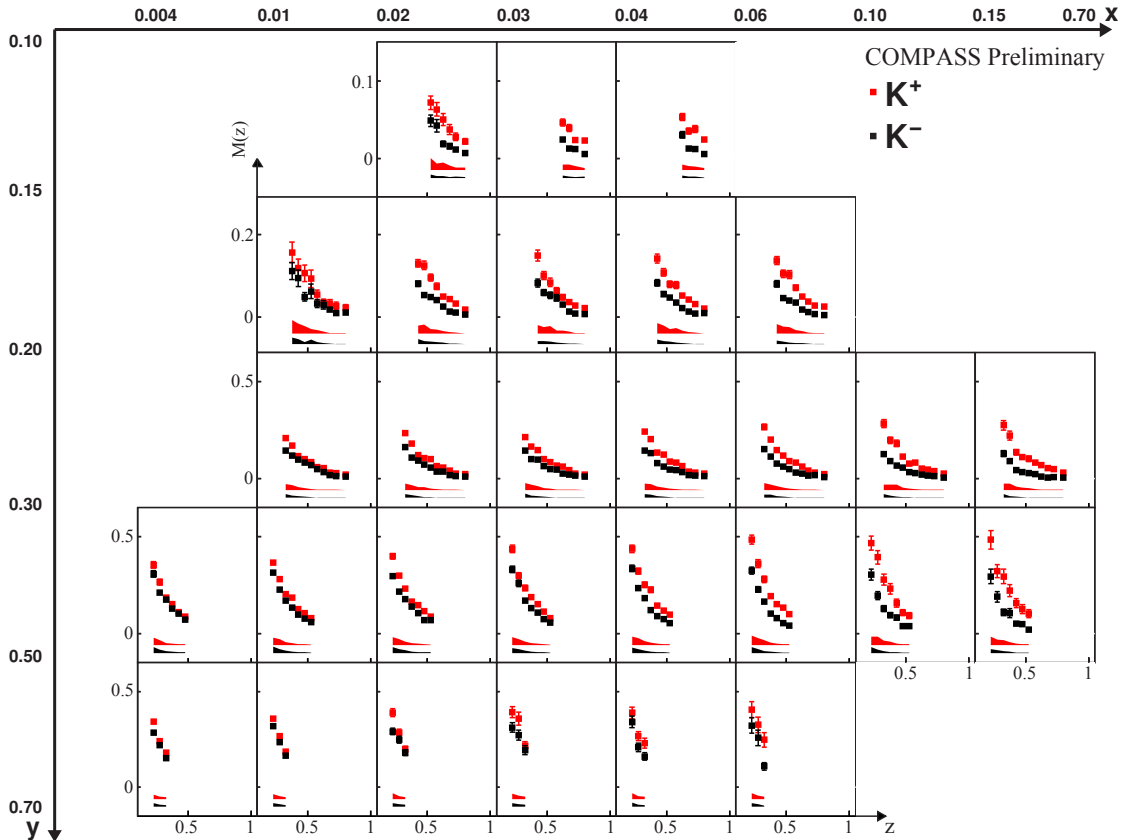


Figure 2: The preliminary, corrected pion hadron multiplicities in bins of x , y and z for positive kaons (red) and negative kaons (black). The systematic uncertainties are shown as error bands.

the spectrometer and for the particle identification efficiency. The acceptance has been determined with a Monte Carlo simulation of the COMPASS experiment. It includes the LEPTO [7] generator which contains the parton distribution functions MSTW08 and the JETSET [8] package for the hadronisation model according to the Lund string model. The produced events are reconstructed in a GEANT3 model of the COMPASS experiment using the COMPASS tuning [9]. The three dimensional acceptance correction is flat in z and reaches values from 0.4 to 0.6. Due to the hadron momentum cut some LEPTO extrapolation into the non-measured range is necessary. To avoid model dependence, all kinematic bins where the extrapolation contribution is higher than 10% are excluded. The RICH efficiency is determined by analysing the final-states of known decays (K_S^0 , ϕ and Λ). The identification efficiency for pions is 98% with a systematic uncertainty of 1% to 3%, depending on the hadron momentum and the entrance angle in the detector. The misidentification of kaons to pions is less than 3%.

Figure 1 and Figure 2 show the preliminary results for pion and kaon multiplicities for both charges: red (gray) for positive and black for negative hadrons. The systematic uncertainties are shown as bands in the corresponding x , y and z bins. It dominates the overall uncertainties, even in the kaon multiplicities, where the statistics is limited. The unidentified hadron multiplicities, which are not shown here, and the pion multiplicity are very similar, since 70% of the produced hadrons are in fact pions. The multiplicities show a strong dependence on the hadron energy fraction z and a small dependence on

y . The dependence on x is rather small and is due to the parton distribution functions. In the pion case, a small difference between positive and negative hadrons is observed. With higher x the positive pion multiplicities are larger than the negative ones. For the kaon multiplicities, the charge difference and its x and y dependence is much more pronounced. This difference is explained by the quark content of the kaons. K^+ mesons can be produced off valence quarks and sea quarks, while K^- mesons can only be produced off sea quarks.

In Figure 3, the sum of the charged kaon multiplicities is shown as a function of x , averaged over y and integrated over the measured range of the fractional hadron energy z . The charge sum is related to the strange quark distribution $S(x) = s(x) + \bar{s}(x)$ and the strange fragmentation function D_S^K , shown in Equation (2). With decreasing x , one expects an increase of the strange parton distribution, hence an increase of the sum of the kaon multiplicities. The data presented in Figure 3 do not exhibit the expected dependence, thus the strange fragmentation function to kaons seems to be small.

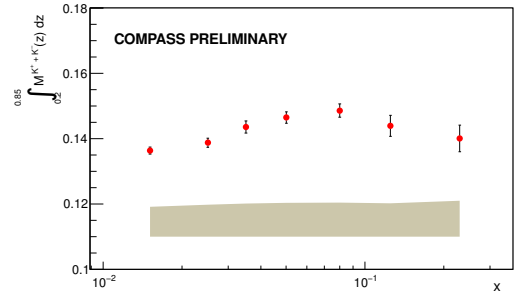


Figure 3: The charge sum of the corrected kaon multiplicities integrated over the measured z range.

$$\int M^{K^+K^-}(z)dz = \frac{Q(x) \int D_Q^K(z)dz + S(x) \int D_S^K(z)dz}{5Q(x) + 2S(x)} \propto \frac{S(x)}{Q(x)} \left(\frac{\int D_S^K(z)dz}{\int D_Q^K(z)dz} - \frac{2}{5} \right) \quad (2)$$

In conclusion, COMPASS has measured the hadron multiplicities for pions and kaon from deep inelastic scattering off an isoscalar target with a systematic uncertainty up to 3 (10)% for pions (kaons), depending on the kinematic range. Also under studies are the determination of the K_S^0 multiplicities, where soon results are expected. In 2012, COMPASS took data with an unpolarised liquid hydrogen target. More data will be taken in the future, most likely after 2015. The large data sample will allow the measurement of hadron multiplicities $M^h(x, y, z, p_t, \theta_h)$ with the hadron transverse momentum p_t and the hadron azimuthal angle θ .

References

- [1] G. Altarelli, Phys. Rept. **81** (1982) 1
- [2] P. Abbon, Nucl. Instr. and Methods **A577** (2007) 455
- [3] V.Yu. Alexakhin, Phys. Lett. **B647** (2007) 8
- [4] M.G. Alekseev, Phys. Lett. **B693** (2010) 227
- [5] M. Arneodo, Nucl. Phys. **B321** (1989) 541
- [6] D. de Florian, Phys. Rev. **D75** (2007) 114010
- [7] G. Ingelman, Comput.Phys.Commun. **101** (1997) 108
- [8] T. Sjöstrand, Comp. Phys. Comm. **82** (1994) 74
- [9] C. Adolph Phys. Lett. **B82** (2013) 922

THE (Q_{weak}) EXPERIMENT. FIRST DIRECT MEASUREMENT OF THE PROTON'S WEAK CHARGE

J.R. Hoskins^{1†} on behalf of the Q_{weak} Collaboration

(1) *College of William and Mary, Williamsburg, VA 23185 USA*

† *E-mail: jhoskins@jlab.org*

Abstract

The Q_{weak} experiment, which completed running in May of 2012 at Jefferson Laboratory, has measured the parity-violating asymmetry in elastic electron-proton scattering at four-momentum transfer $Q^2=0.025$ (GeV/c)² in order to provide the first direct measurement of the proton's weak charge, Q_w^p . The Standard Model makes firm predictions for the weak charge; deviations from the predicted value would provide strong evidence of new physics beyond the Standard Model. Using an 89% polarized electron beam at 145 μ A scattering from a 34.4 cm long liquid hydrogen target, scattered electrons were detected using an array of eight fused-silica detectors placed symmetric about the beam axis. The parity-violating asymmetry was then measured by reversing the helicity of the incoming electrons and measuring the normalized difference in rate seen in the detectors. The low Q^2 enables a theoretically clean measurement; the higher order hadronic corrections are constrained using previous parity-violating electron scattering world data. The experimental method will be discussed, with recent results constituting 4% of our total data and projections of our proposed uncertainties on the full data set.

1 Introduction

The Standard Model (SM), while being successful in describing the fundamental interactions found in nature, is thought to be an effective low-energy theory of a more fundamental underlying physics. There are two complementary methods of searching for new physics: that of high energy experiments which strive to excite matter into new forms, and that of precision experiments which aim to measure observables in the SM that are precisely predicted. The weak charge of the proton, Q_w^p , which is the neutral-weak analog of the proton's electric charge [1], is both precisely predicted and suppressed in the SM. This provides an excellent candidate for indirect searches of new physics; specifically parity-violating (PV) physics in the coupling between electrons and light quarks. The Q_{weak} experiment, which ran at Thomas Jefferson National Accelerator Facility(JLab) from November 2010 - May 2012, provides the first direct determination of Q_w^p via precise measurement of the PV asymmetry in $\vec{e}p$ scattering at low momentum transfer ($Q^2 \sim 0.025 GeV^2$). The choice of low momentum transfer and the use of parity-violating electron scattering (PVES) world data allows for a theoretically clean extraction of Q_w^p using only 4% of the our full data set [2]. Precise measurement of $Q_w^p = -2(2C_{1u} + C_{1d})$, which can be written in terms of the vector quark weak charges,

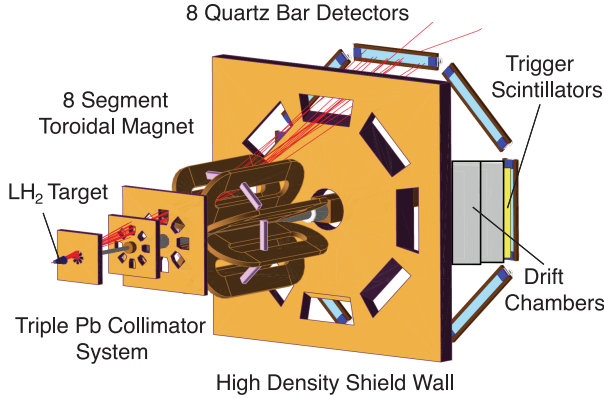


Figure 1: The basic experimental design showing the target, collimation, magnet coils, electron trajectories, and detectors. Elastically scattered electrons (red tracks) focus at the detectors while inelastically scattered electrons (not shown), are swept away from the detectors (to larger radii).

also provides an important compliment to precision atomic parity-violation (APV) experiments. APV experiments on ^{133}Cs [3] provide a different linear combination of the vector quark weak charges that can be used to separate and determine C_{1u} and C_{1d} . Determination of the vector quark weak charges can in turn be used to calculate the neutron's weak charge, $Q_w^n = -2(C_{1u} + 2C_{1d})$.

2 Experiment

The Q_{weak} experiment proposes to be the most precise electron-proton parity violating scattering measurement to date. In order to achieve this goal a custom apparatus was designed and built in Hall C of JLab [4] with the goals of providing high statistics through high current polarized beam and a high power target, low noise by minimizing target density fluctuations and high detector resolution, and controlling systematics by minimizing helicity-correlated beam properties, backgrounds, and a precision Q^2 determination. The longitudinally polarized beam had a helicity reversal of 960 Hz of $(+ - - +)$ or $(- + + -)$ chosen pseudo-randomly. The sequences made up helicity quartets and were helpful in reducing noise due to slow linear drifts, while the rapid reversal minimized effects of target boiling. The acceptance-averaged energy of the $145 \mu\text{A}$ electron beam was $1.155 \pm 0.003 \text{ GeV}$ at the target. Incoming electrons scattered from a 34.4 cm long liquid hydrogen target and into a triple lead collimator system which defined the experimental polar acceptance of $7.9^\circ \pm 3^\circ$. The azimuthal acceptance covered 49% of 2π resulting in a solid angle of 43 msr. A toroidal spectrometer focused elastically scattered electrons on to eight radiation-hard quartz Cerenkov detectors situated azimuthally symmetric about the beamline. The experiment was run in two modes: Current-mode and tracking-mode. Current-mode was the default high statistics running mode for measurement of the PV asymmetry. In current-mode, detector currents corresponding to 640 MHz/detector were read out in integrating mode using low-gain photomultiplier tubes (PMTs). Each detector was equipped with 2 cm thick Pb pre-radiators that amplified the electron signal and suppressed soft backgrounds. The tracking mode consisted of low current (0.1-200 nA) beam and used a system of horizontal and vertical drift chambers and trigger scintillators to characterize the experimental Q^2 .

3 Formalism

The PV asymmetry (A_{ep}) for longitudinally polarized electrons scattering from unpolarized protons can be defined as the difference between the scattering cross section of positive and negative helicity electrons over the total scattering cross section,

$$A_{ep} = \frac{\sigma_+ - \sigma_-}{\sigma_+ + \sigma_-}. \quad (1)$$

At tree level this can be expressed in terms of the Sachs electromagnetic form factors G_E^γ, G_M^γ , the weak neutral form factors G_E^Z, G_M^Z , and the neutral weak axial form factor G_A^Z as [5]:

$$A_{ep} = A_0 \left[\frac{\varepsilon G_E^\gamma G_E^Z + \tau G_M^\gamma G_M^Z - (1 - 4 \sin^2 \theta_W) \varepsilon' G_M^\gamma G_A^Z}{\varepsilon (G_E^\gamma)^2 + \tau (G_M^\gamma)^2} \right] \quad (2)$$

where

$$A_0 = \frac{-G_F Q^2}{4\pi\alpha\sqrt{2}}, \quad \varepsilon = \frac{1}{1 + 2(1 + \tau) \tan^2 \frac{\theta}{2}}, \quad \text{and} \quad \varepsilon' = \sqrt{\tau(1 + \tau)(1 - \varepsilon^2)} \quad (3)$$

are kinematic quantities, G_F the Fermi constant, $\sin^2 \theta_W$ the weak mixing angle, $-Q^2$ the four-momentum transfer squared, α the fine structure constant, $\tau = Q^2/4M^2$, M the proton mass, and θ the laboratory electron scattering angle. In the forward angle limit this can be rewritten in a more insightful form as,

$$A_{ep}/A_0 = Q_w^p + Q^2 B(Q^2, \theta). \quad (4)$$

Here Q_w^p is the intercept of a fit of A_{ep}/A_0 versus Q^2 . The $Q^2 B(\theta, Q^2)$ term, which contains information about the electromagnetic, weak, and strange form factors and is relatively suppressed at low Q^2 , was determined from the global fit of existing world PVES data up to 0.63 GeV². The extraction of Q_w^p comes from extrapolation as $Q^2 \rightarrow 0$ of Eq. 4. Because of the relatively small Q^2 which we report here we expect the extrapolation to $Q^2 = 0$ to be reliable. In the forward-limit the dominant energy-dependent radiative

Table 1: Recent calculations of $\square_{\gamma Z}^V(E, Q^2)$ and its uncertainty at the kinematics of this measurement.

Reference	$\square_{\gamma Z}^V(E, Q^2)$	$\Delta \square_{\gamma Z}^V(E, Q^2)$
Sibirtsev, et al. [6]	0.0047	$\begin{smallmatrix} +0.0011 \\ -0.0004 \end{smallmatrix}$
Rislow, et al. [7]	0.0057	0.0009
Gorchtein, et al. [8]	0.0054	0.0020
Hall, et al. [9]	0.0056	0.00036

correction to Eq. 4 comes from the $\gamma - Z$ box diagram ($\square_{\gamma Z}^V(E, Q^2)$) which arises in the axial-vector coupling at the electron vertex. This correction has been evaluated using dispersion relations [6–9] independently by several groups, and is summarized in Table 1. The most recent calculation [9] of $\square_{\gamma Z}^V(E, Q^2)$, uses parton distributions and benchmarking with recent $\vec{e}d$ PV data at JLab [10] to reduce uncertainties. Their result corresponds to a contribution to the asymmetry at Qweak kinematics that is equivalent to a shift in the proton’s weak charge of $7.8 \pm 0.5\%$ of the tree-level SM value.

4 Analysis

The raw asymmetry for each detector is calculated on the quartet level using the beam charge normalized integrated PMT yield for each helicity state. The acceptance averaged raw asymmetry is given by:

$$A_{raw} = \frac{Y^+ - Y^-}{Y^+ + Y^-} \quad (5)$$

where Y^\pm is the average charge-normalized yield measured by the detector array for each helicity state. The raw asymmetry was measured to be $A_{raw} = -169 \pm 31$ parts per billion (ppb). The raw asymmetry is corrected for the effects of false asymmetries resulting from helicity-correlated beam properties in the following way:

$$A_{msr} = A_{raw} + A_T + A_L + A_{reg}. \quad (6)$$

Here A_T is a correction for the residual transverse polarization in the beam asymmetry. This effect is greatly suppressed due to the azimuthal symmetry of the detector array. The term A_L accounts for potential non-linearities in the PMT response and A_{reg} corrects false asymmetries due to helicity-correlated beam position differences. The position sensitivities used in A_{reg} were determined using linear regression of the natural beam motion in X, θ_X, Y, θ_Y , and beam energy. A charge feedback loop was used to drive the charge asymmetry toward zero and a number of studies using different sets of BPMs, including and excluding charge asymmetry, were performed to study the effect on the regression correction. The full expression for the corrected asymmetry is,

$$A_{ep} = R_{tot} \frac{A_{msr}/P - \sum_{i=1}^4 f_i A_i}{1 - \sum f_i}. \quad (7)$$

Here $R_{tot} = 0.98$ accounts for effects due to ordinary radiative corrections determined from simulations, measured light yield and non-uniform Q^2 across the detector bars, and uncertainty in the determination of Q^2 . The beam polarization is represented by P , and was measured to be 0.890 ± 0.018 . The experimental backgrounds are accounted for in $f_i A_i$, where f_i represents the dilution factors and A_i represents the background asymmetries. Each of these backgrounds was explicitly measured and arose from the aluminum target cell windows, soft backgrounds, the beamline, and inelastic events. The largest correction was due to the aluminum target cell windows with a dilution of 3.2% and a measured asymmetry of 1.76 ppm. The total dilution was found to be $f_{total} = \sum f_i = 3.6\%$. The final corrected asymmetry reported here, for 4% of our total data set, is $A_{ep} = -279 \pm 35(\text{statistical}) \pm 31(\text{systematic})$ ppb. This represents the measurement of the PVES asymmetry from the proton with the highest absolute precision to date.

5 Results

The corrected asymmetry reported above, combined with results from PVES world data [11–22] from hydrogen, deuterium, and helium, is used in a global fit to Eq. 4. All data up to $Q^2=0.63 \text{ GeV}^2$ are used in the fit which follows the basic prescription found in [23]. The five parameter fit includes: the vector quark weak charges C_{1u} and C_{1d} , the

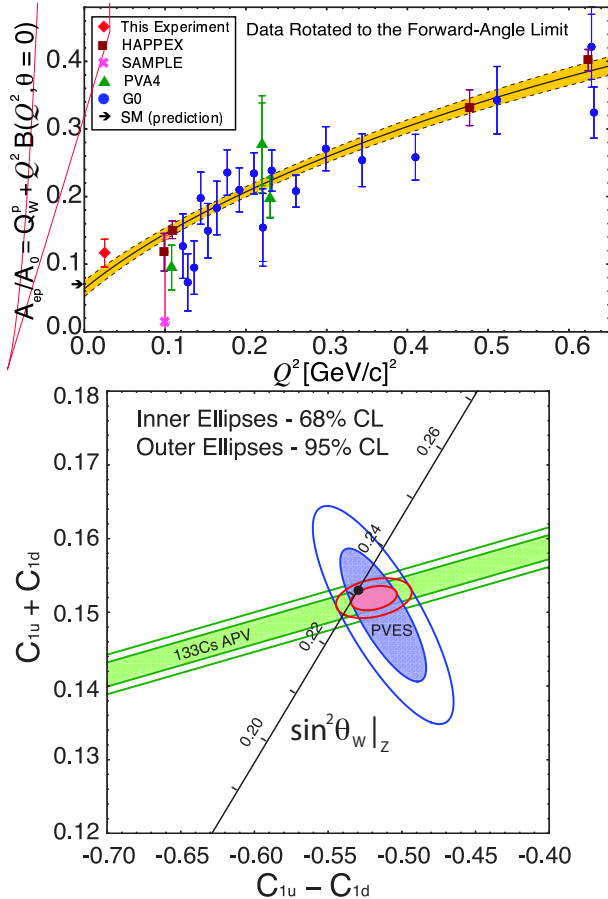


Figure 2: Global fit result (solid line) presented in the forward angle limit, derived from this measurement as well as other PVES experiments up to $Q^2 = 0.63 \text{ GeV}^2$. Fit includes data from proton, helium and deuterium targets. The additional uncertainty arising from the rotation is indicated by outer error bars on each data point, visible only for the more backward angle data. The yellow shaded region indicates the uncertainty in the fit. Q_w^p is the intercept of the fit. The SM prediction [24] is also shown (arrow).

Figure 3: Constraints on the neutral-weak quark coupling constants $C_{1u} - C_{1d}$ (isovector) and $C_{1u} + C_{1d}$ (isoscalar). The near horizontal (green) APV band constrains the isoscalar combination from ^{133}Cs data. The vertical (blue) ellipse represents the global fit of the existing $Q^2 < 0.63 \text{ (GeV)}^2$ PVES data including the new result reported here at $Q^2 = 0.025 \text{ (GeV)}^2$. The small (red) ellipse near the center of the figure shows the result obtained by combining the APV and PVES information. The SM prediction [24] as a function of $\sin^2 \theta_W$ in the \overline{MS} scheme is plotted (diagonal black line) with the SM best fit value indicated by the (black) point at $\sin^2 \theta_W = 0.23116$.

strange quark charge radius ρ_s and magnetic moment μ_s , and the isovector axial form factor $G_A^{Z(T=1)}$. All $\vec{e}p$ data were corrected for the energy-dependent $\square_{\gamma Z}^V(E, Q^2)$ term before fitting. In order to illustrate the A_o/A global fit in a single dimension, all data were converted to reduced A_o/A asymmetries and the angular dependence were removed by rotating all data to the forward limit. The global fit to the data can be seen in Fig. 2. From the fit the intercept gives $Q_w^p(\text{PVES}) = 0.064 \pm 0.012$. At tree level, the proton's weak charge is related to the weak mixing angle through $Q_w^p = 1 - 4 \sin^2 \theta_W$. Figure 4 shows the SM evolution of $\sin^2 \theta_W$ with Q^2 including the extracted Qweak value of $\sin^2 \theta_W$ (after correcting for radiative corrections as prescribed in ref. [33]) and results from other neutral current measurements.

As mentioned previously, the current results presented here can be used to constrain the weak vector quark charges. Combining our result with world PVES measurements of the weak charges and the most recent APV results [25] yields: $C_{1u} = -0.1835 \pm 0.0054$ and $C_{1d} = 0.3355 \pm 0.0050$ with a correlation coefficient of -0.980 . Recalling from above that Q_w^p can be written in terms of the weak quark charges we obtain, $Q_w^p(\text{PVES+APV}) = -2(2C_{1u} + C_{1d}) = 0.063 \pm 0.012$, which agrees perfectly with the results from PVES alone. Additionally, one can use the C_1 's to calculate the neutron's weak charge which yields $Q_w^N = -0.975 \pm 0.010$. Extractions of both Q_w^p and Q_w^n are in agreement with SM predicted values [24] of $Q_w^p(\text{SM}) = 0.0710 \pm 0.0007$ and $Q_w^n(\text{SM}) = -0.9890 \pm 0.0007$.

The commissioning data presented here make up 4% of the total data collected by the experiment. We anticipate the completion of the analysis of the full data set in late 2014. The full data set is expected to have a factor of 5 reduction in the statistical error of the measured asymmetry.

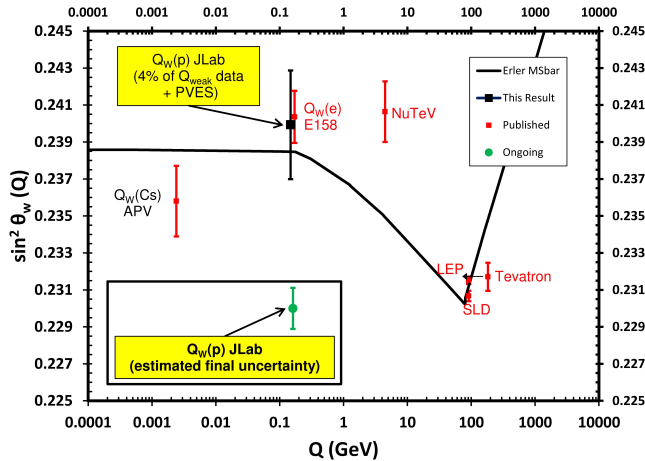


Figure 4: The calculated running of the weak mixing angle is shown in the \overline{MS} renormalization scheme [26, 27]. The red data points indicate published results; atomic parity violation [28, 29], PV Moller scattering (SLAC E158) [30, 31], deep inelastic neutrino-nucleus scattering (NuTeV) [32], and the Z-pole measurements at LEP and SLAC [28]. The black data point indicates the current published Q_{weak} value based on 4% of the total data set [2], and the green point shows the estimated final uncertainty for the Q_{weak} experiment placed arbitrarily on the vertical axis.

References

- [1] J. Erler and M.J. Ramsey-Musolf, Prog. Part. Nucl. Phys. **54**, 351 (2005)
- [2] D. Androic et al., "The First Determination of the Weak Charge of the Proton", Phys. Rev. Lett. **111**, 141803 (2013)
- [3] C.S. Wood, et al., Science **275**, 1759 (1997).
- [4] R.D. Carlini et al., The Q_{weak} Experiment: A Search for New Physics at the TeV Scale via a Measurement of the Proton Weak Charge, JLAB-PHY-12-1478, arXiv:1202.1255 (2007).
- [5] M.J. Musolf, T.W. Donnelly, J. Dubach, S.J. Pollock, S. Kowalski., Phys. Rep. **239**, 1 (1994)
- [6] A. Sibirtsev, P.G. Blunden, W. Melnitchouk, and A.W. Thomas, Phys. Rev. D **82**, 013011 (2010).
- [7] B.C. Rislow and C.E. Carlson, Phys. Rev. D **83**, 113007 (2011).
- [8] M. Gorchtein, C.J. Horowitz, and M.J. Ramsey-Musolf, Phys. Rev. C **84**, 015502 (2011)
- [9] N.L. Hall, P.G. Blunden, W. Melnitchouk, A.W. Thomas and R.D. Young, Phys. Rev. D (2013) 013011
- [10] D. Wang et al., Phys. Rev. Lett. **111**, 082501 (2013)
- [11] D.T. Spayde et al. (SAMPLE), Phys. Lett. B **583**, 79 (2004).
- [12] T.M. Ito et al. (SAMPLE), Phys. Rev. Lett. **92**, 102003 (2004).
- [13] K.A. Aniol et al. (HAPPEX), Phys. Rev. Lett. **82**, 1096 (1999).
- [14] K.A. Aniol et al. (HAPPEX), Phys. Rev. Lett. **96**, 022003 (2006).
- [15] K.A. Aniol et al. (HAPPEX), Phys. Lett. B **635**, 275 (2006).
- [16] A. Acha et al. (HAPPEX), Phys. Rev. Lett. **98**, 032301 (2007).
- [17] Z. Ahmed et al. (HAPPEX), Phys. Rev. Lett. **108**, 102001 (2012).
- [18] D.S. Armstrong et al. (G0), Phys. Rev. Lett. **95**, 092001 (2005).
- [19] D. Androic et al. (G0), Phys. Rev. Lett. **104**, 012001 (2010).
- [20] F.E. Maas et al. (PVA4), Phys. Rev. Lett. **93**, 022002 (2004).
- [21] F.E. Maas et al. (PVA4), Phys. Rev. Lett. **94**, 152001 (2005).
- [22] S. Baunack et al. (PVA4), Phys. Rev. Lett. **102**, 151803 (2009).
- [23] R.D. Young, R.D. Carlini, A.W. Thomas, and J. Roche, Phys. Rev. Lett. **99**, 122003 (2007)
- [24] J. Beringer et al., (Particle Data Group) Phys. Rev. D **86** 010001, (2012).
- [25] V.A. Dzuba, J.C. Berengut, V.V. Flambaum and B. Roberts, Phys. Rev. Lett. **109**, 203003 (2012).
- [26] J. Erler and M.J. Ramsey-Musolf, Phys. Rev. **D72**, 073003 (2005).
- [27] J. Beringer, et al., (Particle Data Group) Phys. Rev. **D86**, 010001 (2012).
- [28] S.C. Bennet and C.E. Wieman, Phys. Rev. Lett. **82**, 2484 (1999).
- [29] V.A. Dzuba, J.C. Berengut, V.V. Flaumbaum and B. Roberts, Phys. Rev. Lett. **109**, 203003 (2012).
- [30] P.L. Anthony, et al., Phys. Rev. Lett. **92**, 181602 (2004).
- [31] P.L. Anthony, et al., Phys. Rev. Lett. **95**, 081601 (2005).
- [32] G.P. Zeller, et al., Phys. Rev. Lett. **88**, 091802 (2002).
- [33] J. Erler, A. Kurylov, and M.J. Ramsey-Musolf, Phys. Rev. **D68**, 016006 (2003)

MEASUREMENT OF SPIN-DEPENDENT STRUCTURE FUNCTION g_1^p WITH 200 GeV BEAM AT COMPASS (CERN)

A.V. Ivanov^{1†}, for the COMPASS collaboration
(1) *Joint Institute for Nuclear Research, Dubna, Russia*
† *E-mail: artem.ivanov@cern.ch*

Abstract

Abstract: The longitudinal inclusive spin asymmetry A_1^p and the spin-dependent structure function of the proton g_1^p as a function of x and Q^2 in deep-inelastic muon-proton scattering have been measured at COMPASS (SPS, CERN). The results have been obtained with data collected in 2011 for the longitudinal polarised NH_3 solid target and polarised muon beam of 200 GeV. The high energy of the beam allows extension of the measured region to lower x (down to 0.0025) and larger Q^2 (up to $100 (\text{GeV}/c)^2$).

The longitudinal spin-dependent structure function of the nucleon, g_1 , is the subject of profound theoretical and experimental interest. The main reason for this interest is the results of the EMC experiment in 1988. They had shown that only a small fraction of the nucleon spin is carried by quarks, $\Delta\Sigma = 0.12 \pm 0.09(\text{stat}) \pm 0.14(\text{syst})$ [1]. It was far from the predicted expectations of 60% [2] at that time. The “spin crisis” urged further investigations in an attempt to find the missing component. The SMC and COMPASS experiments at CERN, as well as E142, E143, E154, E155 at SLAC, and the HERMES experiment at DESY confirmed the EMC observation with a better accuracy. More recent estimation of the contribution of quarks to the spin of the nucleon gives $\Delta\Sigma = 0.30 \pm 0.01(\text{stat}) \pm 0.02(\text{syst})$ [3]. The value of $\Delta\Sigma$ is obtained in \overline{MS} scheme.

The longitudinal spin-dependent structure function, g_1 , can be measured in the polarised deep-inelastic scattering (DIS) processes where an incoming lepton scatters off a polarised fixed nucleon target. Structure function, g_1 , is expressed through the double-spin asymmetry of the cross sections, $A_{||}$, by

$$A_{||} = \frac{d\sigma^{\uparrow\downarrow} - d\sigma^{\uparrow\uparrow}}{d\sigma^{\uparrow\downarrow} + d\sigma^{\uparrow\uparrow}}, \quad (1)$$

where the arrows indicate the relative direction of the beam particle spin (\uparrow) and the target nucleon spin (\uparrow). The asymmetry $A_{||}$ is related to the longitudinal virtual photon nucleon asymmetry, A_1 , as

$$A_{||} = D(A_1 + \eta A_2), \quad (2)$$

where D is a depolarisation factor, which gives the information about a spin transfer from a lepton to a virtual photon. In the kinematic region of the COMPASS experiment the factor η is small. The contribution of A_2 is included into the systematic error. In view of the previous facts, Eq. (2) could be rewritten as $A_{||} \approx DA_1$. The longitudinal spin-dependent structure function, g_1 , relates to A_1 by

$$g_1 = \frac{F_2}{2x(1+R)} A_1, \quad (3)$$

where F_2 is the spin-independent structure function and R is the ratio of cross sections for absorption of longitudinal and transverse polarised photons, $R = \sigma^L/\sigma^T$.

The new measurements were performed with the COMPASS (COmmon Muon and Proton Apparatus for Structure and Spectroscopy) setup at the M2 beamline of the SPS accelerator of CERN. The new proton data were collected during the year 2011 using a 200 GeV longitudinally polarised muon beam and longitudinally polarised proton (NH_3) with an average polarisation 80% and 85%, respectively. The target was composed of three cells in which the neighboring target cells are polarised in the opposite direction. Every 24 hours the spin directions in all cells were reversed by rotating the magnetic field direction in order to cancel out a contribution of acceptance in the asymmetry calculations. Detailed description of the COMPASS setup can be found in Ref. [4].

All events used in the analysis were required to have a reconstructed primary interaction vertex by the incoming and the scattered muon inside one of the target cells. In order to cancel out the muon flux normalization in the asymmetry calculation were required to cross the three cells of the target. Events were selected by cut on the four-momentum transfer squared, $Q^2 > 1 \text{ (GeV/c)}^2$, which defines the region DIS and cut on the fractional energy of the virtual photon, $0.1 < y < 0.9$. The Bjorken scaling variable interval was $0.0025 < x < 0.7$. The statistics available for the analysis after all cuts is about 78 million events.

The starting point for the A_1 asymmetry extraction is the number of events detected in each target cell before and after reversal of the target polarisation direction,

$$N = a\Phi n\bar{\sigma}(1 \pm fDP_B P_T A_1), \quad (4)$$

where a is a acceptance of the spectrometer, Φ is an incoming muon flux, n is a number of target nucleons, $\bar{\sigma}$ is a total cross-section, P_B is a beam polarisation, P_T is a target polarisation and f is a dilution factor, which means the ratio of photon-absorption a polarized cross-sections on a proton to the onces on all nuclei that fill the target cells.

Radiative corrections were taken into account in the dilution factor calculation. The average value of D and f is equal to 0.6 and 0.16, respectively. In order to minimize the statistical error of the asymmetry, each event is weighted by $\omega = fDP_B$.

The four relations $(P_1 P_4)/(P_2 P_3)$ relates to A_1 through a second order equation, where $P_i = \sum_j^{N_i} \omega_j$, $i = 1(2)$ denotes combination of data sets for the upstream and the downstream cells before (after) reversal of the target spin directions, $i = 3(4)$ denotes data set for the center cells taken before (after) reversal of the target spin directions.

The new values of $A_1^p(x)$ on a proton as a function of x obtained at 200 GeV are shown in Fig. 1 together with the published COMPASS results obtained at 160 GeV in 2007 [3]. The higher beam energy in comparison with the 2007 data allows to obtain an

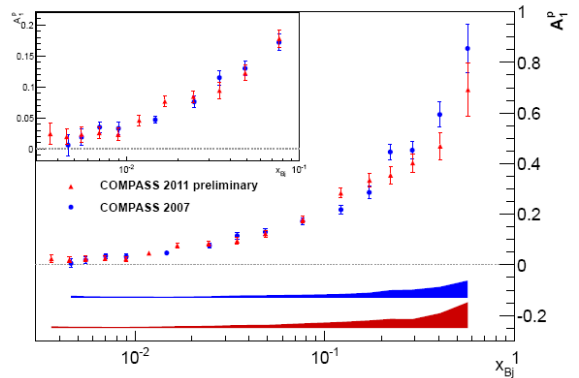


Figure 1: The asymmetry $A_1^p(x)$ measured at 200 GeV in 2011 is shown together with previous COMPASS results measured at 160 GeV in 2007. The bands at the bottom of the figure show the systematic errors of the COMPASS measurements.

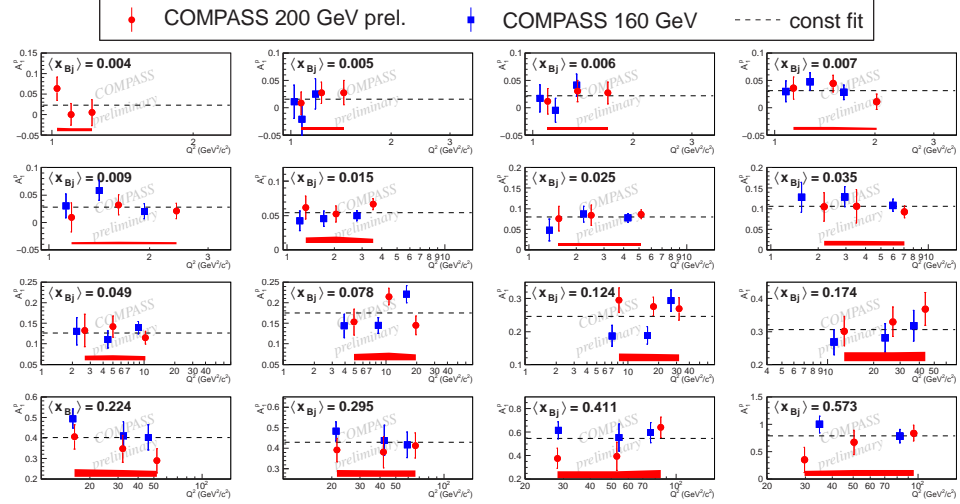


Figure 2: Values of $A_1^p(x, Q^2)$ as a function of Q^2 in intervals of x . The band at the bottom of the figure is the systematic uncertainty. The dashed lines show the results of fits to a constant.

additional point in the low x region: $0.0025 < x < 0.004$. The full systematic error of the new results for $A_1^p(x)$ is shown by the band at the bottom of Fig. 1. The systematic error of 2011 contains the contributions of the uncertainties on the target polarisation 5%, the beam polarisation 5%, the dilution factor 2–3% and the depolarisation factor 2%. Another possible contributions to the systematic error is the contribution from the neglected of the transverse asymmetry, A_2^p , which is less than 0.002 in the full range of x and the contribution from radiative effects, $10^{-5} - 10^{-3}$. Also there is a contribution from false asymmetries generated by instabilities in some components of the spectrometer. Its limit of $\sigma_{syst} < (0.36 \div 0.84)\sigma_{stat}$ was obtained at 68% CL for σ_{stat} .

The asymmetries $A_1^p(x, Q^2)$ as a functions of Q^2 for 16 fixed intervals of x are shown in Fig. 2. The dashed lines indicate the results of fits to a constant. The bands at the bottom correspond to the systematic uncertainty. No significant Q^2 dependence is observed in any interval of x .

The value of $g_1^p(x, Q^2)$ was obtained from Eq. (3) using the SMC parametrisation of the spin-independent structure function F_2^p from Ref. [5] and the SLAC parametrisation of R from Ref. [6]. The new results for $g_1^p(x, Q^2)$ splitted into 2–3 bins of Q^2 at each x value are shown in Fig. 3. New data are compared to the previous COMPASS data at 160 GeV and to other experiments. The dashed line indicates the results of NLO QCD fit from LSS05 [7].

A new measurement of $g_1^p(x, Q^2)$ at 200 GeV beam energy was performed. The mea-

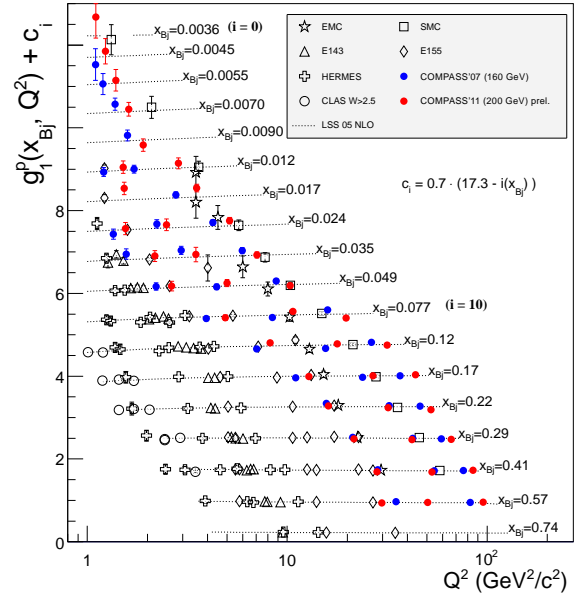


Figure 3: The world data measurement of g_1^p versus Q^2 , only statistical errors are plotted.

surement region was enhanced to lower x and larger Q^2 . For the first time, the results for smaller x ($0.0025 < x < 0.004$) were obtained. The new data will be used to update the Bjorken sum rule [3] and indirect measurement of ΔG via COMPASS NLO QCD fit of world g_1 data [8].

References

- [1] J. Ashman *et al.* [European Muon Collaboration], “An Investigation of the Spin Structure of the Proton in Deep Inelastic Scattering of Polarized Muons on Polarized Protons,” Nucl. Phys. B **328** (1989) 1.
- [2] F. E. Close and R. G. Roberts, “Consistent analysis of the spin content of the nucleon,” Phys. Lett. B **316** (1993) 165 [hep-ph/9306289].
- [3] M. G. Alekseev *et al.* [COMPASS Collaboration], “The Spin-dependent Structure Function of the Proton g_1^p and a Test of the Bjorken Sum Rule,” Phys. Lett. B **690** (2010) 466 [arXiv:1001.4654 [hep-ex]].
- [4] “The COMPASS experiment at CERN,” Nucl. Instrum. Meth. A **577** (2007) 455 [hep-ex/0703049].
- [5] B. Adeva *et al.* [Spin Muon Collaboration], “A Next-to-leading order QCD analysis of the spin structure function $g(1)$,” Phys. Rev. D **58** (1998) 112002.
- [6] V. Y. Alexakhin *et al.* [COMPASS Collaboration], “The Deuteron Spin-dependent Structure Function $g_1(d)$ and its First Moment,” Phys. Lett. B **647** (2007) 330 [hep-ex/0609038].
- [7] E. Leader, A. V. Sidorov and D. B. Stamenov, “Longitudinal polarized parton densities updated,” Phys. Rev. D **73** (2006) 034023 [hep-ph/0512114].
- [8] C. Adolph *et al.* [COMPASS Collaboration], “Leading and Next-to-Leading Order Gluon Polarization in the Nucleon and Longitudinal Double Spin Asymmetries from Open Charm Muoproduction,” Phys. Rev. D **87** (2013) 052018 [arXiv:1211.6849 [hep-ex]].

INVESTIGATION OF DEUTERON BEAM INTERACTION WITH CARBON AND POLYETHYLENE TARGETS AT INTERMEDIATE ENERGIES BY MEANS OF GEANT4 SIMULATION.

M. Janek^{1†}, Yu.V. Gurchin², A.Yu. Isupov², J-T. Karachuk^{2,3}, A.N. Khrenov², A.K. Kurilkin², P.K. Kurilkin², V.P. Ladygin², A.N. Livanov², G. Martinska⁴, S.M. Piyadin², S.G. Reznikov², G. Tarjanyiova¹, A.A. Terekhin², B. Trpisova¹, and T.A. Vasiliev².

(1) *Physics Dept., University of Zilina, 010 26 Zilina, Slovakia*

(2) *LHEP-JINR, Dubna, Moscow region, Russia*

(3) *Advanced Research Institute for Electrical Engineering, Bucharest, Romania*

(4) *P.J. Safarik University, Kosice, Slovakia*

† *E-mail: janek@fyzika.uniza.sk*

Abstract

The GEANT4 simulations of the $dp \rightarrow ppn$ non-mesonic breakup reaction at deuteron energies of 300 and 500 MeV for various configurations of scintillation detectors were performed. Liege and Binary Cascade model are used in calculations. Applicability of the subtraction procedure on obtained missing mass specters is discussed.

1 Introduction

In case of the $dp \rightarrow ppn$ non-mesonic reaction, the short range nucleon correlations are represented mainly by the NN potentials (*e. g.* CD-Bonn [1]) and the 3NFs. This reaction is one of the simplest ones in which the structure of these objects can be studied.

The dp breakup possesses rich kinematics or phase space. The effects originating from the 3NFs dominate some regions of the phase space, the relativistic effects other. The Coulomb effects can be investigated in regions of the phase space where the 3NFs and relativistic effects are weak. Thus, to obtain data for a large region of the phase space it is desirable to get complementary information about the reaction mechanism and the structure of the objects involved in the dp breakup. Using the pd breakup data collected at 19 MeV [2] a discrepancy between the data and the calculations that included the 3NFs has been found. Inclusion of the Coulomb interaction is very significant but in this case didn't completely remove discrepancy. Large discrepancies between experiment and theoretical calculations based on various NN and 3N potentials have also been found in case of the dp breakup measured at 130 MeV [3]. It has been shown, however, that theoretical calculations based on low energy expansion of QCD, *i. e.* the Chiral Perturbation Theory (χPT), can satisfactorily describe data obtained for energies up to 100 MeV/nucleon.

The currently known NN and 3N potentials are in many cases in good agreement with experiment but in some cases they are not.

2 Experiment and GEANT4 simulation

The dp non-mesonic breakup reaction is experimentally studied at deuteron energy from 300 to 500 MeV. Eight ΔE -E scintillation detectors are used. Each detector consists of two scintillators ΔE and E. Both scintillators are of a tube shape, the thin one of a height of 1 cm, the thick one of a 20 cm height, with the diameter of the cross section 8 cm and 10 cm, respectively. Two Photomultiplier tubes PMTs-85 are positioned opposite to each other at the outside cylindrical surface of the thin scintillator. At the end of the E scintillator a photomultiplier tube PMT-63 is positioned. More details about ΔE -E detectors can be found in [4].

Each detector is positioned at a certain distance so that the angle whose vertex is the target subtended by the diameter of the thin scintillator is 4.6° . Longitudinal axes of detectors which work in coincidence pass through the target and make angles that we designated Θ_1 and Θ_2 with the trajectory of the incoming deuterons. The angle between detectors in plane perpendicular to the direction of the deuteron beam is denoted by Φ . The three angles Φ , Θ_1 and Θ_2 specify a detector configuration and the configurations for which we present our results are given in Table 1.

configuration	Θ_1	Θ_2	Φ
2	$22.4^\circ - 27.0^\circ$	$31.0^\circ - 35.6^\circ$	40°
5	$22.4^\circ - 27.0^\circ$	$40.9^\circ - 45.5^\circ$	180°
1	$22.4^\circ - 27.0^\circ$	$22.4^\circ - 27.0^\circ$	180°
3	$22.4^\circ - 27.0^\circ$	$31.0^\circ - 35.6^\circ$	140°
7	$22.4^\circ - 27.0^\circ$	$51.0^\circ - 55.6^\circ$	140°

Table 1: Detector configurations description.

As one can notice, the angles Θ_1 and Θ_2 appear as an interval of angles, which is due to the finite size of the detectors' cross section. The target (polyethylene, carbon) have a shape of a thin thread of thickness $10 \mu\text{m}$.

GEANT4 toolkit [5] was used to select signal events from background for various detector configurations. Plot of deposited energies in ΔE and E detectors with applied cuts is shown on the Figure 1. The leg in figure is caused mainly by the protons with energy above 180 MeV which coming out from the E scintillator which is due to not sufficient length of detector.

On the Figure 2, missing mass distributions for polyethylene (non shaded spectra) and carbon (shaded spectra) target in case of deuterons with energy of 300 (1st and 2nd row) and 500 MeV (3rd, 4th and 5th row) are presented. The detector configurations are 2 (1st row), 5 (2nd row), 1 (3rd row), 3 (4th row) and 7 (5th row), respectively. See Table 1 for detector configuration description. First, second and third column corresponds to the spectra when cut1 (Liege model), cut1

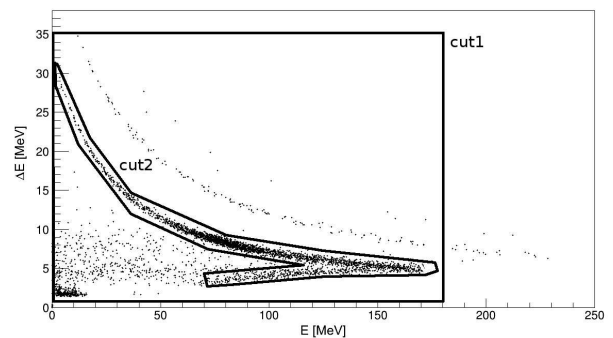


Figure 1: Plot of energies deposited in the ΔE and E detectors with applied cuts.

(Binary Cascade model) and cut2 (Binary Cascade model) is applied.

One can see that signal (dp breakup) events can be obtained subtracting carbon spectra from the polyethylene one after normalisation in the regions where only the carbon content is expected. Cut1 contains also events which have uncorrelated ΔE and E energies. These events make a "tail" in missing mass distributions (1st and 2nd column in Figure 2). Cut2 produces narrower missing mass spectra (3rd column in Figure 2). It can be seen mainly at 500 MeV. Thus, one can conclude that cut1 is more useful to obtain signal events because of the larger region where the normalisation procedure can be performed.

We found that signal events for configuration 1 and 3 are shifted towards the right part of the spectra. Since GEANT4 gives the incoming energies (before detector) of the particles, we could calculate the missing mass for these events with the correct value of their kinetic energy and we found that these events are also the dp breakup events, *i. e.* the signal events. Shift is caused by not sufficient length of detector.

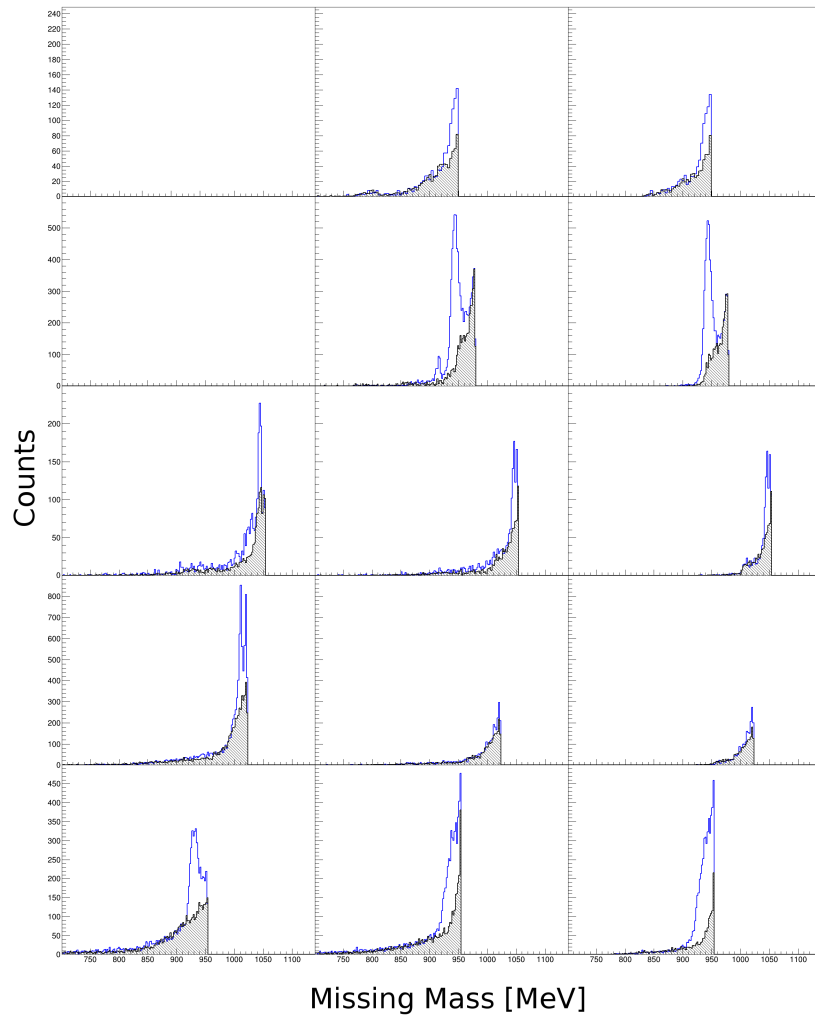


Figure 2: Missing mass distribution for polyethylene (non shaded spectra) and carbon (shaded spectra) target in case of deuterons with energy of 300 (1st and 2nd row) and 500 MeV (3rd, 4th and 5th row). The detector configurations are 2 (1st row), 5 (2nd row), 1 (3rd row), 3 (4th row) and 7 (5th row), respectively. First, second and third column corresponds to the cut1 (Liege model), cut1 (Binary Cascade model) and cut2 (Binary Cascade model).

The main reason of the peak spreading in the missing mass spectra is connected with using in the calculation of the invariant mass instead of the actual values of the scattering angles of the particles hitting the detector the angle at which main axis of the detector is placed. Other reasons of the peak spreading are associated with the detector response. We also modelled the effect of the spherical steel hull which enclosed target on energy and direction of motion of the particles going out of the target. But the hull affects the scattering angles and causes considerable energy losses for particles of only very low energies (roughly of energies smaller than 35 MeV) and these are cut out by the $\Delta E - E$ coincidence condition, that means, they stop already in the thin scintillator.

From the comparison of Liege and Binary Cascade model when cut1 is applied at 500 MeV follows. The signal events can be obtained by subtraction procedure but yields vary with detector configuration. The obtained missing mass spectra at 500 MeV for the 1st configuration (3rd row) and 7th one (5th row) are more or less similar. For the configuration 3 (4th row) there are significant discrepancy. But at the moment of simulations the Liege model was in experimental stage which can be cause of observed discrepancy.

3 Conclusion

We present results of the GEANT4 simulations of the dp non-mesonic breakup reaction at deuteron energies of 300 and 500 MeV for Liege and Binary Cascade model for various configurations of two $\Delta E - E$ detectors and discussed the usefulness of the subtraction procedure.

Acknowledgements This work was supported partly by the scientific cooperation program JINR-Slovak Republic in 2013 and by the Russian Foundation for Basic Research under grant no.13-02-00101a.

References

- [1] R. Machleidt, F. Sammarruca and Y. Song, Phys. Rev. **C53**, (1996), R1483.
- [2] J. Ley et al., Phys. Rev. **C73**, (2006), 064001.
- [3] S. Kistryn, et al., Phys. Rev. **C68**, (2003), 054004.
- [4] S. M. Piyadin et al., Physics of Particles and Nuclei Letters, **V.8**, no. 2, (2011), pp. 107-113.
- [5] S. Agostinelli et al., Nucl. Instrum. Meth. A, **V.506**, no. 3, (2003), pp. 250-303.

INVESTIGATION OF THE DEUTERON SHORT-RANGE SPIN STRUCTURE AT NUCLOTRON

P.K. Kurilkin^{1†}, V.P. Ladygin¹, Yu.V. Gurchin¹, S.M. Piyadin¹, A.A. Terekhin¹,
A.Yu. Isupov¹, M. Janek^{1,2}, J.-T.Karachuk^{1,3}, A.N. Khrenov¹, V.A. Krasnov¹,
A.K. Kurilkin¹, N.B. Ladygina¹, A.N. Livanov¹, G. Martinska⁴, V.L. Rapatsky¹,
S.G. Reznikov¹, V.V. Ryabchuk⁵, B. Trpišová², T.A. Vasiliev¹ and I.E. Vnukov⁵

(1) *Joint Institute for Nuclear Research, 141980 Dubna, Russian Federation*

(2) *Physics Dept, University of Žilina, 010 26 Žilina, Slovak Republic*

(3) *National Institute for Research and Development in Electrical Engineering ICPE-CA,
030138 Bucharest, Romania*

(4) *P.-J.Shafarik University, 041 80 Košice, Slovak Republic*

(5) *Physics Dept, Belgorog State National Research University, 308015 Belgorog, Russian
Federation*

† *E-mail: author@somewhere.org*

Abstract

The study of the deuteron and three-nucleon systems short-range spin structure via the measurements of the polarization observables in the deuteron induced reactions are planned at Nuclotron. The measurements of the analyzing powers for dp -elastic scattering and dp - non-mesonic breakup will be performed at Internal Target Station. The tensor analyzing power T_{20} and spin correlation parameter $C_{y,y}$ in the $d^3He \rightarrow p(0)^4He$ reaction will be measured in the energy range of 1000 - 2000 MeV using extracted polarized deuteron beam.

1 Introduction

The investigation of light nuclei spin structure has been performed at different experiments over the world at RIKEN, KVI, IUCF, RCNP and JINR during last decades. The goal of such investigations is to establish the nature of $2N$ and $3N$ forces, the role of the nonnucleon degrees of freedom and relativistic effects. The theoretical analysis results of the experimental data obtained at low and intermediate energies for the deuteron induced reactions (see recent review [1] and references therein) were the motivation of the research program of the DSS project [2].

It experimental program [2] includes several tasks. First one is to obtain the information on the spin τAY dependent parts of 2-nucleon and 3-nucleon forces from two processes: dp -elastic scattering in a wide energy range and dp non-mesonic breakup with two protons detection at energies 200 - 500 MeV. The second one is the measurement of the T_{20} and C_{yy} for the $^3He(d,p)^4He$ reaction at the energy range of 1.0-2.0 GeV using polarized deuteron beam and polarized 3He target. The development of the high precision deuteron beam polarimetry is important for these investigations.

The experimental program on the deuteron structure investigation at Nuclotron was started by the measurements of the vector A_y and tensor A_{yy} and A_{xx} analyzing powers in

dp - elastic scattering at T_d of 880 MeV [3] and 2000 MeV [4]. The calculations performed within relativistic multiple scattering model [5] describes the data on the vector analyzing power A_y . However, there are the problems in the description of the tensor analyzing powers at large angles in the c.m.. The goal of this paper is to report about the latest results devoted to the study of the deuteron structure and present the program of the future investigation at Nuclotron at JINR.

2 Experiment

The measurements were performed using internal target station (ITS) at Nuclotron [6] with new control and data acquisition system [7]. The $10\mu\text{m}$ CH_2 foil and $8\mu\text{m}$ carbon wire were used as the targets. The effect on the hydrogen has been obtained using $\text{CH}_2\text{-C}$ subtraction.

The schematic view of the experiment [8] to study the dp - elastic scattering at ITS is shown in Fig. 1a. The detection apparatus consists of 4 proton and deuteron scintillation counters based on FEU-85 photomultiplier tubes. The signals from the P, D detectors give coincidences for dp -elastic and quasi-elastic reactions, PP-L and PP-R register protons from pp -quasi-elastic reaction at 90° in the c.m. This reaction is used as the relative intensity monitor of the interacting beam with the target for calculation of cross-section of dp -elastic scattering reaction.

The amplitudes of the signals and timing information from the detectors and also information from target position monitor were recorded and used in the further data analysis for the dp - elastic scattering events selection. The scintillation counters coupled to Hamamatsu H7416MOD PMTs were used for the measurements at $T_d > 1000$ MeV because of better timing and amplitude resolution than FEU-85 PMTs.

The $dp \rightarrow ppn$ reaction will be investigated using $\Delta E\text{-}E$ techniques for the detection of both protons at ITS at Nuclotron. The details of the experimental setup with 8 $\Delta E\text{-}E$ detectors are presented in ref. [9].

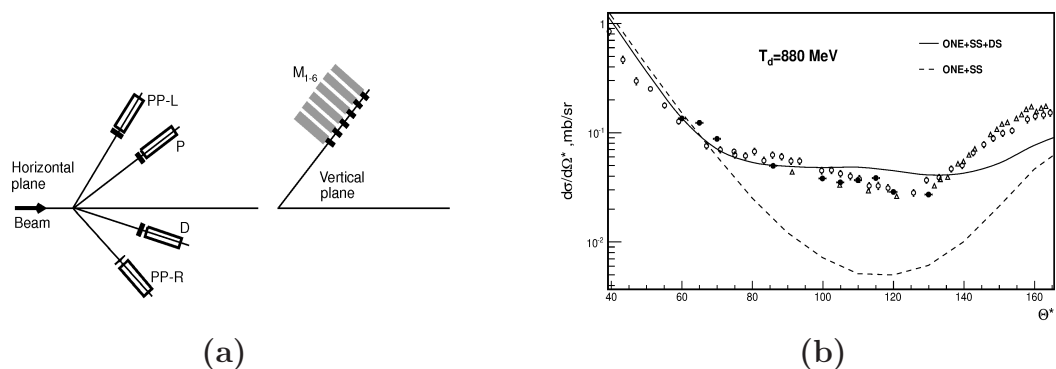


Figure 1: (a) Scheme of the experimental setup at the internal target station: P- proton detector , D- deuteron detector, PP-L and PP-R are the detectors for pp -quasi-elastic scattering, M1-M6- monitor counters. (b) The differential cross section of dp - elastic scattering obtained at 880 MeV at Nuclotron (solid circles), at 850 MeV [10] (open circles) and at 940 MeV [11] (open triangles). The lines are explained in the text.

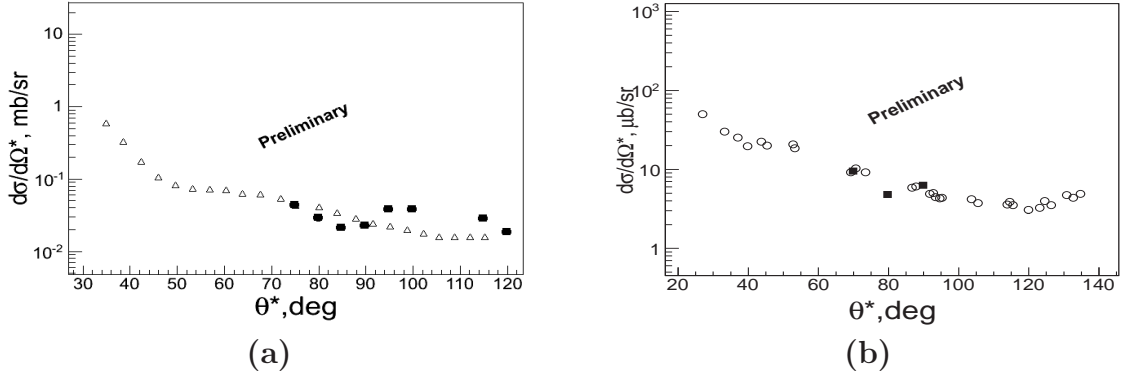


Figure 2: (a) The differential cross section of dp - elastic scattering at 1300 MeV: BNL data [13] (open triangles) and preliminary Nuclotron data (solid circles). (b) The differential cross section of dp - elastic scattering at 2000 MeV: ANL data [14] (open circles) and preliminary Nuclotron data (solid squares).

3 Results

The measurements of the angular dependence of the differential cross section of dp - elastic scattering were carried out at Nuclotron at the energies of 400, 500, 600, 700, 800, 880, 1000, 1300, 1500 and 2000 MeV. Fig. 1b presents the results of the measurement at 880 MeV at Nuclotron depicted by the solid circles. They are compared with the data obtained at 850 MeV [10] and 940 MeV [11] given by open circles and triangles, respectively. The dashes and solid lines are the calculation of the relativistic multiple scattering model [12] without and with double scattering taken into account. The model [12] describes the behaviour of the data, however, some deviation at large scattering angles still remains. The description between the cross section data and theoretical calculations at large angles could be improved by taking into account the short-range $3N$ forces.

The preliminary data on the differential cross section of dp - elastic scattering obtained at Nuclotron at 1300 and 2000 MeV and given in Fig.1a and Fig.1b by the solid symbols. They are compared with the data obtained previously at BNL [13] and at ANL [14] depicted in Fig.1a and Fig.1b by the open triangles and circles, respectively.

The data for different kinematic configuration for the $dp \rightarrow ppn$ reaction have been obtained at 300, 400 and 500 MeV. The preliminary results for the $dp \rightarrow ppn$ events selection obtained at $T_d=400(500)$ MeV for the two protons detection angles, namely, $\theta_1=25^\circ$, $\theta_2=33.7^\circ$ and $\phi=44.6^\circ$) are presented in Fig.3a(b). The data analysis is in progress.

4 Conclusion

The data on the analyzing powers A_y , A_{yy} and A_{xx} in dp - elastic scattering have been measured at ITS at the Nuclotron at the energies of 880 and 2000 MeV [3, 4].

The data on the energy dependence of the dp - elastic scattering cross section have been accumulated at 400-2000 MeV. The data analysis is in progress.

The data on dp -non-mesonic breakup have been obtained at 300, 400 and 500 MeV for different kinematic configurations.

Future studies of deuteron-induced reactions like $dp \rightarrow pd$, dp - breakup, $dd \rightarrow {}^3Hp({}^3Hen)$ and $d{}^3He \rightarrow p{}^4He$ at Nuclotron are related with new PIS developed at LHEP-JINR [15].

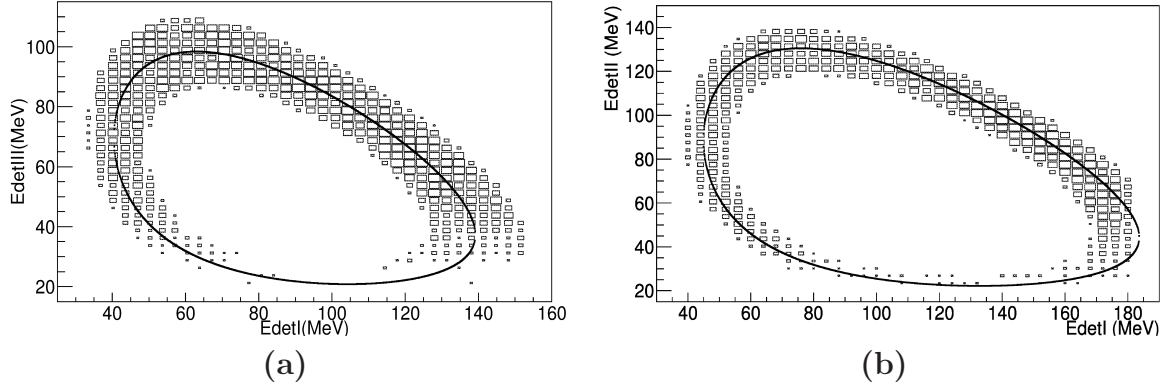


Figure 3: (a) Two detected proton energies correlation for the $dp \rightarrow ppn$ reaction at $T_d=400$ MeV ($\theta_1=25^\circ$, $\theta_2=33.7^\circ$ and $\phi=44.6^\circ$). (b) Two detected proton energies correlation for the $dp \rightarrow ppn$ reaction at $T_d=500$ MeV ($\theta_1=25^\circ$, $\theta_2=33.7^\circ$ and $\phi=44.6^\circ$).

These new experimental data and further development in theoretical approaches will be important for adequate description of the short-range light nuclei spin structure.

The work has been supported in part by the RFBR grant No.13-02-00101a.

References

- [1] N. Kalantar-Nayestanaki et al., Rept.Prog.Phys. **75**, (2012) 016301.
- [2] V.P. Ladygin et al., EPJ Web Conferences 3, (2010) 04004.
- [3] P.K. Kurilkin et al., Phys.Lett. **B715**, (2012) 61-65.
- [4] P.K. Kurilkin et al., Phys.Part.Nucl.Lett.**8**, (2011) 1081-1083.
- [5] . N.B.Ladygina, Phys.Atom.Nucl.**71**, (2008) 2039-2051.
- [6] A.I. Malakhov et al., Nucl.Instrum.Meth. in Phys.Res. **A440**, (2000) 320-329.
- [7] A.Yu. Isupov et al., Nucl.Instrum.Meth. in Phys.Res. **A698**, (2013) 127–134.
- [8] Yu.V. Gurchin et al., Phys.Part.Nucl.Lett.**8**, (2011) 950-958.
- [9] S.M.Piyadin et al., Phys.Part.Nucl.Lett.**8**, (2011) 107-113.
- [10] N.E. Booth et al. Phys.Rev. **D4**, (1971) 1261-1267.
- [11] J.C. Alder et al. Phys.Rev. **C6**, (1972) 2010-2019.
- [12] N.B. Ladygina., Eur.Phys.J. **A42**, (2009) 91-96
- [13] E. Culmez et al., Phys. Rev. C **5**, (1991) 2067.
- [14] G.W.Bennett et al., Phys.Rev.Lett.**19**, (1967) 387-390.
- [15] V.V. Fimushkin et al., Eur.Phys.J.ST **162**, (2008) 275-280.

EXPERIMENTAL PROGRAM FOR BARYONIC MATTER STUDIES¹

V.P. Ladygin^{1,†}, E.L. Bratkovskaya^{2,3}, O.Yu. Derenovskaya¹, K.K. Gudima⁴,
A.M. Korotkova¹, P.K. Kurilkin¹, N.B. Ladygina¹, A.A. Lebedev^{1,5}, O.V. Teryaev¹,
A.I. Zinchenko¹ for the BM@N collaboration.

(1) *Joint Institute for Nuclear Research, 141980 Dubna, Russia*

(2) *Institut für Theoretische Physik, Goethe Universität, 60438 Frankfurt, Germany*

(3) *Frankfurt Institute for Advanced Studies, 60438 Frankfurt, Germany*

(4) *Institute of Applied Physics, ASM, MD-2028 Kishinev, Moldova*

(5) *GSI Helmholtz-Zentrum für Schwerionenforschung GmbH, D-64220 Darmstadt, Germany*

† *E-mail: vladygin@jinr.ru*

Abstract

The major goal of the Baryonic Matter at Nuclotron (BM@N) project is to perform a research program focused on the production of strange matter in heavy-ion collisions at beam energies between 2 and 6 A·GeV. The study of the NN , NA and dA reactions for the reference is assumed. The extension of the experimental program at BM@N is related with the study of the in-medium modification of the polarization for the strange and multi-strange baryons and the spin alignment for vector mesons decaying in hadronic modes. The studies of the spin effects in NN and dA reactions also can be performed with the minor modification of the beam transportation line.

1 Introduction

The Nuclotron at JINR will provide beams of heavy ions with energies up to 6 A·GeV for isospin symmetric nuclei, and 4.65 A·GeV for Au nuclei. In central heavy-ion collisions at these energies, nuclear densities of about 4 times nuclear matter density can be reached. These conditions are well suited to investigate the equation-of-state (EOS) of dense nuclear matter which plays a central role for the dynamics of core collapse supernovae and for the stability of neutron stars. At the same time, heavy-ion collisions are a rich source of strangeness, and the coalescence of kaons with lambdas or of lambdas with nucleons will produce a vast variety of multi-strange hyperons or of light hypernuclei, respectively. Even the production of light double-hypernuclei or of double-strange dibaryons is expected to be measurable in heavy-ion collisions at Nuclotron energies. The observation of those objects would represent a breakthrough in our understanding of strange matter, and would pave the road for the experimental exploration of the 3-rd dimension of the nuclear chart [1]. These studies are complimentary to the CBM experimental program at SIS100 [2].

High-energy heavy-ion collisions offer the unique possibility to create and to investigate hot and dense nuclear matter in the laboratory. The nucleon densities in the collision zone of two gold nuclei exceed the saturation density by a factor of 3-4 at Nuclotron

¹Authors list of the BM@N collaboration can be found at <http://nica.jinr.ru>

beam energies [3]. At these densities the nucleons start to overlap, and it was speculated that under such extreme conditions the onset of chiral symmetry restoration may occur while the quarks are still confined. In this case, the bulk properties (for example the energy density) are dominated by quarks which occupy the Fermi sea, whereas baryons represents the excited states. Due to the increase of the degrees-of-freedom with respect to hadronic matter this particular state can be regarded as a new phase of nuclear matter where quarks and baryons coexist. This so called "quarkyonic" phase [4] is predicted to be located at large baryo-chemical potentials and moderate temperatures, and, therefore, may be produced in heavy-ion collisions at Nuclotron beam energies.

The production of multi-strange hyperons is expected to be enhanced at high densities, and their yield is sensitive to the baryon density reached in the fireball. Therefore, systematic measurements of Ξ^- and Ω^- hyperon production as function of beam energy and size of the colliding nuclei offer the possibility to study the nuclear matter equation-of-state, or baryon density fluctuations as they are expected to occur when the system undergoes a first-order phase transition. These fluctuations may also indicate the existence and the location of a QCD critical endpoint. Moreover, the energy distributions of multi-strange hyperons provide information on the fireball temperature and the radial flow at the time when they are emitted. The BM@N experiment [1] would deliver the first data on the production of multi-strange hyperons in heavy-ion collisions at Nuclotron beam energies. Also we propose to produce hypernuclei (single- and double-lambda) in heavy-ion collision via coalescence of lambdas with nucleons or light fragments. In central $Au + Au$ collisions at 4 A·GeV still 4 lambdas are produced. The probability for coalescence of lambdas with protons or light nuclei like He , however, increases with decreasing beam energy, i.e. with decreasing temperature of the fireball, and, hence, increasing He yield. According to the estimations from ref. [5], one can expect at Nuclotron energies yield of $3 \cdot 10^{-8}$ ${}_{\Lambda\Lambda}{}^6He$, 10^{-6} ${}_{\Lambda\Lambda}{}^5H$, and $2 \cdot 10^{-2}$ ${}^3_{\Lambda}H$ per central collision. Experimentally one has to reconstruct the decay chain of the hypernuclei (if it exists), for example: ${}_{\Lambda\Lambda}{}^5H \rightarrow {}^5_{\Lambda}He + \pi^-$, ${}^5_{\Lambda}He \rightarrow {}^4He + p + \pi^-$. The ${}^6_{\Omega}H$ (if it exists) can be detected using the following chain ${}^6_{\Omega}H \rightarrow {}^6_{\Xi}He + \pi^-$, ${}^6_{\Xi}He \rightarrow {}_{\Lambda\Lambda}{}^6He \rightarrow {}^5_{\Lambda}He + p + \pi^-$, ${}^5_{\Lambda}He \rightarrow {}^4He + p + \pi^-$. The systematic studies of neutron-rich and halo(loosely bound) hypernuclei (${}^3_{\Lambda}H$, ${}^4_{\Lambda}H$, ${}^6_{\Lambda}He$ etc.) [6] can be performed simultaneously. Part of these measurements requires the detection of light nuclear fragments (for instance, 4He) what can be performed using amplitude information from STS (or from the scintillation detectors placed in front of STS). These measurements can be performed for the beams of 4He and 6Li [6].

New signature can be the change of in the polarization properties of the secondary particles in the nucleus-nucleus collisions compared to the nucleon-nucleon collisions. A number of polarization observables have been proposed as a possible signature of phase transition, namely, decreasing of the Λ^0 transverse polarization in central collisions [7–9], non-zero $\bar{\Lambda}^0$ longitudinal polarization [10, 11], non-zero J/Ψ polarization at low p_T [12], anisotropy in di-electron production from vector mesons decay [13], global hyperon polarization [14] and spin-alignment of vector mesons [15] in non-central events etc. The study of the modification of the Λ^0 transverse polarization and global Λ^0 polarization at NICA and FAIR energies has been proposed in ref. [16]. Recently the vorticity and hydrodynamical helicity in noncentral heavy-ion collisions were studied for Nuclotron/NICA energies as the functions of the energy collision, system size etc. [17].

Some modification of the transportation line can allow to measure the tensor analyzing

power T_{20} and spin correlation $C_{y,y}$ in the ${}^3\text{He}(d,p){}^4\text{He}$ reaction in the kinetic energy range between 1.0 and 1.75 GeV can be performed at the BM@N area using polarized ${}^3\text{He}$ target [18]. A number of polarization observables for the $d(p,p)d$, $d(d,p)t$, $d(A,pp)X$ reactions as well as for polarized neutron induced reactions (with the proton spectator detection) at intermediate energies also can be studied with new polarized deuteron source [19] developed at LHEP.

2 BM@N Detector

Schematic view of the BM@N setup is shown in Fig.1(a). The heart of the BM@N setup is the Silicon Tracking System (*STS*) (similar to the CBM *STS* [20]) placed in the magnetic field with the maximal field integral of ~ 2 T·m. The Silicon Tracking System comprises 8 stations of increasing size, and will be operated at -10° C. Therefore, the STS sits in a thermal enclosure which fits into the gap of the dipole magnet as show in Fig.1(a). The double-sided silicon micro-strip sensors will be read out via ultra-thin micro-cables by a free-streaming (i.e. untriggered) front-end-electronics. The sensors, the cables and the electronics are mounted on light-weight carbon ladders which form the stations.

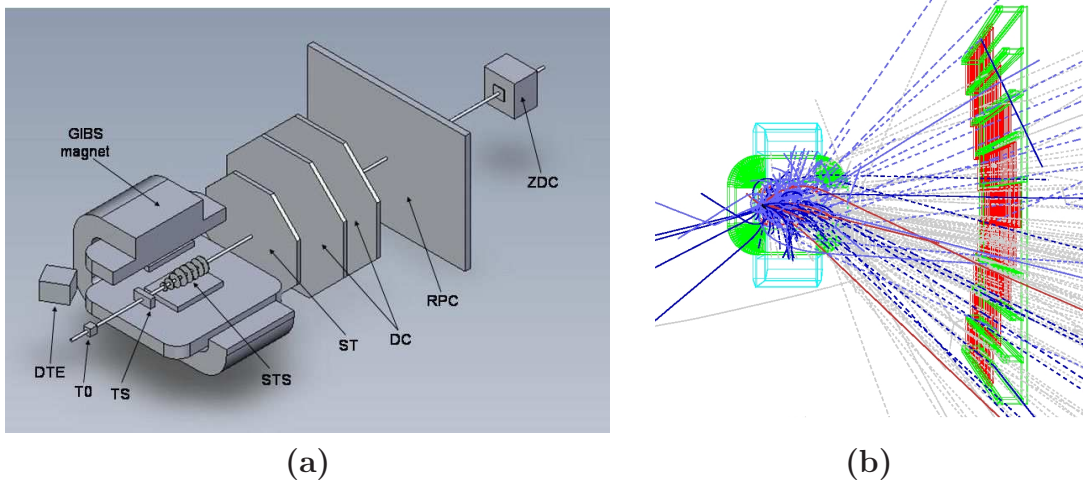


Figure 1: (a) Schematic view of the BM@N setup with the large aperture dipole analyzing magnet SP41. *TS*- target station, *T0*- start diamond detector, *STS*- silicon tracker, *ST*- straw tracker, *DC*- drift chambers, *RPC*- resistive plate chambers, *ZDC*- zero degree calorimeter, *DTE*- detector of transverse energy. (b) One UrQMD central $\text{Au} + \text{Au}$ collision at 4 A-GeV within BM@N detector.

For intermediate tracking two drift chambers from NA48 (delivered from CERN to JINR) can be used [21]. Each drift chamber is composed of eight planes of wires arranged in four views (x, y, u, v) with two planes of staggered wires in each view to resolve the right-left ambiguities. The wire orientations in the (x, y, u, v) views are at multiples of 45 degrees to the horizontal plane and perpendicular to the beam. Sense wire spacing is 1.0 cm; one wire plane extends over 2.40 m and has 256 sense wires. The coordinate accuracy is found to be $110 \mu\text{m}$ for four planes measurements case. In addition the straw tubes plane developed for muon system of CBM can be used to improve the quality of the tracking. It consists of 3 double-layer planes.

The particle identification will be provided by the *TOF*- wall based on *mRPCs* [22–24]. The simulation performed for the central *Au + Au* at 3.5 A·GeV and *Cu + Cu* at 5 A·GeV collisions shown good separation of the secondary particles using $m^2 : p$ plot [1]. The working conditions of proposed experiment for the *T0* detector require the use of diamond pixel or strip detector because of high radiation hardness. Two technologies are considered, namely, mono-crystalline pad diamond detector applied recently for HADES [25] and poly-crystalline double-sided strip module developed for ATLAS [26].

The centrality of the event will be measured using zero degree calorimeter (*ZDC*). For this purpose the reassembled the WA98 *ZDC* [27] will be used. This hadron calorimeter consists of lead/scintillator sandwich modules with the sampling satisfying the compensating condition. The cross section of the module is $15 \times 15 \text{ cm}^2$. The energy resolution is about $50\% / \sqrt{E(\text{GeV})}$ for hadrons. The transverse cross section of *ZDC* will be $150 \times 150 \text{ cm}^2$. The independent estimation of the centrality can be performed using *DTE* based on *PINOT* electromagnetic calorimeter [28]. Also the multiplicity in *TOF* detector can be used as an independent way to measure the centrality.

The *DAQ* system should be able to store and analyze the data obtained from the different detectors both in free-streaming (*STS*) and triggered (for instance, *RPCs* or *ZDC*) modes. The high counting rate expected during the experiment requires the development of high-speed methods, algorithms and software tools of parallel processing for solving problems on multiprocessor and distributed computing complexes, including the use of Grid-technologies. The use of SIMD instructions, simultaneous multi-threading (SMT), algorithmic languages Ct, OpenCL and CUDA for solving problems on the multi-core, multiprocessor distributed computer complexes. These methods, algorithms and software will be used for the charged particles momenta reconstruction with the high accuracy and their identification, for the simulation of the physical processes in heavy ion collisions at Nuclotron energies, the calibration and alignment of the setup detectors. The data taking and analysis will be performed using distributed systems for the data processing.

3 Simulation results

The software framework based on the FAIR root has been developed for the feasibility studies and BM@N setup optimization. Fig.1(b) demonstrates the BM@N magnet with silicon tracker, time-of-flight system and tracks for one central *Au + Au* event at 4 A·GeV. This framework includes the geometry and calculated field for the BM@N magnet, the 8 stations *STS* (with last 5 of the same size), beam pipe and *TOF* wall. Fig.1(b) demonstrates the detectors of the BM@N setup and tracks for one UrQMD central *Au + Au* event at 4 A·GeV.

The results of the simulations are shown in Fig.2 which depicts the invariant mass spectra for K_s^0 mesons and Λ hyperons for UrQMD central *Au + Au* collisions at 4 A·GeV. The analysis is based on topological cuts only, without particle identification via the time-of-flight determination. The combinatorial background can be further reduced by identifying the decay protons by the time-of-flight measurement. For the reference the simulation for the CBM setup has been performed. The results are summarized in table 1. The reconstruction efficiencies are $\sim 11\%$ and $\sim 15\%$ for the K_s^0 and Λ with quite good signal/background ratios for BM@N setup. The reconstruction efficiencies for the CBM setup are similar, however, the *S/B* ratios are slightly better than for BM@N setup. Note,

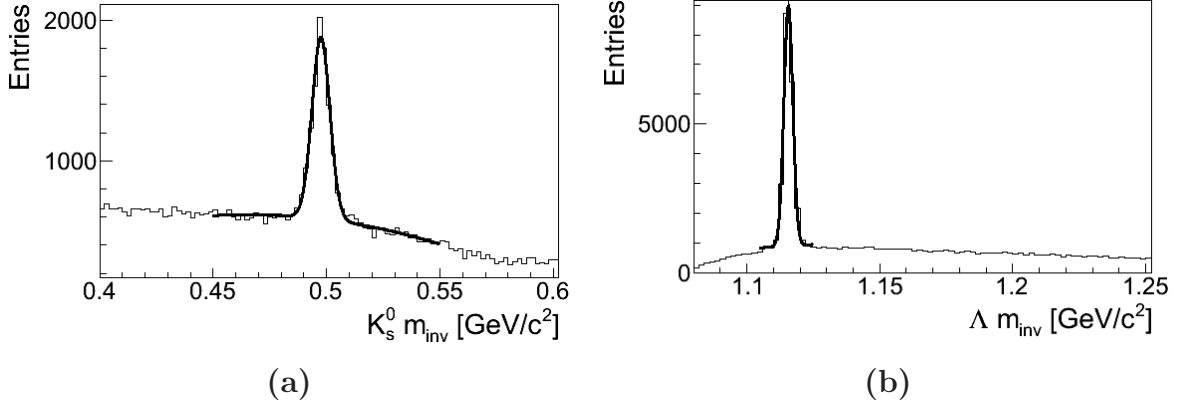


Figure 2: Reconstructed K_s^0 mesons (a) and Λ hyperons (b) from the UrQMD central $Au + Au$ collisions at 4 A·GeV.

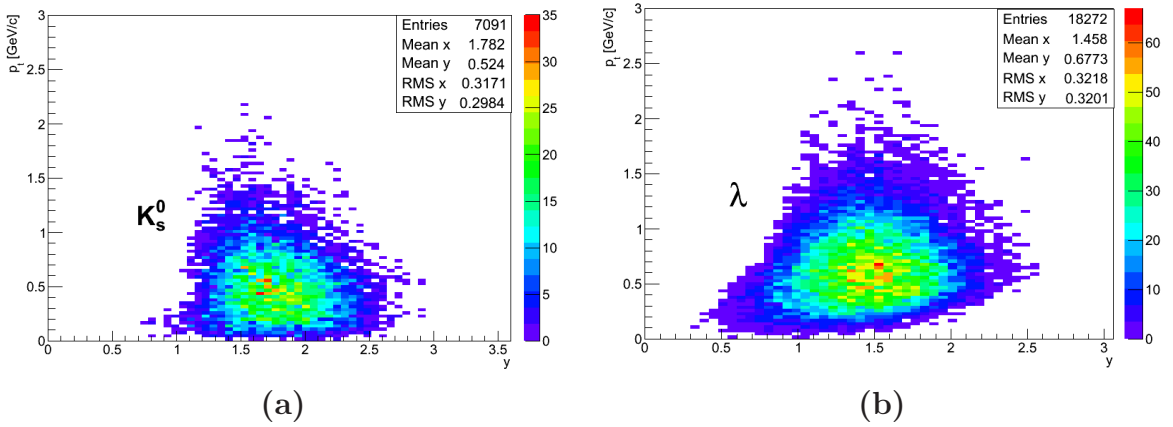


Figure 3: The $y - p_T$ acceptances for K_s^0 mesons (a) and Λ hyperons (b) from the UrQMD central $Au + Au$ collisions at 4 A·GeV.

that efficiencies reconstructions for the primary V^0 particles are larger for BM@N setup, while they are larger for the V^0 's coming from the cascade hyperons for CBM setup due to larger acceptance of STS .

The $y - p_T$ acceptances for K_s^0 mesons and Λ hyperons from the central $Au + Au$ collisions at 4 A·GeV are shown in Fig.3. One can see that acceptances are large enough and cover mostly forward rapidities.

Table 1: The efficiencies ϵ and signal to background ratios S/B of the K_s^0 and Λ reconstruction produced in the central $Au + Au$ collisions at 4 A·GeV for the BM@N and CBM setups.

Setup	$\epsilon(K_s^0)$	$\frac{S}{B}(K_s^0)$	$\epsilon(\Lambda)$	$\frac{S}{B}(\Lambda)$
BM@N	11.05%	1.32	14.65%	6.35
CBM	12.37%	1.43	14.65%	5.44

The simulation results for selection of ${}^3_\Lambda H$ produced in the central $Au + Au$ collisions at 4 A·GeV from the Dubna Cascade Model (DCM) event generator [29] are shown in Fig.4. One can see good identification for two- and three-body decay channels depicted in Fig.4(a) and Fig.4(b), respectively. The simulation for the CBM setup has been performed

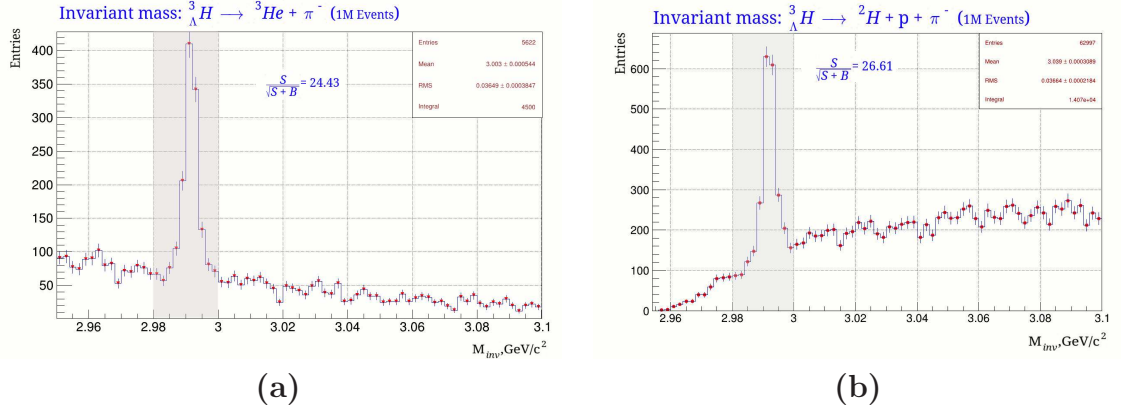


Figure 4: Reconstruction of the hyper-tritons (${}^3_{\Lambda}H$) from the DCM [29] central $Au + Au$ collisions at 4 A·GeV for 2- (a) and 3-body (b) decay channels.

Table 2: The efficiencies ϵ and significance of the ${}^3_{\Lambda}H$ reconstruction produced in the central $Au + Au$ collisions at 4 A·GeV for 2-body (${}^3_{\Lambda}H \rightarrow {}^3He + \pi^-$) and 3-body (${}^3_{\Lambda}H \rightarrow d + p + \pi^-$) decay channels for BM@N and CBM setups.

Setup	$\epsilon(2\text{-body})$	$\frac{S}{\sqrt{S+B}}(2\text{-body})$	$\epsilon(3\text{-body})$	$\frac{S}{\sqrt{S+B}}(3\text{-body})$
BM@N	11.4%	24.4	16.8%	26.6
CBM	7.8%	19.3	9.1 %	24.6

for the reference. The comparison of the results on the efficiencies and significances of the ${}^3_{\Lambda}H$ reconstruction for the BM@N and CBM setups are presented in table 2. One can see good signal to background ratio for the both setups, however, the reconstruction efficiency for the BM@N setup is 50-60% larger than in the case of CBM.

The simulation for Ξ^- reconstruction and the simulation for the cascade Ξ^- hyperon has been performed for $5 \cdot 10^5$ UrQMD central Au+Au collisions at 4 A·GeV. The selection of Xi^- requires the effective reconstruction of Λ decay in the $p\pi^-$ mode and the secondary vertex reconstruction for $\Lambda\pi^-$. The efficiency of the reconstruction was found $\sim 3\%$ with signal to background ratio of $\sim 5\%$.

For the simulation we used parallelized algorithms using LIT firmware with manycore computer. The maximal speed is provided by the Intel X5660 at 2.80 GHz with 24 logical cores, e.g. about 2700 minimum bias or 1200 central events per second.

The simulation framework is still under development. The optimization of the BM@N detector is continued.

4 Experiment status

During last years a significant progress in the preparation of the BM@N experiment has been achieved. The measurements with 3.42 A·GeV carbon [30] and 1.0-4.0 A·GeV deuteron [31] beams demonstrated the feasibility of the experiment with the existing beam lines. On the base of these measurements the technical requirements to the Nuclotron parameters, beam transportation conditions and experimental cave details were formulated.

The experimental zone is now under reconstruction. New beam stopper, target station and beam pipe is prepared. The aperture of the BM@N magnet was enlarged up to 1 m in the vertical direction. The preparation to the magnetic field measurements are in progress now.

The simulation shown that the counting rate at *mRPCs* requires the use of warm float glass techniques use. Such detectors were developed at IHEP and tested U70 Accelerator complex using specially constructed muon beam line. The scintillation fiber hodoscopes based on the use multi-anode PMTs H6568 are under construction and testing at internal Nuclotron beam. The prototype of the *ZDC* module has been prepared on the base of the equipment from WA98 *ZDC* delivered from CERN to JINR in 2012 and tested with muon beam at U70. The work on the electronics and *DAQ* concept is in progress.

5 Conclusions

- BM@N experiment has high discovery potential and can provide new insight to the strangeness production in a GeV energy range. This experiment is comprehensive to the CBM experiment planned at FAIR [2].
- Measurements of the hyperons polarization, heavy mesons spin alignment etc. [13, 16, 17] can significantly enrich the physics at BM@N.
- First stage of the BM@N setup is well suited for the physics with polarized deuterons [18] using new PIS [19].

The authors are indebted to V.V.Ivanov, I.V.Kisel, P.Senger, Yu.O.Vassiliev for useful discussions. They are grateful to I.Kulakov, E.I.Litvinenko, V.A.Vasendina and M.Zyzak for their help in the simulation. The investigation has been supported in part by the Russian Foundation for Basic Research (Grant No.13-02-00101a).

References

- [1] V. Ladygin et al., PoS Baldin-ISHEPP-XXI (2012) 038.
- [2] P.Senger and V.Friese, CBM Report 2011-1; <https://www.gsi.de/documents/DOC-2011-Aug-29-1.pdf>.
- [3] B. Friman, W. Nörenberg and V.D. Toneev, Eur. Phys. J. **A3** (1998) 165.
- [4] A. Andronic et al., Nucl.Phys. **A837** (2010) 65.
- [5] A. Andronic, P. Braun-Münzinger, J. Stachel and H. Stöcker, Phys. Lett. **B695** (2011) 203.
- [6] Yu.A. Batusov, J. Lukstins, L. Majling and A.N. Parfenov, Phys. Elem. Part. Atom. Nucl. **36** (2005) 169.
- [7] A.D. Panagiotou, Phys.Rev. **C33** (1986) 1999.
- [8] A. Ayala, E. Cuautle, G. Herrera and L.M. Montano, Phys.Rev. **C65** (2002) 024902.
- [9] A.Ya. Berdnikov et al., Acta Phys. Hungary.**A22** (2005) 139.
- [10] M. Jacob, Z.Phys. **C38** (1988) 273.

- [11] G. Herrera, G. Magnin and L.M. Montano, Eur.Phys.J. **C39** (2005) 95.
- [12] B.L. Ioffe and D.E. Kharzeev, Phys.Rev. **C68** (2003) 061902(R).
- [13] E.L. Bratkovskaya et al., Phys. Lett. **B348** (1995) 283; *ibid.* **B348** (1995) 325; *ibid.* **B362** (1995) 17; *ibid.* **B376** (1996) 12; Z.Phys. **C75** (1997) 119.
- [14] Z.-T. Liang Z.-T. and X.-N. Wang, Phys.Rev.Lett. **94** (2005) 102301.
- [15] Z.-T. Liang Z.-T. and X.-N. Wang, Phys.Lett. **B629** (2005) 20.
- [16] V.P. Ladygin, A.P. Jerusalimov and N.B. Ladygina, Phys.Part.Nucl.Lett. **7** (2010) 349.
- [17] M. Baznat, K. Gudima, A. Sorin and O.Teryaev, E-Print: arXiv:1301.7003 [nucl-th].
- [18] V.P. Ladygin et al., EPJ Web Conferences **3** (2010) 04004.
- [19] V.V. Fimushkin et al., Eur.Phys.J. ST **162** (2008) 275.
- [20] J.M. Heuser, Nucl.Instrum. and Meth. **A582** (2007) 910.
- [21] D. Bederede et al., Nucl.Instrum. and Meth. **A367** (1995) 88; I. Augustin et al., Nucl.Instrum. and Meth. **A403** (1998) 472.
- [22] I. Deppner et al., Nucl.Instrum. and Meth. **A661** (2012) S121.
- [23] V.V. Ammosov et al., Instrum.Exp.Tech. **53** (2010) 175.
- [24] Y. Wang et al., Nucl.Instrum.Meth. **A661** (2012) S134.
- [25] J. Pietraszko et al., Nucl.Instrum.Meth. **A618** (2010) 121.
- [26] M. Mikuz et al., Nucl.Instrum.Meth. **A579** (2007) 788, V. Adam et al., Eur.Phys.J. **C33** (2004) s1014, Doi:10.1140/epjcd/s2004-03-1798-6.
- [27] V.A.Arefiev et al., JINR Rapid Communications **5[79]-96** (1996) 15.
- [28] E.Chiavassa et al., IEEE Trans. Nucl.Sci. **33** (1986) 209.
- [29] V.D. Toneev and K.K. Gudima, Nucl.Phys. **A400** (1983) 173c; V.D. Toneev, N.S. Amelin, K.K. Gudima and S.Yu. Sivoklov, Nucl.Phys. **A519** (1990) 463c; N.S. Amelin, E.F. Staubo, L.S. Csernai et al., Phys.Rev. **C44** (1991) 1541.
- [30] S.M. Piyadin et al., Phys. Part. Nucl. Lett. **9** (2012) 589.
- [31] A.A. Terekhin et al., PoS Baldin-ISHEPP-XXI (2012) 005.

POLARIZATION EFFECTS IN THE QUASI-ELASTIC ($p, 2p$)-REACTION WITH NUCLEI AT 1 GeV

O.V. Miklukho, G.M. Amalsky, V.A. Andreev, S.V. Evstiukhin, O.Ya. Fedorov,
G.E. Gavrilov, A.A. Izotov, A.Yu. Kisselev, L.M. Kochenda, M.P. Levchenko,
V.A. Murzin, D.V. Novinsky, A.N. Prokofiev, A.V. Shvedchikov, S.I. Trush,
A.A. Zhdanov

B.P. Konstantinov Petersburg Nuclear Physics Institute, Gatchina, 188300, Russia

Abstract

New experimental data on the polarization and spin-correlation parameters in the ($p, 2p$) reaction with nuclei at 1 GeV are presented. The experiment was aimed to study a modification of the proton–proton scattering matrix.

Introduction. There were some speculations on modifications of nucleon and meson masses and sizes, and of meson–nucleon coupling constants, and, as a consequence, of nucleon–nucleon scattering matrix in nuclear medium [1–3]. These speculations were motivated by a variety of theoretical points of view, including the renormalization effects due to strong relativistic nuclear fields, deconfinement of quarks, and partial chiral symmetry restoration.

This work is a part of the experimental program in the framework of which the medium–induced modifications of the nucleon–nucleon scattering amplitudes are studied at the PNPI synchrocyclotron with the 1 GeV proton beam [4–8]. The intermediate–energy quasi–free ($p, 2p$) reaction is a good experimental tool to study such effects, since in the first approximation, this reaction can be considered as a proton–proton scattering in the nuclear matter. Usage of S–shell protons (with zero orbital momentum) is preferred because interpretation of obtained data in this case is essentially simplified since the effective polarization is not involved [9]. The polarization observables in the reaction are compared with those in the elastic pp scattering. In our exclusive experiment, a two–arm magnetic spectrometer is used, the shell structure of the nuclei being evidently distinguished. To measure polarization characteristics of the reaction, each arm of the spectrometer was equipped with a multi–wire–proportional chamber polarimeter.

In the early PNPI–RCNP experiment [5], the polarizations P_1 and P_2 of both secondary protons from the ($p, 2p$) reactions at 1 GeV with the $1S$ –shell protons of the nuclei ${}^6\text{Li}$, ${}^{12}\text{C}$ and with the $2S$ –shell protons of the ${}^{40}\text{Ca}$ nucleus has been measured at nuclear proton momenta close to zero. The polarization observed in the experiment, as well as the analyzing power A_y in the RCNP experiment at the 392 MeV polarized proton beam [10, 11], drastically differed from those calculated in the framework of non–relativistic Plane Wave Impulse Approximation (PWIA) and of spin–dependent Distorted Wave Impulse Approximation (DWIA) [12], based on free space proton–proton interaction. This difference was found to have a negative value and to increase monotonously with the effective mean nuclear density $\bar{\rho}$ [10]. The latter is determined by the absorption of initial and secondary protons in nucleus matter. The observed inessential difference

between the non-relativistic PWIA and DWIA calculations pointed out only to a small depolarization of the secondary protons because of proton-nucleon rescatterings inside a nucleus. All these facts strongly indicated a modification of the proton-proton scattering amplitudes due to the modification of the main properties of hadrons in the nuclear matter.

Later, the results of the experiment with a ${}^4\text{He}$ target broke the above-mentioned dependence of the difference between the experimental polarization values and those calculated in the framework of the PWIA on the effective mean nuclear density [6]. The difference for the ${}^4\text{He}$ nucleus proved to be smaller than that for the ${}^{12}\text{C}$ nucleus. This evidently contradicts the elastic proton-nucleus scattering experiment. According to the experiment, the ${}^4\text{He}$ nucleus has the largest mean nuclear density. The important feature of the experiment with the ${}^4\text{He}$ nucleus was a possibility to see the medium effect without any contribution from multi-step processes (for instance, from the $(p, 2pN)$ reactions). These processes could take place when there were nucleons of outer shells as in other nuclei. Therefore, they could not cause the systematic difference between the polarizations P_1 and P_2 clearly obtained for the first time in the experiment [6].

Here we present the polarization data for the reaction with the nuclei ${}^4\text{He}$, ${}^6\text{Li}$, ${}^{12}\text{C}$ ($1S$ -shell), and ${}^{40}\text{Ca}$ ($2S$ -shell) obtained with a much better statistical accuracy in our last experiments. New data on the polarization in the reaction with the $1S$ -shell protons of the ${}^{28}\text{Si}$ nucleus are presented. The $1S$ -state of the ${}^{28}\text{Si}$ nucleus has a larger value of the mean proton binding energy E_s (50 MeV) than that of the ${}^{12}\text{C}$ nucleus (35 MeV). We also present the polarization measured in the reaction with the P -shell and D -shell protons of the ${}^{12}\text{C}$ and ${}^{28}\text{Si}$ nuclei, respectively.

In recent experiments, the research program was extended to measure the spin correlation parameters C_{ij} in the $(p, 2p)$ reaction with the ${}^4\text{He}$ and ${}^{12}\text{C}$ nuclei. Measurements of the parameters in the reaction with nuclei were for the first time performed. The main attention was concentrated on the spin correlation parameter C_{nn} since its value is the same in the center-of-mass and laboratory systems. Besides, this parameter is not distorted by the magnetic fields of the two-arm spectrometer because of the proton anomalous magnetic moment [13]. Since the polarization and the spin correlation parameter C_{nn} are expressed differently through the scattering matrix elements [3], the measurement of both these polarization observables can provide a more comprehensive information about a modification of the hadron properties in the nuclear medium.

Experimental method. The general layout of the experimental setup is shown in Fig. 1 [14]. The experiment is performed at non-symmetric scattering angles of the final state protons in the coplanar quasi-free scattering geometry with a complete reconstruction of the reaction kinematics. The measured secondary proton momenta K_1 , K_2 (kinetic energies T_1 , T_2) and the scattering angles Θ_1 , Θ_2 are used together with the proton beam energy T_0 to calculate nuclear proton separation energy $\Delta E = T_0 - T_1 - T_2$ and the residual nucleus momentum K_r for each $(p, 2p)$ event. In the impulse approximation, the K_r is equal to the momentum K of the nuclear proton before the interaction ($\mathbf{K}_r = -\mathbf{K}$).

External proton beam of the PNPI synchrocyclotron was focused onto the target TS of a two-arm spectrometer consisting of the magnetic spectrometers MAP and NES. The beam intensity was monitored by the scintillation telescope M1, M2, M3 and was at the level of about $5 \cdot 10^{10}$ protons/(s·cm²).

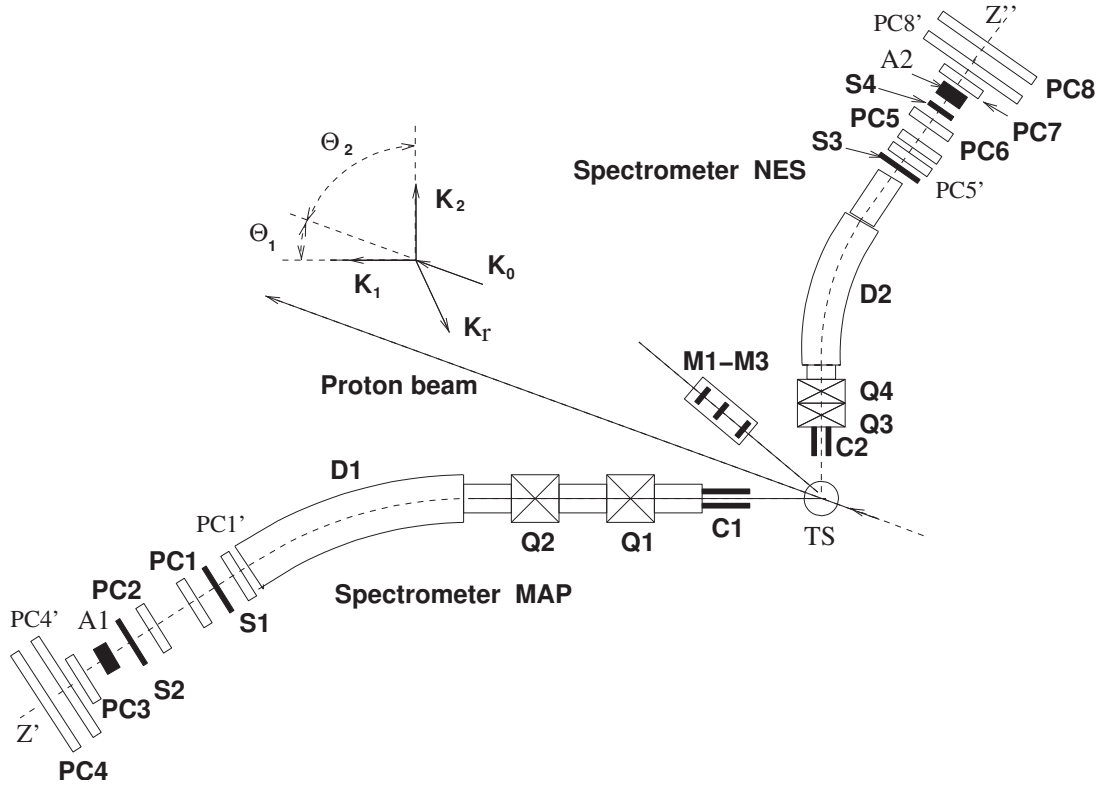


Figure 1: The experimental setup. TS is the target of the two-arm spectrometer; Q1÷Q4 are magnetic quadrupoles; D1, D2 are dipole magnets; C1, C2 are collimators; S1÷S4 and M1÷M3 are scintillation counters; PC1÷PC4, PC1', PC4' (PC5÷PC8, PC5', PC8') and A1 (A2) are the proportional chambers and the carbon analyzer of the high-momentum (low-momentum) polarimeter, respectively.

Solid nuclear targets TS made of CH_2 (for the setup calibration), ${}^6\text{Li}$, ${}^{12}\text{C}$, ${}^{28}\text{Si}$, and ${}^{40}\text{Ca}$, as well as a cryogenic target made of liquid helium ${}^4\text{He}$ (or liquid hydrogen for calibration) were used in the experiment [6, 14].

The spectrometers were used for registration of the secondary protons from the $(p, 2p)$ reaction in coincidence and for measurement of their momenta and outgoing angles. The polarization of these protons P_1 and P_2 , and the spin correlation parameters C_{ij} were measured by the polarimeters located in the region of focal planes of the spectrometers MAP and NES (Fig. 1). The first index of the C_{ij} , i (where i is n or s'), and the second index j (where j is n or s'') correspond to the forward scattered proton analyzed by the MAP polarimeter and the recoil proton analyzed by the NES polarimeter, respectively. The unit vector \mathbf{n} is perpendicular to the scattering plane of the reaction. Unit vectors \mathbf{s}' and \mathbf{s}'' are perpendicular to the vector \mathbf{n} and to the coordinate axes z' and z'' (Fig. 1) of the polarimeters.

The overall energy resolution (on ΔE) of the spectrometer estimated from the elastic proton-proton scattering with the 22 mm in thick cylindrical CH_2 target was about 5 MeV (FWHM) [14].

The track information from the proportional chambers of both polarimeters was used in the off-line analysis to find the azimuthal ϕ_1 , ϕ_2 and polar θ_1 , θ_2 angles of the proton scattering from the analyzers A1, A2 for each $(p, 2p)$ event.

The polarization parameters were estimated by folding the theoretical functional shape of the azimuthal angular distribution into experimental one [8], using the CERNLIB

MINUIT package and a χ^2 likelihood estimator. This method permits to realize the control over χ^2 in the case the experimentally measured azimuthal distribution is distorted due to the instrumental problems.

The time difference (TOF) between the signals from the scintillation counters S2 and S4 was measured. It served to control the accidental coincidence background. The events from four neighboring proton beam bunches were recorded. Three of them contained the background events only and were used in the offline analysis to estimate the background polarization parameters and the background contribution at the main bunch containing the correlated events [14].

The recoil proton spectrometer NES was installed at a fixed angle $\Theta_2 \simeq 53.2^\circ$. At a given value of the S -shell mean binding energy of the nucleus under investigation, the angular and momentum settings of the MAP spectrometer and the momentum setting of the NES spectrometer were chosen to get a kinematics of the $(p, 2p)$ reaction close to that of the elastic proton-proton scattering. In this kinematics, the momentum K of the nuclear S -proton before the interaction is close to zero. At this condition, the counting rate of the S -shell proton knockout reaction should be maximal.

Results and discussion. In Fig. 2, the polarizations P_1 , P_2 in the $(p, 2p)$ reaction with the S -shell protons of the nuclei ${}^4\text{He}$, ${}^6\text{Li}$, ${}^{12}\text{C}$, ${}^{28}\text{Si}$, ${}^{40}\text{Ca}$ are plotted versus the S -shell proton binding energy E_s [14]. For all nuclei (excluding ${}^4\text{He}$), the effective mean nuclear density $\bar{\rho}$, normalized on the saturation nuclear density $\rho_0 \approx 0.18 \text{ fm}^{-3}$, is given. The actual calculation of the effective mean nuclear density $\bar{\rho}$, which is determined by absorption of the incident and both outgoing protons, was carried out following a procedure [10] using the computer code THREEDEE [12]. The potential model of a nucleus employed by the code is not correct for the ${}^4\text{He}$ nucleus. The calculated value of the $\bar{\rho}$ in this case is strongly unreliable [6]. The ${}^4\text{He}$ data should be excluded in comparison with theoretical models which differ from the PWIA.

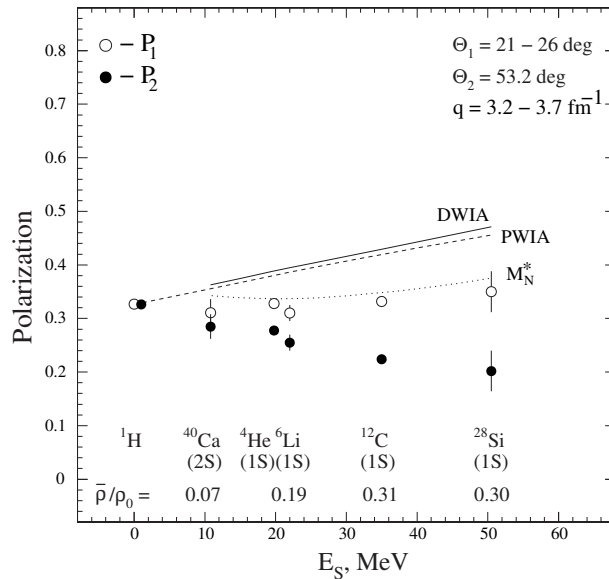


Figure 2: Polarizations P_1 and P_2 of the protons scattered at the angles Θ_1 (○) and Θ_2 (●) in the $(p, 2p)$ reaction with the S -shell protons of nuclei at 1 GeV. The points at $E_s = 0$ correspond to the elastic proton-proton scattering. The curves correspond the theoretical calculations described in the text.

The points (\circ) and (\bullet) in the figure correspond to the polarizations P_1 and P_2 of the forward scattered protons at the angle $\Theta_1 = 21^\circ \div 25^\circ$ (with energy $T_1 = 745 \div 735$ MeV) and of the recoil protons scattered at the angle $\Theta_2 \simeq 53.2^\circ$ (with energy $T_2 = 205 \div 255$ MeV). The points at the $E_s=0$ are the polarizations P_1 and P_2 in the elastic proton-proton scattering at the angles $\Theta_1 = 26.0^\circ$ and $\Theta_2 = 53.2^\circ$ ($\Theta_{cm} = 62.25^\circ$). In Fig. 2, the experimental data are compared with the results of the non-relativistic PWIA, DWIA calculations (the dashed and solid curves, respectively) [14] and the DWIA* calculation with the relativistic effect, the distortion of the nucleon Dirac spinor in nuclear medium, taken into account (the dotted, M_N^* , curve) [2,14]. For the calculations, the computer code THREEDEE was used [12] using an on-shell factorized approximation and the final energy prescription. A global optical potential, parametrized in the relativistic framework and converted to the Shrödinger-equivalent form, was used to calculate the distorted wave functions of incident and outgoing protons in the case of DWIA and DWIA*. A conventional well-depth method was used to construct the bound-state wave function. The DWIA* calculations were carried out in the Shrödinger-equivalent form [5]. In this approach, a modified NN interaction in medium is assumed due to the effective nucleon mass (smaller than the free mass), which affects the Dirac spinors used in the calculations of the NN scattering matrix. A linear dependence of the effective mass of nucleons on the nuclear density was assumed in the calculations.

The results of the polarization studies:

1. The difference of the final proton polarizations P_1 and P_2 found in the PWIA, DWIA and DWIA* is quite small (less than 0.005) for all nuclei under investigation.
2. The difference between the PWIA and DWIA results is small. This indicates that the distortion in the conventional non-relativistic framework does not play any essential role in the polarization for the kinematic conditions under consideration (the transferred momenta $q = 3.2 \div 3.7$ fm $^{-1}$).
3. Predictions of the DWIA* with relativistic corrections (distortion of the proton Dirac spinor in nuclear medium) are close to experimental data for the forward scattered proton polarization P_1 .
4. A significant difference is observed between the measured polarization of the scattered proton P_1 and that of the recoil proton P_2 .

Note that the difference between the measured polarizations P_1 and P_2 was also observed in the reaction with the D -shell protons of the ^{28}Si nucleus and was not seen in the reaction with the P -shell protons of the ^{12}C (Fig. 3).

The experimental data on the spin correlation parameters C_{ij} in the reactions with the ^4He and ^{12}C are given in Fig. 4. The dashed and dotted curves in the figure correspond to the PWIA calculations of the C_{nn} and $C_{s,s'}$ parameters using the current Arndts group phase-shift analysis (SP07). The mixed $C_{s,s'}$ parameter was found by taking into account its distortion in the magnetic fields of the spectrometers. The points at the $E_s = 0$ correspond to the elastic proton-proton scattering.

As seen in Fig. 4, the C_{nn} data (as well as the $C_{s,s'}$ data) are described in the framework of the PWIA. The question arises, there is no the nuclear medium modification of the C_{nn} parameter as it is for the polarization of the final protons (Fig. 2)? Whether this fact is connected to the strong polarization dropping for the recoil proton? It is possible that some spin-flip mechanism compensates the nuclear medium effect in the C_{nn} .

Due to the parity conservation in the elastic proton-proton scattering, the spin correla-

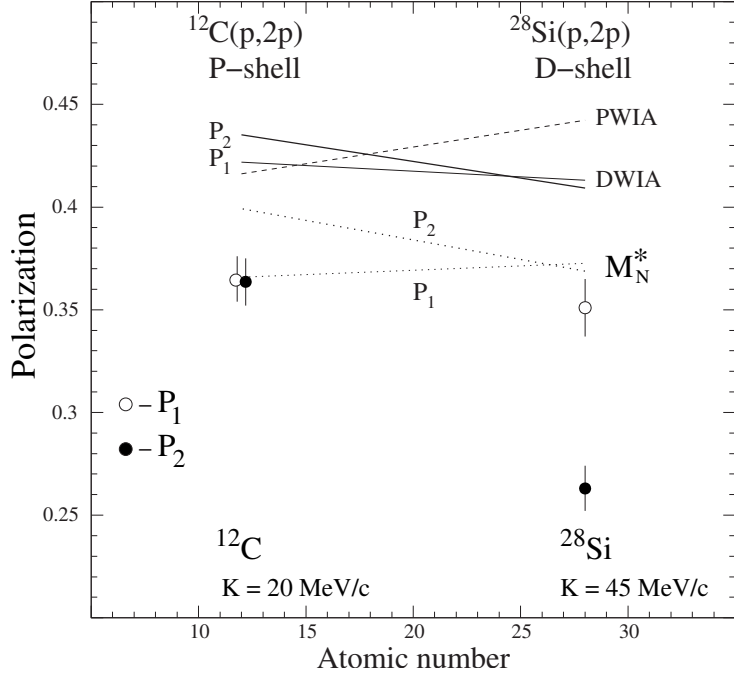


Figure 3: Polarization in the $(p, 2p)$ reaction with the external shell protons of the ^{12}C and ^{28}Si .

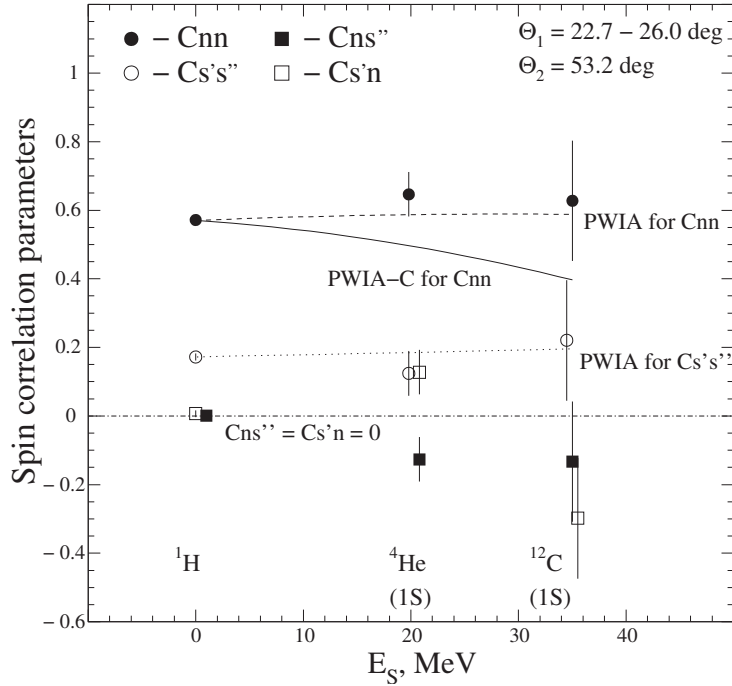


Figure 4: Spin correlation parameters C_{ij} in the $(p, 2p)$ reaction at 1 GeV with the S -shell protons of the ^4He and ^{12}C nuclei at the secondary proton scattering angles $\Theta_2 = 53.22^\circ$, $\Theta_1 = 24.21^\circ$ and $\Theta_2 = 53.22^\circ$, $\Theta_1 = 22.71^\circ$, respectively. The points at $E_s = 0$ correspond to the elastic proton-proton scattering ($\Theta_1 = 26.0^\circ$, $\Theta_{cm} = 62.25^\circ$). The curves are the results of calculations described in the text.

tion parameters $C_{ns''}$ and $C_{s'n}$ should be equal to 0. This is confirmed by the experimental data at the $E_s = 0$ in the Fig. 4. For the $(p, 2p)$ reaction, we see some deviation of the parameters from zero. It may be related to the spin-flip mechanism mentioned above. Note

that test calculations of all spin correlation parameters for the accidental coincidence background give zero values as should be expected.

To find an explanation of the observed effects, let us assume that there is a spin-flip interaction of the recoil (nuclear) proton with the residual nucleus, which is not taken into account by the theoretical approaches. This additional interaction mechanism, governed by the Pauli exclusion principle in a nucleus, reverses the proton spin direction and, as a consequence, changes the signs of the polarization and the spin correlation parameter C_{nn} .

The relative contribution (α) of the spin-flip mechanism in the interaction with a residual nucleus, which is mainly determined by the proton-nucleon rescatterings at small angles, can be found from experiment via the relative polarization dropping (g_p) for the recoil proton. First define the averaged polarization of the recoil proton:

$$\langle P_2 \rangle = \frac{P_2 + \alpha(-P_2)}{1 + \alpha} = \frac{P_1 + \alpha(-P_1)}{1 + \alpha} = \frac{(1 - \alpha)P_1}{1 + \alpha}. \quad (1)$$

In the equation we used the fact that all employed theories give equal values of the polarizations P_1 and P_2 . The averaged value of the C_{nn} can also be calculated using the equation:

$$\langle C_{nn} \rangle = \frac{C_{nn} + \alpha(-C_{nn})}{1 + \alpha} = \frac{(1 - \alpha)C_{nn}}{1 + \alpha}. \quad (2)$$

The relative polarization dropping g_p is determined as:

$$g_p = \frac{P_1 - \langle P_2 \rangle}{P_1} = g_{C_{nn}} = \frac{C_{nn} - \langle C_{nn} \rangle}{C_{nn}} = \frac{2\alpha}{1 + \alpha}. \quad (3)$$

It can be seen that the proposed spin-flip interaction couples in simple form the relative dropping of the polarization and the C_{nn} parameter $g_p = g_{C_{nn}}$. From experimental data we find $g_p(^4\text{He}) = 0.153 \pm 0.018$, $g_p(^{12}\text{C}) = 0.325 \pm 0.031$ and make corrections to the PWIA calculations using the formula $C_{nn\text{-cor}} = (1 - g_p)C_{nn}$ (the solid curve, PWIA-C, in Fig. 4). One can see from the figure that the the experimental C_{nn} points lie above the curve. So it can be expected that the nuclear medium modification enhances the C_{nn} parameter, while the polarization is reduced.

From the experimental g_p data, the probability of the spin-flip interaction can be defined for the corresponding residual nuclei: $\alpha(^3\text{H}) = 0.083 \pm 0.010$, $\alpha(^{11}\text{B}) = 0.194 \pm 0.022$.

What could be the nature of the considered spin-flip interaction? D.I. Blokhintsev was first to propose that there are the fluctuations of nuclear density in nuclei, or dense nucleon associations [15]. The reflection of the recoil proton off the objects is similar to the spin-flip interaction considered above. As a result, a proton belonging to a correlation, with opposite spin direction (due to the Pauli principle) is detected.

Nucleon correlations are intensively studied in the JLAB using electron beam. The CLAS collaboration gives the probability for a given nucleon to belong to a two-nucleon correlation in nucleus with A nucleons $a_{2N}(^3\text{He}) = 0.080 \pm 0.016$, $a_{2N}(^{12}\text{C}) = 0.193 \pm 0.041$ [16].

We can see that there is a coincidence between the PNPI α and the JLAB a_{2N} for the corresponding residual nuclei. The model of the spin-flip interaction for explanation of the PNPI polarization data is currently being developed. Preliminary results suggest that the ratio of the α and a_{2N} is very close to unity.

References

1. G.E. Braun and M. Rho, Phys. Lett. **66** (1991) 2720 .
2. C.J. Horowitz and M.J. Iqbal, Phys. Rev. **C33** (1986) 2059.
3. G. Krein *et al.*, Phys. Rev. **C51** (1995) 2646.
4. O.V. Miklukho *et al.*, Nucl. Phys. **A683** (2001) 145.
5. V.A. Andreev *et al.*, Phys. Rev. **C69** (2004) 024604.
6. O.V. Miklukho *et al.*, Phys. Atom. Nucl. **69** (2006) 474.
7. G.C. Hillhouse and T. Noro, Phys. Rev. **C74** (2006) 064608.
8. O.V. Miklukho *et al.*, Phys. Atom. Nucl. **73** (2010) 927.
9. G. Jacob *et al.*, Nucl. Phys. **A257** (1976) 517.
10. K. Hatanaka *et al.*, Phys. Rev. Lett. **78** (1997) 1014.
11. T. Noro *et al.*, Nucl. Phys. **B633** (2000) 517 .
12. N.S. Chant and P.G. Roos, Phys. Rev. **C27** (1983) 1060.
13. W.O. Lock and D.F. Measday, *Intermediate-Energy Nuclear Physics* (Methuen, London, 1970; Atomizdat, Moscow, 1973).
14. O.V. Miklukho *et al.*, Phys. Atom. Nucl. **76** (2013) 871.
15. D.I. Blokhintsev, Sov.J. ZhETF **33** (1957) 1295 [in Russian].
16. K.S. Egiyan *et al.*, Phys. Rev. Lett. **96** (2006) 082501.

RECENT RESULTS FROM HERMES

W.-D. Nowak¹, A. Rostomyan², G. Schnell^{3,4†}, and C. Van Hulse³

[On behalf of the HERMES Collaboration]

(1) *DESY, 15738 Zeuthen, Germany*

(2) *DESY, 22603 Hamburg, Germany*

(3) *Department of Theoretical Physics, University of the Basque Country UPV/EHU, 48080 Bilbao, Spain*

(4) *IKERBASQUE, Basque Foundation for Science, 48011 Bilbao, Spain*

† *E-mail: gunar.schnell@desy.de*

Abstract

HERMES collected a wealth of deep-inelastic scattering data using the 27.6 GeV polarized HERA lepton beam and various pure, polarized and unpolarized, gaseous targets. This unique data set opens the door to observables sensitive to the multi-dimensional structure of the nucleon. Among them are semi-inclusive deep-inelastic scattering measurements of azimuthal modulations sensitive to the Sivers and Boer-Mulders distributions as well as of light-meson multiplicities, all providing information on the three-momentum-dependent quark distributions. Inclusive hadron production on transversely polarized protons provides complementary information. Knowledge on the quark distribution as a function of longitudinal momentum and transverse position in impact-parameter space can be accessed, e.g., through deeply virtual Compton scattering, in particular through its improved, background-free measurement via recoil-proton detection. The various measurements of the observables providing insight into the multi-dimensional nucleon structure are presented.

1 Introduction

The HERMES experiment at DESY collected data from 1995 until 2007 using the 27.6 GeV HERA lepton beam. In the experiment, longitudinally polarized electrons or positrons were scattered off stationary gaseous hydrogen, deuterium, helium, or heavier targets, with hydrogen longitudinally or transversely polarized or unpolarized, deuterium and helium longitudinally polarized or unpolarized, and the heavier targets unpolarized. The scattered lepton and particles produced in the collision were detected by a forward spectrometer. Here, lepton-hadron separation was performed by a transition-radiation detector, a preshower, and a calorimeter, with an identification efficiency exceeding 98% and a misidentification contamination below 1%. Hadron identification was performed by a ring-imaging Cherenkov detector, allowing the discrimination of pions, kaons, and protons. In the last two years of data collection, a recoil detector was installed around the target cell, filled with unpolarized hydrogen or deuterium, in order to detect low-momentum particles outside the acceptance of the forward spectrometer. This detector consisted of a silicon-strip detector, a scintillating-fibre tracker, and a photon detector.

Data collected on unpolarized targets were used to extract multiplicities in semi-inclusive deep-inelastic scattering (DIS). They provide information on the fragmentation of quarks into final-state hadrons. The measurement of pion and kaon multiplicities from data taken with a hydrogen and deuterium target as well as a re-evaluation of the strange-quark distribution using the extracted kaon multiplicities are presented in section 2.

Extending the analysis to the azimuthal distribution of hadrons provides access to the Boer-Mulders distribution [1] and the Collins fragmentation function [2]. The former describes the distribution of transversely polarized quarks in an unpolarized nucleon and correlates the transverse momentum of the quarks with their spin, while the latter describes the fragmentation of a transversely polarized quark into an unpolarized hadron. Results sensitive to these two quantities are presented in section 3.

Semi-inclusive DIS off a transversely polarized target allows, among others, to access the Sivers [3] and transversity distributions. The Sivers distribution describes the distribution of unpolarized quarks in a transversely polarized nucleon, correlating quark transverse momentum with the nucleon's transverse spin, while the transversity distribution describes the distribution of transversely polarized quarks in a transversely polarized nucleon. Measurements accessing these distributions are discussed in section 4 together with results on single-spin asymmetries in inclusive hadron production.

Turning to exclusive reactions, deeply virtual Compton scattering (DVCS) provides the cleanest access to generalized parton distributions (GPDs) [4]. The Fourier transforms in impact-parameter space of these probability amplitudes describe the distribution of quarks as a function of their longitudinal momentum and transverse position [5]. At HERMES various azimuthal asymmetries have been extracted with data collected using a (longitudinally polarized) positron and electron beam on hydrogen and deuterium targets in various polarization states (see, e.g., Refs. [6–11]), providing sensitivity to different GPDs. Without the usage of the recoil detector, the selected data sample contains a 12% contribution from associated production, where, e.g., the proton is excited to a Δ resonance. With the active detection of protons (and pions) using the recoil detector, this contribution of associated production is reduced to a negligible level. In addition, the recoil detector allows the measurement of associated DVCS. Results on the latter two measurements are discussed in section 5.

2 Charge-separated pion and kaon multiplicities and re-evaluation of the strange-quark distribution

Hadron multiplicities, i.e., hadron numbers per DIS event, were measured in three-dimensional bins in $(Q^2, z, P_{h\perp})$ and in $(x_B, z, P_{h\perp})$ for charge-separated pions and kaons, using unpolarized protons and deuterons [12]. Here, $-Q^2$ represents the squared four-momentum of the virtual photon that mediates the lepton-nucleon interaction, z denotes, in the target-rest frame, the fractional hadron energy with respect to the virtual-photon energy, $P_{h\perp}$ the magnitude of the hadron momentum-component transverse to the virtual-photon three-momentum, and x_B the x -Bjorken variable. The experimentally extracted multiplicities are corrected for QED radiative effects, limited geometric and kinematic acceptance of the spectrometer, losses due to decay in flight and secondary strong interactions, and finite detector resolution using an unfolding procedure, based on a LEPTO

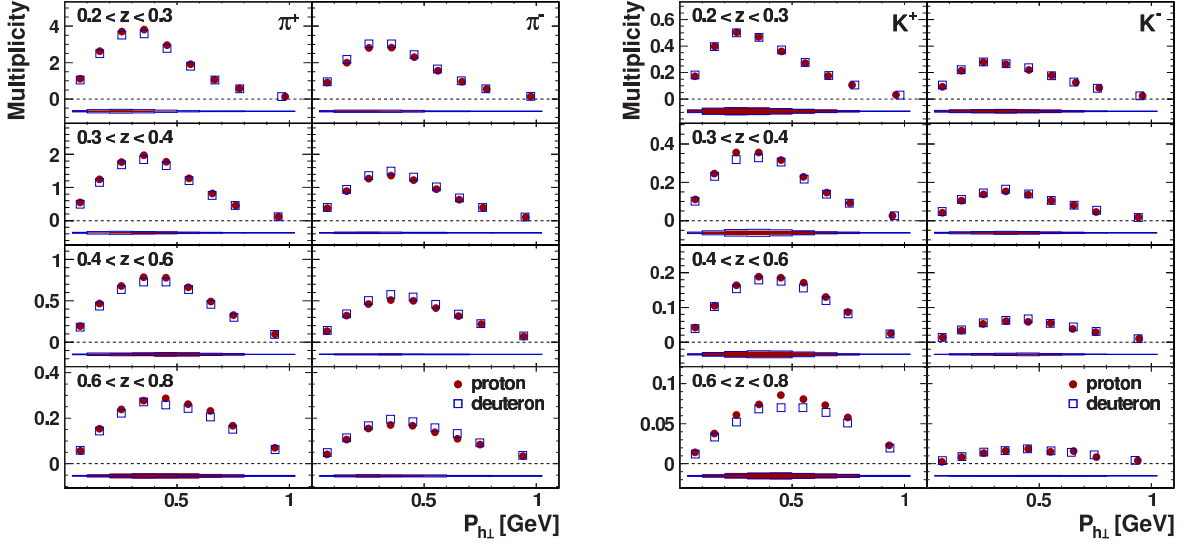


Figure 1: Charge-separated pion (left) and kaon (right) multiplicities from protons (filled circles) and deuterons (open squares) as a function of $P_{h\perp}$ in slices of z . Statistical (systematic) uncertainties are given as error bars (bands).

and JETSET Monte-Carlo simulation, similar to the procedure described in Ref. [13]. Results are available with and without the subtraction of the contributions originating from exclusive vector-meson production. The pion and kaon “Born” multiplicities with exclusive vector-meson contributions removed are presented in Fig. 1 for protons (filled circles) and deuterons (open squares), as a function of $P_{h\perp}$ for various slices in z .

As can be seen in Fig. 1, π^+ multiplicities for protons are larger than for deuterons, whereas for π^- the opposite is true. In addition, the ratio of the π^+ and π^- multiplicities on proton (deuteron) ranges from 1.2 (1.1) in the first z bin to 2.6 (1.8) in the last z bin. These observations can be understood by the dominance of scattering off a u -quark and a subsequent favored fragmentation of a u -quark into a π^+ over an unfavored fragmentation of a u -quark into a π^- , together with the increased d -quark content in deuterons in conjunction with a favored d -quark to π^- fragmentation. For kaons an analogous behavior is observed in the comparison of the multiplicity ratio of both kaon types and in the comparison of K^+ multiplicities for protons and deuterons. However, the K^- multiplicities seem to be insensitive to the target type. These results reflect the fact that K^- can not be produced through favored fragmentation of nucleon valence quarks as it is composed of valence quark types present in the nucleon only as sea quarks,

Similar considerations can also explain the observed transverse-momentum distributions from Fig. 1. The transverse hadron momentum reflects both the intrinsic transverse momentum of the struck quark inside the nucleon and the transverse momentum that is acquired during the fragmentation process. Negative kaons exhibit a broader multiplicity distribution than positive kaons and pions. This can arise from a more complicated hadronization process for negative kaons. Considering, e.g., the LUND model, which models the fragmentation process in terms of string breaking, unfavored fragmentation is characterized by at least one more string break in comparison with favored fragmentation, resulting in a broader distribution of the transverse momentum. These data thus provide essential input to extractions of the flavor-separated transverse-momentum dependences of parton distribution and fragmentation functions as, e.g., demonstrated in Ref. [14].

Based on the above discussed multiplicities, a new extraction at leading-order in α_S of the strange-quark distribution $S(x_B) = s(x_B) + \bar{s}(x_B)$ was performed [15]. A previous extraction of this distribution [16] was based on multiplicities that used an unfolding procedure in only one dimension: x_B . The new three-dimensional unfolding procedure resulted in significant changes for the obtained multiplicities. The then extracted strange-quark distribution $x_B S(x_B)$, evolved to $Q^2 = 2.5 \text{ GeV}^2$, is shown in Fig. 2. For this extraction, the non-strange-quark distribution from CTEQ6L was used, and the value for the z -integrated kaon fragmentation function $S(x_B) \rightarrow K = K^+ + K^-$ was chosen to be 1.27 [17]. The latter only enters as a normalization factor. Irrespective of its chosen value, the shape of the strange-quark distribution is in contradiction with the predictions.

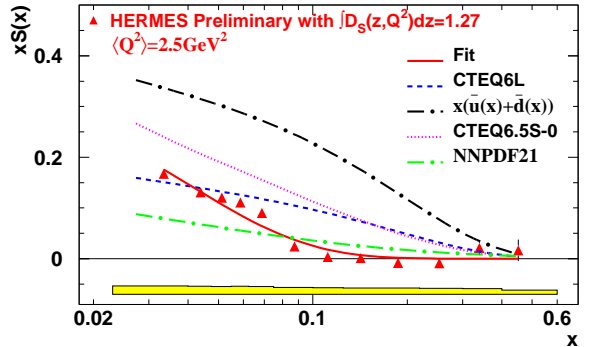


Figure 2: The strange-quark distribution $x_B S(x_B)$ (with x_B labeled as x) obtained from the HERMES multiplicities for charged kaons, evolved to $Q^2 = 2.5 \text{ GeV}^2$, assuming the z -integrated kaon fragmentation function to be equal to 1.27 ± 0.13 . The red solid curve is a result of a fit of the form $x_B^{-0.867} e^{-x_B/0.033} (1 - x_B)$; the blue dashed (black dashed-dotted) curve gives $x_B S(x_B)$ (the sum of the light antiquarks) from CTEQ6L; the magenta dotted (green dashed-dotted) curve gives $x_B S(x_B)$ from CTEQ6.5S-0 [18] (the neural-network PDFs set NNPDF21 [19]). The band at the bottom represents the propagated experimental systematic uncertainties.

3 Azimuthal distributions of charge-separated identified hadrons

When considering the non-collinear semi-inclusive DIS cross section two additional structure functions appear compared to the collinear case. One appears at leading twist as a $\cos(2\phi)$ modulation, and the other at sub-leading twist as a $\cos(\phi)$ modulation. Here, ϕ denotes the angle between the lepton-scattering and the hadron-production planes. The $\cos(2\phi)$ term is a convolution of the Boer-Mulders distribution and the Collins fragmentation function. The sub-leading twist modulation contains the same contribution but also terms related to the Cahn effect [20] as well as to quark-gluon-quark correlations.

The $\cos(\phi)$ and $\cos(2\phi)$ moments were extracted from data collected on hydrogen and deuterium targets, using a fully differential unfolding procedure in x_B , y , z , and $P_{h\perp}$ in order to eliminate moments induced by higher-order QED effects or detector acceptance [13]. In the target rest frame y represents the fractional virtual-photon energy with respect to the beam-lepton energy.

In Fig. 3 the extracted $\cos(2\phi)$ moments projected in bins of x_B , y , z , and $P_{h\perp}$ are presented for π^+ (left, top panels), π^- (left, bottom panels), K^+ (right, top panels), and K^- (right, bottom panels) for data collected on proton (filled symbols) and deuteron (open symbols). The pion $\cos(2\phi)$ moments for data collected on protons and on deuterons are compatible. This hints at similar Boer-Mulders distributions for u -quarks and d -quarks. On the other hand, positive moments for π^- and small but negative moments for π^+ are observed. This is compatible with a favored Collins fragmentation function (e.g.,

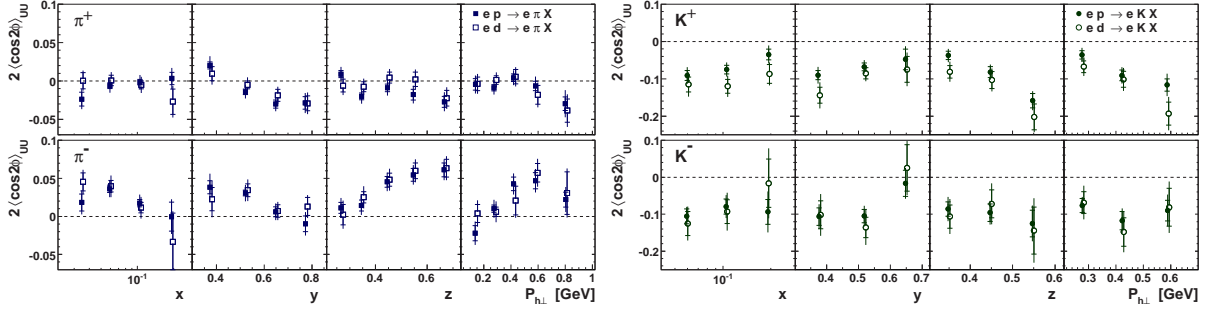


Figure 3: Charge-separated $\cos(2\phi)$ moments for pions (left panels) and kaons (right panels) versus x_B (here labeled as x), y , z , and $P_{h\perp}$ for protons (filled symbols) and deuterons (open symbols). Statistical uncertainties are represented by the inner error bars, while the total error bars represent the quadratic sum of statistical and systematic uncertainties.

$u \rightarrow \pi^+$) with equal magnitude but opposite sign compared to the unfavored Collins fragmentation function (e.g., $u \rightarrow \pi^-$), as obtained from the measurements related to the transversity distribution [21]. For kaons, large negative amplitudes are observed. The K^- amplitude is similar to the K^+ amplitude, both significantly larger than the pion amplitudes. These differences could, e.g., stem from different Collins fragmentation functions for kaon production from u -quarks as compared to pion production, or hint at a significant role of sea quarks.

4 Single-spin asymmetries measured from a transversely polarized proton target

Single-spin asymmetries measured from a transversely polarized proton show characteristic angular modulations. Each of the corresponding azimuthal amplitudes is related to convolutions of different distribution and fragmentation functions. The amplitude of the $\sin(\phi - \phi_S)$ modulation, with ϕ_S being the azimuthal angle of the transverse component of the target-spin vector about the virtual-photon direction with respect to the lepton scattering plane, is interpreted as the convolution of the Sivers distribution function and the spin-independent fragmentation function. The $\sin(\phi + \phi_S)$ modulation is proportional to the convolution of transversity and the Collins fragmentation function. These two azimuthal amplitudes were extracted from a transversely polarized hydrogen target as a function of x_B , z , and $P_{h\perp}$ for charged and neutral pions, and for charged kaons. The results on the Sivers amplitudes were published in Ref. [22], while for the Collins effect results are available in Ref. [23].

The Sivers π^+ amplitude was found to be significantly positive, rising with z and with $P_{h\perp}$ at low values of $P_{h\perp}$, after which it reaches a plateau at higher $P_{h\perp}$ values. Assuming u -quark dominance, this positive amplitude corresponds to a negative u -quark Sivers distribution function. The π^- amplitude is consistent with zero, which can be attributed to canceling contributions from the Sivers u - and d -quark distributions, while for the π^0 amplitude, isospin symmetry is fulfilled. The K^+ Sivers amplitude shows a similar kinematic dependence as the π^+ amplitude, but has a larger magnitude. This may hint at a non-trivial role of sea quarks. The K^- amplitude is observed to be (slightly) positive.

The Collins amplitudes were found to have opposite signs for charged pions, with π^+

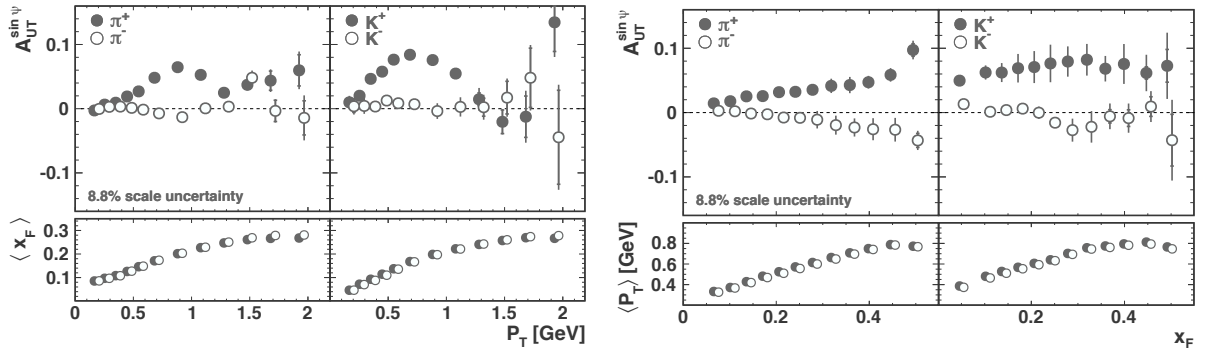


Figure 4: $A_{UT}^{\sin \psi}$ amplitudes for charged pions and kaons as a function of P_T (top) and x_F (bottom), where ψ denotes the angle about the lepton-beam direction between the hadron production plane and the target-spin vector. Positive (negative) particles are denoted by closed (open) symbols. Inner error bars show the statistical uncertainties, while the total ones represent the quadratic sum of statistical and systematic uncertainties. There is an additional 8.8% scale uncertainty due to the precision in the measurement of the target polarization. The bottom subpanels show the P_T (x_F) dependence of the average x_F (P_T). Data points for negative particles are slightly shifted horizontally for legibility.

being smaller in magnitude than π^- . This resulted in the afore-mentioned conclusion of favored and disfavored pion Collins fragmentation functions of similar size but of opposite sign. For kaons, large positive amplitudes were found for K^+ and vanishing ones for K^- .

Inclusive lepto-production of charged pions and kaons from transversely polarized protons serves as an additional probe of spin-momentum correlations. Large transverse single-spin asymmetries in inclusive hadron production in pN collision originally lead to the ideas of the Sivers [3] and Collins [2] effects. The HERMES experiment recently provided the first such measurement in ep scattering [24]. The resulting asymmetries are reminiscent of the Sivers effect, with large positive amplitudes for π^+ and K^+ , slightly larger for kaons than for pions, and small, almost vanishing, amplitudes for π^- and K^- . A two-dimensional extraction of the asymmetry amplitudes [24], performed by binning simultaneously in the component of the hadron momentum transverse to the incoming lepton beam, P_T , and the Feynman- x variable, x_F , results in amplitudes for π^+ which are essentially independent of x_F . An apparent increase with x_F after integration over P_T (see Fig. 4) is mostly a reflection of the underlying dependence on P_T . For negative pions, and less significantly for negative (positive) kaons, the asymmetry amplitudes decrease (increase) with x_F . The amplitudes as a function of P_T are positive for the positive hadrons and slightly larger for K^+ compared to π^+ . They rise smoothly with P_T from zero at low P_T up to a maximum value of approximately 0.06 (0.08) for pions (kaons) at $P_T \simeq 0.8$ GeV and then decrease with increasing P_T .

5 Azimuthal asymmetries in elastic and associated deeply virtual Compton scattering

At the HERMES experiment, DVCS is accessed through azimuthal asymmetries, where the azimuthal angle ϕ is the angle between the photon-production and the lepton-scattering planes. These asymmetries probe the contribution from the interference of the DVCS and Bethe-Heitler processes. In the latter process, the real photon is not emitted by

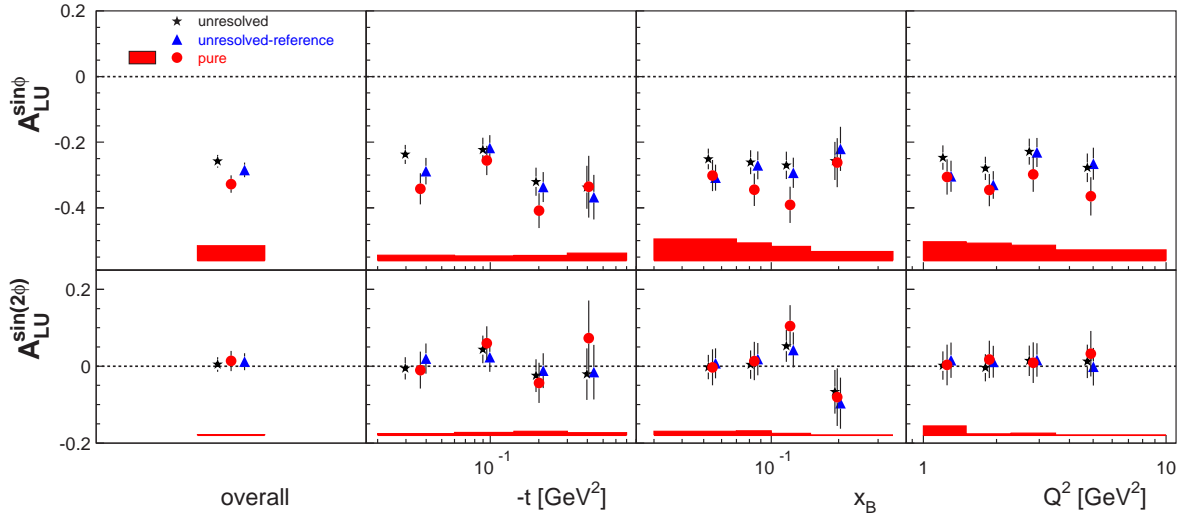


Figure 5: Amplitudes of single-charge beam-helicity asymmetry in DVCS shown in projections of $-t$, x_B , and Q^2 . Statistical uncertainties are shown by error bars. The bands represent the systematic uncertainties of the amplitudes extracted from the pure sample. A scale uncertainty arising from the beam-polarization measurement amounts to 1.96%. Shown are amplitudes extracted from a) the pure sample (red circles, shown at their kinematic values); b) the unresolved-reference sample (blue triangles, shifted to the right for legibility); c) the unresolved sample (black stars, shifted to the left for legibility).

the quark probed by the virtual photon, but by the incident or scattered lepton. Before the installation of the recoil detector [25], the recoiling proton was reconstructed through the determination of its missing mass using the scattered lepton and the real photon, the latter two detected by the forward spectrometer. With active detection of the recoil proton by the recoil detector, the background contribution, which consists mainly of associated production (around 12%), could be reduced to a negligible level of below 0.2% [26].

In order to separate the effect of the recoil-detector acceptance from the removal of background, a so-called unresolved-reference sample was constructed. This sample consists of events where, based on the reconstructed photon and scattered-lepton kinematics using the forward spectrometer only, the recoiling proton was determined to lie within the recoil-detector acceptance. This unresolved-reference sample is estimated to contain 14% of associated background contribution. The asymmetries extracted from the data sample using the forward spectrometer only without considering the recoiling proton (unresolved), from the unresolved-reference sample, and from the data sample with active recoiling-proton detection (pure) are presented in Fig. 5 as a function of $-t$, x_B , and Q^2 , with t being the square of the difference between the initial and final four-momenta of the target proton. The leading twist-2 $\sin(\phi)$ asymmetry from the pure sample increases by 0.054 ± 0.016 with respect to the asymmetry from the unresolved-reference sample. This effectively indicates that the asymmetry from the associated process acts as a dilution. The same conclusion can be drawn from the measurement of associated DVCS, where events originating from associated production for the channels $ep \rightarrow e\gamma\pi^0 p$ and $ep \rightarrow e\gamma\pi^+ n$, around the Δ mass, are selected. The measured asymmetries show a leading asymmetry amplitude compatible with zero [27]. The sub-leading twist asymmetries for DVCS and associated DVCS are found to be compatible with zero [26, 27].

References

- [1] D. Boer and P. J. Mulders, Phys. Rev. **D57** (1998) 5780.
- [2] J. C. Collins, Nucl. Phys. **B396** (1993) 161.
- [3] D. W. Sivers, Phys. Rev. **D41** (1990) 83.
- [4] D. Müller et al., Fortschr. Phys. **42** (1994) 101.
- [5] M. Burkardt, Phys. Rev. **D66** (2002) 114005.
- [6] A. Airapetian et al. [HERMES Collaboration], JHEP **06** (2008) 066.
- [7] A. Airapetian et al. [HERMES Collaboration], Nucl. Phys. **B829** (2010) 1.
- [8] A. Airapetian et al. [HERMES Collaboration], JHEP **06** (2010) 019.
- [9] A. Airapetian et al. [HERMES Collaboration], Phys. Lett. **B704** (2011) 15.
- [10] A. Airapetian et al. [HERMES Collaboration], Nucl. Phys. **B842** (2011) 265.
- [11] A. Airapetian et al. [HERMES Collaboration], JHEP **07** (2012) 32.
- [12] A. Airapetian et al. [HERMES Collaboration], Phys. Rev. **D87** (2013) 074029.
- [13] A. Airapetian et al. [HERMES Collaboration], Phys. Rev. **D87** (2013) 012010.
- [14] A. Signori et al., JHEP **11** (2013) 194.
- [15] A. Airapetian et al. [HERMES Collaboration], arXiv:1312.7028.
- [16] A. Airapetian et al. [HERMES Collaboration], Phys. Lett. **B666** (2008) 446.
- [17] D. de Florian, R. Sassot, and M. Stratmann, Phys. Rev. **D75** (2007) 114010.
- [18] H. L. Lai et al., JHEP **04** (2007) 089.
- [19] R. D. Ball et al. [NNPDF Collaboration], Nucl. Phys. **B855** (2012) 153.
- [20] R. N. Cahn, Phys. Lett. B **78** (1978) 269.
- [21] A. Airapetian et al. [HERMES Collaboration], Phys. Rev. Lett. **94** (2005) 012002.
- [22] A. Airapetian et al. [HERMES Collaboration], Phys. Rev. Lett. **103** (2009) 152002.
- [23] A. Airapetian et al. [HERMES Collaboration], Phys. Lett. **B693** (2010) 11.
- [24] A. Airapetian et al. [HERMES Collaboration], Phys. Lett. **B728** (2014) 183.
- [25] A. Airapetian et al., JINST **8** (2013) P05012.
- [26] A. Airapetian et al. [HERMES Collaboration], JHEP **10** (2012) 042.
- [27] A. Airapetian et al. [HERMES Collaboration], JHEP **01** (2014) 077.

LONGITUDINAL DOUBLE SPIN ASYMMETRY A_1^p AND SPIN-DEPENDENT STRUCTURE FUNCTION g_1^p OF THE PROTON AT LOW x AND LOW Q^2 FROM COMPASS

A.S. Nunes^{1†}, on behalf of the COMPASS Collaboration

(1) *LIP, 1000-149 Lisbon, Portugal*

[†]*E-mail: Ana.Sofia.Nunes@cern.ch*

Abstract

The COMPASS experiment at CERN has collected a large sample of events of inelastic scattering of longitudinally polarised muons off longitudinally polarised protons in the non-perturbative region (four-momentum transfer squared $Q^2 < 1$ (GeV^2/c^2), with a Bjorken scaling variable in the range $4 \times 10^{-5} < x < 4 \times 10^{-2}$. The data set is two orders of magnitude larger than the similar sample collected by the SMC experiment. These data complement our data for polarised deuterons. They allow the accurate determination of the longitudinal double spin asymmetry A_1^p and of the spin-dependent structure function g_1^p of the proton in the region of low x and low Q^2 . The preliminary results of the analysis of these data yield non zero and positive asymmetries and of the structure function g_1^p . This is the first time that spin effects are observed at such low x .

In processes of inelastic scattering of leptons off nucleons, the region of low values of x corresponds to high parton densities. Among experiments with polarisation, only fixed target experiments have been able, up to now, to probe that poorly known region. In this kind of experiments there is a strong correlation between x and Q^2 , which makes low x measurements also low Q^2 ones, for which perturbative QCD is not valid. However, there are models that allow a smooth extrapolation to the low Q^2 region, while matching the perturbative QCD behaviour at high Q^2 , including resummation or vector meson dominance [1, 2]. The SMC experiment at CERN has done pioneer measurements of longitudinal double spin asymmetries A_1^p and of the spin-dependent structure function g_1^p of the proton down to $x = 6 \times 10^{-5}$ [3], but the measurements had a limited precision, that COMPASS can now improve. Furthermore, the non-singlet structure function $g_1^{\text{NS}} = g_1^p - g_1^n$, which decouples from gluons, can be extracted with increased precision when combining our published and structure function g_1^d of the deuteron at low x [8] with these new preliminary results of g_1^p .

The COMPASS experiment is described in detail in [4]. It is a fixed target experiment at the SPS using a tertiary, naturally polarised, muon beam. It consists of a large acceptance two-staged spectrometer with trackers and calorimetry in its two stages, and a RICH detector. A beam momentum of 160 GeV/c was used in 2007, changed to 200 GeV/c in 2011 to allow reaching lower values of x for a given Q^2 . The 1.2 meter-long polarised target was divided in three independent cells, to allow simultaneous data taking in two opposite spin configurations of the target material. In 2007 and 2011, the target consisted on polarisable protons from ammonia (NH_3). The polarisation of the target is built by the process of dynamic nuclear polarisation, using a superconducting solenoid

with 2.5 T; in the frozen spin mode, the target material is kept at temperatures down to 50 mK using a $^3\text{He}/^4\text{He}$ dilution refrigerator. Typical values of polarisation obtained were of the order of 85%; the dilution factor, *i.e.* the percentage of polarisable material, was around 16%.

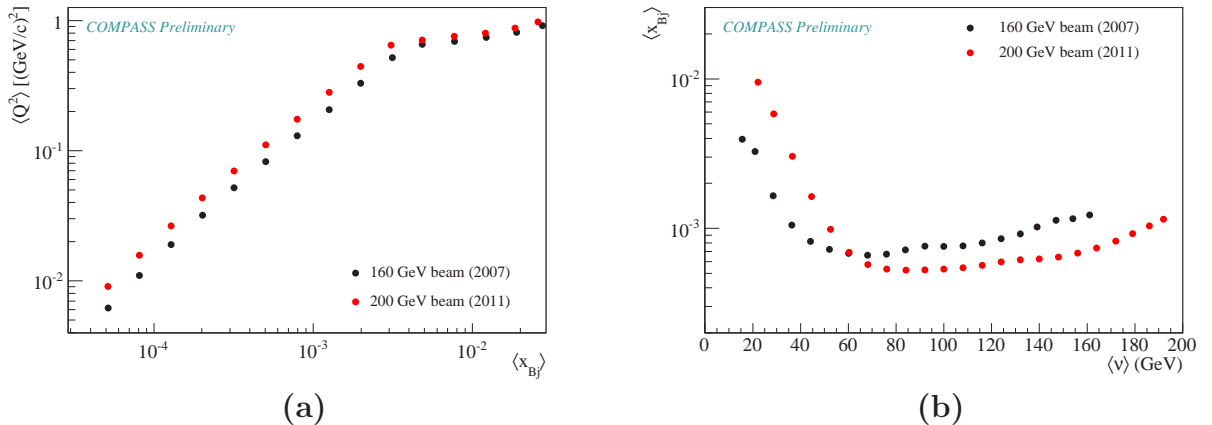


Figure 1: (a) Average values of Q^2 versus average values of x of the bins used in the $A_1^p(x)$ and $g_1^p(x)$ extractions, for the 2007 and 2011 data samples. (b) Similar plot, but for average values of x versus average values of ν of the bins used in the $A_1^p(\nu)$ and $g_1^p(\nu)$ extractions.

For the present analysis, data taken in 2007 and 2011 with a longitudinally polarised target of protons (from NH_3 divided in three cells, with neighbouring cells with opposite polarisation) and a longitudinally polarised muon beam with 160 or 200 GeV, respectively, were used. The main selection criteria of events were: (a) $Q^2 < 1$ $(\text{GeV}/c)^2$; (b) $x \geq 4 \times 10^{-5}$; (c) the fraction of the muon energy transferred to the proton, in the laboratory, satisfied $0.1 < y < 0.9$; (d) there was at least one additional track besides the scattered muon in the interaction vertex (to better discriminate the target cell in which the interaction occurred); (e) the event was not due to elastic scattering of a muon off a target electron (which is an important contamination of the sample, peaked at $x = m_e/m_p \sim 5.5 \times 10^{-4}$), as in [8].

The number of events in the two final samples with different beam energies are, respectively, 447×10^6 and 229×10^6 , *i.e.* the COMPASS sample is about 150 times larger than the SMC one. The average values, for the bins used in the analysis, of selected kinematic variables in the final samples are presented in Fig. 1.

The number of events in the antiparallel (parallel) spin configurations are given by:

$$N^{\vec{\uparrow}, \vec{\uparrow}} \simeq a\phi n\bar{\sigma}(1 \pm P_{\text{beam}}P_{\text{target}}fA_1^p)$$

The longitudinal double spin asymmetries of the proton, A_1^p , were extracted from data using a method [5, 10] that weights each event by a factor $\omega = fDP_b$, *i.e.* the product of the dilution factor, the depolarisation factor and the polarisation of the beam, in order to reduce the statistical errors. Great care was taken to minimize possible sources of false asymmetries. This was done, on one hand, by only selecting events for which the beam track extrapolation crosses all the target cells, in order to have the same beam flux in all cells; and, on the other hand by using three target cells, by reversing the spin configuration of the target cells about every 24 hours, by measuring asymmetries independently in

periods of data taken in about 48 hours, and by changing the combination of the target field and the spin configuration of the target cells at least once per year of data taking, to minimize the respective correlation.

The asymmetries were obtained independently in bins of x and in bins of the virtual photon energy ν . Unpolarised radiative corrections taken from the program TERAD [11] were included in an effective dilution factor, whereas polarised radiative corrections were taken from the program POLRAD [12], and are less or equal than 25% of the statistical errors. The asymmetries were further corrected for the presence of polarisable ^{14}N in the target material, the corrections being less or equal than 1% of the statistical errors. Thorough checks on possible sources of false asymmetries (which dominate the systematic errors) were done, and the systematic errors are expected to be smaller than the statistical errors. The preliminary results obtained for A_1^p are shown in Fig. 2.

The spin dependent structure function of the proton, g_1^p , was also obtained independently in bins of x and in bins of ν , the virtual photon energy, according to

$$g_1^p = \frac{F_2^p(\langle x \rangle, \langle Q^2 \rangle)}{2x[1 + R(\langle x \rangle, \langle Q^2 \rangle)]} A_1^p,$$

where F_2 was obtained from a parameterisation from the SMC within its validity range [6], or from a model otherwise (low x and Q^2) [7]; and R was taken from data or, in the case of low x , from a parameterisation, as described in [8]. The preliminary results obtained for g_1^p are presented in Fig. 3.

In both cases of A_1^p and g_1^p the preliminary results obtained with different beam energies of 160 GeV and 200 GeV are compatible within errors. No special dependence with ν is observed. Furthermore, the results are incompatible with zero and positive in the measured ranges. This is the first time that spin effects are observed at such low values of x . It will now be possible to extract a more precise non-singlet structure function g_1^{NS} from the COMPASS results of g_1^p and g_1^d for $Q^2 < 1$ (GeV/c) 2 , in order to compare it with theoretical predictions.

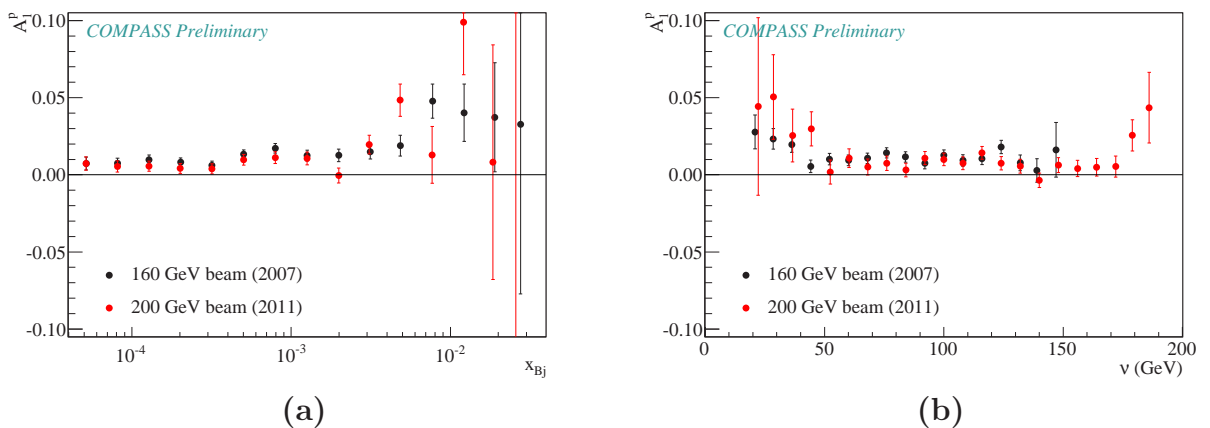


Figure 2: (a) Longitudinal double spin asymmetries A_1^p as a function of x , obtained from 2007 and 2011 data, after corrections due to the polarised radiative asymmetry and the presence of ^{14}N in the ammonia target. The results for the two beam energies are compatible within errors. The systematic errors are expected to be smaller than the statistical errors. The asymmetries are mostly incompatible with zero and positive. (b) The same, but for A_1^p as a function of ν .

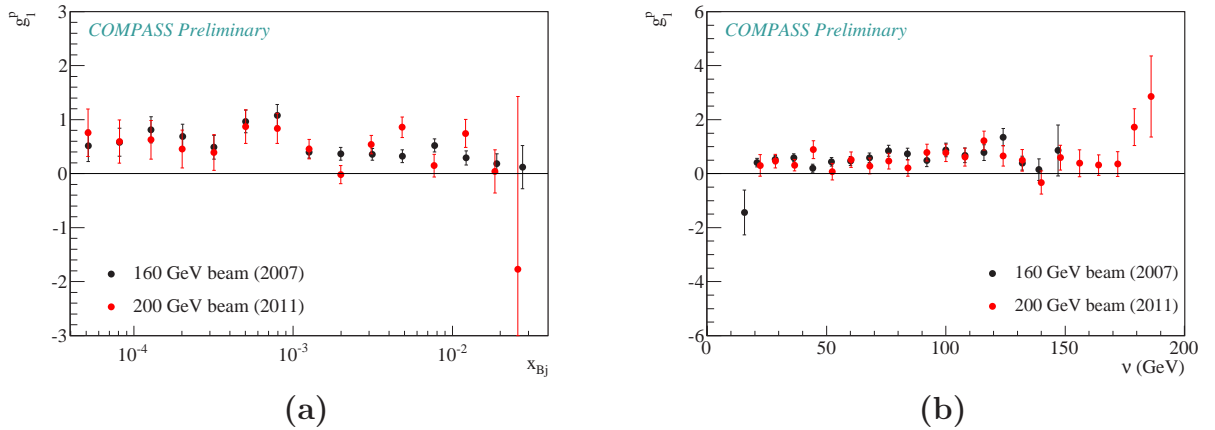


Figure 3: (a) Spin dependent structure function g_1^p as a function of x , obtained from 2007 and 2011 data. The results for the two beam energies are compatible within errors. The systematic errors are expected to be smaller than the statistical errors. The asymmetries are mostly incompatible with zero and positive. (b) The same, but for g_1^p as a function of ν .

References

- [1] B. Badełek, J. Kiryluk & J. Kwieciński, Phys.Rev. D **61** (1999) 014009; B. Badełek, J. Kwieciński & B. Ziaja, Eur.Phys.J. C **26** (2002) 45.
- [2] B.I. Ermolaev, M. Greco & S.I. Troyan, Eur.Phys.J. C **58** (2008) 29; B.I. Ermolaev, M. Greco & S.I. Troyan, Eur.Phys.J. C **50** (2007) 823; B.I. Ermolaev, M. Greco & S.I. Troyan, Phys.Lett. B **622** (2005) 93; B.I. Ermolaev, M. Greco & S.I. Troyan, Riv.Nuovo Cim. **33** (2010) 57.
- [3] B. Adeva et al. (SMC Collaboration), Phys.Rev. D **60** (1999) 072004; B. Adeva et al. (SMC Collaboration), Phys.Rev. D **62** (1999) 079902.
- [4] P. Abbon et al. (COMPASS Collaboration), Nucl. Instr. and Meth. A **577** (2007) 455; A. Bressan, these proceedings.
- [5] E.S. Ageev et al. (COMPASS Collaboration), Phys.Lett. B **612** (2005) 154; A. Ivanov, these proceedings.
- [6] B. Adeva et al. (SMC Collaboration), Phys.Rev. D **58** (1998) 112002.
- [7] J. Kwieciński & B. Badełek, Z.Phys. C **43** (1989) 251; B. Badełek & J. Kwieciński, Phys.Lett. B **295** (1992) 263.
- [8] E.S. Ageev et al. (COMPASS Collaboration), Phys.Lett. LB **647** (2007) 330.
- [9] V.Yu. Alexakhin et al. (COMPASS Collaboration), Phys.Lett. B **647** (2007) 8.
- [10] M.G. Alekseev et al. (COMPASS Collaboration), Phys.Lett. B **690** (2010) 466.
- [11] A.A. Akhundov et al., Sov.J.Nucl.Phys. **26** (1977) 660.
- [12] I. Akushevich et al., Comput.Phys.Commun. **104** (1997) 201.

THE POLARIZED BEAM TAGGING SYSTEM OF THE EXPERIMENTAL SET-UP SPASCHARM

S.B. Nurushev¹, M.A. Chetvertkov², V.A. Chetvertkova², A.P. Meshchanin¹,
V.V. Mochalov^{1,†}, M.B. Nurusheva², M.F. Runtso³, A.V. Ridiger², P.A. Semenov¹,
M.N. Strikhanov³, A.N. Vasiliev¹, V.N. Zapolsky¹

(1) *State Research Center of Russian Federation – Institute for High Energy Physics, Protvino, Russia*

(2) *Federal state budget organization State center Interphysica, Ministry of education and science, Moscow, Russia*

(3) *National Research Nuclear University MEPHI, Moscow, Russia*

† *E-mail: mochalov@ihep.ru*

New experimental program SPASCHARM [1] at IHEP will measure systematically spin effects. The main motivation of the SPASCHARM experiment is to study the dynamics of the strong interaction of hadrons and quarks. Since the SPASCHARM experimental set-up (Fig.1) will have wide aperture, it will be possible to study dependence of the polarization effects on kinematic values in a wide kinematic range: ($0 < x_F < 1, 0 < p_T < 2.5 \text{ GeV}/c$).

The physics program of the experiment will cover wide spectra of the reactions. The measured observables are: an analyzing power A_N , which can be measured with high precision due to the full azimuthal angle set-up coverage and large acceptance; the hyperon transverse polarization P_N , which can be measured using angular distributions of the hyperon decay products in its rest frame; the density matrix element ρ_{00} , which can be measured for 2-boson decays of vector mesons; another observable $\alpha = (\sigma_T - 2\sigma_L)/(\sigma_T + 2\sigma_L)$ can be measured for vector meson decay into a fermion-antifermion pair.

The first stage of the experiment will be carried out with the use of the polarized frozen target. Nevertheless the main goal of spin program is to carry out experiment with both polarized beam and target. The project of the polarized beam construction is in the

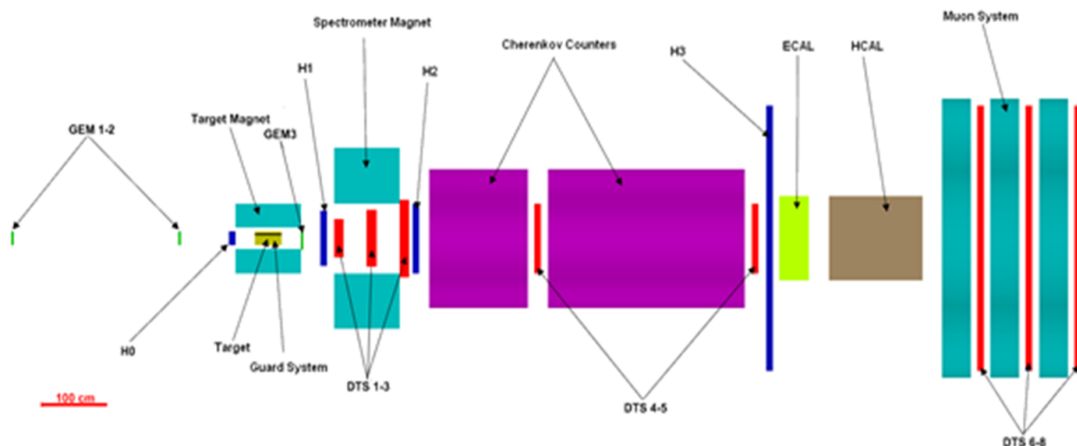


Figure 1: Experimental Setup SPASCHARM.

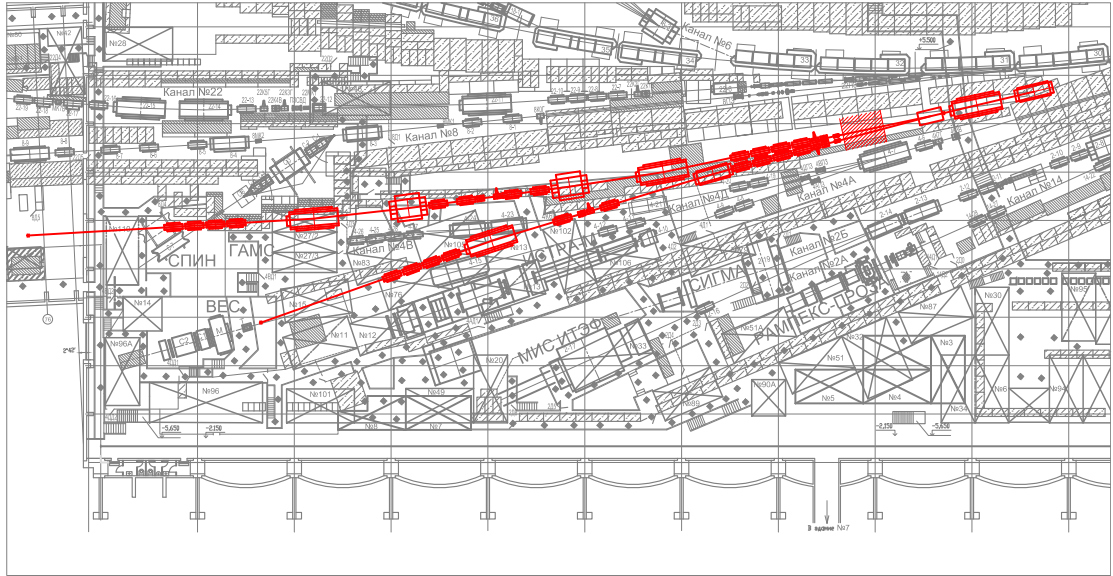
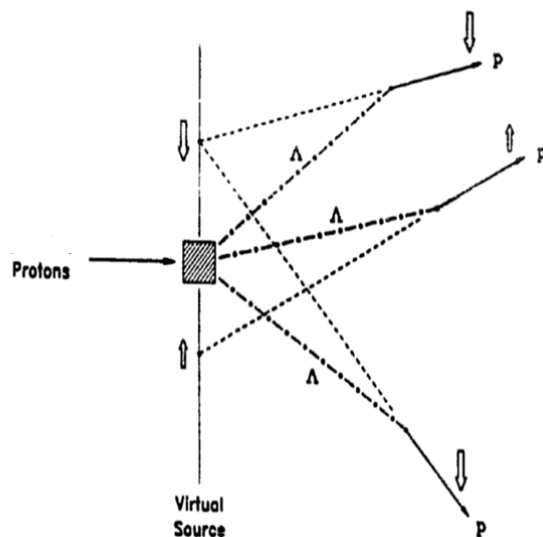


Figure 2: High intensity extracted beams from external target. The top line corresponds to the polarized beam channel.

stage of working design. The scheme of the polarized beam channel in the experimental Hall is presented on Fig. 2.

The intensive (up to 10^{13} protons/cycle) beam from the accelerator will be extracted into external target to create two secondary beams. One beam line (bottom on the Fig. 2) will be used for spectroscopy experiment, another one for polarized beam. The polarization will be created from Λ^0 -decay using standard technique. The method was suggested almost 50 years ago by O.E. Overseth and J.Sandweiss [2].

Since Λ -hyperons create the longitudinally polarized protons aligned with the proton momentum (in the Λ -hyperon rest frame), the protons will have transverse spin component in the laboratory frame depending on the proton emission angle (see Fig. 3). Therefore the spin states of protons are separated in space and proton spin correlates with the coordinate in the plane of primary target (at a virtual source).



268
Figure 3: Polarization scheme from Λ -decay.

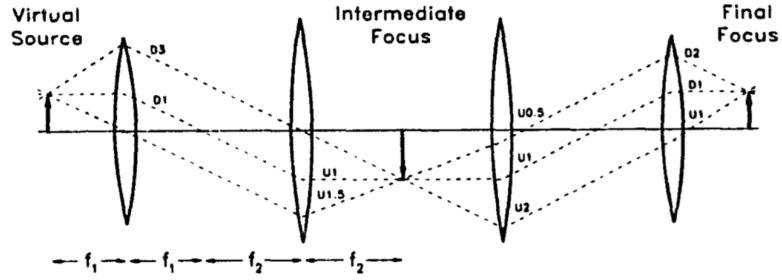


Figure 4: Simplified beam optics.

In this case we can use the optical scheme to have the image of this virtual source in the target region and inverse image in the intermediate focus (see Fig. 4). This method was successfully used for E-704 (FNAL) [3] and FODS (IHEP, Protvino) [4] experiments.

In our case full size of the virtual source is 77 mm and maximal proton emission angle is 96.1° in the Λ rest frame. The calculated dependence of the beam polarization on the vertical coordinate at the virtual source is presented on Fig. 5 together with the polarization curve for E-704 experiment. The minimal beam momentum spread of the proton beam at IHEP ($\Delta p/p$) will be about 5% (without momentum collimators). The calculated intensity of the beam at 40 GeV is $5 \cdot 10^7$ protons/cycle. The dependence of the beam polarization on the coordinate on virtual source is also presented on Table 1.

Table 1: Beam polarization at Virtual source.

Coordinate (mm)	$Pol(\Delta p/p = 1\%)$	$Pol(\Delta p/p = 5\%)$
± 40	$\pm 58\%$	$\pm 53\%$
± 30	$\pm 54\%$	$\pm 50\%$
± 20	$\pm 48\%$	$\pm 44\%$
± 15	$\pm 44\%$	$\pm 39\%$
± 10	$\pm 36\%$	$\pm 31\%$
± 5	$\pm 19\%$	$\pm 16\%$

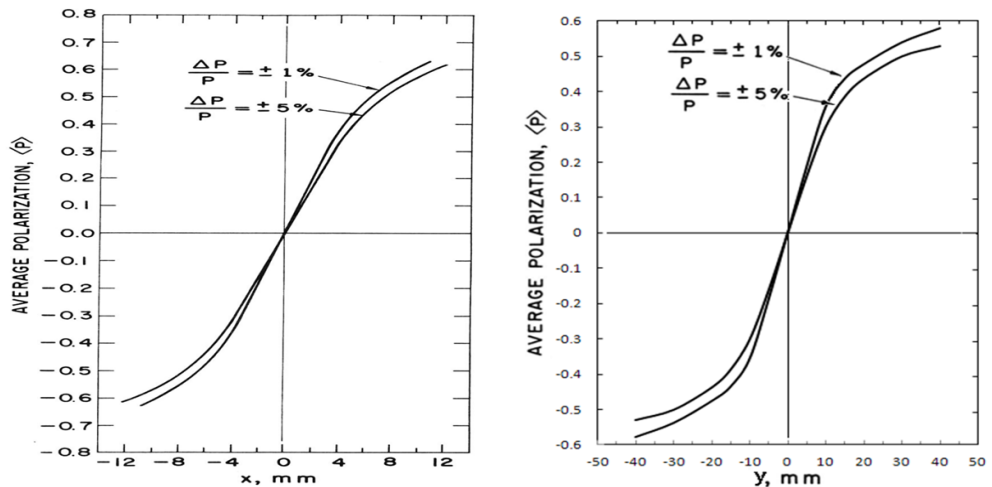


Figure 5: Polarization calculations for E-704 (left) and SPASCHARM (right) experiments.

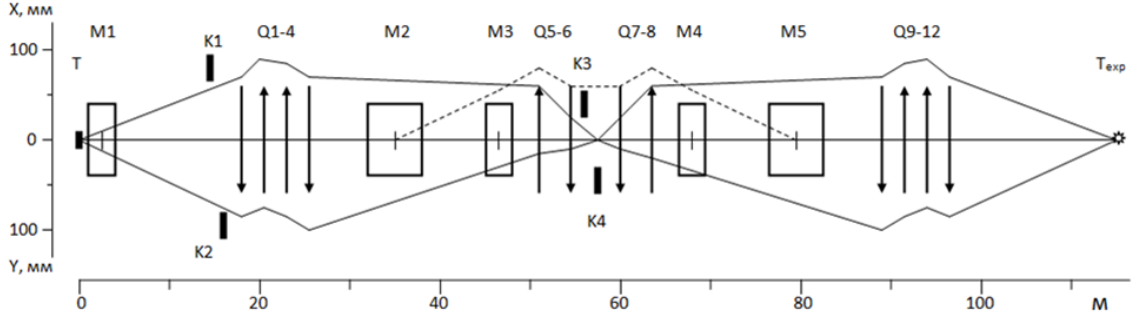


Figure 6: Optical schema of the polarized particle channel at IHEP. Q – quads, M – dipoles, K – collimators, T , T_{exp} – targets (channel and experiment).

Main optic scheme for the polarized beam was calculated to have the polarized proton beam from Λ -hyperon decay up to $p = 50 GeV/c$. The scheme is shown on Fig. 6.

The optics was calculated to have the beam size amplified by factor 1.7 at the intermediate focus for better tagging. Full size of the beam in the intermediate focus will be about 130 mm.

The tagging system proposed is similar to the hodoscope system used in E581/E704 experiment at Fermilab, is shown on Fig. 7 and allows to measure beam online polarization with accuracy 5%. It will be placed between quads $Q6$ and $Q7$ (see Fig. 6). Since the vertical collimator $K4$ will be placed exactly in the position of the intermediate focus, three scintillator detectors $POL1-POL3$ will be used to measure vertical coordinate in the intermediate focus with required accuracy. The effective polarization of the beam is higher if will know beam momentum with better resolution (see Table.1). Six scintillator detectors $MOM1-MOM6$ will be used in addition for fast momenta calculation better than 1%. They will help to improve beam polarization measurements by 5% and exclude π^0 -mesons at elastic scattering. The beam tagging system is required also as a diagnostic tool for optimization of the beam parameters.

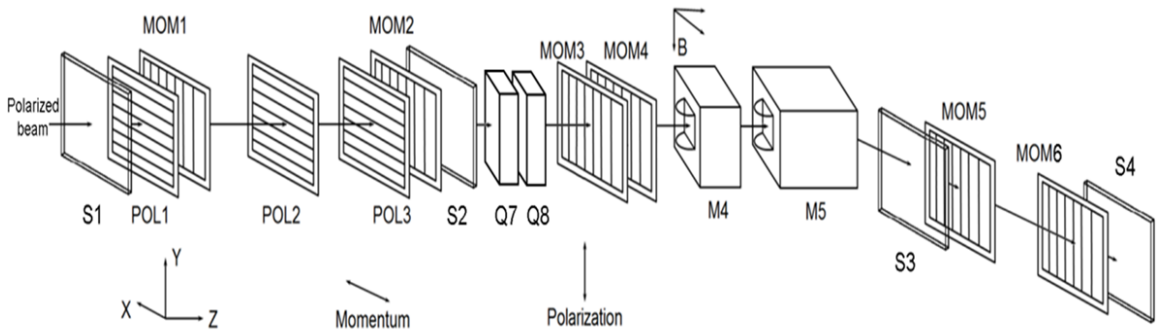


Figure 7: The scheme of the SPASCHARM beam tagging system.

Each scintillation hodoscope will consist of 16 overlapping scintillator counters and will be divided into 31 segments (see Fig. 8). The dimensions and the numbers of elements used in the beam tagging system detectors are presented on Table 2.

The SPASCHARM polarized beam will have one more advantage. Example of the usual proton polarization distribution is presented on Fig. 9 (the relative polarization resolution is estimated to be $\pm 5\%$). Usually only left and right “polarized” parts of the

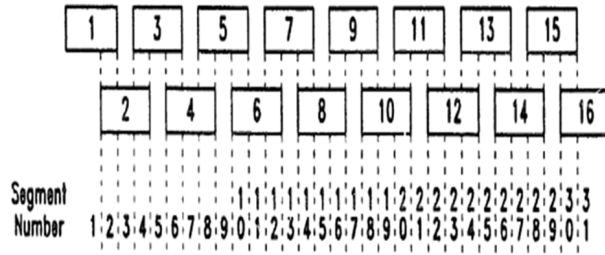


Figure 8: Scintillation detector for tagging system.

Table 2: Beam tagging system scintillation detectors.

Name	Number of PMT's	Sensitive area, $X \times Y$, mm	Scintillator dimensions, mm	Step, mm
POL1	16	70×132	$70 \times 12 \times 5$	4
POL2	16	70×132	$70 \times 12 \times 5$	4
POL3	16	70×132	$70 \times 12 \times 5$	4
MOM1	10	68×132	$12 \times 132 \times 5$	4
MOM2	10	68×132	$12 \times 132 \times 5$	4
MOM3	10	68×132	$12 \times 132 \times 5$	4
MOM4	10	68×132	$12 \times 132 \times 5$	4
MOM5	16	145×180	$15 \times 180 \times 5$	5
MOM6	16	145×180	$15 \times 180 \times 5$	5

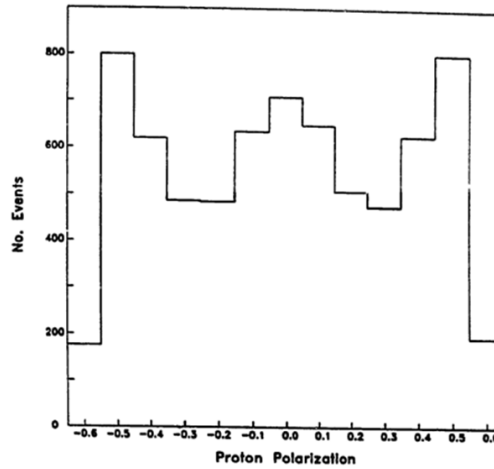


Figure 9: Profile of the beam polarization.

distribution are used for the polarization measurements, since central part of the distribution has zero polarization. In our case beam is turned on about 160 mrad (see Fig. 2). It will happen that in this case longitudinal polarization will be transformed into the horizontal one due to the spin precession. It means due to full azimuthal coverage of the SPASCHARM setup we will have the possibility to use the central part of the beam to measure “up-down” asymmetry simultaneously with “left-right” asymmetry measurements.

The beam tagging system will give us relative calibration. At the same time it will be calibrated by the absolute polarimeter. We propose to use two methods for absolute polarization measurements.

The first polarimeter will be based on pp -elastic scattering in the diffraction cone at $0.04 \leq |t| \leq 0.5(\text{GeV}/T\text{B})^2$. This polarimeter will use existing data from HERA experiment carried out at Protvino at 42.5 GeV [3].

The second method is based on pp -elastic scattering in CNI region at $0.002 \leq |t| \leq 0.05(\text{GeV}/c)^2$ based on RHIC data [5,6].

As a consequence combined polarimeter will give us the possibility to have absolute polarization measurements at $0.002 \leq |t| \leq 0.5(\text{GeV}/T\text{B})^2$.

The description of the polarimeters for SPASCHARM experiment is described in more details in the A. Bogdanov talk [8].

The work was partially supported by RFBR grant 12-02-00737. We express our deep appreciations for useful discussions and helps in preparation to Dr. Y.V.Kharlov, Dr. M.N.Ukhanov, Mrs. G.S.Chetverkova, D.Underwood and F.Luehring

References

- [1] V. Mochalov, Phys.Part.Nucl. **44** N 6, 930 (2013).
- [2] O.E. Overseth and J. Sandweiss, A Polarized Proton Beam From Λ^0 Decay; O.E. Overseth, Polarized Protons at the 200-GeV Accelerator, Proceedings of the 1969 NAL Summer Study, Published in eConf C690609 (1969) 006.
- [3] D.P. Grosnick et al., Nucl.Instrum.Meth. **A290**,269 (1990).
- [4] N.A. Galyaev et al., In *Washington 1993, Particle accelerator, vol. 1* 454-456.
- [5] A. Gaidot et al., Phys. Lett. **61B**, 103(1976).
- [6] A. Bazilevski, et al., Journal of Phys.: Conf. Series **295**, 012096 (2011).
- [7] I.G. Alekseev, et al., Phys. Rev. D **79**, 094014 (2009) **C8** (1999) 409.
- [8] A.A. Bogdanov et al., These Proceedings.

THE η -MESON PRODUCTION WITH THE POLARIZED PROTON BEAM WITH WASA-AT-COSY

I. Ozerianska^{1,†}, M. Hodana¹ and P. Moskal¹

(1) Jagiellonian University, Cracow, Poland

† E-mail: i.ozerianska@gmail.com

Abstract

In November 2010, the azimuthal symmetric WASA detector and the polarized proton beam of COSY, have been used to collect a high statistics sample of $\vec{p}p \rightarrow pp\eta$ reactions in order to determine the analyzing power as a function of the invariant mass spectra of the two particle subsystems. Here, we show studies of the influence of the beam and target characteristics such as location and direction on the determination of the polarization.

The production mechanism of the η meson and meson-nucleon final state interaction for the $\vec{p}p \rightarrow pp\eta$ reaction can be studied via measurements of the analyzing power $A_y(\theta)$. Up to now, only three experiments [1-4] investigated A_y and the results have poor statistics and large uncertainties .

For a precise study of the η meson production in terms of $A_y(\theta)$, in November 2010 the high statistics sample of $\vec{p}p \rightarrow pp\eta$ reaction has been collected using the azimuthal symmetric WASA-at-COSY detector [5]. The measurement was performed using polarized protons for two beam momenta corresponding to 15 MeV and 72 MeV excess energies. Monitoring of the beam polarization, the luminosity and the detector performance, was done using $\vec{p}p \rightarrow pp$ reaction. Additionally, in order to control the effects caused by potential asymmetries in the detector setup the beam - spin flipping - technique has been used.

The degree of polarization was determined based on the analysis of the elastic scattering reaction, for which the values of the analyzing power have been extracted from the EDDA [7] results. After the identification of protons the number of events corresponding to $\vec{p}p \rightarrow pp$ reaction, has been determined for each angular bin $N(\theta, \varphi)$ separately. The polarization, $P(\theta)$, can be written as

$$P(\theta) \equiv \frac{1}{A_y(\theta) \cdot \cos(\varphi)} \cdot \epsilon(N(\theta, \varphi), N(\theta, \varphi + \pi)), \quad (1)$$

where ϵ denotes the asymmetry, which is defined as:

$$\frac{N(\theta, \varphi) - N(\theta, \varphi + \pi)}{N(\theta, \varphi) + N(\theta, \varphi + \pi)} \equiv \epsilon(N(\theta, \varphi), N(\theta, \varphi + \pi)). \quad (2)$$

The data analysis shows that the polarization was stable during the whole measurement time, but its value differs for the spin up and the spin down mode. In the part of

the measurement where the unpolarized beam was used, the calculated value of the polarization slightly deviates from zero. The systematic uncertainty in the determination of the polarization might be due to the false number of events in the individual θ_{CM} ranges, originating from the possible misalignment of the beam's and/or target's position.

One of the ways to control the location of the vertex position in the experiment was proposed in [6]. Using this method we have extracted the vertex position x_v, y_v, z_v . To learn how the vertex position influences the determination of the polarization we have implemented the simulations shifting of the vertex coordinate. The distribution of the polarization as a function of applied shift is done for each of three coordinates separately and the result is shown in Fig. 1 (left).

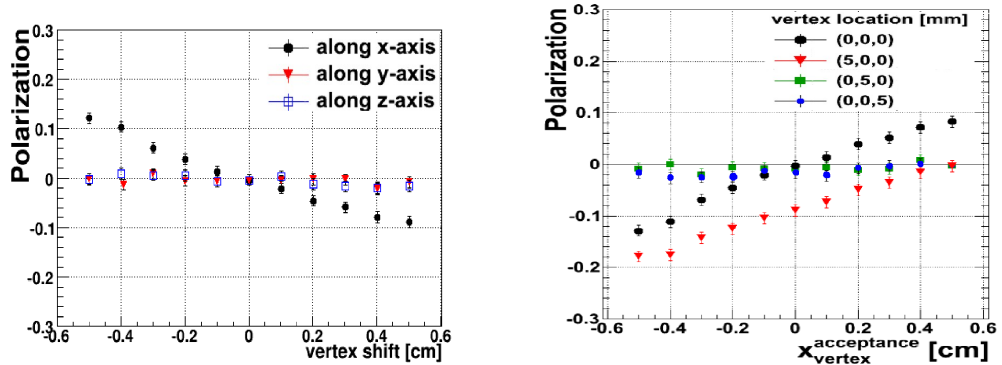


Figure 1: Left: Polarization as a function of vertex shift along the x-, y- and z-axis (see the legend). Right: Polarization as a function of the vertex position corrected for the acceptance. Vertex positions are shown in the legend.

The simulated data for each vertex position (as indicated in the legend), has been acceptance corrected assuming different values of the x_v coordinate, $x_{vertex}^{acceptance}$. Analysis shows that the change of the y_v or z_v coordinates does not affect the result of the polarization. However polarization strongly depends on a change in the x_v coordinate. Figure 1 (Right) shows that to achieve uncertainties of the polarization of about 0.03 the accuracy of the vertex position has to be controlled with a precision better than 1mm. Furthermore, the analysis shows that a shift of a given coordinate within a $[-0.5, 0.5]$ cm window does not affect the extraction of remaining coordinates [8]. From Fig. 2 it can be seen at once that the vertex position in both coordinates x and y is stable.

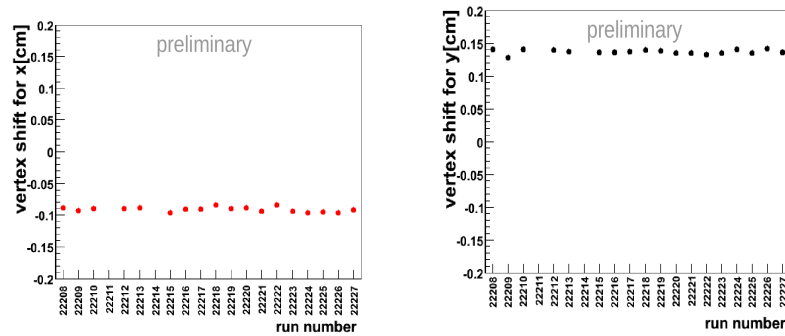


Figure 2: Vertex position extracted from the experimental data. Each plot shows different coordinate, calculated with the method adopted from [6].

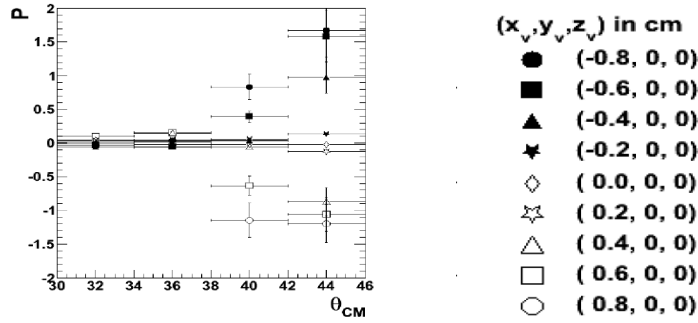


Figure 3: Distribution of the polarization as a function of the θ_{CM} angle.

The distribution of the polarization as a function of the scattering angle of the forward going proton calculated in the center of mass system, θ_{CM} , made for different vertex positions (x- coordinate of the vertex) is shown in Fig. 3. One can see that for a higher θ_{CM} angle ($\theta_{CM} > 38^\circ$), the polarization starts to deviate from expected value of zero when the vertex is shifted by more than 0.5 cm along the x-direction.

Furthermore, the influence of the tilt of the beam on the polarization value has been studied. The maximum allowed range of tilts of the beam at WASA-at-COSY is between -0.05 mrad and 0.05 mrad (symmetrically around the z-axis) [9]. In Fig.4, the polarization as a function of the α angle for both types of studied beam tilts is shown. There are no effects observed in the studied range of the α angle ($\alpha \in [-0.5; 0.5]$ mrad) except that the polarization slightly differs from zero (up to 0.01).

In this report the methods to monitor the location of the vertex have been demonstrated and it was shown how the mis-location of the vertex impacted the obtained degree of polarization. The study concluded that to have the systematic uncertainty of the polarization smaller than 0.01, we need to control the position of the interaction point with a precision higher than 1 mm. Due to the high sensitivity of the result to the scattering angle it is better to calculate the polarization taking into account only scattering angles smaller than $CM_s = 38^\circ$. Furthermore, the investigation shows that the tilt of the beam does not influence the degree of polarization significantly.

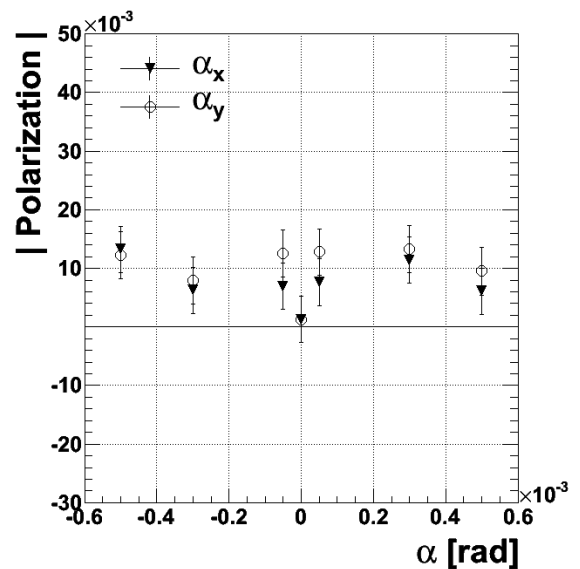


Figure 4: The value of the polarization as a function of the tilt of the beam spin α given in radius.

We acknowledge support by the Polish National Science Center through grant No. 2011/03/B/ST2/01847, by the FFE grants of the Research Center Juelich, by the EU Integrated Infrastructure Initiative HadronPhysics Project under contract number RII3-CT-2004-506078 and by the European Commission under the 7th Framework Programme through the Research Infrastructures action of the Capacities Programme, Call: FP7-

References

- [1] R. Czyżykiewicz et al., Phys. Rev. Lett. **98** (2007) 122003.
- [2] F. Balestra et al. Phys. Rev. **C 69** (2004) 064003.
- [3] P. Winter et al., Eur. Phys. J. **A 18** (2003) 355.
- [4] P. Winter et al., Phys. Lett. **B544** (2002) 251-258.
- [5] P. Moskal, M. Hodana, J.Phys.Conf.Ser.295:012080, 2011.
- [6] L. Demirors PhD Hamburg University (2005).
- [7] M. Altmeier et al., Phys. Rev. Lett. **85** (2000).
- [8] M.Hodana et al., Acta Phys.Polon.Supp. 6 (2013) 1041-1052.
- [9] D. Prashun private communication (2013).

THE FLAVOR STRUCTURE OF THE NUCLEON SEA

J.C. Peng^{1†}, W.C. Chang², H.Y. Cheng² and K.F. Liu³

(1) *Department of Physics, University of Illinois at Urbana-Champaign, Urbana, Illinois 61801, USA*

(2) *Institute of Physics, Academia Sinica, Taipei 11529, Taiwan*

(3) *Department of Physics and Astronomy, University of Kentucky, Lexington, Kentucky 40506, USA*

† *E-mail: jcpeng@illinois.edu*

Abstract

We discuss two topics related to the flavor structure of the nucleon sea. The first is on the identification of light-quark intrinsic sea from the comparison between recent data and the intrinsic sea model by Brodsky et al. Good agreement between the theory and data allows a separation of the intrinsic from the extrinsic sea components. The magnitudes of the up, down, and strange intrinsic seas have been extracted. We then discuss the flavor structure and the Bjorken- x dependence of the connected sea (CS) and disconnected sea (DS). We show that recent data together with input from lattice QCD allow a separation of the CS from the DS components of the light quark sea.

1 Introduction

The flavor structure of the nucleon sea can provide new insight on the nature of QCD at the confinement scale. Perturbative QCD predicts a largely flavor symmetric $\bar{u}, \bar{d}, \bar{s}$ sea, as the $g \rightarrow Q\bar{Q}$ process, in which a gluon split into a quark antiquark pair ($Q\bar{Q}$), is insensitive to the current-quark masses of the u, d , and s , which are small relative to the QCD scale. Indeed, in the 1980s, it was commonly assumed that the nucleon's sea is $\bar{u}, \bar{d}, \bar{s}$ flavor symmetric, notwithstanding the fact that ideas based on meson-cloud [1], Pauli-blocking [2], and intrinsic sea [3], already led to predictions of a flavor asymmetric nucleon sea. We emphasize that the term “flavor asymmetry” does not imply that any fundamental symmetry principle is violated, it merely refers to the differences between the \bar{u}, \bar{d} , and \bar{s} sea quark distributions in the proton.

The earliest evidences for a flavor asymmetric nucleon sea came from the observation of possible violation of the Gottfried sum rule, suggesting $\bar{u} \neq \bar{d}$, and the charm production in neutrino-induced deep-inelastic scattering (DIS), showing that strange quark sea is suppressed relative to the up and down quark seas. This topics continues to attract intense theoretical and experimental interest. We discuss some recent progress in our understanding of the flavor structure of the nucleon sea. We first present the recent analysis which leads to a determination of the intrinsic sea components for \bar{u}, \bar{d} , and \bar{s} in the proton. We then discuss some recent effort to interpret the flavor structure and momentum dependence of sea quark distributions in the context of connected and disconnected seas in the framework of lattice QCD.

2 Intrinsic versus extrinsic sea

Brodsky, Hoyer, Peterson, and Sakai (BHPS) proposed some time ago that the $|uudc\bar{c}\rangle$ five-quark Fock state in the proton can lead to enhanced production rates for charmed hadrons at forward rapidity region [3]. The $c\bar{c}$ component in the $|uudc\bar{c}\rangle$ configuration is coined “intrinsic” sea in order to distinguish it from the conventional “extrinsic” sea originating from the $g \rightarrow c\bar{c}$ QCD process. The maximal probability for the $uudc\bar{c}$ Fock state occurs when all five quarks move with similar velocities. The larger mass of the charmed quark implies that the c and \bar{c} quarks would carry a large fraction of proton’s momentum. This leads to the expectation that the intrinsic charm has a momentum distribution which is valence-like, peaking at relatively large x . In contrast, the extrinsic charm, which results from gluon splitting, is dominant at the small x region. While some tentatizing evidences for intrinsic charm have been reported, a study by the CTEQ Collaboration [4] concluded that the existing data are not yet sufficiently accurate to confirm or refute the existence of intrinsic charm.

It is natural to pose the question, “are there any evidences for intrinsic sea of lighter quarks, i.e., the $|uudu\bar{u}\rangle$, $|uudd\bar{d}\rangle$, and $|uuds\bar{s}\rangle$ Fock states?”. In the BHPS model, the probability for the $|uudQ\bar{Q}\rangle$ Fock state is expected to be roughly proportional to $1/m_Q^2$, where m_Q is the mass of quark Q . This suggests significantly larger probabilities for these light-quark intrinsic sea than for the intrinsic charm. Therefore, it is potentially easier to find evidences for these light-quark intrinsic sea. The challenge, however, is to come up with ways to disentangle the intrinsic sea from the more abundant extrinsic sea.

In a recent attempt to search for evidences for intrinsic light-quark sea, two approaches were adopted in order to disentangle the intrinsic from the extrinsic sea [5]. The first approach is to select experimental observables which have either very little or no contributions from the extrinsic sea. The other approach is to rely on the different dependences for the intrinsic and extrinsic seas. As mentioned earlier, the intrinsic sea is valence-like and is more abundant at large x while the extrinsic sea is dominant at the small x region.

One example of an observable free from the contribution of the extrinsic sea is $\bar{d}(x) - \bar{u}(x)$. The perturbative $g \rightarrow Q\bar{Q}$ process is expected to generate $u\bar{u}$ and $d\bar{d}$ pairs with equal probability and would have no contribution to $\bar{d}(x) - \bar{u}(x)$. Figure 1 shows the $\bar{d}(x) - \bar{u}(x)$ data from the Fermilab E866 Drell-Yan experiment [6] in comparison with the calculation using the BHPS model. The \bar{u} and \bar{d} are predicted to have identical x dependence if $m_u = m_d$. The exact values for the probabilities of the $|uudd\bar{d}\rangle$ and $|uudu\bar{u}\rangle$ configuration, $\mathcal{P}_5^{d\bar{d}}$ and $\mathcal{P}_5^{u\bar{u}}$, are not predicted by the BHPS model and must be determined from experiments. However, the difference between $\mathcal{P}_5^{d\bar{d}}$ and $\mathcal{P}_5^{u\bar{u}}$ is known from the moment of $\bar{d}(x) - \bar{u}(x)$, namely,

$$\int_0^1 (\bar{d}(x) - \bar{u}(x)) dx = \mathcal{P}_5^{d\bar{d}} - \mathcal{P}_5^{u\bar{u}} = 0.118 \pm 0.012, \quad (1)$$

where the moment is evaluated using the $\bar{d}(x) - \bar{u}(x)$ data from the Fermilab E866 experiment. Figure 1 compares the $\bar{d}(x) - \bar{u}(x)$ data with the calculation (dashed curve) using the BHPS model and the constraint given by Eq. (1). The BHPS calculation is in apparent disagreement with the $\bar{d}(x) - \bar{u}(x)$ data. However, the relevant scale, μ , for the BHPS model calculation is at the confinement scale, which is much lower than the $Q^2 = 54 \text{ GeV}^2$ scale of the E866 data. It is

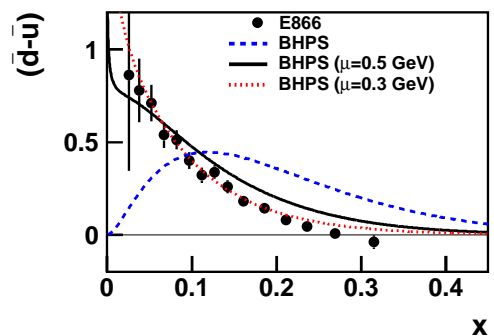


Figure 1: Comparison of the $\bar{d}(x) - \bar{u}(x)$ data at $Q^2 = 54 \text{ GeV}^2$ with calculations. The dashed curve corresponds to the calculation for the BHPS model, and the solid and dotted curves are obtained by evolving it to $Q^2 = 54 \text{ GeV}^2$ from $\mu = 0.5 \text{ GeV}$ and $\mu = 0.3 \text{ GeV}$, respectively.

therefore necessary to evolve the BHPS result from the initial scale to $Q^2 = 54 \text{ GeV}^2$. Figure 1 shows that good agreement between the calculation (solid curve) and the data is achieved when the initial scale is chosen as $\mu = 0.5 \text{ GeV}$. Note that an even better agreement with the data is obtained by lowering the initial scale to $\mu = 0.3 \text{ GeV}$.

An example for identifying the intrinsic sea component by making use of its valence-like x distribution has been reported recently [7]. Figure 2 shows the extraction of $x(s(x) + \bar{s}(x))$ from a measurement of charged kaon production in semi-inclusive DIS by the HERMES Collaboration [8]. An intriguing feature of Fig. 2 is that the strange sea falls off rapidly with x for $x < 0.1$, and becomes a broad peak at the large x region. The HERMES result suggests the presence of two distinct components of the strange sea, one at the small x ($x < 0.1$) region and another centered at the larger x region. This is in qualitative agreement with the expectation that extrinsic and intrinsic seas have dominant contributions at small and large x region, respectively. A comparison between the data and calculations using the BHPS model is shown in Fig. 2 for $\mu = 0.5$ and $\mu = 0.3 \text{ GeV}$. The data at $x > 0.1$ are quite well described by the calculations, supporting the interpretation that the $x(s(x) + \bar{s}(x))$ in the valence region is dominated by the intrinsic sea. From the normalization of the BHPS calculations shown in Fig. 2, one can extract the probability of the $|uuds\bar{s}\rangle$ as

$$\mathcal{P}_5^{s\bar{s}} = 0.024 \quad (\mu = 0.5 \text{ GeV}); \quad \mathcal{P}_5^{s\bar{s}} = 0.029 \quad (\mu = 0.3 \text{ GeV}). \quad (2)$$

Another quantity which is largely free from the extrinsic sea is $\bar{u}(x) + \bar{d}(x) - s(x) - \bar{s}(x)$. Under the assumption that the perturbative $g \rightarrow Q\bar{Q}$ process leads to $\bar{u}, \bar{d}, \bar{s}$ flavor symmetric sea, only the intrinsic sea component can contribute to $\bar{u}(x) + \bar{d}(x) - s(x) - \bar{s}(x)$. From the HERMES measurement of $x(s(x) + \bar{s}(x))$ and the $x(\bar{u}(x) + \bar{d}(x))$ from the CTEQ6.6 PDF [9], we obtain $x(\bar{u}(x) + \bar{d}(x) - s(x) - \bar{s}(x))$ as shown in Fig. 3. We note that Chen, Cao, and Signal [10] have also examined this quantity earlier in the context of the meson-cloud model. Figure 3 shows a remarkable feature that the $x(\bar{u} + \bar{d} - s - \bar{s})$ distribution is valence-like and peaking at $x \sim 0.1$. One can compare it with the BHPS model calculation using the following expression

$$x(\bar{u}(x) + \bar{d}(x) - s(x) - \bar{s}(x)) = x(P^{u\bar{u}}(x_{\bar{u}}) + P^{d\bar{d}}(x_{\bar{d}}) - 2P^{s\bar{s}}(x_{\bar{s}})), \quad (3)$$

where $P^{Q\bar{Q}}(x_{\bar{Q}})$ is the x distribution of \bar{Q} in the $|uudQ\bar{Q}\rangle$ Fock state. Since the quantity $\bar{u} + \bar{d} - s - \bar{s}$ is flavor non-singlet, it can be readily evolved from the initial scale μ to $Q^2 = 2.5 \text{ GeV}^2$. Figure 3 shows a good agreement between the BHPS model calculation and the data. From the comparison between the BHPS calculations and the data shown in Figs. 1-3, the probabilities for the $|uudu\bar{u}\rangle$, $|uudd\bar{d}\rangle$, $|uuds\bar{s}\rangle$ Fock states can be determined as follows (using $\mu = 0.5 \text{ GeV}$):

$$\mathcal{P}_5^{u\bar{u}} = 0.122; \quad \mathcal{P}_5^{d\bar{d}} = 0.240; \quad \mathcal{P}_5^{s\bar{s}} = 0.024. \quad (4)$$

It is remarkable that the existing data on $\bar{d}(x) - \bar{u}(x)$, $s(x) + \bar{s}(x)$, and $\bar{u}(x) + \bar{d}(x) - s(x) - \bar{s}(x)$ not only provide a test of the BHPS model on the intrinsic sea, but also allow an extraction of

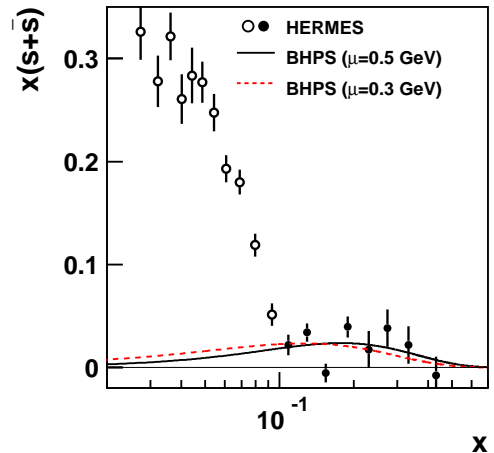


Figure 2: Comparison of the $x(s(x) + \bar{s}(x))$ data from HERMES with calculations. The solid and dashed curves are obtained by evolving the BHPS result to $Q^2 = 2.5 \text{ GeV}^2$ from $\mu = 0.5 \text{ GeV}$ and $\mu = 0.3 \text{ GeV}$, respectively. The normalizations of the calculations are adjusted to fit the data at $x > 0.1$.

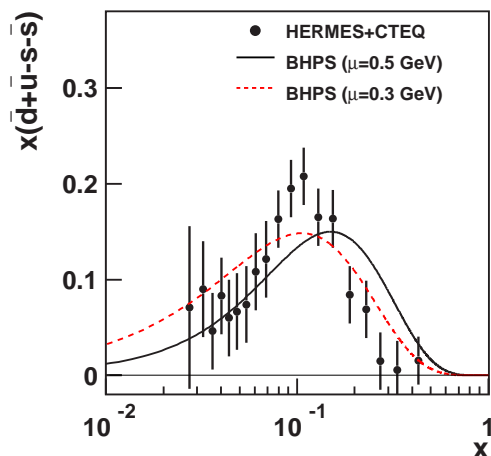


Figure 3: Comparison of $x(\bar{d}(x) + \bar{u}(x) - s(x) - \bar{s}(x))$ with calculations. The solid and dashed curves are obtained by evolving the BHPs model calculation to $Q^2 = 2.5 \text{ GeV}^2$ from $\mu = 0.5 \text{ GeV}$ and $\mu = 0.3 \text{ GeV}$, respectively.

the probabilities of various five-quark Fock states involving light antiquarks. This result could also be extended to possible future studies on some related topics. Some examples of these topics include:

- Search for intrinsic charm and beauty. From the expectation that the probability for the $|uudQ\bar{Q}\rangle$ Fock state is proportional to $1/m_Q^2$ and from the values listed in Eq. (4), one can readily estimate that the probability for the intrinsic charm $|uudc\bar{c}\rangle$ Fock state, $\mathcal{P}_5^{c\bar{c}}$, to be roughly $(m_s^2/m_c^2)\mathcal{P}_5^{s\bar{s}} \sim 0.003$, which is smaller than earlier estimate [3]. Therefore, future measurements with higher precision, possibly at RHIC and LHC, would be very valuable.
- Search for intrinsic gluons. The Fock state $|uudg\rangle$ would provide a valence-like gluon component in the proton [11]. It remains a challenge to identify experimental signatures for such valence-like gluons.
- Spin and transverse-momentum dependent observables of intrinsic sea. Only the spin-averaged distributions for the intrinsic sea has been considered so far. It would be very interesting to explore the implications of intrinsic sea on the spin-dependent and possibly transverse-momentum dependent parton distributions of the proton.
- Intrinsic sea for mesons and hyperons. It is straightforward to extend the formulation for the nucleon's intrinsic sea to the cases for mesons and hyperons. The presence of these valence-like seas could affect, for example, the meson- or hyperon-induced Drell-Yan cross sections in the forward rapidity region.
- Connection between the intrinsic sea and other models. It is important to understand the similarities and differences between the BHPs intrinsic sea model and other theoretical models such as the meson-cloud model [12] and the multi-quark model [13]. Some recent study [14] has been carried out to elucidate the connection between the intrinsic/extrinsic seas and the connected/disconnected seas in the lattice QCD formulation, as discussed next.

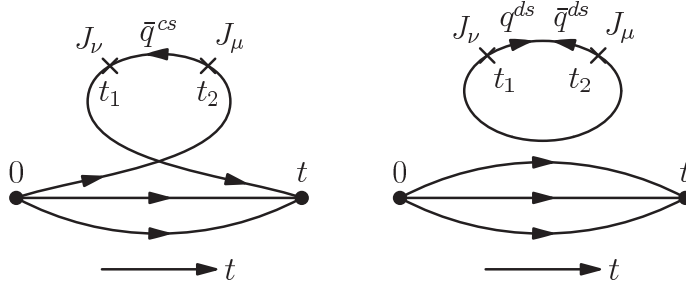


Figure 4: Diagram for (a) connected sea (left) and (b) disconnected sea (right).

3 Connected versus disconnected sea

In order to gain further insight on the flavor structure of the nucleon sea, we note that, according to the path-integral formalism of the hadronic tensor, there are two distinct sources of nucleon sea, namely, the connected sea (CS) and the disconnected sea (DS). Figure 4 shows the two diagrams for the connected and disconnected seas. In Fig. 4 (a), the quark line propagating backward in time between t_1 and t_2 corresponds to the connected-sea antiquarks \bar{q}^{CS} (\bar{u}^{CS} or \bar{d}^{CS}), which have the same flavors as the valence quarks. Figure 4 (b) shows the DS component q^{DS} and \bar{q}^{DS} for $q = u, d, s, c$. These two different sources of sea quarks have distinct quark flavor and x -dependence [14]. While the \bar{u} and \bar{d} seas can originate from both the CS and DS, only DS is present for the $s(\bar{s})$ and $c(\bar{c})$ sea. At the small- x region, the CS and DS are also expected to have different x dependences. Since only reggeon exchange occurs for CS, one expects $\bar{q}^{CS} \propto x^{-1/2}$ at small x . The presence of pomeron exchange implies that $\bar{q}^{DS} \propto x^{-1}$ at small x .

The distinct x dependences of CS and DS remain to be checked experimentally. Since s and \bar{s} sea is entirely originating from the DS, the HERMES measurement of $s(x) + \bar{s}(x)$ provides valuable information on the shape of the x dependence for the DS, which is not yet available from lattice QCD calculations. The \bar{u} and \bar{d} seas contain contributions from both the CS and DS. It is of interest to separate these two components. A first attempt to separate the CS from the DS was reported for the $\bar{u} + \bar{d}$ sea using the following approach [14]. First, a plausible ansatz that $\bar{u}^{DS}(x) + \bar{d}^{DS}(x)$ is proportional to $s^{DS}(x) + \bar{s}^{DS}(x)$ (or equivalently, $s(x) + \bar{s}(x)$, since only DS contributes to strange sea) is adopted. A recent lattice calculation [15] gives the ratio R for the moment of the strange quarks over that of the \bar{u} plus \bar{d} for the disconnected diagram as

$$R = \frac{\langle x \rangle_{s+\bar{s}}}{\langle x \rangle_{\bar{u}^{DS}+\bar{d}^{DS}}} = 0.857(40). \quad (5)$$

Therefore, one can readily separate the CS and DS components for $\bar{u}(x) + \bar{d}(x)$ as follows:

$$\bar{u}^{DS}(x) + \bar{d}^{DS}(x) = \frac{1}{R}(s(x) + \bar{s}(x)) \quad (6)$$

and

$$\bar{u}^{CS}(x) + \bar{d}^{CS}(x) = \bar{u}(x) + \bar{d}(x) - \frac{1}{R}(s(x) + \bar{s}(x)). \quad (7)$$

Figure 5 shows the decomposition of $x(\bar{u}(x) + \bar{d}(x))$ into the CS and DS components, using Eqs. (6) and (7). The x dependences for CS and DS are very different and are in qualitative agreement with the expectation discussed earlier. This agreement lends support to the ansatz and approach adopted in this analysis.

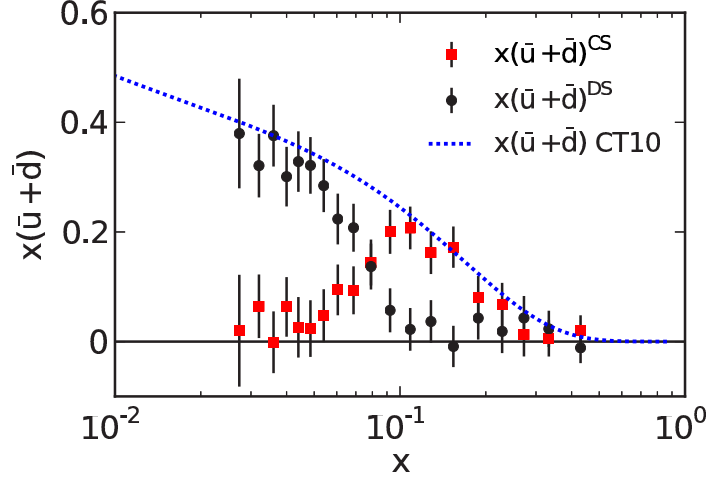


Figure 5: Decomposition of $x(\bar{u}(x) + \bar{d}(x))$ into the connected sea (CS) and the disconnected sea (DS) components using the procedure described in the text. The CT10 parameterization of $x(\bar{u}(x) + \bar{d}(x))$ is also shown.

From Fig. 5 one could also calculate the momentum fractions carried by the CS and DS. It is interesting that the momentum fraction of the $\bar{u}(x) + \bar{d}(x)$ is roughly equally divided between the CS and DS at $Q^2 = 2.5 \text{ GeV}^2$. We also note that in a very recent work [16], the possible sign-change of $\bar{d}(x) - \bar{u}(x)$ at $x \sim 0.3$ as well as a qualitative explanation for this sign-change in the context of lattice QCD are discussed.

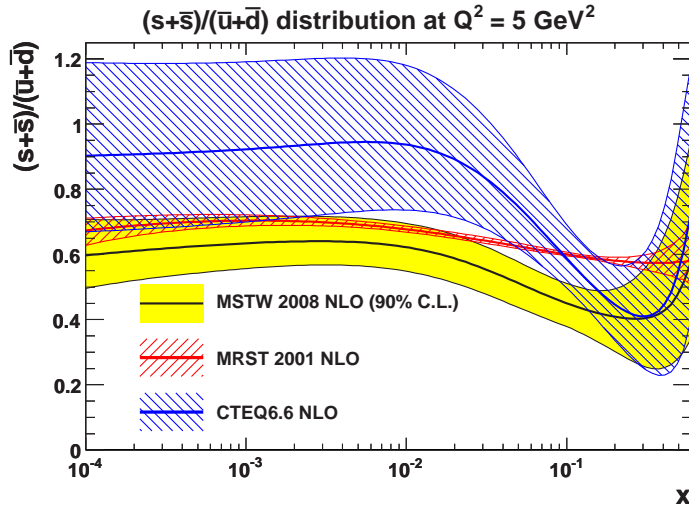


Figure 6: Ratio of $s + \bar{s}$ over $\bar{u} + \bar{d}$ versus x at $Q^2 = 5 \text{ GeV}^2$ from various recent PDFs [17].

The formulation of CS and DS can also explain qualitatively the x dependence of the $R(x) = (s(x) + \bar{s}(x))/(\bar{u}(x) + \bar{d}(x))$ ratio. Figure 6 shows the ratio $R(x)$ from some recent PDF sets [17]. While $R(x)$ is roughly constant at the small x region, it falls with increasing x in the region $0.01 < x < 0.3$. At small x , the DS component is expected to dominate, due to its x^{-1}

dependence. Therefore, it is expected that $R \rightarrow 0.857$ at small x , according to the lattice QCD calculation for the DS [15]. The recent measurement of W and Z boson productions in pp collision at 7 TeV by the ATLAS Collaboration gives $r_s = (s + \bar{s})/2\bar{d}$ at $x = 0.023$ to be $1.0 + 0.25 - 0.28$ [18]. Both the CTEQ6.6 and ATLAS result are consistent with a roughly $\bar{u}, \bar{d}, \bar{s}$ flavor symmetric sea at small x . At the larger x region, the valence-like CS can contribute to \bar{u} and \bar{d} , but not to s and \bar{s} . This results in smaller values of $R(x)$ at larger x . It is expected that future W and Z production data as well as semi-inclusive kaon production data would further improve our knowledge on the x dependence of the strange quark sea.

4 Conclusion

In summary, we have generalized the BHPS model to the light-quark sector and compared the model calculations with the $\bar{d}-\bar{u}$, $s+\bar{s}$, and $\bar{u}+\bar{d}-s-\bar{s}$ data. The qualitative agreement between the data and the calculations provides strong evidence for the existence of the intrinsic u , d , s quark sea. This analysis also allows the extraction of the probabilities for these Fock states. The concept of connected and disconnected seas in lattice QCD offers new insights on the flavor and x dependences of the nucleon sea. Ongoing and future Drell-Yan (and W/Z production) and semi-inclusive DIS experiments will provide new information on the flavor structure of the nucleon sea.

We acknowledge helpful discussion with Stan Brodsky and Paul Hoyer.

References

- [1] A. W. Thomas, Phys. Lett. **B126** (1983) 97.
- [2] R. D. Field and R. P. Feynman, Phys. Rev. **D15** (1979) 2590.
- [3] S. J. Brodsky, P. Hoyer, C. Peterson, and N. Sakai, Phys. Lett. **B93** (1980) 451; S. J. Brodsky, C. Peterson, and N. Sakai, Phys. Rev. **D23** (1981) 2745.
- [4] J. Pumplin, H. L. Lai, and W. K. Tung, Phys. Rev. **D75** (2007) 054029.
- [5] W. C. Chang and J. C. Peng, Phys. Rev. Lett. **80** (2011) 252002.
- [6] E. A. Hawker *et al.* (E866/NuSea Collaboration), Phys. Rev. Lett. **80** (1998) 3715; J. C. Peng *et al.*, Phys. Rev. **D58** (1998) 092004; R. S. Towell *et al.*, Phys. Rev. **D64** (2001) 052002.
- [7] W. C. Chang and J. C. Peng, Phys. Lett. **B704** (2011) 197.
- [8] A. Airapetian *et al.* (HERMES Collaboration), Phys. Lett. **B666** (2008) 446.
- [9] P. M. Nadolsky *et al.*, Phys. Rev. **D78** (2008) 013004.
- [10] H. Chen, F. G. Cao, and A. I. Signal, J. Phys. **G37** (2010) 105006.
- [11] P. Hoyer and D. P. Roy, Phys. Lett. **B410** (1997) 63.
- [12] J. P. Speth and A. W. Thomas, Adv. Nucl. Phys. **24** (1998) 83.
- [13] Y. Zhang, L. Shao, and B. Q. Ma, Phys. Lett. **B671** (2009) 30.
- [14] K. F. Liu, W. C. Chang, H. Y. Chang, and J. C. Peng, Phys. Rev. Lett. **109** (2012) 252002.

- [15] T. Doi *et al.*, Proc. Sci. LAT2008 (2008) 163.
- [16] J. C. Peng, W. C. Chang, H. Y. Cheng, T. J. Hou, K. F. Liu, and J. W. Qiu, arXiv:1401.1705.
- [17] A. Martin, W. Stirling, R. Thorne, and G. Watt, Eur. Phys. J. **C63** (2009) 189.
- [18] G. Aad *et al.* (ATLAS Collaboration), Phys. Rev. Lett. **109** (2012) 012001.

THE THREE FORM FACTOR RECOIL POLARIZATION EXPERIMENTS AT JEFFERSON LAB

C.F. Perdrisat[†]

College of William and Mary, Williamsburg, Virginia, 23187 USA

† E-mail: perdrisa@jlab.org

Abstract

The use of polarization observables to obtain the form factors of the nucleon, has resulted in a drastic change in the way we understand the structure of both proton and neutron. In particular, the results for the two non-zero components of the recoil proton polarization in the elastic $\bar{e}p \rightarrow e'\bar{p}$ reaction in 3 experiments at JLab, have resulted in determining the ratio G_{Ep}/G_{Mp} up to a Q^2 of 8.5 GeV². These experiments were done with two different proton polarimeters, capable of good performance from a few GeV/c to 5.5 GeV/c proton momenta [1,2,3,4,5,6]. An approved and currently planned experiment, which will become possible with 11 GeV electron beams in Hall A after the JLab energy upgrade, is being designed and should reach proton momentum of 8 GeV/c, corresponding to $Q^2=15$ GeV² [7]. It will require a new polarimeter to be added to the super bigbite spectrometer facility (SBS). The evolution of the design and performance of the 3 polarimeters will be discussed in some details.

The use of the recoil polarization technique to obtain the elastic form factors of proton and neutron at large Q^2 has become possible with the development of highly polarized and high luminosity electron beams in the multi-GeV energy range; in particular at the Thomas Jefferson National Accelerator Facility (TJNAF or JLab) electron accelerator (or CEBAF). It is one of the two double-polarization techniques that can be used, the other being polarized electron on a polarized target (proton or neutron), measuring the asymmetry. Here we will discuss the evolution of the recoil polarization technology, which started in 1998, with the first experiment to obtain the elastic electric, G_{Ep} , to magnetic, G_{Mp} , Sachs form factor ratio G_{Ep}/G_{Mp} at JLab Halls A and C.

The first suggestion that double polarization would be a better way to obtain nucleon form factors in elastic **ep** scattering goes back to Akhiezer and Rekalov [8]. Until the late 1990's the only way to obtain the proton form factors was through measurement of the differential cross section. In Born approximation, that is, assuming that single virtual photon exchange is the dominant process in elastic **ep** scattering, the **ep** cross section is the product of the Mott cross section times a factor $\epsilon G_{Ep}^2(Q^2) + \tau G_{Mp}^2(Q^2)$. Q^2 is the negative of the square of the invariant energy transfer, $Q^2 = -(\omega^2 - q^2)$, with (ω, \vec{q}) the virtual photon four-momentum. $\epsilon = (1 + 2(1 + \tau) \tan^2 \frac{\theta_e}{2})^{-1}$ and $\tau = Q^2/4M_p^2$ are the kinematic factor (or polarization of the virtual photon) and the dimension-less momentum transfer squared, respectively. The well known Rosenbluth separation method consists then in measuring the differential cross section for several values of ϵ by changing both beam energy and detector angle, while maintaining Q^2 constant.

In Born approximation and for polarized incident electrons, the recoiling proton is polarized, with a longitudinal component along the final proton momentum, P_ℓ , and a transverse component in the reaction plane, P_t . Measuring these two components determines G_{Ep} and

G_{Mp} , provided one knows both beam polarization and analyzing power of the polarimeter used for the measurement of the proton polarization. Here we discuss the technique related to recoil polarization transfer as used for elastic electron scattering on a free proton in the course of about 10 years, to obtain the form factor ratio over the the large Q^2 range 0.5 to 8.5 GeV².

In the energy range of interest here, i.e. proton momenta from about 0.7 GeV/c to 7-8 GeV/c, the proton polarization components perpendicular to the proton momentum can be obtained by scattering the proton in an analyzer block made preferentially of CH₂, and observing the azimuthal asymmetry with appropriate tracking detectors downstream of the analyzer. The asymmetry in such collisions is caused by the $\vec{L}\cdot\vec{S}$ coupling in NN interaction. As only polarization components perpendicular to the proton momentum can be determined with this method, it is necessary to rotate the longitudinal polarization component, P_ℓ^{target} , so as to produce as large a normal component, P_n^{fpp} , as possible. This rotation is obtained with a dipole, which, at least in first order, does not precess the transverse component, P_t^{target} , if the B-field is perpendicular to the proton momentum, as illustrated in Fig. 1. The azimuthal distribution of the scattered proton will then be $I(\phi) = I_0(1 + A_y(\theta)\vec{P}^{fpp}\cdot\vec{n})$, where θ and ϕ are the polar and azimuthal scattering angles, respectively; \vec{n} is the normal to the **ep**-scattering plane and \vec{P}^{fpp} is the proton polarization vector. Fig. 2 is a schematic illustration of a polarimeter, with its front- and back tracking detectors determining θ and ϕ . The expected azimuthal distribution will then be of the form $N^+(\theta, \phi) = N_0 \frac{\eta(\theta, \phi)}{2\pi} [1 + A_y P_t^{fpp} \cos \phi - A_y P_n^{fpp} \sin \phi]$ for positive helicity of the electron beam. $\eta(\theta, \phi)$ is the efficiency of the polarimeter; its ϕ -dependence is the results of instrumental asymmetries, which can be partially canceled by forming the helicity difference $N^+ - N^-$. $P_t^{fpp} \sim P_t^{target}$ and $P_n^{fpp} \sim P_\ell^{target} \sin \chi$ are the normal and transverse polarization components at the polarimeter, $\chi = \gamma \Theta_{bend}(\mu_p - 1)$ is the spin precession angle, Θ_{bend} is the dipole magnet bend angle. γ and μ_p are the relativistic boost factor and the magnetic moment of the proton, respectively.

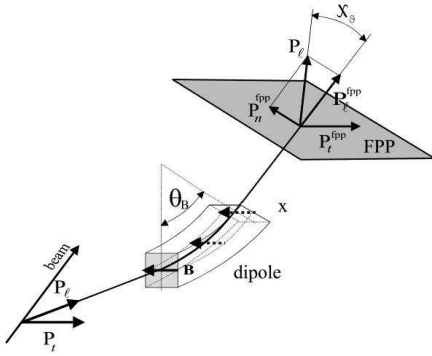


Figure 1: Precession of P_ℓ in typical recoil polarization experiment.

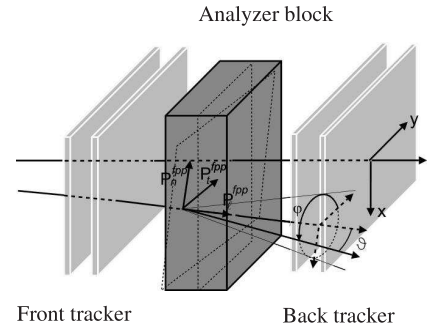


Figure 2: Determination of the azimuthal asymmetry in a polarimeter.

The first polarization transfer experiment at JLab was inspired by the pioneering theoretical work of several authors [8–10]. The GEp(1) experiment used analyzing power data obtained at the accelerator SATURNE with the polarimeter POMME, and shown in Fig. 3, for polarized proton beams of energy up to 2.4 GeV (3.2 GeV/c) [11]. In the GEp(1) experiment the ratio G_{Ep}/G_{Mp} was, for the first time, measured directly, from the ratio $P_t^{target}/P_\ell^{target}$, as had been proposed by Punjabi and Perdrisat in the original proposal [9]. The main advantage of this

method is that the ratio is independent of the beam polarization as well as the analyzing power A_y . In addition, as two physics quantities have been measured, two results can be obtained: the second is the analyzing power, shown in Fig. 4. A_y determines the error bars on the ratio, as in first approximation $\Delta P_t^{fpp} = \Delta P_\ell^{fpp} = \sqrt{(\frac{2}{\eta A_y^2 N})}$, where N is the number of **ep** events, A_y is an average analyzing power, and η the efficiency of the polarimeter.

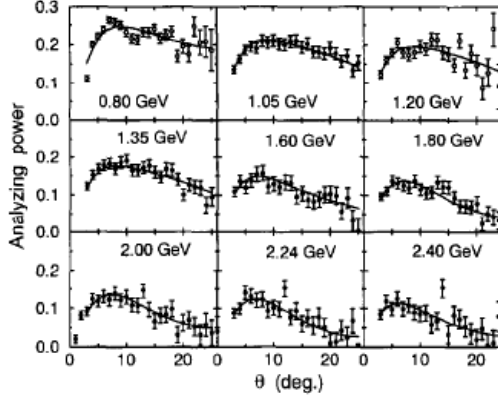


Figure 3: Analyzing powers A_y for pC [11]; the fits are 8-parameter polynomials. The maximum energy corresponds to a Q^2 of 4.5 GeV^2 in elastic **ep**.

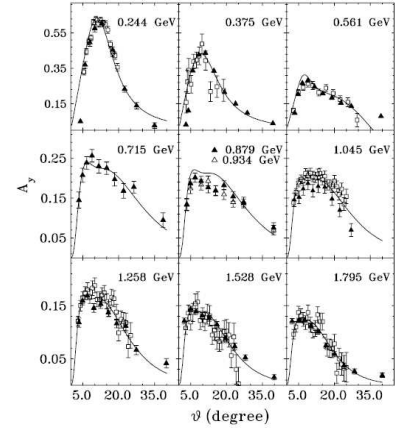


Figure 4: pC analyzing powers obtained from the first GEp experiment in 1998; some of the data points from Fig. 3 are included.

Until the first GEp experiment at JLab, the proton form factors had been obtained almost exclusively by Rosenbluth separation of cross section data. These measurements showed that, individually, the Q^2 dependence of the two form factors was similar to the dipole form factor $G_D = (1 + \frac{Q^2}{0.71})^{-2}$, resulting in an approximately constant G_{Ep}/G_{Mp} ratio. The results of GEp(1) in Fig. 5 strongly suggested [2], that the recoil polarization results may not be in agreement with the Rosenbluth data base. Interestingly, cross section measurements in the 1970's, shown in Fig. 6, indicate a Q^2 dependence similar to that of GEp(1); but later cross section measurements, as seen in Fig. 5, presented a very different picture.

One possible source of systematic error which could have explained the difference between the cross section and double-polarization data may have been in the method used to reconstruct the target polarization components, $(P_t^{target}, P_\ell^{target})$ from the measured focal plane polarimeter polarization components P_t^{fpp} and P_n^{fpp} . The data in Fig. 7 were obtained by choosing a kinematics such that the precession in the HRS dipole would be near 180° . Events in the HRS acceptance then provide a range of precession angles, and the values of the asymmetry amplitude $A_y P_n^{fpp}$ do indeed go through zero very close to 180° precession angle, corresponding to $P_n^{fpp} = P_\ell^{target} \sin \chi = 0$, and validating the calculation of the spin precession.

The results of the second GEp experiment at JLab are published in Ref. [3]. The data have been re-analyzed since and are published in Ref. [14]. The analyzing power results of GEp(2) are shown in Fig. 8; note that the maximum of A_y appears at a nearly constant transverse momentum p_T of ≈ 0.3 - 0.4 GeV/c over the range of proton momentum 2.6 to 3.8 GeV/c . These results confirm the data obtained in a calibration experiment at JINR/Dubna, Ref. [27]. The apparent "scaling" of A_y^{max} versus $1/p$, with p the proton momentum, seen in Fig. 9, was first observed in Ref. [27].

So far the tracking of the polarimeters used at JLab did not allow for particle identification.

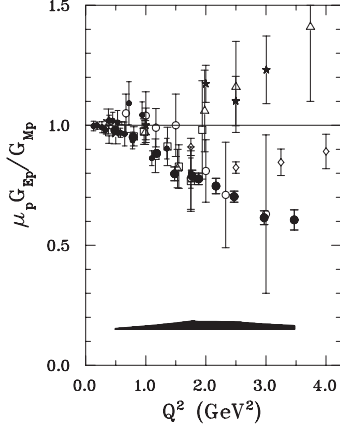


Figure 5: The results of the first recoil polarization experiment, GEp(1), [2] (filled circles), are incompatible with the cross section data of Refs. [16, 17].

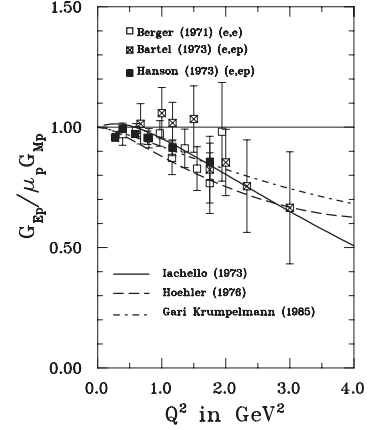


Figure 6: The Sachs form factor ratio from cross section existing in the 1970's display a similar Q^2 dependence as the recoil polarization data shown in Fig. 5.

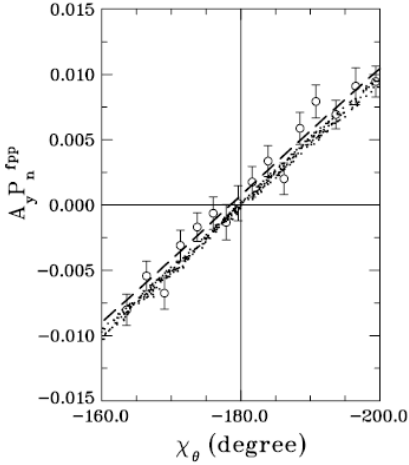


Figure 7: Zero crossing of precessed longitudinal component of the polarization; the small dots are simulation data. The dashed line is a fit to the data, and the solid line fit to the simulation.

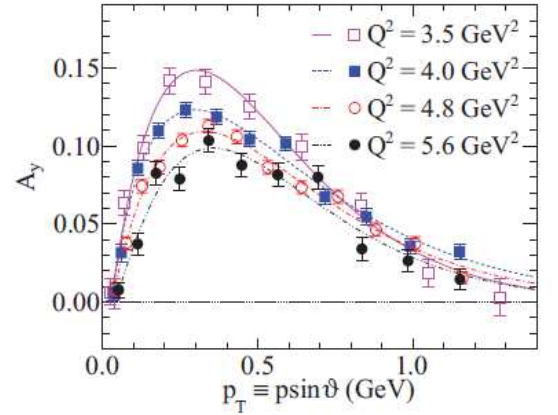


Figure 8: Analyzing powers from GEp(2) using CH_2 as analyzer material. The maximum Q^2 corresponds to 3.8 GeV/c momentum.

As the proton energy increases, the fraction of single-track events decreases, approximately like the ratio of the elastic to inelastic pN total cross section. The undesirable effect of the inelastic contribution, which can only partially be suppressed by selecting single-track events (some inelastic channels results in a single charged final state, example $pn \rightarrow pn\pi^0$), decreases the effective analyzing power A_y . In future experiments, better tracking resolution and crude measurement of energy behind the polarimeter should increase the effective analyzing power.

The third GEp experiment at JLab in 2007-8 used a double polarimeter installed in the Hall C HMS spectrometer [13]; the polar angle dependence of the analyzing powers obtained over the proton momentum range 3.6 to 5.4 GeV/c are shown in Fig. 10.

Fig. 11 shows all values of $\mu_p G_{Ep}/G_{Mp}$ obtained in recoil polarization experiments at JLab so far; as well as values obtained in a number of other experiments to check the polarimeter performance. The results of the 3 most recent Rosenbluth experiments ([16, 17, 20]) are also

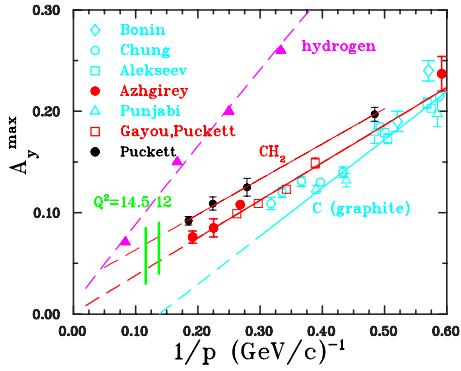


Figure 9: Scaling of A_y^{max} versus $1/p$ discovered in Ref. [27]. The scatter of the data from different experiments reflects their efficiency for single-track identification; Refs. [12, 11, 13, 27, 2, 3, 14, 13], [14] for hydrogen.

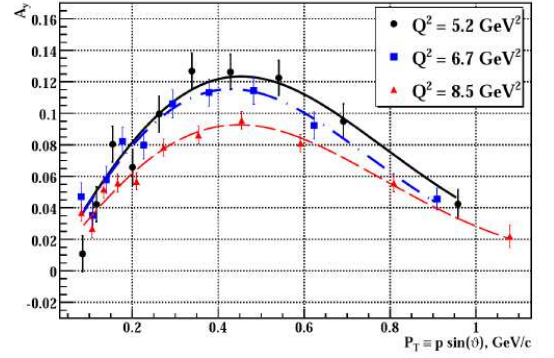


Figure 10: Analyzing powers for CH_2 from GEP(3), using CH_2 as analyzer material; the highest Q^2 value corresponds to a proton momentum of 5.4 GeV/c [17].

shown for comparison.

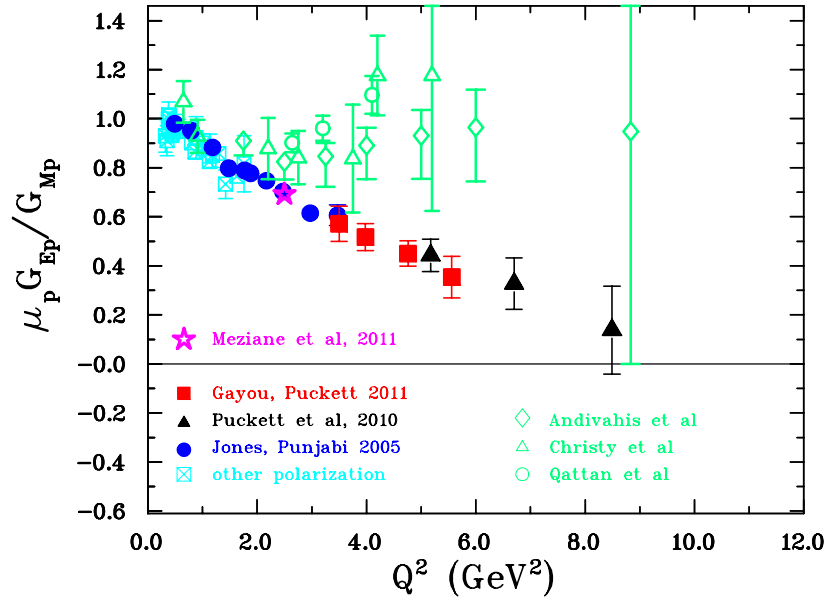


Figure 11: Results of the three JLab GEP experiments obtained by the recoil polarization method. The Rosenbluth data are from [16, 17, 20].

Conclusions

Recoil polarization experiments to measure G_{Ep}/G_{Mp} to large Q^2 became possible with JLab; the technique had been first tested at Bates at $Q^2 < 0.5 \text{ GeV}^2$ in 1996 [21].

Results of recoil polarization experiments were unexpected, showing an irreducible difference between double polarization results and Rosenbluth separation results.

It is now commonly assumed that the difference is due primarily to incomplete radiative corrections to the cross section data, including double virtual photon exchange. The size of the

two-photon exchange has yet to be determined experimentally; the e^+e^- cross section ratio recently measured in three Laboratories should resolve the puzzle soon.

The author acknowledges support from the NSF USA, grant number 1066374 (CFP).

References

- [1] M.K. Jones et al. P.R.L. 84, 1398 (2000).
- [2] V. Punjabi et al. P.R. C 71 055202 (2005), errat. ibid C71,069902 (2005).
- [3] O. Gayou et al., P.R.L. 88, 092301 (2002).
- [4] A.J.R. Puckett et al., P.R. C 85 (2012), 045203.
- [5] A.J.B. Puckett et al., P.R.L. 104, 242301 (2010).
- [6] M.Meziane et al. P.R.L. 106 (2011) 132501.
- [7] C.F. Perdrisat et al., proposal PR12-07-109, JLAB PAC 32 (2007)
- [8] A.I. Akhiezer and M.P. Rekalo, Sov. J. Part. Nucl. 3, 277 (1974).
- [9] N. Dombey, Rev. Mod. Phys, 41, 236 (1969).
- [10] R.G. Arnold, C.E. Carlson and F. Gross, P.R. C 23, 363 (1981).
- [11] E. Chung et al. N.I.M. in P.R. A363 (1995) 561.
- [12] B. Bonin et al., N.I.M.A434 (1999).
- [13] I.J. Alekseev et al., N.I.M. in P.R, A434, 254 (1999).
- [14] H. Spinka et al. N.I.M. 212, 239 (1983)
- [15] C.F. Perdrisat and V. Punjabi, "Electric Form Factor of the Proton by Recoil Polarization, JLab PAC6, (1989).
- [16] L.S. Azhgirey et al, N.I.M. in P.R. A 538 (2005), 431.
- [17] A.J.R. Puckett, unpublished, PhD thesis, MIT (2009).
- [18] L. Andivahis et al., P. R. D 50, 5491 (1994).
- [19] Christy et al., P.R. C 70, 015206 (2004).
- [20] I.A. Qattan I. A. et al., P. R. L. 94, 142301 (2005).
- [21] B.D. Milbrath et al. P.R.L. 80 (1998), 452; erratum P.R.L. 82 (1999),221.

THE Dp NON-MESONIC BREAKUP DATA AT 300–500 MeV OF THE DEUTERON ENERGY OBTAINED AT NUCLOTRON

S.M. Piyadin^{1†}, M. Janek², B. Trpišová², Yu.V. Gurchin¹, A.Yu. Isupov¹, J.-T. Karachuk^{1,3},
A.N. Khrenov¹, V.A. Krasnov¹, A.K. Kurilkin¹, P.K. Kurilkin¹, V.P. Ladygin¹,
A.N. Livanov¹, G. Martinska⁴, S.G. Reznikov¹, A.A. Terekhin¹

(1) *LHEP-JINR, 141-980 Dubna, Moscow region, Russia*

(2) *Physics Dept, University of Žilina, 010 26 Žilina, Slovakia*

(3) *Advanced Research Institute for Electrical Engineering, Bucharest, Romania*

(4) *P.J. Safarik University, Kosice, Slovakia*

† *E-mail: piyadin@jinr.ru*

Abstract

One of the main objectives of the Deuteron Spin Structure project is to obtain the information on the spin dependent parts of 2-nucleon and 3-nucleon forces. As the first step of this program recent results on the study of the dp -breakup reaction with 300-500 MeV unpolarized deuteron beam at Internal Target Station at Nuclotron-M are discussed. Selection procedure of useful events for the $dp \rightarrow ppn$ reaction with the registration of two protons is shown. Further scientific program with polarized and unpolarized deuterons is discussed.

The purpose of Deuteron Spin Structure experimental program is to obtain the information on the spin τAY dependent parts of 2-nucleon and 3-nucleon forces from two processes: dp -elastic scattering in a wide energy range and dp non-mesonic breakup with two protons detection at energies 200 - 500 MeV [1].

Properties of few-nucleon system at moderate energies are determined mainly by pairwise nucleon-nucleon interactions. Models of NN forces describe the long range interaction part according to the meson-exchange, while the short range is based on phenomenology, adjusted by fitting a certain number of parameters to the NN scattering data. Nowadays a new generation of the NN potentials (AV-18 [2], CD-Bonn [3], Nijmegen [4] etc.) was obtained. They reproduce data on the nucleon nucleon scattering up to 350 MeV with very good accuracy. However, these modern $2N$ forces fail to provide the experimental binding energies of few-nucleon systems. Moreover the data on the dp - elastic scattering and deuteron breakup are not described properly.

Precise predictions for observables in the $3N$ system can be obtained via exact solutions of the $3N$ Faddeev equations for any nucleon-nucleon (NN) interaction, even with the inclusion of a $3NF$ model [5]. Incorporation of the $3N$ forces makes it possible to reproduce the binding energy of the three-nucleon bound systems and also data on unpolarized dp - interaction. Nevertheless, polarization data for the reactions with participation of three and more nucleons are not described even with inclusion of $3NF$. Therefore, the obtaining of the additional polarization data in the dp - interaction in the wide energy range more is very desirable for the study of the spin structure of $2N$ and $3N$ forces [6]. To investigate the details of the $3N$ system dynamics, in addition to elastic Nd scattering data, reliable deuteron breakup data sets, covering large regions of the available phase space, are needed.

The experimental data on the deuteron analyzing powers for dp -breakup for large phase space were obtained at 130 MeV at KVI [7]. A_y , A_{yy} and A_{xx} analyzing powers in dp -breakup will be investigated at Internal Target Station at 200-500 MeV. The predictions for analyzing

powers and differential cross section in the selected dp -breakup configurations at 200 MeV were obtained in [8]. It was shown large sensitivity of these observables to the model of $3NF$.

In this report the status of the experiment at ITS at Nuclotron preparation and first results with unpolarized deuterons are presented.

The dp breakup reaction is investigated using ΔE - E techniques for the detection of protons. 8 detectors of this kind are used in the experiment. The details of the ΔE - E detector construction are presented in [9].

Each detector consists of two scintillators ΔE and E . The first scintillator has the cylindrical form with the height 10 mm and the diameter 80 mm. Two PMTs-85 view through given scintillator and they are located the friend opposite to the friend (see Fig. 1). Two planes have been made on the scintillator and photocatode of the PMT-85. These planes have been polished. ΔE scintillator is covered by a white paper. Digital dividers of the high voltage are used for PMT-85.

E scintillator also has the cylindrical form with height 200 mm and diameter 100 mm. PMT-63 view through this scintillator. Given PMT has been chosen because of the suitable size of the cathode (100 mm) with both good time and amplitude properties. E scintillator has been wrapped by a white paper. The part which is located to ΔE scintillator has been covered by a black paper. It is made to exclude possibility of hit the light from one plastic scintillator to another. The calibration for ΔE - E counters were performed with cosmic muons and pp -quasi elastic scattering.

The experiment with 8 ΔE - E detectors at ITS has been performed at the initial deuteron kinetic energy of 300 MeV, 400 MeV and 500 MeV on CH_2 target. During this experiment a DAQ-system based on the VME - standard has been used. The detection angles for registration of two protons for study the $dp \rightarrow ppn$ reaction are presented in Fig. 2.

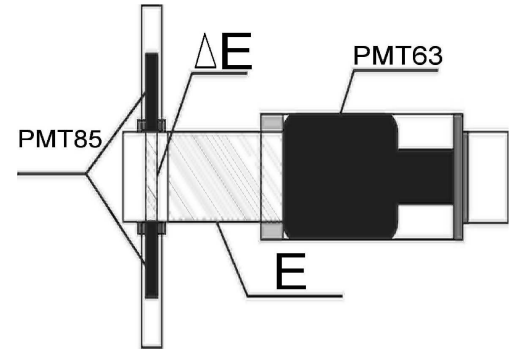


Figure 1: The ΔE - E detector for the detection of protons.

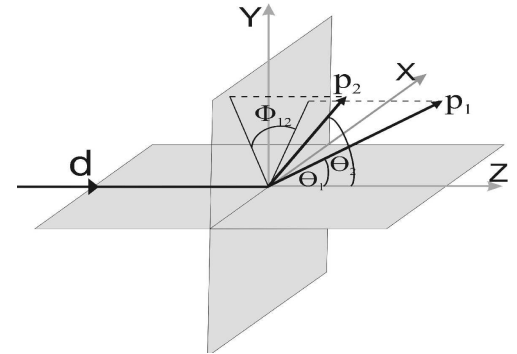


Figure 2: Detection angles for registration of two protons.

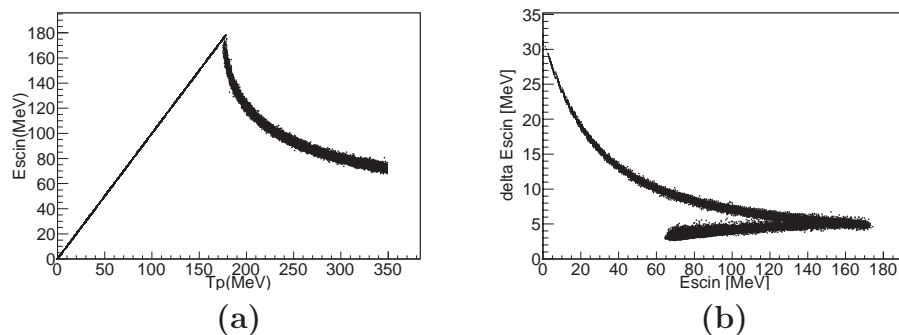


Figure 3: (a) Simulation results of the energy losses of the protons passed through ΔE and E scintillators when the length of a scintillator is 21 cm ($\Delta E + E$) (b) Simulation results of the energy losses of the protons passed through ΔE and E scintillators in thin scintillator versus thick.

The simulation results on the energy losses of the protons which passes through the scintil-

lators are presented in Fig. 3. In (b) figure the energy losses of the proton in thin scintillator are plotted versus ones of the thick scintillator. The events were selected in the region of approximate linear dependence of the energy losses in the scintillator versus the incident proton energy. Therefore the following conditions on the ΔE and E information were imposed: $5 \text{ MeV} < \Delta E < 35 \text{ MeV}$ and $0 \text{ MeV} < E < 180 \text{ MeV}$.

The missing mass has been calculated using the kinematic formulas (see Fig. 4). Histogram was obtained for the kinematical configuration $\Theta_1=25^\circ, \Theta_2=43.6^\circ, \Phi_{12}=178.5^\circ$ and deuteron energy of 400 MeV. One can see clearly the allocated the dp -breakup reaction and dp -elastic scattering. Useful events were obtained with the cut on missing mass: less than 950 MeV for the configuration register dp -elastic scattering and dp -breakup are detected; $940 \text{ MeV} \pm 10 \text{ MeV}$ for the configuration when only dp -breakup events are registered.

Correlations of the proton energies with the cut on missing mass neutron are presented in Fig. 5.

Data were acquired for deuteron breakup reaction with deuteron energies 300 MeV, 400 MeV and 500 MeV on CH_2 at Internal Target Station at Nuclotron. Black curve is the kinematic locus for deuteron breakup reaction at 300-500 MeV energy of deuteron for different angle configuration. The correlation of the proton energies were plotted with the cut on mass of neutron ($\pm 10 \text{ MeV}$).

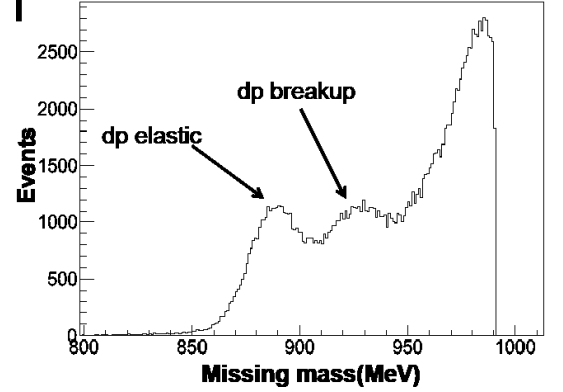


Figure 4: The missing mass for the kinematical configuration $\Theta_1=25^\circ, \Theta_2=43.6^\circ, \Phi_{12}=178.5^\circ$.

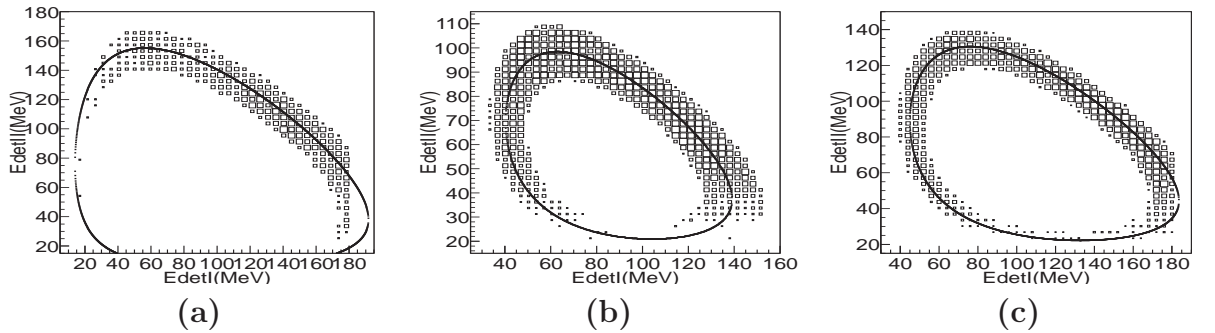


Figure 5: (a) Correlation of the protons energies with the cut on missing mass neutron for $(\Theta_1 = 25.2^\circ, \Theta_2 = 33.9^\circ, \Phi_{12} = 135.3^\circ)$ configuration with deuteron energy 300 MeV. (b) Correlation of the protons energies with the cut on missing mass neutron for $(\Theta_1 = 25^\circ, \Theta_2 = 33.7^\circ, \Phi_{12} = 44.6^\circ)$ configuration with deuteron energy 400 MeV. (c) Correlation of the protons energies with the cut on missing mass neutron for $(\Theta_1 = 24.7^\circ, \Theta_2 = 33.3^\circ, \Phi_{12} = 44.6^\circ)$ configuration with deuteron energy 500 MeV.

Conclusion

The preliminary results for $dp \rightarrow ppn$ reaction at 300-500 MeV for different geometry at Internal Target Station at Nuclotron are obtained. The procedure of selection of events relating to the dp -breakup reaction is established. The setup for the studies of deuteron non-mesonic breakup reaction was put into operation.

The future plans are to continue to process the obtained data and to estimate a contribution of background events to these results for the study of dp-breakup reaction. We are going to take the data on dp τ AY breakup using with polarized deuteron beams at Nuclotron. New source will provide up to $2 * 10^{10}$ ppp and higher values of polarization than POLARIS. Part of the IUCF source is used for the construction. The putting into operation of new PIS is planned in 2014.

The work has been supported in part by RFBR grant 13-02-00101a and JINR grants for young scientists.

References

- [1] V.P. Ladygin et al., EPJ Web Conferences **3**, **04004**, (2010).
- [2] R.B. Wiringa, V.G.J. Stoks, and R. Schiavilla., Rhys. Rev. **C51**, (1995) 38.
- [3] R. Machleidt, Phys.Rev. **C63**, (2001) 024001.
- [4] V.G.J. Stoks, R.A.M. Klomp, C.P.F. Terheggen, and J.J. de Swart., Rhys. Rev. **C49**, (1994) 2950.
- [5] W. Glockle, H. Witala, D. Huber, H. Kamada, and J.Golak, Phys. Rep. **274**, 107 (1996).
- [6] T. Uesaka, V.P. Ladygin, et al., Phys.Part.Nucl.Lett. **3**, (2006) 305.
- [7] St. Kistryn et al., Phys.Rev. **C72**,044006, (2005).
- [8] J. Kuros-Zolnierczuk et al., Phys.Rev., **044006**, (2005).
- [9] S.M. Piyadin et al., Phys.Part.Nuc.Lett., **8**, (2011) 107.

PROTON FORM FACTOR MEASUREMENTS AT JEFFERSON LAB IN 12 GeV ERA

Vina Punjabi[†]

Norfolk State University, Norfolk, Virginia 23504, USA

[†] *E-mail: vapunjabi@nsu.edu*

Abstract

Jefferson Lab is in the middle of an upgrade construction program, which will double the electron beam energy to 12 GeV. The doubling of the energy enables the extension of recent programs to fully characterize the electric form factors of the proton to significantly higher Q^2 . There is an approved experiment at JLab, GEp(5), that will measure the ratio G_{Ep}/G_{Mp} to Q^2 of 12 GeV². A dedicated experimental setup, the Super Bigbite Spectrometer (SBS) facility, is being built for this purpose. It will be equipped with a focal plane polarimeter to measure the polarization of the recoil protons. The scattered electrons will be detected in an electromagnetic calorimeter. In this presentation, I will describe the new experiment which will measure G_{Ep}/G_{Mp} to Q^2 of 12 GeV², also I will review the status of the proton elastic electromagnetic form factors and discuss a number of recent theoretical approaches.

1 Introduction

The proton electromagnetic form factor results from Jefferson Lab at high values of four-momentum transfer Q^2 have had a big impact on progress in hadronic physics; these results have required a significant rethinking of nucleon structure. Since the publication of the JLab ratio measurements, there have been a huge amount of theoretical activity, and several reviews of nucleon form factors [1–6] have been published. New information on hadron structure, such as role of quark orbital angular momentum, transverse charge density distribution, dressed quark form factor has followed in short order. It is clear that the only way to achieve clarity in discriminating between theoretical explanations of G_{Ep}/G_{Mp} data is to measure it with considerable precision to high values of Q^2 . New experiment GEp(5) in preparation for the 12 GeV era, will provide answers to some of the open questions crucial to our understanding of the fundamental proton properties and the nature of QCD in the confinement regime

2 Recoil Polarization Method

The relationship between the Sachs electromagnetic form factors and the degree of polarization transfer in $^1H(\vec{e}, e'\vec{p})$ scattering was first developed by Akhiezer and Rekalov [7], and later discussed in more detail by Arnold, Carlson, and Gross [8].

For single photon exchange, the transferred polarization can be written in terms of the Sachs form factors:

$$P_n = 0 \quad (1)$$

$$\pm h P_l = \pm h \left(\frac{E_e + E'_e}{M} \right) \frac{\sqrt{\tau(1+\tau)} G_{Mp}^2(Q^2) \tan^2 \frac{\theta_e}{2}}{G_{Ep}^2(Q^2) + \frac{\tau}{\epsilon} G_{Mp}^2(Q^2)} \quad (2)$$

$$\pm h P_t = \mp h \frac{2\sqrt{\tau(1+\tau)} G_{Ep} G_{Mp} \tan \frac{\theta_e}{2}}{G_{Ep}^2(Q^2) + \frac{\tau}{\epsilon} G_{Mp}^2(Q^2)} \quad (3)$$

where $\tau = \frac{Q^2}{4m_p^2}$, ϵ is the longitudinal virtual photon polarization, and the \pm stands for the two possible orientations of the electron beam helicity.

An important realization of the double-polarization approach to obtain the ratio at the large momentum transfer by measuring two polarization components simultaneously was first proposed at JLab in 1989 [9]; it is based on a combination of spin precession in a magnetic spectrometer and uses a proton polarimeter. The major advantage of the method, compared to cross section measurements, is that in the Born approximation the form factor ratio, G_E^p/G_M^p , is directly proportional to the measured transverse and longitudinal proton polarization components P_t/P_l . For each Q^2 , a single measurement of the azimuthal angular distribution of the proton scattered in a secondary target (described later) gives both the longitudinal and transverse polarizations. Combining Eqs. 2 and 3 give:

$$\frac{G_{Ep}}{G_{Mp}} = -\frac{P_t}{P_l} \frac{(E_e + E'_e)}{2M} \tan \frac{\theta_e}{2}; \quad (4)$$

thus the ratio of electric to magnetic form factors of the proton is obtained directly from a simultaneous measurement of the two recoil polarization components. The kinematic factors in Eq. 4 are typically known to a precision far greater than the statistical precision of the recoil polarization components.

3 Results of JLab GEp Experiments and comparison to Theoretical Model Calculations

The striking disagreement of the JLab double polarization proton form factor ratio results [10–15] with the Rosenbluth results [16–18] is illustrated in Fig. 1. Use of the double-polarization technique to obtain the elastic nucleon form factors has resulted in a dramatic improvement of the quality of the proton electromagnetic form factors. It has also changed our understanding of the proton structure, having resulted in a distinctly different Q^2 -dependence for the electric form factor G_{Ep} and the magnetic form factor G_{Mp} , contradicting the prevailing wisdom of the 1990's based on cross section measurements, namely that G_{Ep} and G_{Mp} obey a “scaling” relation $\mu G_{Ep} \sim G_{Mp}$. A related consequence of the faster decrease of G_{Ep} revealed by the Jefferson Lab (JLab) polarization results was the disappearance of the early scaling of $F_2/F_1 \sim 1/Q^2$ predicted by perturbative QCD.

The data from the GEp(3) experiment [14] at higher Q^2 show a slowing decrease of G_E^p/G_M^p with Q^2 relative to the linear decrease observed in the Hall A data for $Q^2 \leq 5.6 \text{ GeV}^2$. Although the statistical significance of this change in behavior is somewhat marginal, its physical implications are interesting to consider. A constant ratio G_{Ep}/G_{Mp} at asymptotically large Q^2 is a signature of the onset of the dimensional scaling expected from perturbative QCD for a nucleon consisting of three weakly interacting quarks.

Predicting nucleon form factors in the non-perturbative regime, where soft scattering processes are dominant, is very difficult. As a consequence there are many phenomenological models

which attempt to explain the data in this domain. There are several approaches to calculate nucleon form factors in the non-perturbative regime. The list includes vector meson dominance (VMD) models, relativistic constituent quark models (rCQM), the cloudy bag model, the diquark model and the Dyson-Schwinger equation (DSE) model and more. In the VMD approach, the photon couples to the nucleon via vector mesons, whereas in QCD models the photon couples to the quarks directly. The generalized parton distributions (GPD) represent a framework within which hadrons are described in terms of quarks and gluons. Perturbative QCD predicts form factor values for large Q^2 . We show results from some of these calculations [19–25] here in Fig. 1.

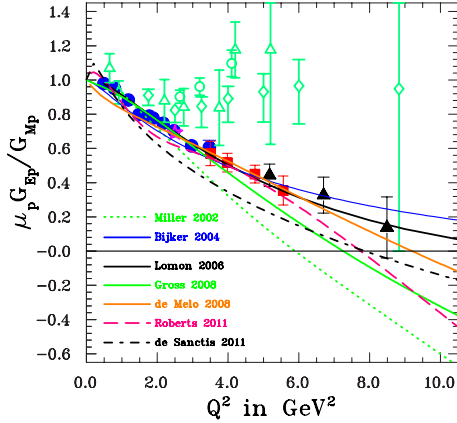


Figure 1: All recoil polarization results from three JLab GEp experiments; also included are selected Rosenbluth results (empty symbols).

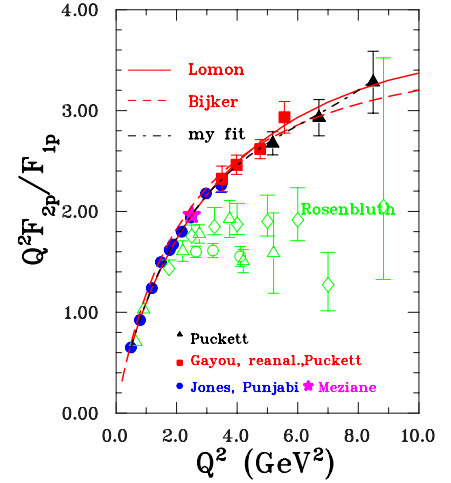


Figure 2: Perturbative QCD behavior of the Fermi and Dirac form factor ratio for the proton, a slow down of the rise is visible.

4 Proton Form Factors with 11 GeV

The measurement of the ground-state electromagnetic form factors of the proton becomes quite challenging at high momentum transfers, because the effective rate drops as roughly E_{beam}^2/Q^{16} . The polarization-transfer method also requires very large statistics because of the relatively low analyzing power of the recoil polarimeter. Figure 3 shows maximum value of the analyzing power A_y^{max} versus the inverse of the proton momentum. The values from GEp(3) (black circles) are systematically larger than those in Azhgirey et al. [27]. The difference is thought to be due to the strict selection of single track events in the GEp(3) experiment. The GEp(5) experiment meets these challenges through an innovative approach. The spectrometer in the proton arm is based on a large open-geometry dipole magnet that is placed quite close to the target, and at a small angle, a configuration that provides large solid angle [26]. The use of gas electron multiplier (GEM) chambers solves the main challenge of this spectrometer, the very high counting rates due to open geometry, allowing tracking at very high background rates.

GEp(5) is a coincidence experiment, conceptually similar to the three previous GEp experiments at JLab. This experiment will be done in Hall A; it requires a proton detector with magnetic analysis of proton momentum, followed by a polarimeter to measure the transferred polarization of the recoiling proton from the elastic reaction $^1H(\vec{e}, e'\vec{p})$. As a new feature the proton detector will also include a highly-segmented hadron calorimeter to provide its own fast trigger and also provide fast information on the approximate angle of the incident proton. The

electron will be detected in coincidence by the reconfigured electromagnetic calorimeter BigCal, used in GEp(3) experiment. BigCal will be large enough to match the acceptance of the proton arm, and will also be equipped with a coordinate detector to further improve position resolution. The GEp(5) experiment will use the 11 GeV polarized electron beam and a 40-cm long liquid hydrogen target. A schematic representation of the experiment is shown in Figure 4. The new experiments will push the invariant momentum transfer squared to a significant higher value, ultimately to 14 GeV^2 , to be compared with 8.5 GeV^2 in the GEp(3) experiment.

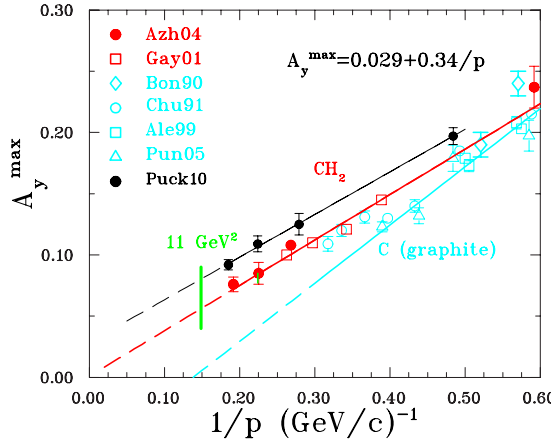


Figure 3: Maximum value of the analyzing power A_y^{max} versus the inverse of the proton momentum.

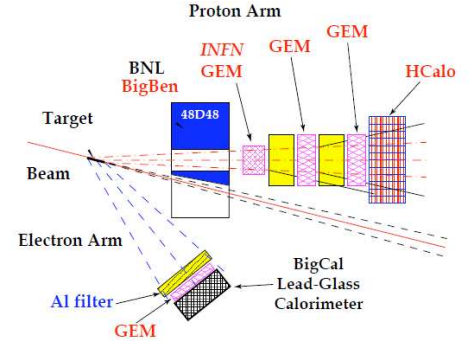


Figure 4: Schematic floor plan arrangement for the GEp(5) experiment using the SBS.

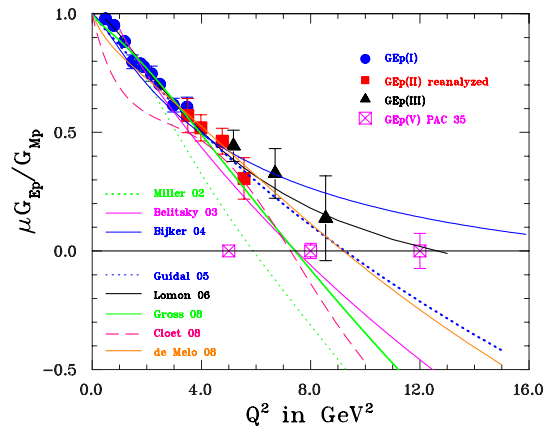


Figure 5: The anticipated results of GEp(5). A wide range of phenomenological model predictions are shown, underlining the potential ability of this experiment, to narrow the range of models able to reproduce the future data.

The expected error bars for GEp(5) [28] are shown in Fig.5.

5 Conclusions

The unexpected results of the proton form factor ratios using double-polarization high-precision experiments at JLab, have challenged the theoretical understanding of the structure of the

proton. These results, together with the anticipated results following the 12 GeV upgrade of the JLab accelerator, will provide answers to a number of open questions crucial to the understanding of fundamental properties of the proton, and the nature of QCD in the confinement regime.

6 Acknowledgments

The author wish to thank the organizers of the Dubna Dspin-13 workshop for the invitation to present this paper. The author is supported by grant from the DOE(USA), DE-FG02-89ER40525.

References

- [1] H.Y. Gao, Int. J. Mod. Phys. E **12**, 1 (2003) [Erratum-ibid. E **12**, 567 (2003)].
- [2] C.E. Hyde-Wright and K. de Jager, Ann. Rev. Nucl. Part. Sci. **54**, 217 (2004).
- [3] C.F. Perdrisat, V. Punjabi and M. Vanderhaeghen, Journal of Progress in Particle and Nuclear Physics, **59**, 694 (2007).
- [4] J. Arrington, C. D. Roberts and J. M. Zanotti, J. Phys. G **34**, S23 (2007) [arXiv:nucl-th/0611050].
- [5] C.F. Perdrisat and V. Punjabi, [http://www.scholarpedia.org/article/Nucleon Form Factor](http://www.scholarpedia.org/article/Nucleon_Form_Factor).
- [6] J. Arrington, K. de Jager, C. F. Perdrisat, J. Phys. Conf. Ser. **299**, 012002 (2011).
- [7] A. I. Akhiezer and M. P. Rekalov, Sov. J. Part. Nucl. **4**, 277 (1974); Fiz. Elem. Chast. Atom. Yadra **4**, 662 (1973).
- [8] R.G. Arnold, C.E. Carlson, F. Gross, Phys. Rev. C **23**, 363 (1981).
- [9] C.F. Perdrisat, V. Punjabi and M. Jones, “Electric Form Factor of the Proton by Recoil Polarization”, Jefferson Lab experiment 89-014 and 93-027 (1993).
- [10] M.K. Jones *et al.*, Phys. Rev. Lett. **84**, 1398 (2000).
- [11] V. Punjabi *et al.* Phys. Rev. C **71** (2005) 055202.
- [12] O. Gayou *et al.*, Phys. Rev. Lett. **88**, 092301 (2002).
- [13] A.J.R Puckett *et al.*, Phys. Rev. C **85**, 045203 (2012).
- [14] A.J.R Puckett *et al.*, Phys. Rev. Lett. **104**, 242301 (2010).
- [15] M. Meziane *et al.* [GEp2gamma Collaboration], Phys. Rev. Lett. **106**, 132501 (2011).
- [16] L. Andivahis *et al.*, Phys. Rev. D **50** 5491 (1994).
- [17] M.E.Christy *et al.*, Phys. Rev. **C70** 015206 (2004).
- [18] I.A. Qattan *et al.*, Phys. Rev. Lett. **94** 142301 (2005).
- [19] M.R. Frank, B.K. Jennings, and G.A. Miller, Phys. Rev. C **54**, 920 (1996); G.A. Miller and M.R. Frank, Phys. Rev. C **65**, 065205 (2002).

- [20] R. Bijker and F. Iachello, Phys.Rev. C **69** (2004) 068201.
- [21] E.L. Lomon, nucl-th/0609029v2.
- [22] F. Gross and P. Agbakpe, Phys. Rev. C **73**, 015203 (2006).
- [23] J.P.B. de Melo, T. Frederico, E. Pace, S. Pisano and G. Salme, Phys. Lett. B **671**, 153 (2009).
- [24] I.C. Cloët and C.D. Roberts, Proc. of Sc. LC2008:047 (2008); arXiv:0811.2018 [nucl-th] (2008); I.C. Cloët, G. Eichmann, B. El-Bennich, T. Klähn and C.D. Roberts, Few Body Syst. **46**, 1 (2009).
- [25] M. de Sanctis *et al*, Phys. Rev. C **76**, 062201 (2007).
- [26] <http://hallaweb.jlab.org/12GeV/SuperBigBite/>
- [27] L.S. Azhgirey *et al.*, Nucl. Inst. Meth. A **538**, 431 (2005).
- [28] <http://hallaweb.jlab.org/collab/PAC/PAC32/PR12-07-109-Ratio.pdf>

SPIN AND PARITY DETERMINATION OF 125 GeV PARTICLE WITH THE CMS DETECTOR

A. Rinkevicius^{1,2†} for the CMS collaboration

(1) *University of Florida, Florida, USA*

(2) *CERN, Geneva, Switzerland*

† *E-mail: aurelijus.rinkevicius@cern.ch*

Abstract

We present results of studies aiming to establish the spin–parity quantum numbers of the newly discovered boson with a mass near 125 GeV. The final states exploited in these studies are $ZZ(4\ell)$, $WW(2\ell 2\nu)$, and $\gamma\gamma$. The dataset used in the analyses corresponds to integrated luminosities of 19.6 and 5.1 fb⁻¹ collected in pp collisions at 8 and 7 TeV, respectively. The hypotheses excluded at 95% CL or higher are pseudoscalar, vector, pseudovector, and massive graviton-like spin-2 tensor. The latter model is studied in assumptions of either gluon–gluon or quark–antiquark production mechanisms. The limit on the fractional presence of a pseudoscalar component is $\sigma(0-)/[\sigma(0+) + \sigma(0-)] < 0.58\%$ at 95% CL.

The Compact Muon Solenoid (CMS) [1] detector is a general-purpose particle detector collecting the resulting particles from the proton–proton collisions produced by the Large Hadron Collider (LHC) near Geneva, Switzerland. During the Run I that covered years 2009–2012, the CMS experiment collected data of the amount that corresponds to the integrated luminosities of 19.6 fb⁻¹ at 8-TeV center-of-mass collisions and 5.1 fb⁻¹ at 7-TeV center-of-mass collisions.

The collected data in particle physics is of the statistical nature, thus it imposes a requirement of the statistical treatment and hypothesis testing. The CMS performs the statistical analysis roughly in three generic steps:

1. Data selection and preparation.
2. Statistical likelihood template preparation (PDFs/PMFs).
3. Performing pseudoexperiments and comparing it to the observation.

The most complex step is step 1, where an extensive data filtration is being performed, a specific physics-object-oriented search. Step 2 is much more generic and differs mostly by the discriminating-variable-map choice and the theoretical expectations. The last, step 3, is an all-analysis common, pseudoexperiment-distribution generation and the statistical significance extraction wrt generated distributions. In the presented analyses the test statistic is chosen to be $q = -2 \ln \frac{L_1}{L_2}$, where L_i is a total likelihood for a particular hypothesis, while CL_S criterion is defined as

$$\text{CL}_S = \frac{P(q \geq q_{\text{obs}} | q \sim S_2 + B)}{P(q \geq q_{\text{obs}} | q \sim S_1 + B)}, \quad (1)$$

where S_1 corresponds to the null hypothesis (Standard-Model [SM] signal: a Higgs boson) and S_2 corresponds to the alternative hypothesis (an exotic signal). In both cases the background B is considered to have been observed, i.e., contributing some events.

The CMS had three different analyses, namely, $\gamma\gamma$, WW, and ZZ [2–4], that were able to investigate the compatibility between various exotic models and the SM Higgs boson. The final states that each analyses corresponds to are the following: $\gamma\gamma$, $2\ell 2\nu$, and 4ℓ , accordingly. All the described analyses were aiming to test the spin–parity properties by the use of different alternative models that are summarized in Table 1. Every alternative resonance under the alternative model we call an alternative signal. For the presented analyses, the Monte–Carlo (MC) data were generated using JHUGen event generator, Ref. [6].

The most prominent analysis in the 126-GeV resonance properties’ studies is the $H/X \rightarrow ZZ \rightarrow 4\ell$ [2]. This mode has a mass resolution of 1–2%, a good signal-to-background ratio, and many independent degrees of freedom (8 + unused boosts) that can be used in the presented studies. However, the channel suffers from the low expected number of events $\sim O(20)$. It is worth mentioning that the mainline analysis had an expected significance for the SM Higgs signal of 7.2σ and the actual observation went up to 6.7σ . The observed mass by this analysis is reported to be

$$m_H = 125.8 \pm 0.5(\text{stat.}) \pm 0.2(\text{syst.}) \text{ GeV.}$$

In order to perform the model testing we need to choose a set of coordinates/observables that would allow us to distinguish between the hypotheses. The chosen coordinate variables we call the discriminants or kinematical discriminants (KDs) while the key ingredient in making them in the ZZ analysis is the use of Matrix Element Method (MEM). The baseline strategy in applying MEM was to use JHUGen [6] matrix elements (MEs) for the signal and the MCFM [13] MEs for the background, while the calculations were validated by the MEs provided by the MEKD [12] (MadGraph5 [11] + FeynRules [10]) in all final states ($4e$, $2e2\mu$, and 4μ) and by MEs provided by the analytical approach, which is accessible via MELA package [7, 8, 14, 15], in the $2e2\mu$ (no-interference) final state. Important whole analysis cross-checks were performed using Boosted Decision Tree [16, 17] (BDT) and Bayesian Neural Network [18, 19] (BNN) techniques. In the end, the actual KDs, which are normalized between 0 and 1, take the following shape:

$$\mathcal{D}_{\text{bkg}} = \left[1 + c(m_{4\ell}) \times \frac{|\mathcal{M}_{ZZ}(p_{\ell_i}|m_{4\ell})|^2 \times \mathcal{P}_{ZZ}^{\text{mass}}(m_{4\ell})}{|\mathcal{M}_{0_m^+}(p_{\ell_i}|m_{4\ell})|^2 \times \mathcal{P}_{0_m^+}^{\text{mass}}(m_{4\ell}|m_H)} \right]^{-1}, \quad (2)$$

$$\mathcal{D}_{JP} = \left[1 + c_{JP} \times \frac{|\mathcal{M}_{JP}(p_{\ell_i}|m_{4\ell})|^2}{|\mathcal{M}_{0_m^+}(p_{\ell_i}|m_{4\ell})|^2} \right]^{-1}, \quad (3)$$

where c are the scaling constants to avoid an overcompression, $\mathcal{P}(m_{4\ell})$ are the detector-simulation-based invariant-mass-shape probability density functions (PDFs), and \mathcal{M} are the MEs.

In the ZZ analysis the actual statistical templates are filled in 2D (\mathcal{D}_{bkg} , \mathcal{D}_{JP}) coordinate space, where the \mathcal{D}_{bkg} discriminates between the SM Higgs and the SM background (mostly $q\bar{q} \rightarrow ZZ$) and the \mathcal{D}_{JP} between the SM Higgs and the alternative signal: this is done using the MC data events, except for the reducible background where it is taken from data. It is worth mentioning that each final state has its own templates (fused all-in-one templates are shown here in Fig. 1). The outcome of the statistical analysis is presented in Tab. 2. In the table

Model	Probing channel	Notes
0_m^+	$\gamma\gamma, WW, ZZ$	SM Higgs
0_h^+	ZZ	Scalar with higher-order coupls.
0^-	WW, ZZ	Pseudoscalar
1^-	ZZ	Vector
1^+	ZZ	Pseudovector
2_m^+	$\gamma\gamma, WW, ZZ$	Graviton-like

Table 1: The list of tried models and the affected analyses.

we present the expected separations for different hypotheses using the expected (after the full selection) signal strengths ($\mu = 1$), where the total yields are the same for both hypotheses under the test. In contrast, the observed results are presented with the best-fit signal strengths, in other words, with floating μ , which is done independently for the null hypothesis and the alternative signal. In the end, all the tested models, except the 0_h^+ , were excluded with at least the 95% CL_S.

Model	Expected separation, $\mu = 1$	Observed 0^+	Observed J^P	CL _S
0^-	2.8σ	0.5σ	3.3σ	0.16%
0_h^+	1.8σ	0.0σ	1.7σ	8.1%
1^-	3.1σ	1.4σ	$> 4\sigma$	$< 0.1\%$
1^+	2.6σ	1.7σ	$> 4\sigma$	$< 0.1\%$
$2_m^+ (gg)$	1.9σ	0.8σ	2.7σ	1.5%
$2_m^+ (q\bar{q})$	1.9σ	1.8σ	4.0σ	$< 0.1\%$

Table 2: The Moriond 2013 ZZ spin-parity results.

One more performed measurement in the ZZ analysis is a fit of the possible pseudoscalar fraction in the signal. Here a possible figure of merit can be chosen to be f_{a3} and defined as follows:

$$f_{a3} = \frac{\sigma_{0^-}}{\sigma_{0_m^+} + \sigma_{0^-}}, \quad (4)$$

where σ is a partial cross-section for the $2e2\mu$ final state only as ratios of cross-sections differ between different final states. The subscript has the following meaning:

$$\sigma_{0_m^+} : a_1 \parallel \kappa_1 \neq 0 \cup a_3 \parallel \kappa_3 = 0; \quad A = v^{-1} \epsilon_1^{*\mu} \epsilon_2^{*\nu} \left(a_1 g_{\mu\nu} m_V^2 + a_3 \epsilon_{\mu\nu\alpha\beta} q_1^\alpha q_2^\beta \right); \quad (5)$$

$$\sigma_{0^-} : a_1 \parallel \kappa_1 = 0 \cup a_3 \parallel \kappa_3 \neq 0; \quad \mathcal{L}_{J=0} \kappa_1 \frac{m_Z^2}{v} h Z_\mu Z^\mu + \frac{\kappa_3}{2v} h Z_{\mu\nu} \tilde{Z}^{\mu\nu}. \quad (6)$$

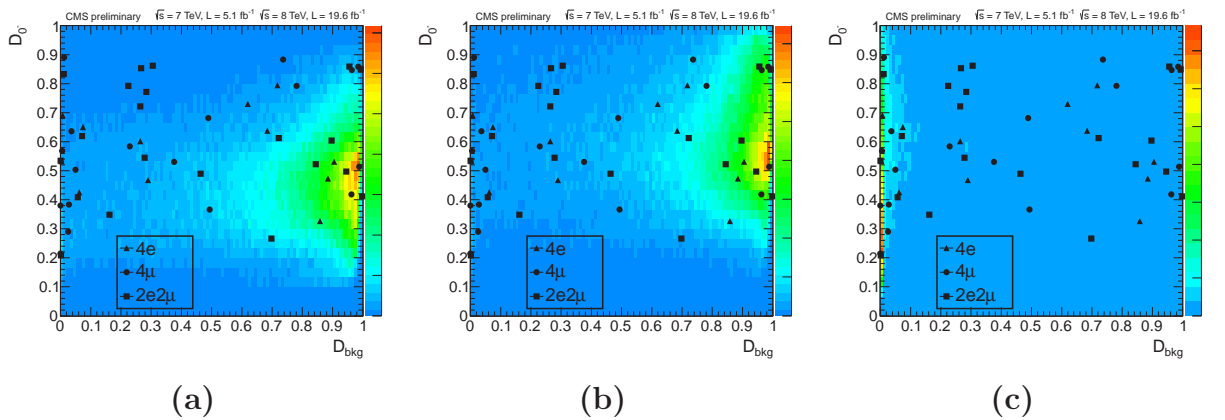


Figure 1: (a) 0^- state fused template with actual data. (b) 0_m^+ (SM Higgs) state fused template with actual data. (c) $q\bar{q} \rightarrow ZZ$ state fused template with actual data.

The observed result can be seen in the Fig. 2 that translates into the exclusion of 0.58 ratio at 95% CL_S (the expected exclusion ratio was 0.76). It can also be written out as

$$f_{a3} = 0.00^{+0.23}_{-0.00}$$

here the nonzero value would indicate a presence of the pseudoscalar state.

The $\gamma\gamma$ analysis [4] has a fair number of signal events $\sim O(400)$ and a good mass resolution of 1–2%. However, in the spin–parity studies it suffers from a few independent degrees of freedom (2 + unused boosts) and a poor signal-to-background ratio. The analysis had an expected significance for the SM Higgs signal of 4.2σ and the actual observation of 3.2σ . The observed mass by this analysis is reported to be

$$m_H = 125.4 \pm 0.5(\text{stat.}) \pm 0.6(\text{syst.}) \text{ GeV.}$$

The $\gamma\gamma$ analysis used $|\cos\theta_{CS}^*|$ as a model discriminating variable, where CS stands for the longitudinally (along the beam axis) colliding partons or Collins–Soper frame. The results are not conclusive on their own and are presented in Tab. 3.

The last standalone analysis presented here is WW [3], which has a fair number of signal events $\sim O(100)$ and a number of three independent degrees of freedom that are useful in the spin–parity studies. On the other hand, it suffers from poor mass resolution of $\sim 20\%$ and signal-to-background ratio. The analysis had an expected significance for the SM Higgs signal of 5.1σ and the actual observation of 4.0σ .

The WW analysis uses the $m_{\ell\ell}$ and m_T parameters as statistical template dimensions in the model studies [$m_T^2 = (m_{\ell_1} + m_{\ell_2})^2 + (p_{\ell_1} + p_{\ell_2})_x^2 + (p_{\ell_1} + p_{\ell_2})_y^2$; $m_{\ell\ell}^2 = (p_{\ell_1} + p_{\ell_2})^2$]. Analysis was done considering only the different-flavor final states, i.e., $e\nu\mu\nu$. Here the direct spin correlations are mostly reflected by $m_{\ell\ell}$. The final results are presented in Tab. 4.

Finally, the combination of results [5]. WW + ZZ gives the combined results that are presented in Tab. 5, which shows a strong exclusion of the minimal-coupling KK graviton. In addition, the $\gamma\gamma + ZZ$ provides the combined mass measurement result: $m_H = 125.7 \text{ GeV}$.

In the end, a number of the most plausible hypotheses, except for the 0_h^+ , are excluded at 99% CL or more (summary Table 6). All the discussed studies show observations that are consistent with the SM Higgs boson. The most important task for the future studies is to continue with the mixed state investigations.

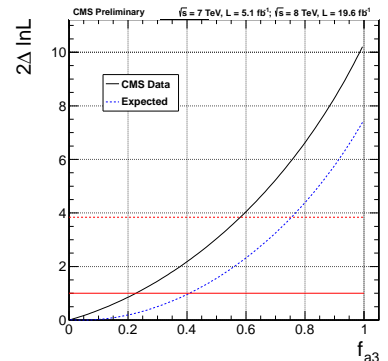


Figure 2: f_{a3} measurement in the ZZ analysis.

Compatibility		Model	CL_S
Source	$\chi^2 p$ -value		
Data vs. 0^+	0.68		
Data vs. 2_m^+ (100% gg)	0.91	2_m^+ (gg)	60.9
Data vs. 2_m^+ (100% $q\bar{q}$)	0.51	2_m^+ ($q\bar{q}$)	16.9
Data vs. 2_m^+ (50% gg , 50% $q\bar{q}$)	0.81		

Table 3: Model study results in $\gamma\gamma$ analysis.

Model	Expected separation, $\mu = 1$	Observed J^P
2_m^+ (gg)	2.2σ	1.3σ

Table 4: Model study results in WW analysis.

Model	CL _S
$P(q \leq q^{\text{obs.}} 0^+)$	-0.34σ
$P(q \geq q^{\text{obs.}} 2_m^+(gg))$	2.84σ
$1 - \text{CL}_S^{\text{obs.}}$	99.4%

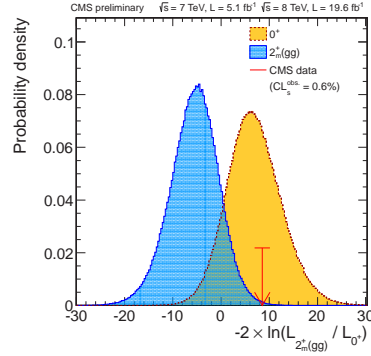


Table 5: Model study results with combined WW + ZZ analysis.

ZZ		$\gamma\gamma$		WW		WW + ZZ	
Model	CL _S	Model	CL _S	Model	CL _S	Model	CL _S
0^-	0.16%	$2_m^+(gg)$	60.9%	0^-	27%	$2_m^+(gg)$	0.6%
0_h^+	8.1%	$2_m^+(q\bar{q})$	16.9%	$2_m^+(gg)$	14%		
1^-	< 0.1%						
1^+	< 0.1%						
$2_m^+(gg)$	1.5%						
$2_m^+(q\bar{q})$	< 0.1%						

Table 6: Model studies summary.

References

- [1] S. Chatrchyan *et al.* [CMS Collaboration], JINST **3** (2008) S08004.
- [2] [CMS Collaboration], CMS-PAS-HIG-13-002.
- [3] [CMS Collaboration], CMS-PAS-HIG-13-003.
- [4] [CMS Collaboration], CMS-PAS-HIG-13-016.
- [5] [CMS Collaboration], CMS-PAS-HIG-13-005.
- [6] <http://www.pha.jhu.edu/spin/>
- [7] Y. Gao, A. V. Gritsan, Z. Guo, K. Melnikov, M. Schulze and N. V. Tran, Phys. Rev. D **81** (2010) 075022 [arXiv:1001.3396 [hep-ph]].
- [8] S. Bolognesi, Y. Gao, A. V. Gritsan, K. Melnikov, M. Schulze, N. V. Tran and A. Whitbeck, Phys. Rev. D **86** (2012) 095031 [arXiv:1208.4018 [hep-ph]].
- [9] A. Belyaev, N. D. Christensen and A. Pukhov, Comput. Phys. Commun. **184** (2013) 1729 [arXiv:1207.6082 [hep-ph]].
- [10] N. D. Christensen and C. Duhr, Comput. Phys. Commun. **180** (2009) 1614 [arXiv:0806.4194 [hep-ph]].
- [11] J. Alwall, M. Herquet, F. Maltoni, O. Mattelaer and T. Stelzer, JHEP **1106** (2011) 128 [arXiv:1106.0522 [hep-ph]].
- [12] P. Avery, D. Bourilkov, M. Chen, T. Cheng, A. Drozdetskiy, J. S. Gainer, A. Korytov and K. T. Matchev *et al.*, Phys. Rev. D **87** (2013) 5, 055006 [arXiv:1210.0896 [hep-ph]].
- [13] <http://mcfm.fnal.gov/>.
- [14] S. Y. Choi, D. J. Miller, M. M. Muhlleitner and P. M. Zerwas, Phys. Lett. B **553** (2003) 61 [hep-ph/0210077].
- [15] . Chen, N. Tran and R. Vega-Morales, JHEP **1301** (2013) 182 [arXiv:1211.1959 [hep-ph]].

- [16] J. Therhaag [TMVA Core Developer Team Collaboration], AIP Conf. Proc. **1504** (2009) 1013.
- [17] J. H. Friedman, Comput. Stat. Data Anal. **35** (2002) 367.
- [18] R. Neal, Lecture Notes in Statistics **118** (1996).
- [19] J. Lampinen and A. Vehtari, Neural Networks **14** (2001) 257.

THE GPD PROGRAM AT COMPASS

A. Sandacz

on behalf of the COMPASS collaboration

National Centre for Nuclear Research, Warsaw, Poland

E-mail: sandacz@fuw.edu.pl

Abstract

The high energy polarised muon beam available at CERN, with positive or negative charge, makes COMPASS a unique place for GPD studies. The GPD program is a part of 'COMPASS-II proposal', which started to be realised in 2012. The new detectors, the large recoil proton detector and a (part of) large angle electromagnetic calorimeter that are essential for measurements of exclusive processes, were constructed and incorporated into the COMPASS setup. A short DVCS pilot run in 2012 was devoted to the commissioning of these new detectors followed by data taking. The COMPASS program of present and future GPD studies is reviewed and various observables for this program and expected accuracies are discussed.

1 Introduction

Generalised Parton Distributions (GPDs) [1–3] contain a wealth of information on the partonic structure of the nucleon. In particular, they allow a novel description of the nucleon as an extended object, sometimes referred to as 3-dimensional 'nucleon tomography' [4]. GPDs also allow access to such a fundamental property of the nucleon as the orbital angular momentum of quarks [2]. For reviews of the GPDs see Refs [5–7]. The mapping of the nucleon GPDs requires comprehensive experimental studies of hard processes, Deeply Virtual Compton Scattering (DVCS) and Hard Exclusive Meson Production (HEMP), in a broad kinematic range.

2 Brief overview of the program

The COMPASS GPD program encompasses the three following activities.

a) The analysis of exclusive vector meson production on polarised ${}^6\text{LiD}$ and NH_3 targets using the data from 2002-2011. Although no recoil proton detector was included in the used experimental setup, which is a disadvantage for measurements of exclusive processes, the analysis of these data allows to obtain valuable results that are sensitive to GPDs E and chiral-odd GPDs. At the moment these GPDs are still poorly constrained experimentally. This subject is covered at this conference in more detail in another contribution from COMPASS [8] and in a theoretical presentation [9].

b) Data taking and analysis of dedicated short 'DVCS test' runs in 2008 and 2009. The setup used in 2008/2009 for the meson spectroscopy with hadron beams (so called 'hadron setup') happened to be an excellent *prototype* to perform validation measurements for DVCS. First measurements of exclusive γ production on a 40 cm long liquid hydrogen (LH_2) target, with detection of the slow recoiling proton in the recoil proton detector (RPD), have been performed during the test runs using 160 GeV highly polarised μ^+ and μ^- beams from the M2 beam line

of the CERN SPS. They were obtained with the hadron setup, all the standard COMPASS tracking detectors, the ECAL1 and ECAL2 electromagnetic calorimeters for photon detection and appropriate triggers. An efficient selection of single photon events, and suppression of the background was possible by using the combined information from the forward COMPASS detectors and the RPD. One of the results from the DVCS test data is discussed in Sec. 3

c) The GPD program of COMPASS-II. This is a part of new 'COMPASS-II proposal' [10], which has been approved in December of 2010 and started to be realised in 2012. The GPD part will be devoted to measurements of both DVCS and HEMP with polarised μ^+ and μ^- beams and a liquid hydrogen target. The following time lines are assumed for the approved part of the proposal. In 2012 there were already performed measurements of pion and kaon polarisabilities using Primakoff reactions with hadron beam scattering off a nickel target. They were followed, still in 2012, by the commissioning and pilot run for DVCS. After a technical stop of the LHC in 2013 and the most part of 2014, the measurements of the Drell-Yan process in scattering of a pion beam on transversely polarised protons will start in late 2014 and will continue in 2015. They will be followed by two years (2016-2017) of data taking for the GPD program (Phase-1) with unpolarised protons accompanied by semi-inclusive DIS (SIDIS) measurements.

Measurements to be pursued by COMPASS-II after 2017 will be a subject of an addendum to the proposal. They will include the GPD E studies (Phase-2) using a transversely polarised target and a recoil proton detector. Also high statistics SIDIS data will be collected with transversely polarised protons and deuterons. Further, measurements of Drell-Yan on transversely polarised protons and deuterons, as well as on unpolarised protons and nuclear targets are foreseen. Hadron spectroscopy in diffractive and central production will be also performed, with an emphasis on a search for glueballs and exotic states.

3 Validation tests

From the theoretical view point DVCS is considered to be the cleanest process among those investigated experimentally, because effects of next-to-leading order and higher twist contributions are under theoretical control [11]. The competing Bethe-Heitler (BH) process, which is elastic lepton-nucleon scattering with a hard photon emitted by either the incoming or outgoing lepton, has a final state identical to that of DVCS so that both processes interfere at the level of amplitudes.

COMPASS offers the advantage to provide various kinematic domains where either BH or DVCS dominates. The collection of almost pure BH events at small x allows one to get an excellent reference yield and to control accurately the global efficiency of the apparatus. In contrast, the collection of an almost pure DVCS sample at larger x will allow the measurement of the x dependence of the t -slope of the cross section, which is related to the tomographic partonic image of the nucleon. In the intermediate domain, the DVCS contribution will be boosted by the BH process through the interference term. The dependence on ϕ , the azimuthal angle between lepton scattering plane and photon production plane, is a characteristic feature of the cross section [11].

The DVCS test runs in 2008 and 2009 with the 40 cm LH₂ target and the small RPD allowed to demonstrate the feasibility to measure exclusive single γ production at COMPASS. A way to identify the observed process, $\mu + p \rightarrow \mu' + \gamma + p'$, to which both the DVCS and Bethe-Heitler process contribute, is to look at the angle ϕ between the leptonic and hadronic planes. The observed distributions, after applying all cuts and selections and for $Q^2 > 1$ (GeV/c)², are displayed in Fig. 1 and compared to the predictions from the Monte Carlo simulations for the BH event yield. The Bethe-Heitler contribution shows a characteristic peak at $\phi \simeq 0$. The overall

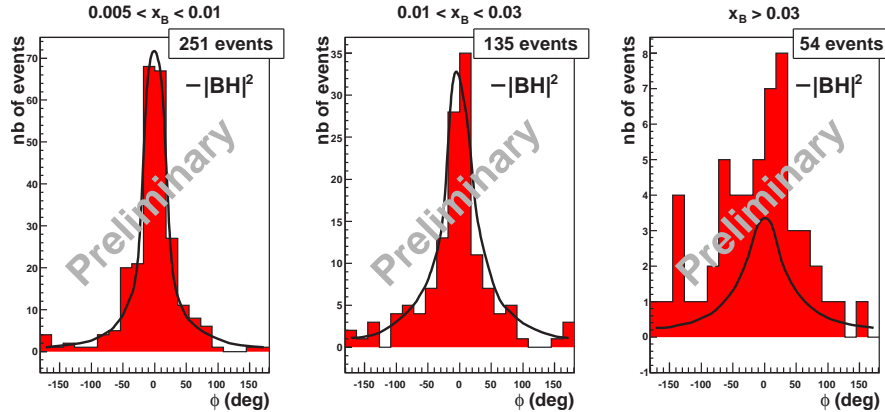


Figure 1: The distribution of the azimuthal angle ϕ for observed exclusive single photon production measured in the 2009 DVCS test run at COMPASS. The lines represent the expected BH event yield.

detection efficiency can be deduced from the relative normalisation of the two distributions for the low x -region dominated by BH. The global efficiency, is equal to 0.14 ± 0.05 in agreement with the value 0.1 assumed for the proposal [10]. It includes the detection efficiency, SPS and COMPASS availabilities, trigger efficiencies and dead time.

4 The proposed setup

The COMPASS apparatus [12] consists of a two-stage spectrometer comprising various tracking detectors, electromagnetic and hadron calorimeters, and particle identification detectors grouped around 2 dipole magnets SM1 and SM2 in conjunction with a longitudinally or transversely polarised target. By installing a large recoil proton detector around the new 2.5 m long LH_2 target COMPASS has been converted into a facility measuring exclusive reactions within a kinematic domain from $x \sim 0.01$ to ~ 0.1 , which cannot be explored at any other existing or planned facility in the near future.

The recoil proton detection is based on a ToF measurement between two barrels of 24 scintillator slats read out at both ends. The inner barrel (Ring A) of 2.75 m length with diameter of 50 cm and surrounding directly the target is made of slats of 4 mm thickness to allow low-momentum-proton detection down to about 260 MeV/c. The outer barrel (Ring B) is made of 3.6 m long and 5 cm thick slats and has a diameter of 2.2 m.

Given the time window of about 150 ns dictated by the dispersion in proton momentum, vertex position along the target and light propagation in the scintillators, a high counting rate in all elements of the RPD is expected, in particular in Ring A, where the dominant source is the production of δ -rays in the target material and walls. A line-shape analysis of the PMT signal is used to obtain precise ToF information and improve background rejection. Given the high counting rates, a dedicated readout called GANDALF based on a 1 GHz digitiser has been designed and implemented.

An entirely new calorimeter ECAL0 covering large photon angles is being constructed. Compared to the existing electromagnetic calorimeters, it will increase the accessible domain in x for DVCS and exclusive π^0 production, and therefore it will provide an overlap with HERMES and JLAB experiments. ECAL0 will provide an improved hermeticity for detection of exclusive events and contribute to reduce background to single-photon production that originates from π^0 and other decays. It will also have a significant impact on the uniformity of acceptance as a

function of angle ϕ [10].

ECAL0 will be located immediately downstream from the RPD. With the transverse size of $216 \times 216 \text{ cm}^2$ and a $80 \times 64 \text{ cm}^2$ central hole it will cover the polar angle range 0.15 - 0.6 mrad and the energy range from 0.2 GeV to 30 GeV. ECAL0 will consist of about 1700 cells arranged in 9-cell modules. Each cell will contain a stack of lead/scintillator plates that have the sampling 'shashlik' structure. The light collected and transported by WLS fibers will be detected by Multipixel Avalanche PhotoDiode (MAPD) detectors.

The central 56 ECAL0 modules, out of the total number of 194, were already calibrated with the beam and made available for the 2012 DVCS pilot run. The complete ECAL0 will be ready for the restart of the GPD program in 2016.

For the GPD program the data will be collected with polarised μ^+ and μ^- beams. Assuming in total 280 days of data taking, μ^+ beam flux of $4.6 \cdot 10^8 \mu$ per SPS spill and three times smaller flux for μ^- beam, a reasonable statistics for the DVCS process can be accumulated for Q^2 values up to 8 GeV^2 . The upper limit of Q^2 -range is driven by the luminosity, and the quoted number corresponds to the present beam intensity and spill structure. In the following sections we show projections for DVCS measurements with an unpolarised proton target (5.1 and 5.2) and with a transversely polarised ammonia target (5.3). For each target the integrated muon flux was taken the same as described above and the value of the global efficiency was assumed to be equal to 0.1.

5 Planned measurements

The complete GPD program at COMPASS-II will comprise the measurements of the DVCS cross section with polarised positive and negative muon beams and at the same time the measurements of exclusive production of a large set of mesons (ρ , ω , ϕ , π , η , ...). In the following we show selected projections for DVCS, while that for exclusive ρ^0 production is given in Ref. [8].

5.1 x -dependence of the t -slope of DVCS

The t -slope parameter $B(x)$ of the DVCS cross section $d\sigma/dt(x) \propto \exp(-B(x)|t|)$ can be obtained from the beam charge and spin sum of the cross sections after integration over ϕ and BH subtraction. The expected statistical accuracy of the measurements of $B(x)$ at COMPASS is shown in Fig. 2. The upper set of COMPASS points corresponds to the acceptance of the existing electromagnetic calorimeters, while the lower one is obtained assuming that in addition the new calorimeter ECAL0 is also available. The systematic errors are mainly due to uncertainties involved in the subtraction of the BH contribution. At $x > 0.02$ they are small compared to the statistical errors. For the simulations the simple ansatz $B(x) = B_0 + 2\alpha' \log(x_0/x)$ was used. As neither B_0 nor α' are known in the COMPASS kinematics, for the projections of expected uncertainties shown in Fig. 2 we chose the values $B_0 = 5.83 \text{ GeV}^2$, $\alpha' = 0.125$ and $x_0 = 0.0012$. The precise value of the t -slope parameter $B(x)$ in the COMPASS x -range will yield new and significant information in the context of the 'nucleon tomography' as it is expected in Ref. [13].

5.2 Beam charge and spin difference of cross sections

COMPASS is presently the only facility to provide polarised leptons with either charge: polarised μ^+ and μ^- beams. Note that with muon beams one naturally reverses both charge

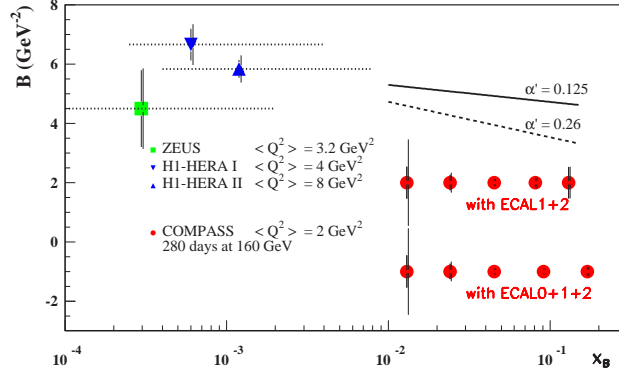


Figure 2: The x dependence of the fitted t -slope parameter B of the DVCS cross section. COMPASS projections for expected uncertainties are calculated for $1 < Q^2 < 8 \text{ GeV}^2$ and compared to HERA results for which the mean value $\langle Q^2 \rangle$ is in this range. The two curves in the right part of the figure represent $B(x)$ dependence for different values of α' .

and helicity at once. Practically μ^+ are selected with a polarisation of -0.8 and μ^- with a polarisation of $+0.8$. The difference and sum of cross sections for μ^+ and μ^- combined with the analysis of ϕ dependence allow us to isolate the real and imaginary parts of the leading twist-2 DVCS amplitude, and of higher twist contributions.

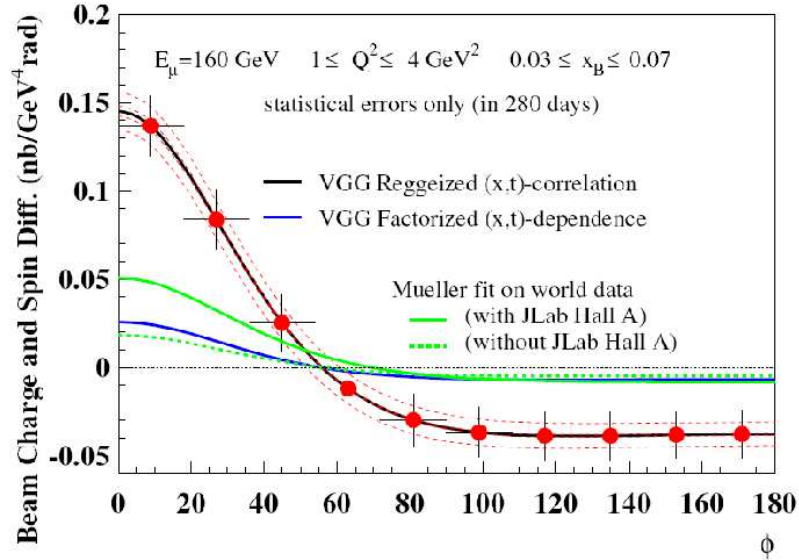


Figure 3: Projections for the beam charge and spin difference of cross sections measured at COMPASS for $0.03 \leq x \leq 0.07$ and $1 \leq Q^2 \leq 4 \text{ GeV}^2$. The red and blue curves correspond to two variants of the VGG model [14] while the green curves show predictions based on the first fits to the world data [15].

Fig. 3 shows the projected statistical accuracy for the beam charge and spin difference of cross section $\mathcal{D}_{CS,U}$ measured as a function of ϕ in a selected (x, Q^2) bin. The difference is defined as

$$\mathcal{D}_{CS,U} = d\sigma^{\leftarrow+} - d\sigma^{\rightarrow-}, \quad (1)$$

with arrows indicating the orientations of the longitudinal polarisation of the beams. The difference $\mathcal{D}_{CS,U}$ is sensitive to the real part of the DVCS amplitude which is a convolution of GPDs with the hard scattering kernel over the whole range of longitudinal momenta of exchanged

quarks. Therefore measurements of this asymmetry provide strong constraints on the models of GPD. Two of the curves shown in the figure are calculated using the 'VGG' GPD model [14]. As this model is meant to be applied mostly in the valence region, typically the value $\alpha' = 0.8$ is used in the 'reggeized' parameterisation of the correlated x, t dependence of GPDs. For comparison also the model result for the 'factorised' x, t dependence is shown, which corresponds to $\alpha' \approx 0.1$ in the reggeized ansatz. A theoretical development [15] exploiting dispersion relations for Compton form factors was successfully applied to describe DVCS observables at very small values of x typical for the HERA, and extended to include DVCS data from HERMES and JLAB. The prediction for COMPASS from this analysis are shown as additional curves.

As the overall expected data set from the GPD program for COMPASS will allow about 10 bins in x vs. Q^2 , each of them expected to contain statistics sufficient for stable fits of the ϕ dependence, a determination of the 2-dimensional x, Q^2 (or x, t) dependence will be possible for the various Fourier expansion coefficients c_n and s_n [11], thereby yielding information on the nucleon structure in terms of GPDs over a range in x . These data are expected to be very useful for future developments of reliable GPD models able to simultaneously describe the *full* x -range.

5.3 Predictions for the transverse target spin asymmetry

Transverse target spin asymmetries for exclusive photon production are important observables for studies of the GPD E , and for the determination of the role of the orbital momentum of quarks in the spin budget of the nucleon. The sensitivity of these asymmetries to the total angular momentum of u quarks, J_u , was estimated for the transversely polarised protons in a model dependent way in Ref. [16].

The transverse target spin asymmetries for the proton will be measured with the transversely polarised ammonia target, similar to the one used in the past by COMPASS. Two options are considered for the configuration of the target magnet and the RPD, each with a different impact on the range of measurable energy of the recoil proton.

The transverse spin dependent part of the cross sections will be obtained by subtracting the data with opposite values of the azimuthal angle ϕ_s , which is the angle between the lepton scattering plane and the target spin vector. In order to disentangle the $|DVCS|^2$ and the interference terms with the same azimuthal dependence, it is necessary to take data with both μ^+ and μ^- beams, because only in the difference and the sum of μ^+ and μ^- cross sections these terms become separated. Both asymmetries for the difference and the sum of μ^+ and μ^- of transverse spin dependent cross sections will be analysed. The difference (sum) asymmetry $A_{CS,T}^D$ ($A_{CS,T}^S$) is defined as the ratio of the μ^+ and μ^- cross section difference (sum) divided by the lepton charge-averaged, unpolarised cross section. Here CS indicates that both lepton charge and lepton spin are reversed between μ^+ and μ^- , and T is for the transverse target polarisation.

As an example, the results from the simulations of the expected statistical uncertainty of the asymmetry $A_{CS,T}^{D,\sin(\phi-\phi_s)\cos\phi}$ are shown in Fig. 4 as a function of $-t$, x and Q^2 for the two considered configurations of the target region. Here $\sin(\phi - \phi_s)\cos\phi$ indicates the type of azimuthal modulations. This asymmetry is an analogue of the asymmetry $A_{UT}^{\sin(\phi-\phi_s)\cos\phi}$ measured by HERMES with unpolarised electrons, also shown in the figure. Typical values of the statistical errors of $A_{CS,T}^{D,\sin(\phi-\phi_s)\cos\phi}$, as well as of the seven remaining asymmetries related to the twist-2 terms in the cross section, are expected to be ≈ 0.03 .

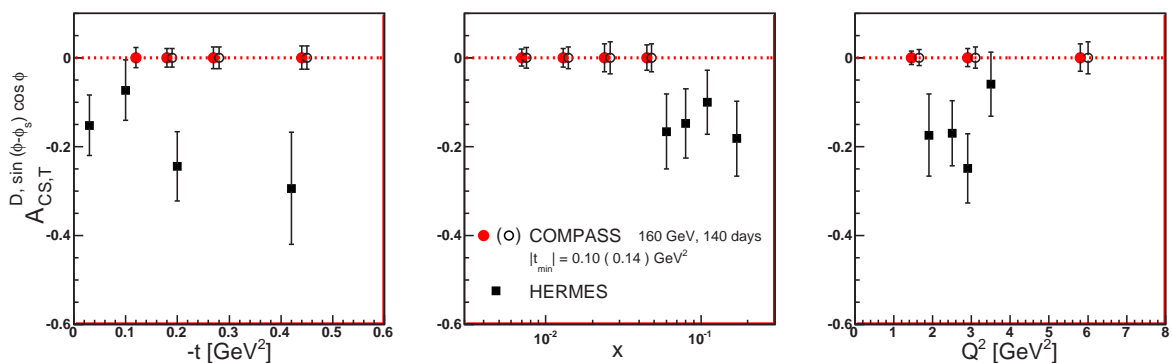


Figure 4: The expected statistical uncertainty of $A_{CS,T}^{D, \sin(\phi-\phi_s)\cos\phi}$ as a function of $-t$, x and Q^2 . Solid and open circles correspond to the simulations for the two considered configurations of the target region. Also shown is the asymmetry $A_{U,T}^{\sin(\phi-\phi_s)\cos\phi}$ measured by HERMES [16] with its statistical errors.

6 Summary

COMPASS has a great potential for the GPD physics. It is unique due to the availability of polarised μ^+ and μ^- and a favourable kinematic range in x . The GPD program required major upgrades of the existing apparatus. For measurement with the liquid hydrogen target (Phase-1) the large RPD was build and a part of the large angle electromagnetic calorimeter ECAL0 was already available for the DVCS pilot run in 2012. For measurements with transversely polarised protons (Phase-2), which are planned after 2017, a new recoil proton detector has to be incorporated into a large polarised target.

Investigation of GPDs with DVCS and HEMP on unpolarised protons will allow to determine the x -dependence for t -slopes of the differential cross sections. That is related to the transverse distribution of partons and the 'nucleon tomography'. Measurements of the beam charge and spin sum and difference of single- γ cross sections will give access to the real and imaginary parts of the DVCS amplitude, and will allow to further constrain GPDs H . Studies of exclusive production of vector mesons (ρ , ω , ϕ) will lead to the quark flavour and gluon separation for GPDs H , while that of exclusive π^0 production will provide constrains on the GPD \tilde{E} and on chiral-odd GPDs.

The main goal of future measurements with transversely polarised target is to constrain GPDs E , which are related to the orbital momentum of partons, and also to investigate the role of chiral-odd GPDs in exclusive meson production.

References

- [1] D. Mueller *et al*, Fortsch. Phys. **42** (1994) 101.
- [2] X. Ji, Phys. Rev. Lett. **78** (1997) 610; Phys. Rev. D **55** (1997) 7114.
- [3] A.V. Radyushkin, Phys. Lett. B **385** (1996) 333; Phys. Rev. D **56** (1997) 5524.
- [4] M. Burkardt, Phys. Rev. D **62** (2000) 071503; erratum-ibid. D **66** (2002) 119903; Int. J. Mod. Phys. A **18** (2003) 173; Phys. Lett. B **595** (2004) 245.
- [5] K. Goeke, M.V. Polyakov and M. Vanderhaegen, Prog. Part. in Nucl. Phys. **47** (2001) 401.
- [6] M. Diehl, *Generalized Parton Distributions*, DESY-thesis-2003-018, hep-ph/0307382.
- [7] A.V. Belitsky and A.V.Radyushkin, Phys. Rep. **418** (2005) 1.

- [8] P. Sznajder, *Exclusive meson production at COMPASS*, this conference.
- [9] S. Goloskokov, *Role of transversity in spin effects in meson leptonproduction*, this conference.
- [10] The COMPASS Collaboration, *COMPASS-II Proposal*, CERN-SPSC-2010-014, SPSC-P-340, May 17, 2010.
- [11] A.V. Belitsky, D. Müller and A. Kirchner, Nucl. Phys. B **629** (2002) 323.
- [12] P. Abbon *et al*, Nucl. Instr. Meth. A **577** (2007) 455.
- [13] M. Strikman and C. Weiss, Phys. Rev. D **69** (2004) 054012.
- [14] M. Vanderhaeghen, P.A.M. Guichon and M. Guidal, Phys. Rev. Lett. **80** (1998) 5064; Phys. Rev. D **60** (1999) 094017.
- [15] K. Kumericki and D. Mueller, Nucl. Phys. B **841** (2010) 1.
- [16] A. Airapetian *et al*, JHEP **06** (2008) 066.

SPIN OBSERVABLES IN ANTIHYPERON-HYPERON PRODUCTION WITH PANDA

K. Schönning^{1†}, E. Thomé¹ for the PANDA collaboration

(1) *Uppsala University, Sweden*

† *E-mail: karin.schonning@physics.uu.se*

Abstract

Hyperon production is an excellent probe of the strong interaction in the confinement domain. The spin observables provide a powerful tool in understanding the underlying physical processes. Seven polarisation parameters of the Ω baryon can be extracted from the decay angular distributions as recently derived by the Uppsala group. Simulation studies show that all strange and single charmed hyperon channels have great prospects with the PANDA experiment.

Hyperon production in $\bar{p}p \rightarrow \bar{Y}Y$ reaction gives important insights into strangeness and charm production. In this work, we consider single- and multi-strange and single-charmed hyperons. Their production from light-quark systems like $\bar{p}p$ implies processes where light quarks are replaced by heavier quarks. The relevant degrees of freedom of a certain process are given by its energy scale, which for strangeness production is governed by the mass of the strange quark, $m_s \approx 100$ MeV. This is close to the QCD cut-off, $\Lambda_{QCD} \approx 200$ MeV, where the strong coupling constant α_s grows so large that perturbative QCD breaks down. It is therefore unclear what the relevant degrees of freedom are: quarks and gluons, or hadrons? The production of strange hyperons therefore probes QCD in the region below the perturbative regime, *i.e.* the confinement domain, that we up to now know very little about. The scale of charm production is governed by $m_c \approx 1300$ MeV, more than ten times larger than m_s . The strong coupling constant in this region is $\alpha_s \approx 0.3$, just barely enough for a perturbative treatment to be valid. Comparing the production of strange hyperons with charmed could thus give important insights into the differences in the underlying physics at these two separate energy scales. Theoretical models describing hyperon production in $\bar{p}p \rightarrow \bar{Y}Y$ reactions are often based on the quark-gluon picture [1]. For strange hyperons, there are also kaon exchange models, where the production of single (multiple) strangeness hyperons are modeled by the single (multiple) exchange of a t-channel kaon [2].

Spin variables are often very powerful in discriminating between different theoretical models. The hyperon spin variables can be related to the spin of individual quarks. The Λ hyperon can be modeled by a ud spin 0 di-quark combined with an s -quark that carries the spin of the hyperon. A similar picture can be drawn for the Λ_c hyperon, and by comparing spin observables of Λ and Λ_c , we can learn about the role of spin degrees of freedom in the creation of s - and c -quarks.

Another interesting aspect of hyperons is CP violation. CP violation has been observed in meson decays, but so far never for baryons. For hyperons, CP violation observables are accessible *via* angular distributions of hyperon decay products.

All physics information about a quantum mechanical ensemble is contained within the density matrix ρ . In an expansion of hermitian matrices Q_M^L and polarisation parameters r_M^L [3], the density matrix of a particle of arbitrary spin j is given by

$$\rho = \frac{1}{2j+1}I + \sum_{L=1}^{2j} \frac{2j}{2j+1} \sum_{M=-L}^L Q_M^L r_M^L \quad (1)$$

where the first term denotes the unpolarised differential cross section I and the second the polarised part, containing the r_M^L parameters. L is the angular momentum and M its third component. In the case of spin $\frac{1}{2}$ particles, the Q_M^L are the Pauli matrices and the polarisation parameters correspond to the vector polarisations P_l , P_m and P_n . The indices are defined in the coordinate system in the left panel of Fig. 1. For particles produced from unpolarised particles in parity conserving processes, *e.g.* $\bar{p}p \rightarrow \bar{\Lambda}\Lambda$ with unpolarised p and \bar{p} , symmetries of the spin density matrix imply that $P_l = P_m = 0$. This gives non-zero polarisation only perpendicular to the production plane.

The weak, parity violating decay of the hyperons means that the decay products are preferentially emitted along the spin of the parent hadron. This makes the polarisation straight-forward to be measured experimentally. In the case of $\Lambda \rightarrow p\pi^-$, the angular distribution of the proton is related to the Λ polarisation by

$$I(\cos \theta_p) = \frac{1}{4\pi}(1 + \alpha_\Lambda P_n \cos \theta_p). \quad (2)$$

where $\alpha_\Lambda = 0.64$ [6] is the asymmetry parameter. Some hyperons decay into other hyperons, *e.g.* the Ξ baryons, as illustrated in the right panel of Fig. 1. In the $\Xi^- \rightarrow \Lambda\pi^-$, $\Lambda \rightarrow p\pi^-$ process, additional asymmetry parameters β and γ of the Ξ^- hyperon are accessible *via* the angular distribution of the protons [4]:

$$I(\theta_p, \phi_p) = \frac{1}{4\pi}(1 + \alpha_\Xi \alpha_\Lambda \cos \theta_p + \frac{\pi}{4} \alpha_\Lambda P_\Xi \sin \theta_p (\beta_\Xi \sin \phi_p - \gamma_\Xi \cos \phi_p)). \quad (3)$$

Comparing α and β for hyperons and antihyperons provides sensitive tests of CP violation.

Not only the polarisation of individual hyperons are of interest, but also their correlations. In Ref. [8], the derivation of the spin observables for the spin $\frac{1}{2}$ case is performed in detail. The spin observables of the $\bar{p}p \rightarrow \bar{Y}Y$ reaction can be written in terms of the momentum vectors of the final state antibaryon \bar{B} and baryon B from the \bar{Y} and Y decays:

$$I_0^{\bar{B}B} = \frac{I_0^{\bar{Y}Y}}{64\pi^3} \sum_{\mu,\nu=0}^3 \sum_{i,j=0}^3 \bar{\alpha} \alpha P_i^{\bar{p}} P_j^p \chi_{ij\mu\nu} \bar{k}_\mu k_\nu \quad (4)$$

where $I_0^{\bar{Y}Y}$ is the unpolarised angular distribution, α ($\bar{\alpha}$) denotes the asymmetry parameter of the Y (\bar{Y}) and P_j^p ($P_i^{\bar{p}}$) the polarisation of the initial state proton (antiproton) where $P_0 = 1$ by convention. Furthermore, k_ν (\bar{k}_μ) denotes the momentum vector of the final state decay baryon (antibaryon) and $\chi_{ij\mu\nu}$ the 256 spin observables. For the case of an unpolarised beam and an

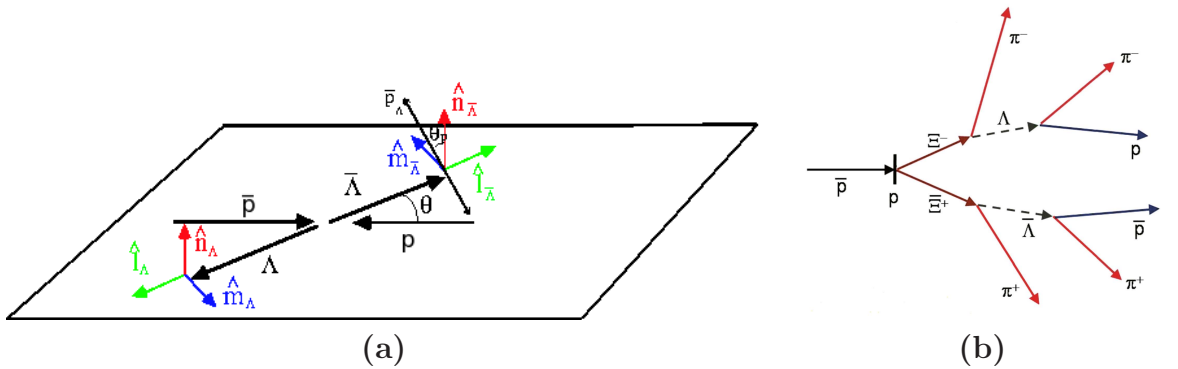


Figure 1: (a) Coord. system of $\bar{p}p \rightarrow \bar{Y}Y$. (b) The $\bar{p}p \rightarrow \bar{\Xi}\Xi$, $\Xi \rightarrow \Lambda\pi$, $\Lambda \rightarrow p\pi$ decay.

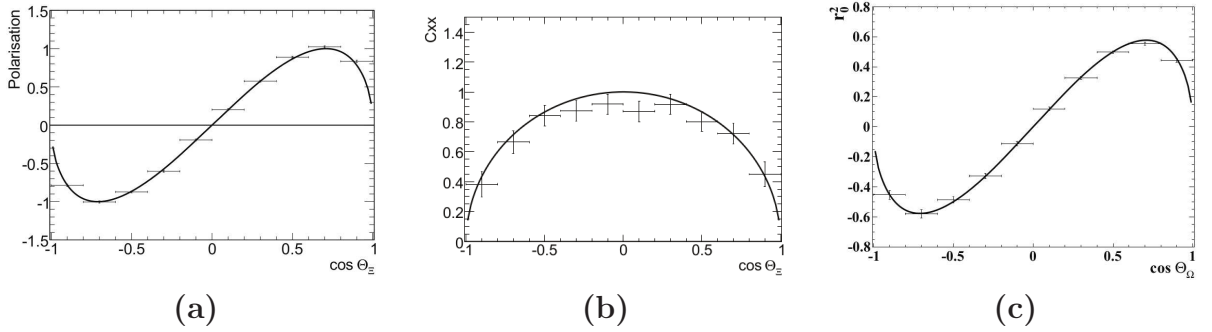


Figure 2: (a) The polarisation of the Ξ^- as a function of the Ξ^- scattering angle $\cos \theta_{\Xi}$. (b) The spin correlation in the x direction (m in Fig. 1) of the Ξ^+ and the Ξ^- . (c) The polarisation parameter r_0^2 of the Ω as a function of $\cos \theta_{\Omega}$. The points represent reconstructed values and the lines the input trigonometric functions.

unpolarised target, $i = j = 0$, giving sixteen accessible observables. Due to symmetries, only six of these are non-zero: the polarisations $P_{\bar{Y},\mu} = \chi_{00\mu 0}$ and $P_{Y,\nu} = \chi_{000\nu}$ and the spin correlations between the Y and the \bar{Y} , $C_{\mu\nu} = \chi_{00\mu\nu}$.

For spin $\frac{3}{2}$ hyperons, *e.g.* the Ω , the spin structure is more complicated. In this work, we consider the polarisation parameters of individual spin $\frac{3}{2}$ hyperons only, and no correlations. The L number in Eq. 1 can be 3, 2 or 1 in this case. This gives three Q_M^1 , five Q_M^2 and seven Q_M^3 matrices, all in all fifteen Q_M^L matrices with fifteen corresponding r_M^L parameters. The spin density matrix was derived in Ref. [5]. Using symmetries imposed by strong interaction, eight polarisation parameters were found to be zero.

In the case of $\Omega \rightarrow \Lambda K^-$, three parameters, r_0^2 , r_1^2 and r_2^2 , can be extracted from the angular distributions of the Λ , if one assumes that $\alpha_{\Omega} = 0$ in line with previous measurements [6]. For details, see [5]. More information about the remaining four non-zero polarisation parameters, r_{-1}^1 , r_{-1}^3 , r_{-2}^3 and r_{-3}^3 , is obtained by studying the combined angular distribution of the Λ hyperons from the Ω decay and the protons from the subsequent Λ decay, $I(\theta_{\Lambda}, \phi_{\Lambda}, \theta_p, \phi_p)$ [7].

The foreseen PANDA experiment at FAIR opens up new possibilities in hyperon physics. The antiproton beam from the HESR storage ring, operating in a momentum range between 1.5 GeV and 15 GeV, will interact with an internal hydrogen target. The PANDA experiment will have high luminosity and provide a near 4π acceptance featuring precise tracking and vertex reconstruction, sophisticated particle identification and calorimetry. For further details, see Ref. [9] and references therein. Simulation studies, described in Refs. [5, 10] show excellent prospects: high signal rate, low background rate and good detection efficiency over the full phase space for all single- and multi-strange and single-charmed hyperons. The studies also show that spin observables of all hyperon channels can be well reconstructed in PANDA. Some examples are shown in Fig. 2.

To summarise, the future PANDA experiment at FAIR has a unique opportunity to give new insights into the strong interaction in the confinement domain. Spin observables in antihyperon-hyperon production provide a powerful tool for this purpose. It will be possible to study the $\bar{p}p \rightarrow \bar{\Omega}^+ \Omega^-$ reaction for the first time and the seven non-zero polarisation parameters that have recently been derived by the Uppsala group.

References

- [1] M. Kohno and W. Weise, Phys. Lett. B. **179** (1986) 15; H.R. Rubinstein and H. Snellman, Phys. Lett. B. **165** (1985) 187; S. Furui and A. Faessler Nucl. Phys. A **486** (1987) 669; M. Burkardt and M. Dillig Phys. Rev. C **37** (1988) 1362; M.A. Alberg *et al.* Z. Phys. A **331** (1988) 207.
- [2] F. Tabakin and R.A. Eisenstein R.A. Phys. Rev. C **31** (1985) 1857; M. Kohno and W. Weise Phys. Lett. B. **179** (1986) 15; P. La France *et al.* Phys. Lett. B. **214** (1986) 317; R.G.E. Timmermans *et al.* Phys. Rev. D **45** (1990) 2288; J. Haidenbauer *et al.* Phys. Rev. C **46** (1992) 2516.
- [3] M.G. Doncel *et al.* Nucl. Phys B **38** (1972) 477; M.G. Doncel *et al.* Phys. Rev. D **7** (1973) 815.
- [4] W. Koch *Analysis of scattering and decay* ed. M. Nikolic, Gordon and Breach, new York-London-Paris (1968).
- [5] E. Thomé E. *Multi-Strange and Charmed Antihyperon-Hyperon Physics for PANDA* Ph. D. Thesis, Uppsala University (2012).
- [6] W.M. Yao *et al.* [Particle Data Group] *J. Phys. G* **33** (2006) 1.
- [7] E. Thomé *A Method for Measurement of Polarisation Parameters in the $\bar{p}p \rightarrow \bar{\Omega}^+ \Omega^-$ Reaction* (in preparation).
- [8] K. Paschke, Ph. D. Thesis, Carnegie Mellon University (2001).
- [9] PANDA collaboration, Technical Progress Report (2005).
- [10] S. Grape *Studies of PWO Crystals and Simulations of the $\bar{p}p \rightarrow \bar{\Lambda}\Lambda, \bar{\Lambda}\Sigma^0$ Reactions for the PANDA experiment* Ph.D. Thesis, Uppsala University (2009).

UNCERTAINTIES IN THE TRANSVERSE DOUBLE SPIN ASYMMETRIES DUE TO THE LUMINOSITY NORMALIZATION

D.N. Svirida^{1†} for the STAR Collaboration

(1) *Institute for Theoretical and Experimental Physics,
25 B. Cheremushkinskaya, Moscow 117218, Russia*

† *E-mail: Dmitry.Svirida@itep.ru*

Abstract

Double spin asymmetries A_{NN} and A_{SS} contain an angular independent term, which is effectively the cross section difference for certain spin combinations. The commonly used "square root formula", which allows to eliminate direct luminosity measurements, can not be applied in this case. Instead, precise luminosity monitor free of spin effects must be used in order to obtain meaningful numbers for the small values of the asymmetries.

Some theoretical estimates of the asymmetry uncertainties, introduced by the luminosity measurements are presented, including leading order influence and evaluation of most important NLO contributions. The results are illustrated by the example of double spin asymmetry analysis of polarized proton-proton elastic scattering data obtained by the STAR experiment at RHIC in the region of Coulomb Nuclear Interference. A method of justifying the spin independence of the luminosity monitor is discussed together with the evaluation of its residual uncertainties.

For the colliding beams of transversely polarized protons the angular distribution of the elastically scattered particles is described by the general formula:

$$2\pi \frac{d^2\sigma}{dt d\varphi} = \frac{d\sigma}{dt} (1 + (P_B + P_Y)A_N \cos \varphi + P_B P_Y (A_{NN} \cos^2 \varphi + A_{SS} \sin^2 \varphi)),$$

where P_B and P_Y are the signed values of the polarization of the two beams and the double spin term can be expressed in the form:

$$A_2(\varphi) = P_B P_Y ((A_{NN} + A_{SS})/2 + (A_{NN} - A_{SS})/2 \cdot \cos 2\varphi).$$

Thus, while $(A_{NN} - A_{SS})$ can be extracted from the angular distributions, $(A_{NN} + A_{SS})$ effectively manifests only as the cross-section difference for parallel and anti-parallel combinations of the beam spin directions. In this case the 'square root formula' [1] cannot be applied and one is bound to rely on normalized event counts, K^{BY} , for the extraction of the raw double spin asymmetries:

$$A_2(\varphi) = A_{2+} + A_{2-} \cos 2\varphi = \frac{(K^{++}(\varphi) + K^{--}(\varphi)) - (K^{+-}(\varphi) + K^{-+}(\varphi))}{(K^{++}(\varphi) + K^{--}(\varphi)) + (K^{+-}(\varphi) + K^{-+}(\varphi))}.$$

In this formula $K^{BY}(\varphi) = N^{BY}(\varphi)/L^{BY}$, N^{BY} are the event counts of the process under study for certain spin combinations in the two colliding beams, 'blue' and 'yellow', $B, Y = +$ or $-$, and L^{BY} are the counts of the luminosity monitor for these combinations.

For the luminosity studies, along with four 'natural' luminosity ratios $r^{BY} = 2L^{BY}/L$, three *independent* ratios were introduced, representing the relative parts of interactions with:

- spin '+' in the 'blue' beam $R_B = (L^{++} + L^{+-})/L$,
- spin '+' in the 'yellow' beam $R_Y = (L^{++} + L^{-+})/L$ and

- parallel spin $R_2 = (L^{++} + L^{--})/L$.

Here L is the total sum of the monitor counts for all spin combinations and simple relations hold between the two sets of ratios:

$$\begin{aligned} r^{++} &= R_2 + R_B + R_Y - 1 & r^{--} &= R_2 + 1 - R_B - R_Y \\ r^{+-} &= R_B + 1 - R_2 - R_Y & r^{-+} &= R_Y + 1 - R_2 - R_B \end{aligned} \quad (1)$$

According to the general rule, uncertainty on the double spin asymmetry is

$$\delta A_2 = \sqrt{(\delta R_2 \cdot \partial A_2 / \partial R_2)^2 + (\delta R_B \cdot \partial A_2 / \partial R_B)^2 + (\delta R_Y \cdot \partial A_2 / \partial R_Y)^2}$$

and thus the partial derivatives $\partial A_2 / \partial R_j$ are the subject of the further discussion.

Starting with the exact formula for the raw transverse double spin asymmetry

$$A_2 = \frac{\frac{N^{++}}{r^{++}} + \frac{N^{--}}{r^{--}} - \frac{N^{+-}}{r^{+-}} - \frac{N^{-+}}{r^{-+}}}{\frac{N^{++}}{r^{++}} + \frac{N^{--}}{r^{--}} + \frac{N^{+-}}{r^{+-}} + \frac{N^{-+}}{r^{-+}}} = \frac{D}{S} \quad (2)$$

one can get the derivatives in the following form:

$$\frac{\partial A_2}{\partial R_j} = \frac{S \cdot \frac{\partial D}{\partial R_j} - D \cdot \frac{\partial S}{\partial R_j}}{S^2} = \frac{\frac{\partial D}{\partial R_j} - A_2 \cdot \frac{\partial S}{\partial R_j}}{S} \approx - \sum_{B,Y=+,-} \pm \frac{N^{BY}}{(r^{BY})^2} \bigg/ \sum_{B,Y=+,-} \frac{N^{BY}}{r^{BY}} \quad (3)$$

Here we neglected the second term in the numerator because of typically very small values of A_2 and took into account that $\partial r^{BY} / \partial R_j$ is ± 1 as follows from (1). It is important that in the sums (3) only $\partial A_2 / \partial R_2$ has all four terms positive, while $\partial A_2 / \partial R_B$ and $\partial A_2 / \partial R_Y$ have equal number of '+' and '-' signs.

Leading order estimates can be made for the case of typical collider running conditions with all spin combinations equally filled $r^{BY} \approx r = 1/2$ and negligible spin asymmetries leading to $N^{++} \approx N^{--} \approx N^{+-} \approx N^{-+} \approx N$. In this case $\partial A_2 / \partial R_2 \approx -1/r = -2$, while the two other derivatives evaluate to 0.

To probe NLO behavior of this result, let us now assume that, as before, all r^{BY} are approximately equal, but the single spin asymmetry A_N is not negligible. Evaluation leads to an expression: $\partial A_2 / \partial R_B \approx -A_Y / r = -2 \cdot A_Y$ and, similarly, $\partial A_2 / \partial R_Y \approx -2 \cdot A_B$. Here A_Y and A_B are the raw single spin asymmetries obtained with only one, 'yellow' or 'blue', beam polarized and the values are below 0.025 as measured in [2].

Another NLO estimate arise with the assumption of 'one bunch missing' and negligible asymmetries. In this case $N^{BY} \sim r^{BY}$ and the resulting estimate is $\partial A_2 / \partial R_B = \pm \frac{2}{3} \cdot \frac{\Delta r}{r}$, where $\Delta r / r$ is the relative difference of the r ratio for the missing bunch combination from its average value of 1/2 and the sign depends on which particular combination is missing. Numerically, for typically 64 colliding bunches, this is 50 times smaller than $\partial A_2 / \partial R_2$. As for $\frac{\partial A_2}{\partial R_Y}$, it has the same value but either the same or opposite sign dependent on the missing combination.

The above estimates show that the uncertainty of the raw asymmetry A_2 is totally dominated by that of the double spin ratio R_2 and is connected to it by a simple equation: $\delta A_2 \approx 2 \cdot \delta R_2$. It is worth mentioning that it manifests as a shift in A_2 , not as a scaling factor, and does not depend on the azimuthal angle φ .

Addressing the issue of physics asymmetries A_{2+} and A_{2-} one should consider the definition (2) as a function of azimuthal angle φ . A_{2+} can be treated as the average of (2) over the full 2π range of φ . Thus all the above conclusions hold, moreover the single spin NLO effect averages out, and $\delta A_{2+} \approx 2 \cdot \delta R_2$. Since the uncertainty has the nature of a shift in A_2 , it is obvious that it will not influence A_{2-} in the leading order and $\delta A_{2-} \approx 0$. Special effort was made to make NLO estimates for A_{2-} which confirmed their very small values, see Tab. 1 for reference.

Table 1: Summary of the uncertainties in double spin asymmetries.

Observable	$\frac{\partial}{\partial R_2}$		$\frac{\partial}{\partial R_B}$		$\frac{\partial}{\partial R_Y}$	
	LO	NLO	LO	NLO	LO	NLO
$A_{2+} = P_B P_Y (A_{NN} + A_{SS})/2$	-2	-	0	$\pm \frac{2}{3} \cdot \frac{\Delta r}{r}$	0	$\pm \frac{2}{3} \cdot \frac{\Delta r}{r}$
$A_{2-} = P_B P_Y (A_{NN} - A_{SS})/2$	0	$-4A_{2-}(R_2 - \frac{1}{2})$	0	0	0	0

The presented mathematical estimates were used in the double spin analysis of the elastic proton-proton scattering data, obtained by the STAR collaboration in the region of Coulomb and nuclear interference at $\sqrt{s} = 200$ GeV. The setup and the event selection procedure is described in [2]. The above conclusions were checked by the calculation of numerical derivatives from the data and were fully confirmed by the resulting numbers. To obtain the final values of the systematic error in the double spin asymmetries due to the luminosity issues, the uncertainties in the normalization ratios δR_j should be estimated. The following discussion illustrates the reasons used for such estimates in the STAR detector environment.

Several STAR subsystems were investigated for monitoring purposes, and two of them were selected for most precise luminosity measurements. ZDCs [3] are the two zero degree calorimeters, located behind the beam bending magnets on both sides of the interaction point and sensitive to forward neutral particles. BBCs [4] are arrays of scintillator tiles surrounding the beam pipe on both sides of the STAR detector magnet.

An assumption was made that two or more different physics processes have the same double spin asymmetry only if it's zero in all of them. In other words, this means that the R_2 values obtained for these monitoring physics channels should be the same. Numerical estimates were based on the analysis of R_2 differences for each pair of compared processes.

First BBC and ZDC were compared as whole detectors and only coincidence of both arms was required in each of the subsystems. The difference ΔR_2 for the running period of this experiment was found to be $1.5 \cdot 10^{-3}$ and far beyond its statistical error of $3.5 \cdot 10^{-4}$. The checks were also made for a set of preceding runs with longitudinal polarization and much higher statistics, and the effect, though ~ 10 times smaller, was statistically significant as well. On the contrary, if random bunch polarization pattern was substituted for the previously mentioned tests, ΔR_2 became comparable with zero. This led to a conclusion that one or both of the two detectors feels double spin effects, but gave no hint which of them makes the best normalization source.

Access to the counts of individual small BBC tiles (see fig. 1a) as well as to any of their combinations provides a powerful tool to study subprocesses within BBC. Three variants of tile hit combinations were used to select substantially different physics conditions:

- exactly one hit in the 'inner' tiles: single particle at small angle;
- exactly one hit in the 'outer' tiles: single particle at twice this angle;
- more than 5 hits in one arm: large forward multiplicity.

In either case at least one hit was required in the opposite arm of the detector. The three channels were separately defined for each of the arms. 'Inner' and 'outer' tiles make two circles around the beam pipe so that the effect dependencies on the azimuthal angle could be checked. High multiplicity events comprise only a small portion of the distribution fig. 1b and are supposed to be evenly spread in azimuthal angle. For each of the three subprocesses the results of the east and west arms coincide well within statistical error and were arm-averaged to be further compared to the whole BBC coincidence count. The resulting ΔR_2 values were all comparable with zero and their spread allowed to estimate the residing R_2 uncertainty at the level of $\delta R_2 = 1.56 \cdot 10^{-4}$. We conclude after comparing different luminosity monitoring subsystems that most of the double

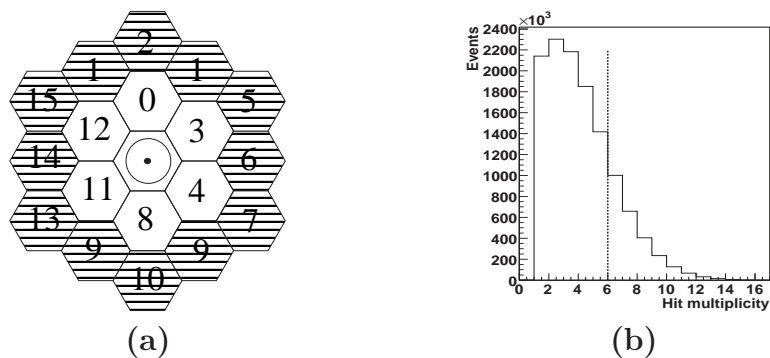


Figure 1: (a) STAR BBC small tiles: white – inner, hatched – outer; the central circle and the dot show the beam pipe and the beam. (b) Hit multiplicity in STAR BBC.

spin effect can be attributed to the ZDC, while the BBC as a whole can be used for precise monitoring at the quoted level of uncertainty.

Single spin ratios R_B and R_Y were also checked for the above physics channels and largest effects were found, as expected, for the tiles in the corresponding polarized beam fragmentation arm. The sign of the angular dependence is opposite for the inner and outer tiles which confirms the statement that the underlying physics is significantly different for the two subprocesses. The maximum ΔR_B and ΔR_Y values were only ~ 5 times larger than ΔR_2 and can be totally neglected in uncertainty estimates.

It was shown both by mathematical derivations and by numerical calculations that the most important role in double spin asymmetry calculations is played by the independent normalization ratio R_2 :

$$\delta[(A_{NN} + A_{SS})/2] \approx \frac{2}{P_B P_Y} \cdot \delta R_2 \quad \delta[(A_{NN} - A_{SS})/2] \approx 0. \quad (4)$$

The analysis of the uncertainty was illustrated by an example of STAR detector data obtained for the elastic scattering analysis in the CNI region [2]. By proper choice of the monitoring subsystem the level of uncertainty can be made as low as $\delta[(A_{NN} + A_{SS})/2] = 8.4 \cdot 10^{-4}$.

References

- [1] R. Battiston et al., Nucl. Instr. Meth. **A238** (1985) 35.
- [2] L. Adamczyk et al., STAR Collaboration, Phys. Lett. **B719** (2013) 62.
- [3] C. Adler et al., Nucl. Instr. and Meth. **A470** (2001) 488.
- [4] C.A. Whitten Jr. for the STAR Collaboration, AIP Conf. Proc. **V.980** (2008) 390.

EXCLUSIVE MESON PRODUCTION AT COMPASS

P. Sznajder
on behalf of the COMPASS Collaboration

National Centre for Nuclear Research, Warsaw
E-mail: pawel.sznajder@fuw.edu.pl

Abstract

Recent and planned measurements of exclusive meson production at COMPASS are discussed. New results on the transverse target spin asymmetries for exclusive ρ^0 production are presented. Some of these asymmetries are sensitive to the GPDs E , which are related to the orbital angular momentum of quarks. Other asymmetries are sensitive to the chiral-odd GPDs H_T , which are related to the transversity.

Introduction Hard exclusive electro- and muoproduction of mesons on nucleons has played an important role in studies of the hadron structure and recently gained renewed interest as it allows access to generalised parton distributions (GPDs). GPDs provide a novel and comprehensive description of the partonic structure of the nucleon and contain a wealth of new information. For instance GPDs give a description of the nucleon as an extended object, referred to as 3-dimensional nucleon tomography, and give access to the orbital angular momentum of quarks.

At leading twist, the chiral-even GPDs H and E are sufficient to describe exclusive vector meson production on a spin $1/2$ target. These GPDs are of special interest as they are related to the total angular momentum carried by partons in the nucleon [1]. GPDs H are well constrained in accessible x_{Bj} range by HERA, HERMES and JLAB data. Constraints on GPDs E are weak and come mainly from measurements of nucleon Pauli form factors. There exist also chiral-odd, "transverse" GPDs, in particular H_T and \bar{E}_T . It was shown [2] that they are required to describe exclusive π^+ production on transversely polarized protons.

In this paper we summarize recent measurement of the transverse target spin asymmetries for exclusive ρ^0 production. These observables are sensitive both to chiral-even and chiral-odd GPDs. The interpretation of results is done in the framework of the GPD model proposed by Goloskokov and Kroll [3]. Planned measurements of exclusive meson production, which are a part of the approved COMPASS-II proposal, are also discussed.

Formalism For exclusive meson production off a transversely polarized target five single (UT) and three double (LT) spin asymmetries can be defined. These are

$$\begin{aligned}
 A_{\text{UT}}^{\sin(\phi-\phi_s)} &= -\frac{\text{Im}(\sigma_{++}^{+-} + \epsilon\sigma_{00}^{+-})}{\sigma_0}, & A_{\text{LT}}^{\cos(\phi-\phi_s)} &= \frac{\text{Re}\sigma_{++}^{+-}}{\sigma_0}, & A_{\text{UT}}^{\sin(\phi+\phi_s)} &= -\frac{\text{Im}\sigma_{+-}^{+-}}{\sigma_0}, \\
 A_{\text{UT}}^{\sin(2\phi-\phi_s)} &= -\frac{\text{Im}\sigma_{+0}^{-+}}{\sigma_0}, & A_{\text{LT}}^{\cos(2\phi-\phi_s)} &= -\frac{\text{Re}\sigma_{+0}^{-+}}{\sigma_0}, & A_{\text{UT}}^{\sin(3\phi-\phi_s)} &= -\frac{\text{Im}\sigma_{+-}^{-+}}{\sigma_0}, \\
 A_{\text{UT}}^{\sin\phi_s} &= -\frac{\text{Im}\sigma_{+0}^{+-}}{\sigma_0}, & A_{\text{LT}}^{\cos\phi_s} &= -\frac{\text{Re}\sigma_{+0}^{+-}}{\sigma_0}. & &
 \end{aligned} \tag{1}$$

The photoabsorption cross sections or the interference terms σ_{mn}^{ij} are proportional to the bilinear combinations of the helicity amplitudes \mathcal{M} for the photoproduction subprocess $\gamma^*p \rightarrow \rho^0p$,

$$\sigma_{mn}^{ij} \propto \sum \mathcal{M}_{m'i',mi}^* \mathcal{M}_{m'i',nj}, \quad (2)$$

where the helicity of the virtual photon is denoted by $m, n = -1, 0, +1$ and the helicity of the initial-state proton is given by $i, j = -1/2, +1/2$. The sum runs over all spin combinations for the final state, given by the spin of the meson $m' = -1, 0, +1$ and the spin of the final-state proton $i' = -1/2, +1/2$. For brevity a dependence on the kinematic variables is omitted here.

The total unpolarized cross section, σ_0 , is given by the sum of cross sections for longitudinally, σ_L , and transversely, σ_T , polarized virtual photons,

$$\sigma_0 = \frac{1}{2} (\sigma_{++}^{++} + \sigma_{++}^{--}) + \epsilon \sigma_{00}^{++} = \sigma_L + \epsilon \sigma_T, \quad (3)$$

and the virtual photon polarization parameter can be approximated by $\epsilon \simeq (1-y)/(1-y+y^2/2)$.

Each asymmetry is related with specific modulation of the cross section in ϕ and ϕ_s angles indicated by the superscript. The angle ϕ is the azimuthal angle between the lepton plane, given by the momenta of the incoming and the scattered leptons, and the hadron plane, given by the momenta of the virtual photon and the meson. The angle ϕ_s is the azimuthal angle between the lepton plane and the spin direction of the target nucleon. Full formula for the cross section can be found in Ref. [4].

The asymmetries are extracted from data selected as described in the following.

Event selection To determine the transverse target spin asymmetries for exclusive production of ρ^0 meson the data taken in 2007 and 2010 with polarized protons were analysed. Each selected event contains a primary vertex with only one incoming and one outgoing muon track and with only two outgoing hadron tracks of opposite charges. It is assumed, that the outgoing hadrons are pions. The ρ^0 resonance is selected by the cut on the reconstructed invariant mass $0.5 \text{ GeV}/c^2 < M_{\pi\pi} < 1.1 \text{ GeV}/c^2$. Because recoiled target particle is undetected, the exclusivity is checked by the missing energy, $E_{miss} = ((p + q - v)^2 - p^2)/2M_p$, where M_p is the mass of the proton and p, q and v are the four-momenta of proton, photon and meson, respectively. For exclusive events the reconstructed values of E_{miss} are close to zero. To select these events the cut $-2.5 \text{ GeV} < E_{miss} < 2.5 \text{ GeV}$ is used. The cut $0.05 (\text{GeV}/c)^2 < p_T^2 < 0.5 (\text{GeV}/c)^2$ is also applied, where p_T^2 is the squared transverse momentum of ρ^0 with respect to the virtual photon direction. The lower cut on p_T^2 suppresses a contribution from the coherent production on the target nuclei, while the upper cut provides a further reduction of non-exclusive background.

The kinematic region is defined by the following cuts: $1 (\text{GeV}/c)^2 < Q^2 < 10 (\text{GeV}/c)^2$, $0.1 < y < 0.9$, $0.003 < x_{Bj} < 0.35$, $W > 5 \text{ GeV}/c^2$ (invariant mass of the virtual photon - nucleon system) and p_T^2 cuts as indicated above. The asymmetries were extracted using the 2D binned likelihood method after subtraction of remaining semi-inclusive background. Details of the analysis can be found in Ref. [5].

Results and discussion The mean values of measured asymmetries are shown in Fig. 1. They are given for the mean values of kinematic variables, $\langle Q^2 \rangle = 2.2 (\text{GeV}/c)^2$, $\langle x_{Bj} \rangle = 0.039$, $\langle p_T^2 \rangle = 0.2 (\text{GeV}/c)^2$, $\langle W \rangle = 8.1 \text{ GeV}/c^2$ and $\langle y \rangle = 0.24$, of the selected data set. The asymmetry $A_{UT}^{\sin\phi_s}$ was found to be $-0.019 \pm 0.008 (stat) \pm 0.003 (sys)$. All other asymmetries were found to be small, consistent with zero within experimental uncertainty. The asymmetries measured as a function of Q^2 , x_{Bj} or p_T^2 can be found in Ref. [5], together with a comparison with predictions of the GPD model proposed by Goloskokov and Kroll [4]. The model agrees well with our data.

For an interpretation of results in the framework of the model of particular interest are the following asymmetries, for which the dependence on the helicity amplitudes reads

$$\begin{aligned}
\sigma_0 A_{UT}^{\sin(\phi-\phi_s)} &= -2\text{Im} \left[\epsilon \mathcal{M}_{0-,0+}^* \mathcal{M}_{0+,0+} + \mathcal{M}_{+-,++}^* \mathcal{M}_{++,++} + \frac{1}{2} \mathcal{M}_{0-,++}^* \mathcal{M}_{0+,++} \right] , \\
\sigma_0 A_{UT}^{\sin(2\phi-\phi_s)} &= -\text{Im} \left[\mathcal{M}_{0+,++}^* \mathcal{M}_{0-,0+} \right] , \\
\sigma_0 A_{UT}^{\sin\phi_s} &= -\text{Im} \left[\mathcal{M}_{0-,++}^* \mathcal{M}_{0+,0+} - \mathcal{M}_{0+,++}^* \mathcal{M}_{0-,0+} \right] .
\end{aligned} \tag{4}$$

The dominant contribution from the $\gamma_L^* \rightarrow \rho_L^0$ transition is given by $\mathcal{M}_{0+,0+}$ and $\mathcal{M}_{0-,0+}$ helicity amplitudes, which are related to chiral-even GPDs H and E , respectively. The suppressed contribution from the $\gamma_T^* \rightarrow \rho_T^0$ transition is given by $\mathcal{M}_{++,++}$ and $\mathcal{M}_{+-,++}$ helicity amplitudes, which are also related to chiral-even GPDs. Description of the $\gamma_T^* \rightarrow \rho_L^0$ transition is possible by inclusion of chiral-odd GPDs H_T and \bar{E}_T , which are related to $\mathcal{M}_{0-,++}$ and $\mathcal{M}_{0+,++}$ helicity amplitudes, respectively. The $\gamma_L^* \rightarrow \rho_T^0$ and $\gamma_T^* \rightarrow \rho_{-T}^0$ transitions are known to be suppressed and are neglected in this formalism.

The vanishing $A_{UT}^{\sin(\phi-\phi_s)}$ asymmetry is interpreted as a cancellation of GPDs E^u and E^d due to their different sign but similar magnitude. A contribution of chiral-odd GPDs is negligible here, as one can see from comparison of calculations of Refs. [3] and [6]. The $A_{UT}^{\sin\phi_s}$ asymmetry represents an imaginary part of two bilinear products of helicity amplitudes. The first product is related with GPDs H and H_T , while the second one is related with GPDs E and \bar{E}_T . The latter product appears also in the $A_{UT}^{\sin(2\phi-\phi_s)}$ asymmetry. The $A_{UT}^{\sin\phi_s}$ asymmetry is found to be different from zero, while the $A_{UT}^{\sin(2\phi-\phi_s)}$ asymmetry vanishes. It implies non-negligible contribution of GPDs H_T . It is the first experimental evidence from hard exclusive ρ^0 production for the observation of these chiral-odd GPDs.

In preparation is a measurement of azimuthal asymmetries for exclusive ω production. The comparison between ρ^0 and ω is of special interest, since they probe different combinations of GPDs for u and d quarks. In particular, for ω the $A_{UT}^{\sin(\phi-\phi_s)}$ asymmetry is expected to be ≈ -0.1 [6].

Future measurements at COMPASS-II The GPD program at COMPASS will be continued. The COMPASS-II proposal [7] of the new measurements has been already approved by CERN. Measurement of exclusive meson production on unpolarized target is one of the main goals of this proposal, together with the measurement of DVCS. The data for the GPD program at COMPASS-II were successfully taken during 2012 pilot run and will be taken in 2016-2017.

For purpose of the GPD program at COMPASS-II the apparatus has been optimized for measurements of exclusive reactions. In particular, new equipment has been build, like a new large angle electromagnetic calorimeter to cover high x_{Bj} region for the DVCS measurement (ECAL0, 1/3 ready in 2012) and a 2.5 m long liquid hydrogen target surrounded by a 4 m long recoil proton detector (CAMERA).

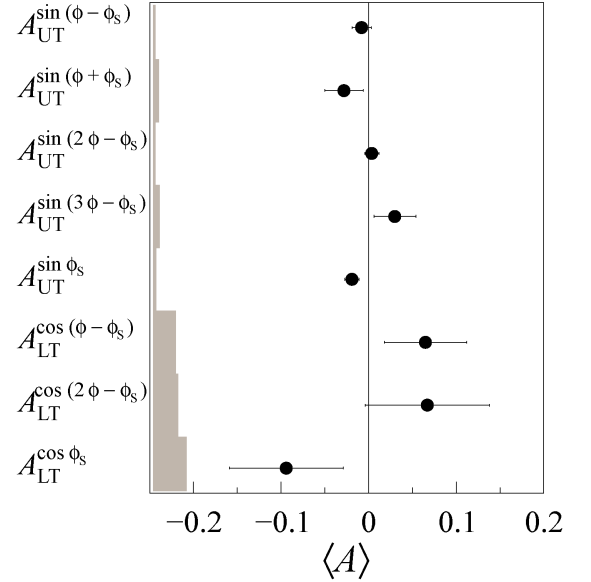


Figure 1: Mean values of azimuthal asymmetries for a transversely polarized proton target. The error bars (left bands) represent the statistical (systematic) uncertainties. Mean values of kinematic variables are indicated in the text.

For the COMPASS-II proposal projections of expected results were made. One of the projections was made to evaluate expected precision of the measurement of slope b of Mandelstam variable t distribution as a function of x_{Bj} for exclusive ρ^0 meson production. The slope is related to the transverse size of the nucleon and thus it can be used for the nucleon tomography. The projection of measurement of slope in four bins of Q^2 for 2016-2017, together with existing data points from ZEUS in a similar Q^2 range, is shown in Fig. 2. In 2012 pilot run $1/10$ expected statistics from 2016-2017 was collected.

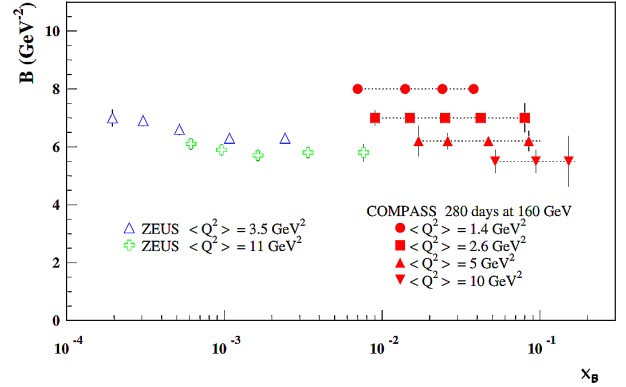


Figure 2: The projection of measurement of slope b for 2016-2017. Also existing data points from ZEUS in a similar Q^2 range are shown.

References

- [1] X. Ji, Phys. Rev. Lett. **78** (1997) 610.
- [2] S.V. Goloskokov and P. Kroll, Eur. Phys. J. **C65** (2010) 137.
- [3] S.V. Goloskokov and P. Kroll, submitted to Eur. Phys. J. C [arXiv:1310.1472].
- [4] M. Diehl and S. Sapeta, Eur. Phys. J. **C41** (2005) 515.
- [5] The COMPASS Collaboration, submitted to Phys. Lett. B [arXiv:1310.1454].
- [6] S.V. Goloskokov and P. Kroll, Eur. Phys. J. **C59** (2009) 809.
- [7] The COMPASS Collaboration, CERN-SPSC-2010-014.

**SPIN ASYMMETRY IN FORWARD POLARIZED pp SCATTERING
AND A BRIEF SUMMARY FROM WORKSHOP ON
"HIGH-ENERGY SCATTERING AT ZERO DEGREE"**

K. Tanida

*Department of Physics and Astronomy, Seoul National University, Seoul 151-742, Korea
E-mail: tanida@phya.snu.ac.kr*

Abstract

A brief summary of the "High-Energy Scattering at Zero Degree", held in Nagoya, Japan, in March 2013 is presented. This workshop focused on high energy interaction in very forward region, which intersects fields of high-energy physics, nuclear physics, and cosmic-ray physics. In particular, single-spin asymmetry (A_N) of very forward neutron in transversely polarized proton collision is discussed as a specific topic related to spin. Energy (\sqrt{s}) and transverse momentum (p_T) dependence of A_N is measured for \sqrt{s} from 62 to 500 GeV. The observed asymmetry linearly increases with p_T up to $\simeq 0.3$ GeV/c. On the other hand, \sqrt{s} dependence, which shows higher asymmetry for higher \sqrt{s} , can be interpreted as due to p_T dependence.

1 A brief summary on workshop "High-Energy Scattering at Zero Degree"

High energy scattering at zero degree is of interest from 3 major fields of physics, namely, particle physics, nuclear physics, and cosmic-ray physics. In particle physics, scattering mechanisms, such as Regge theory with Pomerons, in the region where perturbative QCD is not applicable, are the main interest. In addition, in some experiments, forward scattering are used to calibrate absolute luminosity. Nuclear physicists are mostly interested in properties of nuclear matter by looking at modifications of forward cross sections and energy spectra of produced particles. The main interest of the cosmic-ray field is energy calibration of high energy cosmic-ray from sampling measurements on the earth surface. Presumably, uncertainty of energy scale is the most significant uncertainty in the cosmic-ray flux measurements, and precise measurements on forward scattering are being awaited for to construct reliable interaction models.

In this situation, we had the workshop on "High-Energy Scattering at Zero Degree" (HESZ2013) in Nagoya, Japan, in March 2013. The workshop focused on the following 5 topics:

- Diffraction and very forward p-p and p-A scattering.
- Forward and ultra peripheral A-A scattering.
- Spin asymmetry in forward polarized p-p scattering.
- High energy cosmic ray interaction models.
- QCD aspects in very forward scattering.

There were about 50 participants and 23 talks from the three fields all over the world, and very active discussions were exchanged despite the difference of common knowledge and technical terms. For more information, details of the workshop and used slides can be found in the workshop web-site [1].

Spin related phenomena are rather a new topic in very forward scattering, and there were only two experimental reports, with both from Relativistic Heavy Ion collider (RHIC). One was given by Dr. Lee of Brookhaven National Laboratory (BNL) on "Diffraction at RHIC" [2]. He reported spin asymmetries of proton-proton elastic scattering in the region where Coulomb force interferes with nuclear force, and some other results of measurements in the forward region. The other talk was given by the author on the spin asymmetry of neutrons near zero degree. The content of the talk is discussed hereafter.

2 Single-spin Asymmetry of Very Forward Neutron in Polarized Proton-Proton Collision

Introduction. Needless to say, spin-related measurements played important roles in particle and nuclear physics. (You can find many examples in these proceedings.) For example, single-spin left-right asymmetry, A_N arises from interference of spin-flip and non-flip amplitudes, and thus gives information on both amplitudes and their relative phase. In the case of very forward neutron production, cross-sections measured at ISR [3, 4] can be well reproduced by one-pion exchange (OPE) mechanism where spin-flip amplitude dominates [5, 6]. Here, if there is another mechanism that gives a spin-non-flip amplitude as small as 10% of the spin-flip amplitude, it is hardly seen in the cross-section because, in the cross-section, spin-non-flip amplitude yields only a 1% effect. However, A_N can be as large as an order of 10%, which is rather easy to measure. Therefore, A_N is sensitive to mechanisms that may be hidden under major OPE mechanism. In this sense, it is interesting to see if the OPE mechanism can explain A_N as well, especially its transverse momentum (p_T) dependence. Here we report the \sqrt{s} and p_T dependence of A_N for very forward neutron in transversely polarized proton collisions with \sqrt{s} from 62 to 500 GeV.

Experimental Setup. A plan view of the experimental setup for very forward neutron measurement at the PHENIX experiment in RHIC is shown in Figure 1. Neutrons have been measured by Zero-Degree Calorimeter (ZDC) with a position-sensitive Shower-Max Detector

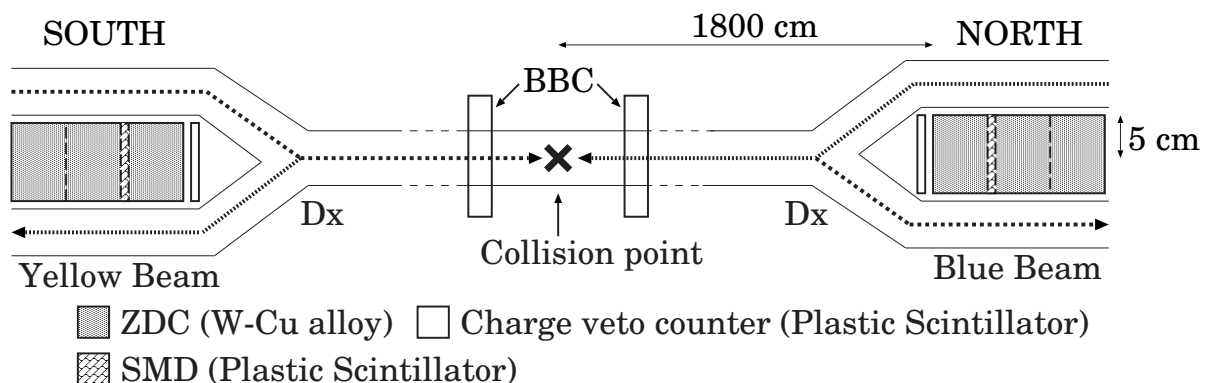


Figure 1: A plan view of the experimental setup at PHENIX (not to scale). Principle components for the leading neutron measurement are shown.

(SMD) [7]. ZDC is composed of copper-tungsten alloy absorbers with optical fibers and each module has 1.7 interaction length (λ_I). A photomultiplier collects Cherenkov lights via the optical fibers in each module. Three ZDCs are located in series (5.1 λ_I in total) at ± 1800 cm away from the collision point within the small acceptance, covering 10 cm in the trasverse plane. SMD consists of x - y scintillator strip hodoscopes and is inserted between the first and second ZDC modules at the position of maximum hadronic shower approximately. The x -coordinate (horizontal) is sampled by 7 scintillator strips of 15 mm width, while the y -coordinate (vertical) is sampled by 8 strips of 20 mm width, tilted by 45 degrees. These detectors are located down stream of the RHIC-DX magnet so that charged particles from collisions are expected to be bent away. A forward scintillation counter, covering 10×12 cm, has been installed in front of the ZDC to remove charged particle backgrounds.

The data was collected by two sets of triggers for the neutron measurement. One is the ZDC trigger for neutron inclusive measurements by requiring energy deposit in either side of the ZDC (the north side or the south side) above 5 GeV. The other is a coincidence trigger of the ZDC trigger with hits in Beam Beam Counter (BBC), which consists of 64 sets of quartz Cherenkov counters covering $\pm(3.0-3.9)$ in pseudorapidity and 2π in azimuthal angle.

An absolute scale for the energy measurement is determined by the 100 GeV single neutron peak from peripheral heavy ion collisions. The response of the detectors was studied by GEANT3 with GHEISHA, which well reproduced the response of the prototype ZDC. The energy resolution obtained from the simulation can be described by $\Delta E/E = 65/\sqrt{E} \text{ (GeV)} + 15(\%)$, which is consistent with the observed width of one neutron peak at 100 GeV.

Neutron position is reconstructed by the energy deposit in SMD scintillators with the centroid method. The position resolutions were estimated by the simulation to be around 1 cm for the neutron energy at 100 GeV. The reliability of the position measurement was checked by comparing hadron shower shapes of the real and simulation data. Then, based on the obtained position and neutron energy (E_n), p_T was calculated as $p_T = E_n \sin \theta_n \sim E_n r/d$, where θ_n is the reaction angle, r is the distance from the beam center to the hit position at ZDC, and $d = 1800$ cm is the distance from the collision point to the ZDC. The single-spin asymmetry, A_N , was calculated using the square-root-formula. Smearing due to finite position resolution and finite acceptance is corrected for using simulations.

Results and Discussions. First, the cross section was measured at $\sqrt{s} = 200$ GeV, and the obtained x_F spectrum [8] was consistent with ISR results at lower energies [3, 4]. In the same paper, x_F dependence of A_N was also reported to be not significant.

A_N for forward neutrons at three different energies are plotted in Figure 2, as functions of reaction angle. A_N for backward neutrons are all consistent with zero. The observed \sqrt{s} dependence could be interpreted as p_T dependence, as shown in Figure 3, which shows a linear increase of A_N with respect to p_T . As p_T is proportional to \sqrt{s} for the same θ_n and x_F , the asymmetry could be larger for higher \sqrt{s} even if there would be no actual \sqrt{s} dependence.

On the theory side, Kopeliovich *et al.* give their calculation for $\sqrt{s} = 200$ GeV based on an interference of Reggeons with OPE [9]. When they consider OPE only, small asymmetries ($|A_N| < 0.01$) for $p_T < 0.2$ GeV/ c which is the range of our measurement at $\sqrt{s} = 200$ GeV, are obtained and thus the present result is not reproduced. However, once they take into account other Reggeons such as a_1 , and their interference with OPE, the present result can be nicely explained. This indicates usefulness of A_N to pick up small contributions beyond the OPE mechanism.

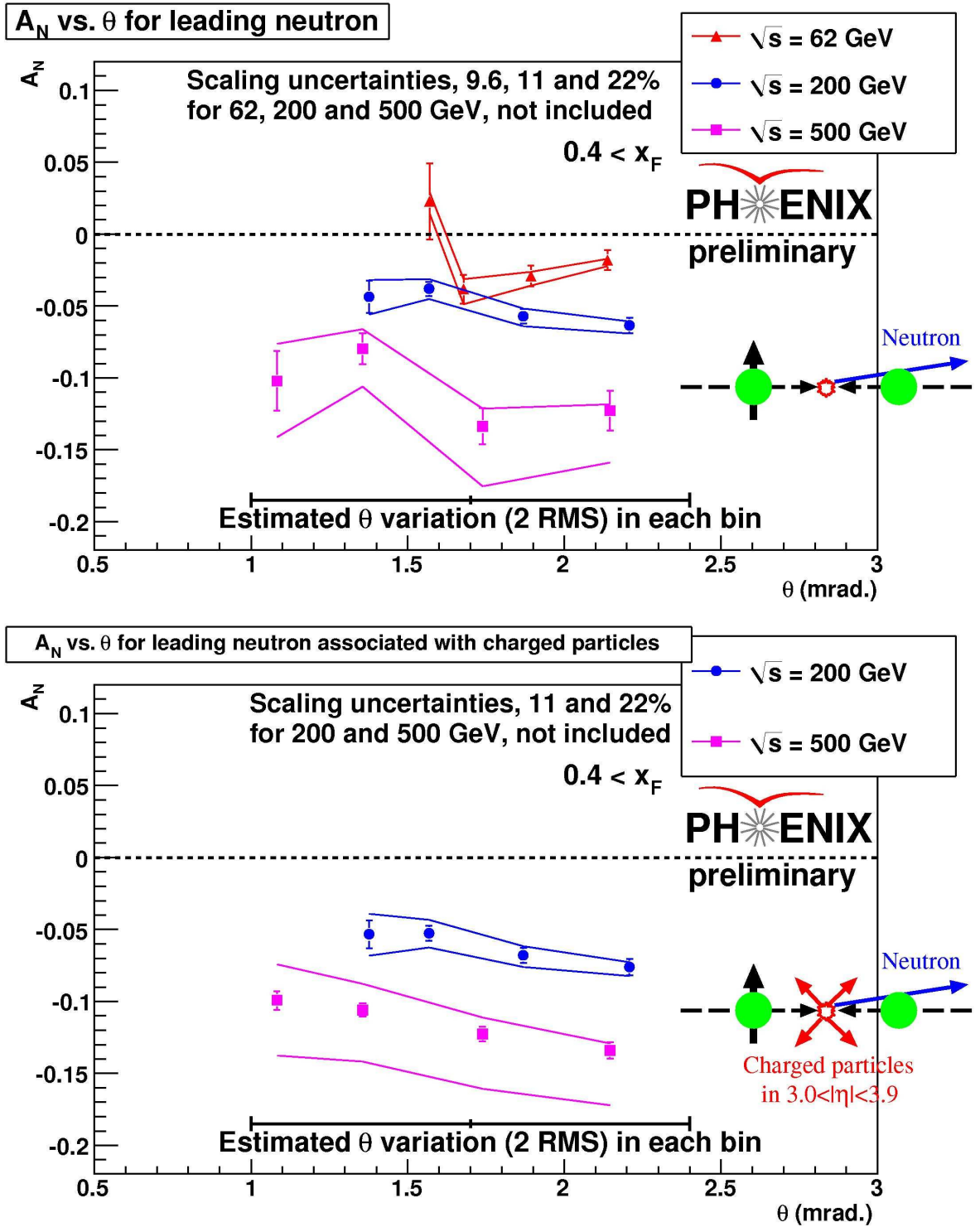


Figure 2: The measured asymmetries for forward neutrons as functions of reaction angle. Top: for inclusive neutrons (ZDC single trigger). Bottom: for neutrons with associated particles (ZDC-BBC coincidence trigger). Neutrons with $x_F > 0.4$ are selected. For the horizontal axis, the plotted positions give the average angles and their variation is also plotted as horizontal bars.

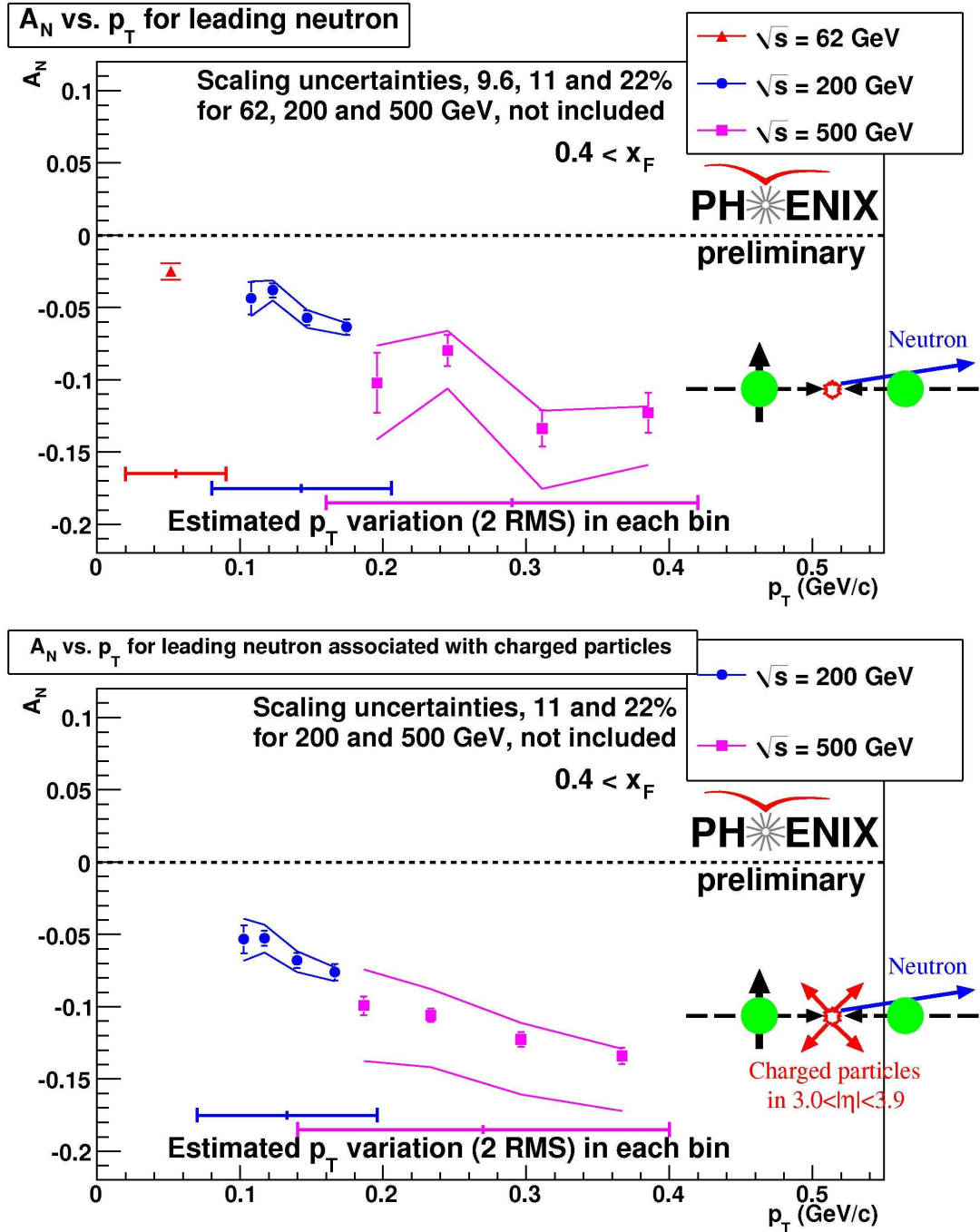


Figure 3: The measured asymmetries for forward neutrons as functions of p_T . Top: for inclusive neutrons (ZDC single trigger). Bottom: for neutrons with associated particles (ZDC-BBC coincidence trigger). Neutrons with $x_F > 0.4$ are selected. For the horizontal axis, the plotted positions give the average p_T and its variation is also plotted as horizontal bars.

Acknowledgments. The author would like to thank the support by Basic Research Grant No. 2013R1A1A1013046 from National Research Foundation and WCU program of the Ministry Education Science and Technology in Korea.

References

- [1] <http://www.gcoe.phys.nagoya-u.ac.jp/hesz2013/>
- [2] http://www.gcoe.phys.nagoya-u.ac.jp/hesz2013/files/HESZ2013_03Mar_06_Lee.pdf
- [3] W. Flauger *et al.*, Nucl. Phys. **B109** (1976) 347.
- [4] J. Engler *et al.*, Nucl. Phys. **B84** (1975) 70.
- [5] N.N. Nikolaev, W. Schafer, A. Szczurek and J. Speth, Phys. Rev. D **60** (1999) 014004.
- [6] U. D'Alesio and H.J. Pirner, Eur. Phys. J. A **7** (2000) 109.
- [7] C. Adler *et al.*, Nucl. Instr. Meth. A **470** (2001) 488.
- [8] A. Adare *et al.* (PHENIX Collaboration), Phys. Rev. D **88** (2013) 032006.
- [9] B.Z. Kopeliovich, I.K. Potashnikova, I. Schmidt and J. Soffer Phys. Rev. D **84**, (2011) 114012.

RECENT SPIN RESULTS FROM THE STAR EXPERIMENT AT RHIC

Qinghua Xu[†] for the STAR Collaboration

*School of Physics, Key Laboratory of Particle Physics and Particle Irradiation (MoE),
Shandong University, Shandong 250100, China*

[†] *E-mail: xugh@sdu.edu.cn*

Abstract

The STAR experiment at the RHIC (Relativistic Heavy Ion Collider) at Brookhaven National Laboratory is running polarized proton-proton collisions at $\sqrt{s}=200$ GeV and 500 GeV. The main goal of the RHIC spin physics program is to gain a deeper insight into the spin structure of the nucleon. We will give an overview of recent spin results from STAR experiment, in particular the study of gluon polarization via jet/hadron production and the sea quark polarization via W boson production in longitudinally polarized proton-proton collisions at RHIC. The recent results on transverse single spin asymmetries at STAR will also be given.

1 Introduction

The spin structure of the nucleon has been one of the hot topics in QCD since the late 1980s when polarized lepton-nucleon deep-inelastic scattering (DIS) experiments revealed that only a small portion (20~30%) of the nucleon spin is carried by the spins of quarks and anti-quarks. In the past three decades, a lot of efforts both experimentally and theoretically have been made to elucidate the contribution of gluon spin and the flavor separated contribution of quark and anti-quark, as well as the contribution of orbital angular momentum of the quarks and gluons. The Relativistic Heavy Ion Collider (RHIC) at Brookhaven National Laboratory is the first high energy polarized hadron-hadron collider in the world. The polarized proton-proton collisions at a center-of-mass of energy of 200 GeV and 500 GeV at RHIC provide a unique way to gain new insights into the proton spin structure, especially the gluon polarization and sea quark polarization in the nucleon. The STAR experiment at RHIC is carrying out a rich spin program using longitudinally polarized and transversely polarized proton-proton collisions.

On the precise determination of gluon polarization (Δg), the STAR detector is well suited for the reconstruction of various final states including jets, identified hadrons (π^0 , π^\pm), electron/positrons and photons, which allows for measurements of different gluon involved processes. The recent STAR results of the inclusive jet double spin asymmetry, provides for the first time an evidence of a non-zero gluon polarization in the range $0.05 < x < 0.2$, and the magnitude is even comparable to the total quark spin contribution.

Another main objective of the STAR spin program is the flavor-separation of quark and anti-quark spin to the proton spin via W boson production in polarized proton-proton collisions at $\sqrt{s} = 500$ GeV. The parity violating nature of W boson provides a unique and clean way of measuring the anti-u and anti-d quark polarization, without the involvement of hadronization as in the semi-inclusive DIS process. The recent results of W boson single spin asymmetry from the 2012 data at STAR will be discussed, which provide new constraints to light sea quark polarization.

On the transverse spin program side, STAR is pursuing to understand the origin of large transverse single spin asymmetry (A_N) observed both in hadron and lepton induced reactions, as well as to gain the knowledge of transverse spin structure of proton, i.e., quark transversity. For the A_N study, we measure the asymmetries for identified hadron (π^0, η) and jet, which provide sensitivity for the underlying mechanism of Sivers and Collins function, as well as the high twist effects. With respect to transversity extraction, STAR has been performing measurements of the asymmetries associated with Collins and Interference Fragmentation Functions (IFF).

2 Gluon polarization ΔG measurements

In proton-proton collisions, the gluon polarization can be accessed with strongly interacting probes including jet or hadron production by measuring the double spin asymmetries (A_{LL}),

$$A_{LL} = \frac{1}{P_1 P_2} \frac{N^{++} - RN^{+-}}{N^{++} + RN^{+-}}, \quad (1)$$

where P_1 and P_2 are the beam polarizations, $R = \mathcal{L}^{++}/\mathcal{L}^{+-}$ is the ratio of luminosities, and N^{++} (N^{+-}) are the yields of jet or hadron for equal (opposite) helicity beams.

At STAR, jets were reconstructed from charged tracks with $|\eta| < 1.3$ measured in the Time Projection Chamber (TPC) and energy deposits in the Barrel Electromagnetic Calorimeter (BEMC) with towers at $|\eta| < 1$ and End-cap Electromagnetic Calorimeter (EEMC) at $1 < \eta < 2$. The jet reconstruction was done with midpoint cone algorithm and also checked with anti-kt algorithm. The jet cross section and the first A_{LL} measurements for inclusive jets has been done with 2003 and 2004 data at STAR [1], and updates with higher precision using 2005 and 2006 data have also been

published [2, 3]. We also measured the double spin asymmetries for π^0 at $|\eta| < 1$ [4] and near-forward rapidity at $1 < \eta < 2$ [5]. The early A_{LL} results were included in the DSSV [6] QCD global analysis to provide information for the gluon polarization, and ruled out large positive and negative scenarios with a small value of Δg in the range of $0.05 < x < 0.2$.

After the 2006 run, several improvements at STAR including larger jet trigger efficiency and faster data acquisition system enabled us to improve the A_{LL} precision significantly during the 2009 run. Figure 1 shows the A_{LL} results for inclusive jet versus jet p_T for the 2006 ($-0.7 < \eta < 0.9$) [3] and 2009 ($|\eta| < 1$) [7] data at STAR, where the theoretical predictions are also shown for comparison. The GRSV [9] model is a previous global analysis for polarized parton densities that only included DIS data. The DSSV [6] model, in addition to DIS and SIDIS data, also incorporates RHIC polarized proton-proton data before 2009. The STAR data fall between the predictions of DSSV and GRSV-STD. Compared with 2006 data, the 2009 data are about four time more precise in low- p_T bins and a factor of three in high- p_T bins. The real impact of these data on constraining gluon polarization can be seen from the recently updated DSSV global analysis, and the magenta curve [10] provides a very good description of the 2009 results,

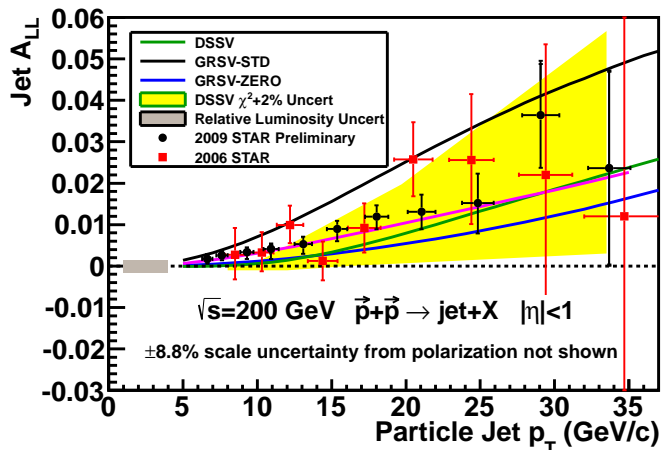


Figure 1: STAR 2009 (black circles) inclusive jet A_{LL} vs. jet p_T for $|\eta| < 1$ in pp collisions at 200 GeV.

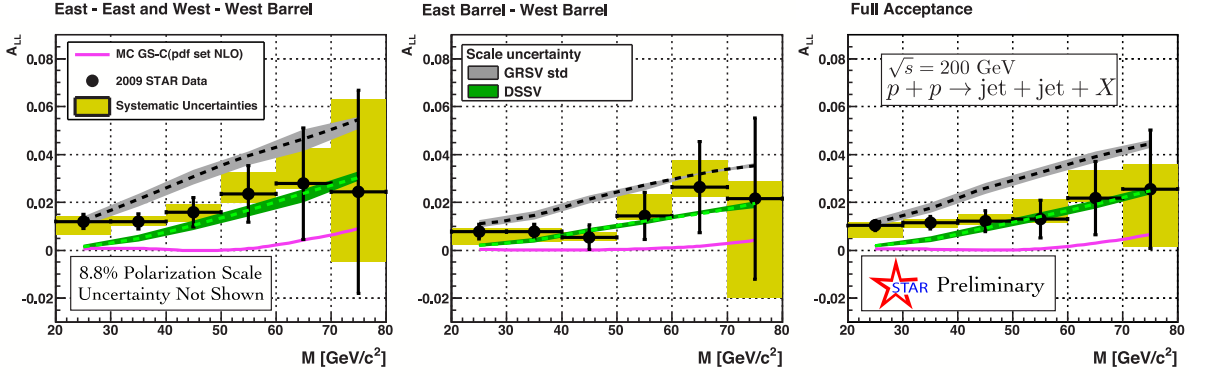


Figure 2: STAR 2009 di-jet A_{LL} for three different η regions for di-jet production as a function of invariant mass M .

corresponding to a truncated integral of $\Delta g(x) \sim 0.13$ over the range $0.05 < x < 0.2$ [10]. A full global analysis incorporating the 2009 A_{LL} results from the STAR inclusive jet channel and PHENIX π^0 channel, suggests a consistent sizable value of the gluon polarization at the level of $\int_{0.05}^{0.2} \Delta g dx (Q^2 = 10 \text{ GeV}^2) = 0.1^{+0.06}_{-0.07}$ [11], which is of similar magnitude as the total quark spin contribution itself.

Di-jet production will allow a better constraint of the partonic kinematics to determine the shape of the gluon polarization. The partonic Bjorken- x of the incoming partons can be extracted at leading order from the pseudo-rapidity plus the transverse momentum of the di-jets. The wide acceptance of the STAR experiment permits reconstruction of di-jet events with different topological configurations. Figure 2 shows the 2009 results of di-jet A_{LL} at STAR [8], as a function of the di-jet invariant mass M , for different pseudo-rapidity regions. The 2009 di-jet A_{LL} measurement is consistent with the inclusive jet results, and also suggests a non-zero gluon polarization in the covered x range. Future inclusive and di-jet A_{LL} measurements at both $\sqrt{s} = 200$ and 500 GeV at STAR will extend the range towards smaller values in Bjorken- x and provide higher precision measurements by approximately a factor of 2 in a few years.

3 Sea quark polarization measurements

The flavor separation of quark polarization in the nucleon, especially the sea quarks \bar{u} and \bar{d} polarization that are not well constrained by semi-inclusive DIS data, can be measured in pp collisions through the production of $W^{+(-)}$ bosons. The large parity-violating longitudinal single-spin asymmetries, $A_L = \frac{(\sigma_+ - \sigma_-)}{(\sigma_+ + \sigma_-)}$, provide unique access to the quark and antiquark helicity distributions, where σ_+/σ_- is the cross section with helicity positive/negative proton beam. $W^{+(-)}$'s are detected through $e^+(e^-)$ with large transverse momentum via $W \rightarrow e\nu$ channel at STAR with BEMC and EEMC. The charge separation is done through the TPC in the mid-rapidity ($|\eta| < 1.3$). The $W \rightarrow e\nu$ events are characterized by an isolated e^\pm with a sizable transverse energy, E_T^e , that peaks near half the W mass (~ 40 GeV). The theoretical framework that describes inclusive lepton production of W 's has been developed, so the measurements can be compared with theoretical prediction. First measurements of the spin asymmetry, A_L , and cross section for W^\pm production were reported by the STAR [12,13] and PHENIX experiments using data collected in 2009 at $\sqrt{s} = 500$ GeV with an integrated luminosity of $\sim 12 \text{ pb}^{-1}$ with an average beam polarization of 39%. These measurements paved the way for further measurements with larger statistics and more pseudo-rapidities bins that will provide real constraints for \bar{u} and \bar{d} polarisation in the nucleon.

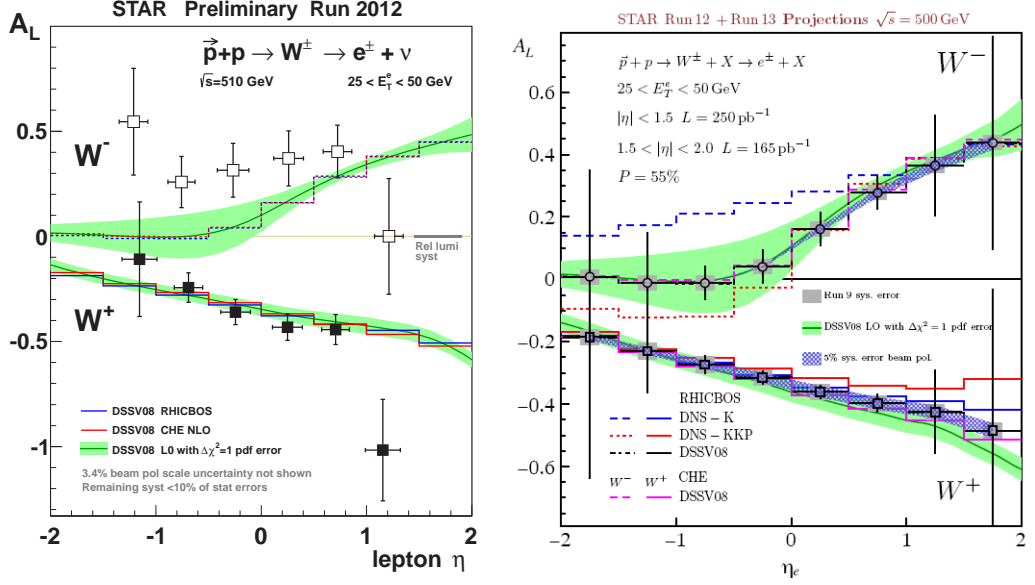


Figure 3: (left) Single-spin asymmetry A_L for W^\pm production as a function of η_e in pp collisions at 510 GeV at STAR; (right) Projections for longitudinal single spin asymmetry A_L for W production with STAR 2012 & 2013 data.

In 2012, STAR experiment collected pp data with an integrated luminosity of 72 pb $^{-1}$ at $\sqrt{s} = 510$ GeV and an average beam polarization of 56%, which is six times larger than the 2009 dataset, thus allowing a pseudo-rapidity dependent measurement of A_L for W 's. The preliminary A_L results with 2012 data [14] are shown in Fig. 3a) for both W^+ and W^- versus lepton pseudo-rapidity, with a comparison to theoretical predictions from NLO (CHE) [15] and fully resummed (RHICBOS) [16] calculations based on the DSSV08 helicity distributions [6]. The $A_L^{W^+}$ data are in good agreement with the predictions. However, the measured $A_L^{W^-}$ asymmetries are in general higher than the theoretical predictions especially in the region of $\eta_{e^-} < -0.5$, which indicates that these data are providing new constraints for $\Delta\bar{u}$ than previous data. The region of $\eta_{e^-} < -0.5$ in particular is expected to be sensitive to the \bar{u} quark helicity distribution, so the enhancement of $A_L^{W^-}$ there prefers to a sizable positive \bar{u} quark polarization relative to that expected from the global analysis of polarized DIS data. The very recent DSSV $^{++}$ global analysis including the new RHIC data especially the STAR 2012 $W A_L$ results shows a significant shift from negative to positive for the best fit value of $\Delta\bar{u}$ with an integral of $0.05 < x < 1$ [11]. RHIC completed a long successful longitudinally polarized $p + p$ run at $\sqrt{s} = 510$ GeV in 2013, and Fig. 3 b) shows the projected precision for the A_L measurement by combining the 2012 and 2013 data, which will further constrain the flavor separated antiquark contributions to the proton spin.

The longitudinal spin transfer D_{LL} of Λ and $\bar{\Lambda}$ hyperons in pp collisions is expected to be sensitive to the helicity distribution function of strange (anti-)quarks, and to the polarized fragmentation functions [17, 18]. A first proof-of-principle measurement of D_{LL} at mid-rapidity has been performed with STAR data taken in 2005 [19]. In 2009, an eightfold larger data sample was collected at STAR, with which the D_{LL} analysis extended hyperon transverse momentum with better precision. Figure 4 shows the obtained D_{LL} results for Λ and $\bar{\Lambda}$ versus p_T for $0 < \eta < 1.2$ in pp collisions at 200 GeV [20]. The data extend out to $p_T = 6$ GeV/ c with a statistical uncertainty about 0.04. The model evaluations of D_{LL} [17] for the combination of Λ and $\bar{\Lambda}$, are consistent with the data and span a range of values that is similar to the experimental uncertainties.

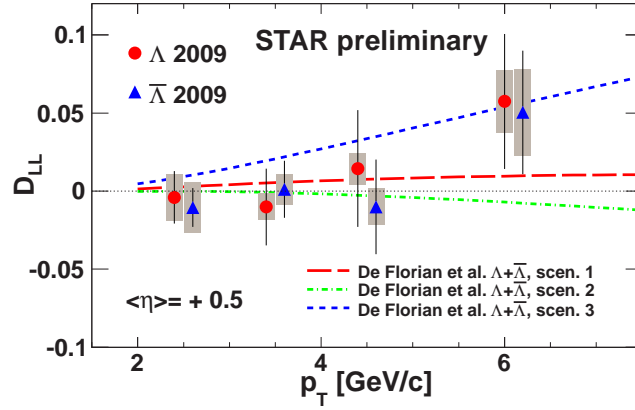


Figure 4: The longitudinal spin transfer D_{LL} for Λ and $\bar{\Lambda}$ in polarized proton-proton collisions at $\sqrt{s} = 200$ GeV for positive η versus p_T . The curves correspond to D_{LL} predictions for $\Lambda+\bar{\Lambda}$ based on different models for polarized fragmentation functions [17].

4 Transverse spin physics

Significant transverse single spin asymmetries (A_N) have been observed in different collisions including semi-inclusive deep inelastic scattering (SDIS) and proton-proton collisions. STAR measurements have demonstrated the persistence of sizeable A_N at RHIC energy [21], and also measured the p_T dependence of π^0 A_N [22,23], and the η -meson A_N [24]. Theoretical studies have shown that these asymmetries are closely related to transverse momentum dependent functions such as the Sivers distribution function and Collins fragmentation functions. It has been shown the Sivers function obtained in SDIS can be different as in pp collisions as it is not universal in QCD factorisation, while Collins functions are universal. Therefore, it is critical to measure the A_N in different channels in pp collisions to further constrain the theoretical models.

Hadron jet correlations in pp collisions provides a direct access to the Collins fragmentation function, and the corresponding A_N is also connected to the proton transversity via the Collins function. Figure 5 shows the preliminary results of the mid-rapidity Collins asymmetries for charge pions versus z and j_T in pp collisions at STAR [25], where z is the momentum fraction of the jet carried by the pion and j_T is the transverse momentum of the pion with respect to the jet

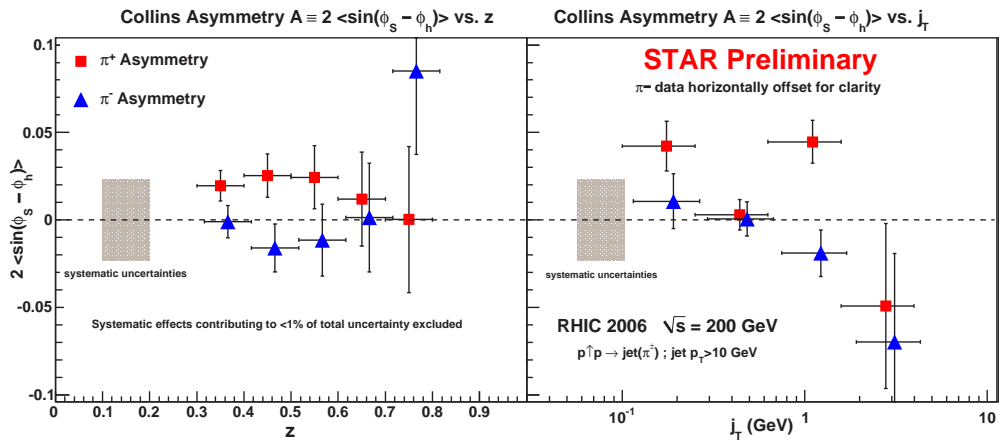


Figure 5: Collins asymmetries for leading π^+ and π^- with mid-rapidity jet in pp collisions at 200 GeV at STAR. ϕ_s and ϕ_h are the azimuthal angle of beam spin direction and hadron production plane respectively.

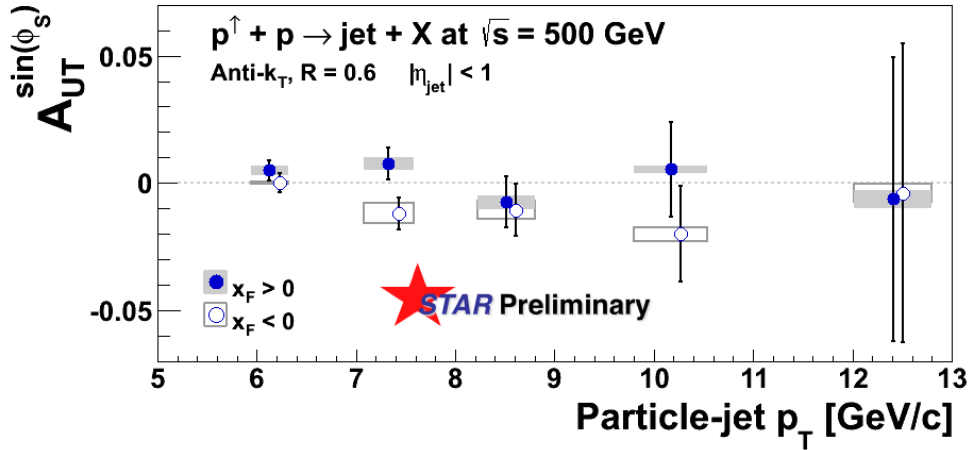


Figure 6: Siverson asymmetry as a function of jet transverse momentum p_T for jet production at mid-rapidity in pp collision at 500 GeV at STAR.

axis. Jets were reconstructed in the same method as mentioned earlier for jet A_{LL} measurements with mid-point cone algorithm. The data in this analysis were taken in 2006 and an analysis with a much larger dataset taken in 2012 at STAR is underway.

The Siverson effect can be studied at STAR by measuring the azimuthal asymmetry of the production of jets, where there is no fragmentation effects. The first measurement of di-jet A_N at mid-rapidity in pp collision at 200 GeV was published using STAR 2006 data and the asymmetry was consistent with zero [26]. Figure 6 shows the new STAR results of Siverson asymmetries (A_N) for inclusive jets at mid-rapidity $|\eta| < 1$ in pp collisions at 500 GeV [27]. Jets are reconstructed utilizing the anti- k_T jet-reconstruction algorithm. The measured asymmetries are quite small, consistent with expectation from measurements at 200 GeV as well as model predictions [28].

STAR also reported the first measurement of di-hadron spin asymmetries at mid-rapidity, which provide another channel to access proton transversity through the analyzing power of interference fragmentation functions (IFF) [29]. The IFF asymmetry $A_{UT}^{\sin\phi}$ takes the form of a spin-dependent azimuthal correlation between the di-hadron plane and the scattering plane, and ϕ is the azimuthal difference of these two planes. Figure 7 shows the preliminary results for the IFF asymmetry $A_{UT}^{\sin\phi}$ at mid-rapidity as a function of di-hadron invariant mass for two

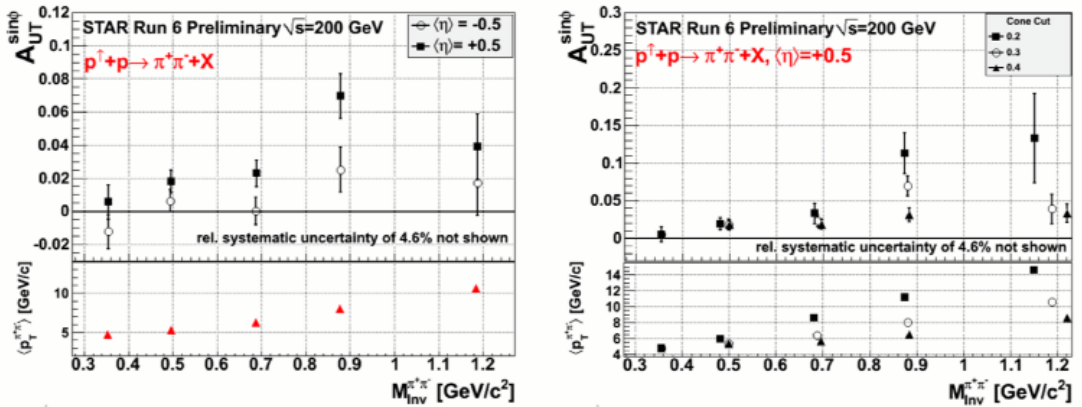


Figure 7: Di-hadron IFF asymmetry at mid-rapidity for $\pi^+\pi^-$ pairs as a function of di-pion invariant mass in pp collisions at 200 GeV at STAR.

pseudo-rapidities bins (left plot), and also for three cone cut radii in $\eta - \phi$ space (right plot). A clear non-zero signal can be seen from this measurement, which will provide an independent constraint on the proton transversity distribution together with IFF measurements from e^+e^- processes. The analysis of a much larger data sample obtained in 2012 at STAR is ongoing.

5 Summary and outlook

RHIC as the current only polarised hadron-hadron collider in the world continues its efforts to deepen our understanding of the nucleon spin structure. New STAR results from 2009 data on jet double spin asymmetry A_{LL} at RHIC-STAR in polarized proton-proton collision at 200 GeV suggest a sizable gluon spin contribution comparable to the quark spin contribution itself. The future jet measurements will double the available data set at 200 GeV and also allow for a high statistics measurement at 500 GeV to provide constraints on Δg at lower x range. Recent measurement of the single-spin asymmetry A_L for W^\pm production from 2012 data at STAR with a data sample about six times larger than the first W measurement, have been included in a preliminary global analysis of the DSSV group reported in Ref. [11], which demonstrate new constraints on the anti-quark helicity distributions $\Delta\bar{u}$ and $\Delta\bar{d}$. The coming measurements, in particular the much larger data sample taken in 2013 at RHIC, will further constrain the gluon polarization and the flavor separated antiquark contributions to the proton spin.

On the transverse spin program, we reported the recent measurements of single spin asymmetries at STAR on the Sivers effect and Collins effect with jet production at mid-rapidity in pp collisions. The measurement of di-hadron spin asymmetries (IFF) at STAR was also reported, which will provide important insights into the proton transversity distribution. The planned forward upgrade at STAR including improved calorimetry, tracking, and potentially particle identification in the forward region, will enable the measurements of jets and prompt photons in $p+p$ and $p+A$ collisions, which will be crucial to understand the origin of the large asymmetries.

The author is supported by the NNSFC, China under Grant No. 11175106 and 11222551, and the NSF of Shandong Province, China, under Grant No. ZR2010AM001.

References

- [1] B.I. Abelev *et al.* [STAR Collaboration], Phys. Rev. Lett. **97**, 252001 (2006).
- [2] B.I. Abelev *et al.* [STAR Collaboration], Phys. Rev. Lett. **100**, 232003 (2008).
- [3] L. Adamczyk *et al.* [STAR Collaboration], Phys. Rev. **D86**, 032006 (2012).
- [4] B.I. Abelev *et al.* [STAR Collaboration], Phys. Rev. **D80**, 111108 (2009).
- [5] L. Adamczyk *et al.* [STAR Collaboration], arXiv:1309.1800 [nucl-ex].
- [6] D. de Florian, R. Sassot, M. Stratmann, and W. Vogelsang, Phys. Rev. Lett. **101**, 072001 (2008).
- [7] P. Djawotho (STAR Collaboration), arXiv/1106.5769.
- [8] M. Walker (STAR Collaboration), arXiv/1107.0917.
- [9] M. Gluck, E. Reya, M. Stratmann, and W. Vogelsang, Phys. Rev. **D63**, 094005 (2001).
- [10] D. de Florian, R. Sassot, M. Stratmann, and W. Vogelsang, Prog. Part. Nucl. Phys. **67**, 251 (2012).
- [11] E. Aschenauer *et al.*, (2013), arXiv/1304.0079.
- [12] M. Aggarwal *et al.* [STAR Collaboration], Phys. Rev. Lett. **106**, 062002 (2011).

- [13] L. Adamczyk *et al.* [STAR Collaboration], *Phys. Rev.* **D85**, 092010 (2012).
- [14] J. R. Stevens (STAR Collaboration), arXiv/1302.6639.
- [15] D. de Florian and W. Vogelsang, *Phys. Rev.* **D81**, 094020 (2010).
- [16] P.M. Nadolsky and C.P. Yuan, *Nucl. Phys.* **B666**, 31(2003).
- [17] D. de Florian, M. Stratmann. and W. Vogelsang, *Phys. Rev. Lett.* **81**, 530(1998).
- [18] Q.H. Xu, Z.T. Liang and E. Sichtermann, *Phys. Rev.* **D73**, 077503 (2006).
- [19] B.I. Abelev *et al.* [STAR Collaboration], *Phys. Rev.* **D80**, 111102 (2009).
- [20] J. Deng (STAR Collaboration), Proc. of SPIN2012.
- [21] J. Adams *et al.* [STAR Collaboration], *Phys. Rev. Lett.* **92**, 171801 (2004).
- [22] B. I. Abelev *et al.* [STAR Collaboration], *Phys. Rev. Lett.* **101**, 222001 (2008).
- [23] S. Heppelmann (STAR Collaboration), Proc. of DIS2013.
- [24] L. Adamczyk *et al.* [STAR Collaboration], *Phys. Rev. D* **86**, 051101 (2012).
- [25] R. Fatemi (STAR Collaboration), AIP Conf. Proc. 1441, 233 (2012).
- [26] B.I. Abelev *et al.* [STAR Collaboration] , *Phys. Rev. Lett.* **99**, 142003 (2007).
- [27] J. Drachenberg (STAR Collaboration), Proc. of MENU2013.
- [28] K. Kanazawa, Y. Koike, *Phys. Lett.* **B 720**, 161 (2013).
- [29] A. Vossen, *Int. J. Mod. Phys. Conf. Ser.* **20**, 37 (2012).

STUDY OF THE SPIN AND PARITY OF HIGGS BOSON WITH ATLAS DETECTOR

Yaquan Fang
(On behalf of the ATLAS Collaboration.)

Institute of High Energy Physics, Beijing
E-mail: fangyq@ihep.ac.cn

Abstract

In this proceeding, the studies of the spin and parity quantum numbers of the Higgs boson with the data collected by the ATLAS experiment are presented. The results include those from the individual channels, i.e. $H \rightarrow \gamma\gamma$, $H \rightarrow ZZ^* \rightarrow 4l$ and $H \rightarrow WW^* \rightarrow l\nu l\nu$ as well as the combination of them. The data are compatible with the Standard Model $J^P = 0^+$ and some specific models $J^P = 0^-, 1^-, 1^+, 2^+$ are excluded at the confidence levels above 97.8%. Thus, the data provide the evidence for the spin-0 with the positive parity being strongly preferred.

1 Introduction

In 2012, a new particle is discovered [1,2] by both ATLAS and CMS in the search for the Higgs Boson [3-6]. The most important task afterwards was to determine whether the discovered particle is the Standard Model (SM) Higgs boson. One interest is to investigate the properties of the spin and parity of the new particle and compare them with the SM predictions for the Higgs boson which is spin-0 and positive parity particle. According to Landau-Yang theorem [7,8], spin-1 hypothesis is strongly disfavored by the observation of $H \rightarrow \gamma\gamma$ signal. In this proceeding, we will compare the hypothesis of the SM, i.e. $J^P = 0^+$, with several alternative hypotheses models $J^P = 0^-, 1^-, 1^+, 2^+$. Three final states $H \rightarrow \gamma\gamma$ and $H \rightarrow ZZ^* \rightarrow 4l, \rightarrow WW^* \rightarrow l\nu l\nu$ with W, Z decaying leptonically are analyzed in this study [9]. The combination of these channels is performed as well in order to improve the sensitivity of the analysis. All three channels are combined for the test of the 2^+ hypothesis; for 1^+ and 1^- hypotheses, the final states of $H \rightarrow ZZ^*, \rightarrow WW^*$ are included in the combination; Only $H \rightarrow ZZ^*$ decay process is used to test the hypothesis of 0^- [9]. In this proceeding, the alternative model descriptions are based on ref. [10]. Since the spin-2 resonance can be produced either via gluon fusion (gg) or via P-wave quark-antiquark annihilation ($q\bar{q}$), the results with different fractions of $q\bar{q}$ production for spin-2 signal are summarized as well.

2 Statistical method

According to the assumption of the spin-parity of the signal, a likelihood function based on the probability density function of the discriminant observables is constructed incorporating with the systematic uncertainties. The profile likelihood ratio between $J^P = 0^+$ hypothesis and alternative hypothesis is used as the test statistic q . Pseudo-experiments are generated to obtain the distributions of q for $J^P = 0^+$ hypothesis and alternative hypothesis. The corresponding p_0 -values of $p_0(0^+)$ (SM prediction) and $p_0(J_{alt}^P)$ (alternative hypothesis) are extracted from the

distributions of q . The exclusion of the alternative hypothesis with respect to prediction can be evaluated in terms of the confidence level $CL_s(J_{alt}^P)$ defined as:

$$CL_s(J_{alt}^P) = \frac{p_0(J_{alt}^P)}{1 - p_0(0^+)}. \quad (1)$$

3 Analyses from individual channels

3.1 Results from $H \rightarrow \gamma\gamma$

The absolute value of the cosine of the polar angle θ^* the photons with respect to the z -axis in the Collins-Soper frame [11] is used as the discriminating variable to separate the spin-0 and spin-2 states. In addition to $|\cos\theta^*|$, $m_{\gamma\gamma}$ is used in the fit as well to separated the signal from the non-resonant background. The $|\cos\theta^*|$ for the signal either with a spin-0 particle or a spin-2 particle is obtained from Monte-Carlo sample, while the background is extracted directly from the sideband of the di-photon mass distribution. Fig. 1(a) and (b) show the distributions of $|\cos\theta^*|$ for spin-0 and spin-2 signals respectively after the subtraction of the background. The distribution of $|\cos\theta^*|$ for the background can be seen from Fig. 1(c). The exclusion of spin-2 model with pure gg fusion configuration from this individual channel reaches 95% using the test statistics described in Section 2.

3.2 Results from $H \rightarrow ZZ \rightarrow 4l$

The discriminating variables which are sensitive to the spin and parity of the Higgs boson are the masses of the reconstructed lepton pairs, the production and the decay angles of the final state leptons as described in Ref. [9]. In order to maximize the discriminating power, a Boost Decision Tree (BDT) is implemented combining these individually reconstructed variables. Fig. 2 shows the distribution for the BDT output for data (points with error bars) and expectations signals of $J^P = 0^+$ (solid line) and $J^P = 0^-$ (dashed line). With same statistical computation, the 0^- and 1^+ are excluded at 97.8% level or higher assuming purely gg production.

3.3 Results from $H \rightarrow WW^* \rightarrow l\nu l\nu$

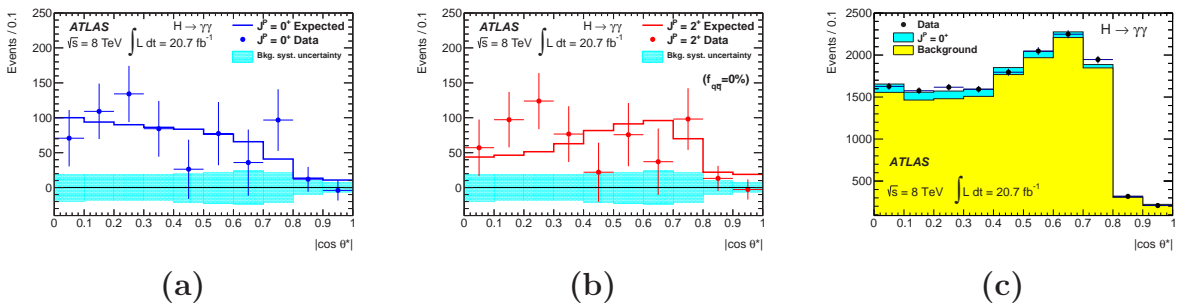


Figure 1: (a) The distribution of $|\cos\theta^*|$ for spin-0 (0^+) particle (solid curve) and data (data point) after the subtraction of the background.

(b) The distribution of $|\cos\theta^*|$ for spin-2 (2^+) particle (solid curve) and data (data point) after the subtraction of the background.

(c) The distribution of $|\cos\theta^*|$ for events in the signal region defined by $122 \text{ GeV} < m_{\gamma\gamma} < 130 \text{ GeV}$. The data (dots) are overlaid with the projection of the signal (blue/dark band) and background (yellow/light histogram) components obtained from the inclusive fit of the data under the spin-0 hypothesis.

The angular distribution as well as the momentum of the final state leptons and missing transverse energy are affected by the spin correlations between the two W 's. Based on these, the invariant mass of the dilepton m_{ll} , the azimuthal separation of the two leptons $\Delta\phi_{ll}$, $E_{T,rel}^{miss}$, the transverse momentum of the dilepton p_T^{ll} are used as the input variables of a BDT based analysis to obtain the best separating power. Two BDT classifiers are developed in this analysis: one classifier is trained to distinguish the $J^P = 0^+$ signal from the sum of all backgrounds, while the other separates the alternative spin hypotheses (1^+ , 1^- , 2^+). In addition, these two-dimensional distributions of the BDT are mapped into an one-dimensional distribution. The mapped distribution for $J^P = 0^+$ and $J^P = 2^+$ are displayed in Fig. 3. The tested 2^+ hypothesis is excluded with a confidence level varying between 95% for a purely $q\bar{q}$ production and 99% for a pure gg production.

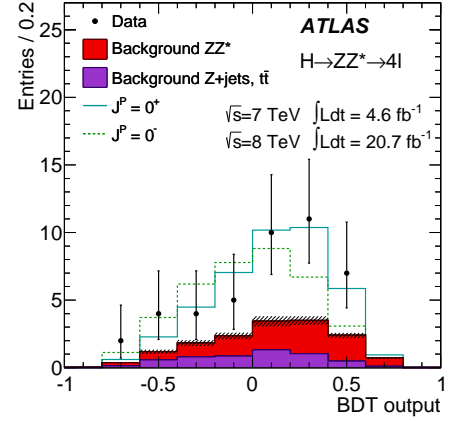


Figure 2: The distributions of the BDT output for data (points with error bars) and expectations based on MC simulation (histograms) for the signals: $J^P = 0^+$ (solid line) and $J^P = 0^-$ (dashed line).

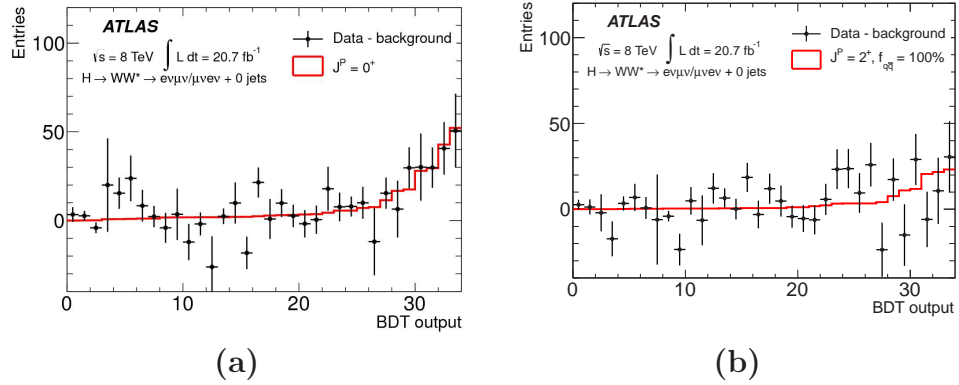


Figure 3: (a) The distribution of the mapped BDT output for spin-0 (0^+) particle (solid curve) and data (data point) after the subtraction of the background. Study of the spin and parity of Higgs boson with ATLAS detector. (b) The distribution of the mapped BDT output for spin-2 (2^+) particle (solid curve) and data (data point) after the subtraction of the background.

4 The results of the combination

As Fig. 4(a) shows, the $J^P = 2^+$ model is rejected at more than 99.9% CL by combining all three channels $H \rightarrow \gamma\gamma$, $H \rightarrow ZZ^* \rightarrow 4l$ and $H \rightarrow WW^* \rightarrow l\nu l\nu$ considering different configuration of the gg and $q\bar{q}$ admixture. the $J^P = 1^+$ and $J^P = 1^-$ model is excluded at more than 99.7% CL by combining $H \rightarrow ZZ^* \rightarrow 4l$ and $H \rightarrow WW^* \rightarrow l\nu l\nu$ which can be found in the second and third bins of Fig. 4(b). $H \rightarrow ZZ^* \rightarrow 4l$ alone rejects the 0^- hypotheses with a confidence level 97.8%. In conclusion, all of the alternative models studied are excluded and the study provides the evidence for the spin-0 nature of Higgs boson, with the positive parity being strongly preferred.

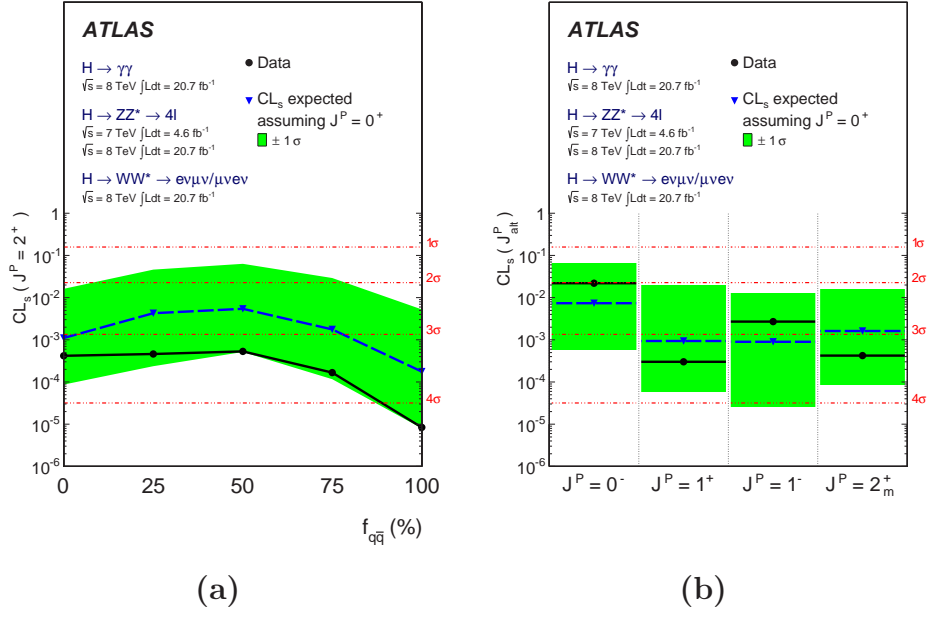


Figure 4: (a) Expected (blue triangles/dashed line) and observed (black circles/solid line) confidence levels, CLs, of the 2^+ hypothesis as a function of the fraction of $q\bar{q}$ for the spin-2 particle. The green bands represent the 68% expected exclusion range for a signal with assumed 0^+ . On the right y-axis, the corresponding numbers of Gaussian standard deviations are given, using the one-sided convention. (b) Expected (blue triangles/dashed lines) and observed (black circles/solid lines) confidence level CLs for alternative spin-parity hypotheses assuming a 0^+ signal. The green band represents the 68% CLs(J^P_{alt}) expected exclusion range for a signal with assumed 0^+ . On the right y-axis, the corresponding numbers of Gaussian standard deviations are given, using the one-sided convention.

References

- [1] ATLAS Collaboration, Phys. Lett. B 716(2012) 1.
- [2] CMS Collaboration, Phys. Lett. B 716(2012) 30.
- [3] F. Englert and R. Brout, Phys. Rev. Lett. 13(1964) 321.
- [4] P.W.Higgs, Phys. Lett. 12(1964) 132, Phys. Rev. Lett. 13(1964) 508, Phys. Rev. 145(1966) 1156
- [5] G.S.Guralnik, C.R. Hagen and T.W.B. Kibble, Phys. Rev. Lett. 13(1964) 585.
- [6] T.W.B Kibble, Phys. Rev. 155(1967) 1554.
- [7] L.D Landau, Dokl. Akad. Nauk Ser. Fiz. 60(1948) 207.
- [8] C.-N. Yang, Phys. Rev. 77(1950) 242.
- [9] ATLAS Collaboration, Phys. Lett. B 726(2013), 120-144.
- [10] Y. Gao et al., Phys. Rev. D 81(2010) 075022.
- [11] J.C. Collins and D.E. Soper, Phys.Rev.D 16(1977) 2219-2225



NICA SPD

POLARIZED DEUTERONS AND PROTONS AT NICA: THE DESIGN CONCEPT DEVELOPMENT

A.D. Kovalenko (for the NICA Collaboration)

Joint Institute for Nuclear Research, 141980 Dubna, Russia

E-mail: kovalen@dubna.ru

Abstract

The possibilities of NICA complex operation in polarized proton and deuteron modes were studied during the last few years. Several schemes of “Siberian Snakes” were considered and the most optimal one have been proposed for the future modeling and technical design. It was shown, average luminosity of polarized pp -collisions higher $1 \cdot 10^{32} \text{ cm}^{-2}\text{s}^{-1}$ at $\sqrt{s_{NN}} \geq 27 \text{ GeV}$ is reachable.

1. Scheme of the complex

The NICA complex at JINR has been approved in 2008 assuming two phases of construction. The first phase realizing now includes construction of facilities for heavy ion physics program [1] while the second phase should include facilities for the program of spin physics studies with polarized protons and deuterons. In this paper we briefly describe the status of design the NICA technical concept in connection with polarized beams.

The main elements of NICA complex are shown in Figure 1. They include: the heavy ion source and source of polarized ions (proton and deuteron), SPI, with corresponding linacs, existing superconducting accelerator, 6 A-GeV strong-focusing synchrotron — Nuclotron, new superconducting Booster synchrotron, new collider NICA with two detectors — MPD (Multi-Purpose Detector for heavy ion studies) and SPD (Spin Physics Detector), as well as experimental hall for fixed target experiments with beams extracted from the Nuclotron.

The functional scheme of facility approved for the first turn construction scenario is presented in Figure 2. The chain of beam injection to the collider rings in the case of polarized protons and deuterons includes: ions source SPI — modernized injection linac LU-20 with the new front-end part (PI) - Nuclotron - Collider. Heavy ion injection line includes respectively: ion source KRION-6T - HILAC - Booster - Nuclotron - Collider.

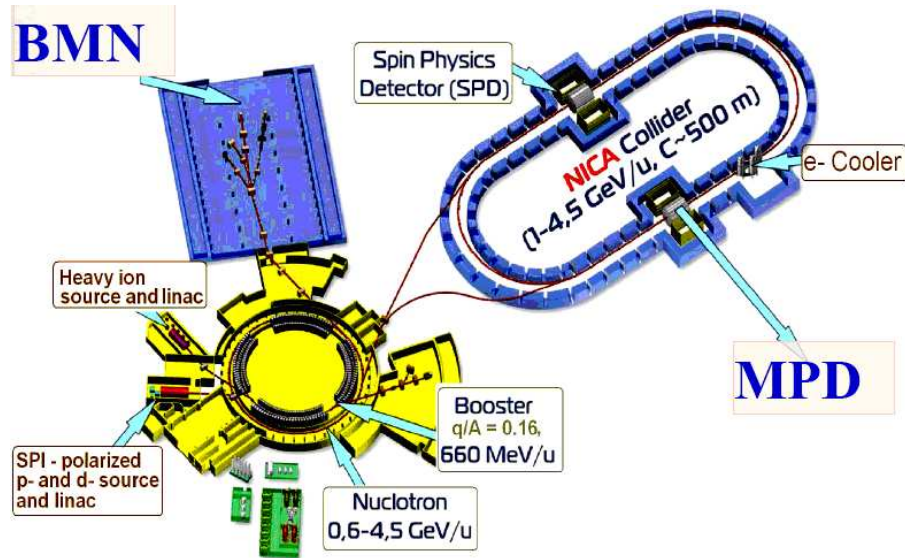


Figure 1: NICA complex at LHEP JINR

It can be also used to inject any light ions, let say, deuterons to the collider. The main goals of the Booster are the following: 1) accumulation and acceleration of about $4 \cdot 10^9$ Au^{32+} ions; up to an energy required for effective stripping; 2) formation of the required beam emittance with electron cooling and 3) fast extraction of the accelerated beam.

The chain with using the booster in the case of polarized protons was proposed and considered also [2], nevertheless the approved scheme do not include direct beam extraction line from the booster to the collider at the first stage of the project realization.

The new polarized ion source is commissioning now. It was designed and constructed as an universal high pulsed intensity source of polarized deuterons and protons based on a charge-exchange plasma ionizer. The output $\uparrow D^+$ ($\uparrow H^+$) current of the source is expected to be at a level of 10 mA. The expected polarization will reach up to 90% of the maximum vector (± 1) for $\uparrow D^+$ ($\uparrow H^+$) and tensor (+1, -2) for $\uparrow D^+$ polarization. The project is designed and constructed in close cooperation with INR of RAS (Moscow). The equipment available from the CIPIOS ion source (IUCF, Bloomington, USA) is partially used for SPI. The source will deliver to the linac 10 mks pulsed polarized proton or deuteron beam with intensity up to $(1 \div 2) \cdot 10^{11}$ part./pulse and repetition rate of 1 Hz [3]. The description of the SPI have been published elsewhere, for example in [4]. The Alvarez-type linac LU-20 used as the Nuclotron injector was put into operation in 1974. It was originally designed as proton accelerator from 600 keV to 20 MeV. Later it was modified to accelerate ions with charge-to-mass ratio $q/A > 0,33$ to 5 MeV/u at $2\beta\lambda$ mode. The pulse transformer voltage up to 700 kV is now used to feed the accelerating tube of the LU-20 pre-injector. The new pre-injector will be based on the RFQ section [5]. The SPI is now commissioning at test bench, whereas the front-end linac section is under manufacturing.

2. Polarized protons and deuterons acceleration at Nuclotron

Polarized deuterons: Acceleration of polarized deuterons at the Synchrotron was done for the first time in 1984 [6] and at the Nuclotron in 2002 [7]. There are no dangerous spin resonances up to to polarized deuteron acceleration at the Nuclotron up

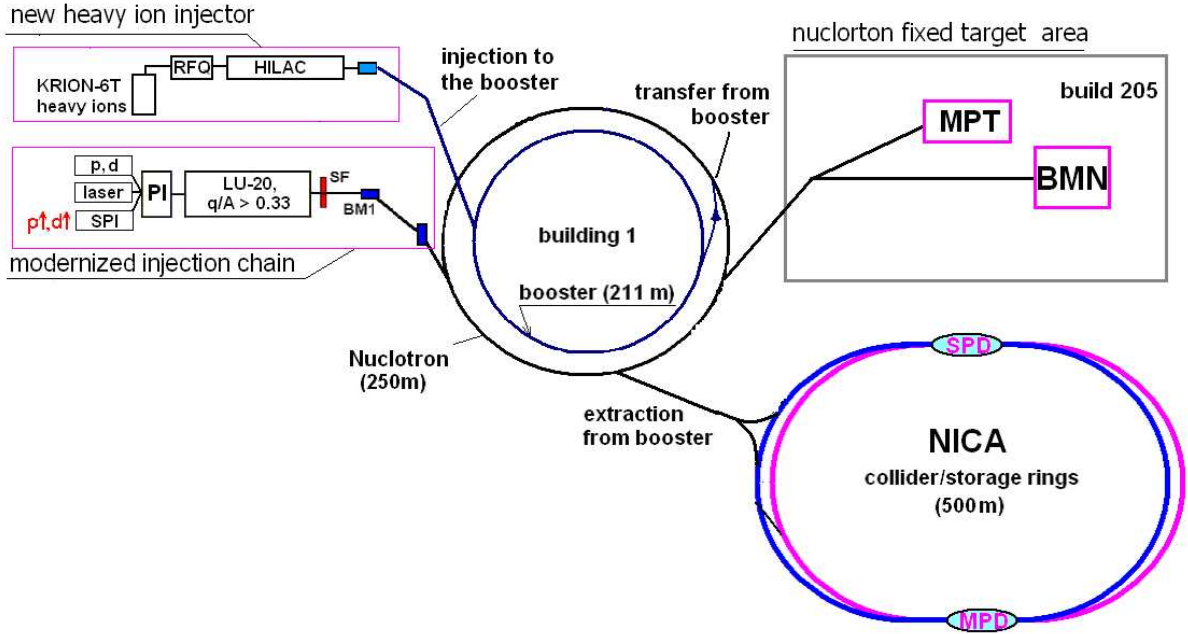


Figure 2: Functional scheme of NICA complex

to an energy of 5,6 GeV/u. This limit is practically very close to maximum design energy of the Nuclotron (6 GeV/u for the particles with charge-to-mass ratio $q/A = 1/2$), thus centre-of-mass energy up to $\sqrt{s_{NN}} \approx 13$ GeV can be provided. Any additional spin control insertions into the Nuclotron lattice are not necessary (vertical spin direction of deuterons is supposed). The only problem in case of deuterons is changing the polarization direction over large angles, say $\pi/2$, in the collider.

Polarized protons: According to the NICA project, experiments with polarized protons should be carried out up to the maximum energy $\sqrt{s_{NN}}$ of 27 GeV and at desired average luminosity $L \geq 1 \cdot 10^{32} \text{ cm}^{-2}\text{s}^{-1}$. The NICA operation in polarized proton mode will need additional acceleration of protons from 5 to 12,5 GeV in the collider, because it is impossible to keep the beam polarization over the total energy range in the Nuclotron. For the successful crossing of numerous spin resonances in Nuclotron, “Siberian snake” insertions will be installed into one of the straight sections of the accelerator ring. Spin resonances, occurring during acceleration cycle at different integer combinations of the betatron (ν_x, ν_y) and spin (ν) frequencies, were analyzed at different integer or half-integer linear combinations between the betatron and spin frequencies during the Nuclotron accelerator cycle. To preserve polarization, we consider “siberian snake” based on solenoids with pulsed magnetic field [8]. The insertions containing transverse magnetic fields would lead to very big closed orbit distortions especially at low energies. Helix snake is much complicated and gives no profit also. The comparison of different “snakes” is considered by A.M. Kondratenko [9]. Orbital parameters of polarized proton beam in Nuclotron with solenoid siberian snake is presented by M.A. Kondratenko et all [10]. The maximum magnetic field integral of the “Snake” solenoid depends on the particle momentum and approximately equal to 21 T·m at the proton Lorenz-factor $\gamma = 6$. Taking into account available empty space for the solenoids within the existing straight section (about $2 \times 3,1$ m without compensation quadrupoles) one can find the needed amplitude of the

solenoid magnetic field $B \approx 3,6$ T. Superconducting pulsed solenoid with the field ramp $dB/dt \approx 3 \div 4$ T/s can be manufactured based on the Nuclotron-type hollow high-current superconducting cable. Assuming outer diameter of the cable 1 cm, double-layer coil and supply current of 15 kA one can obtain the needed parameters. To estimate other important parameters, like stored energy, coil inductance and necessary supply voltage, we should fix inner diameter of the solenoid. Suppose the inner diameter 100 mm (sufficient for the beam circulation), we obtain the following estimates: stored energy of 150 kJ (for the coil length of 3 m), inductance — 1,3 mH, induced voltage 20 V (at $dI/dt = 15$ kA/s). Based on the previous experience of the design and long-term tests of Nuclotron magnets and cables, we can estimate the parameters as feasible.

3. Collider in polarized proton and deuteron modes

The novel scheme of the polarization control at NICA collider, suitable for protons and deuterons, based on the idea of manipulating with polarized beams in zero spin tune vicinity. This approach is actively developed at JLAB for the 8-shaped ring accelerator project [11]. To provide zero spin tune regime at the collider of a racetrack symmetry, it is necessary to install two identical “Siberian snakes” (Sol, $\pi/2$) in the opposite straight sections (Figure. 3). In this scheme any direction of the polarization is reproduced at any azimuth point after every turn. But, if one fix the longitudinal or transverse polarization at SPD then the polarization direction at MPD will obtain some angle in respect to the particle velocity vector. This angle depends on the beam energy. And vice-versa: if the polarization directions are fixed at MPD area, some certain polarization angle will occurred at SPD. Solenoid magnetic field integral in a single (Sol, $\pi/2$)-rotator at the maximum energy is reached of 25 T·m and 80 T·m for proton and deuteron case respectively.

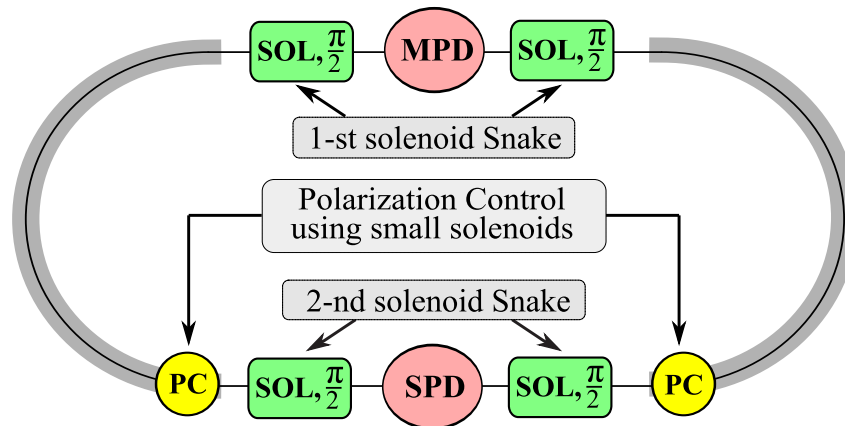


Figure 3: Preliminary positions of the polarization control elements in the collider lattice

The scheme is described in the talk by Yu. Filatov presented at the workshop [12]. The most essential is possibility to manipulate with the polarization vector direction by means of relatively small fields. Design of the final scheme is continuing. Additional analysis of the polarization control at the MPD area will be fulfilled. It is necessary also to define composition of the solenoids, namely: stationary and dynamic parts The final scheme will be approved at the later stages of the project.

4. The luminosity estimates

The NICA peak luminosity in the proton mode is calculated for the proton kinetic energy range from 1 to 12,7 GeV. The last value corresponds to the total collision energy $\sqrt{s} = 27$ GeV and the equivalent fixed target beam kinetic energy $E_{\text{kin}} = 388$ GeV, Figure 4 [13]. The luminosity and total number of the stored particles has been calculated taking into account the space charge limits and the other parameters listed in the Table 2.

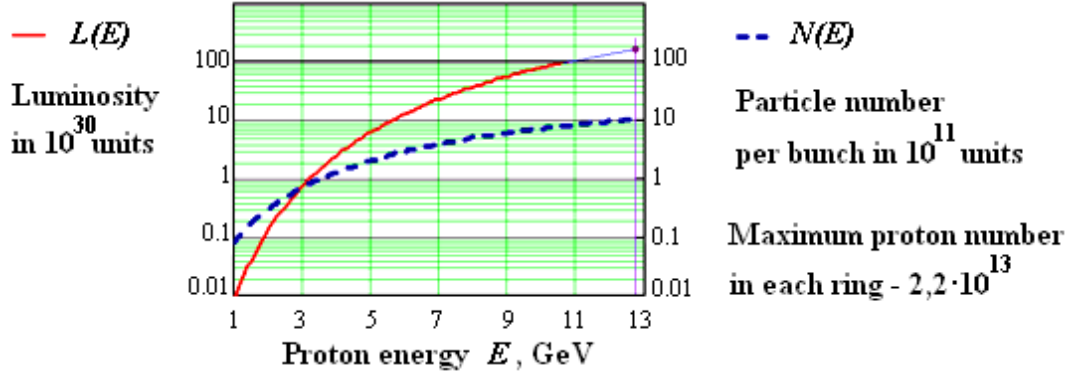


Figure 4: NICA collider pp luminosity in units 10^{30} (left scale, solid line) and maximum number of particles per bunch (right scale, dotted line)

Circumference, m	503
Number of collision points (IP)	2
Beta function β_{min} in the IP, m	0,35
Rms bunch length, m	0,5
Incoherent tune shift, ν_{Lasslett}	0,027
Beam-beam parameter, ξ	0,067
Number of protons per bunch	$\sim 1 \cdot 10^{12}$
Number of bunches	22
Beam emittance (normalized) $\varepsilon_{\text{nrms}}$ at 12,5 GeV, π mm mrad	0,15

Table 1: NICA parameters for $p \uparrow p \uparrow$ -collisions.

As it follow from the calculations, the peak luminosity of $L_{\text{peak}} = 2 \cdot 10^{32} \text{ cm}^{-2}\text{s}^{-1}$ is reached at the beam kinetic energy of 12,6 GeV. From the other hand, the ring filling time will depend on the Nuclotron pulse intensity and cycle duration. The expected proton beam intensity at the Nuclotron output is limited by the source current and the particle losses coming from different reasons. Taking the SPI design current (10 mA) and estimate particle loss coefficient between the source and the Nuclotron (0,5), RF capture (0,8), extraction efficiency (0,9) and the other factors in the synchrotron (0,9), one can expect the output intensity up to $8,5 \cdot 10^{10}$ polarized protons per pulse. Thus, the necessary number of cycles is $2,2 \cdot 10^{13} / 8,5 \cdot 10^{10} \sim 22 \times 12 = 264$ cycles per each ring. The cycle duration depend on the magnetic field ramping time (up and down), the peak value of the magnetic field and necessary pause between the cycles. For our case we take $B = 1$ T, $dB/dt = 1$ T/s and $t_p = 1$ s, i.e. the total cycle duration $T_c = 5$ s and obtain

the ring filling time $T_f \approx 1300$ s (minimum) or 2600 s for the both rings, if a double-spin process is studying.

To estimate the average, one should take into account necessary beam cooling (stochastic) time, the luminosity life time, the machine reliability coefficient. Assuming the cooling time $T_{\text{cool}} = 1500$ s, the luminosity life time $T_{\text{Lif}} = 20000$ s and the reliability coefficient $k_r = 0,95$, it is possible to calculate the average luminosity as $L_{\text{avr}} = L_{\text{peak}}\eta$, where η the ratio of the luminosity life time to the total data taken time and beam preparation time. In the considered case: $L_{\text{avr}} \approx 0,8 \cdot L_{\text{peak}}$. Thus, the average luminosity of $1,6 \cdot 10^{32} \text{ cm}^{-2}\text{s}^{-1}$ can be reachable. The bunch parameters shown in the Table 2 will be optimized at the technical design stage of the facility. So, an increase of the bunch intensity allows increasing the luminosity at the same value of the tune shift. To keep the constant tune shift the beam emittance has to be increased proportionally to the bunch intensity and the luminosity is scaled linearly with the ion number.

References

- [1] *V.D.Kekelidze, A.D.Kovalenko, R.Lednickyy, V.A.Matveev, I.N.Meshkov, A.S.Sorin, G.V.Trubnikov.* Status of NICA project at JINR. PoS(Baldin ISHEPP XXI) 085, pp 1-9, SISSA. It.
- [2] *A.D.Kovalenko et al.* The NICA Facility in Polarized Proton Operation Mode, IPAC'2011 <http://accelconf.web.cern.ch/AccelConf/IPAC2011/papers/tupz004.pdf>
- [3] *V.Fimushkin, A.S.Belov, A.D.Kovalenko et al.* EPJ, Special Topics, 162, pp. 275-280, (2008), Springer
- [4] *V.Fimushkin et al.* Physics of Part.& Nucl., 2014, Vol. 45, No.1, pp. 297-300, Springer 2014.
- [5] *A.Butenko et al.* Development of the NICA Injection Facility
- [6] *N.G.Anishchenko et al.* Journ. de Phys. Colloquia C2, Vol.46, C2-703, (1985)
- [7] *S.Vokal, A.D.Kovalenko, A.M.Kondratenko et al.* Physics of Part.& Nucl., 2009, Vol. 6, No.1, pp. 48-58, Springer 2009.
- [8] *Yu.N.Filatov, A.D.Kovalenko, A.V.Butenko et al.* Physics of Part.& Nucl., 2014, Vol. 45, No.1, pp. 262-264, Springer 2014.
- [9] *A.M.Kondratenko et al.* Comparison of Solenoid, Helix and Dipole Siberian Snakes in the NICA Collider. XV Workshop (DSPIN-13), Dubna, October 8-12, 2013 (this Proceedings).
- [10] *M.A.Kondratenko et al.* Orbital Parameters of Proton Beam in Nuclotron with Solenoid Siberian Snake. XV Workshop (DSPIN-13), Dubna, October 8-12, 2013 (this Proceedings).
- [11] *S. Abeyratne et al.,* Science requirements and conceptual design for a polarized medium energy electron-ion collider at Jefferson lab, edited by Y. Zhang and J. Bisognano, arXiv:1209.0757 [physics.acc-ph] (2012).
- [12] *Yu.N.Filatov, A.M.Kondratenko, A.D.Kovalenko et al.* Proton and Deuteron Polarization Control in NICA Collider Using Small Solenoids. XV Workshop (DSPIN-13), Dubna, October 8-12, 2013 (this Proceedings).
- [13] *I.N.Meshkov.* Private communication

PROTON AND DEUTERON POLARIZATION CONTROL IN NICA COLLIDER USING SMALL SOLENOIDS

Yu.N. Filatov^b, A.D. Kovalenko^a, A.M. Kondratenko^c, M.A. Kondratenko^c and
V.A. Mikhaylov^a

^a *Joint Institute for Nuclear Research, 141980 Dubna, Russia*

^b *Moscow Institute of Physics and Technology, 141700 Dolgoprudny, Russia*

^c *Science and Technique Laboratory “Zaryad”, 630090, Novosibirsk, Russia*

Abstract

The insertion of two identical Siberian Snakes in the NICA collider allows to control effectively the beam polarization by means of small field integrals. The polarization control schemes by application of small solenoids are presented. These devices allow to adjust any proton and deuteron polarization in both MPD and SPD detectors. It makes possible to carry out ultra-high precision experiments with polarized beams.

For spin physics experiments in JINR’s NICA collider deuteron and proton beams with both longitudinal and vertical polarization are required in a momentum range from 2,5 to 13,5 GeV/c [1]. To manipulate polarization of protons as well as deuterons efficiently it was proposed to use the collider in zeroth spin tune mode, wherefore two identical solenoid Siberian Snakes are introduced in the opposite strait sections of the collider [2] (see Fig. 1).

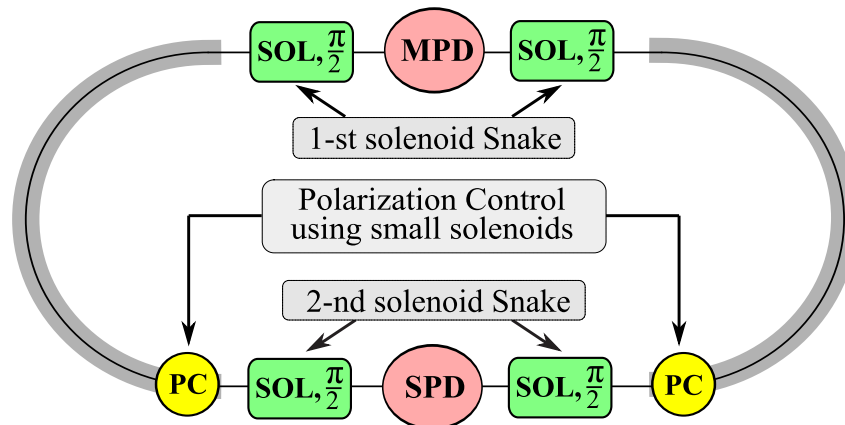


Figure 1: Beam polarization control schematic in the NICA collider.

Each Snake consists of two parts installed symmetrically around the MPD and SPD detectors. In this case the NICA collider with two Snakes becomes similar to figure-8 shaped collider at JLab [3].

The unique feature of a zeroth spin tune accelerator is the possibility to control any particle polarization using small magnetic field integrals [4]. The proton and deuteron polarization in the NICA collider ring can be efficiently controlled by “small” (weak)

solenoids. Any angle lying in the vertical plane of SPD detector can be obtained between the polarization and the beam direction by introducing longitudinal fields in two regions of the collider arcs. Figure 2 shows a symmetric scheme of polarization control with two such insertions located on both sides of the SPD detector.

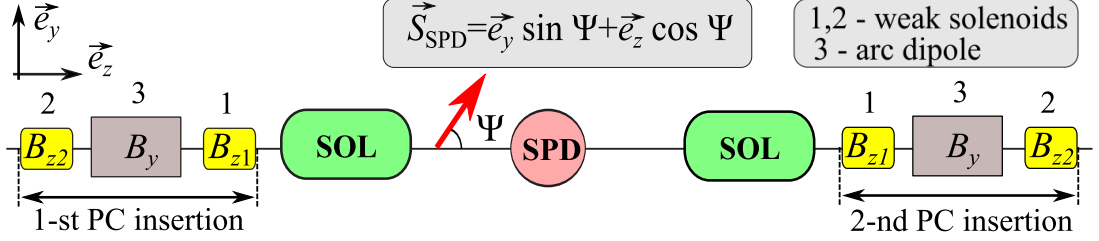


Figure 2: Polarization control by means of small solenoids in NICA collider.

The required spin rotation angles of the longitudinal fields in each insertion are given for small values of the spin tune ν by

$$\varphi_{z1} = \pi\nu \frac{\sin(\varphi_y - \Psi)}{\sin \varphi_y}, \quad \varphi_{z2} = \pi\nu \frac{\sin \Psi}{\sin \varphi_y},$$

where $\varphi_{z1} = (1 + G)(B_z L)_1 / (B\rho)$ and $\varphi_{z2} = (1 + G)(B_z L)_2 / (B\rho)$ are the spin rotation angles of the solenoids, $\varphi_y = \gamma G \alpha$ is the spin rotation angle of the dipole section between the solenoids, α is the orbit bending angle between the solenoids, Ψ is the angle between the polarization and the beam direction, and $B\rho$ is the magnetic rigidity.

To work in the whole proton energy range in the collider, the first solenoid with a field B_{z1} is placed in the experimental straight while the second solenoid with a field B_{z2} is located behind one regular dipole with an orbital bending angle of $4,5^\circ$. The field integrals required in each insertion to obtain the longitudinal $\Psi = 0^\circ$ and vertical $\Psi = 90^\circ$ proton polarizations are shown in figure 3 as functions of the beam momentum. The field integrals dependence on angle Ψ at minimum and maximum beam momentum are shown in figure 4. The spin tune of protons in the collider for the given field integrals has a value of $\nu_p = 0,01$, which exceeds greatly the zeroth resonance strength associated with imperfections of the colliders magnetic structure. The maximum field integral in a single solenoid at the maximum energy does not exceed $0,6 \text{ T}\cdot\text{m}$. Such schemes practically do not influence on orbital characteristics of the NICA collider.

The proton polarization control scheme with one regular dipole in each insertion can be used for deuteron polarization control too, but deuteron spin tune for the given field integrals has a rather small value ν_d of about $0,0003$. One can increase spin tune of the deuteron beam up to the value of $0,003$, which is sufficient to suppress the zeroth spin resonance strength. For that it is necessary to put the second solenoid with a field B_{z2} behind twenty regular dipoles with a total orbital bending angle of 90° , i.e. to install second solenoids in the arc centers.

The half Snake located behind SPD detector rotates spin from the detector's vertical plane to the collider's orbit plane. Thus, by choosing the necessary field integrals, the presented scheme allows to obtain any polarization orientation in the collider's orbital plane at any orbital location, which can be used both for matching the polarization at the beam injection and for obtaining the desired polarization in the MPD detector. The

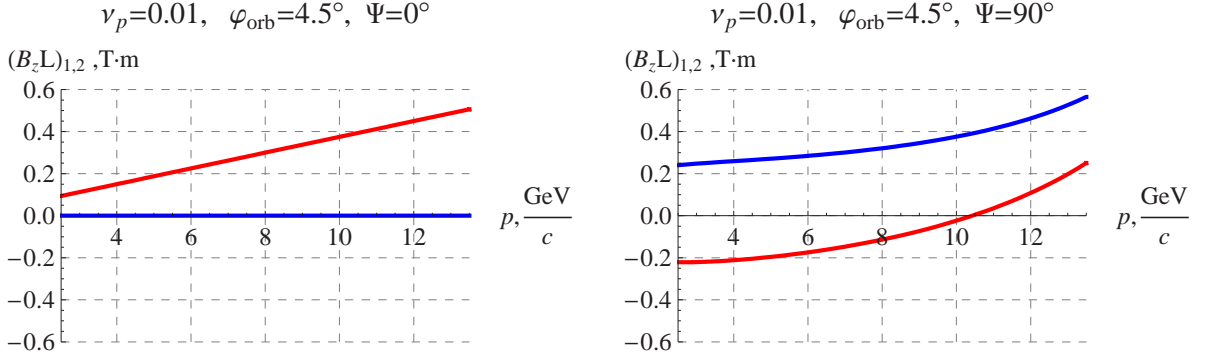


Figure 3: Dependencies of the insertions longitudinal field integrals (T·m) on the beam momentum (GeV/c) for the longitudinal (left) and radial (right) polarizations of the proton beam in the NICA collider rings.

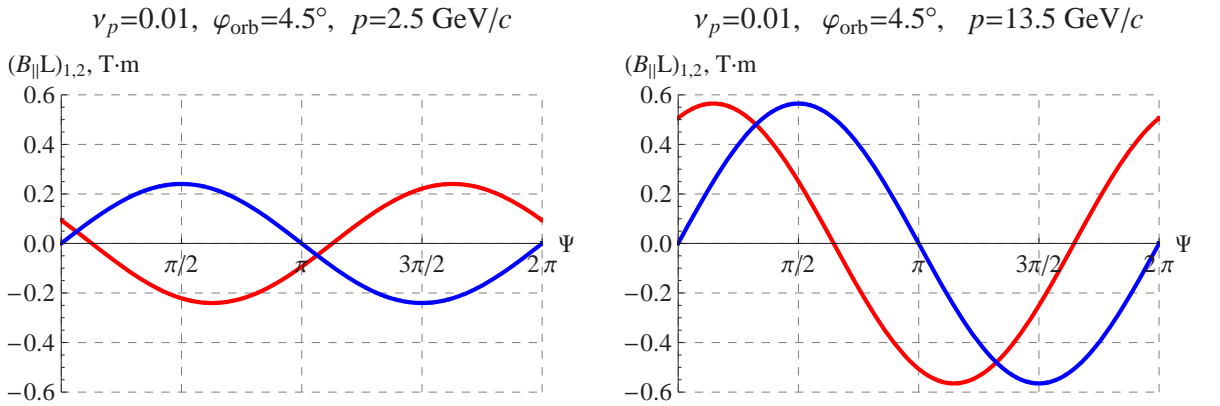


Figure 4: Dependencies of the insertions longitudinal field integrals (T·m) on the Ψ angle between the polarization and the beam direction for proton in the NICA collider rings.

scheme also provides capabilities of reversing the beam polarization during an experiment or changing it from the longitudinal to radial and vice-versa.

The strength of the zeroth spin resonance is determined by the excursions of particle trajectories from the collider's plane. In practice, the excursion of the beam's closed orbit due to imperfections of the collider's magnetic structure substantially exceeds the beam size. Therefore, dependence of the strength on the beam emittances is much less significant. The coherent part of the resonance strength due to the structure's imperfections can be compensated by corrector magnets. There is a unique opportunity of building an "ideal" collider with polarized beams using a real magnetic structure. The polarization orientation can be controlled by ultimately-small magnetic field integrals. It will allow polarized beam experiments with the highest precision levels.

To summarize, let us briefly state the main conclusions. Polarization schemes have been developed for the NICA collider to (i) allow control of the beam polarization using weak solenoids without significant orbit perturbation, (ii) make it possible to control efficiently the polarization of particles with any anomalous magnetic moment including those with a small one, such as deuterons, (iii) allow matching the polarization at the beam injection and obtaining the desired polarization in both MPD and SPD detectors, (iv) allow reversing the beam polarization during an experiment or changing it from the lon-

gitudinal to radial and vice-versa, and (v) make possible ultra-high precision experiments with polarized beams.

References

- [1] V.D.Kekelidze, A.D.Kovalenko et al. Scientific Program of NICA Project @ JINR, ICHEP-2012, Melbourne, Australia, July (2012).
- [2] A.D.Kovalenko et al. Polarized Deuterons and Protons at NICA@JINR, PEPAN, Vol. 45, No. 1 (2014).
- [3] Y. Zhang and J. Bisognano, arXiv:1209.0757v2[physics.acc-ph].
- [4] V.Morosov et al. Ion polarization control in MEIC rings using small magnetic field integrals. To be published in proceedings of Workshop on Polarized Sources, Targets and Polarimetry (PSTP 2013), USA(2013).

PROPOSAL ON THE SPIN PHYSICS DETECTOR (SPD) AT NICA

G.V. Meshcheryakov^{1†}, A.P. Nagaytsev¹ and V.K. Rodionov¹

(1) *Joint Institute for Nuclear Research, 141980 Dubna, Russia*

† *E-mail: glebvm@gmail.com*

Abstract

The SPD-T_HNICA project is under preparation at the second interaction point of the NICA collider. The purpose of this experiment is to study the nucleon spin structure with high intensity polarized light nuclear beams. The design of the collider can allow us to reach for proton beams a very high collision energy up to $\sqrt{s} \sim 26$ GeV with the average luminosity up to $10^{32} \text{cm}^2/\text{s}$, and for deuteron beams - a collision energy per nucleon up to $\sqrt{s} \sim 12$ GeV, the average luminosity reaches up to $10^{31} \text{cm}^2/\text{s}$. Both proton and deuteron beams will be effectively polarized. All these advantages give us unique possibilities to investigate the nucleon spin structure and various polarization phenomena. The preliminary design of the SPD detector for spin physics studies is proposed.

The possible SPD design is based on these main physics tasks proposed for the spin program at NICA [1]. Preliminary considerations of the event topologies require SPD to be equipped with the following sub-detectors covering $\sim 4\pi$ angular region around the beam interaction point: vertex detectors, tracking detectors, electromagnetic calorimeters, hadron detectors and muon detectors. Some of them must be in the magnetic field for which there are two options: toroid or solenoid. The main systems of SPD (Fig1.) are: a magnet (solenoid version) vertex detector (silicon), a central tracker (straw tubes), a trigger system (RPC, scintillator counters), a ECAL-muon/hadron system (range system RS).

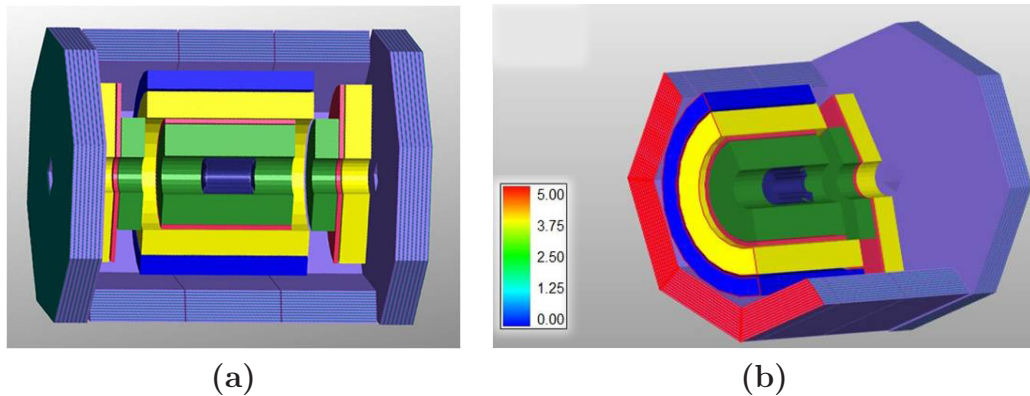


Figure 1: (a) The view of the SPD. (b) The inner view of the SPD.

Preliminary data on the size of the detector systems were used to simulate the ones given below. For barrel, detector positions in radius - the vertex detector :0.16 m – 0.34 m, with a length of 1 m; for the central tracking : 0.38m – 0.98m with a length of 2.5 m; for TOF/RPC: 1.00m – 1.08m with a length of 2.5 m; for ECAL: 1.10 m – 1.60 m with a length of 3.2 m, and for the solenoid magnet yoke: 1.65m – 2.00 m with a length of 3.2 m; for RS: 2.05m - -2.65m with a length of 5.50 m.

A toroid magnet provides a field-free region around the interaction point and does not disturb the beam trajectories and polarizations. It can consist of 8 superconducting coils symmetrically placed around the beam axis. A support ring upstream (downstream) of the coils hosts the supply lines for electric power and for liquid helium. At the downstream end, a hexagonal plate compensates magnetic forces to hold the coils in place. The field lines of an ideal toroid magnet are always perpendicular to the particles originating from the beam interaction point. Since the field intensity increases inverse proportion to the radial distance greater bending power is available for particles scattering at smaller angles and having higher momenta. These properties help to design a compact spectrometer that keeps the investment costs for the detector tolerable. The production of such a magnet requires insertion of the coils into the tracking volume occupying a part of the azimuthal acceptance. Preliminary studies show that the use of superconducting coils, made out of Nb_3Sn -Copper core surrounded by a winding of aluminium for support and cooling, allows one to reach an azimuthal detector acceptance of about 85%. No field is in the beam pipe.

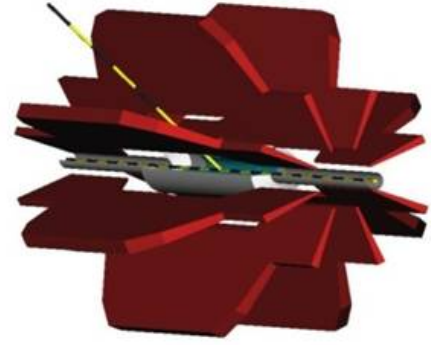


Figure 2: Preliminary view of the toroid magnet.

Concerning the proposal on solenoid magnet, shown in Fig.1: the maximum magnetic field of $\sim 1T$ over a length of about 3.2m and a diameter of 1.8m, the field homogeneity is foreseen to be better than 2% over the volume of the vertex detector and central tracker and one needs to have a special magnetic shield for transverse polarized beams. The design of the SPD solenoid would be very similar to MPD magnet.

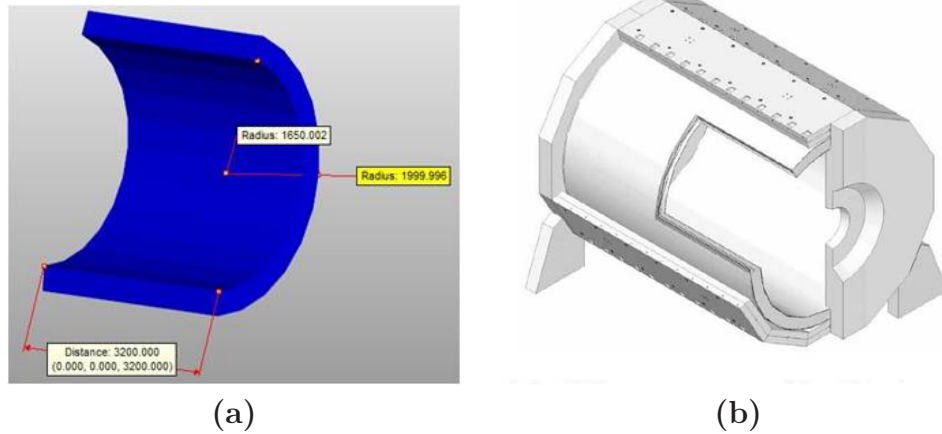


Figure 3: (a) The view of a part of SPD solenoid. (b) The technical view of the solenoid magnet.

One can propose to use Silicon layers as a vertex detector, which can be located outside the beam pipe. Several layers of double sided silicon strips can provide a precise vertex reconstruction and tracking of the particles before they reach the general SPD tracking system. The design should use a small number of silicon layers to minimize the radiation length of the material. With a pitch of 50-100 μm it is possible to reach the spatial

resolution of 20-30 μm . Such a spatial resolution would provide 50-80 μm for precision of the vertex reconstruction. This permits to reject the secondary decay vertexes.

Straw tubes can be used for the main detector of SPD Tracking System. This choice is due to the following properties of the straws tubes: -the minimum material for secondary particles ($X_0 \sim 0.1$); - the time (~ 200 -300 ns) and spatial resolutions ($100 \mu\text{m}$); expected particle rates (DAQ rates ~ 100 KHz). Two various technologies of straw production were developed at JINR [2], [3], which can be applied for SPD.

The main task of the trigger system is to provide separation of a particular reaction from all reactions occurred in collisions. Each of them will be pre-scaled with: two muons (or electrons/positrons) in final states; various types of hadrons in final states ($\pi^{+/-}$, K, p), photons, (π_0 , ω , η) and other reactions. The RPC is proposed to be used as the main trigger detector. Also Hodoscopes of scintillating counters can be used for triggering. They can be located before and after RS (or mounted in the last layers of RS) and before ECAL. The ECAL modules will also be used in the trigger system.

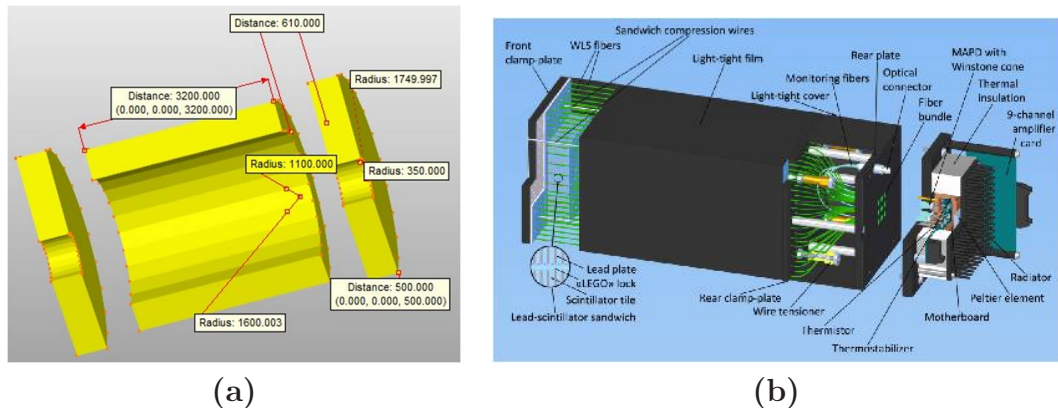


Figure 4: (a) The view of ECAL for SPD. (b) The design of an ECAL module.

ECAL can provide measurements for photon energy range 0.1 – 10GeV. Taking into account the space limitation in the barrel region, the total length of a module of ECAL should be less than 50 cm. The required energy resolution is $>10.0\%/\sqrt{E}$ (GeV). The latest version of the electromagnetic calorimeter (ECAL) modules, developed at JINR for the COMPASS-II experiment at CERN can be a good candidate for ECAL at SPD [4]. This “shashlyk”-type of modules utilises new photon detectors – Avalanche Multichannel Photon Detectors (AMPD). AMPD can work in a strong magnetic field [5].

The range system (RS) technique is proposed to be used as a hadron/muon detector(Fig.5). The laminated iron absorber structure and thickness are subjects of optimization for these purposes developed in [6].

One of the important points of Monte-Carlo studies is the background estimations. The following sources of background to the DY events are to be considered: decays of D mesons, J/ψ and ϕ' , K decays, π decays. Sources coming from detector uncertainties should be considered also:particle misidentification; vertex resolution; time (trigger) resolution.

The Letter of Intent (LoI) on spin physics experiments with SPD at the 2nd interaction point of the collider NICA is under preparation. The preliminary design of SPD is proposed. The main physics topics can be studied with the proposed detector:

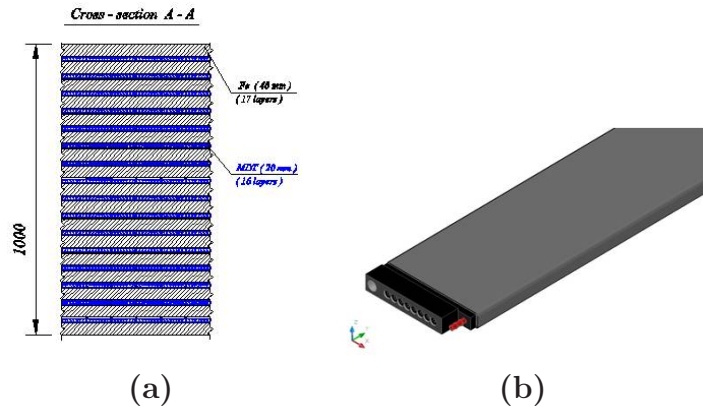


Figure 5: (a) The view of a muon system module (RS). (b) The view of the muon system module.

1. Studies of DY processes with unpolarized, longitudinally and transversely polarized p and D beams. Extraction of unknown (poorly known) parton distribution functions (PDFs).
2. PDFs from J/ψ production processes.
3. Prompt photons.
4. Spin effects in one and two hadron production processes.

References

- [1] A.P. Nagaytsev, Phys.Part.Nucl. 44 (2013) 6, 937-941.
- [2] V.A. Baranov et al ., Instrum.Exp.Tech. 55 (2012) 26-28.
- [3] V.D. Kekelidze et al., Phys.Part.Nucl.Lett. 9 (2012) 180-185.
- [4] N. Anfimov et al., Nucl.Instrum.Meth. A617 (2010) 78-80.
- [5] N. Anfimov et al., Nucl.Instrum.Meth. A628 (2011) 369-371.
- [6] FAIR/PANDA Collaboration, Technical Design Report - Muon System, September 2012.

THE FEASIBILITY OF DRELL-YAN PROCESSES AT NICA

R.R. Akhunzyanov

Joint Institute for Nuclear Research, Dubna, Russia

Abstract

The estimations of the feasibility of Drell-Yan processes at NICA are performed on the first “ideal level” (without any estimations of background and peculiarities of NICA-SPD setup). The expected high luminosity (up to $10^{32} \text{ cm}^{-2}\text{s}^{-1}$) presumably allows us to obtain good Drell-Yan statistics even above J/ψ resonance. Feasibility of measurements of single-spin asymmetries is estimated. Such measurements would give access to the transversity, Boer-Mulders, and Sivers PDFs, or at least, would allow to observe the sign of these PDFs.

Study of the Drell-Yan processes is the main topic of spin physics program at the future collider experiment NICA in JINR. In this work we provide some estimations of feasibility of such measurements.

The first step is to estimate total cross section and total number of events per year obtainable in the experiment. Such estimations are presented in Table 1. To calculate cross section simple leading order formulas were used:

$$\frac{d^2\sigma}{dQ^2 dx_1} = \frac{1}{sx_1} \frac{4\pi\alpha^2}{9Q^2} \sum_{f,\bar{f}} e_f^2 [f(x_1, Q^2)\bar{f}(x_2, Q^2)]_{x_2=Q^2/sx_1}, \quad (1)$$

$$\sigma_{tot} = \int_{Q_{min}^2}^{Q_{max}^2} dQ^2 \int_{x_{min}}^1 dx_1 \frac{d^2\sigma}{dQ^2 dx_1}, \quad (2)$$

where $x_{min} = Q^2/s$, and $Q \equiv M_{l+l-}$ is the mass of lepton pair. The number of events per year is then estimated as

$$N = \sigma_{tot} L t k_{acc}, \quad (3)$$

where $t = 1 \text{ year} \simeq 3.1 \cdot 10^7 \text{ s}$, L is luminosity, which depends on \sqrt{s} and amounts to about $10^{32} \text{ cm}^{-2}\text{s}^{-1}$, $k_{acc} \simeq 0.5$ is a factor accounting to useful part of the accelerator’s working time. From Table 1 one can see that even above the J/ψ region the expected statistics is rather high - of the order of 10^5 events per year, what, as we will show below, presumably gives possibility to measure the various leading-twist PDFs, such as, for example, transversity, Boer-Mulders PDF, and Sivers PDF.

All variants of beam polarization would be possible in NICA, and therefore, in principle, all leading twist PDFs could be extracted from data. In this paper we focus on single polarized Drell-Yan processes with transverse polarization of hadrons. Its cross section is

lower cut on M_{l+l^-} , GeV	2.0	3.1	3.5	4.0
$\sqrt{s} = 24$ GeV ($L \simeq 1.0 \cdot 10^{32}$ cm $^{-2}$ s $^{-1}$)				
σ_{DY} total, nb	1.15	0.20	0.115	0.059
N events per year, 10^3	1800	313	179	92
$\sqrt{s} = 26$ GeV ($L \simeq 1.2 \cdot 10^{32}$ cm $^{-2}$ s $^{-1}$)				
σ_{DY} total, nb	1.30	0.24	0.140	0.074
N events per year, 10^3	2490	460	269	142

Table 1: Total cross section and number of Drell-Yan events per year expected at NICA, corresponding to different values of the lower cut on the mass of lepton pair.

given by formula [1]:

$$\begin{aligned}
\frac{d\sigma(H_1 H_2^\dagger \rightarrow l \bar{l} X)}{d\Omega dx_1 dx_2 d^2 \mathbf{q}_T} &= \frac{\alpha^2}{12Q^2} \sum_{q, \bar{q}} e_q^2 \left\{ (1 + \cos^2 \theta) \mathcal{F}[f_1 \bar{f}_1] \right. \\
&+ \sin^2 \theta \cos(2\phi) \mathcal{F} \left[\frac{(2\hat{\mathbf{h}} \cdot \mathbf{k}_{1T} \hat{\mathbf{h}} \cdot \mathbf{k}_{2T} - \mathbf{k}_{1T} \cdot \mathbf{k}_{2T})}{M_1 M_2} h_1^\perp \bar{h}_1^\perp \right] \\
&+ (1 + \cos^2 \theta) \sin(\phi - \phi_{S_2}) \mathcal{F} \left[\frac{\hat{\mathbf{h}} \cdot \mathbf{k}_{2T}}{M_2} \bar{f}_1 f_{1T}^\perp \right] - \sin^2 \theta \sin(\phi + \phi_{S_2}) \mathcal{F} \left[\frac{\hat{\mathbf{h}} \cdot \mathbf{k}_{1T}}{M_1} \bar{h}_1^\perp h_1 \right] \\
&\left. - \sin^2 \theta \sin(3\phi - \phi_{S_2}) \mathcal{F} \left[\frac{2\hat{\mathbf{h}} \cdot \mathbf{k}_{2T} [2(\hat{\mathbf{h}} \cdot \mathbf{k}_{1T})(\hat{\mathbf{h}} \cdot \mathbf{k}_{2T}) - \mathbf{k}_{1T} \cdot \mathbf{k}_{2T}] - \mathbf{k}_{2T}^2 (\hat{\mathbf{h}} \cdot \mathbf{k}_{1T})}{2M_1 M_2^2} \bar{h}_1^\perp h_{1T}^\perp \right] \right\} \quad (4)
\end{aligned}$$

where

$$\begin{aligned}
\mathcal{F}[w(\mathbf{k}_{1T}, \mathbf{k}_{2T}) f_1 \bar{f}_2] &\equiv \int d^2 \mathbf{k}_{1T} d^2 \mathbf{k}_{2T} \delta^{(2)}(\mathbf{k}_{1T} + \mathbf{k}_{2T} - \mathbf{q}_T) w(\mathbf{k}_{1T}, \mathbf{k}_{2T}) \times \\
&\times (f_1(x_1, \mathbf{k}_{1T}^2) \bar{f}_2(x_2, \mathbf{k}_{2T}^2) + \bar{f}_1(x_1, \mathbf{k}_{1T}^2) f_2(x_2, \mathbf{k}_{2T}^2)).
\end{aligned}$$

Applying integration over the angles with the properly chosen weights that allows to separate the contributions containing different transverse momentum dependent PDFs, one may easily construct single-spin asymmetries (SSA) that give access to such important and still poorly known PDFs as transversity h_1 and Boer-Mulders PDF h_1^\perp :

$$A_{UT}^{\sin(\phi + \phi_S)} = \frac{\int d\Omega d\phi_S \sin(\phi + \phi_S) [d\sigma(\mathbf{S}_{2T}) - d\sigma(-\mathbf{S}_{2T})]}{\int d\Omega d\phi_S [d\sigma(\mathbf{S}_{2T}) + d\sigma(-\mathbf{S}_{2T})]/2} = -\frac{1}{2} \frac{\sum_q e_q^2 \mathcal{F} \left[\frac{\hat{\mathbf{h}} \cdot \mathbf{k}_{1T}}{M_1} \bar{h}_{1q}^\perp h_{1q} \right]}{\sum_q e_q^2 \mathcal{F} [f_{1q} f_{1q}]}, \quad (5)$$

to Siverts PDF f_{1T}^\perp :

$$A_{UT}^{\sin(\phi - \phi_S)} = \frac{\int d\Omega d\phi_S \sin(\phi - \phi_S) [d\sigma(\mathbf{S}_{2T}) - d\sigma(-\mathbf{S}_{2T})]}{\int d\Omega d\phi_S [d\sigma(\mathbf{S}_{2T}) + d\sigma(-\mathbf{S}_{2T})]/2} = \frac{\sum_q e_q^2 \mathcal{F} \left[\frac{\hat{\mathbf{h}} \cdot \mathbf{k}_{2T}}{M_2} \bar{f}_1^q f_{1T}^{\perp q} \right]}{\sum_q e_q^2 \mathcal{F} [\bar{f}_{1q} f_{1q}]}, \quad (6)$$

and similarly to pretzelocity h_{1T}^\perp .

However, it is rather difficult to deal with convolutions entering these asymmetries since we do not know the dependence of PDFs on transverse quark momenta. One possibility is to apply simple Gaussian model (see for example, [2]). Another, very attractive

way to deal with the convolutions is to apply integration over q_T with appropriately chosen weight [3–5] which allows to factorize the convolutions into the simple algebraic products. So, we consider the q_T -weighted asymmetries

$$A_{UT}^{\sin(\phi \pm \phi_S) \frac{q_T}{M_N}} = \frac{\int d\Omega d\phi_S \int d^2\mathbf{q}_T (|\mathbf{q}_T|/M) \sin(\phi \pm \phi_S) [d\sigma(\mathbf{S}_{2T}) - d\sigma(-\mathbf{S}_{2T})]}{\int d\Omega d\phi_S \int d^2\mathbf{q}_T [d\sigma(\mathbf{S}_{2T}) + d\sigma(-\mathbf{S}_{2T})]/2}, \quad (7)$$

one of which gives access to Boer-Mulders PDF with transversity:

$$A_{UT}^{\sin(\phi + \phi_S) \frac{q_T}{M_N}} = -\frac{\sum_q e_q^2 [\bar{h}_{1q}^{\perp(1)} h_{1q} + (q \leftrightarrow \bar{q})]}{\sum_q e_q^2 [\bar{f}_{1q} f_{1q} + (q \leftrightarrow \bar{q})]}, \quad (8)$$

while the other provides access to Sivers PDF:

$$A_{UT}^{\sin(\phi - \phi_S) \frac{q_T}{M_N}} = 2\frac{\sum_q e_q^2 [\bar{f}_1^q f_{1T}^{\perp q(1)} + (q \leftrightarrow \bar{q})]}{\sum_q e_q^2 [\bar{f}_{1q} f_{1q} + (q \leftrightarrow \bar{q})]}. \quad (9)$$

To estimate the feasibility of these asymmetries we performed simulations with the generator of polarized Drell-Yan events [5] at NICA kinematics.

We prepared two samples with statistics 100K and 50K of pure Drell-Yan events for each of two Q^2 ranges: $2 < Q^2 < 8.5 \text{ GeV}^2$ and $Q^2 > 11 \text{ GeV}^2$. The cut $2 < Q^2 < 8.5 \text{ GeV}^2$ is applied to avoid misidentification of lepton pairs due to numerous background processes below $Q^2 < 2 \text{ GeV}^2$ and to exclude lepton pairs coming from the J/ψ region. The cut $Q^2 > 11 \text{ GeV}^2$ is also applied to avoid the lepton pairs coming from the J/ψ region. The results are presented at Figs. 1-4. The results at Figs. 1 and 3 show that at statistics of 100K pure Drell-Yan events one can hope to reconstruct the functional forms of the single-spin asymmetries. But even at the relatively low statistics of 50K Drell-Yan events (Figs. 2 and 4) one would observe, at least, the sign of the single-spin asymmetries, what is very important in order to check the fundamental QCD prediction of the sign change for the Sivers and Boer-Mulders PDFs.

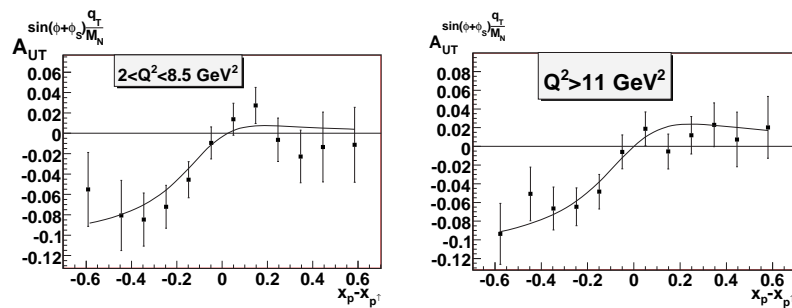


Figure 1: Estimation of asymmetry $A_{UT}^{\sin(\phi + \phi_S) \frac{q_T}{M_N}}$ for NICA, $\sqrt{s} = 24 \text{ GeV}$. Here Boer model [1] is used for Boer-Mulders PDF and evolution model is used for transversity. The points with errors bars are obtained by using simulations with the polarized DY event generator at the applied statistics of 100K pure Drell-Yan events.

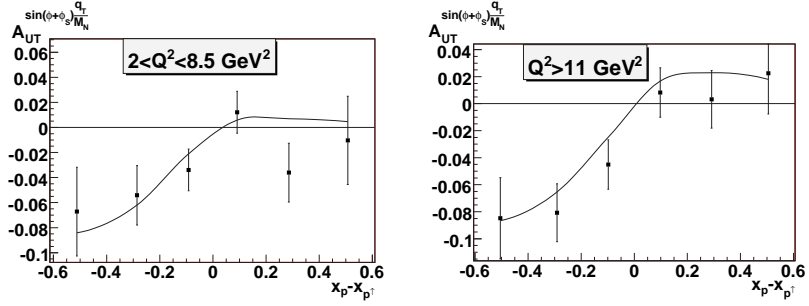


Figure 2: Same as Fig. 1, but for 50K Drell-Yan events.

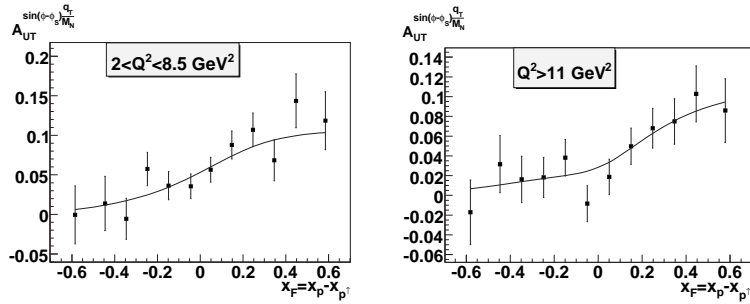


Figure 3: Estimation of asymmetry $A_{UT}^{\sin(\phi-\phi_S)\frac{q_T}{M_N}}$ for NICA, $\sqrt{s} = 24$ GeV. Here fit from [3] is used for Siverts PDF. The points with errors bars are obtained by using simulations with the polarized DY event generator at the applied statistics of 100K pure Drell-Yan events.

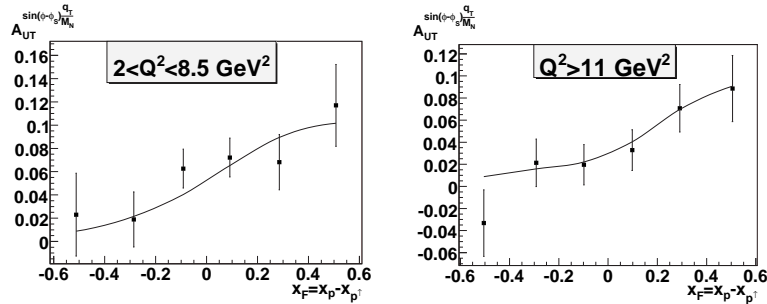


Figure 4: Same as Fig. 3, but for 50K Drell-Yan events.

References

- [1] D. Boer, Phys. Rev. D 60 (1999) 014012.
- [2] J.C. Collins et al, Phys. Rev. D 73 (2006) 094023.
- [3] A. V. Efremov et al, Phys. Lett. B 612 (2005) 233.
- [4] A. Sissakian, O. Shevchenko, A. Nagaytsev and O. Ivanov, Phys. Rev. D 72, 054027 (2005).
- [5] A. Sissakian, O. Shevchenko, A. Nagaytsev, O. Ivanov, Eur. Phys. J. C 59 (2009) 659.

SPIN PHYSICS WITH DIRECT PHOTONS AT NICA SPD

A. Guskov^{1†}

(1) *Joint Institute for Nuclear Research, Dubna*

† *E-mail: guskov@jinr.ru*

Abstract

Registration of direct photons at NICA SPD can be used for study of gluon distributions in nucleons. Single transverse spin asymmetry A_N provides access to Sivers gluon function, while double longitudinal spin asymmetry A_{LL} is related to gluon polarization Δg .

Production of direct photons in the non-polarized and polarized pp (pd) reactions provides information on the gluon distributions in nucleons. There are two main hard processes where direct photons can be produced: gluon Compton scattering, $gq \rightarrow \gamma X$, and quark-antiquark annihilation, $q\bar{q} \rightarrow \gamma X$ (Fig. 1). The total cross section of the prompt photon production in the pp -collision at $\sqrt{s} = 24 \text{ GeV}$ via the first process (according to PYTHIA 6.4 [1]) is 1080 nbn, while the cross section of the second process is about 210 nbn. So, the gluon Compton scattering is the main mechanism of the direct photon production at NICA SPD.

The non-polarized cross section for production of a photon with the transverse momentum p_T and rapidity y in the $pp \rightarrow \gamma X$ can be written [2] as follows:

$$d\sigma = \sum_i \int_{x_{min}}^1 dx_a \int d^2\mathbf{k}_{Ta} d^2\mathbf{k}_{Tb} \frac{x_a x_b}{x_a - (p_T/\sqrt{s})e^y} [q_i(x_a, \mathbf{k}_{Ta}) G(x_b, \mathbf{k}_{Tb}) \times \quad (1)$$

$$\times \frac{d\hat{\sigma}}{d\hat{t}}(q_i G \rightarrow q_i \gamma) + G(x_a, \mathbf{k}_{Ta}) q_i(x_b, \mathbf{k}_{Tb}) \frac{d\hat{\sigma}}{d\hat{t}}(G q_i \rightarrow q_i \gamma)],$$

where k_{Ta} (k_{Tb}) is the transverse momentum of the interacting quark (gluon), x_a (x_b) is the fraction of the proton momentum carried by them and $q_i(x, k_T)$, ($G(x, k_T)$) is the quark (gluon) distribution function with the specified k_T . One can show [2], that the above expression can be used also for extraction of the polarized gluon distribution (Sivers gluon function) from measurement of the transverse single spin asymmetry A_N :

$$A_N = \frac{\sigma^\uparrow - \sigma^\downarrow}{\sigma^\uparrow + \sigma^\downarrow} \quad (2)$$

Here σ^\uparrow and σ^\downarrow are the cross sections of the direct photon production for the opposite transverse polarizations of one of the colliding protons. In [3] it has been pointed out that the asymmetry A_N at large positive x_F is dominated by quark-gluon correlations while at large negative x_F [5] it is dominated by pure gluon-gluon correlations. The further development of the corresponding formalism can be found in [5], [6].

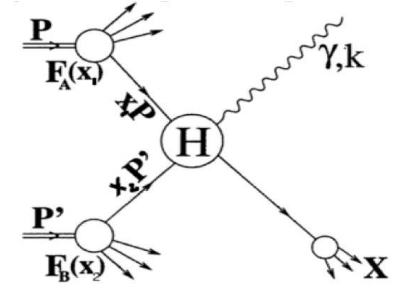


Figure 1: Diagram of the direct photon production. Vertex H corresponds to $qg \rightarrow q\gamma$ or $q\bar{q} \rightarrow g\gamma$ hard processes.

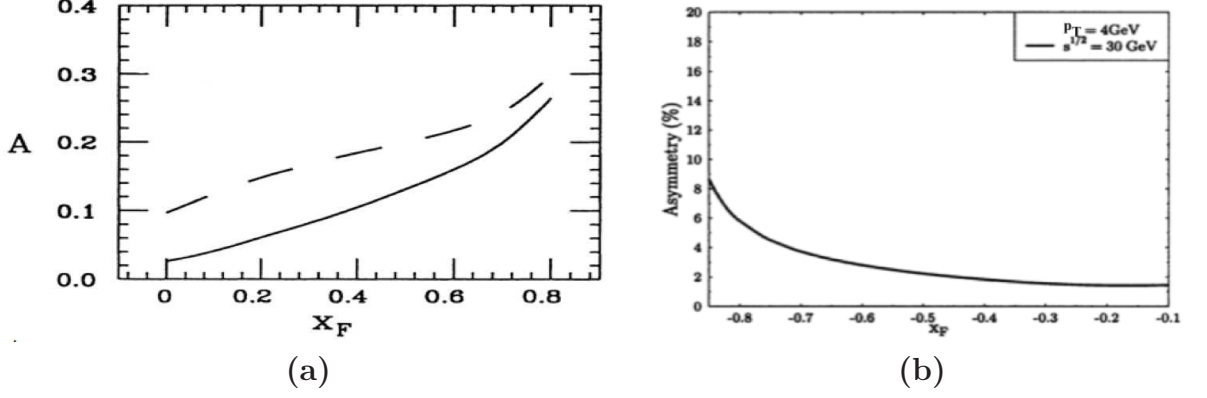


Figure 2: Theoretical predictions for A_N at $\sqrt{s}=30$ GeV, $p_T=4$ GeV/c (a) from [5], (b) from [3].

Predictions for the value of A_N at $\sqrt{s} = 30$ GeV, $p_T = 4$ GeV/c can be found in [5] for negative x_F (Fig. 2 (a)) and in [3] for positive x_F (Fig. 2 (b)). In both cases the A_N values remain sizable.

The first attempt to measure A_N at $\sqrt{s} = 19.4$ GeV was performed in the fixed target experiment E704 at Fermilab [7] in the kinematic range $-0.15 < x_F < 0.15$ and 2.5 GeV/c $< p_T < 3.1$ GeV/c. Results are consistent with zero within large statistical and systematic uncertainties. The single spin asymmetries in the direct photon production will be measured also by PHENIX [8] and STAR [9] at RHIC.

Production of direct photons at large transverse momentum with longitudinally polarized proton beams is a very promising method to measure gluon polarization Δg [10]. Longitudinal double spin asymmetry A_{LL} , defined as:

$$A_{LL} = \frac{(\sigma_{++} - \sigma_{--}) - (\sigma_{+-} - \sigma_{-+})}{(\sigma_{++} + \sigma_{--}) + (\sigma_{+-} + \sigma_{-+})}, \quad (3)$$

where $\sigma_{\pm\pm}$ are cross sections for all four helicity combinations, can be written (assuming dominance of the Compton process) as [10]:

$$A_{LL} \approx \frac{\Delta g(x_1)}{g(x_1)} \cdot \left[\frac{\sum_q e_q^2 [\Delta q(x_2) + \Delta \bar{q}(x_2)]}{\sum_q e_q^2 [q(x_2) + \bar{q}(x_2)]} \right] \cdot \hat{a}_{LL}(gq \rightarrow \gamma q) + (1 \leftrightarrow 2), \quad (4)$$

where the second factor is known as A_{1p} asymmetry from polarized SIDIS and $a_{LL}(gq \rightarrow \gamma q)$ is spin asymmetry for sub-process $gq \rightarrow \gamma q$. Measurement of A_{LL} at $\sqrt{s} > 100$ GeV is included in the long range program of RHIC [11].

In order to study of direct photon production in pp-collisions at NICA SPD ($\sqrt{s} = 24$ GeV) a sample of MC events was generated using the PYTHIA 6.4.2 code. Five hard processes with direct photons in the final state were used: $qg \rightarrow q\gamma$, $q\bar{q} \rightarrow g\gamma$, $gg \rightarrow g\gamma$, $q\bar{q} \rightarrow \gamma\gamma$ and $gg \rightarrow \gamma\gamma$. Relative probabilities of the first two processes are 85% and 15%, respectively, while the contribution of all others is less than 0.2%. CTEQ

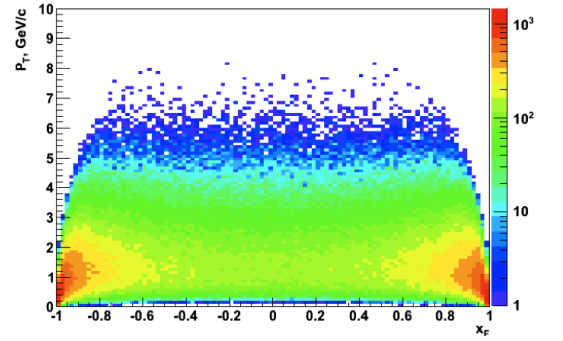


Figure 3: The plot p_T vs. x_F for direct photons.

5L is used for the set of PDFs. No special kinematic cuts are applied. The p_T vs. x_F distribution for direct photons is shown in Fig 3. The photon energy, E_γ , is plotted vs. the photon scattering angle θ in Fig 4(a). The Figure 4 (b) shows the corresponding plot for minimum bias photons (mainly from π^0 decay). The MC simulation shows that for $p_T > 4 \text{ GeV}$ signal-to-background ratio is about 5% that is in good agreement with the data of the UA6 experiment for unpolarized protons at $\sqrt{s} = 24.3 \text{ GeV}$ [12].

For effective registration and identification of direct photons, the SPD detector should have:

- an electromagnetic calorimeter (ECAL) with a geometry close to 4π and with granularity optimized to the expected occupancy;
- a tracking system capable to distinguish between clusters from neutral and charged particles in ECAL. It also should be capable to reconstruct the interaction point;
- a trigger system based on ECAL. Since for A_N and A_{LL} measurements quite energetic photons are needed only, for the main trigger one can require an energy of above 2-3 GeV deposited in any cell of ECAL. Expected trigger rate is 70 kHz for 2 GeV and 25 kHz for 3 GeV threshold;
- a DAQ system with a bandwidth up to 100 kHz;
- a luminosity monitor;
- a local polarimetry.

Estimations of direct photon production rate for $\sqrt{s} = 24 \text{ GeV}$ and $\sqrt{s} = 26 \text{ GeV}$ are presented in Tab. 1. Estimate statistical accuracy of A_N and A_{LL} measurement one assumes that beam polarization (both transversal and longitudinal) $P = \pm 0.8$. General detector efficiency (acceptance, efficiency of event reconstruction and selection criteria) is assumed to be 50%. After 7000 hours of data taking with maximal luminosity A_N and A_{LL} could be measured with statistical accuracy 0.11% and 0.18% correspondently in each of 18 bins of x_F in the range $-0.9 < x_F < +0.9$. Large statistics provides opportunity

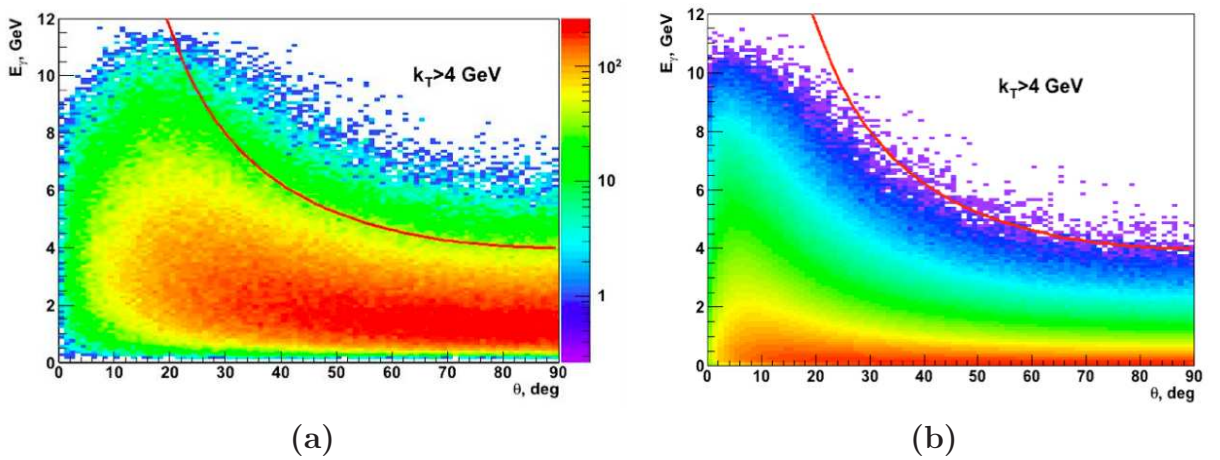


Figure 4: Distribution of energy E_γ as a function of scattering angle θ . Red lines correspond to $p_T = 4 \text{ GeV}$. (a) for direct photons, (b) for minimum bias photons.

to measure precisely also two-dimensional dependence of the asymmetries on x_F and p_T . As for systematic uncertainty, it will depend mainly on precision of luminosity and beam polarization control, accuracy of π^0 and η background rejection and contribution of fragmentation photons.

Table 1: Expected rates of direct photon production events.

$\sqrt{s}=24$ GeV $L = 1.0 \times 10^{32}, cm^{-1}s^{-1}$	$\sigma_{tot},$ nbarn	$\sigma_{P_T>4 GeV/c},$ nbarn	Events/7000 h, 10^6	Events/7000 h, $10^6 (P_T > 4 GeV/c)$
All processes	1290	42	3260	105
$qg \rightarrow q\gamma$	1080	33	2730	84
$q\bar{q} \rightarrow g\gamma$	210	9	530	21
$\sqrt{s}=26$ GeV $L = 1.2 \times 10^{32}, cm^{-1}s^{-1}$	$\sigma_{tot},$ nbarn	$\sigma_{P_T>4 GeV/c},$ nbarn	Events/7000 h, 10^6	Events/7000 h, $10^6 (P_T > 4 GeV/c)$
All processes	1440	48	4340	144
$qg \rightarrow q\gamma$	1220	38	3680	116
$q\bar{q} \rightarrow g\gamma$	240	10	660	28

References

- [1] Torbjörn Sjöstrand et al, hep-ph/0603175, LU TP 06?13, FERMILAB-PUB-06-052-CD-T (2006).
- [2] I. Schmidt, J. Soffer and J.J. Yang, Phys. Lett. B 612 (2005) 258-262.
- [3] J. Qui and G. Sterman, Phys. Rev. Lett. 67 (1991) 2264; Nucl. Phys. B 378 (1992) 52.
- [4] J. Xiandong, Phys. Lett. B 289 (1992) 137.
- [5] N. Hammon et al., Phys. G: Nucl. Part. Phys. 24 (1998) 991-1001.
- [6] L. Gamberg and Z. Kang, Phys. Lett. B 718 (2012) 181.
- [7] D. L. Adams et al., Phys. Lett. B 345 (1995) 569-575.
- [8] S. Campbell: "Prompt photon measurements with PHENIX's MPC-EX detector", talk at Nuclear Dynamics 2013, <https://www.phenix.bnl.gov/phenix/WWW/talk/archive/2013/ndww13/t2103.pdf>
- [9] Len K. Eun, <http://meetings.aps.org/link/BAPS.2011.DNP.HC.3>.
- [10] Cheng HY, Lai SN. Phys. Rev. D 41:91 (1990) 91-102.
- [11] G. Bunce et al. Ann.Rev.Nucl.Part.Sci.50:525-575, (2000).
- [12] G. Sozzi et al., Phys. Lett. B 317 (1993).

POSSIBILITIES FOR THE SPIN-DEPENDENT OBSERVABLES MEASUREMENT IN ELASTIC NN SCATTERING AT NICA

V.I. Sharov¹

*Joint Institute for Nuclear Research,
Veksler and Baldin Laboratory of High Energy Physics,
141980 Dubna, Russia*

Abstract

The possibilities for investigation of the elastic NN scattering observables at $NICA$ collider are shown. The unpolarized differential NN cross section I_{oooo} , analyzing powers for primary reactions with polarized beam A_{oono} or target A_{oon} , and spin correlation parameters A_{oonn} and A_{ookk} in primary reactions with polarized both the beam and target can be measured. The planned luminosity of the polarized colliding beams allows to obtain enough high event rate for such measurements. The colliding polarized beams using has a number of suitable preferences with comparison to the "fixed" target experiments (wider energy range, "target" without background impurities).

One of the main physical task for the $NICA$ collider are research in the particle spin physics [1], continuing the $JINR$ research program in this field to a new level. The $NICA$ will provide the interactions colliding beams of light ions and polarized protons and deuterons beams. Obtaining of new data on the spin dependent observables for elastic NN scattering in energy region above 1 GeV is one of the priority areas for such research.

Why this problem is relevant today? "The theory of the nucleon-nucleon (NN) interaction in the range of about 1 – 10 GeV is one of the most pressing open questions of modern nuclear / particle physics. Below that energy range, chiral effective field theory applies as well as meson theory. At very high energies ($\sim 100 GeV$) perturbative QCD can be used. But it is the "intermediate" region of a few GeV where theory has big problems. Meaningful theoretical work cannot be done unless we have also data in that critical region. The data for np are very scarce, too few to even pin down a reasonable phenomenology" [2].

Currently full phenomenological description (energy dependent phase shift analysis) of NN interactions are possible now only up to 3 GeV for pp and 1.3 GeV for np collisions. In addition, there is no dynamical theory (meson exchange, nonperturbative QCD) which can describe measured NN spin dependent observables over energy region $> 1 GeV$. "For the past 30 years QCD -based calculations have continued to disagree with the ZGS 2-spin and AGS 1-spin elastic data and the ZGS , AGS , $Fermilab$ and $RHIC$ inclusive data. These large spin effects do not go to zero at high energy or high- P_{\perp} as was predicted. ... These precise spin experiments provide experimental guidance for the required modification of the theory of Strong Interactions" [3].

To show the benefits of the elastic NN scattering investigation we list some options why the spin-dependent observables for elastic NN scattering are the most preferred for

¹ e-mail: sharov@sunhe.jinr.ru

experimental studies and attempts to describe the dynamic of strong interactions.

1. The inelasticities do not complicate the attempts of dynamical models creation.
2. The corresponding formal description of the NN interaction (S matrix theory) exists.
3. "Elastic scattering is especially important, because it is the: Only exclusive process that is large enough to be measured at TeV energy. This is because proton-proton elastic scattering is dominated by the diffraction due to the millions of inelastic channels competing for the $\sigma_{TOT} \leq 100$ millibarns at TeV energies" [3].
4. Some of the spin effects remain large enough over a wide energy region of the interacting nucleons up to $RHIC$ energies.
5. The experimental data for the elastic spin-dependent NN observables contain sufficient information about the properties of NN interaction: the pp data for the isovector part, and the np data for the isoscalar one.

In this contribution we used the NN formalism and notations for elastic nucleon-nucleon scattering observables from [4-6]. In four-subscript notation X_{srbt} for experimental quantities, introduced by [6], subscripts s , r , b , and t refer to the polarization components of the scattered, recoil, beam, and target particles, respectively. If an initial particle is unpolarized or a final particle polarization is not analyzed, the corresponding subscript is set equal to zero.

Which spin-dependent elastic NN observables can be measured by the detectors for $NICA$? A compact design of complex detector for the colliders does not allow the scattered and recoil particles polarizations measurements. For these purposes the secondary scattering of analyzed particle and large enough devices (polarimeters) are needed. Therefore the detectors for $NICA$ allow to measure the following elastic NN observables: unpolarized differential NN cross section I_{0000} , analyzing powers for primary reactions with polarized beam A_{00i0} or target A_{000k} , and spin correlation parameters A_{00ik} in primary reactions with the beam and target both polarized.

In principle, 256 experimental quantities exist, which can be defined as components of various tensors. Due to the symmetry principles there remain only 25 linearly independent experimental quantities. For any CM observable X_{pqik} , the following expression holds: $d\sigma/d\Omega X_{pqik} = \frac{1}{4}Tr(\sigma_{1p}\sigma_{2q}M\sigma_{1i}\sigma_{2k}M^+)$, where $d\sigma/d\Omega I_{0000} = \frac{1}{4}Tr(MM^+)$ is the unpolarized differential cross section. Some of CM experimental quantities in term of scattering amplitudes are listed below: $d\sigma/d\Omega I_{0000} \equiv \frac{1}{2}(|a|^2 + |b|^2 + |c|^2 + |d|^2 + |e|^2)$, $d\sigma/d\Omega P \equiv d\sigma/d\Omega P_{n000} = d\sigma/d\Omega P_{0n00} = d\sigma/d\Omega A_{00n0} = d\sigma/d\Omega A_{000n} = Re e a * e$, $d\sigma/d\Omega A_{00nn} = \frac{1}{2}(|a|^2 - |b|^2 - |c|^2 + |d|^2 + |e|^2)$, $d\sigma/d\Omega A_{00kk} = -Re e a * d \cos \theta + Re e b * c + Im m d * e \sin \theta$, $d\sigma/d\Omega A_{00ss} = Re e a * d \cos \theta + Re e b * c + Im m d * e \sin \theta$, $d\sigma/d\Omega A_{00sk} = -Re e a * d \sin \theta - Im m d * e \cos \theta$.

What experimental quantities should be measured to obtain the spin-dependent NN observables? Expression for the differential cross sections for scattering of polarized nucleon beam with energy E on the polarized target nucleons with the scattered particle detection at an angle of θ is [4]: $d\sigma/d\Omega^{pol}(E, \theta) = d\sigma/d\Omega^0(E, \theta)[1 + A_{00n0}(E, \theta)PB_n + A_{000n}(E, \theta)PT_n + A_{00nn}(E, \theta)PB_nPT_n + A_{00ss}(E, \theta)PB_sPT_s + A_{00kk}(E, \theta)PB_kPT_k + A_{00sk}(E, \theta)(PB_sPT_k + PB_kPT_s)]$, where $d\sigma/d\Omega^0(E, \theta)$ is the cross section for unpolarized nucleons, and PB_k and PT_k are the polarization values of the colliding beams.

Using this formula one can obtain the expression for an asymmetry \mathbf{a} in the NN scattering with opposite signs of nucleon beam polarizations. For example, for $PB_n = PT_n = PB_s = PT_s = 0$ and $PB_k \neq 0, PT_k \neq 0$ and sign $PB_k = T - 1$ we have

$$[d\sigma/d\Omega]^+ - [d\sigma/d\Omega]^- = 2[d\sigma/d\Omega]^o A_{00kk} |PB_k|PT_k \text{ and}$$

$$[d\sigma/d\Omega]^+ + [d\sigma/d\Omega]^- = 2[d\sigma/d\Omega]^o, \text{ and the asymmetry will be}$$

$$\mathbf{a} = ([d\sigma/d\Omega]^+ + [d\sigma/d\Omega]^-) / ([d\sigma/d\Omega]^+ - [d\sigma/d\Omega]^-) = A_{00kk} |PB_k|PT_k .$$

Thus in order to obtain the values of the spin-dependent NN observables we have to measure the asymmetry \mathbf{a} , that is ratio of the difference and sum of the elastic NN differential cross sections for opposite signs of the polarizations of colliding polarized particles. To find the $d\sigma/d\Omega(E, \theta)$ values it is necessary to measure the angular distributions of the elastically scattered nucleons. Relative monitoring of the obtained angular distributions of elastic NN scattering events can be made by using information (readings) from the pickup electrodes placed at both sides of the intersection beams point. Since the measured value of the asymmetry is the ratio of difference and sum of the elastic event yields, measured in the same data taking run, the absolute beams intensity monitoring is not required.

Also we need to know the polarization of the colliding beams PB_k and PT_k , measured under the same conditions. For the measurement and continuous monitoring of the values and signs of colliding beam polarizations a complete and reliable polarimetry system is needed. It is desired to have the beam line polarimeters to be placed:

1. before the polarized beam injection into Nuclotron - low energy polarimeter;
 2. polarimeter inside the Nuclotron ring (using internal target station);
 3. special devices (polarimeters) placed at each of accumulated polarized colliding beam.
- Besides detection by SPD detector cases of the elastic NN scattering will make it possible to determine the left-right asymmetries of the reaction yield. This will enable us to estimate the polarization values of the colliding beams directly at the interaction point. This could be done for both proton and deuteron colliding beams.

At the *NICA* collider, currently under construction, it is planned to have the colliding beams of polarized protons and deuterons. Range of kinetic energy of the colliding beams of polarized protons $p \uparrow p \uparrow$ expected to be $5 \div 12.6 \text{ GeV}$ ($\sqrt{s_{NN}} = 12 \div 25 \text{ GeV}$). Proton number per bunch: 6^{10} , number of bunches: 10 and luminosity $L = 1.1^{30} \text{ cm}^{-2} \cdot \text{s}^{-1}$. Range of kinetic energy of the colliding beams of polarized deuterons $d \uparrow d \uparrow$ expected to be $2 \div 5.9 \text{ GeV}/u$ ($\sqrt{s_{dd}} = 4 \div 13.8 \text{ GeV}$) [7].

The minimal nucleon kinetic energy at which the proton beam can be successfully extracted from the Nuclotron $T_{p,min} \sim 0.5 \text{ GeV}$ (from the discussions with accelerator specialists). This value correspond to the incident nucleon laboratory kinetic energy $T_{n,Lab} \sim 2.5 \text{ GeV}$ for "fix" target experiment. This is the possible lower boundary of energy range acceptable for colliding beams at *NICA*. The upper boundary of energy range for colliding beams at *NICA* will be approximately $T_{n,max} \sim 6.0 \text{ GeV}/u$. This value corresponds to the incident nucleon kinetic energy $T_{n,Lab} \sim 100 \text{ GeV}/u$ for "fix" target experiment.

To measure the elastic NN differential cross section we have to select the elastic NN events among all inelastic ones. For the elastic NN interaction in the centre-of-mass system the outgoing nucleons have the following kinematical characteristics:

1. This nucleons have equal momentum values.
2. The nucleon momenta have opposite directions.
3. The nucleon momenta do not depend from the scattering angle θ_{CM} .
4. The absolute values of nucleon momenta are near to the colliding nucleon ones.

Listed items cause the requirements to the Spin Physics Detector (*SPD*) for the elastic events selection. The *SPD* should provide the energy and track (momentum) measurements of the scattered nucleons, as well as the determination of the interaction point of the primary colliding particles

Using the $p \uparrow p \uparrow$ polarized colliding beams the isospin $I = 1$ spin-dependent observables can be measured in elastic pp collisions. In polarized $d \uparrow d \uparrow$ collisions both the $pp(I = 0)$ and $np(I = 1 \text{ and } I = 0)$ quasielastic A_{00i0} and A_{00ik} observables can be measured over wide CM angular range. Nucleons in deuteron have the same polarization value $P_N = P_d$ and half deuteron kinetic energy $T_N = \frac{1}{2}T_d$.

If we will have a possibility for extrapolation of the measured differential cross section to zero CM angle, then we can obtain the spin-dependent total cross sections differences $\Delta\sigma_{L,T}(E)$.

Now we estimate the elastic event yields of for measurement of the spin-dependent NN observables at *NICA*. The event rate R in the collider is proportional to the interaction cross section σ_{int} and luminosity L : $R = \sigma_{int} \times L$. The luminosity of polarized proton beams at *NICA* is estimated as $L = 1.1 \times 10^{30} \text{ cm}^{-2} \text{ s}^{-1}$ [7]

To determine the A_{00kk} , A_{00nn} , and $\Delta\sigma_{L,T}$ values we have to measure the differential CM cross sections for elastic NN interaction. The CM values of the $d\sigma/d\Omega_{NN}$ over angular range of $\theta_{CM} \sim 10^\circ \div 30^\circ$ equals $\sim 15 \div 20 \text{ mb/sr}$ at $T_n \sim 3 \text{ GeV}$ and the event rate have to be $\sim (15 \div 20) \times 10^3 \text{ events sr}^{-1} \text{ s}^{-1}$.

The $d\sigma/d\Omega_{NN}$ values for case of $\theta_{CM} \sim 180^\circ$ equals $\sim 4 \text{ mb/sr}$ at $T_n \sim 3 \text{ GeV}$ and the event rate have to be $\sim 4 \times 10^3 \text{ events sr}^{-1} \text{ s}^{-1}$. The differential CM cross section for elastic NN interaction at $T_n \sim 2.2 \text{ GeV}$ near CM angle $\theta_{CM} \sim 90^\circ$ equal $\simeq 0.12 \text{ mb/sr}$ and the event rate have to be $\sim 120 \text{ events sr}^{-1} \text{ s}^{-1}$.

We made also the event rate comparison for the collider and "fix" target experiments. Planned luminosity in the spin experiments at the collider is estimated by a value of $L = 1 \times 10^{30} \text{ sm}^{-2} \text{ s}^{-1}$ for the polarized $p \uparrow p \uparrow$ colliding beams. Thus 1 count per second will be for the events with total cross section of $\sigma_{tot} \sim 10^{30} \text{ sm}^{-2}$ ($1 \mu\text{b}$). In the "fix" target experiments with polarized proton target ($n_H \sim 10^{24} \text{ sm}^{-2}$) and for the polarized proton beam intensity of $I \sim 10^{10} \text{ p/cycle}$, 1 count per second will be for the events with total cross section of $\sigma_{tot} \sim 10^{-34} \text{ sm}^{-2}$ (100 pb).

References

- [1] Conceptual project "Design and construction of Nuclotron-based Ion Collider fAcility (NICA) and Mixed Phase Detector (MPD)", NICA project. Dubna, JINR P9-2008-153, 2008, 51 pages.
- [2] Ruprecht Machleidt, Professor of Physics, Private communication.
- [3] Prof. A.D. Krisch. Invited talk at DSPIN-09, 1-5 September 2009, JINR, Dubna.
- [4] Bystricky J., Lehar F., Winternitz P., J. Phys. (Paris). **v. 39**, 1978, p. 1.
- [5] Bilenky S.M., Lapidus L.I. and Ryndin R.M. Usp. Fiz. Nauk, **v. 84**, 1964, p. 243.
- [6] Puzikov L.D., Ryndin R.M. and Smorodinskii Ya.A., Zh. Eksp. Teor. Fiz., **v. 32**, 1957, p. 592.
- [7] I.N. Meshkov, Talk: Status of NICA Project. 23 - 29 August 2010, JINR Dubna.

ORBITAL PARAMETERS OF PROTON BEAM IN NUCLOTRON WITH SOLENOID SIBERIAN SNAKE

M.A. Kondratenko^c, A.V. Butenko^a, Yu.N. Filatov^b, A.D. Kovalenko^a,
A.M. Kondratenko^c and V.A. Mikhaylov^a

^a *Joint Institute for Nuclear Research, 141980 Dubna, Russia*

^b *Moscow Institute of Physics and Technology, 141700 Dolgoprudny, Russia*

^c *Science and Technique Laboratory "Zaryad", 630090, Novosibirsk, Russia*

Abstract

A possibility to use a booster as a polarized protons injector in NICA collider up to energy of 5 GeV was discussed since 2011 [1]. To preserve the polarization in the booster a solenoid Siberian Snake was used. Possible ways of usage a solenoid Siberian Snake in Nuclotron was shown in the paper [2]. Solenoids introduce betatron oscillation coupling and distort focusing Nuclotron lattice. In this paper, we present partial and full solenoid Siberian Snake designs in the real Nuclotron lattice, both with coupling compensation and without it.

Solenoid Siberian Snake in Nuclotron

Nuclotron is a conventional accelerator with eight superperiods and maximum magnetic rigidity $B\rho=45$ T·m. Nuclotron consists of superconducting elements with guiding magnetic field ramp of about 1 T/s. Figure 1 shows β -functions and dispersion functions on one Nuclotron superperiod for betatron tunes $\nu_x = 6, 8$ and $\nu_y = 6, 85$. To insert Siberian Snake we plan to use two free spaces with the length of 3,505 m separated by structural defocusing quadrupole in the second superperiod.

For a full Siberian Snake which rotates spin around longitudinal direction by angle of π radian on 5 GeV energy, one has to introduce a $BL = 22$ T·m longitudinal field integral. The full Siberian Snake eliminate overcoming of all spin resonances with any betatron tunes. The partial Siberian Snake can also preserve the beam polarization during the acceleration, but the allowed betatron tunes range is decreased. For a half Siberian Snake, which rotates spin by angle of $\pi/2$ radian, the longitudinal field integral is equal to $BL = 11$ T·m. In this case, the allowed betatron tunes must lie in the range $|\nu_{x,y} - k| \leq 0,25$, where k is the nearest integer to $\nu_{x,y}$.

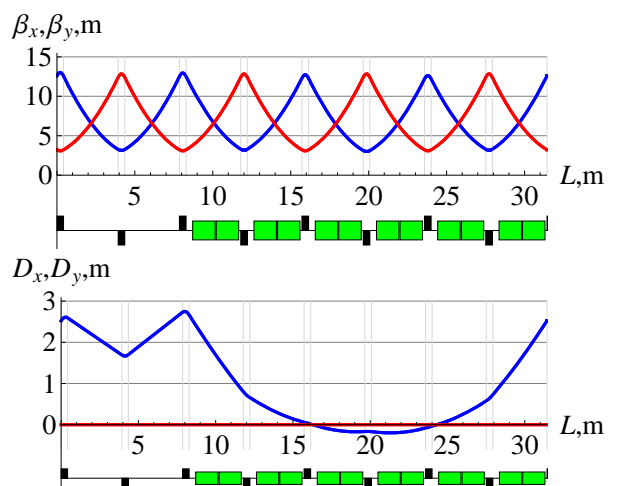


Figure 1: β -functions and dispersion functions in Nuclotron.

A stable spin polarization directions in Nuclotron with a full and a half Siberian Snakes are shown in Fig. 2. If a full Siberian Snake is inserted in the 2-nd superperiod, the polarization is directed along velocity in the opposite 6-th superperiod. During the particle motion in the arcs of the first half of Nuclotron spin turns around vertical direction and is rotated around the velocity in the Siberian Snake. Further, spin turns in the arcs of the second half of Nuclotron and restores its longitudinal direction in the 6-th superperiod.

In case of a half-Snake usage there appears a constant vertical spin projection in Nuclotron arcs. The angle between spin and vertical direction is 45° . While there is a decrease of solenoid field this angle is reducing and spin tend to vertical direction. The acceptable betatron tunes range is decreasing as well. When solenoid field turns off spin gets vertical orientation and, as a result, it becomes impossible to avoid dangerous resonances crossing.

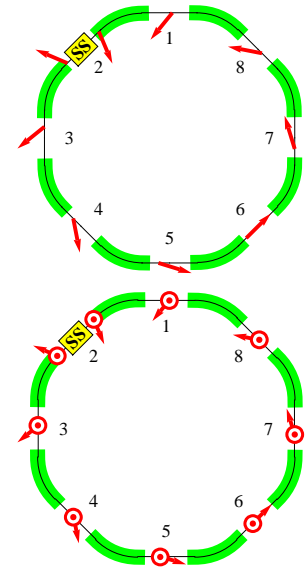


Figure 2: Stable polarization in Nuclotron with a full (on the left) and a half (on the right) Siberian Snakes.

Solenoidal Snake with Coupling Compensation

To localize betatron oscillation coupling it is usually used a system of quadrupoles in the Snake insert.

Focal strength of compensating quadrupoles q_i does not depend on coupling angle φ , but is determined by the characteristic length L of Snake insert [3,4]. Thus, it is necessary to use strong quadrupoles in conventional schemes with strengths several times more than lattice quadrupoles ones. The Nuclotron free space limitation makes it unfeasible to apply strong quadrupoles schemes (SQ schemes) there.

Weak quadrupole schemes (WQ schemes) with focal strength of compensating quadrupoles proportional to coupling angle are analyzed in paper [2]. The quadrupole strengths in SQ schemes become close to the strengths in WQ schemes at maximum coupling angle $\varphi \sim \pi$. Even in case of a full Snake the value of a coupling angle is about $\sim \pi/5$, and for a half Snake it is only $\sim \pi/10$ radian. Thus, the quadrupole strength in WQ schemes is about one fifth of that in SQ schemes for a full Snake and about one tenth for a half Snake. It solves the problem of a Snake installation in Nuclotron and allows to localize the coupling in the Snake insert (see Table 2).

Scheme	q_i	Full Snake	Half Snake
SQ (strong quads)	doesn't depend on coupling angle	$q_i \sim \frac{\pi}{L}$	$q_i \sim \frac{\pi}{L}$
WQ (weak quads)	proportional to coupling angle $\propto \varphi$	$q_i \sim \frac{\pi}{5L}$	$q_i \sim \frac{\pi}{10L}$

Table 1: Comparison of compensation quadrupoles.

A half Snake schematic with coupling compensation, using four compensating quadrupoles which are orientated by $\pm 45^\circ$ angles is shown in fig. 3. Here above the elements the values of solenoid fields and quadrupole gradients in the units of magnetic rigidity are given. Below the elements there are the values of their length. On the plots of β -functions and dispersion functions the place of solenoid insert is marked as a circle.

In this scheme the free space is used rather efficiently – more than a half of space is occupied by solenoids. The strengths of compensating quadrupoles are not more than lattice quadrupoles ones. Vertical dispersion function is excited only at the place of insert. Betatron tunes shifts are compensated by means of two families of focusing and defocusing lattice quadrupoles. The maximum value of the solenoid field is 3 T at kinetic energy of 5 GeV.

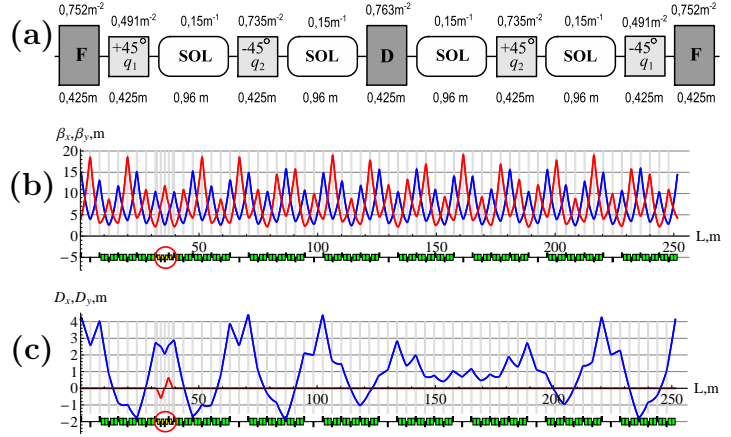


Figure 3: Half Siberian Snake with coupling compensation. (a) Snake schematic, (b) β -functions, (c) dispersion functions.

A similar scheme for a full Snake may be proposed too. But compensating quadrupoles in this case should be twice as strong as lattice quadrupoles and the maximum value of solenoid field is 6 T at kinetic energy of 5 GeV.

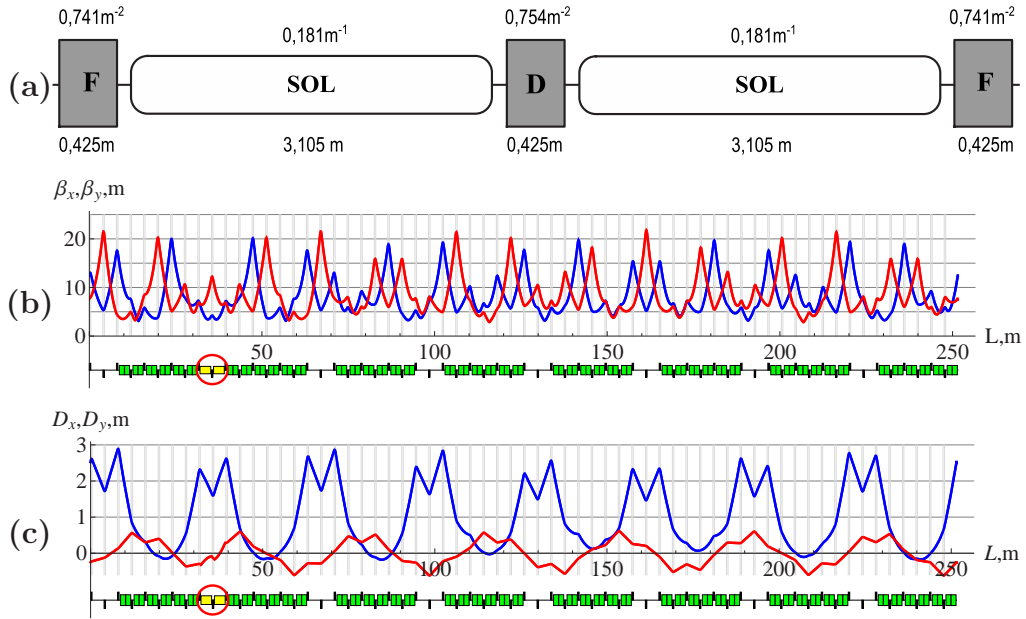


Figure 4: Full Siberian Snake without coupling compensation. (a) Snake schematic, (b) β -functions, (c) dispersion functions.

Solenoid Snake without Coupling Compensation

The condition of coupling compensation is unnecessary to maintain a stable orbital motion. Moreover, the refusal of coupling compensation gives additional possibilities to optimize orbital motion parameters. Quadrupoles and solenoids both may introduce strong betatron oscillations coupling. However, they influence on spin and beam focusing in quite different ways. In Nuclotron energy region solenoids impact on spin is very effective, but beam focusing is determined mainly by quadrupoles. That is why the absence of compensating quadrupoles reduces significantly the influence of Snake on the orbital motion. The result of direct solenoids influence on orbit is the rotation of normal mode oscillation planes. Coupling angle – the angle between orbit plane and normal mode oscillation plane – is a periodical function of azimuth, which is repeated every revolution and determined by magnetic structure of the whole ring.

In Figure 4 it is shown an example of a full Snake scheme without compensating quadrupoles. The beam motion stability is provided by means of two families of focusing and defocusing lattice quadrupoles. In this example the values of betatron tunes are equal to $\nu_x = 6,94$ and $\nu_y = 6,86$. The maximum solenoid field is 3,6 T for a full Snake instead of 6 T for a full Snake with coupling compensation at energy of 5 GeV. Moreover, it becomes possible to use a full Snake in all range of Nuclotron energy. The direct impact of solenoid Snake without compensating quadrupoles on orbital motion may be reduced to small rotations of normal mode oscillation planes in the places of beam injection and extraction.

Summary

- The proposed solenoid Snakes allow to use Nuclotron as an injector for NICA collider and carry out experiments both on internal and external targets.
- The similar Snake design may be applied to preserve polarization in Booster.
- The solenoid Snakes without compensating quadrupoles allow to preserve the polarization in all Nuclotron energy range.
- A solenoid Snake without compensating quadrupoles uses free space efficiently, and it makes possible to use solenoids for polarized deuteron control in NICA collider.
- Nuclotron can be used to test solenoid Siberian Snake for NICA collider.

References

- [1] *A.D. Kovalenko et al.* The NICA Facility in polarized proton operation mode, IPACT11.
- [2] *A.D. Kovalenko et al.* Polarized Proton Beam Acceleration at Nuclotron with the use of the Solenoid Siberian Snake, DSPIN 2012.
- [3] *A. Zholents, V. Litvinenko* BINP (Novosibirsk) Preprint 81-80 (1981).
- [4] *H. Sayed, A. Bogacz and P. Chevtsov* Proceedings of IPAC 10, Tyoto, Japan, p. 1626 (2010).

COMPARISON OF SOLENOID, HELIX AND DIPOLE SIBERIAN SNAKES IN THE NICA COLLIDER

A.M. Kondratenko^c, Yu.N. Filatov^b, A.D. Kovalenko^a, M.A. Kondratenko^c and V.A. Mikhaylov^a

^a Joint Institute for Nuclear Research, 141980 Dubna, Russia

^b Moscow Institute of Physics and Technology, 141700 Dolgoprudny, Russia

^c Science and Technique Laboratory "Zaryad", 630090, Novosibirsk, Russia

Abstract

To control the particles polarization in the NICA collider in a momentum range from 2,5 to 13,5 GeV/c, we plan to use two identical Siberian Snakes with a longitudinal axes of spin rotation. The comparison of solenoid, helix and dipole Siberian Snake main parameters is presented. The impact on the beam orbital characteristics caused by such Snakes is analyzed in the NICA collider.

A polarization control scheme of protons and deuterons (see Fig. 1), which provides longitudinal and vertical polarization in both SPD and MPD detectors in NICA collider was proposed in paper [1].

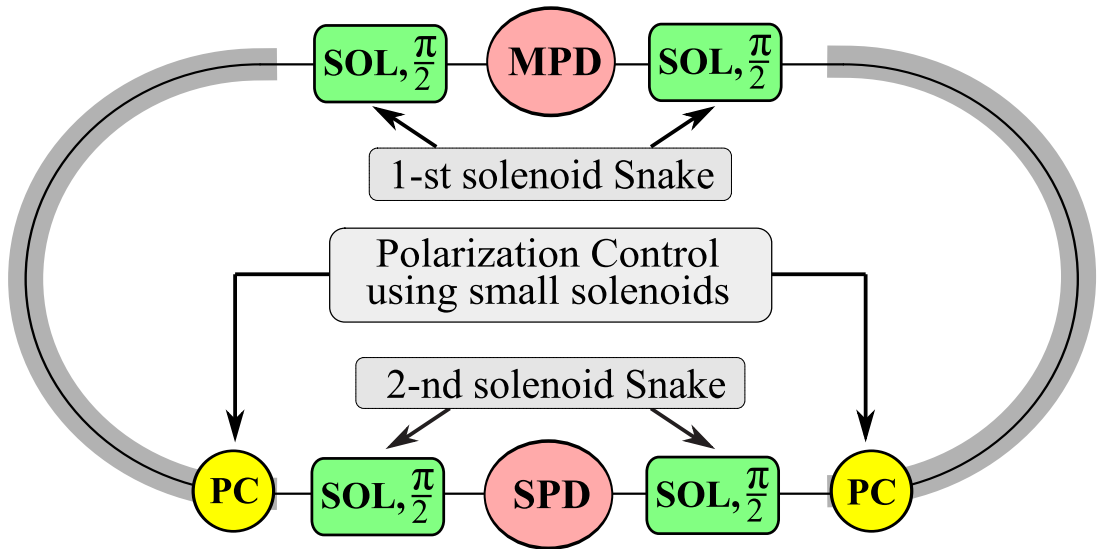


Figure 1: The polarization control scheme of protons and deuterons in NICA collider.

The main elements of this scheme are two identical solenoid Siberian Snakes, which are located in opposite straight sections and make spin to rotate around longitudinal direction. Each of the Snakes symmetrically separated by MPD and SPD detectors. Two solenoid Snakes provide zero spin tune. Thereby NICA collider with two Snakes becomes similar to JLAB figure-8 shaped collider [2].

The unique feature of zero spin tune accelerator is possibility to control any particle polarization using small magnetic field integrals. So, polarization in vertical plane (yz) of detectors is provided by means of two couples of weak solenoids with field integrals less then 0,5 T·m both for proton and deuteron beam. These solenoids allow to flip particles polarization during experiment as well as obtain any polarization direction in the accelerator plane for matching polarization during beam injection into accelerator in arcs. However, to provide zero spin tune one needs to introduce strong solenoids with large field integral. So, the total longitudinal field integral of all Snakes changes in the boundary $B_{\parallel}L = 4 \times (4,7 \div 25,3)$ T·m for protons and $B_{\parallel}L = 4 \times (15,3 \div 82,4)$ T·m for deuterons at a momentum range of NICA collider $p = (2,5 \div 13,5)$ GeV/ c . Thus, solenoid field for deuterons is about three times as strong as protons one.

It was suggested to use helical magnets for Snakes instead of strong solenoids for proton beams in NICA collider [3, 4]. As far as it is unfeasible to use helical Snake for deuterons, it was suggested to use only vertical polarization for them, as well as in conventional accelerators. It should be noted, that proton polarization control by means of a Snake with dipole magnets was analyzed in paper [5]. Thereby it is interesting to make a comparative analysis of helical, dipole and solenoid of half Siberian Snake for protons.

Prior to discussion a proper Snakes design, let's consider qualitatively the impact of the main lattice elements (quadrupoles, dipoles, solenoids) on the spin and orbit motions (see Table 2). The table shows that betatron coupling may be strong for each of the element. The impact of solenoids and dipoles on spin is rather strong in NICA energy range. In contrast to dipoles solenoids and quadrupoles don'tt change closed orbit. The strong impact of dipoles on closed orbit occurs at low energies. Accelerator focusing properties depend mainly on quadrupoles.

Element	Spin	Closed orbit deviation	Focus	Coupling
Quadrupole	Negligible	Negligible	Strong	May be strong
Dipole	Strong	Strong at low energy	Weak	May be strong
Solenoid	Strong at low energy	Negligible	Weak	Strong

Table 1: Impact of the lattice elements on the spin and orbit motions.

To localize betatron oscillations coupling in the scheme containing solenoids, one usually introduces compensation quadrupoles [6]. It was shown, that the condition of coupling compensation is not necessary one, and avoiding compensation quadrupoles allow to use collider space more efficiently. Thus, the solenoid Snake without coupling compensation used in JINRTs Nuclotron is chosen for the comparison of Snakes. As far as the field values of dipole and helix Snakes do not much differ, only 4-twist helical Snake with longitudinal axes is chosen for comparison with solenoid Snake [3, 8] (see Fig. 2).

In Table 1 there are the results of calculation of helix and solenoid Snakes at three values of the proton beam momentum $p = 2,5$ GeV/ c , $p = 7$ GeV/ c , $p = 13,5$ GeV/ c . Here ρ is maximum closed orbit deviation, B is magnitude of magnetic field, α is coupling angle of insertion, L_{tot} is total length of insertion.



Figure 2: Half Snake schematics: a) solenoid Snake, b) helix Snake with longitudinal axes.

	Helix	Solenoid	Helix	Solenoid	Helix	Solenoid
p , GeV/ c	2,5		7		13,5	
ρ , cm	2,9	0	1,1	0	0,6	0
B , T	4	1,1	4	3,1	4	6
α , deg	3,6	16	0,5	16	0,15	16
L_{tot} , m	4,6	4,2	4,6	4,2	4,6	4,2

Table 2: Impact of the lattice elements on the spin and orbit motions.

We made calculations for the maximum field of 4 T in helix and of 6 T in solenoid Snakes. Helix magnets of 4 T are applied in RHIC (BNL) [9], and fast-ramped (~ 1 T/s) solenoids with maximum field of 6 T can be constructed according to JINR technology [10].

Comparison of a half helix and solenoid Siberian Snakes in NICA collider allows to make the following conclusion. Usage of helix Snake is limited by closed orbit deviation at low energies. On the contrary, solenoid Snake does not change the closed orbit at all. That is, one needs helical magnets with a large aperture to work at low energies. Solenoid Snake requires smaller place. The solenoid can be split and installed in strait between lattice quadrupoles. Moreover, usage of fast-ramped solenoids is unnecessary in collider. It allows to apply solenoids with a stronger field. Both types of Snakes introduce betatron oscillations coupling, but the coupling angle in solenoids doesn't depend on energy. The advantages of dipole-based Snakes appear at higher energies than energy range of NICA collider.

Thereby, solenoid Snake is more efficient in NICA collider for proton beam. Moreover, solenoid Snake without compensation quadrupoles is feasible even for deuteron beam. The half Snake with total length of 9 m requires solenoids with field of 9 T at maximum collider energy.

References

- [1] *V.D.Kekelidze, A.D.Kovalenko et al.*, Scientific Program of NICA Project @ JINR, ICHEP-2012, Melbourne, Australia, July (2012).

- [2] *Y. Zhang and J. Bisognano*, arXiv:1209.0757v2[physics.acc-ph].
- [3] *A.Krish*, Spin-Praha@NICA-Spin-2013, Czech Rep., July (2013).
- [4] *Y.Shatunov*, Spin-Praha@NICA-Spin-2013, Czech Rep., July (2013).
- [5] *I.Meshkov and Y.Filatov*, JPCS 295,012144 (2011).
- [6] *A. Zholents, V. Litvinenko*, BINP (Novosibirsk) Preprint 81-80 (1981).
- [7] *M.A. Kondratenko et al.*, Orbital Parameters of Proton Beam in Nuclotron with Solenoid Siberian Snake, DSPIN2013, Dubna, (2013).
- [8] *E.D. Courant*, Proc. SPIN 1988 AIP Conf Proc 187, 1085.
- [9] *V. Ptitsin and Y. Shatunov*, NIM A398, 126 (1997).
- [10] *A. M. Baldin et al.*, IEEE Trans. on Applied. Superconductivity 5, 875 (1995).

TECHNICS
and
NEW DEVELOPMENTS

ABSOLUTE pp POLARIMETER FOR CALIBRATION OF THE BEAM TAGGING SYSTEM AT THE SPASCHARM SET-UP

A.A. Bogdanov^{1†}, M.A. Chetvertkov², V.A. Chetvertkova², A.P. Meshchanin³,
V.V. Mochalov³, M.B. Nurusheva², S.B. Nurushev³, A.V. Ridiger², P.A. Semenov³,
M.N. Strikhanov¹, A.N. Vasiliev³, V.N. Zapolsky³

(1) *National Research Nuclear University MEPhI, Moscow, Russia*

(2) *Federal state budget organization State center Interphysica, Ministry of education and science, Moscow, Russia*

(3) *State Research Center of Russian Federation - Institute for High Energy Physics, Protvino, Russia*

† *E-mail: bogdanov411@mail.ru*

Abstract

We propose to use polarimeters based on elastic pp -scattering for the calibration of the polarized beam tagging system. We propose to measure beam polarization using both elastic scattering in the CNI and in the diffraction regions using existing data from BNL and Protvino.

New experimental program SPASCHARM at IHEP to study systematically spin effects with polarized proton and anti-proton beams [1] requires the beam tagging system (BTS). The system will measure the polarization of the protons and anti-protons on the dependence of their coordinates and momentum. At the same time the absolute calibration of the BTS is important to measure the proton beam polarization with good accuracy [2]. We propose to measure beam polarization using both elastic scattering in the CNI and in the diffraction regions.

pp elastic scattering in the region of diffraction cone will be used as a reaction for this absolute polarimeter (Diffraction polarimeter). HERA Collaboration at IHEP performed fairly precise measurements of the analyzing power P of this process in the diffractive region $-t = 0.04 - 0.7(\text{GeV}/c)^2$ at 45 GeV/c [3]. The results are presented in Table 1. Polarization was about 2% in the range $0.04 < -t(\text{GeV}/c)^2 < 0.5$. The relative accuracy of the measurements was 10%. Overall data in this range of measurements led to analyzing power value $A_N = (2.370 \pm 0.12)\%$. We will use these data for the calibration of the BTS. The expected accuracy of the beam polarization measurements is 10% due to 5% error of the measurements and 5% accuracy of the target polarization scale factor.

Each kinematic interval of elastic scattering corresponds to two intervals of proton angles: scattering angles and recoil angles. Diffraction polarimeter will consist of a scintillation hodoscopes overlapping these two intervals of angles. The main background will be inelastic diffraction scattering,

We simulated signal (S) and background (B) events using PYTHIA 6.1. 5 000 000 events were analyzed in each kinematic region. Since it is possible to separate in the experiment inelastic events from elastic and diffractive ones, these events are only elastic and diffractive. We fixed the kinematic interval (and therefore two intervals of angles) in the simulation. These two intervals of angles were defined as sensitive regions. Each

Table 1: Polarization, kinematic parameters and background for diffraction events.

$-t, (GeV/c)^2$	$\eta=S/(S+B)$	P [3]	FoM, $\frac{\mu b}{(GeV/c)^2}$	$\theta_{scat}, ^\circ$	$\theta_{recoil}, ^\circ$
0.04-0.075	0.994	0.03 ± 0.01	38.7	0.285-0.395	81.5-84
0.075-0.125	0.984	0.026 ± 0.002	18.9	0.39-0.51	79.07-81.5
0.125-0.175	0.978	0.023 ± 0.002	7.8	0.51-0.60	77.13-79.08
0.175-0.225	0.968	0.022 ± 0.002	5.3	0.60-0.69	75.47-77.13
0.225-0.275	0.960	0.016 ± 0.002	1.6	0.69-0.76	74.01-75.47
0.275-0.325	0.944	0.021 ± 0.004	1.8	0.76-0.82	72.69-74.01
0.325-0.375	0.924	0.009 ± 0.005	0.2	0.82-0.88	71.49-72.69
0.375-0.425	0.884	0.009 ± 0.005	0.1	0.88-0.94	70.38-71.49
0.425-0.475	0.861	0.009 ± 0.008	0.07	0.94-0.99	69.33-70.37
0.475-0.525	0.814	0.007 ± 0.010	0.03	0.99-1.05	68.37-69.33

elastic interaction will be registered in both sensitive regions. Inelastic diffraction events interaction will be registered when at least one charged particle reaches each sensitive region.

Cross sections of the pp elastic scattering measured at 44.5 GeV/c is [4]

$$\frac{d\sigma}{dt} = (8.826 \pm 0.073)mb/(GeV/c)^2$$

at $-t = 0.22(GeV/c)^2$. We calculated, that time required to measure polarization with 10% accuracy is about 120 hours, if the beam intensity is 10^6 p/cycle. The simulation was done with point-like beam-size.

We defined factor of merit for each kinematic interval $FoM = P^2 \frac{d\sigma}{dt}, \frac{\mu b}{(GeV/c)^2}$ (see Table. 1). FoM increases with the decreasing of $-t$. This immediately suggests to explore the possibilities of simultaneous use of diffraction polarimeter and polarimeter based on effect of the Coulomb-nuclear interference (CNI). These two polarimeters are planned to be joined in one paired polarimeter.

Polarization in elastic pp scattering was not measured in the CNI region at 45 GeV. However, such measurements were carried out at RHIC at $\sqrt{s} = 6.8, 7.7, 13.7, 21.7$ GeV [5, 6]. We used RHIC data to calculate analyzing power in the CNI range at 45 GeV/c with the use of results from reference [7]:

$$\begin{aligned} \frac{M_p A_N}{\sqrt{-t}} \frac{16\pi}{\sigma_{tot}^2} \frac{d\sigma}{dt} e^{-Bt} &= [k(1 - \rho\delta_C) - 2(Im(r_5) - \delta_C Re(r_5))] \frac{t_C}{t} - 2Re(r_5) + 2\rho Im(r_5) \\ \frac{16\pi}{\sigma_{tot}^2} \frac{d\sigma}{dt} e^{-Bt} &= \left(\frac{t_C}{t}\right)^2 - 2(\rho + \delta_C) \frac{t_C}{t} + (1 + \rho^2); \quad t_C \cong \frac{8\pi\alpha}{\sigma_{tot}}. \end{aligned}$$

Real $Re(r_5)$ and imaginary $Im(r_5)$ parts of the parameter r_5 have to be defined at $\sqrt{s}=9.3$ GeV to calculate analyzing power at this energy. RHIC spin data were fitted using power law to find $Re(r_5)$ and $Im(r_5)$.

$$r = p_0 \left(\frac{s}{s_0}\right)^{p_1},$$

where p_0 and p_1 are fit parameters. $s_0=1 \text{ GeV}^2$. RHIC spin r_5 data and fit result for $\sqrt{s}=9.3 \text{ GeV}$ are presented in table 2.

Table 2: r_5 experimental RHIC data and prediction for $\sqrt{s}=9.3 \text{ GeV}$.

\sqrt{s} , GeV	6.8	7.7	13.7	21.7	9.3
$Re(r_5)$	-0.008 ± 0.001	-0.016 ± 0.02	-0.0008 ± 0.0005	-0.002 ± 0.02	-0.004 ± 0.006
$Im(r_5)$	-0.109 ± 0.03	-0.055 ± 0.04	-0.015 ± 0.001	-0.005 ± 0.04	-0.04 ± 0.09

Analyzing power at $\sqrt{s}=9.3 \text{ GeV}$ at CNI region was calculated using the data. Figure 1 shows range of analyzing power under uncertainty of data. One experimental point of HERA experiment also is shown on this figure. Time to measure polarization with 10% accuracy is about to 110 hours. This calculation was made at $-t=0.015 \text{ (GeV/c)}^2$ using the same (10^6) beam intensity and $\frac{d\sigma}{dt} = (67.4 \pm 3.9) \text{ mb}/(\text{GeV/c})^2$.

The CNI polarimeter consists of the liquid hydrogen target (LHT), six GEM detectors G1-G6, six beam hodoscopes H1-H6 and spectrometer magnet SP12 (see Fig. 2). GEM detectors are grouped as pair 4m apart. G1-G2 have dimensions $100 \times 100 \text{ mm}^2$ each, G3-G6 dimensions are $300 \times 300 \text{ mm}^2$. Such dimensions and selected distances between pairs allow to cover the $-t$ region $2 \times 10^{-3} - 5 \times 10^{-2} (\text{GeV/c})^2$.

Scintillator hodoscope with the coordinate resolution about 600μ will be used as fast trigger. The GEM detector with coordinate resolution about 70μ will significantly improve angular and momentum resolutions in off-line analysis.

The magnet of the SP12 type will be used as a spectrometer one. The integral field of 5.4 Tm will give the bent angle 36 mrad at 45 GeV . Therefore the momentum resolution will be around 1% and 0.2% for hodoscopes for GEM detectors correspondingly. This resolution will be adequate for measurement of analyzing power in the CNI region.

Special triggers are required for the polarimetry measurements. CNI measurements will require following trigger:

- only one hit in any array of beam hodoscopes;
- all events with scattering angle less than 0.7 mrad must be excluded from trigger;
- all events with momentum differing from momentum of initial momentum by 2% should be rejected;
- anti coincidence with beam halo events.

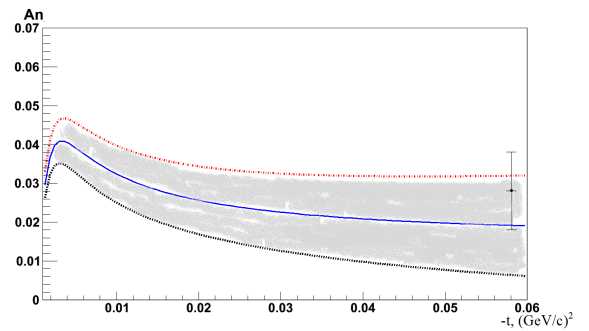


Figure 1: Analyzing power in CNI region at $\sqrt{s}=9.3 \text{ GeV}$.

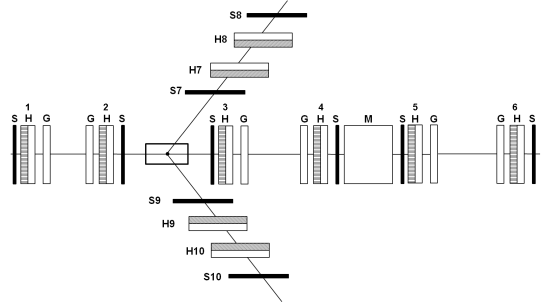


Figure 2: Paired polarimeter Setup.

Table 3: Hodoscope's structure

Hodoscopes	Distance from target, mm	Hodoscope's size,mm	Element's size, mm		Number of elements		
			X	Y	X	Y	Σ
			Beam hodoscopes				
		X×Y	X	Y	X	Y	Σ
H1	-4.25	54×54	6×3×54	6×3×54	13	13	26
H2	-0.25	54×54	6×3×54	6×3×54	13	13	26
			Forward detector				
		X×Y	X	Y	X	Y	Σ
H3	0.25	62×70	6×3×62	6×3×70	15	17	32
H4	4.25	190×110	6×3×190	6×3×110	47	27	74
H5	5.25	238×126	6×3×238	6×3×126	59	31	90
H6	9.25	358×158	6×3×358	6×3×158	99	39	138
			Recoil detector				
		X×Y	X	Y	X	Y	Σ
H7	0.1	246×118	6×3×246	6×3×118	61	29	90
H8	0.3	294×230	6×3×294	6×3×230	73	57	130
H9	0.1	246×118	6×3×246	6×3×118	61	29	90
H10	0.3	294×222	6×3×294	6×3×230	73	57	130

Trigger for the diffraction polarimeter will require in addition to have the coincidence with the signal from recoil hodoscopes. Structure of hodoscopes is presented in table 3.

As a conclusion – we propose to use absolute polarimeter for measuring the beam polarization at momentum of 45 GeV/c both at CNU and diffraction regions. If we will use both methods at 45 GeV, we will have absolute values for CNI polarimeter, since we have already analyzing power for diffraction region as a reference. Then we may calculate analyzing power for CNI measurements for different energies to measure polarization at other (not 45 GeV) energies without additional experimental measurements.

The preliminary estimates show that 10% precision in polarization calibration may be reached. Such measurements will require around one week of data taking.

The work was partially supported by RFBR grant 12-02-00737. We appreciate Dr. V.V. Grushin, Dr. Y.V.Kharlov and mrs. G.S.Chetverkova for useful discussions.

References

- [1] V. Mochalov, Phys.Part.Nucl. **44** N 6, 930 (2013).
- [2] S.B. Nurusev et al., The polarized beam tagging system at the experimental set-up SPASCHARM (this Proceedings).
- [3] A. Gaidot et al., Phys. Lett. **61B**, 103(1976).
- [4] C. Bruneton, Nucl. Phys, **B124**, 391 (1977).
- [5] A. Bazilevski, et al., Journal of Phys.: Conf. Series **295**, 012096 (2011).
- [6] I.G. Alekseev, et al., Phys. Rev. D **79**, 094014 (2009) **C8** (1999) 409.
- [7] N.H. Buttimore et al., Phys. Rev. D **59**, 114010 (1999).

POLARIZED TARGET FOR DRELL–YAN EXPERIMENT AT COMPASS

M. Finger Jr.^{1,2}, M. Finger^{1,2}, J. Matoušek^{1†} and M. Pešek¹, A. Srnka³

On behalf of the COMPASS Collaboration and the Polarized Target Group.

(1) *Charles University in Prague, Faculty of Mathematics and Physics, Czech Republic*

(2) *Joint Institute for Nuclear Research, Dubna, Russia*

(3) *Institute of Scientific Instruments, ASCR, Brno, Czech Republic*

† *E-mail: jan.matousek@cern.ch*

Abstract

In the polarized Drell–Yan experiment at the COMPASS facility in CERN a pion beam with momentum of 190 GeV/ c and intensity up to 10^8 pions/s will interact with transversely polarized proton target. The muon pair produced in Drell–Yan process will be detected. The solid-state NH₃ as polarized proton target will be polarized by dynamic nuclear polarization at very low temperatures. The maximum polarization reached during data taking is expected to be up to 90%. The non-interacting beam and other particles produced inside the target except the muons will be stopped in the hadron absorber after the target. Two target cells, each 55 cm long and 4 cm in diameter separated by a 20 cm gap, will be used. In total the target material volume will be about 691 cm³.

Drell–Yan data taking is expected to start in 2014–2015 for period of approximately 180 days. The current status of the target, the required modifications and the future plans are presented.

1 Introduction

COMPASS [1] is a fixed-target experiment situated at CERN Super Proton Synchrotron North Area. For physics data taking it uses either hadron or muon beams¹. The beam interacts with a target, which can be polarized. COMPASS detector is a universal spectrometer with good particle tracking and identification capability.

COMPASS experiment focuses on spin structure studies and hadron spectroscopy [2]. A set of measurements to study the structure of hadrons was proposed [3], including the first ever measurement of a single-polarized Drell–Yan process using a pion beam and a transversely-polarized proton target. It aims to confirm some crucial predictions of QCD, namely pseudo-universality i.e. change of sign of the Sivers and Boer–Mulders TMDs when measured in Semi-Inclusive Deep Inelastic Scattering and in Drell–Yan processes.

As the Drell–Yan cross section is small, the luminosity should be as high as possible. In COMPASS case this corresponds to the beam intensity of about 10^8 pions/s. That is the highest hadron beam intensity COMPASS has ever used, which leads to several challenges for the detection, data acquisition and polarized target.

¹Produced by proton beam from the Super Proton Synchrotron accelerator hitting a Be target. The beam can be either positive or negative with momentum up to 280 GeV/ c . Muons are naturally longitudinally polarized.

2 Polarized target

The Polarized Target system [1,4] has an essential role in C spin structure studies. It can provide large amount² of target material polarized to a high degree³.

The cooling is provided by a Dilution Refrigerator, which has a cooling power of about 5 mW at 75 mK [7]. A large-aperture superconducting magnet provides a field up to 2.5 T parallel and 0.64 T perpendicular to the beam axis. Homogeneity of the longitudinal field is about 10^{-5} T.

The target material is polarized by Dynamic Nuclear Polarization method [6] at about 0.5 K. When the optimal polarization is reached, the target is switched to a "frozen spin" mode at about 50 mK. A long spin-lattice relaxation time at such temperature (in order of 10^3 hours) allows to perform reasonably efficient experiment. Two Microwave systems for Dynamic Nuclear Polarization allow to have target cells with opposite polarization to reduce systematic errors in measured asymmetries. The polarization is measured by a continuous-wave NMR.

3 Drell–Yan program at COMPASS

Drell–Yan process can be represented by the Feynman graph on Fig. 1. The main advantage of Drell–Yan process for hadron structure studies is that there are leptons in the final state, which means that the cross section does not involve any fragmentation function but only convolution of structure functions of both hadrons. The process is very well calculable, dedicated calculations of the pion-induced Drell–Yan process for the COMPASS kinematics were recently published [8].

The disadvantage of the Drell–Yan process is a small cross section. To overcome this a high-intensity pion beam will be used resulting in a large secondary-hadron flux. A special hadron absorber was designed to stop the non-interacting beam and all secondary particles except muons right after the target to avoid a spectrometer flooding-up [3]. It will be made of stainless steel and alumina, with a tungsten beam plug in the center to stop the beam. For the measurement at COMPASS this means worse vertex resolution in comparison with Semi-Inclusive Deep Inelastic Scattering program, as the absorber introduces significant multiple scattering.

The high intensity pion beam together with the hadron absorber will cause higher radiation dose⁴ in the experimental building. Because of that the control room will be moved to another building.

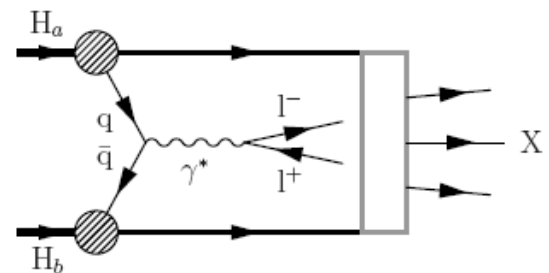


Figure 1: The Drell–Yan process. A quark-antiquark pair from the two hadrons annihilate, producing a lepton-antilepton pair in final state. The gray box denotes hadronization.

²A cylinder of about 4 cm in diameter and about 120 cm long.

³Over 80% in case of H in NH_3 and over 50% in case of D in ^6LiD [5].

⁴About 3.6 $\mu\text{Sv/h}$, which exceeds CERN limit for permanently occupied area.

4 Modifications of the Polarized Target for the Drell–Yan program

The intense pion beam and the presence of the hadron absorber require modifications of Polarized Target, including the target cells. The new cell design consists of two cells (4 cm in diameter, 55 cm long) with 20 cm long Microwave stopper⁵. The wider gap between the target cells is needed to ensure correct assignment of events to the cells.

The NMR system for polarization measurement will have 10 coils. 4 coils will probably be placed outside of each cell (for measurement in longitudinal field) and one inside each cell (coil axis parallel to the beam axis—for measurement in transverse field).

Design of the coils is in development. A special adapter was designed for the Microwave cavity to accommodate one Microwave stopper of 20 cm length instead of two (see the Fig. 2).

Because of the absorber the whole target has to be moved by 2.3 m upstream from the standard (SIDIS) position. The target platform will be lifted by a crane and moved to its new position. A special support craning construction was designed by CERN for this purpose. The helium lines, cabling, Microwave waveguides and other equipment will be moved to the new position as well.

It was decided to abandon the LabVIEWTM system [9] for dilution refrigerator monitoring. A new, more robust, Linux-based software package called pthread is being developed instead. It is written C++ and Perl. It can communicate with the standard COMPASS DCS⁶ using DIM library [10] and write data into MySQL or SQLite database. These features are important for the remote monitoring. The main advantage is that the package is modular and easily adjustable. It can load the target configuration from a file. Fig. 3 shows functionality of the monitoring system.

There is a Programmable Logic Controller unit designed to monitor the most impor-

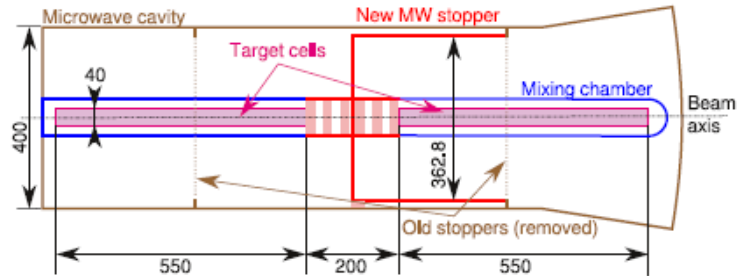


Figure 2: The modified Microwave cavity. The upstream Microwave stopper was removed, the downstream one was replaced by a special adapter and a wider stopper fitting in the 20 cm gap between the 55 cm long target cells.

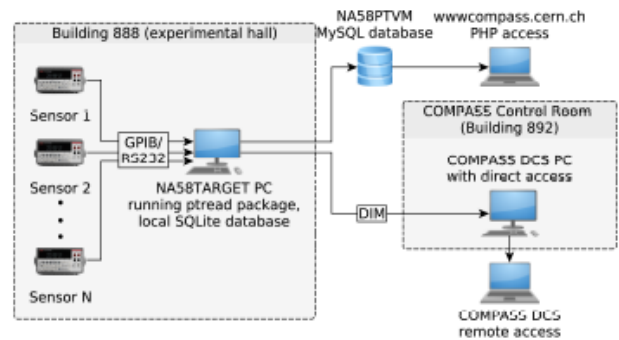


Figure 3: Diagram of pthread communication. The Linux computer with pthread package reads sensors. Data can be stored locally in SQLite database, sent to MySQL database and published by DIM server for COMPASS DCS.

⁵The SIDIS design was three cells (30-60-30 cm long, 4 cm in diameter) with 5 cm long stoppers.

⁶Centralized, PVSS-based detector control system.

tant parameters of Dilution Refrigerator [9]. It runs simultaneously with the standard Dilution Refrigerator control system and is powered from a source not sensitive to power-failures. The needle valves of Dilution Refrigerator will be controlled probably by another Programmable Logic Controller .

The superconducting target magnet is being refurbished by CERN magnet group. The work is almost finished. The group will provide control and safety systems too.

5 Status of the polarized target preparations

The modified Microwave cavity was successfully tested earlier this year. The new target cells are being prepared. The movement of the target platform is planned to be done by the end of 2013. The superconducting magnet refurbishment is finishing, the magnet should be ready for installation in March 2014. The magnet vacuum was successfully tested recently and cooling tests will follow soon. The dilution refrigerator was leak-tested at room temperature, no leaks were found.

Conclusion. COMPASS has now the possibility to make the first-ever measurement of single-polarized Drell–Yan process. Preparation for this involves polarized target modifications which are progressing well. The target should be ready and fully operational by the end of the summer 2014 to allow measurement during the fall 2014 and over the whole 2015.

Acknowledgements. The authors acknowledge support of HP3 EU, MEYS LA08015 and SVV-2013-267303 Czech Republic grants.

References

- [1] P. Abbon et al., NIM **A 577** (2007) 455–518.
- [2] The COMPASS Collaboration, List of COMPASS publications, <http://wwwcompass.cern.ch/compass/publications/>
- [3] The COMPASS Collaboration, COMPASS-II Proposal, CERN-SPSC-2010-014, SPSC-P-340.
- [4] J. H. Koivuniemi et al., Journal of Physics: Conference series **150** (2009) 012023.
- [5] K. Kondo et al., NIM **A 526** 70–75.
- [6] A. Abragam, M. Goldman, Rep. Prog. Phys. **41** (1978) 395.
- [7] N. Doshita et al., NIM **A 526** (2004) 138–143.
- [8] M. Aicher, A. Schäfer and W. Vogelsang, Phys. Rev. **D 83** (2011) 114023.
- [9] F. Gautheron et al., NIM **A 526** (2004) 147–152.
- [10] C. Gaspar et al., Distributed information management system, <http://dim.web.cern.ch/dim/>.

THE METHOD OF ASSEMBLY FUNCTIONS IN THE PROBLEM OF A MOMENTUM RESTORING OF CHARGED PARTICLES

I.P. Yudin

Joint Institute for Nuclear Research, 141980 Dubna, Russia

E-mail: yudin@jinr.ru

Abstract

A problem of a construction of phase-space coordinates transformation between detectors located in an inhomogeneous field of a dipole magnet of a spectrometer is analyzed. It is proposed an analytical dependence between final (detector D_F) and initial (detector D_I) phase-space coordinates of a charged particle. Proposed transformation has been applied to the problem of a momentum restoration of a charged particle in an inhomogeneous field of a dipole magnet of a spectrometer.

A problem of a construction of phase-space coordinates transformation between detectors located in an inhomogeneous field of a dipole magnet of a spectrometer is analyzed. It is proposed an analytical dependence between final (detector D_F) and initial (detector D_I) phase-space coordinates of a charged particle. Proposed transformation has been applied to the problem of a momentum restoration of a charged particle in an inhomogeneous field of a dipole magnet of a spectrometer.

There are continuous requests of the experimentalists to improve a mathematical methods for the calculation of the moments of a charged particles transported through the magnet. As a typical case we can referred the spectrometer [3] setup for a charged particle momentum restoration. The restoration is carried out by the use of the phase-space coordinates which were detected in the planes located before and after a magnet.

The magnet has a field map measured to use an exact calculation procedures. But the exact calculations are consumed in a time and in computer memory.

So, the task is to minimize the resources and the one uses the simplified approach to gain an efficiency of an volume in ours data processing. Descriptions of some approach to reach the goal can be found in [1,2].

Our aim is to use a dipole approximation for the transformation of the phase coordinates. We will describe a procedure which can be used effectively to transport a charged particle from the initial coordinates detector to the final one. The planes of detectors give the phase-space coordinate set x, x', y, y' .

To mark the planes we apply an indexes I and F for initial and final planes correspondingly.

A field map of the real magnet is also used which is taken from the design of the spectrometer [3]. The later task provide the verification of the final step of the particle momentum restoration.

We get the result in a three steps. For the first step a model calculations of the charged particles beam using a real magnetic field map by the program MITRA [2] are produced. In the program MITRA the Runge-Kutta method for a numerical investigation is used. On this step set of a phase-space coordinates is calculated in the output of the magnet.

For the second step we treat to combine the initial and the final phase coordinate sets with the magnetic field values along the trajectories of the particles to find an analytical dependence that is our assembly function [2].

On the third step this analytical dependence permit us to apply it for the momentum restoration of the charged particles.

For a given charged particle transported through a magnetic field, a model task determined as $(B = B(B_x, B_y, B_s))$ is a solution of the Cauchy problem for a system of two nonlinear simple equations of the second order:

$$\begin{cases} x''_{ss} = \frac{A_s}{B\rho} [y'_s \cdot B_s(x, y, s) - (1 + x_s'^2)B_y(x, y, s) + x'_s \cdot y'_s \cdot B_x(x, y, s)], \\ y''_{ss} = \frac{A_s}{B\rho} [x'_s \cdot B_s(x, y, s) - (1 + y_s'^2)B_x(x, y, s) + x'_s \cdot y'_s \cdot B_y(x, y, s)] \end{cases} \quad (1)$$

Where the initial value magnetic field $x(S_o) = x_o$ is determined by the value of $B_o = 0.75$ T and the geometry of the setup: a distance from the source to the magnet – $L_m = 254$ cm, the length of magnet – $L_m = 232$ cm.

To solve the Cauchy problem (1) we used the MITRA [2] program which integrated the equations system (1) by Runge-Kutta method of 5th order.

To find the analytical dependence of the final phase coordinate we considered a linear field approximation for which one there is the following presentation:

$$x_F^l = \sqrt{\rho^2 - (S - C_1)^2} + C_2;$$

$$(x_F^l)' = \frac{S - C_1}{\sqrt{\rho^2 - (S - C_1)^2}};$$

where $S = 232$ cm, $C_1 = \frac{x_o'\rho}{\sqrt{1+x_o'^2}}$, $C_2 = x_o - \frac{\rho}{\sqrt{1+x_o'^2}}$, $\rho = 440 \cdot P$ cm, P – momentum of particle.

For a nonlinear magnetic field

$$x_F^n = x_F^l + \Delta x_F;$$

$$(x_F^n)' = (x_F^l)' + \Delta x_F'.$$

Estimating the results M_k of the modelling we got the next result on the first step (see Fig.1):

$$\Delta x_F = A_1 + A_2(x_o - X_c)^2. \quad (2)$$

The same is for the function of $\Delta x_F'$.

Analyzing $A_1 = A_1(p)$, $A_2 = A_2(p)$ and $x_c = x_c(p)$ we come to the next estimation $A_1 = \alpha_1/p^3$, $A_2 = \alpha_2/p$ and $X_c = x_{cc}/p$, where $\alpha_1 = 0.6038958$, $\alpha_2 = 7.417276 \cdot 10^{-3}$, $x_{cc} = 9.741210$.

So, the equation (2) can be determined as follows:

$$\Delta x_F = \frac{1}{p} \left[\frac{\alpha_1}{p^2} + \alpha_2 \left(x_o - \frac{x_{cc}}{p} \right)^2 \right]. \quad (3)$$

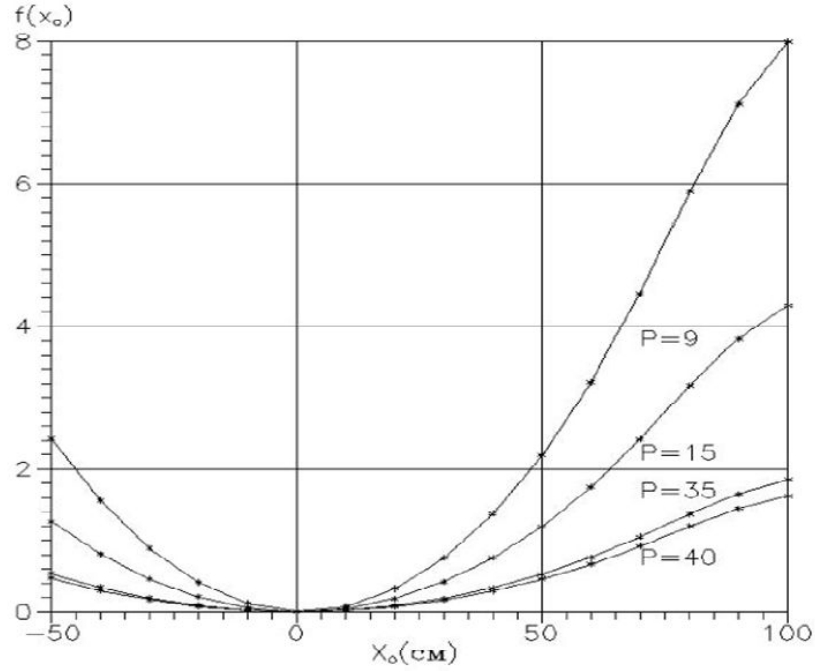


Figure 1: View of function $f(x_o) = \Delta x_F$.

Then we come to iteration procedure of the momentum restoration of the charged particles.

The last analytical presentation for Δx_F (3) (and for $\Delta x'_F$, analogically) permits to use iteration approach to solve the task of the charged particle momentum restoration.

As a initial approximation we have taken the value of the momentum corresponding to the momentum in a uniform magnetic field:

\X0	80	70	60	50	40	30	20	10	0	-10	-20	-30	-40
1.5		10.357	-0.454	-0.254	-0.054	0.042	0.038	-0.013					
2.0		7.016	2.498	1.024	0.473	0.233	0.111	0.089	0.166	0.399			
2.5		4.953	1.130	0.142	-0.053	-0.032	0.007	0.042	0.062	0.096	0.202		
3.0			0.259	-0.411	-0.391	-0.216	-0.067	0.018	0.026	-0.019	-0.079		
4.0			-0.780	-1.061	-0.792	-0.438	-0.163	-0.014	0.000	-0.100	-0.307	-0.584	
5.0			-1.353	-1.411	-1.009	-0.568	-0.221	-0.030	-0.002	-0.122	-0.383	-0.759	
6.0			-1.708	-1.616	-1.140	-0.643	-0.259	-0.042	-0.003	-0.125	-0.414	-0.836	-1.383
7.0			-1.943	-1.763	-1.226	-0.693	-0.285	-0.046	-0.002	-0.128	-0.429	-0.877	-1.460
8.0				-1.860	-1.286	-0.729	-0.304	-0.056	-0.002	-0.129	-0.436	-0.899	-1.506
9.0				-1.930	-1.330	-0.755	-0.318	-0.064	-0.002	-0.129	-0.440	-0.913	-1.534
10.0				-1.984	-1.363	-0.776	-0.330	-0.069	-0.001	-0.128	-0.441	-0.921	-1.552
15.0				-2.126	-1.450	-0.830	-0.361	-0.085	-0.001	-0.123	-0.439	-0.934	-1.586
20.0				-2.186	-1.487	-0.854	-0.372	-0.091	0.000	-0.119	-0.435	-0.934	-1.591
25.0				-2.219	-1.507	-0.868	-0.381	-0.095	0.000	-0.116	-0.429	-0.932	-1.591
30.0				-2.239	-1.517	-0.876	-0.387	-0.097	0.000	-0.114	-0.427	-0.929	-1.589
35.0				-2.253	-1.526	-0.881	-0.391	-0.099	0.000	-0.123	-0.425	-0.927	-1.588
40.0				-2.263	-1.533	-0.885	-0.394	-0.100	0.000	-0.121	-0.424	-0.926	-1.587

Table 1.

$$p_o = \frac{0.03 \cdot B_o \cdot L_m}{\Theta},$$

where $\Theta = \arctan x'_o - \arctan x'_F$, $B_o = 0.75$ T, L_m – length of the magnet.

Iteration method was realized with the INVERS-MOMENTUM program for personal computer.

We find that the precision of method depend on:

- the scattering of $\{\alpha_1 p^3\}$, $\{\alpha_2 p\}$ and $\{x_{cc} p\}$;
- the distance from the source to the magnet.

The calculation results by the INVERSE-MOMENTUM program we present in the Table 1, which give the errors of the momentum determination (in %).

References

- [1] Yudin I.P., Izvestia Saratov State Univ. Seria Physics. 2010, Vol.10, No2, P.25-30.
- [2] Yudin I.P., Preprint JINR, P11-87-349, Dubna, 1987.
- [3] Aleev A.N., Yudin I.P., Nuclear Experimental Technique (PTE) 2009, Vol.52, No 3, P.313-320.

RELATED PROBLEMS

KERR GEOMETRY AS A BRIDGE FROM THEORY OF SUPERSTRINGS TO SPINNING PARTICLES

A.Ya. Burinskii^{1†}

(1) *Theor.Phys.Lab. NSI RAS*

† *E-mail: bur@ibrae.ac.ru*

Abstract

It is broadly discussed that black holes (BH) and theory of superstrings have to be related with elementary particles. However, the path from superstring theory to particle physics represents a still unsolved problem. In the same time, the Kerr geometry of the rotating BH solutions displays surprisingly close relationships with superstring theory and predicts some properties of spinning particles, playing the role of a theoretical guide for unification of strings, gravity and particles.

Superstring theory, being originated from the experimentally supported dual models of elementary particles, should be recognized as a guide to theory of elementary particles. However, the based on string theory "... realistic model of elementary particles still appears to be a distant dream...", (John Schwarz, arXiv:1201.0981). Contrarily, the Kerr-Newman (KN) geometry of the rotating BH solutions displays some surprising relationships to both, the structure of spinning particles and to many of specific structures of superstring theory.

Closed Kerr's string in the electron background. The 4d Kerr-Newman (KN) solution has gyromagnetic ratio $g = 2$; as that of the Dirac electron, and therefore, gravitational and electromagnetic (em) field of the electron should correspond to the Kerr-Newman (KN) solution with great precision. Because of that, the charged Kerr-Newman (KN) solution has paid attention as a classical background for spinning particle, in particular for electron [1]. However, the spin/mass ratio of the spinning particles $a = J/m$ is extremely high. In the dimensionless units $c = G = \hbar = 1$ it is about 10^{44} , while for $a > 1$ the BH horizons disappear, indicating that spinning particles should correspond to over-rotating BH solutions which lose the BH horizons. It means that the electron background should have a topological defect in the form of a naked singular ring of Compton radius $a = \hbar/2mc$. In the our old work [2] this ring was identified as a closed string, excitations of which can create traveling waves generating the spin and mass spectrum of elementary particles as well as zitterbewegung and de Broglie waves of an electron. Twenty years later, it has been shown in the low energy string theory, that the field structure of the Kerr singular ring is very similar to the obtained by Sen solution for fundamental heterotic string [3].

Kerr geometry. Kerr-Schild formalism [4] is a power tool for the treatment of the rotating BH solutions. Kerr-Newman (KN) metric has the form

$$g_{\mu\nu} = \eta_{\mu\nu} + 2Hk_{\mu}k_{\nu}, \quad H = \frac{mr - e^2/2}{r^2 + a^2 \cos^2 \theta}, \quad (1)$$

where $\eta_{\mu\nu}$ is an auxiliary Minkowski background, and k^{μ} is a vortex of the null vector field, $k_{\mu}k^{\mu} = 0$, which is tangent to the *Kerr congruence*, which determines "polarization"

of the Kerr-Schild space-times. Vector potential of the KN electromagnetic (em) field has the corresponding vortex form, aligned with null directions k^μ ,

$$A_{KN}^\mu = Re \frac{e}{r + ia \cos \theta} k^\mu. \quad (2)$$

Kerr Theorem determines the Kerr congruence in terms of twistor coordinates, $T^a = \{Y, \zeta - Yv, u + Y\bar{\zeta}\}$. by a quadratic analytic function $F(T^a)$ as a *quadric* $F(T^a) = 0$ in the projective twistor space. It gives two solutions for the congruence, $k_\mu^+(x)$ and $k_\mu^-(x)$, corresponding to two different metrics $g_{\mu\nu}^\pm$, which leads to *twosheeted* structure of the Kerr space. The branch line is at the Kerr singular ring, $r = \cos \theta = 0$.

Regularization. Singularity of the Kerr *metric* has to be replaced by a regular source, which should suppress gravity in the Compton region of the “dressed” electron in agreement with basic principles of quantum theory. One sees in (1) that gravitational contribution of the term H cancels at the ellipsoidal surface $r = r_e = e^2/2m$ (this surface is oblate ellipsoid since r is the Kerr oblate spheroidal coordinate), and we put the metric flat by $r < r_e$. It gives r_e as the cut off parameter for the metric and the em field, and results in a consistent regular source of Kerr solution in the form of a disk-like rotating soliton, formed by a phase transition from the external exact Kerr-Newman solution to an internal false-vacuum state of Higgs field [1,6]. This model of a “dressed” electron of the Compton size has a few remarkable properties:

i) the Kerr ring is regularized, forming a closed relativistic string along the border of the disklike source,

ii) the Kerr-Newman em potential is dragged by vortex of Kerr congruence and forms a quantum Wilson loop around the disk $\oint e A_\varphi d\varphi = -4\pi ma$, which results in *quantization of the soliton spin*, $J = ma = n\hbar/2$, $n = 1, 2, 3, \dots$,

iii) the Higgs field inside the source is superconducting and oscillates coherently with the frequency $\omega = 2m$.

iv) stringy excitations of the Kerr circular string create a singular pole, which circulates together with traveling waves displaying zitterbewegung of the Dirac electron.

Complex Kerr string. One more string, which is complex and open, was obtained in the complex structure of the Kerr geometry [5]. The KN solution was initially obtained by a “complex trick” from the Kerr solution. The Kerr’s complex radial distance $\tilde{r} = r + ia \cos \theta$ is related with Cartesian coordinates by a complex shift $z \rightarrow z + ia$. As a result, the Kerr solution may be considered as *a point-like source shifted in the complex region*. This source propagates along a complex world-line in complex time $\tau = t + i\sigma$, and the real KN solution is generated by the complex source propagating along this complex world line. There was suggested a special complex retarded-time procedure which generalizes the usual real retarded-time construction. Contrary to the real case, the complex retarded and advanced times may be determined by two different (Left or Right) complex null planes, which are generators of the complex light cone.

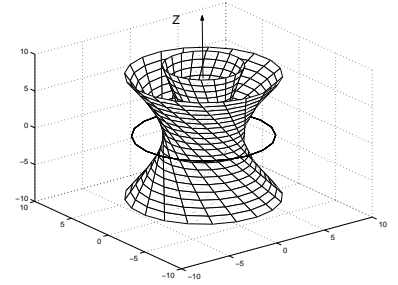


Figure 1: Kerr singular ring and two sheets of the Kerr congruence.

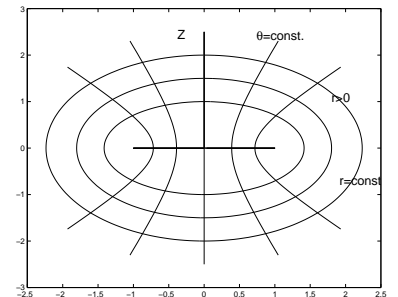


Figure 2: Oblate spheroidal coordinates r and θ .

The two dimensional time parameter $\tau = t + i\sigma$ shows that the complex world-line should be considered as a world-sheet of a complex string. Boundary conditions for this string have some peculiarities and require an *orientifold* structure, which means that the string should be considered as closed one, but folded to form an open string. The world-sheet parity transformation reverses orientation of the world sheet, and covers it second time in mirror direction. Simultaneously, the Left and Right modes are exchanged. The orientifold projection is combined with space reflection R resulting in parity of the retarded and advanced folds, which preserves analyticity of the world-sheet. Endpoints of the resulting string should be associated with the Chan-Paton charges of a quark-antiquark pair. On the real slice, the complex endpoints of the string are mapped to the north and south twistor null lines of the Kerr congruence.

The extra orientifold symmetry of the complex Kerr string creates some extra relations between the retarded and advanced folds of the complex retarded-time construction and results in doubling of the Kerr twosheeted structure. There appears parity between the positive Kerr sheet determined by the Right retarded time and the negative sheet of the the Left advanced time. The Kerr theorem generates different congruences for the retarded and advanced sources. Each of these sources produces a twosheeted Kerr-Schild geometry, and the formal description of the resulting four-folded congruence should be based on the multi-particle Kerr-Schild solutions [7]. The corresponding two-particle generating function of the Kerr theorem will be

$$F_2(T^A) = F_{ret}(T^A)F_{adv}(T^A), \quad (3)$$

where F_{ret} and F_{adv} are determined by the retarded and advanced sources correspondingly. The both factors are quadratic in projective twistor coordinates T^A . The corresponding equation $F_2(T^A) = 0$ represents *quartic* in CP^3 , which gives four sheets of the well known as Calabi-Yau (complex) two-fold, or K3 surface. We obtain that the famous Calabi-Yau space of superstring theory is realized in the projective twistor space CP^3 of the Kerr geometry and describes four sheets of the Kerr Principal Null Congruence [8].

It has been recognized that this parallelism between complex structure of the Kerr geometry and superstring theory is not accidental, and there should be a fundamental structure lying beyond these relationships. Origin of this correspondence we see in twistorial structure of the Kerr-Schild geometry and in the critical N=2 string [9], which is consistent with quantum theory and is based on the underlying twistorial structure too.

N=2 string as the complex Kerr string.

It should be noticed that among the consistent critical strings in dimensions $d=26$ and $d=10$, there is also the complex N=2 string, which has the real critical dimension four and can be used as a basis of some four-dimensional string theory [9]. The principal obstacle for its application emerged earlier from its signature (2,2) or (4,0), which conflicted with its embedding in the real minkowskian space-time. Up to our knowledge, this trouble was not resolved so far, and the initially enormous interest to this string was dampened. We note that N=2 string has organic embedding in the complexified 4d Kerr geometry. In

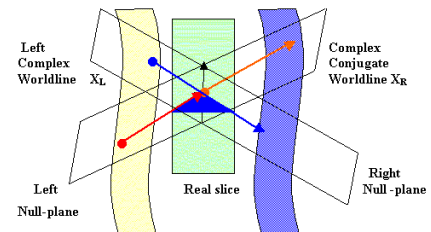


Figure 3: The Left and Right complex world lines and the Left and Right complex null planes form projection on the real space.

particular, the Hermitian action for the Kerr complex world line (CWL), corresponds to bosonic part of the N=2 string. Generalization to complex super-time \mathcal{T} turns CWL into super-world-line $X^\mu(\mathcal{T})$, and leads to action of the N=2 superstring. The extra world-sheet spinor of the N=2 superstring corresponds to the Left null planes of the complex light cones, generators of the real projection of the K3 surface and Kerr congruence. And therefore, twistorial structure of the Kerr geometry turns out to be close related with N=2 supersymmetry. We arrive at the conclusion that the complex N=2 superstring should represent a complex source of the super-Kerr-Newman geometry, and in fact it should represent just the same physics as the complex retarded-time construction. Taking into account the structure of the real Kerr source we arrive at the model of spinning particle as a solitonic field configuration of the N=2 super-multiplet.

Conclusion. Along with wonderful parallelism of the Kerr-Schild geometry with basic structures of the superstring theory, the KN geometry displays very essential peculiarities. One of the principal peculiarities is that all the considered real and complex Kerr stringy structures, including the Calabi-Yau twofold, live in four-dimensional space-time. There appears a wonderful possibility to obtain a four-dimensional superstring theory in which *compactification of higher dimensions is replaced by complexification*. Second peculiarity is related with characteristic parameter of the Kerr strings $a = J/m$, which corresponds to Compton scale of the dressed electron, which makes the Kerr-Schild version of this superstring theory to be much closer to physics of spinning particles. The consistent with gravity Kerr's soliton not only confirm zitterbewegung of the Dirac electron and the Compton size of the its "dressed" image, but also predicts some new features: the disklike shape, Kerr's circular string, Wilson loop and the regularizing role of the oscillating Higgs field. On the other hand, it confirms close relationships with twistors, displays many important structures of superstring theory and reanimates the old mysterious N=2 string as a principal object for future development.

We arrive at the conclusion that the Kerr geometry can be considered as a theoretical bridge between string theory and spinning particles, representing an alternative to higher-dimensions at Planck scale in favor of the four complex dimensions at the Compton level.

References

- [1] A. Burinskii, Physics of Particles and Nuclei, **45**(1) (2014) 202 , [arXiv:1212.2920].
- [2] D.D. Ivanenko, A. Burinskii, Izv. Vuz. Fiz. **5** (1975) 135.
- [3] A. Burinskii, Phys. Rev. **D 52** (1995) 5826, [arXiv:hep-th/9504139].
- [4] G. C. Debney, R. P. Kerr and A. Schild, J. Math. Phys. **10** (1969) 1842 .
- [5] A. Burinskii, "String-like Structures in Complex Kerr Geometry", In: Relativity Today, Edited by R.P.Kerr and Z.Perjes, Akad'emiai Kiad'o, Budapest, 1994, p.149, [arXiv:gr-qc/9303003].
- [6] A. Burinskii, J. Phys. A: Math. Theor. **43** (2010) 392001, [arXiv:1003.2928].
- [7] A. Burinskii, Grav. Cosmol, **11** 301 (2005), [arXiv:hep-th/0506006].
- [8] A. Burinskii, Theor. Math. Phys. **177**(2) (2013) 1492, [arXiv:1307.5021].
- [9] M.B. Green, J. Schwarz, and E. Witten, Superstring Theory, v.I, Cambridge Univ. Press, 1987.

ELECTROMAGNETIC SINGULAR SOLITON AS PARTICLE WITH SPIN AND MAGNETIC MOMENT

A.A. Chernitskii^{1,2}

- (1) *A. Friedmann Laboratory for Theoretical Physics, St.-Petersburg*
(2) *Institute of Management in Saint-Petersburg State University of Economics,
Marata str. 27, St.-Petersburg, Russia, 191002*
E-mail: AAChernitskii@mail.ru, AAChernitskii@engec.ru

Abstract

A space-localized solution of nonlinear electrodynamics is considered as massive charged particle with spin and magnetic moment. The field configurations with two types of singularities are compared. These are solutions with two point dyons (bidyon) and with ring singularity. Advantages and disadvantages of these models are considered from the point of view for representation of real elementary particles.

Singular solitons of nonlinear electrodynamics can be considered as massive charged particles with spin and magnetic moment [1–8]. The appropriate solitons can possess properties of elementary particles and interact like them.

A simplest model of point charged particle without spin has spherical symmetry. To have spin and magnetic moment a soliton field configuration must have the axial symmetry but not spherical one. In this case we must determine the type of singularity for the soliton field configuration.

Here we compare the field configurations with two types of singularities.

The first field configuration called **bidyon** consists of two point dyons with equal electric and opposite magnetic charges [1].

The solitary point dyon has spherical symmetry and point singularity of electromagnetic field. It has both electrical and magnetic charge. But the electromagnetic potential of the dyon has axial symmetry and linear singularity.

Remarkable that the two different functions of electromagnetic potential lead to one dyon configuration of electromagnetic field [1]. The first function has infinite singular line and the second one has semi-infinite singular line beginning from the singular point where the dyon is placed.

Dyon electromagnetic field configuration is the exact solution for any gauge invariant model of nonlinear electrodynamics and has the following form in spherical coordinate system:

$$D_r = \frac{\mathcal{E}}{r^2}, \quad D_\vartheta = D_\varphi = 0, \quad B_r = \frac{\mathcal{M}}{r^2}, \quad B_\vartheta = B_\varphi = 0, \quad (1)$$

where \mathbf{D} and \mathbf{B} are electric and magnetic inductions.

Bidyon has two singular points of electromagnetic field and a singular line segment of electromagnetic potential between the point charges (see Fig. 1). Thus we can talk that in this case we have a segment of singular string.

Let us consider the sum of two dyon field configurations of type (1) with equal electric ($\overset{1}{\mathcal{E}} = \overset{2}{\mathcal{E}} = \mathcal{E}$) and opposite magnetic ($\overset{1}{\mathcal{M}} = -\overset{2}{\mathcal{M}} = \mathcal{M}$) charges placed at different points like on Fig. 1. This sum field configuration can be considered as an initial approximation for the bidyon

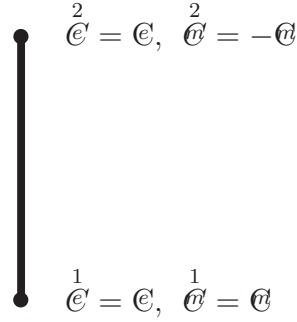


Figure 1: Bidyon as two dyons with equal electric and opposite magnetic charges. Singular line of electromagnetic potential connects two singular points of electromagnetic field.

solution of nonlinear electrodynamics field model. This static electromagnetic field configuration has notable property, namely its full angular momentum or spin does not depend on a distance between the point dyons. The appropriate calculation is an integration of the field angular momentum density over full three-dimensional space. It gives the following expression [1]:

$$s = 2 |\mathcal{G}\mathcal{C}| . \quad (2)$$

The field configuration under consideration looks like electrically charged particle with spin. Its electrical charge is $2\mathcal{C}$ and its spin is $2|\mathcal{G}\mathcal{C}|$. Let us assume that

$$2|\mathcal{C}| = \bar{e}, \quad 2|\mathcal{G}\mathcal{C}| = \frac{\hbar}{2}, \quad (3)$$

where \bar{e} is absolute value of the electron charge and \hbar is Planck constant. In this case we have

$$\frac{|\mathcal{C}|}{|\mathcal{G}|} = \frac{\bar{e}^2}{\hbar} \equiv \alpha, \quad (4)$$

where α is the known fine structure constant.

It is obviously that the field configuration (1) has a magnetic moment. The full energy of this field configuration considered in the model of nonlinear electrodynamics has a finite value [1].

Thus we obtain an electromagnetic model of massive charged particle with spin and magnetic moment.

The second considered field configuration contains the **singular ring** of electromagnetic field [4–6].

This field configuration has a linear charge density distributed along the singular ring. It has also a singular current density along the ring. The charge density gives an appropriate electric field and a full charge of the configuration. The current density gives a magnetic field and an appropriate magnetic moment. Electrical and magnetic fields considered together give momentum density and angular momentum density. An integration of the angular momentum density over full three-dimensional space gives a full angular momentum or spin.

The appropriate exact solution of linear electrodynamics is obtained [4, 7]. But this solution has not finite full energy and full angular momentum.

To obtain finite mass and spin we must consider a nonlinear electrodynamics model. In particular these characteristics are finite for the appropriate solution of Born – Infeld nonlinear electrodynamics [5, 7].

A magnetic moment for this field configuration is characterized by the following expression [5, 7]:

$$\bar{\mu} = \frac{\bar{\beta}\bar{e}\rho_0}{2}, \quad (5)$$

where ρ_o is the radius of the ring, $\bar{\beta} \sim 1$ is a constant defined by concrete soliton solution.

Thus the considered static field configuration with ring singularity looks like massive charged particle with spin and magnetic moment.

The solution of nonlinear electrodynamics which we could consider as more realistic representation for physical particle must contain also a time-periodic part. The time-periodic part leads to wave part for the appropriate moving solution. This wave part gives the observable wave properties of physical particle.

Let us consider a wave which is propagated along the singular ring with phase velocity equal to velocity of light in vacuum. The single-valuedness condition for wave function at the ring gives the following expression for the wave-length of the principal mode:

$$\lambda = 2\pi\rho_o. \quad (6)$$

Combining expressions (5) and (6) we obtain the following expression for magnetic moment of the soliton-particle with ring singularity:

$$\bar{\mu} = \frac{\bar{\beta}\bar{e}\lambda}{4\pi}. \quad (7)$$

This relation between magnetic moment of static part and wave-length of time-periodic part coincides with the corresponding relation of quantum physics.

Really a combination between known expressions for Compton wave-length and magnetic moment of massive charged particle with spin gives the following formula:

$$\bar{\mu} = \frac{\bar{e}\hbar}{2m\epsilon} = \frac{\bar{e}\hbar}{4\pi m\epsilon} = \frac{\bar{e}\lambda_c}{4\pi}, \quad (8)$$

where $\hbar = 2\pi\hbar$ is Planck's constant, m is mass of the particle, ϵ is velocity of light in vacuum, λ_c is Compton wave-length.

As we can see expressions (7) and last expression of (8) are coincided if we take into account that the factor $\bar{\beta} \sim 1$ defines an anomalous magnetic moment.

Generally speaking the last simple expression of (8) for magnetic moment of particle is notable.

In **conclusion** it may be said the following. Bidyon represents spin of particle more directly. But electromagnetic singular ring represents wave properties of particle more directly.

References

- [1] A. A. Chernitskii, J. High Energy Phys. **1999**, 12 (1999) Paper 10, [hep-th/9911093](#).
- [2] A. A. Chernitskii, Encyclopedia of Nonlinear Science, ed. A. Scott, Routledge, New York and London, 2004, 67–69, [hep-th/0509087](#).
- [3] A. A. Chernitskii, Proc. of the 17th. Int. Spin Physics Symposium, SPIN2006, AIP Conf. Proc. **V.915** (2007) 264–267, [hep-th/0611342](#).
- [4] A. A. Chernitskii, Proc. of XII Adv. Res. Workshop on High Energy Spin Physics, DSPIN-07, JINR (2008) 433–436, [arXiv:0711.2499](#).
- [5] A. A. Chernitskii, Proc. of XIII Adv. Res. Workshop on High Energy Spin Physics, DSPIN-09, JINR (2010) 443–446, [arXiv:0911.3230](#).
- [6] A. A. Chernitskii, Proc. of XIV Adv. Res. Workshop on High Energy Spin Physics, DSPIN-11, JINR (2012) 395–398, [arXiv:1112.4437](#).
- [7] A. A. Chernitskii, Nonlinear electrodynamics: singular solitons and their interactions (in Russian), ENGECON, Saint-Petersburg, 2012, 360 p., [en.Publ.su/2012.1.1](#).
- [8] A. A. Chernitskii, Physics of Particles and Nuclei, **45**(1) (2014) 205–206, [arXiv:1212.4468](#).

ON THE DISPUTED $\pi_1(1600)$ AND OBSERVATION OF A NEW ISO-VECTOR RESONANCE

F. Nerling^{1†}

on behalf of the COMPASS collaboration

(1) *Institut für Kernphysik, Universität Mainz, Becherweg 45, 55099 Mainz, Germany*

† *E-mail: nerling@cern.ch*

Abstract

The COMPASS experiment at CERN delivers new results on the search for exotic mesons. A spin-exotic resonance, the $\pi_1(1600)$, was reported by several experiments in the past. Those observations are, however, still to date highly disputed in the community. Especially the $\rho\pi$ decay channel allows for simultaneous observation of well established and less known resonances in different decay modes. The results from amplitude analysis of diffractively produced $(3\pi)^-$ final states show consistently a spin-exotic signal, that appears in agreement previous observations of the $\pi_1(1600)$. The high-statistics 2008 data sample allows and demands for an extended amplitude analysis method that further disentangles resonant and non-resonant particle production. The present status of analysis of COMPASS data and the observation of a new iso-vector meson $a_1(1420)$ is discussed.

Introduction

Exotic mesons have been reported by different experiments and in different decay channels. Quantum Chromodynamics (QCD) allows for and predicts exotic mesons like glue-balls, hybrids or tetraquarks according to several models. The experimental observation of so-called spin-exotic mesons, like the $\pi_1(1600)$ having exotic J^{PC} quantum numbers not accessible within the naive Constituent Quark Model, would be a fundamental confirmation of QCD, for a recent overview see e.g. [1]. Especially the resonant nature of signals observed in the exotic $J^{PC} = 1^{-+}$ partial-wave of the $\rho\pi$ decay channel, accessible via 3π final states, as reported by the E852/BNL and the VES experiments [2, 3] in $\pi^-\pi^+\pi^-$ final states are questioned. The conclusions were withdrawn in later publications [4] and re-analyses of the $(3\pi)^-$ system in two decay modes (charged: $\pi^-\pi^+\pi^-$ and neutral: $\pi^-\pi^0\pi^0$) led to opposite conclusions [5]. One may get a hint at this controversy looking at [6].

The data taken with the COMPASS experiment at the CERN SPS provide excellent opportunity for the search for exotic resonances. In the 2004 pilot run data (π^- beam, Pb target), a significant J^{PC} spin-exotic signal at $1660 \pm 10_{-64}^0$ MeV/ c^2 is observed that is consistent with the disputed $\pi_1(1600)$; it shows a clean phase motion against well-known resonances [7]. The high statistics of the 2008 proton target data allows the search for exotic states in different decay modes in the same experiment, cf. [8]. Employing the same PWA analysis method as in [7], the results obtained for the $J^{PC} M^{\epsilon} = (1^{-+}) 1^+ \rho^- \pi^0$ and $(1^{-+}) 1^+ \rho^0 \pi^-$ intensity and relative phase are similar to the previous observations [9, 10]. Apart of the established resonances $a_1(1260)$, $a_2(1320)$, $\pi_2(1670)$, also $\pi(1800)$ and $a_4(2040)$, an exotic signal in the 1^{-+} wave at around 1.6 GeV/ c^2 is observed, that shows a clean phase motion with respect to well-known resonances. These results are consistently obtained for both $\rho\pi$ decay modes, neutral and charged.

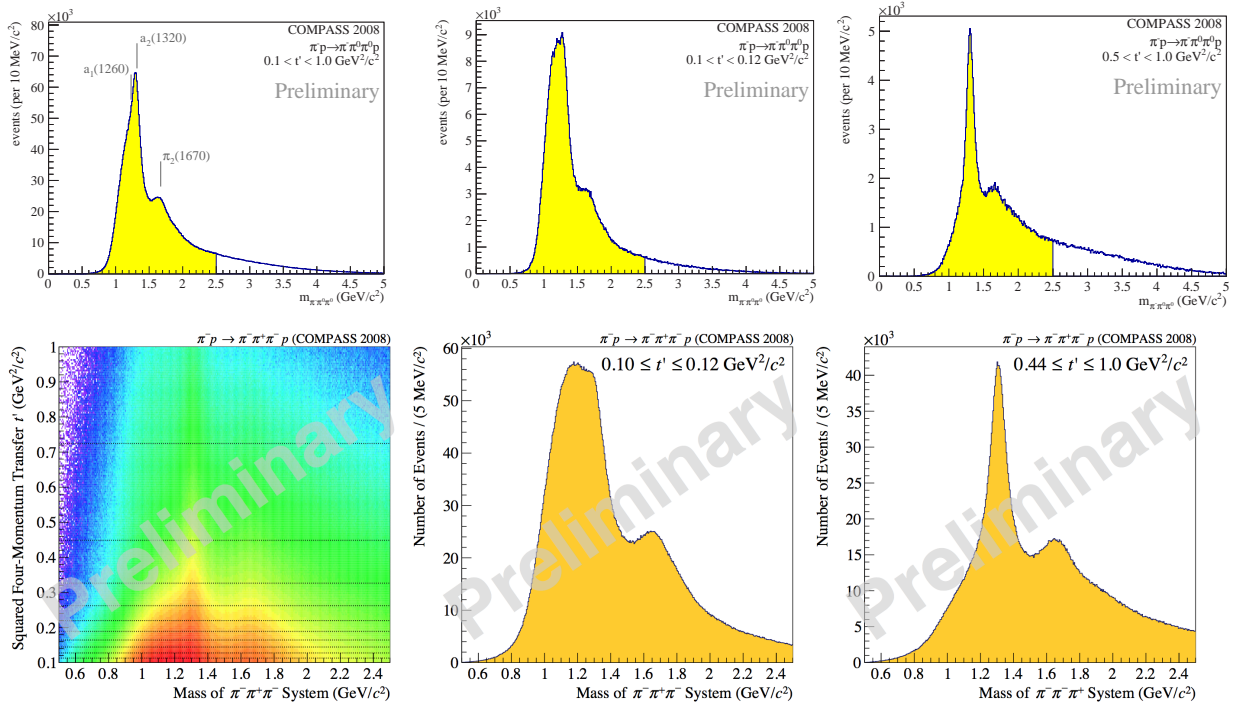


Figure 1: Mass spectra of the $(3\pi)^-$ systems. *Top: Neutral mode* — Different regions of momentum transfer t' : whole t' (left), “low t' ” (centre) and “high t' ” (right). *Bottom: Charged mode* — Correlation of $m_{3\pi}$ and t' (left), “low t' ” (centre) and high t' ” (right).

New Partial-Wave Analysis Results

The data analysed for both $(3\pi)^-$ decay modes has been extended to the full 2008 proton target data. The total outgoing 3π -mass spectrum is shown for the neutral mode data in Fig. 1 (top) for the whole range of momentum transfer t' (Fig. 1, top, left), and for ranges of “low” and “high” (Fig. 1, top, centre and right) t' values, indicating a dependence of $m_{3\pi}$ on t' . This dependence is shown for the charged data (Fig. 1, bottom) at its whole glance in terms of a 2D plot of t' vs. $m_{3\pi}$ (Fig. 1, bottom, left). The two exemplary $m_{3\pi}$ spectra for the “low” and “high” t' values similar to the ones shown for the neutral mode (Fig. 1, top, centre and right) are given for comparison for the charged mode (Fig. 1, bottom, centre and right) as well, illustrating the similarity of the t' dependence observed for both, neutral and charged mode data.

Given the observed dependence on t' and the large statistics (~ 50 M $\pi^-\pi^+\pi^-$, ~ 3.5 M $\pi^-\pi^0\pi^0$ events), the partial-wave analysis (PWA) method has been extended w.r.t. to the previous scheme of a two-step PWA as applied previously [7, 9]. The first step analysis, the mass-independent PWA, has now been performed in different ranges of t' (a scheme already addressed in [11, 5]) with equal statistics contained in each bin, which is then completed by the second step mass-dependent Breit-Wigner χ^2 fit, that takes into account the observed t' dependencies by performing a simultaneous optimisation of the resonant parameters in all t' regions. This procedure disentangles resonant from non-resonant particle production (e.g. dynamically produced components caused by the Deck effect [12]), the former should not depend on t' , whereas non-resonant backgrounds may well do so.

For the results presented here, the data has been divided into 8 and 11 bins of t' for the neutral and charged mode data, respectively, as illustrated for the charged data in Fig. 1 (bottom, left). The mass-independent PWA has been performed for each of the 8 and 11 ranges of t' , whereas 40 MeV/ c^2 (neutral mode) and 20 MeV/ c^2 (charged mode)

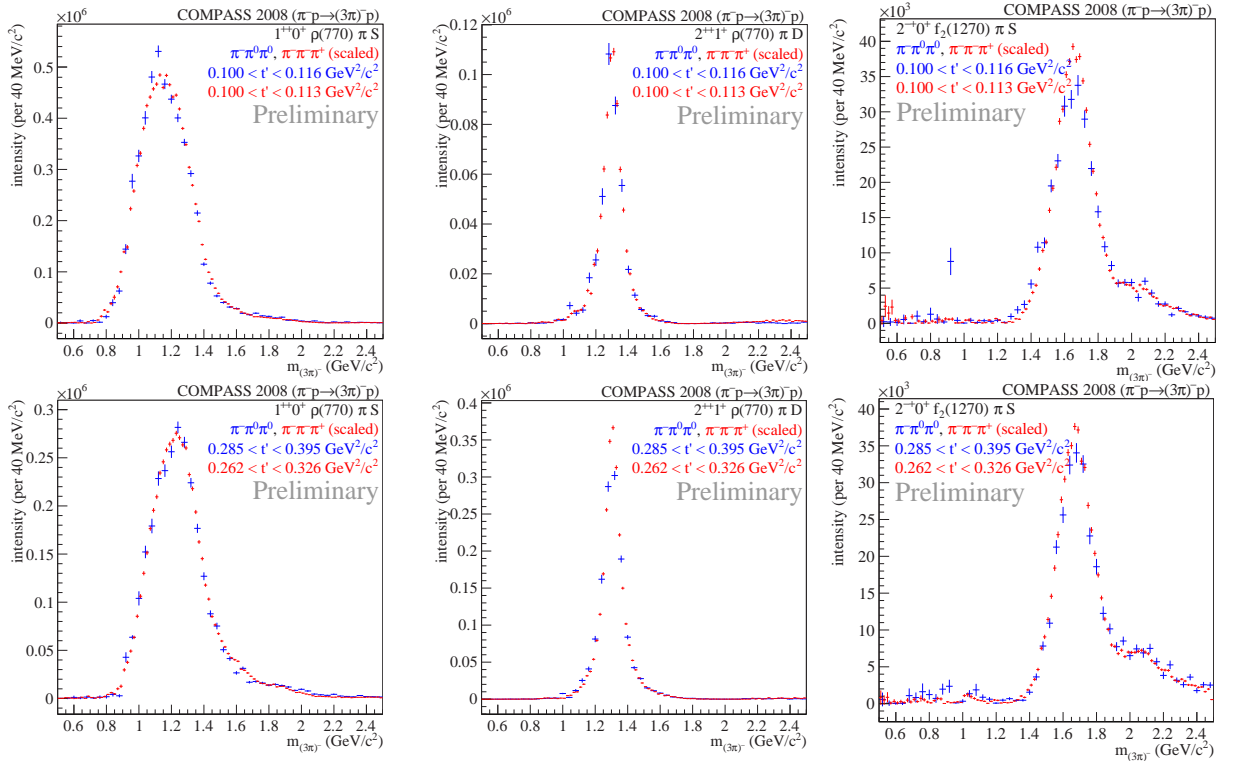


Figure 2: Mass-independent PWA result for neutral (blue) vs. charged (red) mode shown for the major waves for “low” (*top*) and “high” (*bottom*) values of t' . The $a_1(1260)$ in the $(1^{++})0^+\rho(770)\pi$ S -wave (*left*), the $a_2(1320)$ in the $(2^{++})1^+\rho(770)\pi$ D -wave (*centre*) and the $\pi_2(1670)$ in the $(2^{-+})0^+f_2(1270)\pi$ S -wave (*right*) are shown.

wide $m_{3\pi}$ bins have been chosen as previously [9, 10]. The wave-set has been extended from 53 to 88 partial-waves. The mass-dependent PWA including 6 out of the 88 waves is released for public merely for the charged mode data, see also [13, 14] for more details.

In Fig. 2, the mass-independently fitted intensities for the major waves are shown for exemplary two very different ranges of t' (“low” and “high”) for both, the neutral and the charged mode fit results (normalised to the integral for each plot to compare the shapes). The main resonances $a_1(1260)$ (Fig. 2, left), $a_2(1320)$ (Fig. 2, centre), and $\pi_2(1670)$ (Fig. 2, right) are consistently observed for the neutral vs. charged mode data, the shapes are mostly coinciding for the different t' ranges “low” and “high” (Fig. 2, top and bottom). While the $a_2(1320)$ and $\pi_2(1670)$ (Fig. 2, centre and right) are observed rather robust in shape against t' , the $a_1(1260)$ (Fig. 2, left) shows a significant shift in mass for the different t' . In addition, structures around the $a_1(1260)$ and $\pi_2(1670)$ (Fig. 2, left and right) reveal underlying dynamics resulting in a t' dependent shape, which cannot be solely attributed to a resonance. This will be resolved by the completing second step, the mass-dependent fit. Fitting the Breit-Wigner description of the resonances simultaneously to the different t' ranges, while allowing for background contributions, indeed different relative contributions of non-resonant background are found, depending on t' (Fig. 3).

Summing incoherently up the mass-independently fitted intensities of all t' bins, one obtains a similar result as obtained previously [9], where the mass-independent PWA were performed in bins of $m_{3\pi}$ only. The intensity spectra obtained with the extended method discussed here are basically smoother, as the t' dependence is taken into account directly from the data instead of using the t' slopes for the various resonances parameterised from

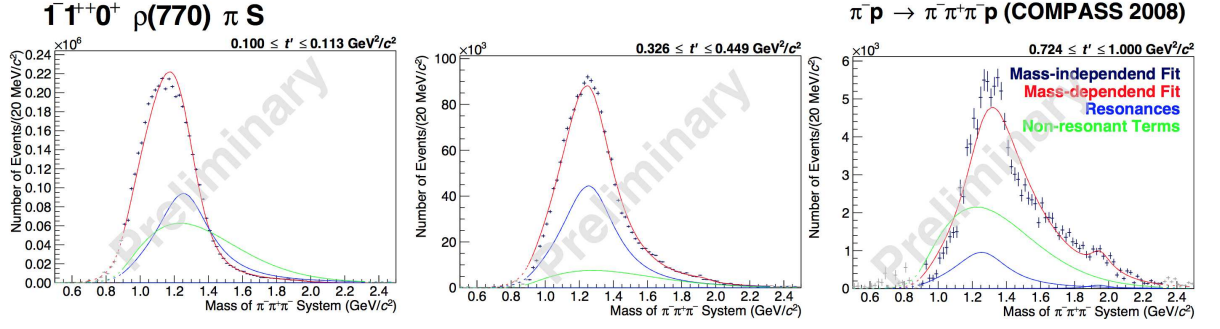


Figure 3: Complete PWA result for the $(1^{++})0^+\rho(770)\pi S$ -wave, in which we observe the $a_1(1260)$, shown for three exemplary bins in t' (“low”, “medium”, and “high”). Shown are the mass-independent fit result (data points) and overlaid the fitted Breit-Wigner (BW) description (red curve), which consists of the BW describing the $a_1(1260)$ (blue curve) and the non-resonant background contribution (green curve).

the data. For the three main waves, in which we observe the $a_1(1260)$, the $a_2(1320)$ and the $\pi_2(1670)$, shown for different t' ranges in Fig. 2, the incoherent sums of intensities over all t' ranges are shown in Fig. 4 (top) for each wave. Further incoherent sums are presented for the $(0^{-+})0^+f_0(980)\pi S$ -wave and the $(4^{++})1^+\rho(770)\pi S$ -wave (Fig. 4, bottom, left and centre), showing the $\pi(1800)$ and $a_4(2040)$, respectively, and the $(0^{-+})0^+(\pi\pi)_s\pi S$ -wave (Fig. 4, bottom, right), where the peak at around $1.8\text{ GeV}/c^2$ can be attributed to the $\pi(1800)$. Other experiments claimed also a $\pi(1300)$ — the object at the mass between 1 and $1.4\text{ GeV}/c^2$ in the $(0^{-+})0^+(\pi\pi)_s\pi S$ -wave shows some differences for the neutral vs. the charged mode COMPASS data.

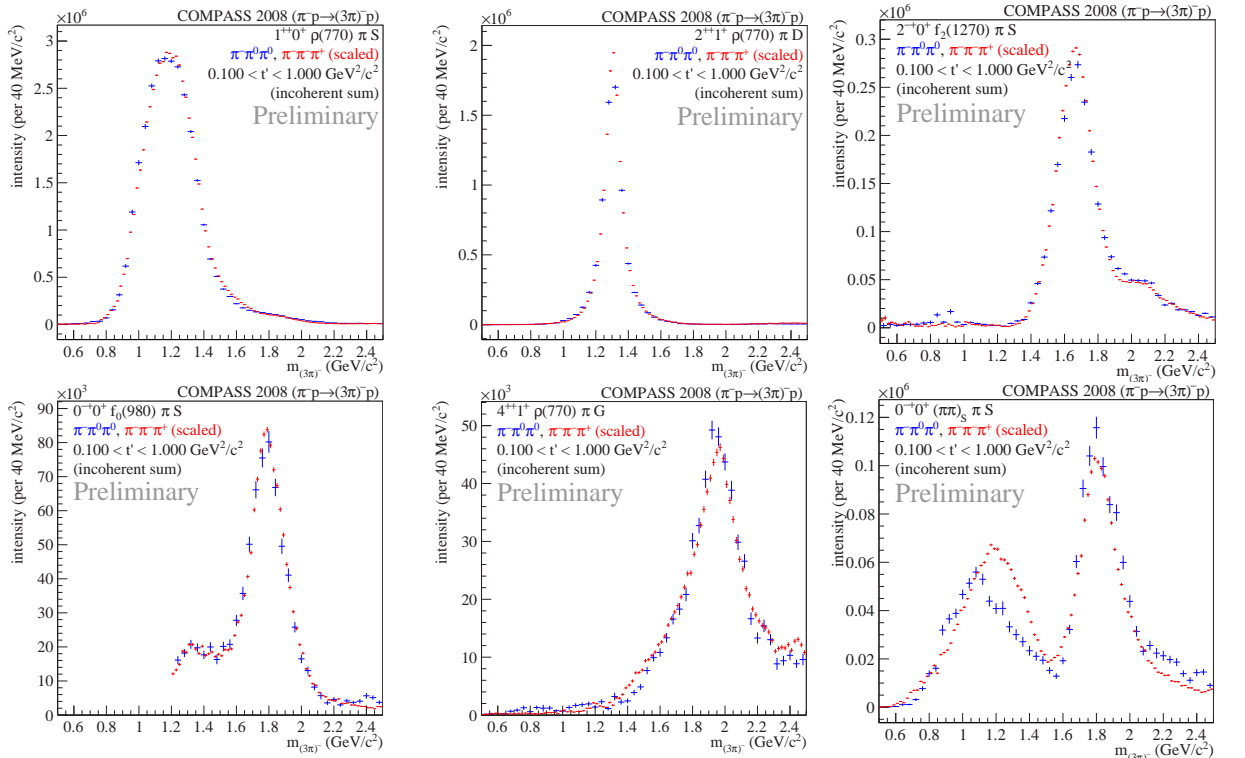


Figure 4: Incoherent sum over the different t' ranges of mass-independently fitted intensities of major and smaller waves compared for neutral (blue) and charged (red) mode data. Shown are the three major waves (cf. also Fig. 2) (top) and those, in which the $\pi(1800)$ (bottom, left and right) and the $a_4(2040)$ (bottom, centre) are observed.

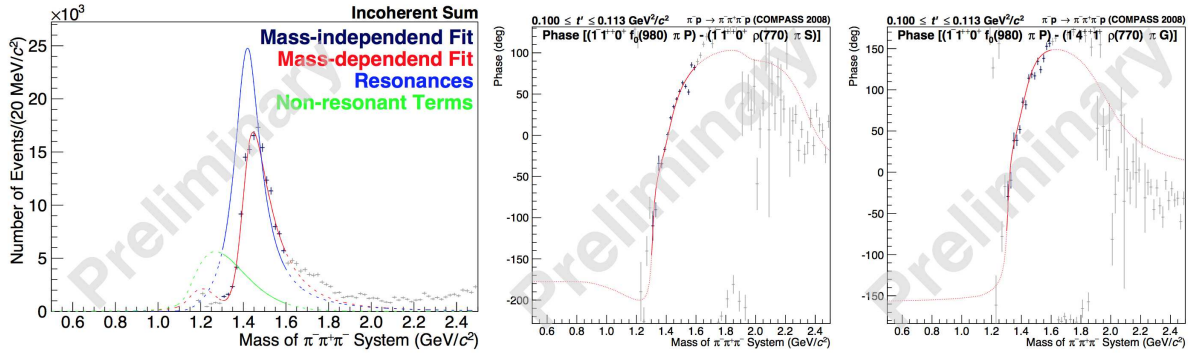


Figure 5: PWA result for the $(1^{++})0^+ f_0(980)\pi$ P -wave. The mass-independently fitted intensities for the neutral and the charged mode data show a narrow structure at $1420 \text{ MeV}/c^2$ (first presented in [14] and [13]). For the charged mode data, the mass-independent fit result is shown (data points) with the fitted BW description (red curve) overlaid, which consists of the BW describing the object at $1420 \text{ MeV}/c^2$ (blue curve) and the non-resonant background contribution (green curve) (*left*). The corresponding relative phases w.r.t. two other waves are shown, again the mass-independent result (data points) with the mass-dependent fit result overlaid (black line) (*centre and right*).

The PWA results for the $(1^{++})0^+ f_0(980)\pi$ P -wave in the charged mode data are displayed in Fig. 5. The mass-independently fitted intensities (incoherent sums of the different t' ranges) are shown (Fig. 5, left). The data exhibits, even though low in intensity, a strong enhancement in form of a clean narrow peak at $1420 \text{ MeV}/c^2$, that is consistently observed for the neutral and the charged mode data, see also [14] and [13], respectively. The mass-independent PWA completed by the simultaneous BW fit to the result obtained from the mass-independent fit performed in the different ranges of t' is shown for the $(1^{++})0^+ f_0(980)\pi$ P -wave in the charged mode data in Fig. 5 (left). Here, the result of the mass-dependent fit is overlaid (curves) in addition. It consists of a BW describing the narrow object and some non-resonant component. No such object has previously been observed.

The relative phases of this object observed in the $(1^{++})0^+ f_0(980)\pi$ P -wave against the $a_1(1260)$ in the $(1^{++})0^+ \rho(770)\pi$ S -wave and the $a_4(2040)$ in the $(4^{++})1^+ \rho(770)\pi$ G -wave are shown in Fig. 5 (centre and right), again with the mass-dependent fit result overlaid. A clean phase motion is observed exactly in the mass region of about $1.3\text{-}1.6 \text{ GeV}/c^2$, where the object is observed in the intensity plots, convincing that the object is of resonant nature.

The neutral and the charged mode results are consistent not only for the well and less established states, but also for this new iso-vector resonance, that we call $a_1(1420)$. The new $a_1(1420)$ decaying into $f_0(980)\pi$ (and not observed in $\rho\pi$) is produced at a rather low intensity (less than 0.25% of the total intensity), which might hint to a large strangeness content and an exotic nature. Similarly to $a_0(980)$ and $f_0(980)$, it might be the isospin-1 partner of the $f_1(1420)$ (that we observe well resolved decaying to $K\bar{K}\pi$ [15]) strongly coupling to KK^* , at least the similarity in width and mass is striking.

Conclusions & Outlook

In summary, we extended our PWA method to disentangle contributions from resonant and non-resonant production. The neutral and the charged mode $(3\pi)^-$ data diffractively produced on a proton target show consistent results concerning major and less known resonances. In particular, we observe a new possibly exotic iso-vector state $a_1(1420)$

decaying into $f_0(980)\pi$ (and not observed in $\rho\pi$), having a width of about $140 \text{ MeV}/c^2$ and showing resonant behaviour. The analyses will be proceeded, including the extraction of the $(\pi\pi)_s$ wave subsystem (not discussed here), before stronger conclusions will be drawn also on the disputed $\pi_1(1600)$ resonance, for which the interpretation as a narrow ($\Gamma=150\text{-}200 \text{ MeV}$) resonance is excluded, and thus its nature can (partly) be connected to dynamical effects on top of a non-resonating Deck-like amplitude.

References

- [1] C.A. Meyer and Y.Van. Haarlem, Phys. Rev. C **82** (2010) 025208.
- [2] G. S. Adams *et al.*, Phys. Rev. Lett. **81**, (1998) 5760.
- [3] Y. Khokhlov, Nucl. Phys. **A663** (2000) 596.
- [4] D. V. Amelin *et al.*, Phys. Atom. Nucl. **68** (2005) 359.
- [5] A.R. Dzierba *et al.*, Phys. Rev. D **73** (2006) 072001.
- [6] J. Beringer *et al.*, (Particle Data Group), Phys. Rev. D **86** (2012) 010001.
- [7] M. Alekseev *et al.*, COMPASS collaboration, Phys. Rev. Lett, **104** (2010) 241803.
- [8] F. Nerling, AIP Conf. Proc. **1257** (2010) 286; arXiv:1007.2951[hep-ex].
- [9] F. Nerling, EPJ Web Conf. **37** (2012) 09025; arXiv:1208.0474[hep-ex].
- [10] F. Haas, Conf. Proc., Hadron2011, Munich (2011); arXiv:1109.1789v2[hep-ex].
- [11] C. Daum *et al.*, Phys. Lett. **89B** (1980) 276; Phys. Lett. **89B** (1980) 281.
- [12] R.T. Deck, Phys. Rev. Lett. **13** (1964) 169.
- [13] S. Paul, Conf. Proc., MENU 2013, Rom, Italy, (2013); arXiv:1312.3678[hep-ex].
- [14] S. Uhl, Conf. Proc., Hadron2013, Nara, Japan, (2013); arXiv:1401.4943[hep-ex].
- [15] J. Bernhard and F. Nerling, Conf. Proc. Hadron2011, Munich (2011); arXiv:1109.0219[hep-ex].

QCD EFFECTIVE COUPLING AND SPECTRA OF ($q\bar{q}$), (gg) STATES WITHIN INFRARED CONFINEMENT

Gurjav Ganbold^{1,2}

(1) *Joint Institute for Nuclear Research, 141980 Dubna, Russia*

(2) *Institute of Physics and Technology, 210651, Ulaanbaatar, Mongolia*

† *E-mail: ganbold@theor.jinr.ru*

Abstract

The spectra of two-particle bound states of spin-half and spin-one constituents are considered within a relativistic model based on the infrared confinement. Masses of conventional mesons are calculated in a wide range (up to 10 GeV). An analytic expression is derived for the lowest-state (gg) glueball mass. The QCD effective coupling is estimated in the low-energy domain by using the masses of ($q\bar{q}$) states and a new, specific infrared-finite behaviour of α_s is obtained below 1 GeV.

1 Introduction

The color confinement is the most crucial feature of QCD explaining the physics phenomenon that color charged particles are not observed. However, we are far from understanding how QCD works at large distances (or, in the infrared (IR) region below $Q \sim 1\text{GeV}$) [1]. The well established conventional perturbation theory cannot be used at low energy, where the most interesting and novel behavior is expected. The calculation of hadron mass characteristics comparable to the precision of experimental data still remains one of the major problems in QCD. Particularly, planned experiments at FAIR (GSI) on annihilation reactions of antiprotons with protons can be used for precise spectroscopy of mesons, baryons and exotic states. The exotic states are intensively searched for in different experiments (e.g., BESIII, Belle II, *BaBar*, CLEO-c Collaborations). Also, the recent evidence for the production of the exotic glueball states and future planned studies (e.g., PANDA experiments at GSI) on their decays open new perspectives in the understanding of the confinement mechanism.

Besides, many quantities in particle physics are affected by the IR behavior of the QCD effective coupling $\alpha_s(Q)$ [2]. Nowadays, the long-distance behavior of α_s is not well defined, it needs to be more specified [3, 4] and correct description of QCD effective coupling in the IR regime remains one of the actual problems in particle physics.

Therefore, it represents a certain interest to investigate some low-energy physics problems, such as hadronisation, glueball states, QCD effective (running) charge within a simple relativistic model based on physically transparent hypotheses, which can be treated by simple analytic methods.

Below, we take into account the dependence of α_s on mass scale M and determine the QCD effective charge in the low-energy region by exploiting the hadron spectrum.

2 IR-confined Propagators and Meson Masses

Consider the model Lagrangian [5]:

$$\mathcal{L} = -\frac{1}{4} (F_{\mu\nu}^A)^2 + \left(\bar{q}_f^a [\gamma_\alpha \partial^\alpha - m_f]^{ab} q_f^b \right) + g \left(\bar{q}_f^a [\Gamma_C^\alpha \mathcal{A}_\alpha^C]^{ab} q_f^b \right), \quad (1)$$

where $\Gamma_C^\alpha = i\gamma_\alpha t^C$. The model parameters are the IR confinement scale Λ and the constituent quark masses $m_f = \{m_{ud}, m_s, m_c, m_b\}$.

For the spectra of two-quark bound states we develop a relativistic quantum-field model based on IR confinement. We take into account the recent theoretical results predicting an IR-finite behavior of the gluon propagator. Consider the gluon and quark propagators exhibiting explicit IR-finite behaviors as follows [6]:

$$\tilde{D}(p) = \frac{1}{p^2} \left(1 - e^{-p^2/\Lambda^2} \right), \quad \tilde{S}_m(\hat{p}) = \frac{i\hat{p} + m_f}{p^2 + m_f^2} \left(1 - e^{-(p^2 + m_f^2)/\Lambda^2} \right). \quad (2)$$

These propagators are entire analytic functions in the Euclidean space.

We write the master equation determining the meson masses as follows [7, 6] :

$$1 + \alpha_s \cdot \lambda_J(M_J^2) = 1 + \frac{16\pi\alpha_s C_J}{9} \iint dx dy U_N(x) \sqrt{D(x)D(y)} U_N(y) \cdot \int \frac{d^4 k}{(2\pi)^4} e^{-ik(x-y)} \text{Tr} \left[O_J \tilde{S}_{m_1}(\hat{k} + \xi_1 \hat{p}) O_J \tilde{S}_{m_2}(\hat{k} - \xi_2 \hat{p}) \right] = 0, \quad p^2 = -M_J^2, \quad (3)$$

where $C_J = \{1, 1, 1/2, -1/2\}$, $\xi_i = m_i/(m_1 + m_2)$, $O_J = \{I, i\gamma_5, i\gamma_\mu, \gamma_5\gamma_\mu\}$ and the polarization kernel $\lambda_{JJ'}(-p^2)$ has been diagonalized on a complete system of orthonormal functions $\{U_N\}$. Note, solution of Eq.(3) is nothing else but the solution of the corresponding ladder Bethe-Salpeter equation [7].

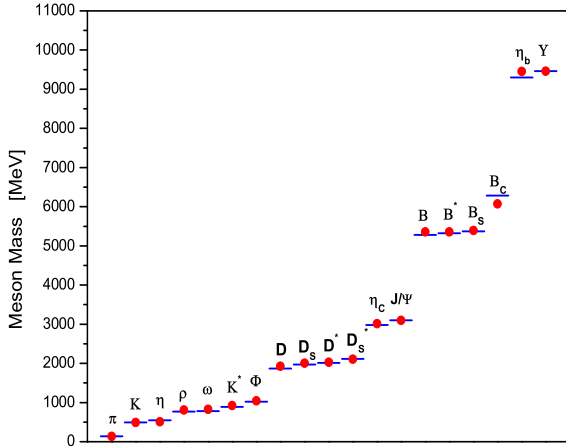


Figure 1: Estimated masses (dots) of conventional mesons (in units of MeV) compared with experimental data (dashes) from PDG-2012.

parameters (in units of MeV):

$$\Lambda = 226, \quad m_{ud} = 115.3, \quad m_s = 392.3, \quad m_c = 1529.8, \quad m_b = 4733.7.$$

4) As application we calculate intermediate and heavy meson masses shown in Fig. 1.

The dependence of meson masses on α_s and other model parameters is defined by Eq.(3). Note, the kernel function λ_N is real and finite, it allows us to derive both analytic and numeric solutions [8].

1) An asymptotic Regge-type behavior is observed: $M_J^2 \approx M_0^2 + J \cdot c(M)$ for $J \geq 3$.

2) For the same quark-antiquark content a vector meson is heavier than its pseudoscalar counterpart: $M_V > M_P$ because of $C_V < C_P$ [7].

3) We derive meson mass formula Eq.(3) and adjust the model parameters by fitting heavy meson masses ($M \geq 2$ GeV). Particularly, we fix a set of model

3 QCD Running Coupling in the IR Region

We consider the meson mass M as an appropriate energy-scale parameter for coupling $\alpha_s(M)$. Having adjusted model parameters, we estimate $\alpha_s(M)$ in the low-energy domain by exploiting meson masses [7]. Then, we perform global evaluation of $\alpha_s(M)$. The resulting curve is plotted in Fig. 2 in comparison with recent experimental data [9].

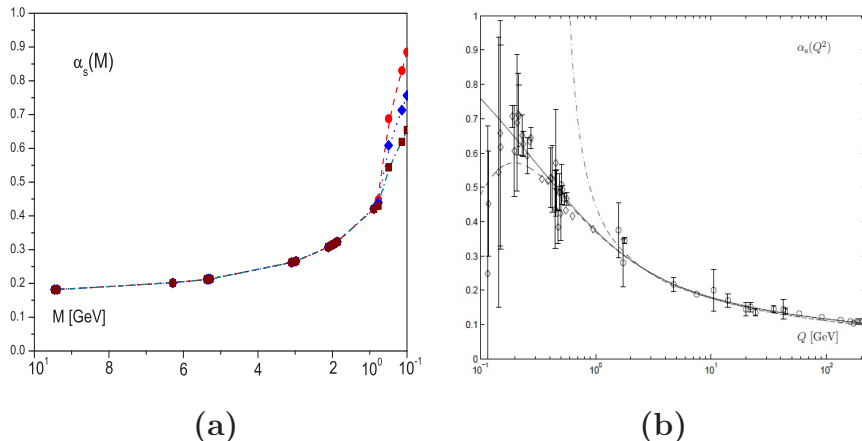


Figure 2: Summary of estimates of $\hat{\alpha}_s(M)$ in interval from 0 to 10 GeV **(a)** at different values of confinement scale: $\Lambda = 200$ MeV (dots), $\Lambda = 226$ MeV (rhombs) and $\Lambda = 250$ MeV (squares) compared with **(b)** $\alpha_s(Q)$ defined in low- (diamonds) and high-energy (circles) experiments. Also shown are the three-loop analytic coupling (solid curve), its perturbative counterpart (dot-dashed curve) both normalized at the Z-boson mass and the massive one-loop analytic coupling (dashed curve) (for details see in [9])

By deriving Eq.(3) for $M = 0$ and $m_1 = m_2 = 0$ we reveal a IR-fixed point:

$$\alpha_s^0 = \alpha_s(0) = 3\pi / (16 \ln(2)) \approx 0.8498 \quad \Rightarrow \quad \alpha_s^0 / \pi = 0.2705.$$

The obtained IR-fixed value of the coupling constant is moderate and is in a reasonable agreement with often quoted estimates: $\alpha_s^0 / \pi \simeq 0.19 - 0.25$ [10], $\alpha_s^0 / \pi \simeq 0.265$ [11], $\alpha_s^0 / \pi \simeq 0.26$ [12] and other phenomenological evidences (e.g., [9]).

4 Glueball Lowest State

The glueball spectrum has been studied by using effective approaches. There are predictions expecting non- $q\bar{q}$ scalar objects, like glueballs and multiquark states in the mass range $\sim 1500 \div 1800$ MeV [13, 14].

Below we consider a two-gluon bound states. First, we isolate the color-singlet term in the bi-gluon spin-zero (scalar) and spin-two (tensor) currents. Further we consider only the scalar component. By omitting details of intermediate calculations we define the Bethe-Salpeter kernel for the two-gluon scalar state:

$$\Pi(z) \doteq \iint dt ds U_n(t) \sqrt{W(t)} D\left(z + \frac{t-s}{2}\right) \cdot D\left(z - \frac{t-s}{2}\right) \sqrt{W(s)} U_n(s).$$

The scalar glueball mass M_G is defined from equation:

$$1 - \frac{\pi g^2}{8} \int dz e^{izp} \Pi(z) = 0, \quad p^2 = -M_G^2. \quad (4)$$

For $\Lambda \approx 226$ MeV and $\alpha_s(M_\tau) = 0.343$ we estimate: $M_G \approx 1790 \pm 25$ MeV.

Our estimate is in reasonable agreement with other predictions [15, 13, 16, 17]. The quenched lattice estimate favors a scalar glueball mass $M_G = 1710 \pm 50 \pm 58$ MeV [18] while recent glueball mass measurements from improved staggered fermion simulations (UKQCD Collaboration) predict the scalar glueball mass at $M_G = 1830$ MeV [19].

To conclude, we have shown that the behavior of the QCD running coupling in the low-energy region may be explained reasonably by using the meson spectrum [6]. A new, independent, and specific IR-finite behavior of QCD coupling is exhibited. At moderate mass scale we obtain α_s in coincidence with the QCD predictions. However, at large mass scale (above 10 GeV) $\hat{\alpha}_s$ decreases much faster than expected by QCD prediction. The reason is the use of simple confined propagators in the form of entire functions. As applications, we performed estimates on conventional meson spectrum and the lowest glueball mass and, the results were in reasonable agreement with experimental data.

References

- [1] J. Beringer et al. (Particle Data Group), Phys. Rev. **D86** (2012) 010001.
- [2] S. Bethke, Eur. Phys. J. **C64** (2009) 689.
- [3] D.V. Shirkov, Theor. Math. Phys. **132** (2002) 1309.
- [4] O. Kaczmarek and F. Zantow, Phys. Rev. **D71** (2005) 114510.
- [5] G. Ganbold, Phys. Rev. **D79** (2009) 034034.
- [6] G. Ganbold, Phys. Part. Nucl. **43** (2012) 79.
- [7] G. Ganbold, Phys. Rev. **D81** (2010) 094008.
- [8] G. Ganbold, Phys. Part. Nucl. **45** (2014) 10.
- [9] M. Baldicchi et al., Phys. Rev. **D77** (2008) 034013.
- [10] S. Godfrey and N. Isgur, Phys. Rev. **D32** (1985) 189.
- [11] T. Zhang and R. Koniuk, Phys. Lett. **B261** (1991) 311.
- [12] F. Halzen, G. I. Krein and A. A. Natale, Phys. Rev. **D47** (1993) 295.
- [13] C. Amsler, N.A. Tornqvist, Phys. Rep. **389** (2004) 61.
- [14] W.-M. Yao et al., J. Phys. **G33** (2006) 1.
- [15] C.J. Morningstar and M. Peardon, Phys. Rev. **D60** (1999) 034509.
- [16] S. Narison, Nucl. Phys. **B509** (1998) 312; Nucl. Phys. **A675** (2000) 54.
- [17] H.B. Meyer and M.J. Teper, Phys. Lett. **B605** (2005) 344.
- [18] Y. Chen et al., Phys. Rev. **D73** (2006) 014516.
- [19] Christopher M. Richards et al., Phys. Rev. **D82** (2010) 034501.

PERSPECTIVE STUDIES OF STRONG INTERACTIONS AND HADRONIC MATTER IN ANTIPROTON-PROTON ANNIHILATION

M.Yu. Barabanov[†], A.S. Vodopyanov.

Joint Institute for Nuclear Research, Joliot-Curie 6, Dubna, Moscow reg., Russia 141980

[†] *E-mail: barabanov@jinr.ru*

Abstract

The spectroscopy of exotic states with hidden charm is discussed. Together with charmonium it is a good testing tool for theories of strong interactions including QCD in both perturbative and non-perturbative regime, lattice QCD, potential models and phenomenological models. An elaborated analysis of exotic spectrum is given, and attempts to interpret recent experimental data in the above $D\bar{D}$ threshold region are considered. Experiments using the antiproton beam have an advantage of the intensive production of particle-antiparticle pairs in antiproton-proton annihilations. Experimental data from different collaborations are analyzed with special attention given to new states with hidden charm which were discovered recently. Some of these states can be interpreted as higher-lying charmonium states and tetraquarks. But much more data on different decay modes are needed before firmer conclusions can be made. These data can be derived directly from the experiments using the high quality antiproton beam with momentum up to 15 GeV/c.

1 Introduction

The study of strong interactions and hadronic matter in the process of antiproton-proton annihilation seems to be a challenge nowadays. One of the main tasks of PANDA physical program is to search for new exotic forms of matter, which must manifest the existence of multiquark states such as meson molecules and tetraquarks [1]. The researches of spectrum of tetraquarks with the hidden charm together with the charmonium and charmed hybrid spectra are promising to understand the dynamics of quark interactions at small distances.

In the last few years we have witnessed the discovery of a number of narrow hadron resonances with charm which do not match the standard quark-antiquark interpretation, thereby named exotic hadrons [2–5]. This has called for alternative interpretations of their inner structure. One of the possible explanations is that these particles are loosely bound molecules of open charm mesons. Another possibility is that new aggregation patterns of quarks in matter are possible. We follow the suggestion of having diquarks as building blocks. Light diquarks have been an object of several lattice studies. The idea that the coloured diquark can be handled as a constituent building block is at the core of the taken approach.

An early quark model prediction was the existence of multiquark states, specifically bound meson antimeson molecular states [4, 5]. In the light quark sector the $f_0(980)$ and $a_0(980)$ are considered to be strong candidates for $K\bar{K}$ molecules. However, in general, it is challenging to definitively identify a light multiquark state in the environment of many broad and often overlapping conventional states. The charmonium spectrum is

better defined so that new types of states can potentially be more easily delineated from conventional charmonium states.

Two generic types of multiquark states have been described in the literature [4, 5]. The first one, the molecular state, is comprised of two charmed mesons bound together to form a molecule. These states are by nature loosely bound. Molecular states bound through two mechanisms: quark/colour exchange interactions at short distances and pion exchange at a large distance (although pion exchange is expected to dominate). Molecular states are generally not isospin eigenstates, which give rise to distinctive decay patterns. Since the mesons inside the molecule are weakly bound, they tend to decay as if they are free.

The second type is a tightly bound four-quark state, so called tetraquark that is predicted to have properties that are different from those of a molecular state. In the model of Maiani [4, 5], for example, the tetraquark is described as a diquark-diantiquark structure in which the quarks group into the colour-triplet scalar and vector clusters and the interactions are dominated by a simple spin-spin interaction. Here, strong decays are expected to proceed via rearrangement processes followed by dissociation that gives rise, for example, to such decays as: $\bar{p}p \rightarrow X \rightarrow J/\Psi\rho \rightarrow J/\Psi\pi\pi$; $\bar{p}p \rightarrow X \rightarrow J/\Psi\omega \rightarrow J/\Psi\pi\pi\pi$, $\bar{p}p \rightarrow X \rightarrow \chi_{cJ}(1P)\pi$ (decays into J/Ψ , $\Psi(2S)$, χ_{cJ} and light mesons); $\bar{p}p \rightarrow X \rightarrow D\bar{D}^* \rightarrow D\bar{D}\gamma$; $\bar{p}p \rightarrow X \rightarrow D\bar{D}^* \rightarrow D\bar{D}\eta$; (decays into $D\bar{D}^*$ pair).

A prediction that distinguishes tetraquark states containing a $c\bar{c}$ pair from conventional charmonia is possible existence of multiplets which include members with non-zero charge $cu\bar{c}\bar{d}$, strangeness $cd\bar{c}\bar{s}$, or both $cu\bar{c}\bar{s}$.

2 Calculation of exotics spectrum

For this purpose we have fulfilled the elaborated analysis of the spectrum of tetraquarks with the hidden charm in the mass region mainly above $D\bar{D}$ threshold. The analysis of spectrum of the singlet $^1S_0, ^1P_1, ^1D_2$ and triplet $^3S_1, ^3P_J, ^3D_J$ charmonium states [6, 7] and charmed hybrids [8, 9] was carried out earlier. Different decay modes of tetraquarks such as decays into light mesons and decays into $D\bar{D}^*$ pair, were, in particular, analyzed. A special attention was given to the new states with the hidden charm discovered recently (XYZ -particles) [2–5]. The experimental data from different collaborations like Belle, BaBar, BES, LHCb CDF, CLEO were carefully analyzed. Using the combined approach based on the quarkonium potential model and confinement model on a three-dimensional sphere embedded into the four-dimensional Euclidian space [10, 11], more than twenty tetraquarks were predicted in the mass region above $D\bar{D}$ threshold (see Fig.1).

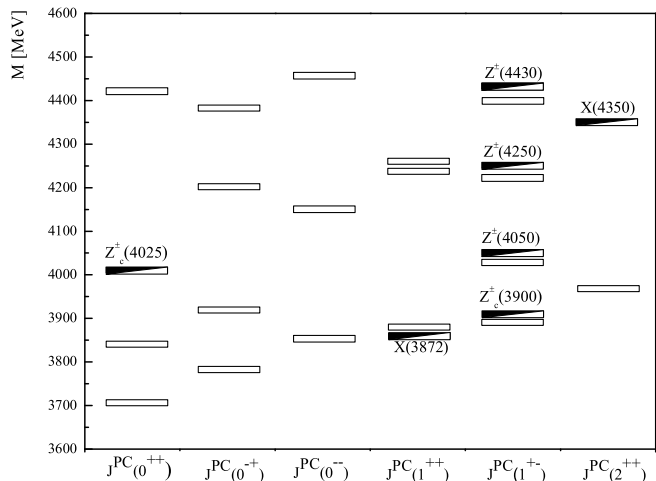


Figure 1: The spectrum of tetraquarks with hidden charm.

The experimental data from different collaborations like Belle, BaBar, BES, LHCb CDF, CLEO were carefully analyzed. Using the combined approach based on the quarkonium potential model and confinement model on a three-dimensional sphere embedded into the four-dimensional Euclidian space [10, 11], more than twenty tetraquarks were predicted in the mass region above $D\bar{D}$ threshold (see Fig.1).

The black-white boxes correspond to the recently revealed XYZ states with the hidden charm that may be interpreted as tetraquarks. White boxes correspond to the tetraquark states which have not been found yet. But a possibility of existence of these states is predicted in the framework of the combined approach. It has been shown that charge/neutral tetraquarks must have their neutral/charged partners with mass values which differ by few MeV. This assumption can shed light on the nature of neutral $X(3872)$, $X(4350)$ and charged $Z(4050)^\pm$, $Z(4250)^\pm$, $Z(4430)^\pm$ states. The quantum numbers J^{PC} of the $X(3872)$ meson have been recently determined by LHCb [12]. One can find that $X(3872)$ may be interpreted as tetraquark state with $J^{PC} = 1^{++}$ and the new state $Z_c(3900)^\pm$ observed by BES [13] as its charged partner. The new state $Z_c(4025)^\pm$ observed by BES [14] may be interpreted as tetraquark state with $J^{PC} = 0^{++}$. The predicted states with the mass equals to 4228 MeV and 4256 MeV and quantum numbers $J^{PC} = 1^{++}$ may be interpreted as their radial excited states, correspondingly. The analogous situation is observed with charged Z^\pm states. The state $Z(4430)^\pm$ may be interpreted as charged tetraquark. The predicted state with a mass equal to 4412 MeV and quantum numbers $J^{PC} = 1^{+-}$ may be interpreted as its neutral partner. The recently observed states $Z(4050)^\pm$ and $Z(4250)^\pm$ may be also interpreted as charged tetraquarks. They must have their neutral partners with the masses equal to 4043 MeV and 4210 MeV, correspondingly. Probably, $Z(4250)^\pm$ and $Z(4430)^\pm$ may be considered as radial excited states of $Z(4050)^\pm$. The new state $X(4550)$ may be interpreted as the tetraquark state with quantum numbers $J^{PC} = 2^{++}$. Two charged states $Z(3750)^\pm$ and $Z(3880)^\pm$ with $J^{PC} = 1^{+-}$ are expected to exist. This hypothesis coincides with that proposed by Maiani and Polosa [15, 16]. But these assumptions need confirmation in PANDA experiment with its high quality antiproton beam in the channels considered above.

To confirm that the predicted states actually exist and can be found experimentally, their widths and branching ratios were calculated [7, 11]. The feature of the considered states is their narrowness compared with light unflavored mesons, baryons and hybrids. The states we find in this model have small widths of the order of several tens of MeV. This fact facilitates experimental searches. The values of the calculated widths coincide (within the experimental error) with the experimentally determined values for the XYZ particles; the correspondence of the mass values has been discussed above. This fact strongly suggests that some of the XYZ particles may be interpreted as higher-lying charmonium states [6, 7] and tetraquarks as it can be verified by the PANDA experiment. The values of branching ratios in the considered decay channels of charmonium and exotics are of the order of $\beta \approx 10^{-1} - 10^{-2}$ dependent of their decay channel (mode). From this one can conclude that the branching ratios are significant and searches for charmonium and exotics and studies of the main characteristics of their spectrum seem to be promising for the PANDA experiment at FAIR.

3 Conclusion

The prospects for future exotics research at FAIR are related with the results obtained below.

A combined approach has been employed to study charmonium and exotics on the basis of the quarkonium potential model and a confinement model that uses a three-dimensional sphere embedded into the four-dimensional Euclidian space of the decay products.

The most interesting and promising decay channels of tetraquarks have been analyzed. More than twenty tetraquark states above the $D\bar{D}$ threshold are expected to exist in framework of this model.

The recently discovered states with the hidden charm above the $D\bar{D}$ threshold (*i.e.*, the XYZ particles) have been analyzed. Seven of these states can be interpreted as higher-lying tetraquark states. The necessity of further studies of the XYZ particles and improved measurements of their main characteristics in PANDA experiment has been demonstrated.

Using the integral approach for the hadron resonance decay, the widths and branching ratios of the expected states of tetraquarks have been calculated and they turn out to be relatively narrow; most are of the order of several tens of MeV. This fact additionally indicates the necessity of further studying tetraquarks in the channels considered above.

References

- [1] W. Erni *et al.*, Physics Performance Report for PANDA: Strong Interaction Studies with Antiprotons, e-Print: arXiv:0903.3905v1 [hep-ex] (2009).
- [2] N. Brambilla *et al.*, Eur. Phys. J. C **71** (2011) 1534.
- [3] J. Beringer *et al.*, Review of Particle Physics, Phys. Rev. **86** (2012).
- [4] S. Godfrey and S. Olsen, Ann. Rev. Nucl. Part. Sci. **58** (2008) 51. arXiv:0801.3867v1 [hep-ph] (2008).
- [5] S. Olsen, arXiv : 0909.2713v1 [hep-ex] (2009).
- [6] M.Yu. Barabanov, A.S. Vodopyanov, Fizika Elementarnyh Chastits Atomnogo Yadra Pisma, **8**, N.10, (2011) 63 / Phys. Part. Nucl. Lett. **8**, N.10, (2011) 1069.
- [7] M.Yu. Barabanov, A.S. Vodopyanov, S. L. Olsen, Yadernaya Fizica, **77**, N.1 (2014) 1 / Phys. At. Nucl., **77**, N.1 (2014) 126.
- [8] M.Yu. Barabanov, A.S. Vodopyanov, the Proceedings of the XXIV International Conference on Particle Physics and Cosmology "24 Rencontres de Blois", Blois, France, May 27 May-June 01, (2012) 99.
- [9] M.Yu. Barabanov, A.S. Vodopyanov, the Proceedings of the XV International Conference on Hadron Spectroscopy, Nara, Japan, November 4-8, in print (2013).
- [10] M.Yu. Barabanov *et al.*, Russ. Phys. J. **50** (2007) 1243.
- [11] M.Yu. Barabanov *et al.*, Hadronic J. **32**, N.2 (2009) 159.
- [12] R. Aaij *et al.*, arXiv: 1302.6269v1 [hep-ex] (2013).
- [13] M. Ablikim *et al.*, arXiv: 1303.5949v1 [hep-ex] (2013).
- [14] M. Ablikim *et al.*, arXiv: 1308.2760v1 [hep-ex] (2013).
- [15] L. Maiani, F. Piccinini, A.D. Polosa, V. Riquer, Phys. Rev. D **71** (2005) 014028.
- [16] N.V. Drenska, R. Fassini, A.D. Polosa, arXiv: 0902.2803 [hep-ph] (2009).

SUMMARY. AN ANALYTICAL REVIEW OF DSPIN-13

A.V. Efremov^{1,†} and J. Soffer^{2,‡}

¹*JINR, Dubna, Russia*

²*Temple University, Philadelphia, USA*

† *E-mail: efremov@theor.jinr.ru* ‡ *E-mail: jacques.soffer@gmail.com*

The XV Workshop on High Energy Spin Physics continued a series of meetings, the first of which was held in Dubna in 1981 on the initiative of a prominent theoretical physicist L.I. Lapidus. Since then, such meetings are taking place in Dubna each odd year. They give the opportunity to present and discuss the accumulated annual news. Another important feature is the possibility of participation for a large number of physicists from the former Soviet Union and Eastern Europe, for whom long-distance travel is difficult by financial (and in past as well by bureaucratic) reasons. In even years large International Symposia on Spin Physics have been held in various countries, including Dubna, Russia in 2012.

This meeting was characterized by a substantial attendance, with a larger than ever number of participants (125 persons) from different countries: Russia 24, USA 10, Belarus 7, Poland 6, Germany 4, Czech Republic 3, Italy 3, France 2, Slovakia 2, Iran 2, China 2 and by one person from Belgium, Bulgaria, India, Portugal, Sweden, Ukraine and South Korea. As always, a lot of physicists from JINR (53) were involved.

The reason for the increasing popularity of the meeting is, apparently, the fact that this year has brought many new experimental results and above all the discovery and determination of the quantum numbers of the Higgs boson at the Large Hadron Collider (LHC), given in talks by A. Rinkevicius (USA) and Yaquan Fang (China).

The talk by X. Artru (France) proposed the development of simple explanation of the Collins effect and the effect of handedness in the model of sequential fragmentation of quark and offered a program of implementation of the model into Monte Carlo simulation.

Classical experiments on the study of the nucleon spin structure at high energies use both scattering leptons on polarized nucleons (HERMES, JLab, COMPASS) and collisions of the polarized protons (RHIC, IHEP, JINR). The joint description of such different high-energy processes becomes possible due to the application of the fundamental theory of strong interactions, quantum chromodynamics (QCD), and its remarkable properties of factorization, local quark-hadron duality and asymptotic freedom which allow one to calculate the characteristics of a process within the framework of perturbation theory (PT). At the same time, parton distribution functions (PDF), correlations and fragmentation functions are universal and do not depend on the process. However since they are not given by the theory, they require some methods to build specific models. A number of reports at the conference were dedicated to the development and application of this type of models (P. Zavada, Czech Republic, the original covariant model of nucleon, J. Soffer, France, quantum statistical model and others). Several talks were devoted to the development of methods of experimental data processing and extraction both polarized and unpolarized PDF. It is particularly worthwhile mention the report of D. Strózik-Kotlorz (Poland) on the development of the method of truncated Mellin moments and generalized

evolution equations for these moments, and the talk of A. Sidorov (Dubna) who demonstrated the particular importance of the knowledge of quark fragmentation functions for the determination of spin dependent PDFs of sea quarks. New data of COMPASS collaboration on measurement of quark fragmentation functions into pions and kaons were presented by N. du Fresne von Hohenesche from Mainz.

The theoretical description of processes involving spin, especially dependent on internal transverse parton motion (TMD), proves to be, as always, more complicated, so that the number of these functions increases and the picture connected with them loses to a considerable degree the simplicity of a parton model with its probabilistic interpretation. One of the difficulties here is the evolution of these functions with a change in the wavelength of a tester. A possible approach to its solution was presented in the talk by I. Cherednikov (Dubna and Antwerpen).

The most widely studied to date is the helicity distribution of quarks in the nucleon g_1 . The COMPASS data (A. Ivanov, Dubna) allow one essentially specify these distributions. New measurements of the structure function g_2 of the proton and neutron (^3He) were presented by Jian-ping Chen from JLab. They show better agreement with the so-called Wandzura-Wilczek approximation relating these distributions at leading-twist. Recent experimental data are precise enough to include in their QCD analysis not only the perturbation corrections, but also the contributions of higher-twist and target mass corrections (F. Arbabifar and F. Abdolghafari, Tehran). In this case, positive polarization of strange quarks is excluded with high probability. New data on the spin distributions of sea \bar{u} and \bar{d} quarks from the W^+ and W^- bosons production processes in polarized proton-proton collision were presented by the STAR collaboration (K. Barish, BNL), in good agreement with the predictions of the statistical model (J. Soffer). The polarization of gluons, however, is consistent with the results of its direct measurements by the COMPASS and PHENIX + STAR collaborations (K. Barish – BNL, Qinghua Xu – China). Its low value seems insufficient for resolving the so-called nucleon spin crisis.

The hope to overcome the crisis lies with contributions of the orbital angular momenta of quarks and gluons which can be determined by measuring the so-called Generalized Parton Distributions (GPD). Theoretical aspects of a model GPD calculation were covered in talks of S. Goloskokov (Dubna) and S. Nair (Bombay). Different experimental aspects of GPD measurement already held (HERMES) and new ones under preparation (COMPASS) were presented by W.-D. Nowak (Freiburg) and A. Sandacz (Warsaw), respectively.

Other important spin distribution functions manifest themselves in scattering of transversely polarized particles. The processes in which the polarization of only one particle (initial or final) is known are especially interesting and complicated from the theoretical point of view (and relatively simple from the point of view of experiment – such complementarities frequently occur). Such single spin asymmetries are related to the T-odd effects, i.e. they seemingly break invariance under time reversal. Here, however, we deal with an effective breaking connected not with the true non-invariance of fundamental (in our case, strong, described by QCD) interactions under the time reversal, but with their simulations by thin effects of rescattering in the final or initial state.

The effects of single spin asymmetries have been studied by theorists (including Dubna theorists who have priority in a number of directions) for more than 20 years, but their study received a new impetus in recent years in connection with new experimental data

on the single spin asymmetry in the semi-inclusive electro-production of hadrons off longitudinally and transversely polarized targets at the facilities COMPASS (F. Bradamante, A. Bressan, Trieste), HERMES (W.-D. Nowak, Freiburg) and CLAS (Jian-ping Chen, Newport News). In particular, data from HERMES for the asymmetry of pions (the so-called "Sivers function") associated with the left-right difference in the distribution of partons in a transversely polarized hadron are described by the existing theory. However, the data for positive kaons in the region of small x about 2.5 times deviate from their predictions. New measurements of the asymmetry by the COMPASS collaboration give evidence in favor of the explanation of this difference by higher-twist contributions. Especially interesting was the comparison of SSA (transversity) in the production of a pair (π^+, π^-) from transversally polarized proton: x -dependence of the pair is almost identical to the x -dependence of π^+ (F. Bradamante, Trieste), which clearly testifies to a sequential fragmentation mechanism proposed by X. Artru. New data on the SSA pions produced in polarized proton-proton collisions at RHIC energies (200×200 GeV) were provided by the STAR collaboration (Qinghua Xu, Shandong). The collaboration confirms surprisingly large asymmetries observed previously at lower energies, which indicates their energy independence. However, new measurements at large p_T show also that asymmetry has roughly constant behavior up to $p_T = 7$ GeV/ c . This creates great difficulties for the modern theoretical understanding of these processes. New data were also obtained for the asymmetry of pairs of hadrons ($\pi^+ \pi^-$), which creates opportunities for measuring the PDF transversity (distribution of transversely polarized quarks in a transversely polarized nucleon). Similar observations were reported by the PHENIX collaboration (K. Barish, BNL). Also, PHENIX does not see much difference in the asymmetries of η^- and π^0 mesons earlier reported by STAR. The specific mechanisms of origin of these asymmetries still remain a mystery. Thus, although in general the single asymmetry is described by the existing theory, its development continues. Appearing here T-odd PDF lose key properties of universality and become "effective" depending on the processes in which they are observed. In particular, the most fundamental prediction of QCD is a change in the sign of the Sivers function in the transition from pion electroproduction to the production of Drell-Yan pairs on a transversely polarized target. This conclusion is supposed to be checked in the COMPASS experiment (O. Denisov, Turin) and at colliders RHIC, NICA (R. Akhudzyanov, Dubna) and PANDA-PAX. We also had a very interesting talk on the importance of the Drell-Yan process and an ongoing experiment to improve our knowledge of the flavor structure of the nucleon sea (Jen Chieh Peng, Illinois).

Considerable interest and discussion were called by new data of the JLab on measurement of the ratio of the electric and magnetic form factors of the proton carried out by "technique of the recoil polarization" presented at the meeting (Ch. Perdrisat – Williamsburg, V. Punjabi – Norfolk State University). Early measurements of the JLab showed that this ratio is not constant, as it has been believed for a long time, and decreases linearly with increasing momentum transfer Q^2 (the so-called "form factor crisis"). New data obtained in 2010 (experiment GEp(3) with JINR participation), point to a flattening of this ratio in $Q^2 = 6 - 8$ GeV². The proposed experiment GEp(5) will advance up to $Q^2 = 15 - 17$ GeV². The question whether this is the behavior due to the influence of radiative corrections, in particular, two-photon exchange, is still open.

Several talks were devoted to theoretical search of Z' features and other exotic at the LHC and the future International Linear Collider (ILC) of electrons and positrons

(V. Andreev, A. Tsitrinov – Gomel).

A separate section was devoted to a problem of localization of energy momentum and spin in the classical field theory. The picture arising in geometrical description in the language of external forms is close to the traditional: if electrons (and quarks) are described by an initial tensor of energy-momentum, for photons (and for gluons!) it is a tensor of Belinfante (F. Hehl, Cologne). This conclusion is very actual in the light of the discussed problem of gluon contribution to the nucleon spin being discussed. The dynamics of spin in gravitational fields and non-inertial reference systems were considered in talks by Yu. Obukhov (IBRAE, Moscow) and A. Silenko (JINR, Dubna). It was shown that particles with spin were the only tester for so-called "torsion" of space-time, and their unitary transformation allow one to pass to a quasi-classical limit and to compare evolutions of quantum spin and classical top.

Calculation of spin and orbital moment contributions on a lattice was discussed in M. Deka's (JINR, Dubna) talk. In particular, essential cancellation of spin and orbital moments of d -quarks was confirmed.

Finally, considerable attention was paid to the history of polarized studies and to further development of the projects of polarization studies at FERMILAB (A. Krisch, Ann Arbor). Plans for further research at the modified accelerator Jlab, as well as plans to create the electron-nuclear colliders in the world: eRHIC, LHeC, MEIC/EIC and especially EIC@HIAF in China were presented by Jian-ping Chen, Newport News.

The program of obtaining of polarized proton and antiproton beams from the decay of Lambda particles at the U-70 IHEP, Protvino, for spin studies at the facility SPASCHARM was presented by S. Nurushev. He stressed the importance of a comparative study of spin effects induced by particles and antiparticles.

Of particular interest were plans to create in IKP (Jülich, Germany), a unique European complex for measurement of the electric dipole moment (EDM) proton and nuclei (N. Nikolaev, Landau ITP). The fact is that the dipole moment of the fundamental particles, if it exists, violates the laws of conservation of spatial and temporal parity. Detection of EDM would indicate violation of the Standard Model and, in particular, would open up the possibility for an approach to the problem of understanding the baryon asymmetry of the Universe. The planned complex will lower the measurement limit of deuteron EDM up to 10^{-29} e-cm.

The talks related to the development of the VBLHEP accelerating complex of JINR were also presented in the program of the conference (V. Ladygin, R. Kurilkin, S. Piyadin, E. Stokovsky – Dubna). They discussed some of the new proposals for research on the basis of the upgraded Nuclotron-M. In particular, the proposal for a new experiment BM@N whose main purpose is to study the properties of dense nuclear matter especially with strange quark participation.

Special plenary and parallel sessions were devoted to the project of the collider complex NICA at JINR. The project has two phases. The first one is the construction of the collider and Multi-Purpose Detector (MPD) for studies of heavy ion collisions to be completed in 2017. The second phase includes the construction of the infrastructure for the acceleration of polarized protons and deuterons in the total energy range 12-27 GeV with luminosity $\geq 10^{32}$ cm⁻²s⁻¹ for protons (talk of A. Kovalenko, Dubna) and a detector for the collision products (SPD) reported by G. Mescheryakov, Dubna. The proposed scheme allows the complex to operate with polarized (longitudinal and transversal) or unpolarized proton

and deuteron beams. The main ideas proposed for the SPD centered around the nucleon spin structure using the Drell-Yan process of lepton pairs (R. Akhunzyanov, Dubna), direct photon (A. Gus'kov, Dubna) and the J/Ψ -mesons production. The possibility of 4π -geometry of SPD for registration of pairs e^\pm , μ^\pm and direct photons can allow one to measure all leading TMD distribution functions of quarks and antiquarks in the nucleon. Some of them were measured recently in SIDIS experiments, some are still unmeasured. One of the main purposes is to check the fundamental QCD predictions for the change of the sign of the T-odd TMD in the Drell-Yan process compared with that of SIDIS. There were also proposals for the study of spin processes in elastic pp -scattering (S. Shimanski and V. Sharov, Dubna), in particular, the so-called "Krisch-effect". Sources of polarized particles and physics of acceleration of polarized beams (Yu. Filatov, Dubna, Yu. and M. Kondratenko, Novosibirsk) were discussed. The spin community presented at the meeting supported plans for a new and unique opportunities for polarization studies at the collider JINR complex. The complex with these features will not have competition with other centers of polarization studies and the data collected will help to solve the riddle of spin effects that has not had solutions since the 70s of the last century.

Special session on the development of the so-called analytic perturbation theory (APT) by Solovtsov-Shirkov was devoted to the blessed memory of Alexander P. Bakulev. As it is known, the effective coupling constant in QCD, $\alpha_s(Q^2)$, has a non-physical pole in the area of 200-300 MeV (the so-called "Landau-Pomeranchuk pole"), which prevents the application of QCD perturbation theory in the region of small momentum transfers. Imposition of an additional condition on the analyticity of divergent series defining $\alpha_s(Q^2)$ eliminates the pole and makes the value of $\alpha_s(Q^2)$ finite up to $Q^2 = 0$. This leads to noticeable stabilization of perturbation theory and to better agreement with experiment up to the small Q^2 , e.g. up to GeV^2 for the value of Γ^{p-n} (talks of V. Khandramai, Gomel). Various aspects of the application of this theory as well as a difficult situation in QCD description of transition form factor $F_{\gamma\gamma^*\pi}$ were the subject of talks by O. Solovtsova (Gomel), A. Oganesian (ITEP, Moscow), N. Stefanis (Bochum), S. Mikhailov, O. Teryaev, A. Pimikov and D. Shirkov (JINR, Dubna) who have had a long collaboration with A.P. Bakulev.

The summary of the meeting was made in the final report by J. Soffer.

The success of the conference was due to the support by the Russian Foundation for Basic Research, International Committee for Spin Physics, Foundation "Dynasty", European Physical Society and the JINR programs for international collaboration: Heisenberg-Landau, Bogolyubov-Infeld and Blokhintsev-Votruba ones. This made possible to provide noticeable financial support to participants from Russia and other JINR Member States and developing countries. The materials of the conference, including all presented talks are available on the site <http://theor.jinr.ru/~spin/2013/>.

List of participants of DSPIN-13

Name	E-mail address	Affiliation
1. Abramov Victor	Victor.AbramovATihep.ru	IHEP Protvino Russia
2. Abdolghafari Fattaneh	fattane67ATyahoo.com	YAZD Uni Iran
3. Ahmadov Azad	ahmadovATtheor.jinr.ru	JINR Dubna Russia
4. Akhunzyanov Ruslan	axruslanATmail.ru	JINR Dubna Russia
5. Alekseev Igor	igor.alekseevATitep.ru	ITEP Moscow Russia
6. Andreev Vasili	selfdeniedATtut.by	Gomel Uni Belarus
7. Anikin Igor	anikinATtheor.jinr.ru	JINR Dubna Russia
8. Arbabifar Fatemeh	farbabifar@gmail.com	IPM Tehran Iran
9. Artru Xavier	x.artruATipnl.in2p3.fr	CNRS Lion France
10. Barabanov Mikhail	barabanovATjinr.ru	JINR Dubna Russia
11. Barish Kenneth	Kenneth.BarishATucr.edu	Uni California USA
12. Bogdanov Alexey	bogdanov411ATmail.ru	MEPhI Moscow Russia
13. Bradamante Franco	franco.bradamanteATts.infn.it	Uni of Trieste Italy
14. Bressan Andrea	Andrea.BressanATts.infn.it	Uni of Trieste Italy
15. Burinskii Alexander	burATibrae.ac.ru	NSI Moscow Russia
16. Bystritskiy Yury	bystrATtheor.jinr.ru	JINR Dubna Russia
17. Chavleishvili Michail	chavleiATyandex.ru	Uni "Dubna" Russia
18. Chen Jian-ping	jpchenATjlab.org	JLab Newport News USA
19. Cherednikov Igor	igor.cherednikovATuantwerpen.be	Uni Antwerpen Belgium
20. Chetvertkov Mikhail	match88ATmail.ru	"Interfizika" Moscow Russia
21. Chetvertkova Vera	tcheATTrambler.ru	"Interfizika" Moscow Russia
22. Christova Ekaterina	echristoATirne.bas.bg	INR&NE Sofia Bulgaria
23. Deka Mridupawan	mpdekaATtheor.jinr.ru	JINR Dubna Russia
24. Denisov Oleg	denisovATto.infn.it	INFN Torino Italy
25. du Fresne v.Hohenesche Nicolas	dufresneATcern.ch	IfK Mainz Germany
26. Efremov Anatoly	efremovATtheor.jinr.ru	JINR Dubna Russia
27. Fang Yaquan	fangyqATihep.ac.cn	IHEP Beijing China
28. Filatov Yury	yuriiiflatoffATmail.ru	JINR Dubna Russia
29. Filip Peter	Peter.FilipATSavba.sk	Inst. Phys. Slovak AS
30. Finger Miroslav	miroslav.fingerATmff.cuni.cz	JINR Dubna Russia
31. Finger Michael	michael.fingerATcern.ch	JINR Dubna Russia
32. Ganbold Gurjav	ganboldATtheor.jinr.ru	JINR Dubna Russia
33. Gerasimov Sergo	gerasbATtheor.jinr.ru	JINR Dubna Russia
34. Glagolev Victor	vglagolevATjinr.ru	JINR Dubna Russia
35. Goloskokov Sergey	goloskkvATjinr.ru	JINR Dubna Russia
36. Gorbunov Ilya	Ilya.GorbunovATcern.ch	JINR Dubna Russia
37. Guskov Alexey	avgATnusun.jinr.ru	JINR Dubna Russia
38. Hehl Friedrich	hehlATthp.Uni-Koeln.DE	Uni Cologne Germany
39. Hoskins Joshua	jrhoskATEmail.wm.edu	Coll. W&M USA
40. Ivanov Artem	artem.ivanovATcern.ch	JINR Dubna Russia
41. Ilgenfritz Ernst-Michael	ilgenfri@theor.jinr.ru	JINR Dubna Russia
42. Janek Marian	ktfATfel.uniza.sk	Zilina Uni Slovakia
43. Khandramai Viacheslav	v.khandramaiATgmail.com	Gomel Tech. Uni Belarus
44. Kistenev Edward	kistenevATbnl.gov	BNL Upton USA
45. Klopov Yaroslav	klopovATtheor.jinr.ru	JINR Dubna Russia
46. Kolganova Elena	keaATtheor.jinr.ru	JINR Dubna Russia

Name	E-mail address	Affiliation
47. Kondratenko Anatoli	kondratenkomATmail.ru	NPO "Zaryad" Russia
48. Kondratenko Mikhail	kondratenkomATmail.ru	NPO "Zaryad" Russia
49. Korchagin Nikolai	kolya.korchaginATgmail.com	JINR Dubna Russia
50. Kovalenko Aleksandr	kovalenATdubna.ru	JINR Dubna Russia
51. Krisch Alan	krischATumich.edu	Uni Michigan Ann Arbor USA
52. Kuraev Eduard	kuraevATtheor.jinr.ru	JINR Dubna Russia
53. Kurbatov Vladimir	kurbatovATjinr.ru	JINR Dubna Russia
54. Kurek Krzysztof	kurekATfuw.edu.pl	NCNR Warsaw Poland
55. Kurilkin Pavel	pkurilkinATjinr.ru	JINR Dubna Russia
56. Ladygin Vladimir	vladyginATjinr.ru	JINR Dubna Russia
57. Larin Sergey	larinATinr.ac.ru	INR Moscow Russia
58. Lednicky Richard	lednickyATfzu.cz	JINR Dubna Russia
59. Lyuboshitz Valery	Valery.LyuboshitzATjinr.ru	JINR Dubna Russia
60. Makhaldiani Nugzar	mnvATjinr.ru	JINR Dubna Russia
61. Matousek Jan	jan.matousekATcern.ch	Charles Uni Prague CR
62. Mescheryakov Gleb	mglebATsunse.jinr.ru	JINR Dubna Russia
63. Mikhailov Sergey	mikhsATtheor.jinr.ru	JINR Dubna Russia
64. Miklukho Oleg	miklukhoATpnpi.spb.ru	PNPI Gatchina Russia
65. Mochalov Vasily	Vasily.MochalovATihep.ru	IHEP Protvino Russia
66. Musulmanbekov Genis	genisATjinr.ru	JINR Dubna Russia
67. Nair Sreeraj	sreeraj_nairATIitb.ac.in	Inst. of Tech. Bombay India
68. Nerling Frank	F.NerlingATgsi.de	HIM GSI Darmstadt Germsny
69. Neznamov Vasily	neznamovATvniief.ru	FNC Sarov Russia
70. Nikolaev Nikolai	nikolaevATitp.ac.ru	Landau ITP Moscow Russia
71. Novak Oleksandr	novak-o-pATukr.net	Inst. Appl. Phys. Sumy Ukraine
72. Nowak Wolf-Dieter	wolf.dieter.nowakATgooglemail.com	Uni of Freiburg Germany
73. Nunes Ana Sofia	Ana.Sofia.NunesATcern.ch	LIP Lisboa Portugal
74. Nurushev Sandibek	Sandibek.NurushevATihep.ru	IHEP Protvino Russia
75. Nurusheva Marina	mbnurushevaATmail.ru	'Interfizika' Moscow Russia
76. Obukhov Yuri	obukhovATibrae.ac.ru	IBRAE Moscow Russia
77. Oganessian Armen	armenATitep.ru	ITEP Moscow Russia
78. Ozerianska Iryna	i.ozerianskaATgmail.com	Jagiellonian Uni Krakow Poland
79. Pankov Alexander	pankovATictp.it	Tech. Uni Gomel Belarus
80. Peng Jen-Chieh	jcpengATuiuc.edu	Uni of Illinois USA
81. Perdrisat Charles	perdrisaATjlab.org	Coll. W&M USA
82. Pesek Michael	michael.pesekATcern.ch	Charles Uni Prague CR
83. Peshekhonov Dmitry	pdvATlhe.jinr.ru	JINR Dubna Russia
84. Pimikov Alexandr	pimikovATtheor.jinr.ru	JINR Dubna Russia
85. Piskunov Nikolay	piskunovATsunhe.jinr.ru	JINR Dubna Russia
86. Piyadin Semen	piyadinATjinr.ru	JINR Dubna Russia
87. Plis Yuri	plisATnusun.jinr.ru	JINR Dubna Russia
88. Punjabi Vina	vapunjabiATnsu.edu	Norfolk Uni USA
89. Ridiger Alexey	1310ATmail.ru	'Interfizika' Moscow Russia
90. Rinkevicius Aurelijus	aurelijus.rinkeviciusATcern.ch	Uni of Florida USA
91. Rodionov Valery	vrodionovATjinr.ru	JINR Dubna Russia
92. Romanenkova Evgeniya	postATjinr.ru	JINR Dubna Russia
93. Runtso Mikhail	mfruntsoATmephi.ru	MEPhI Moscow Russia
94. Sandacz Andrzej	sandaczATfuw.edu.pl	NCNR Warsaw Poland

Name	E-mail address	Affiliation
95. Savin Igor	savinATsunse.jinr.ru	JINR Dubna Russia
96. Schoenning Stina Karin	karin.schoenningATphysics.uu.se	Uppsala Uni. Sweden
97. Selyugin Oleg	seluginATtheor.jinr.ru	JINR Dubna Russia
98. Sharov Vasily	sharovATsunhe.jinr.ru	JINR Dubna Russia
99. Shevchenko Oleg	shevATmail.cern.ch	JINR Dubna Russia
100. Shimanskiy Stepan	shimanskiyATjinr.ru	JINR Dubna Russia
101. Shirkov Dmitry	shirkovdATtheor.jinr.ru	JINR Dubna Russia
102. Sidorov Alexander	sidorovATtheor.jinr.ru	JINR Dubna Russia
103. Silenko Alexander	alsilenkoATmail.ru	INP Belarusian Uni Minsk
104. Sitnik Igor	sitnikATdubna.ru	JINR Dubna Russia
105. Soffer Jacques	jacques.sofferATgmail.com	Temple Uni Philadelphia USA
106. Solovtsova Olga	olsol07ATmail.ru	Gomel Tech. Uni Belarus
107. Stefanis Nikolaos	stefanisATtp2.ruhr-uni-bochum.de	Ruhr Uni Bochum Germany
108. Stokovsky Eugene	strokATjinr.ru	JINR Dubna Russia
109. Stozik-Kotlorz Dorota	d.stozikkotlorzATpo.opole.pl	Opole Uni Tech. Poland
110. Svirida Dmitry	Dmitry.SviridaATitep.ru	ITEP Moscow Russia
111. Szabelski Adam	adam.szabelskiATfuw.edu.pl	NCNR Warsaw Poland
112. Sznajder Pawel	pawel.sznajderATfuw.edu.pl	NCNR Warsaw Poland
113. Tanida Kiyoshi	tanidaATphya.snu.ac.kr	Seoul Uni S. Korea
114. Temerbayev Azamat	adastra.77ATmail.ru	Eurasian Uni Astana Kazakhstan
115. Teryaev Oleg	teryaevATtheor.jinr.ru	JINR Dubna Russia
116. Tsytrinov Andrei	tsytrinATrambler.ru	Gomel Tech. Uni Belarus
117. Uzikov Yuri	uzikovATnusun.jinr.ru	JINR Dubna Russia
118. Xu Qinghua	xuqhATSdu.edu.cn	Shandong Uni China
119. Yudin Ivan	yudinATjinr.ru	JINR Dubna Russia
120. Yuldashev Bekhzod	yuldashevATjinr.ru	JINR Dubna Russia
121. Zakharov Alexander	alex_f_zakharov5ATmail.ru	ITEP Moscow Russia
122. Zavada Petr	zavadaATfzu.cz	Ins. Phys. Prague CR
123. Zemlyanichkina Elena	Elena.ZemlyanichkinaATsunse.jinr.ru	JINR Dubna Russia
124. Zolin Leonid	zolinATjinr.ru	JINR Dubna Russia
125. Zykunov Vladimir	zykunovATrambler.ru	Uni of Transport Gomel Belarus

Научное издание

**XV Advanced Research Workshop on High Energy Spin Physics
(DSPIN-13)**

Proceedings of the Workshop

**XV рабочее совещание по физике спина при высоких энергиях
(DSPIN-13)**

Труды совещания

E1,2-2014-12

Ответственные за подготовку сборника *А.В. Ефремов, С.В. Голоскоков*

Сборник отпечатан методом прямого репродуцирования
с оригиналов представленных оргкомитетом.

Подписано в печать 07.04.2014.

Формат 60×90/16. Бумага офсетная. Печать офсетная.

Усл. печ. л. 26,5. Уч.-изд. л. 46,75. Тираж 180 экз. Заказ 58199.

Издательский отдел Объединенного института ядерных исследований
141980, г. Дубна, Московская обл., ул. Жолио-Кюри, 6

E-mail: publish@jinr.ru

www.jinr.ru/publish/